How to Make Small Things do Big Things: Exploring Engineered Disorder for Massively Scalable Metasurfaces and Metamaterials

Dissertation by

Parker Ryan Wray

In Partial Fulfillment of the Requirements for

the Degree of

Doctor of Philosophy

CALIFORNIA INSTITUTE OF TECHNOLOGY
Pasadena, California

2024

(Defended October 13, 2023)

Parker Ryan Wray
ORCID: 0000-0003-3384-0826

Two roads diverged in a yellow wood,
And sorry I could not travel both
And be one traveler, long I stood
And looked down one as far as I could
To where it bent in the undergrowth;

Then took the other, as just as fair,
And having perhaps the better claim,
Because it was grassy and wanted wear;
Though as for that the passing there
Had worn them really about the same,

And both that morning equally lay
In leaves no step had trodden black.
Oh, I kept the first for another day!
Yet knowing how way leads on to way,
I doubted if I should ever come back.

I shall be telling this with a sigh
Somewhere ages and ages hence:
Two roads diverged in a wood, and I—
I took the one less traveled by,
And that has made all the difference.

- Robert Frost, The Road Not Taken, 1916

ACKNOWLEDGEMENTS

Many of my colleagues have commented to me that their acknowledgements were the most delightful part of the writing process. I could not feel more opposite. I am deeply indebted to too many people. They have given me their time, their support, their trust, their love, and some, their hope. How do I acknowledge such an investment? The thought is paralyzing. I have been stuck on this section for many weeks and have recently decided that it just cannot be done. I tried… I did not succeed. The end. I have multiple published works on complicated topics in electromagnetism and quantum mechanics. Yet these pale in comparison to acknowledgements. To whom it concerns, I am sorry to say, you will not be getting the acknowledgement you deserve. To those friends, family, and colleagues, many of you will not even be on the list. It had to be this way. I'm sorry. You know who you are. You know I could not have done this without you. Below is the very abridged list.

I would like to acknowledge Professor Harry A. Atwater for shepherding me through the Ph.D. process. Professor Atwater is a true leader in every sense of the word. His accomplishments are objectively numerous. Though, this reflects only a fraction of his talent. What lies underneath is the true hallmark. It is clear to me that Harry is a primary contributor to the culture creating the quality and standards that alumni hope Caltech will aspire to. A number of Harry's colleagues could learn a lot from his tutelage. Whatever Caltech is currently paying Harry, it is likely not enough.

I am deeply indebted to Professor Richard De La Garza. Over ten years ago, he accepted me, as an undergraduate freshman, to intern in his lab. This positive and transformative experience catalyzed my pursuit of academia and likely changed my overall life trajectory. It should be noted that my resume (and upbringing) was not that of the privileged who usually got this opportunity. Many of my peers at the time did not go to college. The only thing I had to give was a fiery tenacity that enabled me to push through the nearly one hundred rejections that came before him. Ten years later, Rich is still an active mentor in my life. In many instances he has been a lifeline. I am truly very lucky and very grateful to have met him. He is also not paid enough…

I would like to acknowledge Dr. Mohammad Ali Eslamisaray for his many hours of hard work. Harry and I proposed an ambitious goal for our collaborators; to fabricate pristine crystalline semiconductors well into the Kerker regime. As the chief experimentalist, Ali was burdened with many tough tasks in our collaborative efforts. I was continually elated by his ability to meet these high demands. His willingness to peruse the highest possible quality was inspirational and his work on fabricating c-Si Kerker particles was excellent. It was refreshing to work with someone

who understood the beauty of good quality work. To my knowledge, his synthesized c-Si particles are among the best in the world.

For similar reasons, I would also like to thank Professor Uwe Kortshagen for championing our vision. Prior, quantum dots were a strong focus of our collaborators. When Harry and I initially proposed the synthesis of large particles supporting strong Kerker harmonics, we recognized this represented a radical change to the current status quo. We also believed this endeavor could open new doors for both the photonics and dusty plasma community. Realizing such particles required new synthesis techniques and there was no guarantee of success. After five years of hard work, Professor Kortshagen and Dr. Eslamisaray reported to us a success! I am very grateful to Professor Uwe Kortshagen for making our vision a reality. I hope that he is able to reap many rewards and new research directions from this effort. I also want to deeply thank Professor Kortshagen for collaborating with us in our radiative cooling efforts and managing the multi-university research initiative (MURI).

I would like to thank Elijah Paul for his hard work on the random metasurface filters project. Elijah began working with me as a freshman undergraduate during a summer research rotation. Within the first month of working with Elijah it was clear to me that he could learn fast. After a great rotation, Harry offered Elijah the ability to continue the project. This is certainly a great achievement! Elijah worked with me from his freshman to junior year. This resulted in the completion of a flagship paper for this thesis as well as becoming a semi-finalist in the Perpall competition and attaining many hours of self-directed research experience. All of these accomplishments are a testament to Elijah's hard work and acumen. I am very lucy to have mentored such an intelligent and dedicated individual. I wish Elijah the best on his future goals.

I would like to acknowledge my undergraduate recommendation letter writers, Professor Andrea Alu, Professor Ray T. Chen, and Professor Gustavo de Veciana. My Ph.D. acceptance letters to nearly every top engineering program in the nation was certainly a direct response to your advocacy and excellent teaching. In particular, I would like to thank Professor Chen for allowing me to do research in your lab for over two years. Your guidance prepared me for the Ph.D. process well beyond many of my peers.

Saving the best for last, I must thank my parents. There is no amount of writing that can summarize what you have done for me. Please accept my deepest gratitude and know that I am forever indebted to you for everything you have done. This work is a testament to your work.

ABSTRACT

This dissertation explores a collection of topics broadly related to the theory, application, and measurement of random nanoparticle systems. The underlying motivation is to explore to what extent metasurface, and metamaterial concepts could be applied at a massively large scale; by identifying emergent properties in systems that do not require careful fabrication. Emphasis is placed on exploring theoretical descriptions for systems that do not conform well to existing simpler models.

The dissertation is broken into three distinct parts:

Part I uses a rigorous theoretical description to study emergent phenomena in random metasurfaces, where multiple scattering, multipole scattering, and nearfield interactions are all non-negligible.

Chapter 1 describes the theory behind a custom-built electromagnetic program that solves the infinite many-body random particle problem of suitable systems; by estimating the moments of a particle's local field, based on properly defined Monte Carlo simulations. This quasi-analytic approach offers a powerful tool to describe multiple scattering and correlations of a wide range of particle sizes and spatial distributions; without needing to resort to potentially ill-founded ansatz, such as the Born approximation, ladder diagrams, non-self-referencing interactions, and others. Besides emphasizing rigor and interpretability, this method explicitly links optical properties to particle properties and spatial distribution, which are directly relevant parameters in synthesis and fabrication. Correspondingly, the model connects emergent behavior to actionable parameters in synthesis/fabrication.

Chapter 2 presents a case study of emergent phenomena in random metasurfaces made of Huygens (first order Kerker) particles at packing fractions up to 40% and with Percus-Yevick-like pair correlations. These films show tailorable reflection and transmission spectra in the visible regime, through designing Huygens-like scattering of the constituent particles. The films also show completely indistinguishable behavior between TE or TM polarization at all incidence angles. Silicon and gallium nitride particle films are shown as real material examples describing the two distinct Huygen's regimes: with and without the ability to support backward Huygens. The key insight to the emergent transmission-to-reflection ratio is shown to be the result of uniquely different particle-particle coupling behavior of electric and magnetic-type dipoles. The magnetic dipoles, arising from strong toroidal fields within the core of the particle, weakly couple between particles and act as sharp particle-defined resonances. On the contrary, the electric dipoles strongly couple to create a broadband continuum. The macroscopic directionality is then

understood as a Fano-like effect, controlled, in part, by the quality and spectral location of the optically induced magnetic resonances. Polarization invariance is understood to arise from the unique symmetrical scattering behavior of Huygens particles in the azimuthal plane relative to the direction of incidence. This is distinctly different from, for example, dipole scattering, that has a characteristic donut pattern. Representing the infinite particle film as an effective particle, a macroscopic Kerker condition for the random film system is derived. To the best of my knowledge, this represents the first generalization of the Kerker effect to random film systems. From this description it can be shown that randomly phased polarization conversion occurring from the multiply scattered field always has a deleterious effect on the overall Huygen's behavior. The emergent behavior seen in random films of Huygen's particles inspired the question: to what extent can similar results be seen in particle films exhibiting generalized Kerker? This question motivated the work of Chapter 3 and Chapter 4.

Chapter 3 defines a new a mathematical transform from Mie to "Kerker" harmonics, that are designed to provide an intuitive understanding of directional scattering. This transform maintains nearly all of the benefits of the Mie harmonics while simultaneously providing a unified approach to understand all forms of Kerker scattering (generalized, transverse, regular), as well as general highly directional scatting, in terms of intuitive contours in the complex plane. This represents a paradigm shift in analysis. The Kerker harmonics are decomposed into forward and backward-type, where each harmonic order has a clear notion of directionality, with clearly defined primary and side lobes. Constructive/destructive interference between same type harmonics increases/decreases the directivity in the hemisphere, accordingly. Interference between forward and backward type harmonics is weak, so that scattering in the forward/backward hemisphere is dominated by the forward/backward coefficients, respectively. In summary, interference relationships are intuitive, and this begets intuitive geometric descriptions in the complex plane. For example, the theoretically maximum directionality of any system supporting a finite number of harmonics can easily be derived from geometric arguments. In general, directional scattering/emission is represented as complex interference relations in Mie harmonics, because these harmonics represent non-directional atom-like field patterns. The Kerker harmonics offer an intuitive framework to simplify understanding of directional scattering/emission behavior, even in complex system. This transform is of particular importance when representing a random particle film as an effective particle. The effective particle representation is generally not rotationally symmetric and can have appreciable interference between many polar and azimuthal numbers. The Kerker basis makes understating emergent directionality from these systems substantially more intuitive compared to the Mie framework.

Chapter 4 uses Bayesian inverse design to show that all four canonical filters (shortpass, longpass, bandpass, and bandstop) can be made out of a single layer of randomly sized and

randomly positioned particles, based on experimentally realizable conditions. Importantly, all filters are realized using a single material, germanium. This represents a distinctly different philosophy to design filters, where multiple material compatibilities and fabrication sensitivity are no longer a primary concern. Spectral properties are entirely controlled by probability distributions. This is unlike traditional methods, which rely on deterministic phase delays and/or absorption, usually between multiple different materials. E.g., instead of optimizing the number of layers and each layer's material and thickness in a stack of thin films, you optimize a particle size distribution and the packing fraction. Furthermore, systems of this nature break the primary assumptions of traditional effective medium theories. Single harmonic order (electric dipole), non-resonant, and negligible particle-particle coupling are all invalid ansatz. The filters are designed in the infrared (4 – 9 μm), well below germanium's absorption bands, to show that filtering can be achieved truly through photon redirection and not simply resonant absorption.

Part II transitions the discussion from single layer to multilayer particle films and effective medium representations. Commonly used effective medium theorems are applied to radiative cooling applications and a new model for scale-invariant random fractal spatial distributions is presented.

Chapter 5 summarizes the theory behind constitutive relations for the mean field. I.e., effective mediums. This starts with deriving the Dyson equation and self-energy as a solution to mean field problem. It is then shown that the four most commonly known mixing rules, individual scattering, Maxwell-Garnett, Bruggeman, and Gyorffy, Korringa, and Mills are applications of the quasi-crystalline and coherent potential frameworks. These four well-known approximations are discussed as part of a larger class of mixing rules, that can be described by a single equation, as shown by Sihvola. Importantly, Sihvola introduces a unifying parameter shown to explicitly control the local field assumption. Variational bounds are then discussed to define the encompassing restrictions to the solution space. This detailed discussion on existing theorems is important to understanding Chapter 6. The remainder of this chapter focuses on the regime where Sihvola's unified equation does not apply. Generalizations of well-known theories to support multipoles are presented from the viewpoint of the extinction theorem. Though, these do not account for spatial non-locality or scattering asymmetry. Leveraging concepts discussed in part I, a new Monte Carlo-based effective medium theory is developed that accounts for both spatial non-locality and scattering asymmetry. Scattering asymmetry is resolved through the concept of an effective permeability made from toroidal currents in nonmagnetic materials. This new model is used in Chapter 7 to study a fractal film in the mean field regime.

Chapter 6 compares an entire class of bilayer effective medium models and thin film combinations of silicon dioxide and silicon nitride for radiative cooling applications. In this work, it is shown that a bilayer of nanoparticles will always produce an optimal radiative cooler

compared to a mixture of nanoparticle and thin film or purely thin film structures. Alternatively stated, as long as the particle film satisfies simple fundamental assumptions common to the four main effective medium theories, an optimal radiative cooler can be defined no matter the specifics of the local field behavior. This provides a powerful conclusion as the subtleties of local field effects are often the largest subject of debate when using an effective medium model. Optimality is defined as the ability to produce the most cooling power at a target temperature. Target temperatures between 270 – 300K in a 300K background are considered. In all cases the nanoparticle films are optimal not only in total cooling power at any temperature, but over most angles and polarization. It is show that optimality is achieved due to better impedance matching to free space as well as the ability to spectrally shift absorption resonances using the local field, to better match the atmospheric transmission window. Though both of these phenomena can be achieved in thin films, this approach is angle and polarization dependent. In contrast, the nanoparticle film is controlled through filling fraction, which is angle and polarization robust. The proposed materials are chosen because they are nearly ideal for cooling applications. Silicon dioxide is cheap, abundant, transparent in the visible and has proper phonon resonances in the infrared. Silicon nitride also has the proper spectral qualities and is already commonly used /optimized for solar panel applications. The cooling performance of multiple important works of literature at the time are compared to the proposed structures. It is shown that nanoparticle films could produce similar or better performance. The hope is that these theoretical results inspire experimental study of the cooling applications of these films and their ability to be fabricated at a large scale.

Chapter 7 presents an experimental study of a broadband, angle, and polarization invariant absorber in the visible regime; achieved through leveraging strong nanoparticle absorptions resonances and a fractal-like spatial configuration to trap incident electromagnetic fields. The Monte Carlo-based effective medium model discussed in Chapter 5 is applied to describe the underlying particle shape and local field effects giving rise to the film's measurables. It is shown that the fractal-like clusters making up the film's thickness act as effective particles with shifted and broadened absorption bands. Absorption broadening is shown to be caused by nearfield coupling of electric-type multipoles and is dependent on the number of connected or near connected neighbors.

Part III transitions the discussion to single particle and particle film measurement. This provides an outline, with case studies, on how particle film concepts discussed in this dissertation can be characterized.

Chapter 8 outlines the theory of nanoparticle measurement. Principles of causality, passivity, and superposition are discussed as a restriction of the frequency dependence of material models to Nevanlinna-Herglotz form. Common oscillator models and their application to the mean field

potential (self-energy) are then discussed. A nanoparticle film characterization protocol is outlined for films satisfying the traditional effective medium constraints discussed in part II. The characterization protocol constitutes a model fit procedure using data from angle and polarization resolved Mueller matrix measurements, in combination with normal incidence visible/infrared spectroscopy, scanning and transmission electron microscopy, X-ray photoelectron spectroscopy, profilometry, and film weight measurements. Direct measurement techniques are used to give estimates on model parameters such as filling fraction, film thickness, surface roughness, particle size and shape statistics, and material makeup such as core shell, crystallinity, elemental constituents, et cetera. These direct estimates are then used to guide an optimization procedure to match Mueller matrix and normal incidence spectroscopic data to produce a best fit effective medium and material oscillator model. This section also outlines Beer-Lambert measurements for single particle characterization.

Chapter 9 presents the characterization of, to the best of my knowledge, the first example of Huygens scattering silicon nanoparticles in the visible regime that is synthesized through a nonthermal equilibrium dusty plasma synthesis process. It is shown that optically induced magnetic resonance can be achieved in individual particles and that size parameters can span these resonances across the visible. Particles are shown to maintain strikingly high-quality spherical shape, material purity, and crystallinity. Size distributions are primarily Gaussian, with standard deviations around 1%. This synthesis result, attributed to the hard work of coauthor Ali Eslamisaray, demonstrates the feasibility to make high-quality Huygens particles in a scalable synthesis process. This provides preliminary evidence to the potential of realizing the metasurface concepts discussed in part I on a massive scale.

Chapter 10 uses the measurement protocol discussed in Chapter 8 to characterize the behavior of compact nanoparticle films made of alumina of different phases. This work highlights the applicability of commonly used effective medium methods to freestanding nanoparticle films made directly from nonthermal equilibrium dusty plasma synthesis. This experimental demonstration provides preliminary evidence to the potential of making the radiative cooling films discussed in Chapter 6 at scale.

PUBLISHED CONTENT AND CONTRIBUTIONS

Wray, P. R.; Atwater, H. A. Light–Matter Interactions in Films of Randomly Distributed Unidirectionally Scattering Dielectric Nanoparticles. *ACS Photonics* **2020**, *7* (8), 2105–2114. https://doi.org/10.1021/acsphotonics.0c00545.

P.R.W. conceived the idea, developed the theoretical framework, performed simulations, analyzed results, and wrote the manuscript.

Wray, P. R.; Atwater, H. A. Kerker Transform: Expanding Fields in a Discrete Basis of Directional Harmonics. arXiv March 7, 2023. https://doi.org/10.48550/arXiv.2303.03693.

P.R.W. conceived the idea, developed the theoretical framework, performed simulations, analyzed results, and wrote the manuscript.

Wray, P. R.; Paul, E. H.; Atwater, H. A., Optical Filters Made from Random Metasurfaces using Bayesian Optimization, *Nanophotonics* 2023. (accepted)

P.R.W. conceived the idea, developed the theoretical framework, performed simulations, analyzed results, and wrote the manuscript.

Wray, P. R.; Su, M.; Atwater, H. Design of Efficient Radiative Emission and Daytime Cooling Structures with Si3N4 and SiO2 Nanoparticle Laminate Films. *Opt. Express* **2020**. https://doi.org/10.1364/OE.408845.

P.R.W. conceived the idea, developed the theoretical framework, performed simulations, analyzed results, and wrote the manuscript.

Wray, P. R.[†]; Eslamisaray, M. A.[†]; Nelson, G. M.; Ilic, O.; Kortshagen, U. R.; Atwater, H. A. Broadband, Angle- and Polarization-Invariant Antireflective and Absorbing Films by a Scalable Synthesis of Monodisperse Silicon Nanoparticles. *ACS Appl. Mater. Interfaces* **2022**, *14* (20), 23624–23636. https://doi.org/10.1021/acsami.2c03263.

P.R.W. conceived the effective medium model, developed the theoretical framework, performed simulations, compared results to experiment, and participated in writing the manuscript.

Eslamisaray, M. A.†; **Wray, P. R.†**; Lee, Y.; Nelson, G. M.; Ilic, O.; Atwater, H. A.; Kortshagen, U. R. A Single-Step Bottom-up Approach for Synthesis of Highly Uniform Mie-Resonant Crystalline Semiconductor Particles at Visible Wavelengths. *Nano Lett.* **2023**, *23* (5), 1930–1937. https://doi.org/10.1021/acs.nanolett.2c05084.

P.R.W. performed simulations, counseled in measurement procedure, interpreted measurement results, and participated in writing the manuscript.

Li, Z.; **Wray, P. R.**; Su, M. P.; Tu, Q.; Andaraarachchi, H. P.; Jeong, Y. J.; Atwater, H. A.; Kortshagen, U. R. Aluminum Oxide Nanoparticle Films Deposited from a Nonthermal Plasma: Synthesis, Characterization, and Crystallization. *ACS Omega* **2020**, *5* (38), 24754–24761. https://doi.org/10.1021/acsomega.0c03353.

P.R.W. performed all optical/infrared measurements, developed the material and effective medium model, interpreted measurement results, and participated in writing the manuscript.

† = co-first author.

TABLE OF CONTENTS

LIST OF ILLUSTRATIONS

LIST OF TABLES

SECTION 1

RANDOM METASURFACES

Chapter 1

THEORY OF RANDOM METASURFACES

1.1 INTRODUCTION

In the mid-1970's, the stealth revolution ushered in an era of rapid technology development around controlling the behavior of electromagnetic interactions with objects. Focusing primarily on the radar range, specially designed centimeter to millimeter sized shapes were assembled to render objects obscured to probing radar signals. Later the demand of semiconductor computers brought new control over designs at the nanometer scale. With this came the implication that similar designs used in the radar range could be used to control electromagnetic interactions in the infrared to visible spectral range. Though Maxwell's equations are scale-invariant, light-matter interactions certainly are not. At such energy, field interactions probe the atomic makeup of materials, which manifest as quantized states. Correspondingly, a whole new beast is born where material properties are tailored, formed into micro/nanometer sized shapes, then patterned to provide control of electromagnetic fields in the infrared to visible. Since the patterning is often too small to be seen by eye, the structure gives the illusion of a bulk material with seemingly supernatural properties. Gaining traction in the mid-2000's, these concepts were adorned the prefix "meta," meaning "beyond" in Greek, and the field of metamaterials was formalized. Though it is arguable the prefix "engineered" is more technically correct. Applications of metamaterials are broad and can exist anywhere where current efforts are limited by the behavior of "natural" materials. In 2019, the world economic forum announced optical metamaterials the third most important technology to shape tomorrow's world. General research papers on metamaterials have grown at a rate of 17% per year from 2012 – 2022 in the Web of Science database.

Over time it was learned that patterning in a single surface layer produced easier designs, easier fabrication, and a smaller size footprint compared to volumetric patterning. Termed metasurfaces, these structures have come close to controlling nearly every aspect of light in the visible and infrared. This is certainly an impressive feat considering a thickness on the order of only 100 – 100,000 atoms. Unfortunately, the greatest strength of this technology is also its greatest weakness — nanometer control is hard (and expensive) to produce over large length scales. A meter area metasurface can require the placement of around 10^{12} – 10^{15} elements! This certainly poses a problem if desiring to use metasurfaces to coat windows, solar panels, space crafts, or fighter jets… If metasurfaces are identified that are robust to disorder, then the Achilles

heel of metasurfaces could be removed. After all, precise nanometer control is not necessary if the metasurface works the same way over a large range of fabrication error. This is the underlying premise of Chapters 1 - 6 in this dissertation, which seeks to develop a theoretical description of how random metasurfaces can be used to provide emergent optical phenomena at large scale. The idea is that if the metasurface inherently allows a tolerance for disorder, then fabrication constraints can be relaxed accordingly. The conceptual framework transitions the thinking from studying the effect of precise placement of particular particles, to studying the effect of a probability of placements and a probability of particles. The definitive characteristics underlying emergent properties are then the underlying characteristics of the film's probability distribution.

Of course, not all distributions can be reasonably fabricated. This dissertation was formed in close collaboration with five experimental research labs at four district universities all studying nanoparticle fabrication and deposition. (Prof. Kortshagen, University of Minnesota; Prof. Kushner and Prof. Violi, University of Michigan; Prof. Thimsen, Washington University at St. Louis; and Prof. Goree at the University of Iowa.) From these collaborations it was determined that nanoparticles fabricated using dusty plasma synthesis operating at non-thermodynamic equilibrium could be a scalable technology to grow spherical particles of most semiconductor, metallic, and insulating materials used in metasurfaces. Furthermore, the method has shown pristine control on particle shape, size, and material purity. It was also determined that this method could be coupled to a spray or Langmuir-Blodgett deposition scheme to produce fast metasurface coatings at scale. Though the theoretical work of this dissertation is generalizable, much of the details are formed with this fabrication pipeline in mind.

This chapter outlines the rigorous derivation underlying the theory of random metasurfaces used in this dissertation. The remainder of the chapter is composed of 8 sections and 5 supporting appendices. The first section outlines Maxwell's equations and conventions. The second and third sections derive an exact solution to the multiple scattering problem, from fundamentals, and discuss the vital role of basis expansion in understanding the framework. Having this background in mind, the fourth section formalizes the problem statement. The fifth and sixth sections discuss the role of energy conservation and power flow in understanding the behavior of random films. The seventh section extends the main results of the prior sections to the distribution of all possible random films. Finally, the eighth section outlines how to calculate the reflection, transmission, and absorption of random films as well as their statistical moments using a Monte Carlo integration scheme.

1.2 MAXWELL AND CONVENTIONS

> "From a long view of the history of mankind — seen from, say, ten thousand years from now — there can be little doubt that the most significant event of the 19th century will be judged as Maxwell's discovery of the laws of electrodynamics. The American Civil War will pale into provincial insignificance in comparison with this important scientific event of the same decade."
>
> - Richard Feynman, The Feynman Lectures on Physics, Vol. II, 1964

As discussed in the introduction, light-matter interactions can produce a wide range of changes to an impinging electromagnetic field. Correspondingly, it is necessary to define the models used to describe such interactions. In this dissertation all interactions can be understood classically through Maxwell's equations and the material constitutive relations. Materials under study are passive and isotropic. Impinging fields are assumed in the linear regime for the material and oscillating at infrared to visible frequencies. It is common that materials do not appreciably respond to magnetic fields at these frequencies, so the magnetic permeability of all materials is assumed that of vacuum, $\mu = \mu_o$. From Fourier theory, any time pulse can be composed from the knowledge of the spectra. Therefore, all electric, $\boldsymbol{\mathcal{E}}$, and magnetic, $\boldsymbol{\mathcal{H}}$, vector fields are represented in the time-harmonic form as

$$\begin{aligned} \boldsymbol{\mathcal{E}} &= \boldsymbol{\mathcal{E}}(\boldsymbol{r},\omega)e^{-i\omega t} \\ \boldsymbol{\mathcal{H}} &= \boldsymbol{\mathcal{H}}(\boldsymbol{r},\omega)e^{-i\omega t}, \end{aligned} \qquad 1.2.1$$

where $\boldsymbol{\mathcal{E}}(\boldsymbol{r},\omega) \in \mathbb{C}^3$ and $\boldsymbol{\mathcal{H}}(\boldsymbol{r},\omega) \in \mathbb{C}^3$ are complex-valued and spatial, $\boldsymbol{r} \in \mathbb{R}^3$, and frequency, ω, dependent phasors. t denotes the time and all units follow the International Standard (SI). Following the conventions of others, the time dependence will be implied for all fields and will not be written explicitly. Given the stated definitions, Maxwell's equations in time-harmonic form are,

$$\begin{aligned} \nabla \cdot \left(\varepsilon_o \varepsilon_r(\boldsymbol{r},\omega)\boldsymbol{\mathcal{E}}(\boldsymbol{r})\right) &= 0 \\ \nabla \cdot \boldsymbol{\mathcal{H}}(\boldsymbol{r}) &= 0 \\ \nabla \times \boldsymbol{\mathcal{E}}(\boldsymbol{r}) &= i\omega\mu_o \boldsymbol{\mathcal{H}}(\boldsymbol{r}) \\ \nabla \times \boldsymbol{\mathcal{H}}(\boldsymbol{r}) &= -i\omega\varepsilon_o \varepsilon_r(\boldsymbol{r},\omega)\boldsymbol{\mathcal{E}}(\boldsymbol{r}). \end{aligned} \qquad 2.2.2$$

where ε_o is the permittivity of vacuum. Unlike the magnetic field, appreciable atomic and molecular interactions do occur with the electric field at infrared to visible wavelengths. The result is a conversion of energy between fields and the material, at the relevant energy level transitions. For example, vibrational transitions in the infrared and electronic transitions in the visible. Clearly, such transitions are time-causal and, consequently, absorption coincides with dispersion as dictated by the Kramers-Kronig relations. In the context of Maxwell's equations, these atomic-scale interactions are modeled macroscopically in time-harmonic form as a complex relative permittivity, $\varepsilon_r(\boldsymbol{r},\omega) = \Re[\varepsilon_r] + i\Im[\varepsilon_r]$, where the Fraktur $\Re$ and $\Im$ denote the real and imaginary part, respectively. At the atomic scale, the classical model for the relative permittivity is understood as an excitation of "free" and/or locally "bound" charges responding to the field excitation. Away from material transitions ε_r becomes approximately constant. In particular, the sum rules dictate that at frequencies above the material's highest energy transition the permittivity is constant. The physical interpretation is that the response to such a short-time impulse constitutes a tiny perturbation where collective effects are negligible. Though, the response is not instantaneous due to the inertia of charges.

With regard to computational considerations, both ε_o and μ_o are a floating-point headache. Without loss in generality, all electromagnetic fields will be scaled as

$$\begin{aligned}\boldsymbol{\mathcal{E}} &\rightarrow \boldsymbol{E}/\sqrt{\varepsilon_o} \\ \boldsymbol{\mathcal{H}} &\rightarrow \boldsymbol{H}/\sqrt{\mu_o}.\end{aligned} \tag{1.2.3}$$

Under this transform, Maxwell's equations can be rewritten as

$$\nabla \cdot \left(\sqrt{\varepsilon_o}\varepsilon_r(\boldsymbol{r},\omega)\boldsymbol{E}(\boldsymbol{r})\right) = 0 \tag{1.2.4}$$

$$\nabla \cdot \boldsymbol{H}(\boldsymbol{r}) = 0 \tag{1.2.5}$$

$$\nabla \times \boldsymbol{E}(\boldsymbol{r}) = ik_o\boldsymbol{H}(\boldsymbol{r}) \tag{1.2.6}$$

$$\nabla \times \boldsymbol{H}(\boldsymbol{r}) = -ik_o\varepsilon_r(\boldsymbol{r},\omega)\boldsymbol{E}(\boldsymbol{r}) = \boldsymbol{J}(\boldsymbol{r}). \tag{1.2.7}$$

where $k_o = \omega\sqrt{\varepsilon_o\mu_o}$ is the wavenumber in vacuum. This dissertation is not concerned with electrostatics, so the domain of interest is divergence free, $\varepsilon_r(\boldsymbol{r},\omega) \neq 0$. The coordinate system is defined in figure 1.2.1.

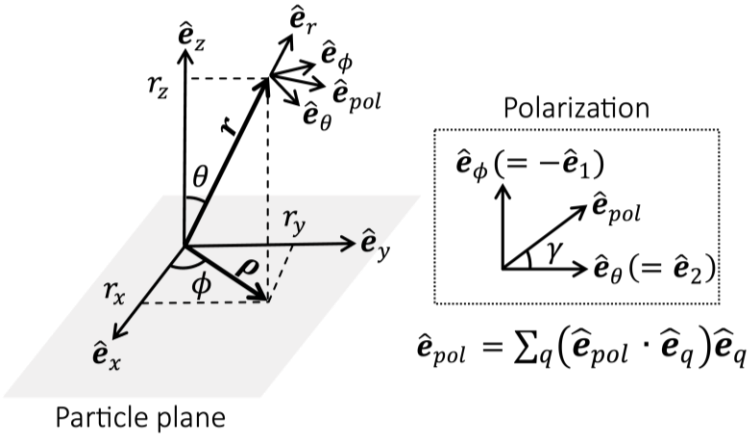

Figure 1.2.1. Coordinate system. $\{\hat{\boldsymbol{e}}_x, \hat{\boldsymbol{e}}_y, \hat{\boldsymbol{e}}_z\}$ and $\{\hat{\boldsymbol{e}}_r, \hat{\boldsymbol{e}}_\phi, \hat{\boldsymbol{e}}_\theta\}$ are the standard basis in Cartesian and polar coordinates, respectively. Spatial vectors are denoted in bold.

1.3 LIPPMANN-SCHWINGER AND FOLDY-LAX

The relative permittivity of an inhomogeneous media can be written as $\varepsilon_r(\boldsymbol{r},\omega) = \epsilon + \delta\varepsilon(\boldsymbol{r},\omega) \in \mathbb{C}$, where $\epsilon \in \mathbb{R}$ is the relative permittivity of the lossless background (so that the far field can be defined) and $\delta\varepsilon(\boldsymbol{r}) \in \mathbb{C}$ is the fluctuation as a result of material changes within the volume. The support of $\delta\varepsilon(\boldsymbol{r})$ is the interior volume of the inhomogeneities, $V_{int} \in \mathbb{R}^3$. For such a system, Maxwell's curl equations in time-harmonic form are

$$\begin{aligned} \nabla \times \boldsymbol{E}(\boldsymbol{r}) &= ik_o \boldsymbol{H}(\boldsymbol{r}) \\ \nabla \times \boldsymbol{H}(\boldsymbol{r}) &= -ik_o \epsilon \boldsymbol{E}(\boldsymbol{r}) + \delta\boldsymbol{J}(\boldsymbol{r}) + \boldsymbol{J}_s(\boldsymbol{r}) \end{aligned} \qquad 1.3.1$$

where Ampere's law makes clear that the permittivity fluctuations cause changes in passive current densities, $\delta\boldsymbol{J}(\boldsymbol{r}) = -ik_o \delta\varepsilon(\boldsymbol{r})\boldsymbol{E} \in \mathbb{C}^3$, whose oscillations emanate scattered fields. The system is excited by an externally driven source current density, $\boldsymbol{J}_s$.Taking the curl of Faraday's law and substituting Ampere's law gives the inhomogeneous wave equation is,

$$\nabla \times \nabla \times \boldsymbol{E}(\boldsymbol{r}) - k^2 \boldsymbol{E}(\boldsymbol{r}) = U(\boldsymbol{r})\boldsymbol{E}(\boldsymbol{r}) + ik_o \boldsymbol{J}_s(\boldsymbol{r}), \qquad 1.3.2$$

where $k^2 = k_o^2 \epsilon$ is the magnitude of the wavenumber in the background media and $U(\boldsymbol{r}) = k^2(\eta_r^2(\boldsymbol{r}) - 1)$ is the fluctuation potential, defined from the relative refractive index, $\eta_r(\boldsymbol{r}) = \sqrt{\varepsilon_r(\boldsymbol{r})/\epsilon}$. The transition to refractive index is done since experimental data of the refractive index is more likely to be reported in literature. Again, all materials are assumed to have a magnetic permeability of free space. The solution to equation 1.3.2 is

$$\boldsymbol{E}(\boldsymbol{r}) = \boldsymbol{E}^{inc}(\boldsymbol{r}) + \left(\bar{\bar{\boldsymbol{I}}} + \frac{1}{k^2}\nabla \otimes \nabla\right) \cdot \int_{V_{int}} d^3\boldsymbol{r}'\, G_o(\boldsymbol{r},\boldsymbol{r}')U(\boldsymbol{r})\boldsymbol{E}(\boldsymbol{r}'), \qquad 1.3.3$$

where $\boldsymbol{E}^{inc}$ is the incident external field excitation onto the inhomogeneous space, $\bar{\bar{\boldsymbol{I}}}$ is the identity dyad, $\otimes$ is the dyadic product, and $G_o(\boldsymbol{r},\boldsymbol{r}') = e^{ik|\boldsymbol{r}-\boldsymbol{r}'|}/4\pi|\boldsymbol{r}-\boldsymbol{r}'|$ is the solution to the scalar Green wave equation with $\delta\varepsilon = 0$. The corresponding dyadic Green's function for the electric field is $\bar{\bar{\boldsymbol{G}}}_{eo}(\boldsymbol{r},\boldsymbol{r}') = \left(\bar{\bar{\boldsymbol{I}}} + \frac{1}{k^2}\nabla \otimes \nabla\right) G_o(\boldsymbol{r},\boldsymbol{r}')$. The second term of the total field is the total scattered field, $\boldsymbol{E}^{sca}(\boldsymbol{r}) = \boldsymbol{E}(\boldsymbol{r}) - \boldsymbol{E}^{inc}(\boldsymbol{r})$, and is a result of the collective excitation of all charges in the inhomogeneous media responding to the incident excitation.

Correspondingly, the scattered field anywhere in the background, $\mathbb{R}^3 - V_{int}$, can be written explicitly in terms of the incident field as

$$\boldsymbol{E}^{sca}(\boldsymbol{r}) = \int_{V_{int}} d^3\boldsymbol{r}'\, \overline{\overline{\boldsymbol{G}}}_{eo}(\boldsymbol{r},\boldsymbol{r}') \cdot \int_{V_{int}} d^3\boldsymbol{r}''\, \overline{\overline{\boldsymbol{T}}}(\boldsymbol{r}',\boldsymbol{r}'') \cdot \boldsymbol{E}^{inc}(\boldsymbol{r}''), \tag{1.3.4}$$

where $\overline{\overline{\boldsymbol{T}}}$ is the incident-to-scattering transition dyad defined by the Lippmann-Schwinger equation,

$$\overline{\overline{\boldsymbol{T}}}(\boldsymbol{r},\boldsymbol{r}') = U(\boldsymbol{r})\delta(\boldsymbol{r}-\boldsymbol{r}')\overline{\overline{\boldsymbol{I}}} + U(\boldsymbol{r}) \int_{V_{int}} d^3\boldsymbol{r}''\, \overline{\overline{\boldsymbol{G}}}_{eo}(\boldsymbol{r},\boldsymbol{r}'') \cdot \overline{\overline{\boldsymbol{T}}}(\boldsymbol{r}'',\boldsymbol{r}'), \tag{1.3.5}$$

where $\boldsymbol{r},\boldsymbol{r}' \in V_{int}$.

For a layer consisting of a mixture of N $(\to \infty)$ particles the inhomogeneity in V_{int} is defined by a collection of individually finite, countable, and non-overlapping hard particles, where each particle is defined by a shape, s, relative refractive index, η_r, and central position in the $x-y$ plane, $\boldsymbol{\rho}$. Therefore, V_{int} can be constrained to extending throughout the $x-y$ plane centered at $z = 0$ and having a finite z-thickness, h, defined by the largest particle height. Furthermore,

$$U(\boldsymbol{r}) = \sum_a^N \left(U_a(\boldsymbol{r}) = \begin{cases} k^2\left(\eta_{r,a}^2(\boldsymbol{r}) - 1\right) & \boldsymbol{r} \in V_a \\ 0 & \boldsymbol{r} \notin V_a \end{cases} \right), \tag{1.3.6}$$

where $V_{int} = \bigcup_a^N V_a$ and V_a is the volume occupied by particle a. Such a system is shown in figure 1.3.1.

Any position inside a particle can be written as $\boldsymbol{r} = \boldsymbol{\rho} + \boldsymbol{s} \in V_a$, where $\boldsymbol{s}$ spans the particle's shape with respect to the particle's center. Correspondingly, $\eta_r(\boldsymbol{\rho} + \boldsymbol{s})$ completely describes the particle. Given the partitioned potential, the total field in the background domain is defined by the Foldy-Lax relations,

$$\boldsymbol{E}(\boldsymbol{r}) = \boldsymbol{E}^{inc}(\boldsymbol{r}) + \sum_a^N \int_{V_a} d^3\boldsymbol{r}'\, \overline{\overline{\boldsymbol{G}}}_{eo}(\boldsymbol{r},\boldsymbol{r}') \cdot \int_{V_a} d^3\boldsymbol{r}''\, \overline{\overline{\boldsymbol{T}}}_a(\boldsymbol{r}',\boldsymbol{r}'') \cdot \boldsymbol{E}_a^{loc}(\boldsymbol{r}''), \tag{1.3.7}$$

where

$$\boldsymbol{E}_a^{loc}(\boldsymbol{r} \in V_a) = \boldsymbol{E}^{inc}(\boldsymbol{r}) + \sum_{b\neq a}^{N} \int_{V_b} d^3\boldsymbol{r}'\, \overline{\overline{\boldsymbol{G}}}_{eo}(\boldsymbol{r},\boldsymbol{r}') \cdot \int_{V_b} d^3\boldsymbol{r}''\, \overline{\overline{\boldsymbol{T}}}_b(\boldsymbol{r}',\boldsymbol{r}'') \cdot \boldsymbol{E}_b^{loc}(\boldsymbol{r}''), \quad 1.3.8$$

and the transition operator, $\overline{\overline{\boldsymbol{T}}}_j$, is found by replacing $U(\boldsymbol{r}) \rightarrow U_j(\boldsymbol{r})$ in the Lippmann-Schwinger procedure. The Foldy-Lax paradigm introduces the concept of multiple scattering and a local field. The Lippmann-Schwinger procedure now defines how a particle will scatter the local field. Equation 1.3.8 defines the local electromagnetic field felt by a particle as the superposition from all other fields besides itself at the location of itself.

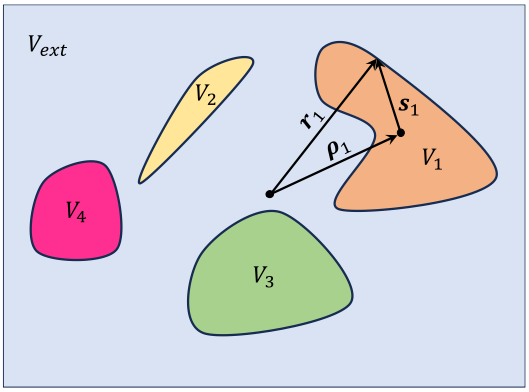

Figure 1.3.1. Example of a countable set of piecewise homogeneous materials embedded in an external homogeneous host material.

The Foldy-Lax and Lippmann-Schwinger equations can be written in operator form as

$$\begin{aligned} \boldsymbol{E} &= \boldsymbol{E}^{inc} + \sum_a^N \mathbb{G}_{eo}\mathbb{T}_a\boldsymbol{E}_a^{loc} \\ \boldsymbol{E}_a^{loc} &= \boldsymbol{E}^{inc} + \sum_{b\neq a}^N \mathbb{G}_{eo}\mathbb{T}_b\boldsymbol{E}_b^{loc} \\ \mathbb{T}_j &= U_j + U_j\mathbb{G}_{eo}\mathbb{T}_j \end{aligned} \quad 1.3.9$$

where $\mathbb{T}_j$ is the transition operator for particle j and $\mathbb{G}_{eo}$ is the source free Green's propagator. In operator notation, the form of the Green's propagator (e.g., electric or magnetic) is implied by the context. This procedure defines a set of coupled linear equations which can be used to solve for the unknown scattered fields given a known incident excitation. Under the concept of multiple scattering, the local field can be explicitly related to the incident field through an infinite series of all multiple scattering terms,

$$\boldsymbol{E}_a^{loc} = (1 + \sum_{b\neq a}^{N} \mathbb{G}_{eo}\mathbb{T}_b + \sum_{\substack{c\neq b \\ b\neq a}}^{N} \mathbb{G}_{eo}\mathbb{T}_b\mathbb{G}_{eo}\mathbb{T}_c + \sum_{\substack{d\neq c \\ c\neq b \\ b\neq a}}^{N} \mathbb{G}_{eo}\mathbb{T}_b\mathbb{G}_{eo}\mathbb{T}_c\mathbb{G}_{eo}\mathbb{T}_d \ldots)\boldsymbol{E}^{inc}. \quad 1.3.10$$

Substituting this expression into the total field gives

$$\boldsymbol{E} = (1 + \sum_{a}^{N} \mathbb{G}_{eo}\mathbb{T}_a + \sum_{\substack{b\neq a \\ a}}^{N} \mathbb{G}_{eo}\mathbb{T}_a\mathbb{G}_{eo}\mathbb{T}_b + \sum_{\substack{c\neq b \\ b\neq a \\ a}}^{N} \mathbb{G}_{eo}\mathbb{T}_a\mathbb{G}_{eo}\mathbb{T}_b\mathbb{G}_{eo}\mathbb{T}_c \ldots)\boldsymbol{E}^{inc}. \quad 1.3.11$$

Equations 1.3.10 and 1.3.11 introduce the concept of "order of scattering," which play an important role in random scattering and effective medium theories. The first summation in equation 1.3.11 is the scattered field from all particles as if no particles interacted. The next terms are the field contribution from all double scattering paths, then triple scattering paths, and so forth. Paths above double can return to a prior particle and this distinction is meaningful. The concept of order of scattering can be understood in the context of Feynman diagrams, as shown in as in figure 1.3.2.

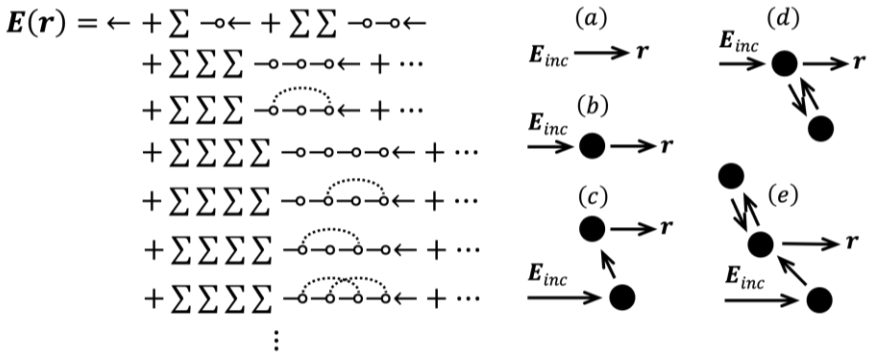

Figure 1.3.2. Graphical description of order of scattering. (Left) Diagrammatic expansion of order of scattering terms. ← represents the incident field, ∘ is the transition operator, − is the propagator, and ←⋯ indicates that the transition operator is owned by the same particle, representing a return loop. (Right) Pictorial examples of order of scattering terms. (a) Incident field contribution. (b) Single scattering. (c) Double scattering. (d) Triple scattering with a self-reference. (e) Quadruple scattering with a single self-reference.

The Foldy-Lax and Lippmann-Schwinger equations defines a self-consistent system of equations that gives an exact solution to the multiple scattering problem. This result offers a powerful framework for analysis as it distinctly elucidates how particle type (through $\mathbb{T}$), position (through $\mathbb{G}$), and the incident field gives rise to emergent scattering phenomena.

1.4 STRATTON-CHU AND MIE

> "The formulation of a problem is often more essential than its solution, which may be merely a matter of mathematical or experimental skill."
>
> - Albert Einstein & Léopold Infeld, Evolution of Physics, 1938

In the generalized form the volume integral Foldy-Lax and Lippmann-Schwinger equations represent a daunting numerical task, for which approaches such as the coupled-dipole method, the dipole-dipole approximation, the method of moments, and others have been used to solve[1]. If the space is piecewise homogeneous, then the volume integrals can be replaced by surface integrals at the interface boundary, ∂V, in all source free domains. Fields in these regions can be described using the Stratton-Chu representation,

$$\pm \boldsymbol{E}(\boldsymbol{r} \in V - \partial V) = \nabla \times \oint_{\partial V} \boldsymbol{d}^2\boldsymbol{r}'\, \boldsymbol{j_m}(\boldsymbol{r}') G_o(\boldsymbol{r}, \boldsymbol{r}') + \frac{i}{k_o \varepsilon_r} \nabla \times \nabla \times \oint_{\partial V} \boldsymbol{d}^2\boldsymbol{r}'\, \boldsymbol{j_e}(\boldsymbol{r}') G_o(\boldsymbol{r}, \boldsymbol{r}'), \quad 1.4.1(a)$$

$$\pm \boldsymbol{H}(\boldsymbol{r} \in V - \partial V) = \nabla \times \oint_{\partial V} \boldsymbol{d}^2\boldsymbol{r}'\, \boldsymbol{j_e}(\boldsymbol{r}') G_o(\boldsymbol{r}, \boldsymbol{r}') - \frac{i}{k_o \mu_r} \nabla \times \nabla \times \oint_{\partial V} \boldsymbol{d}^2\boldsymbol{r}'\, \boldsymbol{j_m}(\boldsymbol{r}') G_o(\boldsymbol{r}, \boldsymbol{r}') \quad 1.4.1(b)$$

where $\boldsymbol{j_e} = \hat{\boldsymbol{n}} \times \boldsymbol{H}$ and $\boldsymbol{j_m} = \hat{\boldsymbol{n}} \times \boldsymbol{E}$ are the electric and magnetic surface currents on ∂V, from the surface equivalence principle. The boundary surface, ∂V, of the volume, V, is approached from the inside the volume such that all values are retrieved from inside that domain and all derived fields are valid only inside the domain. The $\pm$ sign is chosen depending on if the outward pointing surface normal is pointing inside $(+)$ or outside $(-)$ the domain V. Equation 1.4.1 states that for any isotropic and homogeneous media, knowledge of the equivalent surface currents on a closed surface in the domain is sufficient to know the fields anywhere in the domain. This is a direct result of Green's vector theorem.

The continuity conditions of electromagnetic fields in a source free medium,

$$\hat{\boldsymbol{n}} \times \begin{matrix}(\boldsymbol{E}_1 - \boldsymbol{E}_2) \\ (\boldsymbol{H}_1 - \boldsymbol{H}_2)\end{matrix} = \boldsymbol{0} \quad 1.4.2$$

$$\hat{\boldsymbol{n}} \cdot \begin{matrix}(\varepsilon_1 \boldsymbol{E}_1 - \varepsilon_2 \boldsymbol{E}_2) \\ (\mu_1 \boldsymbol{H}_1 - \mu_2 \boldsymbol{H}_2)\end{matrix} = 0, \quad 1.4.2$$

demand that the surface currents and the flux are conserved on the surface between two domains, V_1, V_2. This provides the link between fields in two dissimilar domains and the problem is now reduced to a set of surface integral equations connecting the boundary currents. Though the dimensionality of the problem is reduced, it can still be quite expensive to calculate surfaces in three dimensions. Furthermore, developing physical insight into the behavior of the system is not necessarily straightforward given complex current/field patterns.

To mitigate further the computational complexity as well as to provide potential useful physical insight, it would be nice to be able to project the surface currents at every boundary onto a suitable basis of vector functions. The surface integral problem would then be mapped to a matrix problem connecting basis coefficients between domains. The choice of basis in each sub-domain serves two purposes. First, it intends to reduce the computational burden of the problem. The hope is that the dimension and computational complexity of the coefficient equations are substantially smaller compared to the dimension necessary to solve the surface integration directly, to a similar level of accuracy. Therefore, the goal is to identify a basis that accurately represents the surface fields using the minimal number of elements. From this point of view, the basis is an intelligently designed weight function that uses a priori knowledge of the behavior of the fields to strongly compress the field representation. The second goal is that the basis provides meaningful insight for humans to understand the interaction dynamics. Since the basis ascribes a set of priori patterns to the field, complicated field patterns are now decomposed into a superposition of "simpler" patterns that may have a well-described physical insight. Furthermore, the representation of the transition, propagation, and basis operators may be more digestible. Note that a sparse basis is not necessarily an insightful one, as is commonly found in machine learning. Clearly the sparsest basis is a single coefficient would mean the basis vector is the solution to the problem. This is not insightful at all!

Unfortunately, it is not straightforward to define a vector basis that accurately, sparsely, and meaningfully represents surface currents for an arbitrary surface. Fortunately, under the correct conditions, the physical boundary of an object can be electromagnetically "extended" into a shape where such a basis can be defined. This brings to the analysis the notion of an effective particle, whose input-output relation is identical to the actual shape anywhere outside of the effective shape's domain. This is best understood by returning to the abstract operator notation of Foldy-Lax. Ultimately, $\mathbb{T}$ needs only to map input excitation fields to output scattered fields within the domain of interest. For example, if each oddly shaped particle can be isolated by a circumscribing sphere where no spheres intersect, then the problem can be transformed into a scattering problem of spheres, which has an excellent expansion using the Mie harmonics. All field values outside of a sphere would be exactly the same as that solved by the initial problem.

In this way, the shape complexity is abstracted into $\mathbb{T}$. Traditionally, this procedure is known as the extended boundary condition method, and the derivation by Waterman shows that the method is quite general[2,3]. Other authors have applied it to particles of non-convex shape, layered particles, chiral media, and scattering by more general composites[4–7], though any numerical method capable of solving Maxwell's equations can be used to construct $\mathbb{T}$. Once $\mathbb{T}$ is known, it can be used to solve any coupling problem satisfying the non-intersection condition of the effective particle. (Strictly speaking, this condition is actually overly stringent. Extended boundaries can overlap, but this requires more effort in defining the input-output relations[8,9].) An example of inhomogeneities satisfying the non-overlapping sphere condition is shown in figure 1.4.1.

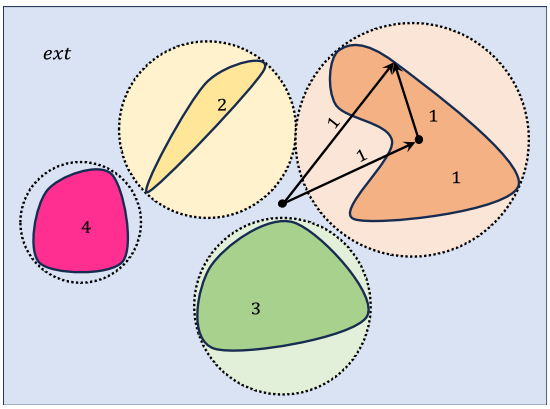

Figure 1.4.1. Example of a countable set of inhomogeneities eligible for domain extension to a minimally circumscribing ball.

For suitable scattering systems a proper basis projection of equivalent surface currents can substantially reduce the computational complexity of the fundamental interaction equations. Furthermore, such an expansion can provide a digestible framework for analysis if the basis has a properly defined physical interpretation.

Fields in the Mie Basis

The topics of this dissertation have been formed in connection with advances in the synthesis of spherical particles, using the nonthermal dusty plasma synthesis method. Correspondingly, the inhomogeneities of interest are random distributions of spheres. Luckily this shape can be exactly projected onto the basis of Mie vector harmonics, without the need for domain extension. Furthermore, the properties of the basis with respect to distance, $|\boldsymbol{r}|$, polar, $\theta \in [0,\pi]$, and azimuthal, $\phi \in [0,2\pi)$, angle offer multiple convenient relations. For this reason, this dissertation adopts the ansatz that the Mie vector harmonics represent a sparse and conceptually meaningful basis to describe the scattered fields in question. Outside of the particle's domain, the Mie harmonics are related to the particle's surface currents through

$$\begin{aligned}&\nabla \times \left(\boldsymbol{v}(\boldsymbol{r}')G_o(k,\boldsymbol{r},\boldsymbol{r}')\right)\\&= \frac{ik^2}{\pi}\sum_n \sum_{m=-n}^{n} \begin{pmatrix} \left(\boldsymbol{v}(\boldsymbol{r}')\cdot \mathrm{Rg}\, \boldsymbol{M}_{n,-m}(k\boldsymbol{r}')\right)\boldsymbol{N}_{n,m}(k\boldsymbol{r}) \\ +\left(\boldsymbol{v}(\boldsymbol{r}')\cdot \mathrm{Rg}\, \boldsymbol{N}_{n,-m}(k\boldsymbol{r}')\right)\boldsymbol{M}_{n,m}(k\boldsymbol{r}) \end{pmatrix} \quad \boldsymbol{r} > \boldsymbol{r}'\end{aligned} \tag{1.4.3}$$

and

$$\begin{aligned}&\nabla \times \nabla \times \left(\boldsymbol{v}(\boldsymbol{r}')G_o(k,\boldsymbol{r},\boldsymbol{r}')\right)\\&= \frac{ik^3}{\pi}\sum_n \sum_{m=-n}^{n} \begin{pmatrix} \left(\boldsymbol{v}(\boldsymbol{r}')\cdot \mathrm{Rg}\, \boldsymbol{M}_{n,-m}(k\boldsymbol{r}')\right)\boldsymbol{M}_{n,m}(k\boldsymbol{r}) \\ +\left(\boldsymbol{v}(\boldsymbol{r}')\cdot \mathrm{Rg}\, \boldsymbol{N}_{n,-m}(k\boldsymbol{r}')\right)\boldsymbol{N}_{n,m}(k\boldsymbol{r}) \end{pmatrix} \quad \boldsymbol{r} > \boldsymbol{r}'\end{aligned} \tag{1.4.4}$$

Here $\boldsymbol{M}$, $\boldsymbol{N}$ and $\mathrm{Rg}\boldsymbol{M}$, $\mathrm{Rg}\boldsymbol{N}$ are the outgoing and regular magnetic and electric-type Mie harmonics, respectively. The harmonics are defined by their integer polar, $n \in [1,\infty)$, and azimuthal, $m \in [-n,n]$, quantum numbers. Further detail can be found in section 1.10, appendix A. $\boldsymbol{v}$ is an arbitrary surface current. Applying equations 1.4.3 and 1.4.4 to equation 1.4.1 gives the scattered field as

$$\begin{aligned}\boldsymbol{E}_{sca,a}(\boldsymbol{r}-\boldsymbol{\rho}_a) &= \sum_n \sum_{m=-n}^{n} b_{n,m}\boldsymbol{M}_{n,m}(\boldsymbol{r}-\boldsymbol{\rho}_a) + a_{n,m}\boldsymbol{N}_{n,m}(\boldsymbol{r}-\boldsymbol{\rho}_a)\\ \boldsymbol{H}_{sca,a}(\boldsymbol{r}-\boldsymbol{\rho}_a) &= -iY\sum_n \sum_{m=-n}^{n} b_{n,m}\boldsymbol{N}_{n,m}(\boldsymbol{r}-\boldsymbol{\rho}_a) + a_{n,m}\boldsymbol{M}_{n,m}(\boldsymbol{r}-\boldsymbol{\rho}_a),\end{aligned} \tag{1.4.5}$$

where $Y = \sqrt{\varepsilon/\mu}$ is the admittance of the media and the coefficients encapsulate the current distribution on the surface through their projection onto the regular harmonics,

$$\begin{matrix} a_{nm} \\ b_{nm} \end{matrix} = \frac{ik^2}{\pi} \oint_{\partial V_a} \boldsymbol{d}^2\boldsymbol{s}' \left(\boldsymbol{j_m}(\boldsymbol{s}') \cdot \begin{matrix} \mathrm{Rg}\boldsymbol{M}_{n,-m}(k\boldsymbol{s}') \\ \mathrm{Rg}\boldsymbol{N}_{n,-m}(k\boldsymbol{s}') \end{matrix} + \frac{i}{Y} \boldsymbol{j_e}(\boldsymbol{s}') \cdot \begin{matrix} \mathrm{Rg}\boldsymbol{N}_{n,-m}(k\boldsymbol{s}') \\ \mathrm{Rg}\boldsymbol{M}_{n,-m}(k\boldsymbol{s}') \end{matrix} \right). \quad 1.4.6$$

Conceptually this expansion transforms a particle (closed inhomogeneity) into an effective "atom" positioned at the center of the particle. The state of this fictitious atom is described by electric, $\boldsymbol{N}$, and magnetic-type, $\boldsymbol{M}$, "orbitals." Type is defined by the form of the field distribution emitted by $\boldsymbol{N}$ and $\boldsymbol{M}$, which mimic the field patterns seen from electric and magnetic multipoles. The oscillation strength and phase of these multipoles is determined by the coefficients, which are superpositions of electric and magnetic equivalent surface currents giving rise to the multipole-like behavior. The local field impinging on a particle is then viewed as driving the atom and the resulting scattered field is the field that emanates from the atom's oscillations. To connect with the operator framework, the Mie harmonic expansion will usually be written in the matrix notation,

$$\boldsymbol{\Psi} c = [\boldsymbol{N} \quad \boldsymbol{M}] \begin{bmatrix} c^E \\ c^M \end{bmatrix}, \quad 1.4.7$$

where

$$\begin{aligned} \boldsymbol{N} c^E &= [\boldsymbol{N}_{1,-1} \quad \boldsymbol{N}_{1,0} \quad \dots \quad \boldsymbol{N}_{2,-2} \quad \dots][a_{1,-1} \quad a_{1,0} \quad \dots \quad a_{2,-2} \quad \dots]^T \\ \boldsymbol{M} c^M &= [\boldsymbol{M}_{1,-1} \quad \boldsymbol{M}_{1,0} \quad \dots \quad \boldsymbol{M}_{2,-2} \quad \dots][b_{1,-1} \quad b_{1,0} \quad \dots \quad b_{2,-2} \quad \dots]^T. \end{aligned} \quad 1.4.8$$

As a shorthand, $l = \{t, n, m\}$ will represent an index for any unique combination of harmonic type, $t = \{N, M\}$, and quantum numbers. The size of all combinations is L. Correspondingly, $\boldsymbol{\Psi} \in \mathbb{C}^{3\times \mathrm{L}}$ and $c \in \mathbb{C}^L$.

The transition operator, which relates the surface currents to the exciting local field, can now be viewed as defining how the "orbitals" of the effective atom arise from a given excitation. As discussed, this operator is defined by the shape and material properties of the particle. From the multipole framework $\mathbb{T}$ can be viewed as defining the "spring constants." When considering a Mie harmonic expansion with origin at the center of the particle, then the transition matrix of a homogeneous and isotropic sphere is a diagonal form, $\mathbb{T}^{t,t'}_{n,m,n',m'} = \delta_{n,n'}\delta_{m,m'}\delta_{t,t'}T^t_{nm} \in \mathbb{C}^{\mathrm{L}\times\mathrm{L}}$, with coefficients, T^t_{nm}, given directly by Mie theory,

$$T_{nm}^{E} = \frac{j_n(kR)d_{k_sR}\left(k_sRj_n(k_sR)\right) - j_n(k_sR)d_{kR}\left(kRj_n(kR)\right)}{j_n(k_sR)d_{kR}\left(kRh_n(kR)\right) - h_n(kR)d_{k_sR}\left(k_sRj_n(k_sR)\right)} \quad 1.4.9(a)$$

$$T_{nm}^{M} = \frac{k^2 j_n(kR)d_{k_sR}\left(k_sRj_n(k_sR)\right) - k_s^2 j_n(k_sR)d_{kR}\left(kRj_n(kR)\right)}{k_s^2 j_n(k_sR)d_{kR}\left(kRh_n(kR)\right) - k^2 h_n(kR)d_{k_sR}\left(k_sRj_n(k_sR)\right)} \quad 1.4.9(b)$$

where R is the sphere's radius, k_s is the wavenumber in the sphere, j_n and y_n are the spherical Bessel functions of the first and second kind, respectively, and $h_n = j_n + iy_n$ is the spherical Hankel function of the first kind.

Under the Mie basis, the electromagnetic field distribution in any particle that can be represented as an effective atom centered about the particle as

$$\boldsymbol{E}_{inc,a}(\boldsymbol{r}) = \mathrm{Rg}\,\boldsymbol{\Psi}(\boldsymbol{r} - \boldsymbol{r}_a)c_{inc} \quad 1.4.10(a)$$

$$\boldsymbol{E}_{loc,a}(\boldsymbol{r}) = \mathrm{Rg}\,\boldsymbol{\Psi}(\boldsymbol{r} - \boldsymbol{r}_a)c_{a,loc} \quad 1.4.10(b)$$

$$\boldsymbol{E}_{sca,a}(\boldsymbol{r}) = \boldsymbol{\Psi}(\boldsymbol{r} - \boldsymbol{r}_a)c_a = \mathbb{T}_a\boldsymbol{E}_{loc,a}. \quad 1.4.10(c)$$

To maximally leverage the basis expansion approach, the goal is to represent the Foldy-Lax equations solely as a relation between expansion coefficients. I.e., each local field equation, $\mathbb{T}_a\left(\boldsymbol{E}_a^{loc} = \boldsymbol{E}^{inc} + \sum_{b\neq a}^{N}\mathbb{G}_{eo}\mathbb{T}_b\boldsymbol{E}_b^{loc}\right)$, should expand so that a common basis can be removed, leaving only a coefficient relation. Unfortunately, each particle is best represented as a Mie expansion centered at their own origin. This is because, as shown in equation 1.4.6, the coefficients are then directly related to the particles' surface currents. In simple geometries like the sphere, this also leads to a sparse representation of the transition matrix. Instead of re-deriving all fields at each new origin, translation relations are defined so that, when necessary, the coefficients of one particle can be represented in an expansion referenced at the center of another particle. The Mie translation operators are

$$\mathrm{Rg}\,\boldsymbol{\Psi}(\boldsymbol{r} - \boldsymbol{r}_b)c_b = \mathrm{Rg}\,\boldsymbol{\Psi}(\boldsymbol{r} - \boldsymbol{r}_a)\mathbb{J}^{ab}(\boldsymbol{d}_{ab})c_b \quad 1.4.11(a)$$

$$\boldsymbol{\Psi}(\boldsymbol{r} - \boldsymbol{r}_b)c_b = \mathrm{Rg}\,\boldsymbol{\Psi}(\boldsymbol{r} - \boldsymbol{r}_a)\mathbb{H}^{ab}(\boldsymbol{d}_{ab})c_b \qquad |\boldsymbol{d}_{ab}| > |\boldsymbol{r} - \boldsymbol{r}_a| \quad 1.4.11(b)$$

$$\boldsymbol{\Psi}(\boldsymbol{r} - \boldsymbol{r}_b)c_b = \boldsymbol{\Psi}(\boldsymbol{r} - \boldsymbol{r}_a)\mathbb{J}^{ab}(\boldsymbol{d}_{ab})c_b \qquad |\boldsymbol{d}_{ab}| < |\boldsymbol{r} - \boldsymbol{r}_a| \quad 1.4.11(c)$$

where $\boldsymbol{d}_{ab} = \boldsymbol{r}_a - \boldsymbol{r}_b$ and their explicit form is given in section 1.13, appendix D . The lettering system of these operators is intentional as $\mathbb{J}^{ab} \to j_n$ is reliant on the first spherical Bessel function and $\mathbb{H}^{ab} = \mathbb{J}^{ab} + i\mathbb{Y}^{ab} \to h_n$ is reliant on the first spherical Hankel function. The $\mathbb{J}^{ab} \in \mathbb{C}^{\mathrm{L}\times\mathrm{L}}$ operator is a true translation. The $\mathbb{H}^{ab} \in \mathbb{C}^{\mathrm{L}\times\mathrm{L}}$ operator not only translates fields but also transforms them from outgoing to incoming harmonics at the new location. The

corresponding transformation from incoming to outgoing harmonics occurs in the $\mathbb{T}_a$ operator as it maps incident to scattered fields.

Under this framework the fundamental interaction equation resulting from the solution to the Foldy-Lax relations is

$$c_a = \mathbb{T}_a \mathbb{J}^{a0}(\boldsymbol{d}_{a0}) c_{inc} + \mathbb{T}_a \sum_{b \neq a} \mathbb{H}^{ab}(\boldsymbol{d}_{ab}) c_b. \qquad 1.4.12$$

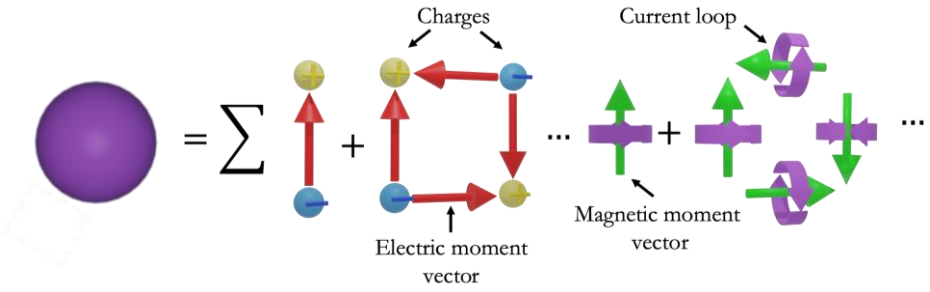

Figure 1.4.2. Schematic representation of the Mie vector harmonic expansion of a sphere as a superposition of electric and magnetic type multipoles.

In the Mie basis the Foldy-Lax equations represent a matrix problem solely relating Mie coefficients between particles. Correspondingly, all electromagnetic behavior can be studied in coefficient space under the atom-atom interaction analogy. This representation also produces a substantial reduction in computational cost compared to a system of numerical integral equations.

1.5 THE PROBLEM STATEMENT

Consider a monolayer consisting of a mixture of N ($\rightarrow \infty$) particles that are dispersed in the x-y plane at z = 0 and embedded in a lossless media defined by the permittivity, ϵ. All particles are assumed spherical, non-overlapping, and are defined by their shape, s (radius), refractive index, η, and center position in the x-y plane, $\boldsymbol{\rho}$. Given the distinct and countable nature of the scattering inhomogeneities, the system is well suited for the scattered field formalism, where the total electric field, $\boldsymbol{E}_{tot}$, from the film is a superposition of the scattered field from each particle, $\sum_a \boldsymbol{E}_{sca,a}$, and the initial field incident on the particle film, $\boldsymbol{E}_{inc}$. This is written as

$$\boldsymbol{E}_{tot}(\boldsymbol{r}) = \boldsymbol{E}_{inc}(\boldsymbol{r}) + \sum_a^N \boldsymbol{E}_{sca,a}(\boldsymbol{r} - \boldsymbol{\rho}_a). \quad 1.5.1$$

Correspondingly, the local electromagnetic field felt by a particle is the superposition from all other fields besides itself at the location of itself,

$$\boldsymbol{E}_{loc,a}(\boldsymbol{\rho}_a) = \boldsymbol{E}_{inc}(\boldsymbol{\rho}_a) + \sum_{b\neq a}^N \boldsymbol{E}_{sca,b}(\boldsymbol{\rho}_a - \boldsymbol{\rho}_b). \quad 1.5.2$$

Let all interactions be in the linear regime, so that the scattering response operator, $\boldsymbol{E}_{sca,a} = \mathbb{T}_a[\boldsymbol{E}_{loc,a}]$, is linear and defined by equation 1.4.9. Let the incident field be a plane-wave in order to match the infinite extent of the particle film so that reflection and transmission are well defined. (Arbitrary spatial and temporal excitations can then be constructed through Fourier transformation.)

Under the proposed framework the problem statement is:

How can spherical particles be engineered to produce emergent transmission, reflection, and absorptions properties when dispersed randomly in a single layer?

1.6 POWER BALANCE

> "The modern view of the world that emerged from Maxwell's theory is a world with two layers. The first layer, the layer of the fundamental constituents of the world, consists of fields satisfying simple linear equations. The second layer, the layer of the things that we can directly touch and measure, consists of mechanical stresses and energies and forces. The two layers are connected, because the quantities in the second layer are quadratic or bilinear combinations of the quantities in the first layer. To calculate energies or stresses, you take the square of the electric field-strength or multiply one component of the field by another… The objects on the first layer, the objects that are truly fundamental, are abstractions not directly accessible to our senses. The objects that we can feel and touch are on the second layer, and their behavior is only determined indirectly by the equations that operate on the first layer."
>
> - Freeman Dyson, Why is Maxwell's Theory so Hard to Understand, 2007

Power balance relations can be found from the conservation of time average power flux formalized using Poynting's theorem in differential form,

$$\frac{1}{2}(\sigma \boldsymbol{E}\cdot\boldsymbol{E}^{*}+\boldsymbol{E}\cdot\boldsymbol{J})=\nabla\cdot\boldsymbol{S}+\frac{i\omega}{2}(\mu \boldsymbol{H}\cdot\boldsymbol{H}^{*}+\epsilon \boldsymbol{E}\cdot\boldsymbol{E}^{*}), \tag{1.6.1}$$

where $\boldsymbol{S}=\frac{1}{2}\boldsymbol{E}\times\boldsymbol{H}^{*}\in\mathbb{C}^{3}$ is the time average Poynting vector. The * superscript denotes the complex conjugate. By applying the divergence theorem to equation 1.6.1 over an integration surface encompassing the entire particle collection the film-level extinction theorem can be derived,

$$W_{ext}=W_{sca}+W_{abs}. \tag{1.6.2}$$

Equation 1.6.2 states that the proportion of incident power converted to either absorption, W_{abs}, or scattered power escaping into the far field, W_{sca}, is equal to the power removed from the incident field, W_{ext}. This result is completely analogous to the extinction theorem derived by Paul Ewald and Carl Oseen when considering the particle collection as a single "particle." The power definitions have the following relations to the individual terms,

$$W_{ext} = \sum_a^N \left(W_{a,inc} + W_{inc,a}\right) \quad 1.6.3(a)$$

$$W_{sca} = \sum_a^N \left(W_{a,a} - \sum_{b\neq a}^N W_{a,b}\right) \quad 1.6.3(b)$$

$$W_{abs} = \iiint dV \, \frac{1}{2}(\sigma \boldsymbol{E}_{tot} \cdot \boldsymbol{E}_{tot}^* + \boldsymbol{E}_{tot} \cdot \boldsymbol{J}_{tot}), \quad 1.6.3(c)$$

where $\boldsymbol{S}_{x,y} = \frac{1}{2}\boldsymbol{E}_x \times \boldsymbol{H}_y^*$ and $W_{x,y} = \oint d^2\boldsymbol{r} \cdot \Re\left[\boldsymbol{S}_{x,y}\right]$, since the power stored in the electromagnetic field is completely reactive, $\Re\left[\frac{i\omega}{2}(\mu \boldsymbol{H} \cdot \boldsymbol{H}^* + \epsilon \boldsymbol{E} \cdot \boldsymbol{E}^*)\right] = 0$.

When treating all particles as a single collective inhomogeneity, the Ewald-Oseen extinction theorem defines the power balance. At the "film-level," the total scattering and absorption results from a removal of power from the incident field.

Particle-level Power Balance

Similarly, a power conservation relation between an individual particle and the remaining environment can be found by integration enclosing the particle of interest. To isolate a power balance relation between an individual particle and its environment, it is generally necessary to define the integration surface as tracing the particle's surface on the side of the embedding media, ∂V^+. Though if the embedding media is lossless then any surface encompassing the particle and no other inhomogeneities will suffice. When possible, integrating over the surface of the smallest ball, $B \in \mathbb{R}^3$, encapsulating the particle has the nice property of leveraging the orthogonality of the Mie basis. For spherical particles this has the further benefit of representing an exact integration over ∂V^+. By applying the divergence theorem to Poynting's theorem over an integration surface encompassing a single particle the particle-level extinction theorem is,

$$W_{abs,a} + W_{a,a} = W_{inc,a} + W_{a,inc} + \sum_{b\neq a}^N \left(W_{a,b} + W_{b,a}\right) \quad 1.6.4$$

Equation 1.6.4 states that the power absorbed and scattered to the far field for an individual particle is equal to the power the particle transferred to/from the incident *and* scattered field of all other particles. This constitutes a generalization to the extinction theorem of Ewald-Oseen. When considering multiple scattering sites, it is possible that any individual particle may *give* power to another particle or even the incident field. I.e., it is not necessary that $W_{inc,a}$, $W_{a,inc}$, $W_{b,a}$, or $W_{a,b}$ are positive. This is a result of the multiple interaction channels for each particle. Only the scattered, $W_{a,a}$, and absorbed, $W_{abs,a}$, power of an individual particle are always

positive, as these quantities define one-way transitions either to the far field or to a non-conserved conversion to another form work, respectively. Note that over the surface enclosing particle a, there is no net power flow from the incident field, $W_{inc} = 0$, the scattered field from other particles, $\sum_{b\neq a}^{N}(W_{b,b} = 0)$, or the interference of the scattered field from other particles and the incident field, $\sum_{b\neq a}^{N}(W_{b,inc} + W_{inc,b} = 0)$. This is because none of these fields originate inside the enclosing surface, so their net influx is balanced by their net outflux.

Inspection of both the particle and film-level power balance makes clear that adding all particle-level powers can derive the film-level balance relation,

$$\begin{aligned}&(W_{ext} = W_{sca} + W_{abs})\\&= \sum_{a}^{N}\left(W_{inc,a} + W_{a,inc} = W_{abs,a} + W_{a,a} - \sum_{b\neq a}^{N}\left(W_{a,b} + W_{b,a}\right)\right),\end{aligned} \qquad 1.6.5$$

where it should be understood that the $\left(W_{a,b} + W_{b,a}\right)$ pair is integrated over a surface enclosing only particle a.

Particle-level power balance introduces new particle-particle interaction channels necessitating a generalized version of the extinction theorem. Adding all particles recovers the traditional Ewald-Oseen extinction theorem.

Connection to Foldy-Lax

The satisfying connection between particle and film-level power conservation provides a quick and insightful method to calculate power flows from the Foldy-Lax relations. It brings to the conversation a connection to the local field. Right multiplying particle a's local electric field by $\times \frac{1}{2}\boldsymbol{H}_{sca,a}^{*}$ and left multiplying the conjugate of particle a's magnetic local field by $\frac{1}{2}\boldsymbol{E}_{sca,a} \times$ gives

$$\begin{aligned}\frac{1}{2}\boldsymbol{E}_{loc,a} \times \boldsymbol{H}_{sca,a}^{*} &= \frac{1}{2}\left(\boldsymbol{E}_{inc} \times \boldsymbol{H}_{sca,a}^{*} + \sum_{b\neq a}^{N}\boldsymbol{E}_{sca,b} \times \boldsymbol{H}_{sca,a}^{*}\right)\\\frac{1}{2}\boldsymbol{E}_{sca,a} \times \boldsymbol{H}_{loc,a}^{*} &= \frac{1}{2}\left(\boldsymbol{E}_{sca,a} \times \boldsymbol{H}_{inc}^{*} + \sum_{b\neq a}^{N}\boldsymbol{E}_{sca,a} \times \boldsymbol{H}_{sca,b}^{*}\right).\end{aligned} \qquad 1.6.6$$

Adding the two relations together, adding $\boldsymbol{S}_{a,a} - \boldsymbol{S}_{a,a}$ to the left-hand side, regrouping terms, and integrating the real part over the particle surface gives

$$W_{a,a} + \oint d^2\boldsymbol{r} \cdot \Re\left[\boldsymbol{S}_{loc-a,a} + \boldsymbol{S}_{a,loc-a} - \boldsymbol{S}_{a,a}\right] = W_{inc,a} + W_{a,inc} + \sum_{b\neq a}^{N}\left(W_{a,b} + W_{b,a}\right). \quad 1.6.7$$

Clearly, $W_{abs,a} = \oint d^2\boldsymbol{r} \cdot \Re\left[\boldsymbol{S}_{loc-a,a} + \boldsymbol{S}_{a,loc-a} - \boldsymbol{S}_{a,a}\right]$. Therefore, the particle's absorption can be calculated directly from a surface integral directly from knowledge of the particle's local and scattered field. Care should be taken as to the interpretation of an "absorption Poynting vector," defined as

$$\boldsymbol{S}_{abs,a} = \frac{1}{2}\left(\boldsymbol{E}_{loc,a} \times \boldsymbol{H}^*_{sca,a} + \boldsymbol{E}_{sca,a} \times \boldsymbol{H}^*_{loc,a} - \boldsymbol{E}_{sca,a} \times \boldsymbol{H}^*_{sca,a}\right). \quad 1.6.8$$

There is likely little physical interpretation of equation 1.6.8 outside of integrating it over the entire surface.

Deriving power balance from the fundamental interaction equations directly identifies the role of the local field in power balance and provides a satisfying consistency check.

A Probabilistic Interpretation

With the powers defined, it is also possible to consider electrical cross sections, C, and conversion efficiencies, Q, defined as

$$C \equiv \frac{W}{I_{inc}}, \quad Q \equiv \frac{C}{A}, \quad 1.6.9$$

where W denotes any of the prior defined power flows, I_{inc} is the intensity of the incident plane wave and A is the geometric cross-sectional area of the particle, as seen from the angle of the plane wave.

From this definition it is clear that the total conservation of power for the film is in fact a conservation of cross sections,

$$\left(C_{ext} = C_{sca} + C_{abs}\right) = \sum_a^N\left(C_{inc,a} + C_{a,inc} = C_{abs,a} + C_{a,a} - \sum_{b\neq a}^{N}\left(C_{a,b} + C_{b,a}\right)\right) \quad 1.6.10$$

This defines the notion of a macroscopic, film-level, cross section as being the sum of the individual particle-level cross sections. Correspondingly, film-level efficiencies for scattering, absorption, and extinction are defined as $Q = \sum_a^N C_a \,/\, \sum_a^N A_a$. If the film is composed of multiple different particle types (defined as a unique shape and/or material), then the summation of all particles can be partitioned by particle type, $\sum^N = \sum^{|\mathcal{T}|} \sum^{|\mathcal{Q}_\mathcal{T}|}$. Here, the total number of unique types is denoted as $|\mathcal{T}|$ where there are $|\mathcal{Q}_\mathcal{T}|$ particles of that type dispersed throughout the film. The total area in the plane composed of particles as seen from the external plane wave is then $A_p = \sum_\mathcal{T}^{|\mathcal{T}|} A_\mathcal{T} |\mathcal{Q}_\mathcal{T}| = N \sum_\mathcal{T}^{|\mathcal{T}|} A_\mathcal{T} P_\mathcal{T}$, where $P_\mathcal{T} = |\mathcal{Q}_\mathcal{T}|/N$ is the probability that any chosen particle in the film is of type $\mathcal{T}$. This second equality is particularly useful because it transforms the problem to the language of probability distributions, which is a meaningful characteristic parameter in the context of random films. Dividing the apparent particle area by the total area of the x-y plane, A_{xy}, gives the fraction of the space seen by the plane wave that is filled with particles, $ff = A_p/A_{xy}$. Correspondingly, the fraction of the space filled with particles of type, $\mathcal{T}$, is $ff_\mathcal{T} = A_\mathcal{T} |\mathcal{Q}_\mathcal{T}|/A_{xy}$. Using the definitions above, the film-level cross-section of a particular particle type is

$$C_\mathcal{T} = ff_\mathcal{T} \left(\frac{1}{|\mathcal{Q}_\mathcal{T}|} \sum_a^{|\mathcal{Q}_\mathcal{T}|} Q_a\right) = ff \left(\frac{A_\mathcal{T} P_\mathcal{T}}{\sum_\mathcal{T}^{|\mathcal{T}|} A_\mathcal{T} P_\mathcal{T}}\right) \left(\frac{1}{|\mathcal{Q}_\mathcal{T}|} \sum_a^{|\mathcal{Q}_\mathcal{T}|} Q_a\right). \tag{1.6.11}$$

and the total cross section is

$$C = \sum_\mathcal{T}^{|\mathcal{T}|} C_\mathcal{T} \,. \tag{1.6.12}$$

Therefore, the film-level power balance can be restated as

$$ff \left(\begin{array}{c} \mathbb{E}\left[\mathbb{E}\left[Q_{ext,a}|\mathcal{T}\right]\right] - \mathbb{E}\left[\mathbb{E}\left[Q_{abs,a}|\mathcal{T}\right]\right] \\ = \mathbb{E}\left[\mathbb{E}\left[Q_{a,a}|\mathcal{T}\right]\right] + \mathbb{E}\left[\mathbb{E}\left[\sum_{b\neq a}^N Q_{a,b}\,|\mathcal{T}\right]\right] \end{array} \right) \tag{1.6.13}$$

where the conditional expectation is $\mathbb{E}[\sigma|\mathcal{T}] = \frac{1}{|\mathcal{Q}_\mathcal{T}|} \sum_a^{|\mathcal{Q}_\mathcal{T}|} Q_a$ and the outer expectation is $\mathbb{E}\big[\mathbb{E}[Q|\mathcal{T}]\big] = \sum_\mathcal{T}^{|\mathcal{T}|} w_\mathcal{T} \mathbb{E}[Q|\mathcal{T}]$. In the context of a random film, the weight factor, $w_\mathcal{T} = A_\mathcal{T} P_\mathcal{T} / \sum_\mathcal{T}^{|\mathcal{T}|} A_\mathcal{T} P_\mathcal{T}$, can be interpreted as the *area* probability density of the particle type, $\mathcal{T}$.

Interestingly, equation 1.6.13 has the form of the law of total expectation, where $w_{\mathcal{T}}$ is the weight factor. This formulation, arising solely from algebraic manipulation, brings the language of probability to a deterministic problem. Summing all contributions to construct the film-level response is equivalent to calculating the expected behavior of each unique particle type. Under this interpretation, $\mathbb{E}[\sigma|\mathcal{T}]$ is understood as the average behavior of a particle's scattering, absorption, or extinction efficiency when considering all possible local fields, a particle of that type may experience. Recall that equation 1.6.13 is just an algebraic repackaging of the fundamental relations. Therefore, it is still equally valid for an ordered system, such as a periodic lattice, or a film of same type particles. In this case the probabilistic interpretation is trivial. Distributions and spatial correlations are simply described by delta functions. In this context the random system can be regarded as the most general definition. Finally, note that equations 1.6.13 is not restricted to the behavior of the coherent field. It is a complete description of all power in the system. No approximations.

Power flow at the macroscopic level can be shown to arise from to the average power conversion efficiency of particles at the nanoscopic level. This is analogous to how permittivity and permeability are related to the average behavior of charges at the atomistic level.

Power in the Mie Basis

As detailed in section 1.11, appendix B the power between any electric and magnetic field over a surface can be written in the Mie basis as

$$\begin{aligned} W_{ab} &= \tfrac{1}{2}\Re[\int d\boldsymbol{A}\cdot(\boldsymbol{E}_a\times\boldsymbol{H}_b^*)] \\ &= \Re\, tr[\int d\mathbb{W}(\boldsymbol{r}-\boldsymbol{\rho})\,\mathbb{c}_{ab}], \end{aligned} \qquad 1.6.14$$

where tr is the trace operation and $\mathbb{c}_{ab} = c_a \otimes c_b^* \in \mathbb{C}^{L\times L}$ is the outer product, $\otimes$, matrix between the coefficient vectors of the two fields. Each element, $\mathbb{c}_{ab_{l,l'}} = c^t_{a,n,m}c^{t'*}_{b,n'm'}$, defines an interference combination between the two fields in coefficient space. $d\mathbb{W}(\boldsymbol{r}-\boldsymbol{\rho}_a) \in \mathbb{C}^{L\times L}$ is a matrix that maps the interference combinations in coefficient space to real space. Each element in $d\mathbb{W}$ takes the form

$$d\mathbb{W}_{ll'}(\boldsymbol{r}-\boldsymbol{\rho}) = \tfrac{1}{2}iYd\boldsymbol{A}\cdot\Big(\boldsymbol{\Psi}_l(\boldsymbol{r}-\boldsymbol{\rho})\times\nabla\times\boldsymbol{\Psi}^*_{l'}(\boldsymbol{r}-\boldsymbol{\rho})\Big), \qquad 3.6.15$$

where $Y = \sqrt{\epsilon/\mu}$ is the admittance at the differential surface area under consideration, $\boldsymbol{dA} = d^2\boldsymbol{r}\,\hat{\boldsymbol{n}}$, which has an outward pointing normal, $\hat{\boldsymbol{n}}$. Equation 1.6.15 necessitates that both fields are expanded in Mie harmonics about the same reference frame. Otherwise, there is little meaning to $\mathbb{c}_{ab}$, so the coefficients may need to be translated to $\boldsymbol{\rho}$. Correspondingly, equation 1.6.15 may take the form $\boldsymbol{\Psi} \times \nabla \times \boldsymbol{\Psi}^*$, $\mathrm{Rg}\boldsymbol{\Psi} \times \nabla \times \boldsymbol{\Psi}^*$, $\boldsymbol{\Psi} \times \nabla \times \mathrm{Rg}\boldsymbol{\Psi}^*$, or $\mathrm{Rg}\boldsymbol{\Psi} \times \nabla \times \mathrm{Rg}\boldsymbol{\Psi}^*$, depending on the chosen reference frame and domain of integration. Finally, it is also implied that the harmonics in equation are valid across the integration domain. As discussed, this precludes surfaces traversing boundaries.

Given the orthogonality of the Mie basis over a closed surface, Parseval-Plancherel's theorem states that the total power over a closed surface is a suitably normalized sum of the inner product of the coefficients. Correspondingly, the film-level power balance in the Mie basis is

$$W_{sca} = I_{inc}\frac{\pi}{k^2}\left(\sum_a^N c_a^\dagger c_a + \Re\left[c_a^\dagger \sum_{b\neq a} \mathbb{J}^{ab} c_b\right]\right) \quad 1.6.16(a)$$

$$W_{abs} = I_{inc}\frac{\pi}{k^2}\sum_a^N \Re\left[c_a^\dagger \mathbb{A}_a c_a\right] \quad 1.6.16(b)$$

$$W_{ext} = I_{inc}\frac{\pi}{k^2}\sum_a^N \Re\left[\tilde{c}_a^\dagger \mathbb{J}^{a0} c_{inc}\right] \quad 1.6.16(c)$$

where the † superscript denotes the Hermitian conjugate, $I_{inc} = \frac{1}{2}Y|\boldsymbol{E}_{inc}|^2$ is the intensity of the incident plane wave, and $\mathbb{A}_a = \Re\left[\mathbb{T}_a^{-1} - 1\right] \in \mathbb{C}^{L\times L}$ is the absorption operator for particle a[4]. Correspondingly, the particle level power balance is

$$W_{a,a} = I_{inc}\frac{\pi}{k^2} c_a^\dagger c_a \quad 1.6.17(a)$$

$$W_{abs,a} = I_{inc}\frac{\pi}{k^2}\Re\left[c_a^\dagger \mathbb{A}_a c_a\right] \quad 1.6.17(b)$$

$$W_{a,b} + W_{b,a} = I_{inc}\frac{\pi}{k^2}\Re\left[c_a^\dagger \sum_{b\neq a} \mathbb{H}^{ab} c_b\right] \quad 1.6.17(c)$$

$$W_{inc,a} + W_{a,inc} = I_{inc}\frac{\pi}{k^2}\Re\left[\tilde{c}_a^\dagger \mathbb{J}^{a0} c_{inc}\right]. \quad 1.6.17(d)$$

Equation 1.6.17 defines the power balance on the surface of particle a, with all fields expanded using particle a as the reference frame. The interference between the other particles and the particle of interest, has a form similar to the film-level extinction, except using the $\mathbb{H}^{ab}$ translation operator instead of $\mathbb{J}^{ab}$. This is necessary because $\mathbb{J}^{ab}$ defines a valid expansion for integration out to the far field. $\mathbb{H}^{ab}$ defines a valid expansion for the integration domain over the particle surface. At first glance, it appears these two representations are incompatible, and the film-level cannot be derived from the particle-level. This "incompatibility" is incorrect because when considering the entire collection, a replacement $\mathbb{H}^{ab} \to \mathbb{J}^{ab}$ occurs. Performing

the summation shows this transformation is due to an exact cancelation when considering all particles,

$$\begin{aligned}
&\textstyle\sum_a^N c_a^\dagger \sum_{b\neq a} \mathbb{H}^{ab} c_b \\
&= \textstyle\sum_a^N \sum_{b=a+1}^N \left(c_a^\dagger \mathbb{H}^{ab} c_b + c_b^\dagger \mathbb{H}^{ba} c_a\right) \\
&= \textstyle\sum_a^N \sum_{b=a+1}^N \left(c_a^\dagger \mathbb{H}^{ab} c_b + c_a^\dagger \mathbb{H}^{ba\dagger} c_b\right) \\
&= \textstyle\sum_a^N \sum_{b=a+1}^N \left(c_a^\dagger (\mathbb{J}^{ab} + i\mathbb{Y}^{ab}) c_b + c_a^\dagger (\mathbb{J}^{ab} - i\mathbb{Y}^{ab}) c_b\right) \\
&= \textstyle\sum_a^N c_a^\dagger \sum_{b\neq a} \mathbb{J}^{ab} c_b \,.
\end{aligned} \qquad 1.6.18$$

Equation 1.6.18 shows that once considering the interference on all particle surfaces the $\mathbb{Y}$ translation term exactly cancels in the film-level power balance. This naturally brings the question, what is the meaning of $c_a^\dagger i\mathbb{Y}^{ab} c_b$? The interpretation in this dissertation is that $c_a^\dagger i\mathbb{Y}^{ab} c_b$ defines power transfer between the portion of particle a and particle b's fields that are trapped inside the film but do not contribute to absorption. By conservation, this contribution must then exactly cancel. Unfortunately, due to this exact cancelation, $c_a^\dagger i\mathbb{Y}^{ab} c_b$ does not contribute to any physically measurable quantity. Correspondingly, it is hard to solidify a physical meaning. The interpretation proposed is a postulate.

Under the Mie expansion, the Foldy-Lax connection offers a very expedient method to calculate total power. Simply multiply the Foldy-Lax relation by $\frac{\pi}{k^2} \tilde{c}_a^\dagger \mathbb{T}_a^{-1}$ to derive the particle-level power balance for every particle! The summation then gives the film-level power. Mie harmonic translations are usually a costly computational process. In many cases generating the interaction matrix requires more computation effort than solving it! Correspondingly, it is ideal to maximally reuse the results of computational effort.

Under the Mie framework, equation 1.6.17 is equivalent to multiplying the coefficient-based Foldy-Lax relation by $\frac{\pi}{k^2} \tilde{c}_a^\dagger \mathbb{T}_a^{-1}$. This gives a computationally efficient and expedient method to calculate power balance for an arbitrary particle and also the particle collection solely through additions and matrix multiplications[4].

1.7 POWER FLOW TO THE FAR FIELD

Ultimately, the goal is to understand how sub-wavelength inhomogeneities alter the transmission, reflection, and absorption spectra of incident radiation. Though section 1.6 describes this emergent connection in terms of power balance, the results provide no statements on the angular redistribution of power. For this it is necessary to study angle-resolved power flow, particularly over the hemisphere in the far field.

In the far field the scalar Green's functions has the asymptotic relations

$$\lim_{r\to\infty} \nabla \times \boldsymbol{v}(\boldsymbol{r}')G(\boldsymbol{r},\boldsymbol{r}') = ik\frac{e^{ikr}}{r}\left(e^{-ik\hat{\boldsymbol{r}}\cdot\boldsymbol{r}'}\left(\hat{\boldsymbol{r}}\times\boldsymbol{v}(\boldsymbol{r}')\right) + O\left(\frac{1}{r}\right)\right) \quad 1.7.1(a)$$

$$\lim_{r\to\infty} \nabla \times \nabla \times \boldsymbol{v}(\boldsymbol{r}')G(\boldsymbol{r},\boldsymbol{r}') = k^2\frac{e^{ikr}}{r}\left(e^{-ik\hat{\boldsymbol{r}}\cdot\boldsymbol{r}'}\left(\hat{\boldsymbol{r}}\times(\boldsymbol{v}(\boldsymbol{r}')\times\hat{\boldsymbol{r}})\right) + O\left(\frac{1}{r}\right)\right). \quad 1.7.1(b)$$

Correspondingly, the far field of an arbitrary surface current distribution has the asymptotic form

$$\lim_{r\to\infty} \boldsymbol{E}_{sca}(\boldsymbol{r}) = \frac{e^{ikr}}{r}\left(\boldsymbol{E}^{\infty}_{sca}(\hat{\boldsymbol{r}}) + O\left(\frac{1}{r}\right)\right), \quad 1.7.2$$

where

$$\boldsymbol{E}^{\infty}_{sca}(\hat{\boldsymbol{r}}) = \frac{ik}{4\pi}\int_{\partial V_a} d^2\boldsymbol{r}'\, e^{ik\hat{\boldsymbol{r}}\cdot\boldsymbol{r}'}\left(\hat{\boldsymbol{r}}\times\boldsymbol{J}_s(\boldsymbol{r}') + \frac{1}{Y}\,\hat{\boldsymbol{r}}\times(\boldsymbol{M}_s(\boldsymbol{r}')\times\hat{\boldsymbol{r}})\right). \quad 1.7.3$$

Clearly, $\boldsymbol{E}^{\infty}_{sca}\cdot\hat{\boldsymbol{e}}_r = 0$ and this means that all fields in the far field are propagating and transverse. Applying Faraday's law to equation 1.7.3 gives a fundamental condition on emanating fields in the far field. They must satisfy the Silver-Müller far field radiation condition,

$$\lim_{r\to\infty} \hat{\boldsymbol{e}}_r\times\sqrt{\mu}\boldsymbol{H}_{sca} + \sqrt{\epsilon}\boldsymbol{E}_{sca} = O\left(\frac{1}{r}\right). \quad 1.7.4$$

The scattered power flow in the far field at any differential solid angle is

$$\frac{dW^{far}_{sca}}{d\Omega} = Y|\boldsymbol{E}^{\infty}_{sca}|^2 + O\left(\frac{1}{r}\right), \quad 1.7.5$$

where the real operator is unnecessary since the far field is composed of a lossless media. Equation 1.7.5 can be easily derived from a circular shift of the scalar triple product, $\hat{\boldsymbol{e}}_r \cdot (\boldsymbol{E}^{\infty}_{sca} \times \boldsymbol{H}^{\infty *}_{sca}) = \boldsymbol{E}^{\infty}_{sca} \cdot (\boldsymbol{H}^{\infty *}_{sca} \times \hat{\boldsymbol{e}}_r) = Y|\boldsymbol{E}^{\infty}_{sca}|^2$. Again, when the inhomogeneities are countable and distinct the currents can be bundled, and the concept of multiple scattering is useful to understand particle-particle interactions. In this case, the total scattered power can be decomposed into scattered power from each inhomogeneity and the interference terms,

$$|\textstyle\sum_a^N \boldsymbol{E}^{\infty}_a|^2 = \sum_a^N (|\boldsymbol{E}^{\infty}_a|^2 + \sum_{b\neq a}^N \Re[\boldsymbol{E}^{\infty}_a \boldsymbol{E}^{\infty *}_b]), \tag{1.7.6}$$

and through the same partitioning scheme discussed in section 1.6,

$$\frac{dQ^{far}_{sca}}{d\Omega} = \mathbb{E}\left[\mathbb{E}\left[\frac{dQ^{far}_{a,a}(\hat{\boldsymbol{r}})}{d\Omega}\middle|\mathcal{T}\right]\right] + \mathbb{E}\left[\mathbb{E}\left[\frac{\sum_{b\neq a}^N dQ^{far}_{a,b}(\hat{\boldsymbol{r}})}{d\Omega}\middle|\mathcal{T}\right]\right]. \tag{1.7.7}$$

The monochromatic incident plane wave can be written in a form like equation 1.7.7 by viewing it as the superposition of an incoming and outgoing spherical wave in the far field,

$$\lim_{r\to\infty} e^{i\boldsymbol{k}_{inc}\cdot\boldsymbol{r}} = \lim_{r\to\infty} \frac{2\pi i}{k}\left(\delta(\hat{\boldsymbol{r}} + \hat{\boldsymbol{k}})\frac{e^{-ikr}}{r} - \delta(\hat{\boldsymbol{r}} - \hat{\boldsymbol{k}})\frac{e^{ikr}}{r}\right). \tag{1.7.8}$$

Therefore, the time-average power resulting from the interference between the incident field and the scattered field in the far field is

$$\lim_{r\to\infty} \frac{dW_{mix-inc}}{d\Omega} = \frac{1}{2} Y \Re\left[\frac{4\pi}{ik}\boldsymbol{E}^{*}_{inc} \cdot \boldsymbol{E}^{\infty}_{sca}\right] \delta(\boldsymbol{k} - \boldsymbol{k}_{inc})\delta(\hat{\boldsymbol{e}} - \hat{\boldsymbol{e}}_{inc}) + O\left(\frac{1}{r}\right). \tag{1.7.9}$$

Equation 1.7.9 is known as the optical theorem. It shows that the net scattered (including multiply scattered interference) and net absorbed power from all particles can be determined by a far field power measurement in the exact direction, $\boldsymbol{k}_{inc}$, and polarization, $\hat{\boldsymbol{e}}_{inc}$, of the exciting plane wave. Furthermore, for multiple scattering, this result holds for each individual particle, $\boldsymbol{E}^{*}_{inc} \cdot \boldsymbol{E}^{\infty}_{sca} = \sum_a^N \boldsymbol{E}^{*}_{inc} \cdot \boldsymbol{E}^{\infty}_{sca,a} \rightarrow W_{mix-inc} = \sum_a^N W_{mix-inc,a}$. Equation 1.7.9 also shows that the reflection direction is composed only of the contribution from the multiply scattered field.

Therefore, it is not necessary to calculate the total transmission explicitly because it can be found through power conservation,

$$\begin{aligned} Ref &= ff \int_{\theta=\pi/2}^{\pi} \int_{\phi=0}^{2\pi} \left(\mathbb{E}\left[\mathbb{E}\left[dQ_{a,a}^{far}(\hat{\boldsymbol{r}}) | \mathcal{T} \right] \right] + \mathbb{E}\left[\mathbb{E}\left[\sum_{b\neq a}^{N} dQ_{a,b}^{far}(\hat{\boldsymbol{r}}) \, | \mathcal{T} \right] \right] \right) \\ Abs &= ff \mathbb{E}\left[\mathbb{E}\left[Q_{abs,a} | \mathcal{T} \right] \right] \\ Trans &= 1 - Ref - Abs. \end{aligned} \tag{1.7.10}$$

The total reflection, transmission, and absorption from an infinite film can be written as the expected value of the far field scattering efficiency of all particles. Optical theorem shows that reflection is purely composed of the scattered field. Correspondingly, computational effort can be saved by evoking power balance to calculate transmission.

Order of Power

The concept of order of scattering can be used to understand power flow as a decomposition of multiple scattering terms. Given that the power is proportional to the product of the field, the order of power is then all combinations of products of scattering paths,

$$\begin{aligned} &\frac{dW_{sca}^{far}}{d\Omega} \propto \\ &= \left| \left(1 + \sum_{a}^{N} \mathbb{GT}_a + \sum_{\substack{b\neq a \\ a}}^{N} \mathbb{GT}_a \mathbb{GT}_b + \sum_{\substack{c\neq b \\ b\neq a \\ a}}^{N} \mathbb{GT}_a \mathbb{GT}_b \mathbb{GT}_c \ldots \right) \boldsymbol{E}^{inc} \right|^2 . \end{aligned} \tag{1.7.11}$$

Figure 1.7.1 describes schematically the order of power. The scattering path on the left of the product at the top and the scattering path on the right of the product at the bottom. Same particles are again connected through a dotted line. Clearly the order of power has substantially more complex behavior as it is a product of all combinations of order of scattering terms.

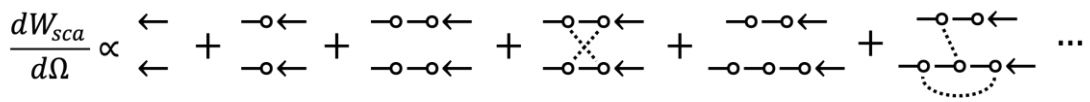

Figure 1.7.1. Decomposition of the scattered power into products of order of scattering terms.

Far Field in the Mie Basis

The electric angular far field vector can be written in Mie harmonics as

$$\boldsymbol{E}_{sca}^{\infty}(\hat{\boldsymbol{r}}) = \frac{1}{k}\boldsymbol{\Psi}^{far}c, \qquad 1.7.12$$

where $\boldsymbol{\Psi}^{far} = [\boldsymbol{N}^{far} \quad \boldsymbol{M}^{far}]$ as detailed in section 1.10, appendix A. Correspondingly, the far field scattering efficiency in any differential solid angle is

$$dQ_{a,b}^{far} = tr\left[\Re[d\mathbb{W}^{far}\mathbb{Q}_{ab}]\right], \qquad 1.7.13$$

where $\mathbb{Q}_{ab} = (c_a \otimes c_b^*)/A_a I_{inc}$ weighs the coefficient space to that resembling a partial efficiency relative to particle a.

Total reflection and transmission in the far field arises from the average angle-resolved power conversion efficiency of particles at the nanoscopic level. Therefore, from designing the efficiency and directionality of scattering particles as well as their response to particle-particle coupling emergent properties can be designed in the far field.

1.8 DISTRIBUTIONS OF RANDOM FILMS

Sections 1.3 - 1.7 outline the theory of multiple scattering for a realized film and show that power balance can be written in a mathematical form resembling particle-level expected values. This section considers the properties of a possible random film from the viewpoint of the statistical moments analyzed across the possible configurations. Generally, a random particle film is composed of particles having different shapes, materials, and positions, where each parameter may be controlled only in the statistical sense. In this case, it is natural to ask how electromagnetic fields behave as a function of the governing distribution. This section shows that, in context of analyzing power flow, the relevant quantitative measures are the field's moments.

To this end, it is important to first define the notion of "random" being addressed. After all, a crystal lattice is a perfectly fine realization in the space of all configurations. In fact, spatial order dominates at high packing fractions of non-penetrable objects, so order cannot be regarded as a vanishingly low probability scenario. Clearly, ordered packings are not the intended systems of study (many of which are already well described using concepts such as Bloch's theorem). The space of all possible configurations, $\mho$, is therefore restricted to the set of films having a form of strong spatial disorder. The first restriction formally imposed is that the average over all potential configurations leads to a constant effective permittivity, $\mathbb{E}[\tilde{U}] = M_U$. Second, for any realization the spatial covariance between particle centers is a function only of the Euclidean distance, $Cov(\boldsymbol{\rho}_a, \boldsymbol{\rho}_b) = Cov(|\boldsymbol{\rho}_a - \boldsymbol{\rho}_b|)$. Finally, for any realization there exists a finite critical distance, d_c, such that any two central points become uncorrelated, $Cov(|\boldsymbol{\rho}_a - \boldsymbol{\rho}_b| \geq d_c) = 0$. These conditions enforce that the spatial properties of any realization are not dependent on global translations or rotations and that all systems lack long-range spatial order. This enforces a form of statistical self-repetition and is a generalization of periodicity, where from the properties of one the whole can be reproduced. I.e., a sufficiently large block of a particular realization can statistically describe the distribution of all possible realizations (and vice versa). Such systems have been found to arise in nature and in particle fabrication/deposition schemes, dictated by the nature of the dominant forces and/or growth mechanisms involved[10–17].

As discussed in section 1.4, particle shape and material define the scattering transition operator and this operator can be encapsulated as describing a particle "type." It is then natural to define the particle type distribution, $P(\tilde{\mathcal{T}})$, with corresponding random variable, $\tilde{\mathcal{T}}$. This distribution is generally neither strictly discrete nor strictly continuous. For example, material is usually considered as categorical, under the assumption that the materials are distinct and countable (variations in material doping being a counter example). Alternatively, particle growth usually

produces a continuum of particle sizes (often Gaussian or Log Normal). Combinations of these are then a piecewise distribution. Another example could be particles of the same material and shape, but the shape is not rotationally symmetric. Though all objects are categorically the same, any non-degenerate rotation would be assigned a unique "type" since particle rotations correspond to a unique scattering behavior. In this context particle type can be synonymous with the transition operator $\mathcal{T} \Leftrightarrow \mathbb{T}$.

Under the constraint of rigid objects, the particle location and type distribution are mutually dependent since particles cannot overlap or stack on top one another. The joint distribution defines the potential distribution, P_U. If the inhomogeneities are distinct and countable then, following a similar framework to Foley, the potential distribution is described as

$$\int_{\mathcal{V}} P_U\left(\tilde{\boldsymbol{\rho}}_1 = \boldsymbol{\rho}_1, \dots, \tilde{\boldsymbol{\rho}}_N = \boldsymbol{\rho}_N, \tilde{\mathcal{T}}_1 = \mathcal{T}_1, \dots, \tilde{\mathcal{T}}_N = \mathcal{T}_{\mathrm{N}}\right) \prod_{a=1}^{N} d\boldsymbol{\rho}_a \, d\mathcal{T}_a = 1, \qquad 1.8.1$$

where the integrand reads as the probability of the first particle being type $\mathcal{T}_1$ and finding it centered in the differential element $d\boldsymbol{\rho}_1$, while simultaneously having the second particle be type $\mathcal{T}_2$ and centered in differential element $d\boldsymbol{\rho}_2$, and so on. All positions where particles would overlap have zero probability, therefore there are at minimum hard-particle correlations. An example of such a correlation is shown in figure 1.8.1.

When considering the moments of an electromagnetic field resulting from the interaction with a random potential, it is important to properly define the notion of "random." This work is concerned with spatial distributions that are rotation and translation invariant and have finite correlation lengths.

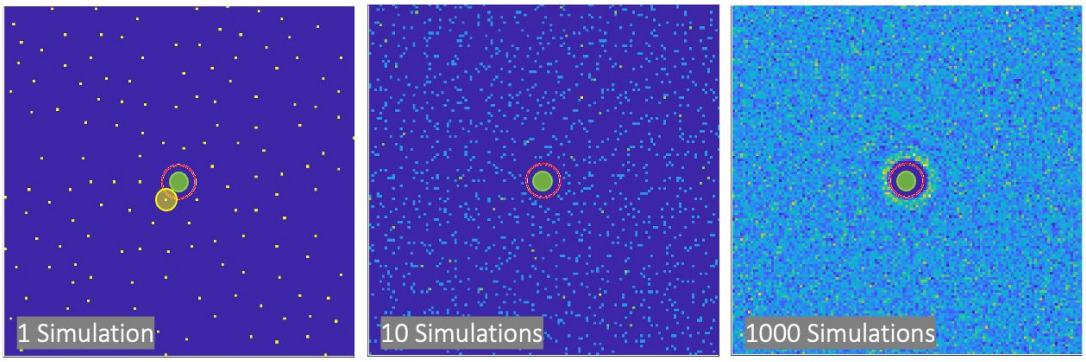

Figure 1.8.1. Progression of hard particle correlation in spherical particles of different radii. Each simulation places a particle at the origin (green circle) and randomly generates particles around it (e.g., yellow circle). Particle centers are recorded with a yellow dot on a dark blue background. The dots are averaged over simulations. As more particle films are added, a pattern emerges. No particle centers can penetrate into where particle touch. Lack of access to these inner locations creates local correlation. Outside of this zone is increased probability. Progressing radially, the probability oscillates until equilibrium to a uniform distribution.

Defining the Moments of the Field Distribution

It is now straightforward to transition the results from sections 1.1.3 – 1.1.7 to define the field moments. Since the fields, Poynting vectors, and conservation relations are defined for each individual configuration, they are also defined over the weight of all configurations. The latter being the definition of expected value, $\mathbb{E}[f(\tilde{X})] = \int dP_X \tilde{f}$, by the law of the unconscious statistician. The wave equation weighed across all possible potentials defines the mean field, $\mathbb{E}[\widetilde{\boldsymbol{E}}]$, as the solution to

$$\int_{\mathcal{U}} dP_U \left(\nabla \times \nabla \times \widetilde{\boldsymbol{E}} - \omega^2 \mu \epsilon \widetilde{\boldsymbol{E}} = \widetilde{U}\widetilde{\boldsymbol{E}}\right), \qquad 1.8.2$$

where $\boldsymbol{E} = \widetilde{\boldsymbol{E}}(\boldsymbol{r} \mid \widetilde{U} = U)$. It is important to note that $\mathbb{E}[\widetilde{U}\widetilde{\boldsymbol{E}}]$ may not be in the support of the possible $\widetilde{U}\widetilde{\boldsymbol{E}}$ configurations, since there is generally no guarantee that the mean of any distribution exist in the distribution. In fact, given sufficient disorder, $\mathbb{E}[\widetilde{U}\widetilde{\boldsymbol{E}}]$ approximates a homogeneous media even when every realization of $\widetilde{U}\widetilde{\boldsymbol{E}}$ is inhomogeneous. Due to the propensity of $\mathbb{E}[\widetilde{U}\widetilde{\boldsymbol{E}}]$ to blur into a continuum, the mean field is often called the "coherent" field. This interpretation is exact if the distribution is self-averaging. In that case, the spatial average of a single film instance is equivalent to the average of all possible realizations. The expectation over distributions is then replaced by a truly complete spatial blurring resulting in an

effective homogeneous media defined by $\mathbb{E}[\widetilde{U}\widetilde{\boldsymbol{E}}]$. Thought, $\mathbb{E}[\widetilde{U}\widetilde{\boldsymbol{E}}]$ may be continuous, the scattered field formalism o still applies as the expectation over film realizations,

$$\begin{aligned}&\int_{\mho} dP_V\left(\widetilde{\boldsymbol{E}}_{tot} = \boldsymbol{E}_{inc} + \sum_a^N \widetilde{\boldsymbol{E}}_a\right)\\&\int_{\mho} dP_V\left(\widetilde{\boldsymbol{E}}_{loc,a} = \boldsymbol{E}_{inc} + \sum_{b\neq a}^N \widetilde{\boldsymbol{E}}_b\right).\end{aligned} \tag{1.8.3}$$

This introduces the concept of order of scattering for the mean field,

$$\begin{aligned}&\mathbb{E}[\widetilde{\boldsymbol{E}}_{tot}]\\&= \mathbb{E}[1 + \sum_a^N \widetilde{\mathbb{G}}\widetilde{\mathbb{T}}_a + \sum_{\substack{b\neq a\\ a}}^N \widetilde{\mathbb{G}}\widetilde{\mathbb{T}}_a\widetilde{\mathbb{G}}\widetilde{\mathbb{T}}_b + \sum_{\substack{c\neq b\\ b\neq a\\ a}}^N \widetilde{\mathbb{G}}\widetilde{\mathbb{T}}_a\widetilde{\mathbb{G}}\widetilde{\mathbb{T}}_b\widetilde{\mathbb{G}}\widetilde{\mathbb{T}}_c \ldots]\boldsymbol{E}^{inc}\\&= \boldsymbol{\varepsilon}_{eff}\boldsymbol{E}^{inc},\end{aligned} \tag{1.8.4}$$

where the last equality interprets the expected total field as a displacement field. An analogous equation can be derived for the magnetic field. It is the subject of effective medium theories to define procedures to truncate the scattering terms in equation 1.8.4 and approximate $\boldsymbol{\varepsilon}_{eff}, \boldsymbol{\mu}_{eff}$ accordingly. Correspondingly, it is also important to note that the mean field is not the same as the field from the mean potential. The latter is substantially easier to define as it requires no concept of order of scattering. This highlights that thought the underlying potential distribution heavily informs the form of the field distribution, the two distributions are not the same.

Equations 1.8.2 - 1.8.4 introduce new concepts and definitions that are useful to understand the behavior of random films in a statistical sense. Realized film configurations are related to the coherent field through

$$\begin{aligned}\Delta\boldsymbol{E}_{sca} &= \boldsymbol{E}_{sca} - \mathbb{E}[\widetilde{\boldsymbol{E}}_{sca}]\\\Delta\boldsymbol{H}_{sca} &= \boldsymbol{H}_{sca} - \mathbb{E}[\widetilde{\boldsymbol{H}}_{sca}],\end{aligned} \tag{1.8.5}$$

where $\Delta\boldsymbol{E}, \Delta\boldsymbol{H}$ are the fluctuations in the realization that deviate from expectation. All fluctuations arise from the scattered field since the incident field is deterministic. The notion of a mean field also gives rise to the notion of a time average Poynting vector for the mean field, $\boldsymbol{S}_{mf} = \frac{1}{2}\mathbb{E}[\widetilde{\boldsymbol{E}}] \times \mathbb{E}[\widetilde{\boldsymbol{H}}^*]$. (Note that $\boldsymbol{S}$ is in the harmonic time-averaged form and the expectation, $\mathbb{E}$, is over ensembles.) Since the expectation of the square is not the same as the square of the expectations, the mean field Poynting vector is not necessarily the same as the mean Poynting vector,

$$\mathbb{E}[\tilde{\boldsymbol{S}}] = \frac{1}{2}\mathbb{E}[\tilde{\boldsymbol{E}} \times \tilde{\boldsymbol{H}}^*] = \boldsymbol{S}_{mf} + 2Var[\tilde{\boldsymbol{S}}]. \quad 1.8.6$$

The difference between the two is the variance,

$$2Var[\tilde{\boldsymbol{S}}] = 2\mathbb{E}\left[\tilde{\boldsymbol{S}} - E[\tilde{\boldsymbol{S}}]\right] = \left(\frac{1}{2}\mathbb{E}[\tilde{\boldsymbol{E}} \times \tilde{\boldsymbol{H}}^*] - \frac{1}{2}\mathbb{E}[\tilde{\boldsymbol{E}}] \times \mathbb{E}[\tilde{\boldsymbol{H}}^*]\right), \quad 1.8.7$$

which is termed the "incoherent Poynting vector." (Note that the multiplication by 2 preserves the 1/2 factor related to the definition of the time average Poynting vector, since $Var[a\tilde{X}] = a^2 Var[\tilde{X}]$.) Equations 1.8.6 and 1.8.7 make clear that the conservation of expected power and expected angular distribution of power cannot be derived directly from the mean field as the field fluctuations about the mean value play an important role in total power flow. Therefore, when considering the expected reflection, transmission, and absorption from a random film it is necessary to work with the field's second moment. This is unfortunate from the mathematical point of view, because $\mathbb{E}[\tilde{\boldsymbol{S}}]$ is usually substantially harder to calculate compared to $\mathbb{E}[\tilde{\boldsymbol{E}}]$. When the correlation length of particle positions is comparable or smaller than the particle's electromagnetic cross section, the fluctuations play an importing role in maintaining power conservation. From the order of scattering framework, field correlations can be viewed from the order of correlation.

Since power conservation occurs for every realization, an analogous conservation occurs for the expected power across all realizations. At the individual particle level this conservation is defined as,

$$\int_{\mho} dP_V \left(\tilde{C}_{inc,a} + \tilde{C}_{a,inc} = \tilde{C}_{abs,a} + \tilde{C}_{a,a} - \sum_{b\neq a}^{N}\left(\tilde{C}_{a,b} + \tilde{C}_{b,a}\right)\right). \quad 1.8.8$$

Similarly, the total film-level/macroscopic expected power conservation can be built from the particle-level,

$$\begin{aligned}&\int_{\mho} dP_V \left(\tilde{C}_{ext} = \tilde{C}_{sca} + \tilde{C}_{abs}\right)\\ &= \int_{\mho} dP_V \left(\sum_{a}^{N}\left(\tilde{C}_{inc,a} + \tilde{C}_{a,inc} = \tilde{C}_{abs,a} + \tilde{C}_{a,a} - \sum_{b\neq a}^{N}\left(\tilde{C}_{a,b} + \tilde{C}_{b,a}\right)\right)\right).\end{aligned} \quad 1.8.9$$

Following the same arguments, the expected angle-resolved power flow in the far field is,

$$\int_{\mho} dP_V \left(\frac{d\widetilde{W}_{sca}}{d\Omega} \xrightarrow{r\to\infty} \sqrt{\frac{\epsilon}{\mu}} \sum_a^N \left(\left| \widetilde{\boldsymbol{E}}_{sca,a}^{\infty} \right|^2 + 2 \sum_{b\neq a}^N \Re\left[\widetilde{\boldsymbol{E}}_{sca,a}^{\infty} \widetilde{\boldsymbol{E}}_{sca,b}^{\infty *} \right] \right) \right), \tag{1.8.10}$$

$$\int_{\mho} dP_V \left(\frac{d\widetilde{W}_{ext}}{d\Omega} \xrightarrow{r\to\infty} \frac{1}{2} \Re \left[\sqrt{\frac{\epsilon}{\mu}} \frac{4\pi}{ik} \boldsymbol{E}_{inc}^{*} \cdot \widetilde{\boldsymbol{E}}_{sca}^{\infty} \right] \delta(\boldsymbol{k} - \boldsymbol{k}_{inc}) \delta(\hat{\boldsymbol{e}} - \hat{\boldsymbol{e}}_{inc}) \right). \tag{1.8.11}$$

Equation 1.8.11 shows that, on average, the expected extinction can be derived purely from the knowledge of only the coherent field. Alternatively stated, only the coherent field removes power from the incident field, on average. Therefore, at the film-level, the field fluctuations do not dictate the expected power extracted from the incident field. Instead, the fluctuations play a role in defining the proportion of the removed power going into either expected absorption or scattering.

For any configuration of an infinite film, the film-level power must be conserved, $(W_{sca} + W_{abs})/W_{inc} \leq 1$. Also, the absorbed and scattered power at the particle-level is always positive, meaning

$$\frac{1}{\int d^2\boldsymbol{\rho}} \sum_a^N \left(C_{mix-inc,a} - C_{mix-sca,a} \; = C_{sca-i,a} + C_{abs,a} \right) \leq 1 \tag{1.8.12}$$

is a monotonic and bounded sequence on each side of the equality. From the monotonic convergence theorem, the sum and expectation can be interchanged,

$$\begin{aligned} &\int_{\mho} dP_V \left(\sum_a^N \left(\tilde{C}_{inc,a} + \tilde{C}_{a,inc} = \tilde{C}_{abs,a} + \tilde{C}_{a,a} - \sum_{b\neq a}^N \left(\tilde{C}_{a,b} + \tilde{C}_{b,a} \right) \right) \right) \\ &= \sum_a^N \int_{\mho} dP_V \left(\tilde{C}_{inc,a} + \tilde{C}_{a,inc} = \tilde{C}_{abs,a} + \tilde{C}_{a,a} - \sum_{b\neq a}^N \left(\tilde{C}_{a,b} + \tilde{C}_{b,a} \right) \right). \end{aligned} \tag{1.8.13}$$

Since $d\,W_{sca}/d\Omega \xrightarrow{r\to\infty} \sqrt{\epsilon/\mu} |\boldsymbol{E}_{sca}^{\infty}|^2 \leq \; W_{sca}$, then by the dominated convergence theorem the sum and expectation can also be interchanged for the angle resolved scattered power,

$$\begin{aligned} &\int_{\mho} dP_V \sum_a^N \left(\left| \widetilde{\boldsymbol{E}}_{sca,a}^{\infty} \right|^2 + \sum_{b\neq a}^N \Re\left[\widetilde{\boldsymbol{E}}_{sca,a}^{\infty} \widetilde{\boldsymbol{E}}_{sca,b}^{\infty *} \right] \right) \\ &= \sum_a^N \int_{\mho} dP_V \left(\left| \widetilde{\boldsymbol{E}}_{sca,a}^{\infty} \right|^2 + \sum_{b\neq a}^N \Re\left[\widetilde{\boldsymbol{E}}_{sca,a}^{\infty} \widetilde{\boldsymbol{E}}_{sca,b}^{\infty *} \right] \right). \end{aligned} \tag{1.8.14}$$

Similarly, since $|\boldsymbol{E}_{sca}^{\infty}|^2 \geq \boldsymbol{E}_{sca}^{\infty}$, the same is true for the extinction. The interchange of summation and expectation make clear that film-level field moments can be derived from the

particle-level field moments then summing all particles. Hence the paradigm of particle-level constructing the film-level applies to the moments as well.

The expected reflection, transmission, and absorption is dictated by the behavior of both the coherent and incoherent field. This necessitates an understanding of both order of scattering and order of correlation. Fortunately, film-level expectations can be constructed from particle-level expectations, so the study of statistical behavior at the particle-level can inform the larger collective.

1.9 SAMPLING STRATEGY

"Essentially, all models are wrong, but some are useful."

- George Box, Science and Statistics, 1976

It is a daunting task to analytically study the moments of fields from random potentials. Order of scattering analysis shows that the expected field is described by an infinite hierarchy of conditional distributions. The expected power flow adds to the complexity a larger and more complicated infinite hierarchy of correlates. Unfortunately, there is no known analytic form for the packing distribution of arbitrary particles in a plane. This is true even if all particles are simply spheres of different radii. For truly analytic study, authors usually constrain the potential to a subspace where approximate formulas of the distribution can be used. With the exception of examples such as well separated particles and quasi-crystallinity, restrictions of this form are still often not descriptive enough for analytic progress. Authors then resort to constraining the field distribution/correlations directly. Clearly the necessity to put the cart in front of the horse in this way requires strong justification and can result in a lack of insight as to what underlying potential actually produces such a field constraint. Nonetheless, much work has been devoted to determining solutions to these problems. For example, the Twersky approximation of non-self-referencing interactions, Maxwell-Garnett, and Bruggeman approximations have been widely used[18]. The goal of these works is to simplify the expression of the structure factor and the local field a particle experiences by a priori neglecting perceived negligible correction terms in the order of scattering/correlation analysis[18].

As stated in the introduction to this chapter, this work is concerned with the electromagnetic response of random monolayers of particles not already well described by prior models. Furthermore, the methodology favors model accuracy and fabrication insight over analytic and/or computational simplicity. Recall that, the moments of interest form an infinite hierarchy that must be simplified through a truncation assumption. The ansatz used in this work is that the moments of the local field for each particle are primarily affected only by the behavior of their local neighbors and that this dependence can be well described by a suitable Monte Carlo scheme. Each Monte Carlo sample is of a finite sized but sufficiently large random distribution of particles such that the center particles of interest "feel" as if they are in an infinite film. Since the finite film problem can be solved exactly, this enables the ability to exactly capture the effect of arbitrary particle shape, material, and position distributions in local regions. In essence, this quasi-analytic framework can study particle distributions that do not have an analytic form

because it offloads the complexity to the computer, which can realize the distribution through a sequence of samples.

Justifying the Form of a Sample

The first assumption of this method is that the moments of the local field inside an infinite film can be well described by moments sampled in the inner region of a large finite film. From the particle point of view, this assumption can be well justified as long as the film is sufficiently sized and correlation lengths are finite. In this case, any two scattered fields impinging on a particle that originate outside of the correlation length have essentially random relative phase. The power of each scattered field decays/spreads as the square of the distance, but the number of additional particles is linear with distance. Therefore, the contribution of scattered fields outside of the correlation zone falls off as $O(\rho^{-1})$. For order of scattering terms beyond single pass scattering, the decay rate is likely even faster as added absorption and/or longer path lengths occur for each additional scattering event. To solidify nomenclature, particles in the zone of non-negligible contribution are said to exist in the "non-negligible zone." Of course, this zone is defined relative to a particle of interest.

One point of concern is that finite size films suffer from diffraction at the edges. Clearly this is an effect not seen in infinite films. Unfortunately, this means that particles close to the edge can have dramatically different scattering behavior compared to internal particles. This is because the scattered fields of the edge particles are primarily responsible for constructing the edge diffraction effect. Since edge particles have their own non-negligible zone, the diffraction effect can appreciably alter neighboring particles within the outer annulus defining the edge particle non-negligible zone. To ensure that the diffraction effect does not alter simulations for the particle of interest deep inside the film, it is necessary that this particle's non-negligible zone not overlap the non-negligible zone of the edge particles. This creates a further size constraint. In general, it may be hard to predict the correct finite size for Monte Carlo simulations and this dissertation makes no attempts in defining bounds or formulas for such a size. After all, it is always possible to increase simulation size progressively until convergence is met.

The reliance on finite sized films also creates another conceptual hurdle. How to deal with the sum of all particles? Clearly this is an important requirement as it connects particle-level to film-level conservation quantities. In the prior section, film-level conservation expressions for the field moments were derived from film-level conservation of each realization, which were, in-tern, derived from particle-level conservation for each particle in each realization. At the onset it is clear that the Monte Carlo method does not have access to film-level conservation relations

for individual realizations, because it does not simulate infinite films. The ansatz is that particle-level quantiles are only locally affected and that therefore film-level field moments can be derived directly from estimating this local behavior. So, for each Monte Carlo sample, how many particles should be used in the estimate? One method would be to simply add all the particles in each finite film. This has the clear benefit that all finite film-level conservation quantities are correct for each realization and, therefore, also for the derived moments. Though, the interpretation of these moments as surrogates for an infinite film may not hold. For very large Monte Carlo samples the area fraction of the diffraction annulus reduces as $O(r^{-1})$. So, it is feasible that there exists a large enough size that particles strongly altered by diffraction phenomena become negligible in the summation of all particles. Another method would be to exclude the problematic particles in the final summation of "all" particles. This has the clear benefit of not needing to out-compete the contributions from the edges, but film-level conservation quantities no longer hold for each individual realization. Clearly any conservation quantity reliant on adding all particles will not hold if you do not add all particles. Since the inaccuracy of this method also comes from the contribution of the edge annulus, similar $O(r^{-1})$ scaling arguments in the correction term can be made. When comparing the two approaches, the exclusion method is the clear conceptual winner. From the onset the Monte Carlo method does not propose to provide film-level conserve quantities of individual realizations for an infinite film. The method only seeks to well estimate the moments from studying local field behavior. Adding all the particles of a finite film preserves the finite film-level conservation relations for each instance, but this is not the conservation of interest. Furthermore, this occurs at the expense of accuracy in our desired estimates.

The exclusion method also has a clear benefit in terms of computational efficiency. In the Monte Carlo framework information about the system increases from either increasing film size or the number of Monte Carlo samples, N_{MC}. A film of N_p particles produce a $2N_pL(L+2)$ large system of equations, where L is the sum of all quantum numbers and harmonic type. For direct methods such as Gaussian elimination, the computational cost is $\propto \left(2N_pL(L+2)\right)^3$. In the limit of large film size, the information gain to computational cost ratio is $\propto O\left(1/N_p^2\right)$. Clearly there are diminishing returns in increasing film size, and it is better to increase sample number, which is $O(1)$. The method which counts edge particles fundamentally relies on large N_p for model accuracy. This is a diametric opposition to computational cost. The accuracy of the exclusion method does not dependent on a large N_p to satisfy accuracy requirements. This is because it only records the particles that are accurate for any given N_p. In this case, the smallest possible film size is one where only the center particle has a non-negligible region that does not overlap the edge non-negligible region.

Of course, larger films are likely best suited for indirect methods, which can have a more favorable computational cost for large film sizes, given the method/preconditioner. In general, the coupled system of equations is a fully populated matrix and particle resonances can result in a poor condition number. Therefore, it is not straightforward to estimate computational cost or determine what iterative method is best to use. In literature, the biconjugate gradient method has been among the best performing[4]. In this dissertation it was found that the exclusion method keeping only the center particle represents a matrix problem which takes seconds to solve using direct methods, without the headache of tuning parameters necessary of an iterative method.

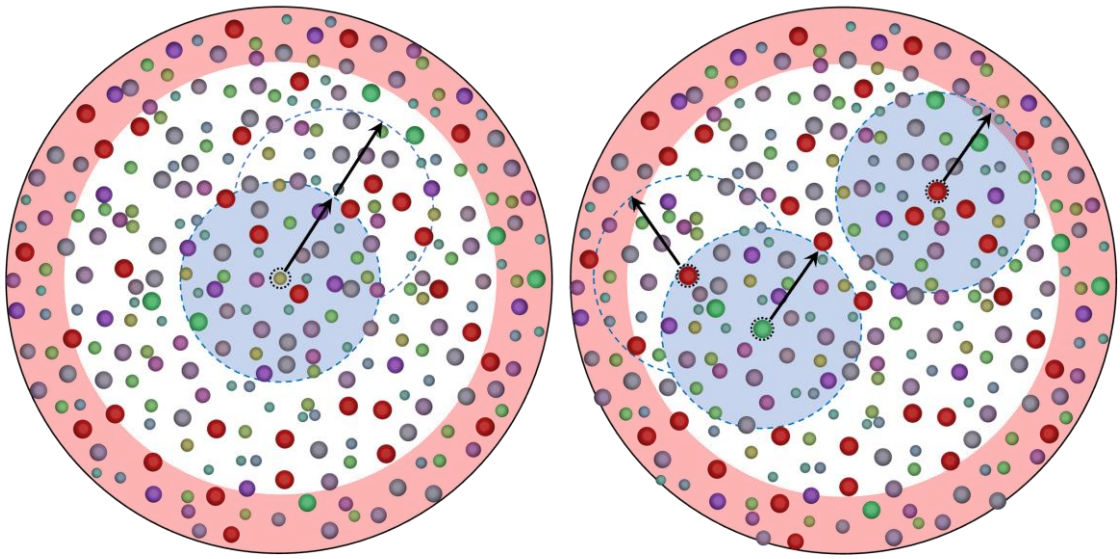

Figure 1.9.1. Examples of sampling methods. (Left) Example of a center observation particle (dotted black circle) where the non-negligible zone (blue shaded region) does not overlap with the diffraction zone annulus (red shaded region). Furthermore, the non-negligible zone of all particles inside the observation particle's non-negligible zone are also outside of the diffraction annulus. (Right) Examples of particles that do not satisfy the requirement of a local field which approximates that of an infinite film. In the lower left corner, the green observation particle is dependent on a red particle whose non-negligible zone overlaps with the diffraction annulus. In the upper right corner, the red observation particle's non-negligible zone directly overlaps with the diffraction annulus.

Deriving the Monte Carlo Field Moments

Recall, the coherent field arises from the expectation of the total scattered field, which is the sum of the expected scattered field from each particle,

$$\mathbb{E}\left[\widetilde{\boldsymbol{E}}_{sca,a}\right] = \mathbb{E}\left[\widetilde{\boldsymbol{\Psi}}(\boldsymbol{r}-\widetilde{\boldsymbol{\rho}}_a)\mathbb{E}\left[\widetilde{\mathbb{T}}_a\tilde{c}_{loc,a}|\widetilde{\boldsymbol{\rho}}_a=\boldsymbol{\rho}_a,\widetilde{\mathbb{T}}_a=\mathbb{T}_a\right]\right]. \tag{1.9.1}$$

Equation 1.9.1 uses the law of total expectation to decompose the problem to first conditioning on known properties for particle a. Given that particle a's type and location are known, the inner expectation in equation 1.9.1 is an expectation of the surrounding environment. It is this inner conditional that is to be estimated using Monte Carlo. The outer expectation then weighs this field for all possible particle types and locations. Since the statistical properties of the potential are translation invariant and the incident field is translation invariant up to a phase shift, the expected scattered field is translation invariant up to the phase shift of the incident field. Let the Monte Carlo expectation of different configurations of neighboring particles be denoted as

$$\begin{aligned}&\mathbb{E}\left[\widetilde{\mathbb{T}}_a\tilde{c}_{loc,a}|\widetilde{\boldsymbol{\rho}}_a=\boldsymbol{\rho}_a,\widetilde{\mathbb{T}}_a=\mathbb{T}_a\right] = e^{i\boldsymbol{k}_{inc}\cdot\boldsymbol{\rho}_a}\mathbb{E}\left[\mathbb{T}_a\tilde{c}_{loc,a}|\widetilde{\boldsymbol{\rho}}_a=\boldsymbol{0},\tilde{\mathcal{T}}_a=\mathcal{T}_a\right]\\ &\approx e^{i\boldsymbol{k}_{inc}\cdot\boldsymbol{\rho}_a}\frac{1}{N_{MC}}\sum^{N_{MC}}c_a^{MC}(\mathcal{T}_a)\equiv e^{i\boldsymbol{k}_{inc}\cdot\boldsymbol{\rho}_a}\overline{c_a^{MC}}(\mathcal{T}_a),\end{aligned} \tag{1.9.2}$$

where $c_a^{MC}(\mathcal{T}_a)$ is the scattering coefficient of particle a, measured from a finite sized but sufficiently large sample simulation generated by randomly placing particles around particle a. In each sample, particle a is centered at the origin and has type $\mathcal{T}_a \Leftrightarrow \mathbb{T}_a$. The expected value of the scattering coefficient is then estimated by the arithmetic mean, $\overline{c_a^{MC}}$, of N_{MC} samples. Choosing $\widetilde{\boldsymbol{\rho}}_a = \boldsymbol{0}$ has implications to Monte Carlo sampling because aligning particle a to the global origin writes the entire system of interaction equations relative to particle a automatically, including the incident field. It is then only necessary to repeat the Monte Carlo process for different $\mathcal{T}_a$, as particle a's type will change the local scattering behavior of neighboring particles. Since each sample is independently generated the law of large numbers guarantees convergence as $N_{MC} \to \infty$.

After estimating the expected local field, the expected scattered field can be decoupled into two independent terms,

$$\mathbb{E}\left[\widetilde{\boldsymbol{E}}_{sca,a}\right] \approx \mathbb{E}\left[\boldsymbol{\Psi}(\boldsymbol{r}-\boldsymbol{\rho}_a)e^{i\boldsymbol{k}_{inc}\cdot\boldsymbol{\rho}_a}\right]\mathbb{E}\left[\overline{c_a^{MC}}(\mathcal{T}_a)\right], \tag{1.9.3}$$

where $\mathbb{E}\left[\boldsymbol{\Psi}(\boldsymbol{r}-\boldsymbol{\rho}_a)e^{i\boldsymbol{k}_{inc}\cdot\boldsymbol{\rho}_a}\right]$ and $\mathbb{E}\left[\overline{c_a^{MC}}(\mathcal{T}_a)\right]$ are expectations solely over particle position, $\boldsymbol{\rho}_a$, and particle type, $\mathcal{T}_a$, respectively. The expectation over particle type will again be found through Monte Carlo since the choice of particle type will change the local field behavior. The type estimation can be written as

$$\begin{aligned}&\mathbb{E}\left[\overline{c_a^{MC}}(\mathcal{T}_a)\right]\\ &\approx \textstyle\sum^{|\mathcal{T}|} P(\mathcal{T}=\mathcal{T}_a)\overline{c_a^{MC}}(\mathcal{T}_a) \equiv \overline{c_a^{MC}}\ ,\end{aligned} \tag{1.9.4}$$

where $P(\mathcal{T}=\mathcal{T}_a)$ is the probability of particle a being type $\mathcal{T}_a$ and is a measurable characteristic of the film.

It is now necessary to address $\mathbb{E}\left[\boldsymbol{\Psi}(\boldsymbol{r}-\boldsymbol{\rho}_a)e^{i\boldsymbol{k}_{inc}\cdot\boldsymbol{\rho}_a}\right]$, which can be calculated directly due to the translation invariance of the potential. Since the expected particle location, $\boldsymbol{\rho}_a$, involves an integration over the particle plane, it is easiest to first transform the Mie harmonics into a plane wave representation,

$$\boldsymbol{\Psi}_l(k\boldsymbol{r}) = \tfrac{1}{2\pi}\textstyle\sum_{q=0}^{1}\int \frac{\partial^2\boldsymbol{k}_\parallel}{k|k_z^{\pm}|} g_{l,q}^{far}\left(\widehat{\boldsymbol{k}}\right)\widehat{\boldsymbol{e}}_q\left(\widehat{\boldsymbol{k}}\right)e^{i\boldsymbol{k}^{\pm}\cdot\boldsymbol{r}}\ . \tag{1.9.5}$$

The integration $d^2\boldsymbol{k}_\parallel = k_\parallel dk_\parallel d\alpha$ is over the wave vector components parallel to the particle plane, where the wave vector is expressed in cylindrical coordinates as $\boldsymbol{k} = k_\parallel\hat{\boldsymbol{e}}_\rho + \alpha\hat{\boldsymbol{e}}_\phi \pm k_z\hat{\boldsymbol{e}}_z$. In general, the integration includes the evanescent fields and the $\pm$ superscript denotes the choice in the root for $k_z = \pm\sqrt{k^2-k_\parallel^2}$. Since the Mie harmonics emanate from the particle, they admit two separate plane wave expansions. The first expansion, $+$, is used in the transmission hemisphere above the particle plane, $r_z > h/2$. In this region the $+$ root guarantees traveling fields propagate and evanescent fields decay away from the film in the upward direction. The second expansion, $-$, is used in the reflection hemisphere below the particle plane, $r_z < -h/2$. The $-$ root guarantees traveling fields propagate and evanescent fields decay away from the film in the downward direction. $g_{l,q}^{far}\left(\widehat{\boldsymbol{k}}\right) = \boldsymbol{\psi}_l^{far}\left(\widehat{\boldsymbol{k}}\right)\cdot\hat{\boldsymbol{e}}_q\left(\widehat{\boldsymbol{k}}\right)$ is the projection of the vector Mie harmonic's angular dependence onto the transverse magnetic (TM), $\hat{\boldsymbol{e}}_0$, and transverse electric (TE), $\hat{\boldsymbol{e}}_1$, vector directions defined with respect to the particle plane.

More information on the plane wave representation of Mie harmonics can be found in section 1.15, appendix F.

Inserting the plane wave representation into the position expectation shows that the expected particle position is equivalent to the Fourier transform, $\mathcal{F}$, of the phase shifted particle position distribution,

$$\begin{aligned}&\mathbb{E}\left[\boldsymbol{\Psi}(\boldsymbol{r}-\boldsymbol{\rho}_a)e^{i\boldsymbol{k}_{inc}\cdot\boldsymbol{\rho}_a}\right] \to \mathcal{F}^{\pm}\left[P(\boldsymbol{\rho}_a)e^{i\boldsymbol{k}_{inc}\cdot\boldsymbol{\rho}_a}\right]\\&= \frac{i}{2\pi}\sum_q \int \frac{\partial^2\boldsymbol{k}_{\parallel}}{k|k_z^{\pm}|}\left(\boldsymbol{\Psi}^{far}\left(\widehat{\boldsymbol{k}}\right)\cdot\hat{\boldsymbol{e}}_q\left(\widehat{\boldsymbol{k}}\right)\right)\hat{\boldsymbol{e}}_q\left(\widehat{\boldsymbol{k}}\right)e^{i\boldsymbol{k}^{\pm}\cdot\boldsymbol{r}}\int P(\boldsymbol{\rho}_a)\,e^{-i(\boldsymbol{k}_{\parallel}-\boldsymbol{k}_{inc,\parallel})\cdot\boldsymbol{\rho}_a}.\end{aligned} \tag{1.9.6}$$

Given that there is no bias in the potential to place particle a at a particular location, the probability of finding particle a in any location is uniform, $P(\boldsymbol{\rho}_a) = 1/\int d^2\boldsymbol{\rho}$, when no other particles have yet been constrained. Therefore,

$$\mathbb{E}\left[\widetilde{\boldsymbol{E}}_{sca,a}\right] \approx \frac{1}{\int d^2\boldsymbol{\rho}}\frac{1}{\cos\theta_{inc}}\frac{2\pi}{k^2}\sum_q E^{\pm}_{coh,a}\hat{\boldsymbol{e}}_q\left(\widehat{\boldsymbol{k}}^{\pm}_{inc}\right)e^{i\boldsymbol{k}^{\pm}_{inc}\cdot\boldsymbol{r}} \tag{1.9.7}$$

where $\boldsymbol{k}^{\pm}_{inc} = \boldsymbol{k}_{inc,\parallel} \pm k_z$ and $E^{\pm}_{coh,a} = \left(\boldsymbol{\Psi}^{far}\left(\widehat{\boldsymbol{k}}^{\pm}_{inc}\right)\cdot\hat{\boldsymbol{e}}_q\left(\widehat{\boldsymbol{k}}^{\pm}_{inc}\right)\right)\overline{c_a^{MC}}$. Equation 1.9.7 shows that in the transmission hemisphere, the particle's coherent field propagates as a plane wave in the same direction as the incident field. In the reflection hemisphere the propagation plane wave is in the reverse direction as the incident field. The amplitude and phase of the coherent field is defined by $E^{\pm}_{coh,a}$. Therefore, the expected scattered field actually behaves as a coherent field. This is a satisfying consistency check to the interpretation of the coherent field as discussed in the prior section.

Equation 1.9.7 can be written in a form analogous to the algebraic repackaging used to derive the probabilistic interpretation of a film instance. Letting

$$\begin{aligned}&\overline{c_a^{MC}}\\&= \left(\frac{\sum_a^N A_a}{\sum_a^N A_a}\right)\sum^{|\mathcal{T}|}\left(\frac{A_{\mathcal{T}_a}}{A_{\mathcal{T}_a}}\right)P(\mathcal{T}=\mathcal{T}_a)\overline{c_a^{MC}}(\mathcal{T}_a)\\&= \left(\sum_a^N A_a\right)\sum^{|\mathcal{T}|} w_{\mathcal{T}_a}\frac{\overline{c_a^{MC}}(\mathcal{T}_a)}{A_{\mathcal{T}_a}},\end{aligned} \tag{1.9.8}$$

where $w_{\mathcal{T}_a} = \left(\frac{A_{\mathcal{T}_a}}{\sum_a^N A_a}\right) P(\mathcal{T} = \mathcal{T}_a)$ is the area probability weight defined in section 1.6. $\overline{c_a^{MC}}(\mathcal{T}_a)/A_{\mathcal{T}_a}$ is the area normalized coefficient, defined now in preparation for later expressing power flows in terms of particle-level efficiencies. $ff = \sum_a^N A_a / \int d^2\boldsymbol{\rho}$ is the fraction of the space filled with particles. The Monte Carlo procedure is shown in figure 1.9.2. It will also be shown later that the samples from this procedure can also be used to calculate the total power.

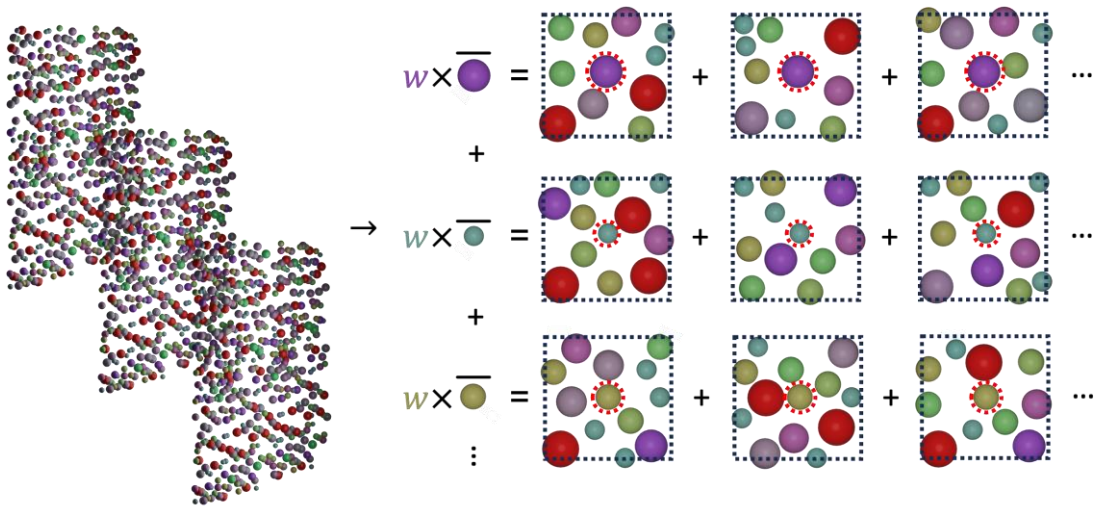

Figure 1.9.2. Schematic representation of the conversion from an expectation across different realizations of random films (left) to a Monte Carlo sampling scheme of individual particle types (right). Different particle types existing within the film distribution are distinguished as spheres of different size and color. The field moments of each particle type are estimated as an ensemble average of film realizations centered around the particle type of interest (red dashed circle). The estimation is then multiplied by a weight, which is the proportion of the filling fraction that is filled by that type of particle.

Under this algebraic repackaging, the coherent scattered field using the Monte Carlo sampling scheme is

$$\mathbb{E}\left[\widetilde{\boldsymbol{E}}_{sca,a}\right] \approx \frac{ff}{\cos\theta_{inc}} \frac{2\pi}{k^2} \sum_q g_{l,q}^{far}\left(\hat{\boldsymbol{k}}_{inc}^{\pm}\right) \hat{\boldsymbol{e}}_q\left(\hat{\boldsymbol{k}}_{inc}^{\pm}\right) e^{i\boldsymbol{k}_{inc}^{\pm}\cdot\boldsymbol{r}} \sum^{|\mathcal{T}|} w_{\mathcal{T}_a} \frac{\overline{c_a^{MC}}(\mathcal{T}_a)}{A_{\mathcal{T}_a}}, \qquad 1.9.9$$

where $\sum^{|\mathcal{T}|} w_{\mathcal{T}_a} \overline{c_a^{MC}}(\mathcal{T}_a)/A_{\mathcal{T}_a} \approx \mathbb{E}\left[\mathbb{E}[c_a/A_a|\mathcal{T}]\right]$.

For the sake of completeness deriving the coherent field is important as a consistency check. Though the primary interest is controlling the total power flow and for this it is necessary only to calculate the total absorption and scattered power in the reflection hemisphere. In deriving

the total scattered power, it is simpler to first derive the conditions for two arbitrary fields. From this the total can be constructed. From section 1.11, appendix B the expected power through a differential area resulting from the interference of two arbitrary scattered fields can be written as

$$\begin{aligned}&\mathbb{E}[dW_{ab}] = \tfrac{1}{2}\Re\left[d\boldsymbol{A}\cdot\mathbb{E}[\boldsymbol{E}_a\times\boldsymbol{H}_b^*]\right]\\&= \Re\, tr\left[\mathbb{E}\left[d\mathbb{W}(\boldsymbol{r}-\tilde{\boldsymbol{\rho}}_a)\,\mathbb{E}[\tilde{\mathbb{c}}_{ab}|\tilde{\boldsymbol{\rho}}_a=\boldsymbol{\rho}_a,\tilde{\mathcal{T}}_a=\mathcal{T}_a]\right]\right],\end{aligned} \tag{1.9.10}$$

where

$$\mathbb{c}_{ab} = \begin{cases} c_a\otimes c_a^* & a=b\\ c_a\otimes(\mathbb{J}(\boldsymbol{\rho}_{ab})c_b)^* + (\mathbb{J}(\boldsymbol{\rho}_{ab})c_b)\otimes c_a^* & a\neq b.\end{cases} \tag{1.9.11}$$

Recall from section 1.6 that $\mathbb{c}_{ab}\in\mathbb{C}^{L\times L}$ is a matrix resulting from the outer product of the two scattering coefficient vectors. Each element, $\mathbb{c}_{ab_{l,l'}} = c^{t}_{a,n,m}c^{t'*}_{b,n'm'}$, defines an interference combination from the two fields in coefficient space. $d\mathbb{W}(\boldsymbol{r}-\tilde{\boldsymbol{\rho}}_a)\in\mathbb{C}^{L\times L}$ is a matrix that maps the interference combinations in coefficient space to real space. Each element in $d\mathbb{W}$ takes the form

$$d\mathbb{W}_{ll'}(\boldsymbol{r}) = \tfrac{1}{2}iYd\boldsymbol{A}\cdot\left(\boldsymbol{\Psi}_l(\boldsymbol{r})\times\nabla\times\boldsymbol{\Psi}^*_{l'}(\boldsymbol{r})\right), \tag{1.9.12}$$

where $d\boldsymbol{A} = d^2\boldsymbol{r}\,\hat{\boldsymbol{n}}$ is the differential surface area under consideration with outward pointing normal, $\hat{\boldsymbol{n}}$.

Equation 1.9.10 again uses the law of total expectation to decompose the problem to first conditioning on known properties for particle $\boldsymbol{a}$. Given that particle $\boldsymbol{a}$'s type and location are known, the inner expectation in equation 1.9.10 is again an expectation of the surrounding environment to be estimated using Monte Carlo. Since the statistical properties of the potential are translation invariant, this inner conditional is also translation invariant. This is sensible as the properties of the surrounding scattered fields onto particle $\boldsymbol{a}$'s field should only depend on relative distances to particle $\boldsymbol{a}$. Correspondingly,

$$\begin{aligned}&\mathbb{E}[\mathbb{c}_{ab}|\tilde{\boldsymbol{\rho}}_a=\boldsymbol{\rho}_a,\tilde{\mathcal{T}}_a=\mathcal{T}_a]\\&=\mathbb{E}[\mathbb{c}_{ab}|\tilde{\boldsymbol{\rho}}_a=\boldsymbol{0},\tilde{\mathcal{T}}_a=\mathcal{T}_a].\end{aligned} \tag{1.9.13}$$

Choosing $\widetilde{\boldsymbol{\rho}}_a = \mathbf{0}$ has implications to Monte Carlo sampling because aligning particle a to the global origin writes the entire system of interaction equations relative to particle a automatically, including the incident field. Hence, the same samples used for the coherent field also provide all information to calculate the multiply scattered coefficient matrix. It is again only necessary to repeat the Monte Carlo process for different $\mathcal{T}_a$, as particle a's type changes the local scattering behavior of neighboring particles. Let the Monte Carlo expectation of different configurations of neighboring particles be denoted as

$$\begin{aligned}&\mathbb{E}[\mathbb{c}_{ab}|\widetilde{\boldsymbol{\rho}}_a = \mathbf{0}, \tilde{\mathcal{T}}_a = \mathcal{T}_a] \\ &\approx \tfrac{1}{N_{MC}} \sum^{N_{MC}} \mathbb{c}_{ab}^{MC}(\mathcal{T}_a) \equiv \overline{\mathbb{c}_{ab}^{MC}}(\mathcal{T}_a)\end{aligned} \qquad 1.9.14$$

where $\mathbb{c}_{ab}^{MC}(\mathcal{T}_a)$ is a finite sized but sufficiently large interference matrix calculated from the same samples as used for the incident field. I.e., randomly placing particles around particle a, which is centered at the origin and having type $\mathcal{T}_a \Leftrightarrow \mathbb{T}_a$. The expected value of the interference coefficient matrix is then estimated by the arithmetic mean, $\overline{\mathbb{c}_{ab}^{MC}}$, of N_{MC} samples, where again the law of large numbers guarantees convergence as $N_{MC} \to \infty$.

As discussed above the inner expectation of equation 1.9.14 has no $\boldsymbol{\rho}_a$ dependence. Correspondingly, the estimation of the expected power flow can be decoupled into two independent terms,

$$\mathbb{E}[dW_{ab}] \approx \Re\, tr\big[\, \mathbb{E}[d\mathbb{W}(\boldsymbol{r} - \widetilde{\boldsymbol{\rho}}_a)]\, \mathbb{E}\big[\overline{\mathbb{c}_{ab}^{MC}}(\tilde{\mathcal{T}}_a)\big]\, \big], \qquad 1.9.15$$

where $\mathbb{E}[d\mathbb{W}(\boldsymbol{r} - \widetilde{\boldsymbol{\rho}}_a)]$ and $\mathbb{E}\big[\overline{\mathbb{c}_{ab}^{MC}}(\tilde{\mathcal{T}}_a)\big]$ are expectations solely over position, $\boldsymbol{\rho}_a$, and type, $\mathcal{T}_a$, respectively. The expectation over particle type is again be found through Monte Carlo,

$$\begin{aligned}&\mathbb{E}\big[\overline{\mathbb{c}_{ab}^{MC}}(\mathcal{T}_a)\big] \\ &\approx \sum^{|\mathcal{T}|} P(\mathcal{T} = \mathcal{T}_a)\mathbb{c}_{ab}^{MC}(\mathcal{T}_a) \equiv \overline{\mathbb{c}_{ab}^{MC}}\ .\end{aligned} \qquad 1.9.16$$

It is now necessary to address $\mathbb{E}[d\mathbb{W}(\boldsymbol{r} - \widetilde{\boldsymbol{\rho}}_a)]$, which can be calculated directly due to the translation invariance of the potential. Since the expected particle location, $\boldsymbol{\rho}_a$, involves an integration over the particle plane, it is again advantageous to express the Mie harmonics in a

plane wave representation. The power operator then admits an upper and lower hemisphere form, $d\mathbb{W}^{\pm}(\boldsymbol{r}-\widetilde{\boldsymbol{\rho}}_a)$, with elements,

$$d\mathbb{W}^{\pm}_{ll'}(\boldsymbol{r}-\widetilde{\boldsymbol{\rho}}_a) = \Re\tfrac{1}{2} iY \textstyle\sum_{q_a,q_b} \iint d^2\boldsymbol{k}_{a,b,\parallel}\, e^{i\left(\boldsymbol{k}_a^{\pm}-\boldsymbol{k}_b^{\pm}\right)\cdot(\boldsymbol{r}-\widetilde{\boldsymbol{\rho}}_a)} g_{lq_a}(\boldsymbol{k}_a^{\pm}) g^{*}_{l'q_b}(\boldsymbol{k}_b^{\pm}) dA_{q_a,q_b}(\boldsymbol{k}_a^{\pm},\boldsymbol{k}_b^{\pm}). \quad 1.9.17$$

$d^2\boldsymbol{k}_{a,b,\parallel} = d^2\boldsymbol{k}_{a,\parallel} d^2\boldsymbol{k}_{b,\parallel}$ is a shorthand notation for two double integrals over the wave vector components parallel to the particle plane. $g_{lq}(\boldsymbol{k}_a^{\pm}) = \boldsymbol{\psi}_{far,l}(\widehat{\boldsymbol{k}})\cdot\hat{\boldsymbol{e}}_q(\widehat{\boldsymbol{k}})/2\pi k|k_z^{\pm}|$ is the plane wave spectral map. $dA = d^2\boldsymbol{\rho}\,\hat{\boldsymbol{z}}^{\pm}\cdot\left(\hat{\boldsymbol{e}}_{q_a}(\boldsymbol{k}_a^{\pm})\times\left(\boldsymbol{k}_b^{\pm}\times\hat{\boldsymbol{e}}_{q_b}(\boldsymbol{k}_b^{\pm})\right)^{*}\right)$ defines the component of the field normal to the differential area element. Equation 1.9.17 makes clear that the expected particle position is equivalent to a form of Fourier transform, $\mathcal{F}$, over the particle position distribution,

$$\mathbb{E}[d\mathbb{W}(\boldsymbol{r}-\widetilde{\boldsymbol{\rho}}_a)] \to \mathcal{F}^{\pm}[P(\boldsymbol{\rho}_a)] = \iint d^2\boldsymbol{\rho}_a\, P(\widetilde{\boldsymbol{\rho}}_a=\boldsymbol{\rho}_a)\, e^{-i\left(\boldsymbol{k}^{\pm}_{\parallel,a}-\boldsymbol{k}^{\pm}_{\parallel,b}\right)\cdot\boldsymbol{\rho}_a} = (2\pi)^2\,\delta^2\left(\boldsymbol{k}_{a,\parallel}-\boldsymbol{k}_{b,\parallel}\right)/\int d^2\boldsymbol{\rho}. \quad 1.9.18$$

The second equality is derived given that there is no bias in the potential to place particle $\boldsymbol{a}$ at a particular location. Furthermore, since both particle $\boldsymbol{a}$ and $\boldsymbol{b}$ emanate from the film, they use the same choice for the $k_z^{\pm}$ root when integrating the plane above or below the particle plane. Correspondingly, $\delta^2\left(\boldsymbol{k}_{a,\parallel}-\boldsymbol{k}_{b,\parallel}\right)$ can be replaced with a more stringent $\delta^3(\boldsymbol{k}_a-\boldsymbol{k}_b)$. Noting that $A_{q_a,q_b}(\boldsymbol{k}^{\pm},\boldsymbol{k}^{\pm}) = \delta_{q_a,q_b}k\left(\hat{\boldsymbol{z}}\cdot\widehat{\boldsymbol{k}}^{*\pm}\right)d^2\boldsymbol{\rho}$, then the elements in the power operator take the final simplified form,

$$\mathbb{E}\left[d\mathbb{W}^{\pm}_{ll'}(\boldsymbol{r}-\widetilde{\boldsymbol{\rho}}_a)\right] = \frac{iY}{2k}\frac{d^2\boldsymbol{\rho}}{\int d^2\boldsymbol{\rho}}\textstyle\sum_q \iint d^2\boldsymbol{k}_{\parallel}\left(\hat{\boldsymbol{z}}\cdot\widehat{\boldsymbol{k}}^{*}\right)\left(\boldsymbol{\psi}_{far,l}(\widehat{\boldsymbol{k}})\cdot\hat{\boldsymbol{e}}_q(\widehat{\boldsymbol{k}})\right)\left(\boldsymbol{\psi}_{far,l'}(\widehat{\boldsymbol{k}})\cdot\hat{\boldsymbol{e}}_q(\widehat{\boldsymbol{k}})\right)^{*}. \quad 1.9.19$$

Equation 1.9.19 states that when looking at all possible film realizations from a translation invariant potential using the Monte Carlo approach, the expected power flow is completely homogenized across the observation plane. Alternatively stated, any differential area $d^2\boldsymbol{\rho}$ in the observation plane contains the same expected power flow as its neighbor. This is in contrast to ordered systems such as a periodic grating that can have clearly defined grating lobes. Note that this result does not preclude phenomena such as speckle, since speckle is a coherence occurring within a specific film instance. If the system is translation invariant, then the expectation of all speckle patterns will produce a homogenized speckle-less blur.

Integrating the area-resolved expected power across the entire observation plane gives the total expected power through the plane. A quick comparison to the derivation in section 1.11, appendix B shows that integrating equation 1.9.19 over the plane gives the same expression as the power operator for a particle at the origin, $\int \mathbb{E}[d\mathbb{W}^{\pm}(\boldsymbol{r}-\tilde{\boldsymbol{\rho}}_a)] = \int d\mathbb{W}^{\pm}(\boldsymbol{r})$.

Now that the expected power flow in either hemisphere is solved between two arbitrary particles, the total film-level power flow is found by simply adding all contributions,

$$\frac{\mathbb{E}[W_{sca}^{\pm}]}{W_{inc}} \approx ff\ \Re\ tr\Big[\int d\mathbb{W}^{\pm}(\boldsymbol{r})\left(\overline{\mathbb{Q}_{aa}^{MC}} + \sum_{b\neq a}\overline{\mathbb{Q}_{ab}^{MC}}\right)\Big], \tag{1.9.20}$$

where again the same partitioning scheme found in section 1.6 can be used to write the ratio of total expected scattered to incident power as a function of the film's fill fraction and expected particle scattering efficiencies.

When adding the contribution from both the upper and lower hemisphere the orthogonality relations can be evoked to calculate the total power from coefficients alone, $\int d\mathbb{W}^{+} + d\mathbb{W}^{-} = \frac{1}{2}Y\frac{\pi}{k^2}\mathbb{I}$. Therefore, the total expected scattered power from the particle film is

$$\frac{\mathbb{E}[W_{sca}]}{W_{inc}} \approx ff\left(\overline{Q_{a,a}^{MC}} + \Re\left[\sum_{b\neq a}\overline{Q_{b,a}^{MC}}\right]\right), \tag{1.9.21}$$

where $\overline{Q_{a,a}^{MC}} = \frac{\pi}{A_a k^2}\overline{\left(c_a^{\dagger}c_a\right)^{MC}}$ and $\overline{Q_{b,a}^{MC}} = \frac{\pi}{A_a k^2}\overline{\left(c_a^{\dagger}\mathbb{J}^{ab}c_b\right)^{MC}}$ are the Monte Carlo expectations of both particle type and the local fields for that type. Inspection of equation 1.9.21 shows that it has the exact same form as the probabilistic interpretation of film-level behavior for an individual film instance, $ff\left(\mathbb{E}\left[Q_{a,a}\right] + \mathbb{E}\left[\sum_{b\neq a}Q_{b,a}\right]\right)$, derived in section 1.6. This is seen once you recall that the local behavior results in the $\mathbb{H}^{ab} \to \mathbb{J}^{ab}$ transition by exact cancelations in the individual instance derivation. The primary difference is then that true expectations are now replaced by Monte Carlo estimates of expectations.

Recall from section 1.6 that a particle's absorption can be calculated directly from the interplay of the particle's scattered field with its own local field. As long as the underlying potential characterizing the film is translation invariant, this equation contains no dependence on absolute position. Correspondingly, the Monte Carlo estimate of the expected film absorption is,

$$\frac{\mathbb{E}[W_{abs,a}]}{W_{inc}} = ff\mathbb{E}\left[\mathbb{E}\left[Q_{abs,a}|\tilde{\mathcal{T}} = \mathcal{T}_a\right]\right] \approx ff\sum^{|\mathcal{T}|} w_{\mathcal{T}_a}\overline{Q_{abs,a}^{MC}}(\mathcal{T}_a) \equiv ff\overline{Q_{abs,a}^{MC}} \quad 1.9.22$$

where $\overline{Q_{abs,a}^{MC}}(\mathcal{T}_a) = \frac{1}{N_{MC}}\sum^{N_{MC}}\frac{\pi}{A_a k^2}\Re\left[c_a^\dagger \mathbb{A}_a c_a\right](\mathcal{T}_a)$ is the arithmetic average of the absorption cross-section calculated for the observation particle, a, having type $\mathcal{T}_a$ and centered at the origin.

It is now possible to calculate the expected transmission, reflection, and absorption spectra from an arbitrary random film as

$$\mathbb{E}[Ref] \approx ff\ \Re\, tr\left[\int_{\theta=\frac{\pi}{2}}^{\pi}\int_{\phi=0}^{2\pi} d\mathbb{W}^-(\boldsymbol{r})\left(\overline{\mathbb{Q}_{aa}^{MC}} + \sum_{b\neq a}\overline{\mathbb{Q}_{ab}^{MC}}\right)\right]$$
$$\mathbb{E}[Abs] \approx\ ff\overline{Q_{abs,a}^{MC}} \quad 1.9.23$$
$$\mathbb{E}[Trans] = 1 - \mathbb{E}[Ref] - \mathbb{E}[Abs].$$

Conceptual Connection to a Film Instance

The formula for the estimated expected reflection, absorption, and transmission spectra is nearly the exact same as the formula for a film instance, when repackaging variables under a probabilistic interpretation. The only difference between the two is the replacement of true expectations with expectation estimates using Monte Carlo. This connection is in fact a satisfying consistency check as long as the probabilistic interpretation of a film instance is properly meaningful. First, a single infinite film should be able to recover the statistical properties of the distribution of all possible films, then the self-averaging property holds. Second, correlation lengths should be finite, so that the local field contribution to any one particle is finite. The Monte Carlo sampling scheme which excludes the diffraction zone can then be interpreted as a process of bouncing around an infinite film instance randomly collecting sample particles. In this picture, the sampling scheme is analogous to a bounce procedure. Collecting only the origin particle is analogous to bouncing to a random location, define a local area, collecting a sample, then mark that area as collected for subsequent bounces. In principle it is necessary to actually sum of all particles in the film. Clearly then the bounce and sum strategy is only approximating the true behavior as it includes only a subset of particles. But, given that the sum of all particles is written in the form of an arithmetic average of particle efficiencies, then barring low probability locations that disproportionately influence the total film behavior, this process should converge to some level of acceptable accuracy given enough samples.

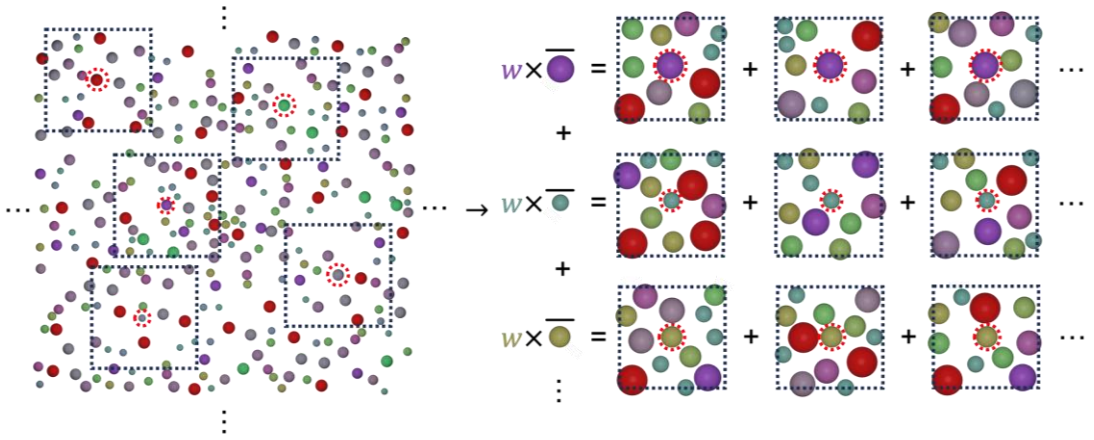

Figure 1.9.3. Schematic representation of the Monte Carlo sampling scheme (right) being an approximate for a bounce, sample, sum strategy (left) in an infinite random film.

Under suitable conditions, the Monte Carlo scheme can be viewed as a "bounce, sample, sum" strategy on a random film instance. This conceptual viewpoint helps to make clear the consequences of sampling and pitfalls of under sampling.

Consequences of Sampling

As discussed, the Monte Carlo method needs to address the conceptual hurdle of how to deal with the sum of all particles. The rationale of the method is that it is better to record only particles that experience a local field mimicking that of an infinite film. This avoids particles tarnished by the diffraction effect. Further considerations, such as the scaling of computational burden, justify more numerous smaller samples over larger ones. E.g., samples where only a single "observation particle" is recorded. After deriving the field moments under the Monte Carlo method and discussing the conceptual connection to the "bounce and sample" strategy of a film instance, the consequences of such a sampling approach can be discussed more concretely. Namely, the consequences inherent to using finite film approximates and under sampling them.

When deriving the expected film-level scattered power, the $\mathbb{J}^{ab}$ translation operator is used at the onset as this is the correct operator for deriving film-level behavior from fundamentals. For expected particle-level behavior the $\mathbb{H}^{ab}$ operator is used. Recall from equation 1.6.18 that the transition $\mathbb{H}^{ab} \rightarrow \mathbb{J}^{ab}$ requires adding every particle in the infinite film. The power transfer from $a \rightarrow b$ added with the transfer of $b \rightarrow a$ creates an exact cancelation of the notorious $c_a^\dagger i\mathbb{Y}^{ab}c_b$ term that exists at the particle-level but is absent at the film-level. Section 1.8 proved that the expectation of film configurations and summation of all particles can be interchanged because the power is exactly balanced in every realization. Therefore, expected film-level power can be derived from expected particle-level power analogous to how film-level power can be derived from particle-level power for an individual realization. As discussed, such a connection is formally broken under the proposed sampling scheme. This is because not all particles are recorded in a sample. The rationale being that only in the inner region is desired as this is where the local environment closely approximates that of an infinite film. In summary, estimating expected particle-level power for particle a using a Monte-Carlo method, then doing the same for particle b using its own samples will likely not produce exact cancelation of $\mathbb{Y}^{ab}$ when adding the two. Clearly this is expected as the expectations of both particles arise from separate sample sets. Using the $\mathbb{J}^{ab}$ operator directly circumvents this term at the film-level and is equivalent to an estimate recording both $b \rightarrow a$, $c \rightarrow a$, $d \rightarrow a$ … and also the $a \rightarrow b$, $a \rightarrow c$, $a \rightarrow d$, … terms necessary for the cancelation of $\mathbb{Y}^{ab}$.

The lack of recording all particles in the film also implies that the Monte Carlo estimates have no guarantee to obey power conservation at all. This is seen in under sampled estimates. For example, consider an estimate of the expected value arising from a single sample, $N_{MC} = 1$, that happens to be of a particularly large scattering efficiency $\gg 1$ for the observation particle. At a high packing fraction, this efficiency would inevitably be balanced by stealing from neighboring

particles in order to balance the total power of the collective. Though the Monte Carlo-derived moments do not consider this balance as they assume the local field on the observation particle is representative. Clearly, the estimated expectation could be well above what is actually capable by power conservation! To circumvent this, it is necessary to rely on the convergence of expectation as $N_{MC} \to \infty$. Fortunately, this can be done in an iterative fashion, scaling as $O(N_{MC})$, until convergence is met. It has been the experience of this dissertation that for lossy systems, 25 - 50 samples are within range for accurate estimates. For lossless systems 100 - 500 samples may be necessary. In all simulation experiments power conservation was reached eventually and estimates matched well with full-wave simulations. Though, this may not formally preclude the existence of counter examples.

The sampling scheme does not guarantee a local-to-macro connection or power conservation as it is equivalent to summing only a subset of particles in a suitably defined infinite film. Conservation properties are approached given sufficient sampling.

A Computational Tradeoff

Though the Mie harmonics represent an efficient expansion to calculate thousands of random film samples, the process is still computationally intensive. For this reason, much work is involved in defining the right sample strategy, optimizing computer code, and computing only the absolutely necessary equations. As discussed, the decision is to sample only the center particle so that the size of each film sample is reduced. Another decision is to calculate transmission directly from power conservation as the Mie harmonics are not orthogonal over the hemisphere. The film's expected absorption can rely on orthogonality for expedient calculation. Unfortunately, calculating the expected reflection requires a much larger matrix multiplication. Since the reflection is solely from the scattered field, it can be rewritten as

$$\mathbb{E}[Ref] \approx {ff\overline{Q_{sca,a}^{MC}}}\Big/{1 + \overline{FBR_a^{MC}}}, \qquad 1.9.24$$

where $\overline{Q_{sca,a}^{MC}}$ is the Monte Carlo estimate of the scattering efficiency, which utilizes the orthogonality conditions. $\overline{FBR_a^{MC}} = \overline{Q_{sca,a}^{MC+}}/\overline{Q_{sca,a}^{MC-}}$ is the estimate of the forward-to-backward hemisphere scattering ratio. By approximating the hemispherical integration by the value only at the poles, $\overline{FBR_a^{MC}} \approx \overline{Q_{sca,a}^{MC+}}(\theta = 0)/\overline{Q_{sca,a}^{MC-}}(\theta = \pi)$, the calculation of the expected reflection is substantially simplified. This is because $\overline{Q_{sca,a}^{MC}}$ is a vector inner product and $\overline{Q_{sca,a}^{MC\pm}}(\theta = 0, \pi)$

considers only the $m = \pm 1$ terms as azimuthal variations have no meaning at the poles. An analysis of the accuracy of this approximation will be delayed until the discussion of the Kerker transform in a later chapter. With this transform, the connection between directionality at the poles and directionality integrated over the hemisphere is better understood. With that said, clearly the approximation for $\overline{FBR_a^{MC}}$ is most accurate when particles are dominantly forward/backward directional scattering. Finally, calculating $c_a^\dagger \mathbb{J}^{ab} c_b$ and/or $c_a^\dagger \mathbb{H}^{ab} c_b$ also represents a large computational task. In fact, in many cases constructing the interaction matrix is more computationally intensive than solving it! For this reason, since calculating $c_a^\dagger \mathbb{H}^{ab} c_b$ is unavoidable for generating the fundamental interaction matrix, performing the approximation $\overline{\left(c_a^\dagger \mathbb{J}^{ab} c_b\right)^{MC}} \approx \overline{\left(c_a^\dagger \mathbb{H}^{ab} c_b\right)^{MC}}$ when calculating the reflection maximizes the reuse of calculations. The implications of this approximation have already been discussed. When showcasing Kerker scattering in random films in a later chapter, the use of both of these approximations will be shown to produce satisfying estimates matching well to full-wave simulation.

Calculating the interaction of all particles and integrating over the hemisphere can represent a bottleneck in simulation. Leveraging orthogonality, simplified expressions for scattering at the poles, the fundamental interaction equation, and power conservation can provide a further approximation to the reflection, transmission, and absorption at a reduced computational effort.

1.10 APPENDIX A: MIE VECTOR HARMONIC EXPANSION

In a medium with permittivity, ε, and permeability, μ, that is linear, isotropic, homogeneous, and lacking a net charge or external sources, Maxwell's equations dictate that any electromagnetic field (and corresponding vector potential and Hertz vector) must obey the homogeneous Helmholtz equation,

$$\nabla^2 \boldsymbol{V} = k^2 \boldsymbol{V}, \qquad 1.10.1$$

where $k^2 = \omega^2 \varepsilon \mu$ is the magnitude of the wavevector, ω is the angular oscillation frequency of the field, $\nabla^2 \boldsymbol{V} = -\nabla \times \nabla \times \boldsymbol{V} + \nabla(\nabla \cdot \boldsymbol{V})$ is the vector Laplacian, and $\boldsymbol{V}$ is any such vector described above.

The goal is to represent any feasible field distribution in this medium as an expansion of functions having known integral/differential properties. Furthermore, it is desired that the expansion be computationally efficient and physically insightful. An approach to find characteristic solutions to 1.10.1 is to reduce the complexity to finding characteristic solutions to the scalar Helmholtz equation,

$$\nabla^2 \psi + k^2 \psi = 0, \qquad 1.10.2$$

where $\nabla^2 \psi = \nabla \cdot (\nabla \psi)$ is the scalar Laplacian. This approach works by recognizing that solutions to 1.10.2 can generate solutions to 1.10.1 through a proper vectorization scheme. In this regard there are 3 mutually perpendicular characteristic vector functions that can be constructed in R^3,

$$\boldsymbol{P} = \nabla \psi \quad \boldsymbol{M} = -\hat{\boldsymbol{e}}_r \times \boldsymbol{P} \left(= \nabla \times (\hat{\boldsymbol{e}}_r \psi)\right) \quad \boldsymbol{N} = \frac{1}{k} \nabla \times \boldsymbol{M}. \qquad 1.10.3$$

The vector functions in equation 1.10.3 are each solutions to 1.10.1 as long as the corresponding ψ is a solution to 1.10.2. For example, from the identity, $\nabla^2 \nabla f = \nabla \nabla^2 f$, you can conclude $\nabla^2 \boldsymbol{P} + k^2 \boldsymbol{P} = \nabla(\nabla^2 \psi + k^2 \psi)$. Since scattered fields are viewed as emanating from the particle

and possibly propagating in any direction of 3D space, it is sensible to solve the governing scalar wave equation in polar form,

$$\nabla^2 = \frac{1}{r^2}\frac{d}{dr}\left(r^2\frac{d}{dr}\right) - \frac{1}{r^2}\boldsymbol{L}\cdot\boldsymbol{L}^*, \qquad 1.10.4$$

where $\boldsymbol{L} = \hat{\boldsymbol{e}}_r \times (-i\nabla)$ is the orbital angular momentum operator (equivalent to the one used in quantum mechanics without Plank's constant) and can be viewed as the generator of rotations. Similarly, $-i\nabla$ is analogous to linear momentum. Though it is not common to derive the Mie harmonics using angular momentum operators, this connection illuminates' important properties of the Mie harmonics. Using the separation of variables technique, the complexity of the problem can be further reduced by enforcing that the scalar field, $\boldsymbol{\psi(r,t)} = R(r)\Theta(\theta)\Phi(\phi)e^{i\omega t}$, is a product of 3 spatially dependent functions each separately managing the spatial dependence on $r,\ \theta,\ \phi$. Under these conditions, the following eigenfunctions can be used to construct solutions to 1.10.2,

$$\frac{d}{dr}\left(r^2\frac{d}{dr}\begin{matrix} j_n(kr) \\ y_n(kr)\end{matrix}\right) = \left((kr)^2 - n(n+1)\right)\begin{matrix} j_n(kr) \\ y_n(kr)\end{matrix}, \qquad 1.10.5(a)$$

$$(\boldsymbol{L}\cdot\boldsymbol{L}^*)\bar{Y}_{nm} = n(n+1)\bar{Y}_{nm}, \qquad 1.10.5(b)$$

and

$$L_z^2 e^{im\phi} = \frac{d^2 e^{im\phi}}{d\phi^2} = m^2 e^{im\phi}, \qquad 1.10.5(c)$$

where

$$\bar{Y}_{nm} = \bar{P}_n^{|m|}(\cos(\theta))e^{im\phi},\ \ \theta \in [0,\pi], \phi \in [0, 2\pi) \qquad 1.10.6$$

is the normalized spherical harmonic in complex form. $\bar{P}_n^{|m|}$ is the normalized associated Legendre polynomial. j_n and y_n are the spherical Bessel functions of the first and second kind, respectively. The eigenvalues in equations 1.10.5(a)-(c) are formed from discrete integers, termed the principal quantum numbers, $n \in \mathbb{Z} \cap [0, \infty]$, and azimuthal quantum numbers, $m \in \mathbb{Z} \cap [-n, n]$. Equation 1.10.5(c) is necessary to enforce that ψ is composed of an azimuthal-specific

function, $\Phi(\phi)$. In the chosen coordinate system, the $\theta \in [0, \pi]$ endpoints lie on the z-axis. $L_z = \boldsymbol{L} \cdot \hat{\boldsymbol{e}}_z$, is the projection of the angular momentum operator onto the z-axis. Correspondingly, this operator generates rotations around the z-axis. In atomic orbital theory, the azimuthal quantum number is often called the magnetic quantum number. Though, the Mie harmonics are separated into electric and magnetic type, which are a different property. To avoid confusion m is denoted as the azimuthal quantum number as this terminology is more explicit to the role m plays as defining the form of oscillation in the azimuthal plane. The weight factor, w_{nm} is used for convenience to normalize orthogonality relations as detailed in section 1.12, appendix C. Under these conditions, equation 1.10.2 admits the eigenfunctions,

$$\begin{matrix} \psi_{nm}(\boldsymbol{r}) \\ \mathrm{Rg}\, \psi_{nm}(\boldsymbol{r}) \end{matrix} = \begin{matrix} h_n(kr) \\ j_n(kr) \end{matrix} \bar{Y}_{nm}(\theta, \phi). \tag{1.10.7}$$

The spherical Bessel function of the first kind, j_n, is used to describe "incoming"/regular (Rg) waves. This solution is mathematically valid everywhere in space, but it does not satisfy the Silver-Muller radiation condition, $\lim_{r \to \infty} \hat{\boldsymbol{e}}_r \times \sqrt{\mu}\boldsymbol{H} + \sqrt{\varepsilon}\boldsymbol{E} = O\left(\frac{1}{r}\right)$, necessary for energy conservation of outward emanating fields in three dimensions. Therefore, this form is used for fields propagating "inwards" toward a point of interest. E.g., a plane wave starting at infinity and converging to a particle. The second option, the spherical Hankel function of the first kind, $h_n^1 = j_n + iy_n$, is singular at the origin, $\lim_{x \to 0^+} y_n(x) = -\infty$, but satisfies the Silver-Muller condition in the far field. This form is used for waves that are emanating outward from a particle and are valid in the domain $R^3 - \{0\}$.

Applying equation 1.10.7 to equation 1.10.3 the Mie vector harmonics are then,

$$\begin{matrix} \boldsymbol{L}_{nm}(\boldsymbol{r}) \\ \mathrm{Rg}\, \boldsymbol{L}_{nm}(\boldsymbol{r}) \end{matrix} = \frac{d}{d(kr)} \begin{matrix} \psi_{nm} \\ \mathrm{Rg}\, \psi_{nm} \end{matrix} \hat{\boldsymbol{e}}_r + \frac{1}{kr} \begin{matrix} h_n^1(kr) \\ j_n(kr) \end{matrix} \left(\hat{\boldsymbol{e}}_r \times \boldsymbol{\psi}_{nm}^{far}\right) \tag{1.10.8(a)}$$

$$\begin{matrix} \boldsymbol{M}_{nm}(\boldsymbol{r}) \\ \mathrm{Rg}\, \boldsymbol{M}_{nm}(\boldsymbol{r}) \end{matrix} = \frac{1}{kr} \begin{matrix} \mathcal{R}(kr) \\ \mathrm{Rg}\mathcal{R}(kr) \end{matrix} \boldsymbol{\psi}_{nm}^{far} \tag{1.10.8(b)}$$

$$\begin{matrix} \boldsymbol{N}_{nm}(\boldsymbol{r}) \\ \mathrm{Rg}\, \boldsymbol{N}_{nm}(\boldsymbol{r}) \end{matrix} = \nabla \times \begin{matrix} h_n^1(kr) \\ j_n(kr) \end{matrix} \boldsymbol{\psi}_{nm}^{far}$$
$$= \frac{1}{kr}\left(n(n+1) \begin{matrix} \psi_{nm} \\ \mathrm{Rg}\, \psi_{nm} \end{matrix} \hat{\boldsymbol{e}}_r + \begin{matrix} \dot{\mathcal{R}}(kr) \\ \mathrm{Rg}\dot{\mathcal{R}}(kr) \end{matrix} \left(\hat{\boldsymbol{e}}_r \times \boldsymbol{\psi}_{nm}^{far}\right) \right) \tag{1.10.8(c)}$$

where

$$\begin{matrix}\mathcal{R}(kr) \\ \mathrm{Rg}\mathcal{R}(kr)\end{matrix} = kr \begin{matrix}h_n^1(kr) \\ j_n(kr)\end{matrix}$$

$$\begin{matrix}\dot{\mathcal{R}}(kr) \\ \mathrm{Rg}\dot{\mathcal{R}}(kr)\end{matrix} = \frac{d}{d(kr)}\left(kr \begin{matrix}h_n^1(kr) \\ j_n(kr)\end{matrix}\right) = kr \begin{matrix}h_{n-1}^1(kr) \\ j_{n-1}(kr)\end{matrix} - n \begin{matrix}h_n^1(kr) \\ j_n(kr)\end{matrix}$$

1.10.9

define the radial dependence of the toroidal terms in terms of Riccati-Bessel functions and their derivatives. The angular dependence of the toroidal terms are defined by the angular Mie vector functions,

$$\boldsymbol{\psi}_{nm}^{far} = \frac{i\boldsymbol{L}\bar{Y}_{nm}}{\sqrt{2n(n+1)}} = e^{im\phi}\left(im\pi_n^{|m|}(\theta)\hat{\boldsymbol{e}}_\theta - \tau_n^{|m|}(\theta)\hat{\boldsymbol{e}}_\phi\right) \quad 1.10.10(a)$$

$$\hat{\boldsymbol{e}}_r \times \boldsymbol{\psi}_{nm}^{far} = \frac{r\nabla\bar{Y}_{nm}}{\sqrt{2n(n+1)}} = e^{im\phi}\left(\tau_n^{|m|}(\theta)\hat{\boldsymbol{e}}_\theta + im\pi_n^{|m|}(\theta)\hat{\boldsymbol{e}}_\phi\right) \quad 1.10.10(b)$$

where

$$\sqrt{2n(n+1)}\pi_n^{|m|}(\theta) = \frac{P_n^{|m|}(\cos\theta)}{\sin(\theta)} \quad 1.10.11(a)$$

$$\sqrt{2n(n+1)}\tau_n^{|m|}(\theta) = \frac{dP_n^{|m|}(\cos\theta)}{d\theta} \quad 1.10.11(b)$$

are given explicit variables since their behavior is critical to understanding the angular pattern of the field. The angular Mie functions are outlined in detail in section 1.12, appendix C. In the far field, the spherical Hankel function has the asymptotic form,

$$\lim_{x\to\infty} h_n(x) = \frac{(-i)^{n+1}e^{ix}}{x}. \quad 1.10.12$$

Correspondingly,

$$\lim_{r\to\infty} \boldsymbol{L}_{nm}(\boldsymbol{r}) = \frac{(-i)^n e^{ikr}}{kr}\bar{Y}_{nm}\hat{\boldsymbol{e}}_r \quad 1.10.13(a)$$

$$\lim_{r\to\infty} \boldsymbol{M}_{nm}(\boldsymbol{r}) = \frac{e^{ikr}}{kr}\left((-i)^{n+1}\boldsymbol{\psi}_{nm}^{far}(\hat{\boldsymbol{r}})\right) = \frac{e^{ikr}}{kr}\boldsymbol{M}_{nm}^{far}(\hat{\boldsymbol{r}}) \qquad 1.10.13(b)$$

$$\lim_{r\to\infty} \boldsymbol{N}_{nm}(\boldsymbol{r}) = \frac{e^{ikr}}{kr}\left((-i)^{n}\left(\hat{\boldsymbol{e}}_r \times \boldsymbol{\psi}_{nm}^{far}\right)\right) = \frac{e^{ikr}}{kr}\boldsymbol{N}_{nm}^{far}(\hat{\boldsymbol{r}}) \qquad 1.10.13(c)$$

(Note: When the domain of interest is not explicitly stated, the outgoing harmonics will be used to keep a less cumbersome notation. Changing to the regular expansion is as simple as appending Rg and rederiving the problem.)

Any feasible field distribution can be found from the vector potential, $\boldsymbol{A}$, that is constructed through properly assigning the complex weight factors $(a_{n,m}, b_{n,m}, c_{n,m})$ associated to each characteristic harmonic

$$\boldsymbol{A} = -\frac{\mathrm{i}}{\omega}\sum_{nm} a_{n,m}\boldsymbol{N}_{n,m} + b_{n,m}\boldsymbol{M}_{n,m} + c_{n,m}\boldsymbol{L}_{n,m}, \qquad 1.10.14$$

where the Lorentz gauge is used.

The complex weight factor is found through projecting the field onto the characteristic harmonic, e.g.,

$$a_{n,m} = \int_{\phi=0}^{2\pi}\int_{\theta=0}^{\pi} \boldsymbol{A}\cdot\boldsymbol{N}_{n,-m}\, sin(\theta)\, d\theta d\phi \Big/ \int_{\phi=0}^{2\pi}\int_{\theta=0}^{\pi} \left|\boldsymbol{N}_{n,m}\right|^2 sin(\theta)\, d\theta d\phi. \qquad 1.10.15$$

The integration domain is chosen to leverage the orthogonality relation of the Mie vector harmonics detailed in section 1.12, appendix C and arises from the decision to solve 1.10.2 in polar coordinates using the separation of variables technique. Of the three vector types, $\boldsymbol{L}$ is longitudinal and not divergence free. $\boldsymbol{M}$ and $\boldsymbol{N}$ are solenoidal $(\nabla\cdot\boldsymbol{M} = \nabla\cdot\boldsymbol{N} = 0)$ if $n > 0$. Furthermore, both $\boldsymbol{M}$ and $\boldsymbol{N}$ are related through the curl, $\boldsymbol{M} = \frac{1}{k}\nabla\times\boldsymbol{N}$ and $\boldsymbol{N} = \frac{1}{k}\nabla\times\boldsymbol{M}$. Therefore, $\boldsymbol{M}$ and $\boldsymbol{N}$ satisfy the wave equation, are divergence free, and, by construction, are proportional to one another under the curl as necessary to satisfy the Ampere and Faraday relations. Recognizing that $\mu\boldsymbol{H} = \nabla\times\boldsymbol{A}$, then

$$\boldsymbol{E} = \sum_{n>0} \sum_{m=-n}^{n} b_{n,m}\boldsymbol{M}_{n,m} + a_{n,m}\boldsymbol{N}_{n,m}$$
$$\boldsymbol{H} = -iY \sum_{n>0} \sum_{m=-n}^{n} b_{n,m}\boldsymbol{N}_{n,m} + a_{n,m}\boldsymbol{M}_{n,m}. \quad 1.10.16$$

By looking at the field patterns of $\boldsymbol{N}$ and $\boldsymbol{M}$ it is apparent that these vector harmonics have field distributions mimicking electric ($\boldsymbol{N}$) and magnetic-type ($\boldsymbol{M}$) multipoles. Clearly this is a sensible conclusion given the form of their pilot function, ψ, and their curl relation.

It is often convenient to add an index for the two harmonic types, $t \in \{\text{Electric} = 0, \text{Magnetic} = 1\}$. Then the fields can be written in compact form as

$$\boldsymbol{E} = \sum_{n} \sum_{m=-n}^{n} \sum_{t=0}^{1} c_{n,m}^{t}\, \boldsymbol{\Psi}_{n,m}^{t} = \sum_{l} c_l \boldsymbol{\Psi}_l = \boldsymbol{\Psi} c$$
$$\boldsymbol{H} = -iY \sum_{n} \sum_{m=-n}^{n} \sum_{t=0}^{1} c_{n,m}^{t}\, \boldsymbol{\Psi}_{n,m}^{1-t} = -\frac{iY}{k} \sum_{l} c_l (\nabla \times \boldsymbol{\Psi}_l), \quad 1.10.17$$

where $\boldsymbol{\Psi}_{n,m}^{t} = t\boldsymbol{M}_{n,m} + (1-t)\boldsymbol{N}_{n,m}$ and $c_{n,m}^{t} = t b_{n,m} + (1-t) a_{n,m}$. For a further compact notation, $l = t, n, m$ is a shorthand representing a unique combination of the integer polar quantum number, n, azimuthal quantum number, m, and harmonic type t. The size of all possible combination is L. For the most compact notation, vector harmonics without an index subscript are in matrix form $\boldsymbol{\Psi} \in \mathbb{C}^{3\times L}$ and the correspond coefficients are in column vector form $c \in \mathbb{C}^{L}$. The matrix is written as

$$\boldsymbol{E} = [\boldsymbol{N} \quad \boldsymbol{M}] \begin{bmatrix} c^{E} \\ c^{M} \end{bmatrix}$$
$$\boldsymbol{H} = -iY [\boldsymbol{M} \quad \boldsymbol{N}] \begin{bmatrix} c^{E} \\ c^{M} \end{bmatrix} \quad 1.10.18$$

where,

$$\boldsymbol{N}c^{E} = [\boldsymbol{N}_{1,-1} \quad \boldsymbol{N}_{1,0} \quad \dots \quad \boldsymbol{N}_{2,-2} \quad \dots][a_{1,-1} \quad a_{1,0} \quad \dots \quad a_{2,-2} \quad \dots]^{T}$$
$$\boldsymbol{M}c^{M} = [\boldsymbol{M}_{1,-1} \quad \boldsymbol{M}_{1,0} \quad \dots \quad \boldsymbol{M}_{2,-2} \quad \dots][b_{1,-1} \quad b_{1,0} \quad \dots \quad b_{2,-2} \quad \dots]^{T}. \quad 1.10.19$$

It is often useful to derive fields in terms of the Mie vector harmonics through the Green's function approach. From the results discussed above, the Green's function for the homogeneous scalar wave equation defined by 1.10.2 can be written as,

$$G_o(k, \boldsymbol{r}, \boldsymbol{r}') = \frac{e^{ik|\boldsymbol{r}-\boldsymbol{r}'|}}{4\pi|\boldsymbol{r}-\boldsymbol{r}'|} = \frac{ik}{2\pi} \begin{cases} \sum_{n} \sum_{m=-n}^{n} \psi_{n,-m}(k\boldsymbol{r}')\,\mathrm{Rg}\,\psi_{nm}(k\boldsymbol{r}) & r < r' \\ \sum_{n} \sum_{m=-n}^{n} \mathrm{Rg}\,\psi_{n-m}(k\boldsymbol{r}')\psi_{n,m}(k\boldsymbol{r}) & r > r', \end{cases} \quad 1.10.20$$

where the function is defined for $\boldsymbol{r} \neq \boldsymbol{r}'$. The corresponding dyadic Green's functions are,

$$\begin{aligned}&\overline{\overline{\boldsymbol{G}}}_{mo}(k,\boldsymbol{r},\boldsymbol{r}') = \\ &\frac{ik^2}{\pi}\begin{cases}\sum_n \sum_{m=-n}^{n} \boldsymbol{M}_{n,-m}(k\boldsymbol{r}')\mathrm{Rg}\,\boldsymbol{N}_{n,m}(k\boldsymbol{r}) + \boldsymbol{N}_{n,-m}(k\boldsymbol{r}')\mathrm{Rg}\,\boldsymbol{M}_{n,m}(k\boldsymbol{r}) & r < r' \\ \sum_n \sum_{m=-n}^{n} \mathrm{Rg}\,\boldsymbol{M}_{n,-m}(k\boldsymbol{r}')\boldsymbol{N}_{n,m}(k\boldsymbol{r}) + \mathrm{Rg}\,\boldsymbol{N}_{n,-m}(k\boldsymbol{r}')\boldsymbol{M}_{n,m}(k\boldsymbol{r}) & r > r',\end{cases}\end{aligned} \tag{1.10.21}$$

and

$$\begin{aligned}&\overline{\overline{\boldsymbol{G}}}_{eo}(k,\boldsymbol{r},\boldsymbol{r}') \\ &= -\frac{1}{k^2}\hat{\boldsymbol{r}}\hat{\boldsymbol{r}}\delta(\boldsymbol{r}-\boldsymbol{r}') + \\ &\frac{ik}{\pi}\begin{cases}\sum_n \sum_{m=-n}^{n} \boldsymbol{M}_{n,-m}(k\boldsymbol{r}')\mathrm{Rg}\,\boldsymbol{M}_{n,m}(k\boldsymbol{r}) + \boldsymbol{N}_{n,-m}(k\boldsymbol{r}')\mathrm{Rg}\,\boldsymbol{N}_{n,m}(k\boldsymbol{r}) & r < r' \\ \sum_n \sum_{m=-n}^{n} \mathrm{Rg}\,\boldsymbol{M}_{n,-m}(k\boldsymbol{r}')\boldsymbol{M}_{n,m}(k\boldsymbol{r}) + \mathrm{Rg}\,\boldsymbol{N}_{n,-m}(k\boldsymbol{r}')\boldsymbol{N}_{n,m}(k\boldsymbol{r}) & r > r'.\end{cases}\end{aligned} \tag{1.10.22}$$

Furthermore, the Green's relation to surface currents makes use of the expansions,

$$\begin{aligned}&\nabla \times \left(\boldsymbol{v}(\boldsymbol{r}')G_o(k,\boldsymbol{r},\boldsymbol{r}')\right) \\ &= \frac{ik^2}{\pi}\sum_n \sum_{m=-n}^{n}\begin{cases}\begin{pmatrix}\left(\boldsymbol{v}(\boldsymbol{r}')\cdot\boldsymbol{M}_{n,-m}(k\boldsymbol{r}')\right)\mathrm{Rg}\,\boldsymbol{N}_{n,m}(k\boldsymbol{r}) \\ +\left(\boldsymbol{v}(\boldsymbol{r}')\cdot\boldsymbol{N}_{n,-m}(k\boldsymbol{r}')\right)\mathrm{Rg}\,\boldsymbol{M}_{n,m}(k\boldsymbol{r})\end{pmatrix} & r < r' \\ \begin{pmatrix}\left(\boldsymbol{v}(\boldsymbol{r}')\cdot\mathrm{Rg}\,\boldsymbol{M}_{n,-m}(k\boldsymbol{r}')\right)\boldsymbol{N}_{n,m}(k\boldsymbol{r}) \\ +\left(\boldsymbol{v}(\boldsymbol{r}')\cdot\mathrm{Rg}\,\boldsymbol{N}_{n,-m}(k\boldsymbol{r}')\right)\boldsymbol{M}_{n,m}(k\boldsymbol{r})\end{pmatrix} & r > r',\end{cases}\end{aligned} \tag{1.10.23}$$

and

$$\begin{aligned}&\nabla \times \nabla \times \left(\boldsymbol{v}(\boldsymbol{r}')G_o(k,\boldsymbol{r},\boldsymbol{r}')\right) \\ &= \frac{ik^3}{\pi}\sum_n \sum_{m=-n}^{n}\begin{cases}\begin{pmatrix}\left(\boldsymbol{v}(\boldsymbol{r}')\cdot\boldsymbol{M}_{n,-m}(k\boldsymbol{r}')\right)\mathrm{Rg}\,\boldsymbol{M}_{n,m}(k\boldsymbol{r}) \\ +\left(\boldsymbol{v}(\boldsymbol{r}')\cdot\boldsymbol{N}_{n,-m}(k\boldsymbol{r}')\right)\mathrm{Rg}\,\boldsymbol{N}_{n,m}(k\boldsymbol{r})\end{pmatrix} & r < r' \\ \begin{pmatrix}\left(\boldsymbol{v}(\boldsymbol{r}')\cdot\mathrm{Rg}\,\boldsymbol{M}_{n,-m}(k\boldsymbol{r}')\right)\boldsymbol{M}_{n,m}(k\boldsymbol{r}) \\ +\left(\boldsymbol{v}(\boldsymbol{r}')\cdot\mathrm{Rg}\,\boldsymbol{N}_{n,-m}(k\boldsymbol{r}')\right)\boldsymbol{N}_{n,m}(k\boldsymbol{r})\end{pmatrix} & r > r'.\end{cases}\end{aligned} \tag{1.10.24}$$

Note that $\boldsymbol{M}_{n,-m} \neq \boldsymbol{M}_{n,m}^*$ and $\boldsymbol{N}_{n,-m} \neq \boldsymbol{N}_{n,m}^*$ as the radial functions are not conjugated.

1.11 APPENDIX B: MIE VECTOR HARMONIC POWER FLOW

"What do you get when you cross and elephant and a grape?

Elephant grape sine theta."

- Unknown, A Joke about Cross Products

Power flow analysis with multiple scattering requires calculating the Poynting vector between all field pairs. The time-averaged Poynting vector between any two arbitrary time-harmonic fields is $\boldsymbol{S}_{aa} + \boldsymbol{S}_{bb} + \boldsymbol{S}_{ab} + \boldsymbol{S}_{ba}$, where $\boldsymbol{S}_{ab} = \frac{1}{2}\boldsymbol{E}_a \times \boldsymbol{H}_b^* = \frac{1}{2}iY(\boldsymbol{E}_a \times \nabla \times \boldsymbol{E}_b^*)$. The power flow through a surface is then $W = \int dA\ (\hat{\boldsymbol{n}} \cdot \boldsymbol{S})$, where $\hat{\boldsymbol{n}}$ is the outward pointing normal of the surface. If two time-harmonic fields are written as Mie harmonic expansions referenced to the same origin, then the resulting interference can be written as

$$\begin{aligned}
&\boldsymbol{S}_{ab} = \tfrac{1}{2}\boldsymbol{E}_a \times \boldsymbol{H}_b^* \\
&= \tfrac{1}{2}\textstyle\sum_{nmn'm'} iY \begin{pmatrix} (\boldsymbol{N}_{nm} \times \boldsymbol{M}_{n'm'}^*)(c_{a,nm}^E c_{b,n'm'}^{E*}) \\ +(\boldsymbol{M}_{nm} \times \boldsymbol{N}_{n'm'}^*)(c_{a,nm}^H c_{b,n'm'}^{H*}) \\ +(\boldsymbol{N}_{nm} \times \boldsymbol{N}_{n'm'}^*)(c_{a,nm}^E c_{b,n'm'}^{H*}) \\ +(\boldsymbol{M}_{nm} \times \boldsymbol{M}_{n'm'}^*)(c_{a,nm}^H c_{b,n'm'}^{E*}) \end{pmatrix} \\
&= tr[\mathbb{S}(c_a \otimes c_b^*)],
\end{aligned} \tag{1.11.1}$$

where tr is the trace operator, $\otimes$ is the outer product, and the Mie Poynting vector matrix is

$$\mathbb{S}(\boldsymbol{r}, k) = \tfrac{1}{2}iY \begin{bmatrix} \boldsymbol{N} \otimes (\times \boldsymbol{M}^*) & \boldsymbol{N} \otimes (\times \boldsymbol{N}^*) \\ \boldsymbol{M} \otimes (\times \boldsymbol{M}^*) & \boldsymbol{M} \otimes (\times \boldsymbol{N}^*) \end{bmatrix}$$

$$= \tfrac{1}{2}iY \begin{bmatrix} \boldsymbol{N}_{1,-1} \times \boldsymbol{M}_{1,-1}^* & \cdots & \boldsymbol{N}_{1,-1} \times \boldsymbol{M}_{n,n}^* & \boldsymbol{N}_{1,-1} \times \boldsymbol{N}_{1,-1}^* & \cdots & \boldsymbol{N}_{1,-1} \times \boldsymbol{N}_{n,n}^* \\ \vdots & \ddots & \vdots & \vdots & \ddots & \vdots \\ \boldsymbol{N}_{n,n} \times \boldsymbol{M}_{1,-1}^* & \cdots & \boldsymbol{N}_{n,n} \times \boldsymbol{M}_{n,n}^* & \boldsymbol{N}_{n,n} \times \boldsymbol{N}_{1,-1}^* & \cdots & \boldsymbol{N}_{n,n} \times \boldsymbol{N}_{n,n}^* \\ \boldsymbol{M}_{1,-1} \times \boldsymbol{M}_{1,-1}^* & \cdots & \boldsymbol{M}_{1,-1} \times \boldsymbol{M}_{n,n}^* & \boldsymbol{M}_{1,-1} \times \boldsymbol{N}_{1,-1}^* & \cdots & \boldsymbol{M}_{1,-1} \times \boldsymbol{N}_{n,n}^* \\ \vdots & \ddots & \vdots & \vdots & \ddots & \vdots \\ \boldsymbol{M}_{n,n} \times \boldsymbol{M}_{1,-1}^* & \cdots & \boldsymbol{M}_{n,n} \times \boldsymbol{M}_{n,n}^* & \boldsymbol{M}_{n,n} \times \boldsymbol{N}_{1,-1}^* & \cdots & \boldsymbol{M}_{n,n} \times \boldsymbol{N}_{n,n}^* \end{bmatrix}. \tag{1.11.2}$$

Note that in general the Mie harmonics may be outgoing or regular or a mix of the two. The form of the Poynting matrix would then change accordingly, dependent on the context. The

time-average real power flow over an arbitrary surface of differential area, dA, and outward pointing normal, $\hat{\boldsymbol{n}}$, is

$$\begin{aligned} dW_{ab} &= dA\hat{\boldsymbol{n}} \cdot \Re[\boldsymbol{S}_{ab}] \\ &= \Re\left[\tfrac{1}{2} iY \sum_{n,m,t} \sum_{n',m',t'} c^{t}_{a,n,m} c^{t'*}_{b,n',m'} dA\hat{\boldsymbol{n}} \cdot \left(\boldsymbol{\Psi}^{t}_{n,m} \times \boldsymbol{\Psi}^{(1-t')*}_{n',m'}\right)\right] \\ &= \Re\, tr[d\mathbb{W}(c_a \otimes c_b^*)], \end{aligned} \tag{1.11.3}$$

where the power matrix is

$$d\mathbb{W}(\boldsymbol{r}, k) = \tfrac{1}{2} iY\, d\boldsymbol{A} \cdot \mathbb{S}(\boldsymbol{r}, k) \tag{1.11.4}$$

and the dot product, $d\boldsymbol{A} \cdot \mathbb{S}$, is understood as an element wise inner product with $dA\hat{\boldsymbol{n}}$.

Far Field Power Flow

In the far field the Poynting vector and power matrix take the form,

$$\mathbb{S}^{far} = \tfrac{1}{2} \tfrac{iY}{(kr)^2} \begin{bmatrix} \boldsymbol{N}^{far} \otimes \left(\times \boldsymbol{M}^{far*}\right) & \boldsymbol{N}^{far} \otimes \left(\times \boldsymbol{N}^{far*}\right) \\ \boldsymbol{M}^{far} \otimes \left(\times \boldsymbol{M}^{far*}\right) & \boldsymbol{M}^{far} \otimes \left(\times \boldsymbol{N}^{far*}\right) \end{bmatrix}. \tag{1.11.5}$$

Correspondingly, $d\mathbb{W} = \Re \tfrac{1}{2} \tfrac{Y}{k^2} (\hat{\boldsymbol{e}}_r \cdot \mathbb{S}^{far}) \sin(\theta)\, d\theta d\phi$.

Integration over the Ball Surface

Integrating equation 1.11.3 over a closed spherical surface gives,

$$\begin{aligned} W_{ab} &= \Re \tfrac{1}{2} \sum_{nmn'm'} iY \begin{pmatrix} \oint_{\partial B} d\boldsymbol{A} \cdot (\boldsymbol{N}_{nm} \times \boldsymbol{M}^*_{n'm'}) (c^{E}_{a,nm} c^{E*}_{b,n'm'}) \\ + \oint_{\partial B} d\boldsymbol{A} \cdot (\boldsymbol{M}_{nm} \times \boldsymbol{N}^*_{n'm'}) (c^{H}_{a,nm} c^{H*}_{b,n'm'}) \end{pmatrix} \\ &= \Re \tfrac{1}{2} \sum_{nm} iY \tfrac{\pi}{k^2} \begin{pmatrix} -\dot{\mathcal{R}}_n \mathcal{R}^*_n (c^{E}_{a,nm} c^{E*}_{b,nm}) \\ +\mathcal{R}_n \dot{\mathcal{R}}^*_n (c^{H}_{a,nm} c^{H*}_{b,nm}) \end{pmatrix}. \end{aligned} \tag{1.11.6}$$

If $a = b$ and both fields are outgoing harmonic expansions, then from the Wronskian relation,

$$W_{aa} = \frac{1}{2}\sum_{nm} Y \frac{\pi}{k^2}\left(-\Re\left[i\dot{\mathcal{R}}_n\mathcal{R}_n^*\right]\left|c_{a,nm}^E\right|^2 + \Re\left[i\dot{\mathcal{R}}_n^*\mathcal{R}_n\right]\left|c_{a,nm}^H\right|^2\right)$$
$$= \frac{Y}{2}\frac{\pi}{k^2}\sum_{nm}\left(\left|c_{a,nm}^E\right|^2 + \left|c_{a,nm}^H\right|^2\right). \quad 1.11.7$$

Equation 1.11.7 uses the simplification,

$$\dot{\mathcal{R}}_n\mathcal{R}_n^* = \left(\dot{\mathcal{R}}_n^*\mathcal{R}_n\right)^* = \left(\dot{j}_n + i\dot{y}_n\right)\left(j_n^* - iy_n^*\right)$$
$$\xrightarrow{kr\in\mathbb{R}} \left(\dot{j}_n j_n + \dot{y}_n y_n\right) + i\left(j_n\dot{y}_n - \dot{j}_n y_n\right) = \left(\dot{j}_n j_n + \dot{y}_n y_n\right) + i, \quad 1.11.8$$

where the Wronskian, $\mathcal{W}\left(j_n, y_n\right) = \left(j_n\dot{y}_n - \dot{j}_n y_n\right) = 1$, is used.

If $a \neq b$, then both $\boldsymbol{S}_{ab}$ and $\boldsymbol{S}_{ba}$ terms need to be used to further simplify. First consider the case where one of the fields is regular and the other is outgoing. This situation corresponds to a particle's scattered field interfering with a portion of its local field (E.g., either the incident, multiply scattered, or both). Since the designation is arbitrary let field a be outgoing and field b be incoming. Then,

$$W_{ab} + W_{ba}$$
$$= \Re\frac{Y}{2}\sum_{nm}\frac{\pi}{k^2}\begin{pmatrix} -i\dot{\mathcal{R}}_n\mathrm{Rg}\mathcal{R}_n^*\left(c_{a,nm}^E c_{b,nm}^{E*}\right) - i\mathrm{Rg}\dot{\mathcal{R}}_n\mathcal{R}_n^*\left(c_{a,nm}^{E*}c_{b,nm}^E\right) \\ +i\mathcal{R}_n\mathrm{Rg}\dot{\mathcal{R}}_n^*\left(c_{a,nm}^H c_{b,nm}^{H*}\right) + i\mathrm{Rg}\mathcal{R}_n\dot{\mathcal{R}}_n^*\left(c_{a,nm}^H c_{b,nm}^{H*}\right)\end{pmatrix} \quad 1.11.9$$
$$\xrightarrow{kr\in\mathbb{R}} \frac{Y}{2}\sum_{nm}\frac{\pi}{k^2}\Re\left[c_{a,nm}^E c_{b,nm}^{E*} + c_{a,nm}^H c_{b,nm}^{H*}\right].$$

Equation 1.11.9 uses the simplifications,

$$\mathcal{R}_n\mathrm{Rg}\dot{\mathcal{R}}_n^* A + \mathrm{Rg}\mathcal{R}_n\dot{\mathcal{R}}_n^* A^*$$
$$\xrightarrow{kr\in\mathbb{R}} \mathrm{Rg}\mathcal{R}_n\dot{\mathcal{R}}_n(A + A^*) + \mathcal{W}(\mathcal{R}_n, \mathrm{Rg}\mathcal{R}_n)A = 2\left(\mathrm{Rg}\mathcal{R}_n\dot{\mathcal{R}}_n\right)\Re[A] - iA \quad 1.11.10$$
$$\rightarrow \Re\left[i\left(2\left(\mathrm{Rg}\mathcal{R}_n\dot{\mathcal{R}}_n\right)\Re[A] - iA\right)\right] = \Re[A]$$

and

$$\dot{\mathcal{R}}_n\mathrm{Rg}\mathcal{R}_n^* A + \mathrm{Rg}\dot{\mathcal{R}}_n\mathcal{R}_n^* A^*$$
$$\xrightarrow{kr\in\mathbb{R}} \mathrm{Rg}\dot{\mathcal{R}}_n\mathcal{R}_n(A + A^*) - \mathcal{W}(\mathcal{R}_n, \mathrm{Rg}\mathcal{R}_n)A = 2\left(\mathrm{Rg}\dot{\mathcal{R}}_n\mathcal{R}_n\right)\Re[A] + iA \quad 1.11.11$$
$$\rightarrow \Re\left[-i\left(2\left(\mathrm{Rg}\dot{\mathcal{R}}_n\mathcal{R}_n\right)\Re[A] + iA\right)\right] = \Re[A].$$

If both fields are outgoing harmonics, then the simplification from 1.11.8 can be used and

$$\begin{aligned} &W_{ab} + W_{ba} \\ &= \frac{Y}{2}\frac{\pi}{k^2}\sum_{nm} -2\Re\left[i\dot{\mathcal{R}}_n\mathcal{R}_n^*\right]\Re\left[c_{a,nm}^E c_{b,nm}^{E*}\right] + 2\Re\left[i\dot{\mathcal{R}}_n^*\mathcal{R}_n\right]\Re\left[c_{a,nm}^H c_{b,nm}^{H*}\right] \\ &\xrightarrow{kr\in\mathbb{R}} Y\frac{\pi}{k^2}\sum_{nm}\Re\left[c_{a,nm}^E c_{b,nm}^{E*} + c_{a,nm}^H c_{b,nm}^{H*}\right]. \end{aligned} \qquad 1.11.12$$

Comparing equations 1.11.12 and 1.11.9 shows that the interference between two outgoing harmonics is $2\times$ that of the equation for the outgoing-incoming equivalent. This validates the particle-level versus film-level power flow analysis in section 1.6. Integrating over particle a then integrating over particle b and summing the result gives the same expression as integrating over a surface enclosing both particle a and particle b. If both fields are incoming harmonics, then $\Re\left[i\dot{j}_n j_n\right] = 0$ and there is no net power flow. This also validates the results from section 1.6. When integrating over the surface of particle a, all other multiple scattered fields are incoming harmonics. Correspondingly, on that integration surface, $W_{bb} = W_{inc,b} = W_{b,inc} = 0$.

1.12 APPENDIX C: USEFULL RELATIONS

This appendix is a reference for definitions, properties, and orthogonality relations related to the Mie harmonics. There are multiple different normalization schemes used throughout literature. For this reason, this section derives relations irrespective of the chosen weight, then defines the weight, w_{nm}, for each function used in this dissertation.

Wronskians of the Riccati-Bessel Functions

Let the Wronskian be defined as $\mathcal{W}(f,g) = f\dot{g} - g\dot{f}$. It can be readily verified that the Wronskian has the properties,

$$\mathcal{W}(f+u, g+v) = \mathcal{W}(f,g) + \mathcal{W}(f,v) + \mathcal{W}(u,g) + \mathcal{W}(u,v) \quad 1.12.1$$

$$\mathcal{W}(f,g) = -\mathcal{W}(g,f). \quad 1.12.2$$

When calculating power flow over a closed ball's surface using the Mie harmonic expansion, the Wronskians dictate the radial dependence of the power on the ball's surface. Therefore, it is necessary to understand the Wronskian relations of the Riccati-Bessel functions. This section outlines the Wronskian behavior under the constrain that the argument, $x = kr \in \mathbb{R}$, is real. This constraint is imposed because all power of interest in this dissertation, with the exception of absorption, is in the lossless background. Correspondingly, the Wronskian of any Riccati-Bessel function with itself is zero,

$$\mathcal{W}\begin{pmatrix} xj_n(x) & xj_n(x) \\ xy_n(x), & xy_n(x) \\ xh_n(x) & xh_n(x) \end{pmatrix} = 0. \quad 1.12.3$$

Furthermore,

$$\mathcal{W}(xj_n(x), xy_n(x)) = 1 \quad 1.12.4$$

$$\mathcal{W}(xj_n(x), xh_n(x)) = i. \quad 1.12.5$$

Normalization of the Spherical Vector Harmonics

The orthogonality relation of the spherical harmonics is

$$\begin{aligned}&\int_{\phi=0}^{2\pi}\int_{\theta=0}^{\pi} Y_{n,m}(\theta,\phi)Y^{*}_{n',m'}(\theta,\phi)\sin(\theta)\,d\theta d\phi\\&=\int_{\phi=0}^{2\pi}\int_{\theta=0}^{\pi} Y_{n,m}(\theta,\phi)Y_{n',-m'}(\theta,\phi)\sin(\theta)\,d\theta d\phi\\&=(w_{nm})^2 2\pi\frac{2}{2n+1}\frac{(n+m)!}{(n-m)!}\delta_{m,m'}\delta_{n,n'}\\&=2\pi\delta_{m,m'}\delta_{n,n'}\end{aligned} \qquad 1.12.6$$

where the chosen weight factor for the spherical harmonic is

$$w_{nm}=\left(\frac{2}{2n+1}\frac{(n+m)!}{(n-m)!}\right)^{-1/2}. \qquad 1.12.7$$

This is a result of the orthogonality of Euler's formula,

$$\int_{\phi=0}^{2\pi} e^{i(m-m')\phi}d\phi=2\pi\delta_{m,m'}, \qquad 1.12.8$$

and of the associated Legendre polynomials,

$$\int_{\theta=0}^{\pi} P_n^{|m|}(\cos(\theta))P_{n'}^{|m|}(\cos(\theta))\sin(\theta)\,d\theta=\frac{2}{2n+1}\frac{(n+m)!}{(n-m)!}\delta_{n,n'}. \qquad 1.12.9$$

Relations of the Angular Functions

The far field Mie vector functions make clear that it is also important to consider the relations between the angular vector functions, $Y_{n,m}\hat{\boldsymbol{e}}_r$, $\boldsymbol{\psi}_{nm}^{far}=\boldsymbol{L}Y_{n,m}$, and $\hat{\boldsymbol{e}}_r\times\boldsymbol{\psi}_{nm}^{far}$. The first important property is that each of these functions are point-wise orthogonal,

$$Y_{n,m}\hat{\boldsymbol{e}}_r\cdot\boldsymbol{L}Y_{n,m}=Y_{n,m}\hat{\boldsymbol{e}}_r\cdot\left(\hat{\boldsymbol{e}}_r\times\boldsymbol{L}Y_{n,m}\right)=\boldsymbol{L}Y_{n,m}\cdot\left(\hat{\boldsymbol{e}}_r\times\boldsymbol{L}Y_{n,m}\right)=0. \qquad 1.12.10$$

Recalling that $\boldsymbol{P}_{nm}$, is not divergence free, the second important relation is

$$\begin{aligned}&\nabla\cdot Y_{n,m}\hat{\boldsymbol{e}}_r=\boldsymbol{P}_{nm}\cdot\hat{\boldsymbol{e}}_r\\&\nabla\cdot\boldsymbol{L}Y_{n,m}=\nabla\cdot\left(\hat{\boldsymbol{e}}_r\times\boldsymbol{L}Y_{n,m}\right)=0\rightarrow\nabla\cdot\boldsymbol{M}=\nabla\cdot\boldsymbol{N}=0.\end{aligned} \qquad 1.12.11$$

Correspondingly the curl relation $k\boldsymbol{M} = \nabla \times \boldsymbol{N}$ and $k\boldsymbol{N} = \nabla \times \boldsymbol{M}$ also has an analogy for the angular vector functions,

$$-\boldsymbol{L}Y_{n,m} = \hat{\boldsymbol{e}}_r \times \left(\hat{\boldsymbol{e}}_r \times \boldsymbol{L}Y_{n,m}\right) = -\hat{\boldsymbol{e}}_r \times r\nabla Y_{n,m}. \tag{1.12.12}$$

Equation 1.12.12 comes from the vector identity $\boldsymbol{A} \times \boldsymbol{B} \times \boldsymbol{C} = \boldsymbol{B}(\boldsymbol{A} \cdot \boldsymbol{C}) - \boldsymbol{C}(\boldsymbol{A} \cdot \boldsymbol{B})$ and $\boldsymbol{L}Y_{n,m} \cdot \hat{\boldsymbol{e}}_r = 0$.

Relations of Mie Vector Functions in the Far Field

The Mie vector functions are mutually perpendicular in the far field,

$$\boldsymbol{N}_{nm}^{far} \cdot \boldsymbol{M}_{nm}^{far} = 0. \tag{1.12.13}$$

Correspondingly, the far field Mie vector functions are related through,

$$\begin{aligned} \hat{\boldsymbol{e}}_r \times \boldsymbol{N}_{nm}^{far} &= (-i)^n\left(\hat{\boldsymbol{e}}_r \times \hat{\boldsymbol{e}}_r \times \boldsymbol{L}Y_{n,m}\right) = -(-i)^n \boldsymbol{L}Y_{n,m} = -i\boldsymbol{M}_{nm}^{far} \\ \hat{\boldsymbol{e}}_r \times \boldsymbol{M}_{nm}^{far} &= (-i)^{n+1}\left(\hat{\boldsymbol{e}}_r \times \boldsymbol{L}Y_{n,m}\right) = -i\boldsymbol{N}_{nm}^{far}. \end{aligned} \tag{1.12.14}$$

From the triple product relation $\boldsymbol{A} \cdot (\boldsymbol{B} \times \boldsymbol{C}) = (\boldsymbol{A} \times \boldsymbol{B}) \cdot \boldsymbol{C}$, the following relations are useful for calculating power in the far field,

$$\begin{aligned} &\lim_{r\to\infty} \hat{\boldsymbol{e}}_r \cdot \left(\boldsymbol{N}_{nm} \times \boldsymbol{N}_{n'm'}^{*}\right) \\ &= \frac{1}{(kr)^2}\left(\hat{\boldsymbol{e}}_r \times \boldsymbol{N}_{nm}^{far}\right) \cdot \boldsymbol{N}_{n'm'}^{far*} = \frac{-i}{(kr)^2}\boldsymbol{M}_{nm}^{far} \cdot \boldsymbol{N}_{n'm'}^{far*} = 0, \end{aligned} \tag{1.12.15}$$

$$\begin{aligned} &\lim_{r\to\infty} \hat{\boldsymbol{e}}_r \cdot \left(\boldsymbol{M}_{nm} \times \boldsymbol{M}_{n'm'}^{*}\right) \\ &= \frac{1}{(kr)^2}\left(\hat{\boldsymbol{e}}_r \times \boldsymbol{M}_{nm}^{far}\right) \cdot \boldsymbol{M}_{n'm'}^{far*} = \frac{-i}{(kr)^2}\boldsymbol{N}_{nm}^{far} \cdot \boldsymbol{M}_{n'm'}^{far*} = 0, \end{aligned} \tag{1.12.16}$$

$$\begin{aligned} &\lim_{r\to\infty} \hat{\boldsymbol{e}}_r \cdot \left(\boldsymbol{M}_{nm} \times \boldsymbol{N}_{n'm'}^{*}\right) \\ &= \frac{1}{(kr)^2}\left(\hat{\boldsymbol{e}}_r \times \boldsymbol{M}_{nm}^{far}\right) \cdot \boldsymbol{N}_{n'm'}^{far*} \end{aligned} \tag{1.12.17}$$

$$= \frac{-i}{(kr)^2} \boldsymbol{N}_{nm}^{far} \cdot \boldsymbol{N}_{n'm'}^{far*}$$
$$= \frac{-i}{(kr)^2} (-i)^n (i)^{n'} (\boldsymbol{L}Y_{n,m}) \cdot \left(\boldsymbol{L}Y_{n',m'}\right)^*,$$

and

$$\lim_{r\to\infty} \hat{\boldsymbol{e}}_r \cdot \left(\boldsymbol{N}_{nm} \times \boldsymbol{M}_{n'm'}^*\right)$$
$$= \frac{1}{(kr)^2} \left(\hat{\boldsymbol{e}}_r \times \boldsymbol{N}_{nm}^{far}\right) \cdot \boldsymbol{M}_{n'm'}^{far*} \qquad 1.12.18$$
$$= \frac{-i}{(kr)^2} \boldsymbol{M}_{nm}^{far} \cdot \boldsymbol{M}_{n'm'}^{far*}$$
$$= \frac{-i}{(kr)^2} (-i)^n (i)^{n'} (\boldsymbol{L}Y_{n,m}) \cdot \left(\boldsymbol{L}Y_{n',m'}\right)^*.$$

Relations of Mie Vector Functions

The Mie harmonics have the following relations when integrated over a spherical surface,

$$\int_{\partial B} d^2\boldsymbol{r} \cdot \left(\boldsymbol{N}_{nm} \times \boldsymbol{N}_{n'm'}^*\right)$$
$$= \frac{1}{k^2} \dot{\mathcal{R}}_n \dot{\mathcal{R}}_{n'}^* \int_{\phi=0}^{2\pi} \int_{\theta=0}^{\pi} \hat{\boldsymbol{e}}_r \cdot \left(\left(\hat{\boldsymbol{e}}_r \times \boldsymbol{\psi}_{nm}^{far}\right) \times \left(\hat{\boldsymbol{e}}_r \times \boldsymbol{\psi}_{n'm'}^{far*}\right)\right) \sin(\theta)\, d\theta d\phi$$
$$= \frac{1}{k^2} \dot{\mathcal{R}}_n \dot{\mathcal{R}}_{n'}^* \int_{\phi=0}^{2\pi} \int_{\theta=0}^{\pi} \left(-\boldsymbol{\psi}_{nm}^{far} \cdot \left(\hat{\boldsymbol{e}}_r \times \boldsymbol{\psi}_{n'm'}^{far*}\right)\right) \sin(\theta)\, d\theta d\phi \qquad 1.12.19$$
$$= 0.$$

Similarly,

$$\int_{\partial B} d^2\boldsymbol{r} \cdot \left(\boldsymbol{M}_{nm} \times \boldsymbol{M}_{n'm'}^*\right)$$
$$= \frac{1}{k^2} \mathcal{R}_n \mathcal{R}_{n'}^* \int_{\phi=0}^{2\pi} \int_{\theta=0}^{\pi} \hat{\boldsymbol{e}}_r \cdot \left(\left(\boldsymbol{\psi}_{nm}^{far}\right) \times \left(\boldsymbol{\psi}_{n'm'}^{far*}\right)\right) \sin(\theta)\, d\theta d\phi$$
$$= \frac{1}{k^2} \mathcal{R}_n \mathcal{R}_{n'}^* \int_{\phi=0}^{2\pi} \int_{\theta=0}^{\pi} \left(\left(\hat{\boldsymbol{e}}_r \times \boldsymbol{\psi}_{nm}^{far}\right) \cdot \boldsymbol{\psi}_{n'm'}^{far*}\right) \sin(\theta)\, d\theta d\phi \qquad 1.12.20$$
$$= 0.$$

For opposite harmonics the relations are,

$$\int_{\partial B} d^2\boldsymbol{r} \cdot \left(\boldsymbol{M}_{nm} \times \boldsymbol{N}_{n'm'}^*\right)$$

$$
\begin{aligned}
&= \frac{1}{k^2}\mathcal{R}_n\dot{\mathcal{R}}^*_{n'}\int_{\phi=0}^{2\pi}\int_{\theta=0}^{\pi}\hat{\boldsymbol{e}}_r\cdot\left(\boldsymbol{\psi}^{far}_{nm}\times\left(\hat{\boldsymbol{e}}_r\times\boldsymbol{\psi}^{far*}_{n'm'}\right)\right)\sin(\theta)\,d\theta d\phi\\
&= \frac{1}{k^2}\mathcal{R}_n\dot{\mathcal{R}}^*_{n'}\int_{\phi=0}^{2\pi}\int_{\theta=0}^{\pi}\left(\left(\hat{\boldsymbol{e}}_r\times\boldsymbol{\psi}^{far}_{nm}\right)\cdot\left(\hat{\boldsymbol{e}}_r\times\boldsymbol{\psi}^{far*}_{n'm'}\right)\right)\sin(\theta)\,d\theta d\phi\\
&= \frac{1}{k^2}\mathcal{R}_n\dot{\mathcal{R}}^*_{n}(w_{nm})^2\left(2\pi\frac{2}{2n+1}\frac{(n+m)!}{(n-m)!}n(n+1)\delta_{m,m'}\delta_{n,n'}\right)\\
&= \frac{\pi}{k^2}\mathcal{R}_n\dot{\mathcal{R}}^*_{n}\delta_{m,m'}\delta_{n,n'}.
\end{aligned}
\qquad 1.12.21
$$

Similarly,

$$
\begin{aligned}
&\int_{\partial B} d^2\boldsymbol{r}\cdot\left(\boldsymbol{N}_{nm}\times\boldsymbol{M}^*_{n'm'}\right)\\
&= \frac{1}{k^2}\dot{\mathcal{R}}_n\mathcal{R}^*_{n'}\int_{\phi=0}^{2\pi}\int_{\theta=0}^{\pi}\hat{\boldsymbol{e}}_r\cdot\left(\left(\hat{\boldsymbol{e}}_r\times\boldsymbol{\psi}^{far}_{nm}\right)\times\left(\boldsymbol{\psi}^{far*}_{n'm'}\right)\right)\sin(\theta)\,d\theta d\phi\\
&= -\frac{1}{k^2}\dot{\mathcal{R}}_n\mathcal{R}^*_{n'}\int_{\phi=0}^{2\pi}\int_{\theta=0}^{\pi}\left(\left(\hat{\boldsymbol{e}}_r\times\boldsymbol{\psi}^{far}_{nm}\right)\cdot\left(\hat{\boldsymbol{e}}_r\times\boldsymbol{\psi}^{far*}_{n'm'}\right)\right)\sin(\theta)\,d\theta d\phi\\
&= -\frac{1}{k^2}\dot{\mathcal{R}}_n\mathcal{R}^*_{n}(w_{nm})^2\left(2\pi\frac{2}{2n+1}\frac{(n+m)!}{(n-m)!}n(n+1)\delta_{m,m'}\delta_{n,n'}\right)\\
&= -\frac{\pi}{k^2}\left(\mathcal{R}_n\dot{\mathcal{R}}^*_{n}\right)^*\delta_{m,m'}\delta_{n,n'}.
\end{aligned}
\qquad 1.12.22
$$

1.13 APPENDIX D: MIE VECTOR HARMONIC TRANSLATIONS

The Mie translation operators are

$$\begin{aligned}
&\mathrm{Rg}\,\boldsymbol{\Psi}(\boldsymbol{r}-\boldsymbol{r}_b)c_b = \mathrm{Rg}\,\boldsymbol{\Psi}(\boldsymbol{r}-\boldsymbol{r}_a)\mathbb{J}^{ab}(\boldsymbol{d}_{ab})c_b \\
&\boldsymbol{\Psi}(\boldsymbol{r}-\boldsymbol{r}_b)c_b = \mathrm{Rg}\,\boldsymbol{\Psi}(\boldsymbol{r}-\boldsymbol{r}_a)\mathbb{H}^{ab}(\boldsymbol{d}_{ab})c_b \qquad |\boldsymbol{d}_{ab}| > |\boldsymbol{r}-\boldsymbol{r}_a| \\
&\boldsymbol{\Psi}(\boldsymbol{r}-\boldsymbol{r}_b)c_b = \boldsymbol{\Psi}(\boldsymbol{r}-\boldsymbol{r}_a)\mathbb{J}^{ab}(\boldsymbol{d}_{ab})c_b \qquad |\boldsymbol{d}_{ab}| < |\boldsymbol{r}-\boldsymbol{r}_a|
\end{aligned} \tag{1.13.1}$$

where $\boldsymbol{d}_{ab} = \boldsymbol{r}_a - \boldsymbol{r}_b$. Each element of the operator is calculated as

$$\begin{matrix}\mathbb{H}_{ll'} \\ \mathbb{J}_{ll'}\end{matrix} = \delta_{tt'}\mathbb{A}_{mn,m'n'} + (1-\delta_{tt'})\mathbb{B}_{mn,m'n'} \tag{1.13.2}$$

where

$$\begin{aligned}
&\mathbb{A}_{mn,m'n'} = \\
&e^{i(m-m')\phi_d}\sum_{y=|n-n'|}^{n+n'} a_5(n,m|n',m'|y)\begin{matrix}h_y^{(1)}(kd) \\ j_y(kd)\end{matrix}P_y^{|m-m'|}(\cos(\theta_d))
\end{aligned} \tag{1.13.3}$$

and

$$\begin{aligned}
&\mathbb{B}_{mn,m'n'} = \\
&e^{i(m-m')\phi_d}\sum_{y=|n-n'|}^{n+n'} b_5(n,m|n',m'|y)\begin{matrix}h_y^{(1)}(kd) \\ j_y(kd)\end{matrix}P_y^{|m-m'|}(\cos(\theta_d)).
\end{aligned} \tag{1.13.4}$$

Therefore, $\mathbb{J}^{ab}$ is the same formula defining $\mathbb{H}^{ab}$, but using the spherical Bessel function of the first kind instead of the spherical Hankel function of the first kind. Finally, the transition functions are defined as

$$\begin{aligned}
&a_5(n,m|n',m'|y) \\
&= i^{|m-m'|-|m|-|m'|+n'-n+y}(-1)^{m-m'}\sqrt{\tfrac{(2n+1)(2n'+1)}{2n(n+1)n'(n'+1)}} \\
&\big(n(n+1)+n'(n'+1)-y(y+1)\big)\sqrt{2y+1}\times \\
&\begin{pmatrix} n & n' & y \\ m & -m' & -(m-m') \end{pmatrix}\begin{pmatrix} n & n' & y \\ 0 & 0 & 0 \end{pmatrix}
\end{aligned} \tag{1.13.5}$$

and

$$b_5(n,m|n',m'|y) = i^{|m-m'|-|m|-|m'|+n'-n+y}(-1)^{m-m'}\sqrt{\frac{(2n+1)(2n'+1)}{2n(n+1)n'(n'+1)}} \sqrt{\big((n+n'+n+y)(n+n'+1-y)(y+n-n')(y-n+n')(2y+1)\big)} \times \begin{pmatrix} n & n' & y \\ m & -m' & -(m-m') \end{pmatrix}\begin{pmatrix} n & n' & y-1 \\ 0 & 0 & 0 \end{pmatrix} \quad 1.13.6$$

where $\begin{pmatrix} \cdots \\ \cdots \end{pmatrix}$ denotes the Wigner-3j symbols.

1.14 APPENDIX E: MIE VECTOR HARMONIC ROTATIONS

The Mie rotation operator is

$$\begin{matrix}\mathrm{Rg}\,\boldsymbol{\Psi}(r,\theta,\phi)\\ \boldsymbol{\Psi}(r,\theta,\phi)\end{matrix} c_b = \begin{matrix}\mathrm{Rg}\,\boldsymbol{\Psi}(r,\theta',\phi')\\ \boldsymbol{\Psi}(r,\theta',\phi')\end{matrix} \mathbb{D}(\theta-\theta',\phi-\phi')c_b. \tag{1.14.1}$$

Each element of the operator is calculated as

$$\mathbb{D}_{ll'} = \delta_{tt'}\delta_{nn'}(-1)^{m+m'}e^{im(\phi-\phi')}d^n_{m,m'}(\theta-\theta')\Delta_{m,m'}, \tag{1.14.2}$$

where

$$\Delta_{m,m'} = \begin{cases} 1 & m \geq 0 \quad m' \geq 0 \\ (-1)^{m'} & m \geq 0 \quad m' < 0 \\ (-1)^{m} & m < 0 \quad m' \geq 0 \\ (-1)^{m+m'} & m < 0 \quad m' < 0 \end{cases} \tag{1.14.3}$$

and

$$\begin{aligned} &d^n_{m,m'}(\theta-\theta') \\ &= \sqrt{\tfrac{(n+m')!(n-m')!}{(n+m)!(n-m)!}}\textstyle\sum_\sigma(-1)^{n-m'-\sigma}C^{n-m'}_{n+m}C^{\sigma}_{n-m} \times \\ &\left(\cos\left(\tfrac{\theta-\theta'}{2}\right)\right)^{m+m'+2\sigma}\left(\sin\left(\tfrac{\theta-\theta'}{2}\right)\right)^{2n-m-m'-2\sigma}. \end{aligned} \tag{1.14.4}$$

are the Wigner d-functions.

1.15 APPENDIX F: MIE TO PLANE WAVE TRANSFORM

An arbitrary electromagnetic field can be expanded into a basis of plane waves as

$$\boldsymbol{E}(\boldsymbol{r};\boldsymbol{k}^{\pm}) = \sum_{q=0}^{1}\int \partial^2\boldsymbol{k}_{\parallel}\, g_q(\boldsymbol{k}^{\pm})\, e^{i\boldsymbol{k}^{\pm}\cdot\boldsymbol{r}}\, \hat{\boldsymbol{e}}_q(\boldsymbol{k}^{\pm}) \quad 1.15.1$$

$$\boldsymbol{H}(\boldsymbol{r};\boldsymbol{k}^{\pm}) = -iY\sum_{q=0}^{1}\int \partial^2\boldsymbol{k}_{\parallel}\, g_q(\boldsymbol{k}^{\pm})\, e^{i\boldsymbol{k}^{\pm}\cdot\boldsymbol{r}}\left(\hat{\boldsymbol{k}}^{\pm}\times\hat{\boldsymbol{e}}_q(\boldsymbol{k}^{\pm})\right), \quad 1.15.2$$

where $g_q(\boldsymbol{k}^{\pm})$ is the continuous coefficient representing the field's plane wave spectra. The wave vector is $\boldsymbol{k}$ and $\boldsymbol{k}_{\parallel}$ is the component of the wave vector parallel to the evaluation plane. Given that the domain of interest is above and below the particle plane, an evaluation plane will be defined as a plane parallel to the particle plane such that $\partial^2\boldsymbol{k}_{\parallel} = dk_x dk_y = k_{\parallel}dk_{\parallel}d\alpha = ksin(\beta)d\beta d\alpha$. The $\pm$ superscript denotes the chosen root of $k_z = \pm\sqrt{k^2 - k_{\parallel}^2}$, when writing the wavevector in cylindrical coordinates. Waves traveling toward $z \to \infty$ are given the $+$ superscript. Waves traveling toward $z \to -\infty$ are given the $-$ superscript. In the case that $k^2 < k_{\parallel}^2$, the wave is evanescent, and the sign enforces the proper exponential decay in the direction of travel. $\hat{\boldsymbol{e}}_{\mathbf{q}}^{\pm}$ is the polarization state, where $q = 0$ is the unit vector in the azimuth direction (TE or s-polarization) and $q = 1$ is the unit vector in the polar direction (TM or p-polarization). S-polarization is defined in relation to the normal vector of the evaluation plane and the direction of the wave vector,

$$\hat{\boldsymbol{e}}_0(\boldsymbol{k}^{\pm}) = \frac{(\boldsymbol{k}^{\pm}\times-\hat{\boldsymbol{n}})}{\|\boldsymbol{k}^{\pm}\times-\hat{\boldsymbol{n}}\|} \quad (TE)\,. \quad 1.15.3$$

Correspondingly, TM polarization is defined as

$$\hat{\boldsymbol{e}}_1(\boldsymbol{k}^{\pm}) = \frac{(\hat{\boldsymbol{e}}_0(\boldsymbol{k}^{\pm})\times\boldsymbol{k}^{\pm})}{\|\hat{\boldsymbol{e}}_0(\boldsymbol{k}^{\pm})\times\boldsymbol{k}^{\pm}\|} \quad (TM)\,. \quad 1.15.4$$

The initial choice to define $\hat{\boldsymbol{e}}_1(\boldsymbol{k}^{\pm})$ in terms of $-\hat{\boldsymbol{n}}$ is c for the convenience of being able to write $\pm$ in the components of $\hat{\boldsymbol{e}}_2(\boldsymbol{k}^{\pm})$instead of $\mp$. The two polarization states are orthogonal to the direction of plane wave propagation but $\hat{\boldsymbol{e}}_2(\boldsymbol{k}^{\pm})$ is not orthogonal to the normal of the particle plane. The following identities

$$\widehat{\boldsymbol{k}}^{\pm} \times \hat{\boldsymbol{e}}_q(\boldsymbol{k}^{\pm}) = (-1)^q \hat{\boldsymbol{e}}_{\bar{q}}(\boldsymbol{k}^{\pm}) \quad 1.15.5$$

$$\hat{\boldsymbol{e}}_q(\boldsymbol{k}^{\pm}) \times \hat{\boldsymbol{e}}_{1-q}(\boldsymbol{k}^{\pm}) = (-1)^q \widehat{\boldsymbol{k}}^{\pm} \quad 1.15.6$$

are useful for calculating power flow. A plane wave with arbitrary polarization can always be decomposed to TE and TM polarization states as $\hat{\boldsymbol{e}}(\boldsymbol{k}^{\pm}) = (\hat{\boldsymbol{e}} \cdot \hat{\boldsymbol{e}}_1(\boldsymbol{k}^{\pm}))\hat{\boldsymbol{e}}_1(\boldsymbol{k}^{\pm}) + (\hat{\boldsymbol{e}} \cdot \hat{\boldsymbol{e}}_2(\boldsymbol{k}^{\pm}))\hat{\boldsymbol{e}}_2(\boldsymbol{k}^{\pm})$.

Representing the wavenumber in spherical coordinates, $\boldsymbol{k} = k\hat{\boldsymbol{e}}_r + \alpha\hat{\boldsymbol{e}}_\phi + \beta\hat{\boldsymbol{e}}_\theta$, the regular Mie harmonics can be written in integral representation as

$$\begin{matrix} \mathrm{Rg}\, \boldsymbol{M}_{mn} \\ \mathrm{Rg}\, \boldsymbol{N}_{mn} \end{matrix} = \frac{i}{4\pi} \int_{\beta=0}^{\pi} \int_{\alpha=0}^{2\pi} \sin(\beta)\, d\beta d\alpha \begin{matrix} \boldsymbol{M}_{nm}^{far}(\widehat{\boldsymbol{k}}) \\ \boldsymbol{N}_{nm}^{far}(\widehat{\boldsymbol{k}}) \end{matrix} \boldsymbol{e}^{i\boldsymbol{k}\cdot\boldsymbol{r}}. \quad 1.15.7$$

Since the outgoing harmonics are singular at their reference origin, their integral representation is meaningful only in the domain not including this origin point. For the case of an infinite film, the domains of interest are above and below the particle plane as singular points exist throughout the particle plane. In this context, it is most efficient to write the wavenumber in cylindrical coordinates, $\boldsymbol{k}^{\pm} = k_{\parallel}\hat{\boldsymbol{e}}_\rho + \alpha\hat{\boldsymbol{e}}_\phi \pm k_z\hat{\boldsymbol{e}}_z$. Then the integral representation of the outgoing harmonics, takes the form

$$\begin{matrix} \boldsymbol{M}_{mn} \\ \boldsymbol{N}_{mn} \end{matrix} = \frac{i}{2\pi} \int_{\alpha=0}^{\pi} \int_{k_{\parallel}=0}^{\infty} \frac{d^2\boldsymbol{k}_{\parallel}}{k|k_z|} \begin{matrix} \boldsymbol{M}_{nm}^{far}(\widehat{\boldsymbol{k}}) \\ \boldsymbol{N}_{nm}^{far}(\widehat{\boldsymbol{k}}) \end{matrix} \boldsymbol{e}^{i\boldsymbol{k}^{\pm}\cdot\boldsymbol{r}} \quad 1.15.8$$

where $\boldsymbol{k}^{+}$ is used in the transmission hemisphere and $\boldsymbol{k}^{-}$ is used in the reflection hemisphere.

It is now clear that the spherical harmonics can be written as a plane wave expansion by projecting their integral representation onto the TE and TM polarizations. Correspondingly an electric field in the Mie basis can be expanded in a plane wave basis with spectral coefficients,

$$g_q(\boldsymbol{k}^{\pm}) = \frac{i}{2\pi k|k_z|} \left[\boldsymbol{N}^{far}(\widehat{\boldsymbol{k}}) \cdot \hat{\boldsymbol{e}}_q(\boldsymbol{k}^{\pm}) \quad \boldsymbol{M}^{far}(\widehat{\boldsymbol{k}}) \cdot \hat{\boldsymbol{e}}_q(\boldsymbol{k}^{\pm}) \right] \begin{bmatrix} c^E \\ c^M \end{bmatrix}. \quad 1.15.9$$

Chapter 2

PRESERVATION OF THE KERKER EFFECT IN RANDOM FILMS

Wray, P. R.; Atwater, H. A. Light–Matter Interactions in Films of Randomly Distributed Unidirectionally Scattering Dielectric Nanoparticles. *ACS Photonics* **2020**, *7* (8), 2105–2114. https://doi.org/10.1021/acsphotonics.0c00545.

ABSTRACT

We theoretically investigate the light scattering characteristics of monolayer films composed of randomly positioned unidirectionally scattering dielectric nanoparticles that support overlapping electric and magnetic dipole modes. We show using generalized Mie theory that the optical response of both sparse and dense nanoparticle films can be understood from the scattering properties of the individual dielectric nanoparticles, despite random particle-particle coupling effects, and validate these results with full wave electromagnetic simulations. The spectral, angular, and polarization dependent reflection and transmission scattering characteristics of these random particle films are also shown to be strikingly different from those of homogeneous dense solid thin films of equivalent dielectric permittivity.

2.1 INTRODUCTION

Scattering objects made of a high index dielectrics offer the ability to generate low-loss electric and magnetic Mie resonances for light manipulation below the free-space diffraction limit[19–25]. Of notable interest, the addition of magnetic Mie resonances in spherical dielectric particles enables field distributions not achievable in metal counterparts, which support only resonant electric Mie modes [22,23,26–28]. This degree of freedom provides a compelling argument for the use of high index dielectrics in next generation metamaterial technologies. For example, overlapping electric and magnetic Mie modes have shown to produce dramatic unidirectional scattering, termed Kerker scattering[23,27,29]. Through precise particle placement, research in Kerker scattering particle films has shown new ways to design antireflective coatings, reflectors, absorbers, and other wavefront manipulating metasurfaces[19,21,24–26,29–35]. We expand on this growing body of research by studying the behavior of Kerker metasurfaces composed of randomly positioned but uniformly sized particles. We find the spectral, angular, and polarization response of these random Kerker metasurfaces are dramatically distinct from dense solid thin films of equivalent dielectric permittivity. The particle films exhibit no polarization dependence and transmission and reflection peaks can be directly manipulated through proper design of the constituent particle. The results suggest that random films of Kerker particles could be used in designs of polarization invariant antireflective coatings or reflectors. Notably, random Kerker metasurfaces can be synthesized without the need for precise lithographic patterning, self-assembly, or layer stacking and thus could be fabricated using low-cost deposition methods such as plasma synthesis.

A scattering object with overlapping electric dipole (ED) and magnetic dipole (MD) modes and suppressed higher order modes will have a far field scattering distribution which mimics an idealized point source (i.e., an only forward or backward propagating spherical wavelet) that is described by the Huygens-Fresnel principle[36]. Objects of this type are characterized by extreme forward-to-backward scattering ratios (FBR) dictated by the phase relationship between the ED and MD modes. They are also characterized by an even distribution in energy between the two modes, which gives rise to polarization invariance; meaning the scattering pattern looks the same in the direction parallel and perpendicular to the electric field[29,37]. The concept of overlapping electric and magnetic scattering modes was first introduced by Milton Kerker, in the context of elastic scattering from magnetic particles[37]. For this reason, the unique scattering behavior is often called Kerker scattering.

In recent years there has been rapidly expanding interest in Kerker scattering based on small dielectric particles. Though not magnetic, these particles support spectrally overlapping electric

and magnetic dipole modes in the visible wavelength range. This is done by creating an optically-induced magnetic resonance[22,23,26–29,32,34,38–40]. The use of Kerker particles in the context of antenna arrays has been explored to produce highly directional scattering[41]. Previous research has shown that precise placement of Kerker particles in chains along the plane wave propagation direction can lead to a polarization-invariant scattered far field. Backward reflection could be substantially suppressed and forward directivity and side lobes could be tuned through particle spacing[42]. Particle clusters have been studied which were shown to collectively exhibit Kerker scattering behavior[43–45]. Random silicon trimer and quadrimer particle clusters in different orientations were shown to behave like effective Kerker particles[45]. The magnetic response was attributed to the individual nanoparticle, whereas the electric component was attributed to gap modes between particles[45]. Films composed of Kerker particles have also been studied in 2D and 3D ordered periodic arrays. Lattices of various types have been studied in the metasurface regime, where the sub-wavelength periodicity produces no diffraction orders, and in the grating regime where diffraction is present at various orders[46,47]. This body of work has led to the theoretical predictions and experimental verification of near prefect transmission[48,49], reflection[50,51], and absorption[34,52] in ordered arrays, through particle design and lattice spacing.

In this paper, we show that 2D films of randomly placed Kerker particles also give rise to behavior which cannot be replicated by equivalent homogeneous dense thin film analogs. The key finding is that, in an average sense, nanoparticles will retain their Kerker behavior in the presence of random interparticle coupling. This occurs despite the stringent requirement placed on both the amplitude and phase of the ED and MD modes. The result is that the optical properties of both sparse and dense monolayer films of randomly distributed Kerker particles can be accurately predicted from the scattering characteristics of single particle building blocks. The specular, angular, and polarization dependent properties are distinctly different from dense homogeneous thin film analogs. Our analysis uses generalized Mie theory, which completely accounts for particle coupling. This framework creates satisfying parallels between studying random Kerker particle films and the use of traditional Mie theory for the design of isolated Kerker particles.

2.2 DESIGN OF ED/MD OVERLAPING KERKER PARTICLES

The phenomenon of Kerker scattering from a spherical particle can be directly seen from Mie theory[53]. In the far field limit, the amplitude response of elastic scattering from a wave incident on a particle can be written in a convenient matrix form

$$\begin{bmatrix} E_s^{\parallel} \\ E_s^{\perp} \end{bmatrix} = \frac{e^{ikR}}{-ikR} \begin{bmatrix} S_2 & S_3 \\ S_4 & S_1 \end{bmatrix} \begin{bmatrix} E_i^{\parallel} \\ E_i^{\perp} \end{bmatrix}, \quad 2.2.1$$

where E_s is the elastic scattered electric field amplitude, E_i is the incident field amplitude, $\parallel$ and $\perp$ represent the planes parallel and perpendicular to the scattering plane[53], k is the wavenumber in the surrounding media, and R is the radial observation distance from the particle's origin. S_j ($j = 1,2,3,4$) are the elements of the amplitude scattering matrix. For a single particle under plane wave illumination, there is no polarization conversion $(S_3 = S_4 = 0)$[53]. If all scattering coefficients beyond the first order are negligible, the angle-resolved far field scattering efficiency parallel, $Q_s^{\parallel}(\theta)$, and perpendicular, $Q_s^{\perp}(\theta)$, to the scattering plane are given by

$$Q_s^{\parallel}(\theta) = \frac{\|S_2\|^2}{x^2} = \frac{1}{x^2}\left(\|a_1\|^2\tau_1^2 + \|b_1\|^2\pi_1^2 + (a_1 b_1^* + b_1 a_1^*)\pi_1\tau_1\right) \quad 2.2.2$$

and

$$Q_s^{\perp}(\theta) = \frac{\|S_1\|^2}{x^2} = \frac{1}{x^2}\left(\|b_1\|^2\tau_1^2 + \|a_1\|^2\pi_1^2 + (a_1 b_1^* + b_1 a_1^*)\pi_1\tau_1\right), \quad 2.2.3$$

where $\tau_n = \frac{dP_n^1(\cos(\theta))}{d\theta}$ and $\pi_n = \frac{P_n^1(\cos(\theta))}{sin\theta}$ are the angle-dependent basis functions, based on the associated Legendre polynomial (P_n^m) of order n and degree $m = 1$. The coefficients for this basis are a_n for transverse magnetic (TM) modes and b_n for transverse electric (TE) modes. These coefficients are found by applying the boundary conditions of field continuity between the particle and environment, leading to the well-known Mie solutions[53]. The asterisk over the variable denotes the complex conjugate and the $n = 1$ subscript represent the dipole modes. The argument $x = \frac{2\pi r}{\lambda_0}$, called the size parameter, is a unitless ratio between the particle radius (r) and the free-space wavelength (λ_0). In the forward $(\theta = 0°)$ and backward $(\theta = 180°)$ scattering directions the parallel and perpendicular scattering efficiencies are the same.

Therefore, the forward-to-backward ratio (FBR) is defined as $FBR = Q_s(\theta = 0°) / Q_s(\theta = 180°)$, where either $Q_s^{\parallel}(\theta)$ or $Q_s^{\perp}(\theta)$ can be used.

Kerker's condition for forward scattering requires $a_1 = b_1$ and backward scattering requires $a_1 = -b_1$ [37]. The condition $\|a_1\|^2 = \|b_1\|^2$ creates polarization invariance. Therefore, Kerker scattering requires an even distribution of energy between the transverse electric (TE) and transverse magnetic (TM) modes, while the propagation direction is directly related to the relative phase of the coefficients, due to the interference term. Figure 2.2.1 depicts the entire particle parameter space where the Kerker conditions are satisfied for the first order (dipole). The contribution of higher order modes is shown in the figure 2.5.1. The plots assume a particle with lossless permittivity ($\epsilon = \epsilon_r$) and unity relative permeability (μ_r = 1) with a background of free space. The assumption of negligible loss is justified in figure 2.5.2. Figure 1a shows the difference in energy distribution between the first order TE and TM modes. The dotted and dashed magenta line indicate where the TE and TM mode energies are equal. Figure 2.2.1b shows the relative phase between these two modes. From the phase profile we see the dashed magenta line corresponds to the forward Kerker condition whereas the dotted magenta line is approaching the backward Kerker condition with increasing permittivity. Between these two regions is an optically-induced artificial magnetic resonance[26]. Figure 2.2.1c shows the resulting FBR that would be achieved as a result of the magnitude and phase relationships from figure 2.2.1a and 2.2.1b. This figure shows that there are two distinct Kerker regimes for real passive materials: (1) a region where forward-scattering is always dominant and (2) a region producing a backward-to-forward scattering transition.

As an example of Kerker scattering for passive materials, figure 2.2.2 shows the response of an 88 nm diameter silicon (Si[54]) particle illustrating the backward-to-forward scattering regime, and a 280 nm diameter gallium nitride (GaN[55]) particle, as an example of the forward-only scattering regime. For the 88 nm diameter Si particle, the wavelength range from 400 nm to 500 nm is sufficient to study backward-to-forward scattering. In the case of the 280 nm diameter GaN particle, we find forward-only scattering with optimal forward scattering from 675-800 nm. We find wavelength ranges from 550 nm to 600 nm are shown to have appreciable second order terms. This region is not considered in our analysis, despite maintaining forward dominant scattering, since we are primarily interested in overlapping ED and MD modes. All calculations for figures 2.2.1 and 2.2.2 were done using a Mie theory scattering formalism[56].

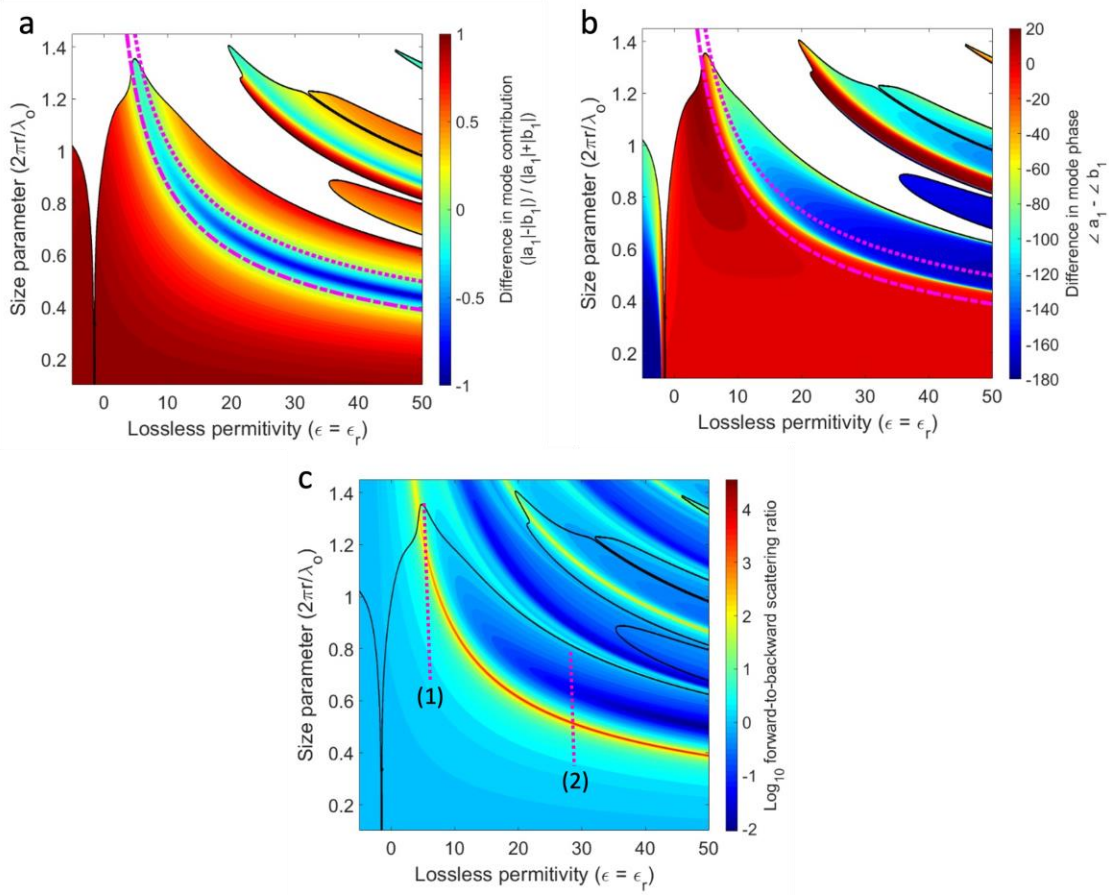

Figure 2.2.1. Parameter space for the single particle scattering coefficients, showing the different Kerker regimes. (a) Normalized difference between the first order TM and TE scattering coefficients, as a function of size parameter and lossless permittivity. The dashed and dotted magenta line show the region where $\|a_1\|^2 = \|b_1\|^2$. The dashed line is under the dotted line. The white region is where the particle supports more than one mode, which is defined when the first order modes contribute less than 99% of the scattering cross-section. (b) The phase difference between the first order TM and TE mode. The dashed and dotted magenta lines are transferred from Figure 2.2.1a, to show the phase relationship in the regions where TM and TE mode energy is equal. The white region is also transferred from Figure 2.2.1a. (c) Log base 10 of the FBR which would occur from the magnitude and phase results in Figure 2.2.1a and 2.2.1b. The black outline denotes the transition region from single to multi-mode. Multi-mode regions are not overlaid with white. The first magenta dashed line shows and the forward-only scattering region. The second magenta line shows the region of backward-to-forward scattering transitions.

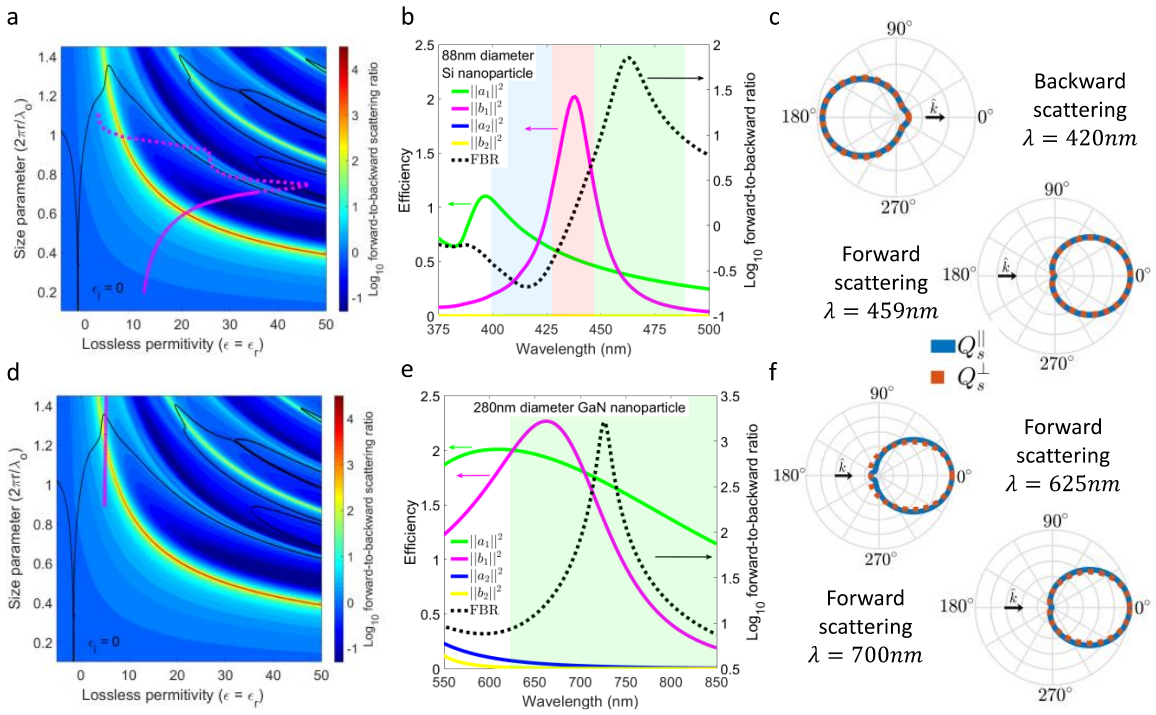

Figure 2.2.2. Scattering profiles of a 88 nm diameter Si particle and a 280 nm diameter GaN particle. (a) The log base 10 FBR from Figure 2.2.1c, with the permittivity of silicon overlaid in magenta, as a function of size parameter $(x = 2\pi\ 44\ [nm]/\lambda_o\ [nm])$. The dashed magenta line represents the region of Si permittivity that is not applicable for the graph, due to material loss. The solid magenta line is the region of Si applicable to the graph $(\epsilon_i < 0.7)$. (b) Efficiency scaled magnitude response of the dominant scattering coefficients in the Si particle's scattering cross-section (solid lines). he dashed black line plots the log base 10 FRB of the Si particle, as a function of wavelength, in the regions showing the backward scattering (blue), the optically-induced artificial magnetic resonance (red), and the forward scattering (green) regime. (c) The angle-resolved far field scattering profiles near the backward and forward Kerker resonances in the Si particle. (d-f) The analogous graphs from (a-c) for a 280 nm diameter GaN particle. For 280 nm diameter GaN, only forward-dominant scattering is present and second order modes become appreciable at shorter wavelengths $(\lambda < 650\ nm)$. All magnitude responses are efficiency scaled based on the formula $\frac{2}{x^2}(2n+1)\|\delta_n\|^2$, where $\delta_n = a_n$ or b_n and n is the mode order.

2.3 EFFECT OF RANDOM COUPLING ON KERKER PARTICLES

As described in the previous sections, Kerker scattering requires a particle to satisfy stringent magnitude and phase relationships between modes. To study the effect of random nanoparticle coupling, we generate random monolayer films of same sized Kerker particles and calculate how interparticle coupling alters the scattering behavior of an individual particle within the film. This is done using generalized Mie theory, which is a complete analytical solution to the problem of multiple scattering and interparticle coupling between particles[57,58]. Interestingly we find that, the average response will continue to satisfy Kerker's stringent amplitude and phase conditions. This is true even when the average nearest neighbor distance is well within the near field coupling regime. We then show, in the next section, that this average response has a direct relationship to the scattering behavior of an infinite randomly distributed particle film.

When dealing with coupled nanoparticles, polarization conversion can occur. Since this property is not seen in isolated Mie theory, it is necessary to work with the full scattering matrix from of equation 2.2.1 to define a particle's scattering response. The particle's angle resolved scattering efficiency is written in general form

$$Q_s^{\parallel}(\theta) = \frac{1}{x^2}(\|S_2\|^2 + \|S_3\|^2 + S_2S_3^* + S_2^*S_3)\,, \qquad 2.3.1$$

and

$$Q_s^{\perp}(\theta) = \frac{1}{x^2}(\|S_4\|^2 + \|S_1\|^2 + S_4S_1^* + S_4^*S_1). \qquad 2.3.2$$

Furthermore, in generalized Mie theory, it cannot be assumed that degree (m) in the modal expansion is unitary. Therefore, the scattering amplitude elements $(S_1 - S_4)$ are fully expanded with respect to degree (m), order (n), and type (TE or TM). The derivation for converting the scattering amplitude elements from isolated Mie theory to generalized Mie theory is presented in section two of the supplementary information.

Using the generalized framework, we simulate finite sized random monolayer nanoparticle films with 10%, 20%, 30%, and 40% area fill fraction. The packing densities correspond to an average nearest neighbor distance ranging from 68nm to 10nm. Gap distances as small as zero (i.e., touching particles) are allowed and do occur. Simulations are done for both 88 nm diameter Si and 280 nm diameter GaN particles, to study both the forward-to-backward and forward-only

Kerker scattering regimes. The method emulates simulating a particle in an infinite film by deterministically placing an "observation particle" at the origin, then generating a sufficiently large number of particles surrounding it. The surrounding particles are placed based on a uniform distribution (i.e., equal probably of finding a particle at any location where particles do not overlap) around the observation particle. The spatial autocorrelation of these random particle distributions is shown in figure 2.6.3 for Si and figure 2.6.4 for GaN. The generalized Mie program is then run on each finite particle film and the resulting scattering coefficients for the observation particle is recorded, accounting for all interparticle coupling. This process is repeated for 50 unique particle distributions, simulating both parallel and perpendicular incident polarization at normal incidence (100 simulations in total). Repeating the simulation procedure on unique distributions is designed to mimic randomly sampling particles in an infinite film.

In both the loose and densely packed cases, we find the average response of the observation particle is weakly affected by coupling between surrounding particles. The effect of particle coupling became more pronounced as fill fraction increased. Though, on average, the resulting spectral profile exhibits the same type of Kerker scattering as is seen for isolated particles. We find that particle coupling does not excite higher order modes within the Kerker particles, as all scattering coefficients having orders greater than one $(n > 1)$ were shown to be negligible (detail for 88 nm diameter Si particles is shown in figure 2.6.5 and for 280 nm diameter GaN particles in figure 2.6.6). Therefore, we need only consider $mn = \{11, -11\}$. Unlike the isolated Mie solution, in both Si and GaN, polarization conversion was present. For the scattering coefficients associated with polarization conversion, their phase profiles mimicked a uniform distribution. Their magnitudes mimicked the parallel-to-parallel or perpendicular-to-perpendicular coefficients with, on average, an order of magnitude less strength (detail for 88 nm diameter Si particles is shown in figure 2.6.5 and for 280 nm diameter GaN particles in figure 2.6.6). In other words, the polarization conversion scattering elements, S_3 and S_4, had random phase. They also had magnitudes that were one order of magnitude less than S_1 and S_2 and have similar spectral shape. This result simplifies equations 2.3.1 and 2.3.2 with respect to the average response since $E[S_2 S_3^* + S_2^* S_3] \approx E[S_4 S_1^* + S_4^* S_1] \approx 0$. We can intuit the random phase of the polarization converted field from the fact that this field is a direct result of the scattered field from the surrounding particles impinging on the observation particle. Since these particles are a random distance from the observation particle, their phase profiles do not coherently overlap.

In general particle clusters are not rotationally symmetric, so scattering coefficients for parallel and perpendicular incident polarization are different. We can intuitively understand this lack of symmetry by considering particle dimers. In dimers the electric field distribution can be different depending on if particles are aligned on or off axis with respect to the incident polarization. For

an infinite film we can remove this polarization dependence, with respect to the average response, by including particle distributions rotated by 90 degrees when performing the average. Removing the negligible higher order terms and incorporating all relevant simplifications discussed above, the average angle-resolved scattering efficiency for a particle in a randomly positioned Kerker film can be simplified to

$$\mathbb{E}[Q_s^{\parallel}(\theta)] = \frac{1}{x^2}\mathbb{E}\begin{bmatrix}(\|A_{11}\|^2 + \|A_{11}^{\times}\|^2)\tau_{11}^2 + \\ (\|B_{11}\|^2 + \|B_{11}^{\times}\|^2)\pi_{11}^2 + \\ (A_{11}B_{11}^* + A_{11,j}^* B_{11})\tau_{11}\pi_{11}\end{bmatrix} \quad 2.3.3$$

and

$$\mathbb{E}[Q_{s,j}^{\perp}(\theta)] = \frac{1}{x^2}\mathbb{E}\begin{bmatrix}\left(\|B_{11,j}\|^2 + \|B_{11,j}^{\times}\|^2\right)\tau_{11}^2 + \\ \left(\|A_{11,j}\|^2 + \|A_{11,j}^{\times}\|^2\right)\pi_{11}^2 + \\ (A_{11,j}B_{11,j}^* + A_{11,j}^* B_{11,j})\tau_{11}\pi_{11}\end{bmatrix}. \quad 2.3.4$$

The variables A_{mn} and B_{mn} are the TM and TE modes associated with energy transfer between same polarization states. The variables $A_{mn}^{\times}$ and $B_{mn}^{\times}$ account for cross-polarization energy transfer. Averaging is taken over observation particles (j), including sets of 90-degree rotations.

Equations 2.3.3 and 2.3.4 show a surprising result. A first order Kerker particle's average scattering response function in a random film is nearly identical to its isolated scattering response function shown in equations 2.2.2 and 2.2.3. The difference is only in the addition of first order incoherent polarization conversion terms. Consequently, the FBR of the average scattering response can be written in similar form to the isolated Mie case, as $FBR_A = \frac{\mathbb{E}[Q_s(\theta=0°)]}{\mathbb{E}[Q_s(\theta=180°)]}$. Either $\mathbb{E}[Q_s^{\parallel}(\theta)]$ or $\mathbb{E}[Q_s^{\perp}(\theta)]$ can be used as long as we are considering all sets accounting for 90-degree rotations. Justification for the definition of the FBR_A is provided in section four of the supplementary information. For randomly distributed Kerker particles, the phase relationship that determines forward or backward Kerker scattering is given by only the primary first order modes, $\mathbb{E}[A_{11}B_{11}^* + A_{11}^* B_{11}]$. Therefore, for both forward and backward Kerker scattering, it is necessary that $\mathbb{E}[\|A_{11}\|^2] = \mathbb{E}[\|B_{11}\|^2]$ and that $\mathbb{E}[\|A_{11}^{\times}\|^2]$ and $\mathbb{E}[\|B_{11}^{\times}\|^2]$ approach zero, since the cross-polarization coefficients are not present in the interference term. The condition of polarization invariance is generalized to $\mathbb{E}[\|A_{11}\|^2 + \|A_{11}^{\times}\|^2] = \mathbb{E}[\|B_{11}\|^2 +$

$\|B_{11}^{\times}\|^2]$, indicating that it is not necessary for cross polarization terms to vanish in order to satisfy polarization invariance.

Figure 2.3.1 shows the average magnitude response of the prominent scattering coefficients found in a randomly coupled Kerker particle as well as the particle's FBR_A. The results are shown for 88 nm diameter Si nanoparticle films with (a) 10% and (d) 40% fill fraction and for 280 nm diameter GaN nanoparticle films with (b) 10% and (e) 40% fill fraction. Results for 20% and 30% fill fraction are shown in figure 2.6.7. We see, for nanoparticles in both the forward-only and backward-to-forward Kerker scattering regimes (280nm diameter GaN and 88 nm diameter Si, respectively), the average scattering coefficients mimic the overall shape of the mode profiles for the isolated Mie solution from figure 2.2.2. Furthermore, the FBR_A for the coupled and isolated case follow a similar profile, indicating correct phase behavior. The phase response of the primary scattering coefficients is presented in figure 2.6.5 for 88 nm diameter Si and figure 2.6.6 for 280 nm diameter GaN. From the results above we find that a Kerker particle embedded in a random monolayer film of Kerker particles will retain the Kerker scattering behavior of its isolated particle solution, in an average sense, despite the effects of random particle coupling. All FBR_A's were calculated using the general formulas from equations 2.3.1 and 2.3.2, assuming no simplifications, to validate equations 2.3.3 and 2.3.4. In figure 2.3.1, the mode decomposed independent scattering efficiencies are defined as $\frac{2}{x^2}\mathbb{E}\left[\left\|\Delta_{nm,j}\right\|^2\right]$, where $\Delta = \mathrm{A}, \mathrm{B}, \mathrm{A}^{\times}$, or $B^{\times}$. These mode decomposed efficiencies will sum to the independent particle's scattering efficiency. This is not the same as the total scattering efficiency due to the interference effect between particles. More information about particle efficiencies under the generalized Mie theory framework is presented in section three of the supplementary information.

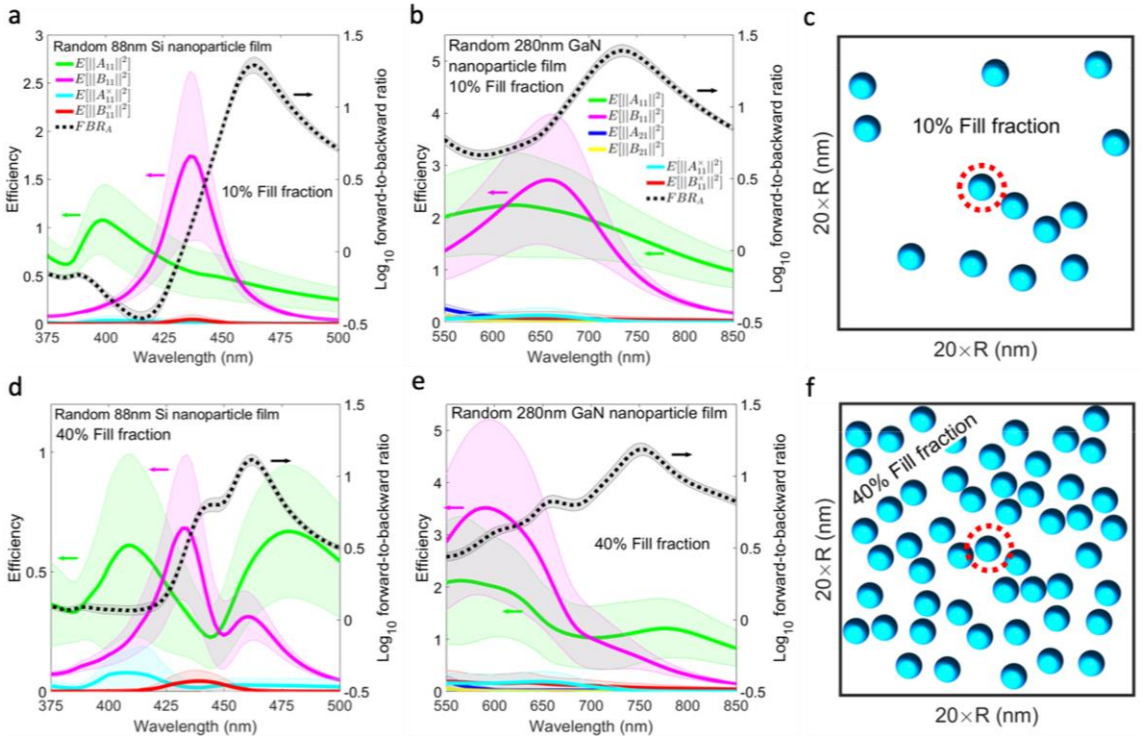

Figure 2.3.1. Scattering behavior of Kerker particles embedded in a random monolayer Kerker particle film. (a,d) Efficiency scaled magnitude of the dominant scattering modes and FBR_A for an 88 nm diameter Si particle embedded in a random particle film with fill fractions of (a) 10% and (d) 40%. (c,e) Corresponding results for 280 nm diameter GaN particle embedded in a random particle film with fill fractions of (b) 10% and (e) 40%. (c,f) Top-view graphical representation of a random particle film with fill fractions of (c) 10%, and (f) 40%. The red dashed circle outlines the observation particle. The length and width of the film are given as a function of particle radius (R). The solid color lines show the average (N=100) mode contribution to the independent scattering efficiency (left y-axis). The dashed black line shows the FBR_A for the average scattering response (right y-axis). The corresponding shaded areas is the area one standard deviation from the mean. All magnitude responses are efficiency scaled based on the formula $\frac{2}{x^2}\mathbb{E}[\|\Delta_{nm}\|^2]$, where $\Delta = \mathrm{A}, \mathrm{B}, \mathrm{A}^{\times}$, or $B^{\times}$.

2.4 MONOLAYER FILMS OF RANDOMLY DISTRIBUTED KERKER PARTICLES

To corroborate our results from generalized Mie theory and further study the reflection, transmission, absorption (RTA), and polarization-dependent behavior of these films, we simulate the random nanoparticle films using full-wave finite-difference time-domain (FDTD) simulations[59].

Random nanoparticle films with length and width dimensions of 40 times the particle radius was repeated using Bloch boundary conditions to model an infinite random structure. Figure 2.4.1a-c shows the RTA behavior of 88 nm diameter Si random nanoparticle films in the backward-to-forward Kerker regime. Area fill fractions ranged from 10-40% and illumination was normal incidence. Figure 2.4.1d-f shows the corresponding RTA results for 280 nm diameter GaN random films in the forward-only regime. In all cases, three distinct random particle distributions were simulated using FDTD. The solid lines are the average from the three distinct simulations. The shaded region represents the area within one standard deviation of the average. In all cases, the reflection and transmission properties of these films were dramatically different from the behavior of a corresponding homogeneous dense thin film. The RTA response of a homogeneous dense thin film with a thickness equal to the corresponding nanoparticle diameter is given by the dashed black line.

We find the dominant scattering feature in these films is like that of an isolated nanoparticle building block. To highlight this, we propose the formula

$$R = \frac{ff\mathbb{E}[\sigma_{sca}]}{1+FBR}, \;\; A = ff\mathbb{E}[\sigma_{abs}], \;\; T = 1 - A - R, \tag{2.4.1}$$

which estimates the film's spectral reflection (R), absorption (A), and transmission (T) response based only on parameters from the average Kerker particle scattering behavior and the particle film's area fill fraction (ff). The FBR_A, average observation particle scattering efficiency ($\mathbb{E}[\sigma_{sca}]$), and average observation particle absorption efficiency ($\mathbb{E}[\sigma_{abs,}]$) are calculated from the simulations performed in section three. The scattering efficiency is determined through the equation

$$\mathbb{E}[\sigma_{ext}] - \mathbb{E}[\sigma_{abs}] = \mathbb{E}[\sigma_{sca-i}] + \mathbb{E}[\sigma_{sca-d}] = \mathbb{E}[\sigma_{sca}], \tag{2.4.2}$$

where $\sigma_{ext,j}$ is the extinction efficiency, $\sigma_{abs,j}$ is the absorption efficiency, $\sigma_{sca-i,j}$ is the independent scattering efficiency, and $\sigma_{sca-d,j}$ is the dependent scattering efficiency of the j'th sampled observation particle[60].

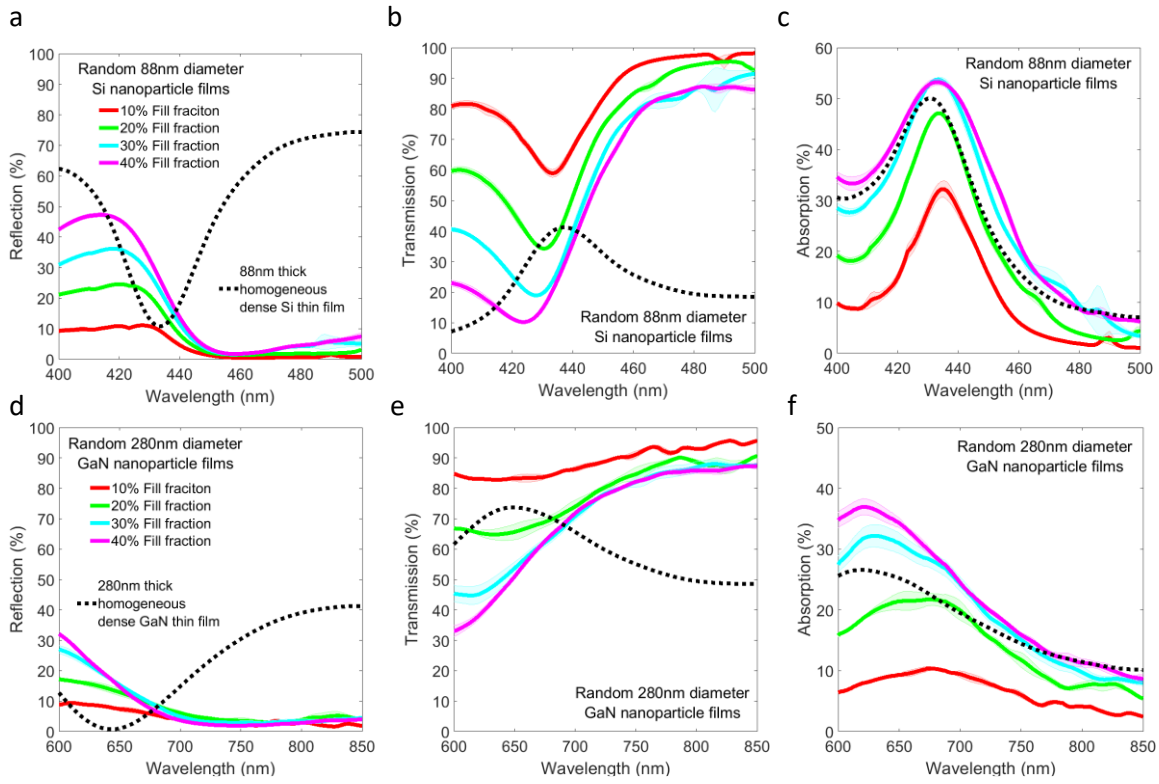

Figure 2.4.1. Reflection, transmission, and absorption of random nanoparticle films made of Kerker particles, calculated using FDTD. (a-c) RTA of random particle films made of 88 nm diameter Si particles for area fill fractions ranging from 10-40%. The colored solid lines represent the average response over 3 simulations of distinct random distributions. The colored shaded region represents the area within one standard deviation of the mean. The dashed black line shows the RTA for an 88 nm thick dense homogenous thin film slab of Si. (d-f) Corresponding results for random particle films of 280 nm diameter GaN particles. The dashed black like shows the corresponding response for a 280 nm thick dense homogeneous thin film slab of GaN.

Figure 2.4.2 compares the result of equation 2.4.1 to the direct calculations from figure 2.4.1. The comparison was done for fill fractions of 10% and 40% in 88 nm diameter Si films (figure 2.4.2a,b) and in 280 nm diameter GaN films (figure 2.4.2c,d). The results for fill fractions of 20% and 30% are shown in figure 2.6.7. Satisfyingly we find a good agreement between equation 2.4.1 and the results from full-wave calculations. Alternatively, effective medium theories such as the Bruggeman and Maxwell-Garnett mixing formulas did not accurately predict the film's RTA response.

Figure 2.4.3 shows the angle- and polarization-dependent RTA responses of both Si and GaN nanoparticle films with 20% fill fraction. The response to the random Si Kerker film is plotted at a wavelength of 420 nm (figure 2.6.9), for backward-Kerker behavior, and at 459 nm (figure 2.4.2a), for forward-Kerker scattering. A comparison to the response of an 88 nm thick Si homogeneous dense thin film is shown in figure 2.4.2d. Figures 2.4.2b,c,e,f show the analogous comparisons for GaN. Unlike the thin film cases, we see that the RTA response of the Kerker particle films are relatively unchanged for angles of incidence lower than 40 degrees. At steeper angles, reflection begins to increase and transmission decreases accordingly, while absorption stays relatively constant. This effect is most pronounced at wavelengths with forward-direction Kerker scattering. The RTA response of the random Kerker films are also invariant to incident polarization state and show no Brewster's angle suppression of transverse magnetic reflective. This behavior is completely different to the case of a homogeneous dense thin film.

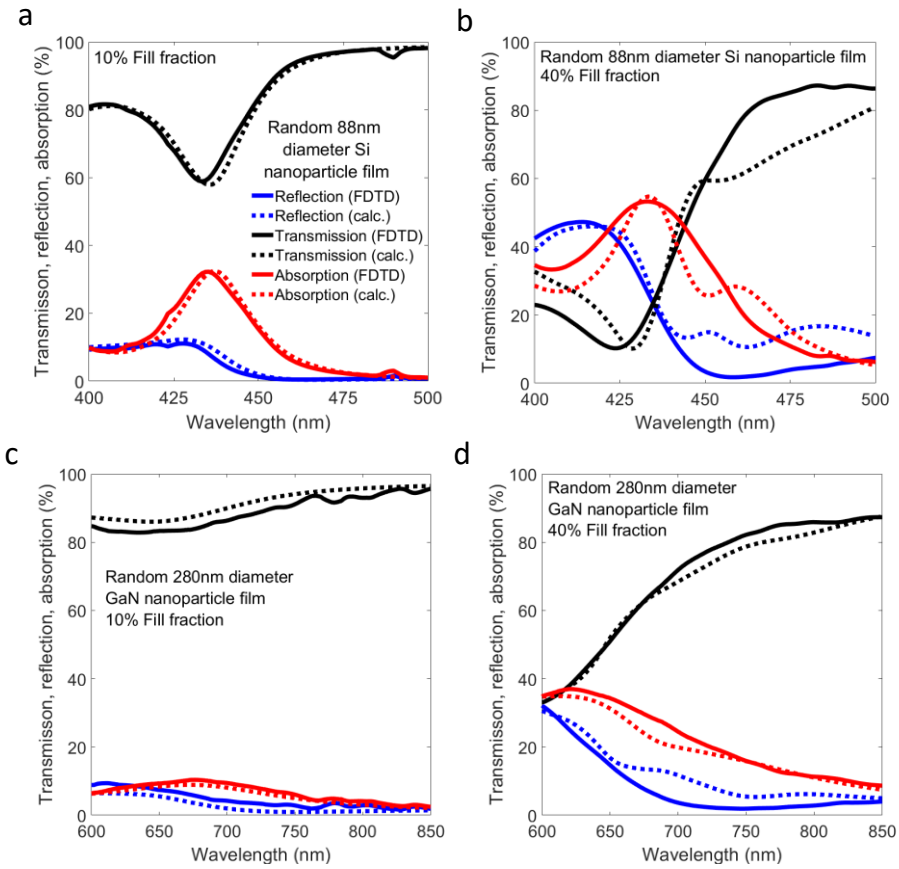

Figure 2.4.2. Comparison of the reflection, transmission, and absorption (RTA) in random monolayer Kerker films at normal incidence. In all cases the solid lines are the average FDTD-based RTA response, taken from Figure 2.4.1, and the dashed lines are the average RTA response predicted from equation 2.4.1 using the data from section two. (a,b) RTA of 88 nm diameter Si random particle films for (a) 10% and (b) 40% fill fraction. (c,d) RTA of the 280 nm diameter GaN random particle films for (c) 10% and (d) 40% fill fraction.

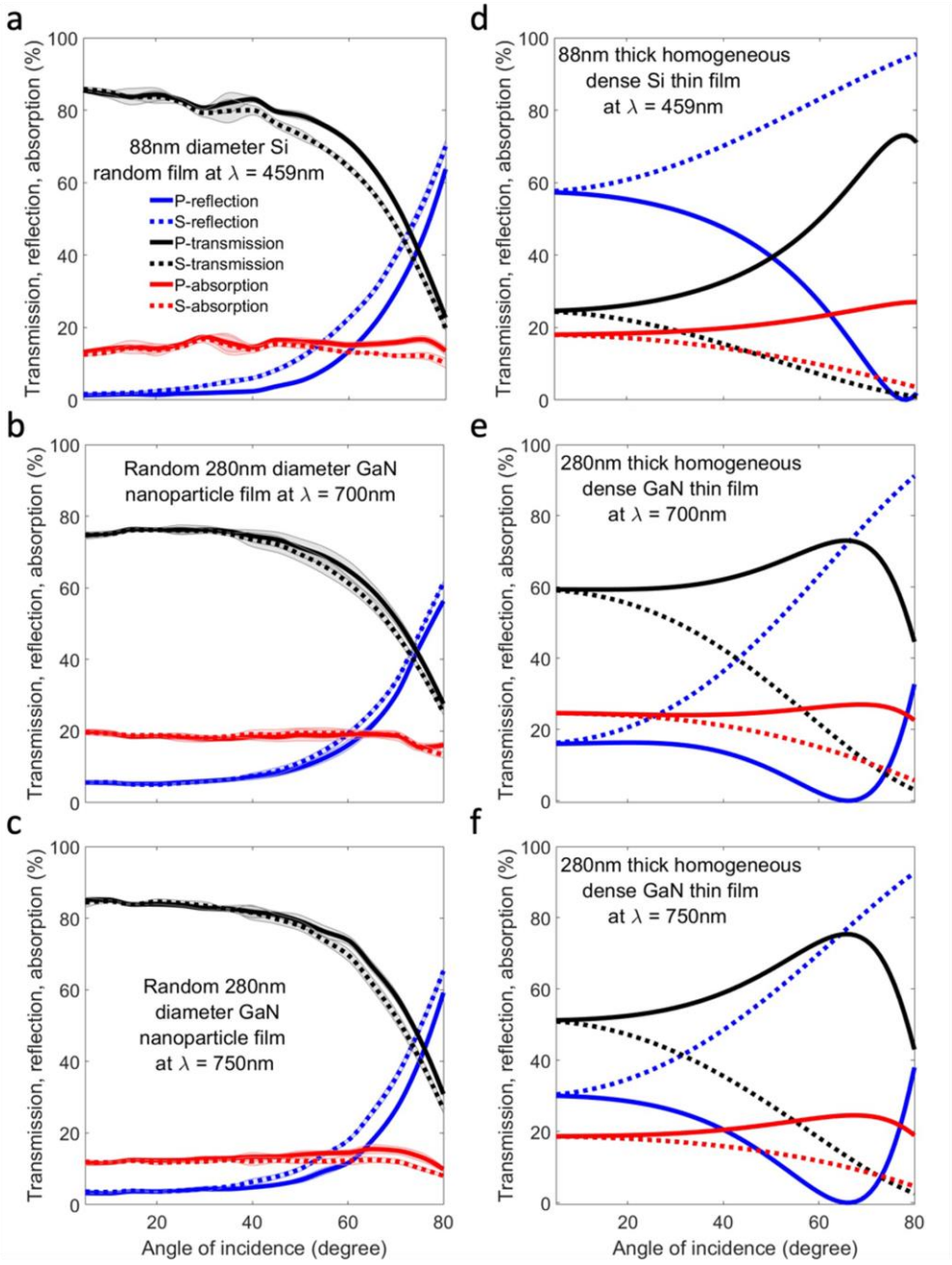

Figure 2.4.3. Angular and polarization response of random Kerker films with a fill fraction of 20% and a comparison to equivalent thickness thin film analogs. For the random films, the particle distributions are the same as the ones used in Figure 2.4.1, for the 20% fill fraction case. For a-c, the lines represent the average from the 3 distinct simulations and the shaded area represents the area within one standard deviation from the mean. All solid lines represent plane wave excitation with p-polarization. All dashed lines represent s-polarization.

2.5 CONCLUSION

In summary, we show that Kerker scattering achieved by ED and MD overlap in small size parameter particles can create either forward-only scattering or scattering with a backward-to-forward transition as the wavelength is varied. Using 280 nm diameter GaN nanoparticles as an example of forward-only scattering and 88 nm diameter Si nanoparticles as an example of a backward-to-forward scattering transition, we study the effect of random particle coupling in monolayer particle films. The scattering properties of an individual Kerker particles in a random film was weakly affected by particle coupling. In an average sense, the scattering properties mimic the isolated Mie response with the introduction of an added cross-polarization term. This term was roughly an order of magnitude weaker than the dominant terms and had random phase. Random films of Kerker particles had reflection and transmission spectra that could be predicted from three values: the average particle scattering cross-section, the forward-to-backward ratio, and the films area fill fraction. In all cases the spectrum was distinctly different from thin-film analogs or effective medium predictions. Finally, we showed that the reflection and transmission response of random Kerker films does not differentiate between s- and p-polarizations and that these films do not exhibit a Brewster angle reflection like that of a thin film sample.

2.6 APPENDIX A: SUPPLEMENTARY FIGURES

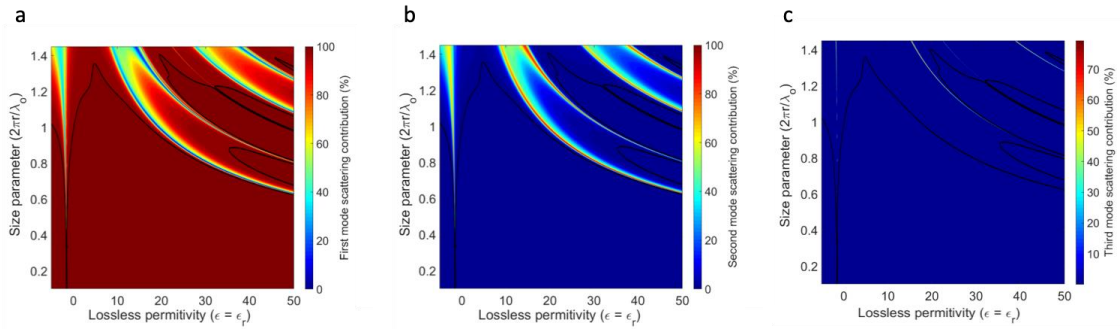

Figure 2.6.1. Mode contribution to the total scattering cross section for a single lossless nanoparticle. (a) Normalized contribution of the first order modes to the total scattering cross section. (b) Normalized contribution of the second order modes to the total scattering cross section. (c) Normalized contribution of the third order modes to the total scattering cross section. All graphs were calculated using Mie theory, up to fifth order modes. No non-zero mode contributions were found for modes above the third order.

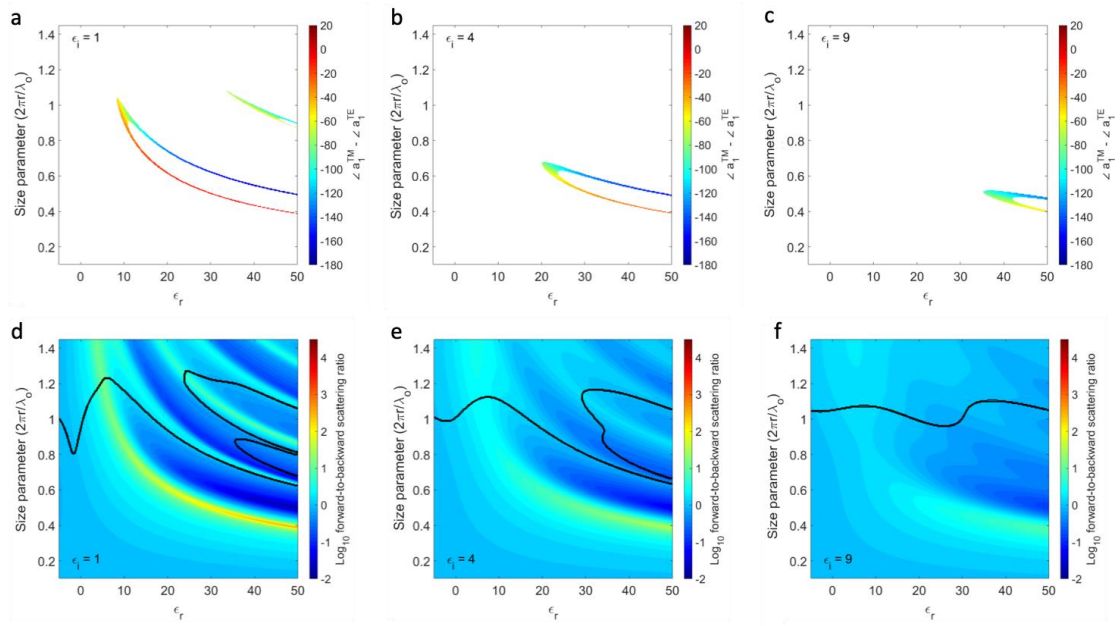

Figure 2.6.2. Effect of material loss on satisfying polarization invariance Kerker condition, and forward-to-backward ratios. Figure 2.6.2a-c shows the phase difference between the first order TM and TE modes, in the regime where the normalized difference in the mode magnitudes is less than one tenth. Figure 2.6.2a-c are plotted for imaginary permittivity equal to one, four, and nine, respectively. Figure 2.6.2d-f, shows the corresponding log base ten forward-to-backward scattering ratios, with a black line overlay showing the cutoff when the first order modes contribute less than ninety nine percent of the scattering cross section.

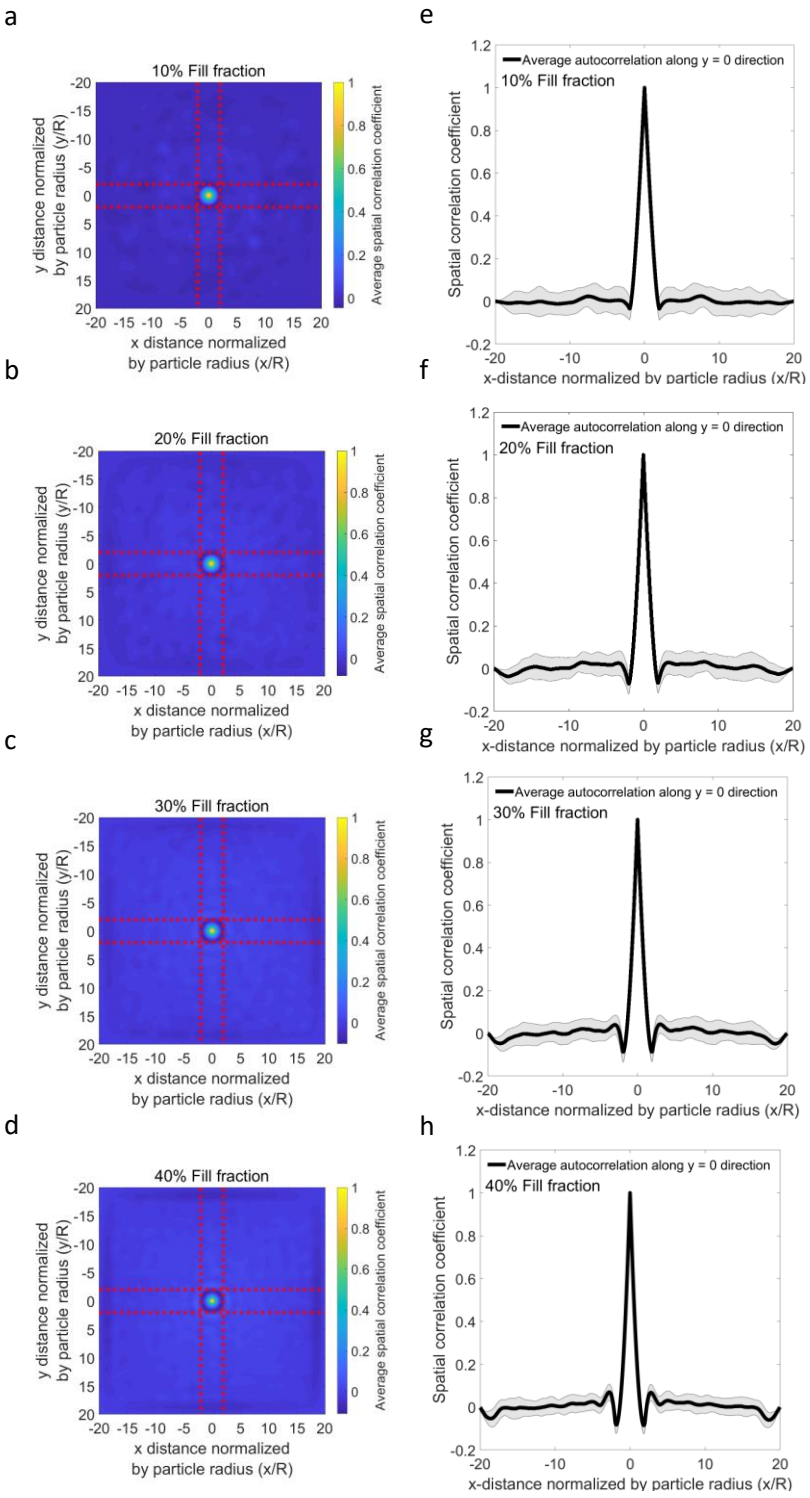

Figure 2.6.3. Average spatial autocorrelation functions of the 50 unique particle distributions and their 90 degree rotations for Si. (a-d) Average spatial autocorrelation function for 88nm diameter Si particles randomly distributed with fill fractions of (a) 10%, (b) 20%, (c) 30%, and (d) 40%. (e-h) Line profile of the autocorrelation along the y = 0 direction. The solid black line represents the average autocorrelation. The shaded area is one standard deviation from the average.

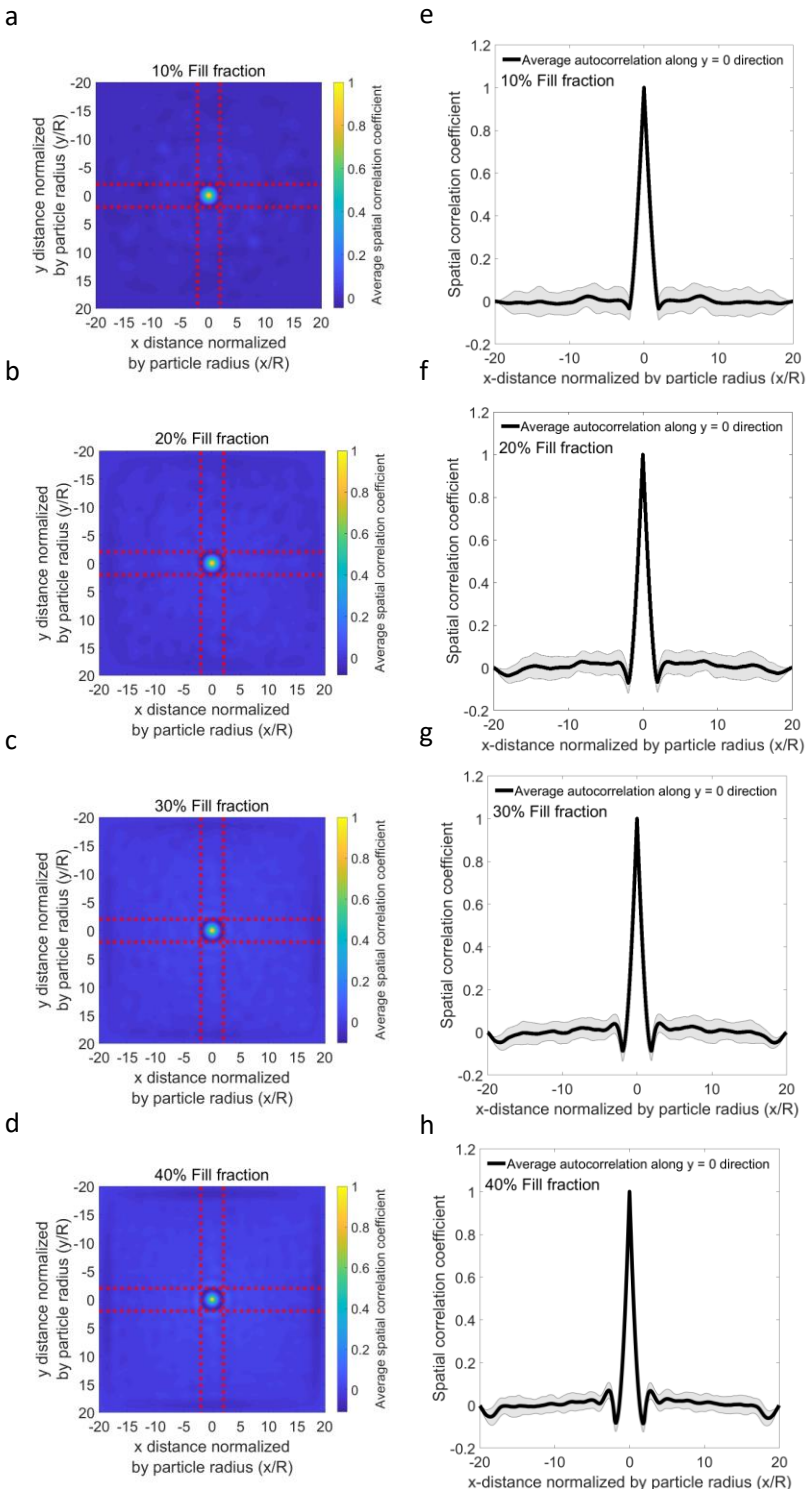

Figure 2.6.4. Average spatial autocorrelation functions of the 50 unique particle distributions and their 90 degree rotations for Si. (a-d) Average spatial autocorrelation function for 88nm diameter Si particles randomly distributed with fill fractions of (a) 10%, (b) 20%, (c) 30%, and (d) 40%. (e-h) Line profile of the autocorrelation along the y = 0 direction. The solid black line represents the average autocorrelation. The shaded area is one standard deviation from the average.

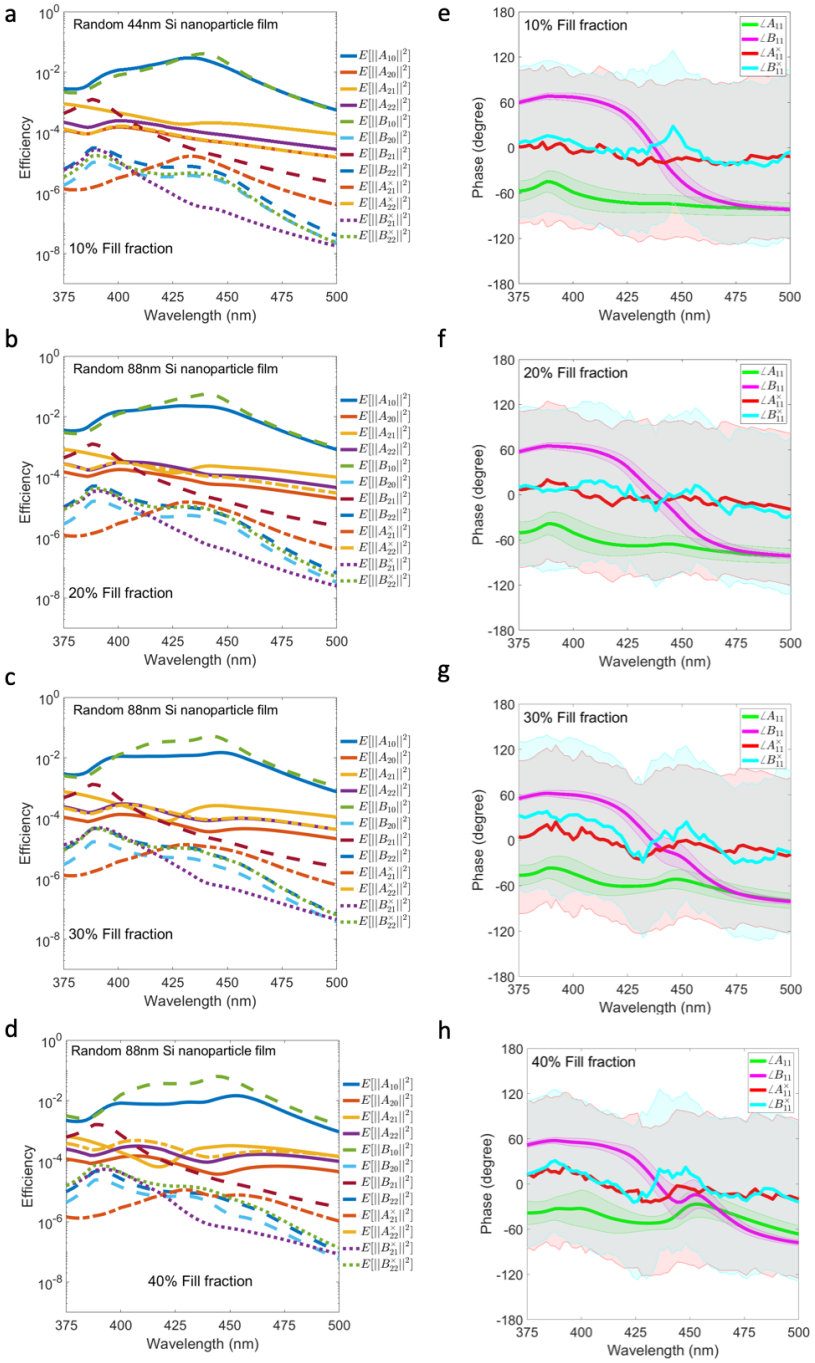

Figure 2.6.5. Contribution of higher order modes to the scattering response and the phase profiles of the dominant scattering modes for an 88nm Si particle embedded in a random Kerker film of 88nm Si particles. (a-d) Average contribution of the $mn = \{01,02,12,22\}$ modes to the independent scattering cross-section for fill fractions of (a) 10%, (b) 20%, (c) 30%, and (d) 40%. (e-h) Phase profile of the dominant scattering modes $mn = \{11\}$, showing the cross-polarization terms have random phase for (e) 10%, (f) 20%, (g) 30%, and (h) 40% fill fraction. The solid lines represent the average response and the corresponding shaded area is the area within one standard deviation of the mean. Statistics were based on 50 unique particle distributions and their 90-degree rotations (100 simulations in total).

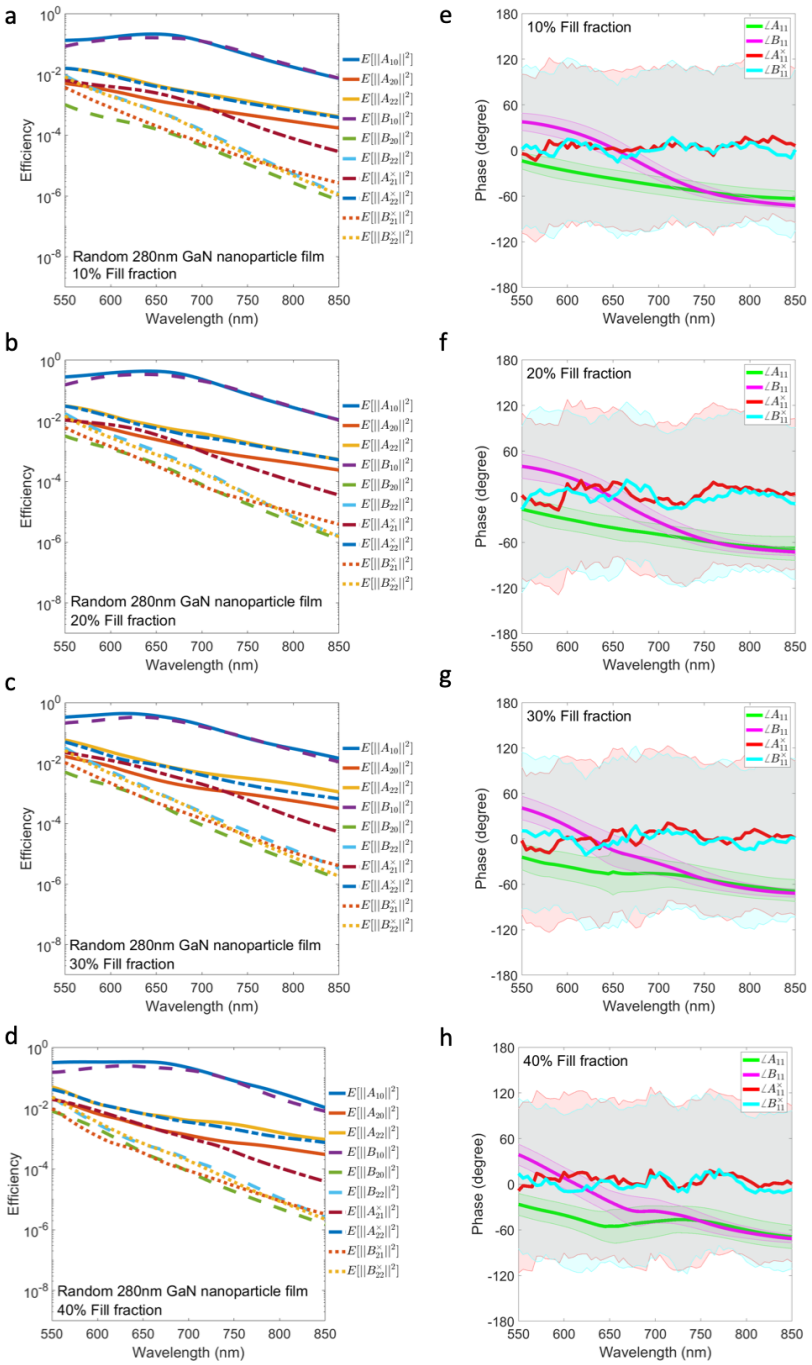

Figure 2.6.6. Contribution of higher order modes to the scattering response and the phase profiles of the dominant scattering modes for an 280nm GaN particle embedded in a random Kerker film of 280nm GaN particles. (a-d) Average contribution of the $mn = \{01,02,12,22\}$ modes to the independent scattering cross-section for fill fractions of (a) 10%, (b) 20%, (c) 30%, and (d) 40%. (e-h) Phase profile of the dominant scattering modes $mn = \{11\}$, showing the cross-polarization terms have random phase for (e) 10%, (f) 20%, (g) 30%, and (h) 40% fill fraction. The solid lines represent the average response and the corresponding shaded area is the area within one standard deviation of the mean. Statistics were based on 50 unique particle distributions and their 90-degree rotations (100 simulations in total).

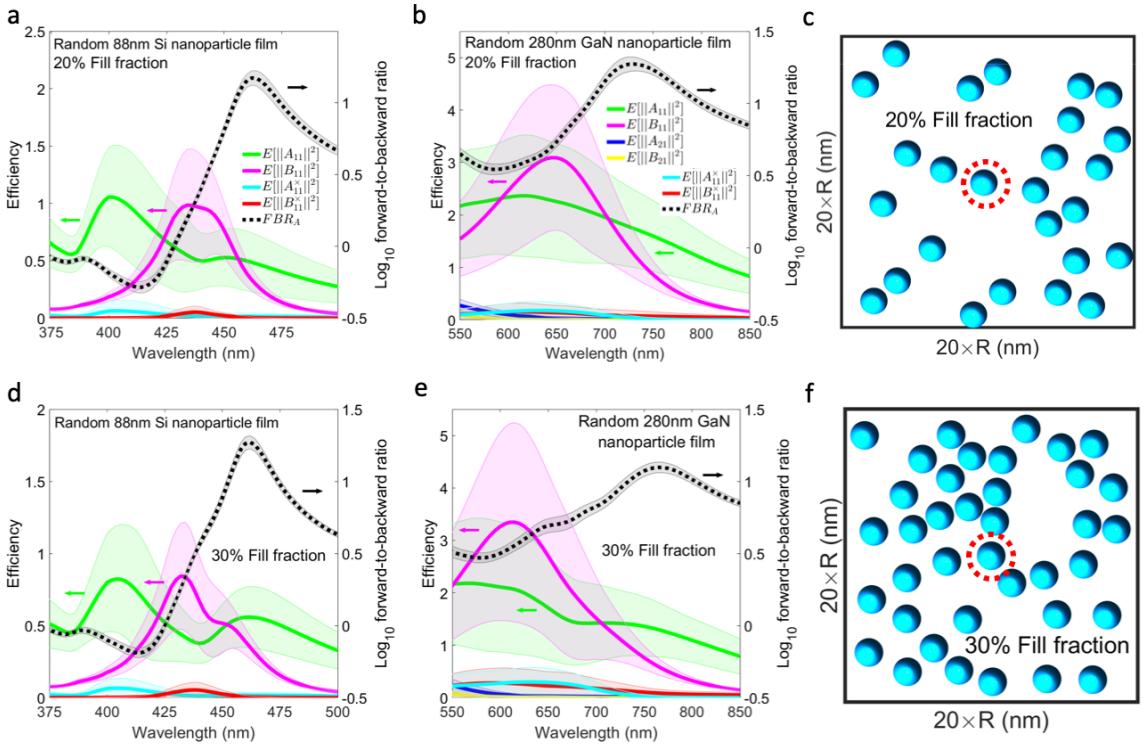

Figure 2.6.7. Scattering behavior of Kerker particles embedded in a random monolayer Kerker particle film. (a,d) Efficiency scaled magnitude of the dominant scattering modes and FBR_A for an 88 nm diameter Si particle embedded in a random particle film with fill fractions of (a) 20% and (d) 30%. (c,e) Corresponding results for 280 nm diameter GaN particle embedded in a random particle film with fill fractions of (b) 20% and (e) 30%. (c,f) Top-view graphical representation of a random particle film with fill fractions of (c) 20%, and (f) 30%. The red dashed circle outlines the observation particle. The length and width of the film are given as a function of particle radius (R). The solid color lines show the average (N=100) mode contribution to the independent scattering efficiency (left y-axis). The corresponding shaded area is the area one standard deviation from the mean. The dashed black line shows the FBR_A for the average scattering response (right y-axis).

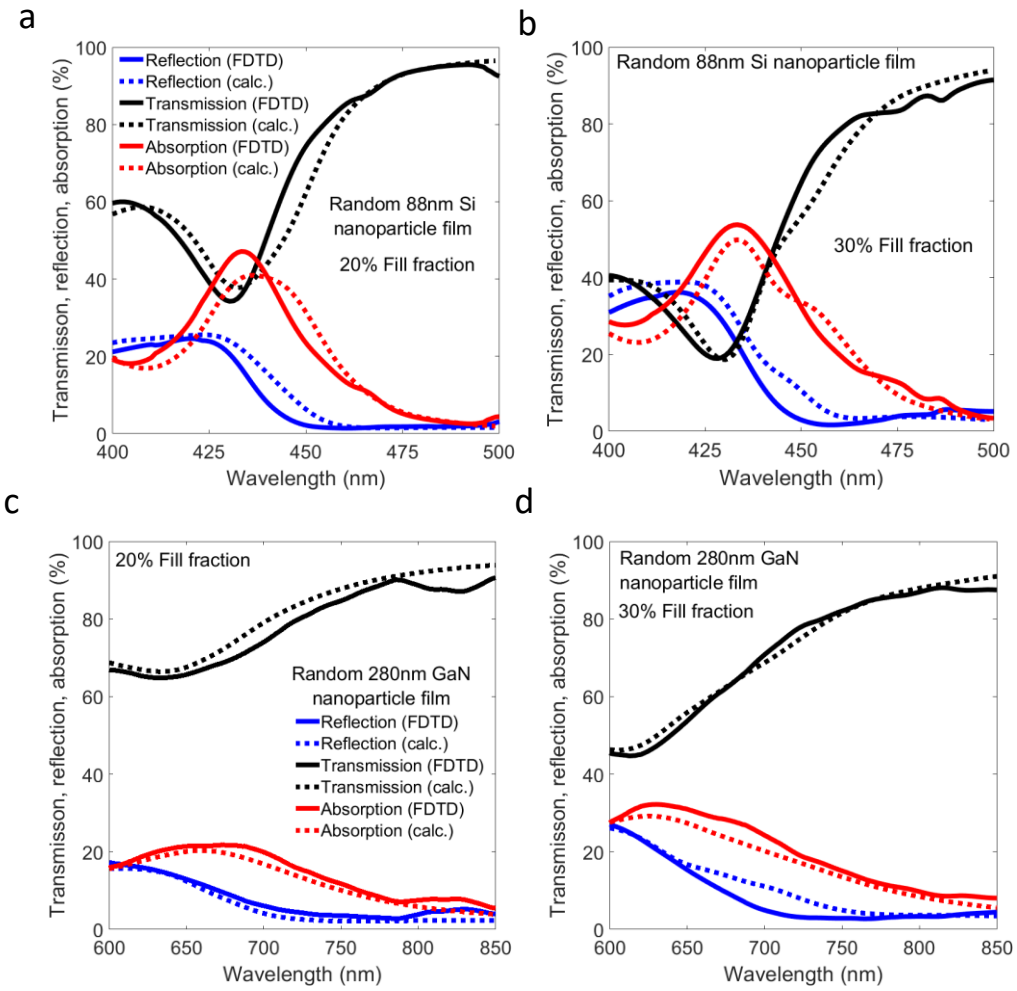

Figure 2.6.8. Comparison of the reflection, transmission, and absorption (RTA) in random monolayer Kerker films at normal incidence. In all cases the solid lines are the average FDTD-based RTA response, taken from the, and the dashed lines are the average RTA response predicted from equation (8) using the data from section 2 in the main text. (a,b) RTA of 88 nm diameter Si random particle films for (a) 20% and (b) 30% fill fraction. (c,d) RTA of the 280 nm diameter GaN random particle films for (c) 20% and (d) 30% fill fraction.

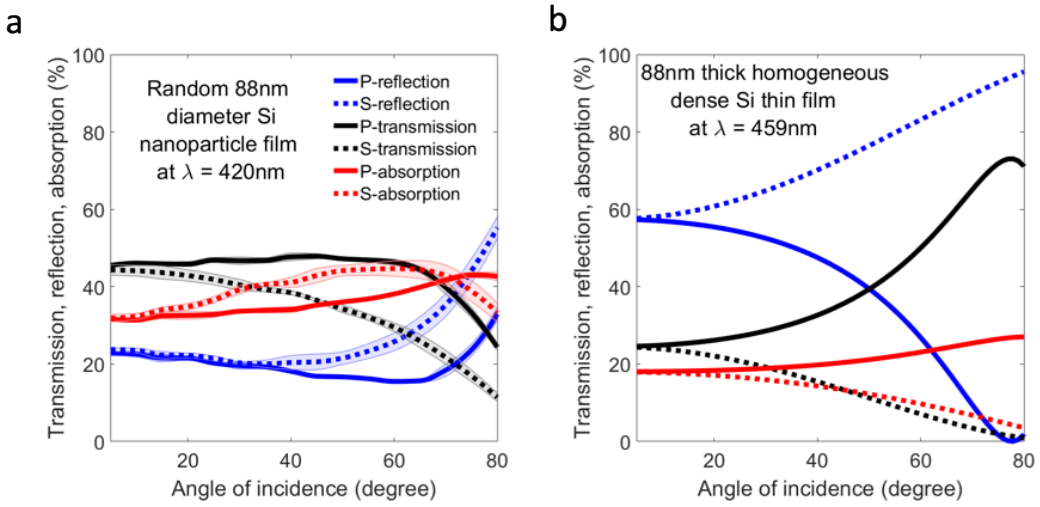

Figure 2.6.9. Angular response of random Kerker films with a fill fraction of 20%. (a) RTA for randomly placed 88 nm Si particles as a function of angle, at a wavelength of 420 nm (backward-Kerker regime). (b) Corresponding RTA angular response for an 88 nm Si slab at a wavelength of 420 nm.

Chapter 3

THE KERKER TRANSFORM

Wray, P. R.; Atwater, H. A. Kerker Transform: Expanding Fields in a Discrete Basis of Directional Harmonics. arXiv March 7, 2023. https://doi.org/10.48550/arXiv.2303.03693.

ABSTRACT

We present a linear coordinate transform to expand the solution of scattering and emission problems into a basis of forward and backward directional vector harmonics. The transform provides intuitive algebraic and geometric interpretations of systems with directional scattering/emission across a broad range of wavelength-to-size ratios. The Kerker, generalized Kerker, and transverse Kerker effect as well as other forms of highly directional scattering/emission are easily understood through open and closed loop contours in the complex plane. Furthermore, the theoretical maximum directivity of any scattering/emissive system is easily defined. The transformed far field harmonics have coordinates that are polar-angle invariant, interference between forward and backward harmonics weakly interact, and interference of same type harmonics alters directivity. Examples of highly directional scattering are presented including a Kerker scattering magnetic sphere, a directional scattering photonic nanojet, both under plane wave illumination, as well as generalized backward Kerker and transverse Kerker emission from sub-wavelength spheres that are near-field coupled to emitters. Solutions of scattering/emission under the Kerker transform are contrasted to the traditional Mie expansion for comparison.

3.1 INTRODUCTION

The spherical harmonics are a set of fundamental modes of vibration on the sphere that provide valuable insights for understanding the scattering/emission of electromagnetic waves from particles[61–63]. Though these harmonics are invaluable to our understanding of scattering/emission from wavelength-sized objects, their atom-like spatial profile does not create a simple representation for describing phenomena such as angular momentum or directional scattering/emission. Fortunately, a linear transform of the spherical harmonics offers an insightful and mathematically simple method to study optical spin and orbital angular momentum[64,65]. In this manuscript we show that by a different but equally simple linear transform, the spherical harmonics can also give an intuitive basis to describe strongly directional scattering/emission. The resulting basis therefore provides a framework to study highly directional phenomena, which is of great value in many subjects in electromagnetics[22,29,34,35,37,66–71], while maintaining may of the beneficial properties that have popularized the spherical harmonics.

Under the Mie (vector spherical harmonic) framework, the Kerker effect is a method of achieving large forward-to-backward scattering/emission ratios through near exact cancelation of either the forward or backward intensity. This is achieved through the precise interference of same order electric ($\boldsymbol{\Psi}^{E}_{nmp}$) and magnetic-type ($\boldsymbol{\Psi}^{M}_{nmp}$) atom-like modes, where n is the polar quantum number, m is the azimuthal quantum number, and p ($0 =$ even and $1 =$ odd) is the azimuthal parity[37]. The case where generalized combinations of harmonics leads to (near) exact forward or backward cancelation is categorized as a generalized Kerker effect[72,29]. This requires no restriction on relative amplitude or phase between modes, only that they collectively interfere for exact cancelation in one direction. Cancelation in both directions is termed the transverse Kerker effect[34]. These conditions of cancelation in the exact forward or backward direction are formalized as the null points in the expression of exact forward ($\theta = 0$) or backward ($\theta = \pi$) power flow[53,73]. In principle, there are an infinite number of these null solutions. Besides a select set of simple examples (e.g., $c^{M}_{n1p} = c^{E}_{n1p}$), these solutions can be hard to intuit as they come from a quadratic polynomial of n, m, p, t terms. Furthermore, directional scattering is a more holistic concept that need not evoke Kerker's conditions. It encompasses other metrics, such as directivity and side lobe behavior. The null conditions of the exact forward and backward power flow do not provide insight to these properties. Many works have shown that other combinations of interference not satisfying the null conditions (e.g., not evoking a Kerker effect) can give highly directional scattering/emission. For example, photonic nanojets typically have large number of side lobes with dominant and highly directive forward power flow, but backward power flow does not approach zero and can still be non-negligible[70]. Therefore, it is

important to note that though the Kerker transform is named after the inspiring work of Milton Kerker, the Kerker basis is intended to efficiently represent all highly directional scattering /emission, not just the Kerker conditions. The basis is also intended to provide insights to metrics describing directionality such as directivity and side lobes.

To illustrate the general complexity of directional scattering in the Mie basis, consider two systems

$$System\ 1: \quad -2a\boldsymbol{\Psi}^{E}_{111} - 2ib\boldsymbol{\Psi}^{E}_{211} + c\boldsymbol{\Psi}^{E}_{311} - ic\boldsymbol{\Psi}^{M}_{310}$$
$$System\ 2: \quad -2a\boldsymbol{\Psi}^{E}_{111} - 2b\boldsymbol{\Psi}^{M}_{210} + c\boldsymbol{\Psi}^{E}_{311} - ic\boldsymbol{\Psi}^{M}_{310},$$

where $a, b, c \in \mathbb{Z}^{+} \ll \infty$. Are these systems directional? Which has the larger forward-to-backward ratio? What is occurring with respect to the side lobes? Can either system be Kerker, generalized Kerker, or transverse Kerker? What can we infer about directivity? How do the answers to these questions dependent on the choice of $a,\ b,$ and c? These questions become more complex with the introduction of phase and as more harmonics are considered. The difficulty stems fundamentally from the Mie harmonics: they are designed to provide intuition of atom-like behavior, not directionality. To add further complication, many examples of directional scattering occur from particles which straddle the wave and ray-optic regime. E.g., photonic nanojets. When inclusions have around 2 appreciable harmonics (e.g., small sized inclusions), the conditions of harmonic interference giving rise to directionality is straightforward. In the limit of a very large number of harmonics (e.g., inclusions much larger than the wavelength) direct harmonic analysis is infeasible, and directionality is understood through a ray-optic approximation. Between the two regimes (2 – 50 harmonics) ray optics may not be accurate and wave optics not intuitive (e.g., the example of 4 harmonic systems proposed above).

The parameter space to achieve directional scattering/emission is vast. Inspired by the Kerker effect we propose a linear coordinate transform which seeks to provide a more intuitive basis for analyzing directional scattering/emission across all size regimes where wave optics is computationally viable, while still maintaining the useful properties which has made the spherical vector harmonics indispensable. The linear transform, termed the Kerker transform, and the resulting basis, termed the Kerker basis, is composed of forward and backward-type harmonics constructed from the Mie harmonics. The Kerker harmonics have the useful properties that forward and backward-type harmonics weakly interact with each other, and interference of same type harmonics is designed to control directivity and side lobes in the respective direction. The algebraic conditions for directional scattering under this framework is found to be simple to

understand and have an intuitive geometric interpretation in the complex plane based on open and closed contours. Notably the conditions for Kerker scattering, transverse Kerker scattering (simultaneous suppression of both forward and backward intensity), and generalized Kerker scattering are easily conceptualized. The condition for theoretically maximal directivity is also easily conceptualized.

The difference between the Kerker and Mie harmonic expansions are summarized as:

The Kerker framework easily represents directional scattering, while atom-like scattering arises from complicated interference. In the Mie framework, atom-like scattering is easily represented, while directional scattering arises from complicated interference.

The remainder of this article is comprised of three sections. In the first section the Mie expansion is briefly reviewed and the Kerker expansion is presented. In the second section, features of the Kerker expansion studied in detail in the context of electromagnetic fields. Areas where the Kerker basis provides new beneficial insights for directional systems is emphasized, discussed, and contrasted to the Mie basis. The last section presents case studies of a Kerker, transverse Kerker, generalized Kerker, and general highly directional scattering/emitting systems, comparing the solutions in both the Kerker and Mie basis. Both scattering and emissive systems across a wide size-to-wavelength regime are discussed. We also provide an answer to our illustrative questions for *System 1* and *System 2*, posed above. Finally, we conclude with a summary of the results.

3.2 THE KERKER TRANSFORM

Mie theory expands outward propagating scattered or emitted electromagnetic fields in terms of electric ($\boldsymbol{\Psi}^{E}_{nmp}$) and magnetic-type ($\boldsymbol{\Psi}^{M}_{nmp}$) spherical vector harmonics. As the names suggest, electric-type harmonics mimic electric atom-like multipole patterns in the far field, whereas magnetic-type harmonics mimic magnetic atom-like multipole field patterns. Time-harmonic electric and magnetic fields in the frequency domain are expanded under the Mie framework as

$$\begin{aligned}\boldsymbol{E} &= \sum_{n=1}^{\infty}\sum_{m=0}^{n}\sum_{p=0}^{1}\left(c^{M}_{nmp}\boldsymbol{\Psi}^{M}_{nmp}(\boldsymbol{r},k)+c^{E}_{nmp}\boldsymbol{\Psi}^{E}_{nmp}(\boldsymbol{r},k)\right)\\ \boldsymbol{H} &= \frac{-ik}{\mu\omega}\sum_{n=1}^{\infty}\sum_{m=0}^{n}\sum_{p=0}^{1}\left(c^{E}_{nmp}\boldsymbol{\Psi}^{M}_{nmp}(\boldsymbol{r},k)+c^{M}_{nmp}\boldsymbol{\Psi}^{E}_{nmp}(\boldsymbol{r},k)\right),\end{aligned} \qquad 3.2.1$$

where c^{E}_{nmp} and c^{M}_{nmp} are the complex electric and magnetic-type scattering coefficients, respectively. Though the coefficients are termed electric and magnetic-type, both coefficients scale either electric or magnetic-type harmonics depending on if one is viewing the electric or magnetic field. (E.g., the magnetic field scales the magnetic-type harmonic with the electric-type coefficient.) This is because $\boldsymbol{H}=\left(\frac{-i}{\mu\omega}\right)\nabla\times\boldsymbol{E}$ and the vector spherical harmonics change type under the curl operator: $\nabla\times\boldsymbol{\Psi}^{t}_{nmp}(\boldsymbol{r},k)=k\boldsymbol{\Psi}^{1-t}_{nmp}(\boldsymbol{r},k)$, where $t=0=M$ and $t=1=E$. The vector spherical harmonics are constructed from the scalar spherical harmonics and the spherical Bessel functions, as detailed in the appendix. All expansions in this text are written in a form general enough to represent any feasible electromagnetic field distribution in a linear, isotropic, and homogeneous host medium, with permeability, μ, and permittivity, ϵ. All fields are assumed time harmonic with angular frequency, ω. Arbitrary time pulses are then generated though Fourier transformation. The harmonic time dependence is implied and not written explicitly. All bold variables are vectors in $\mathbb{C}^3$ or $\mathbb{R}^3$, dependent on the physical context, under the standard spherical basis $\hat{\boldsymbol{e}}_r$, $\hat{\boldsymbol{e}}_\theta$, and $\hat{\boldsymbol{e}}_\phi$. Spatial positions are denoted by $\boldsymbol{r}=\left(r\hat{\boldsymbol{e}}_r+\phi\hat{\boldsymbol{e}}_\phi+\theta\hat{\boldsymbol{e}}_\theta\right)$, where $r,\phi,$ and θ are the radial, azimuthal, and polar coordinates, respectively. The wavenumber of the host media is $k^2=\omega^2\epsilon\mu$. In both the Mie and Kerker expansions we adopt the convenient approach of assigning a type variable, $t\in[0,1]$, and a parity variable, $p\in[0,1]$, to write equations in compact form when applicable. Therefore, $1-t$ is equivalent to flipping the harmonic type and $1-p$ flips parity. This compact form helps to illuminate fundamental differences between the Mie and Kerker basis systems, which we feel is a critically important concept to convey as a first introduction to the Kerker transform. Correspondingly, we also use the cosine and sine expansion of the Mie harmonics (hence the parity variable and $m\geq 0$), because this also best illuminates' difference between the Mie and

Kerker expansions. Though, we note that the complex azimuthal representation would elegantly simplify many of the analytic expressions discussed below. For this reason we encourage the reader to write the expansions on paper for each type and parity and also in the complex azimuthal form. Doing so will illuminate the simplicity of the Kerker transform, which is somewhat obscured by the chosen notation. Throughout the text, the summation bounds for n, m, p, and t are the same as the bounds in equation 3.2.1. We will omit writing summation bounds explicitly and instead use the shorthand, Σ_{nmpt}.

The Kerker basis expands the electric and magnetic fields in terms of highly directional forward ($\boldsymbol{\Upsilon}^f_{nmp}$) and backward-type ($\boldsymbol{\Upsilon}^b_{nmp}$) harmonics. The field expansions under the Kerker framework are

$$\begin{aligned} \boldsymbol{E} &= \sum_{nmp}\left(c^f_{nmp}\boldsymbol{\Upsilon}^f_{nmp}(\boldsymbol{r},k) + c^b_{nmp}\boldsymbol{\Upsilon}^b_{nmp}(\boldsymbol{r},k)\right) \\ \boldsymbol{H} &= \frac{k}{\mu\omega}\sum_{nmp}(-1)^p\left(c^f_{nmp}\boldsymbol{\Upsilon}^f_{nm1-p}(\boldsymbol{r},k) - c^b_{nmp}\boldsymbol{\Upsilon}^b_{nm1-p}(\boldsymbol{r},k)\right), \end{aligned} \qquad 3.2.2$$

where c^f_{nmp} and c^b_{nmp} are the complex forward and backward scattering coefficients, respectively. Unlike the Mie expansion, the Kerker coefficients of one type multiply only the harmonics of the same type. (E.g., in both the electric and magnetic field, the forward coefficient always multiplies the forward harmonic.) This is because the Kerker harmonics do not alter type under the curl operation: $\nabla\times\boldsymbol{\Upsilon}^t_{nmp}(\boldsymbol{r},k) = (-1)^{t-p}ik\boldsymbol{\Upsilon}^t_{nm1-p}(\boldsymbol{r},k)$, where $t=0=f$ and $t=1=b$. Instead, the curl induces a parity change of the Kerker harmonic, and changing parity is equivalent to an azimuthal phase shift, $\boldsymbol{\Upsilon}^t_{nmp}(r,\ \theta,\phi,k) = \boldsymbol{\Upsilon}^t_{nm1-p}\left(r,\ \theta,\phi+\frac{\pi}{2},k\right)$. This type preservation under the curl operation is an important component to simplifying analytic expressions in directional systems. The Kerker harmonics are related to the vector spherical harmonics through the linear transform

$$\boldsymbol{\Upsilon}^t_{nmp}(\boldsymbol{r},k) = (-1)^{t(n+m+1)}(i)^n\left(\boldsymbol{\Psi}^M_{nmp}(\boldsymbol{r},k) + (-1)^{t-p}i\boldsymbol{\Psi}^E_{nm1-p}(\boldsymbol{r},k)\right). \qquad 3.2.3$$

A complete component-wise expansion of the Kerker harmonics is shown in the appendix. The Kerker coefficients are related to the Mie coefficients through

$$c^t_{nmp} = \frac{1}{2}(-1)^{t(n-m-1)}(-i)^n\left(c^M_{nmp} + (-1)^{1-t-p}ic^E_{nm1-p}\right), \qquad 3.2.4$$

where $t = 0 = f$ and $t = 1 = b$. Therefore, electromagnetic scattering/emission problems can be solved in either the Kerker or Mie basis, then subsequently transformed into the other basis when beneficial for analysis.

It is important to note that though the Kerker harmonics are formed from a superposition of electric and magnetic-type Mie harmonics, this basis is not equivalent to the transform used to study angular momenta. The Kerker basis does not preserve circular polarization or helicity (e.g., it is not equivalent to $\boldsymbol{\Psi}^{M}_{nmp} \pm \boldsymbol{\Psi}^{E}_{nmp}$). The Kerker harmonics are not eigenvectors of the orbital angular momentum operator ($\frac{1}{k}\nabla \times$), as evident by the change in parity under the curl discussed above. With that said, multiple reports have studied the connection between Kerker's conditions and helicity preservation that exists in suitably rotationally symmetric scattering/emissive systems[65,74]. Such connections can also be studied in the Kerker basis by forming Kerker harmonics that also preserve handedness. This is achieved through a linear transform of the regular Kerker harmonics to incorporate both parity. E.g., $\boldsymbol{Q}^{t}_{nmh}(\boldsymbol{r}, k) = \boldsymbol{\Upsilon}^{t}_{nm0}(\boldsymbol{r}, k) + (-1)^{t-h} i \boldsymbol{\Upsilon}^{t}_{nm1}(\boldsymbol{r}, k)$, where $h = 0 = L$ for left-handed polarization and $h = 1 = R$ for right-handed polarization. This basis is an eigenvector of the angular momentum operator as, $\nabla \times \boldsymbol{Q}^{t}_{nmh} = (-1)^{h} k \boldsymbol{Q}^{t}_{nmh}$. Therefore, the Kerker harmonics can be used to efficiently understand directional scattering in systems with and without angular momentum preservation.

3.3 FEATURES OF THE KERKER TRANSFORM

A primary benefit of the Kerker basis is having a simplified expression in the far field compared to the Mie harmonics. The far field Kerker harmonics are

$$\boldsymbol{\Upsilon}^{t}_{far,nmp}(\boldsymbol{r},k) = i\frac{e^{ikr}}{kr}X^{t}_{nm}(\theta)\begin{bmatrix} 0\,\hat{\boldsymbol{e}}_r \\ +sin\left(m\phi - p\frac{\pi}{2} + t\pi\right)\hat{\boldsymbol{e}}_\theta \\ +cos\left(m\phi - p\frac{\pi}{2}\right)\hat{\boldsymbol{e}}_\phi \end{bmatrix} + O\left\{\frac{1}{(kr)^2}\right\}, \qquad 3.3.1$$

where

$$X^{t}_{nm}(\theta) = \frac{(-1)^{t(n+m+1)}}{\sqrt{n(n+1)}}\left(\tau^{m}_{n}(\theta) + (-1)^{t}m\pi^{m}_{n}(\theta)\right) \qquad 3.3.2$$

is a real valued function describing the forward, $X^{f}_{nm}(\theta)$, and backward, $X^{b}_{nm}(\theta)$, polar-angle dependence. Equation 3.3.1 shows that the vector components differ only by simple trigonometric relations. Equation 3.3.2 defines the relationship of the Kerker polar angle functions to the Mie polar angle functions, $\tau^{m}_{n}(\theta)$ and $m\pi^{m}_{n}(\theta)$. By construction, all vector components of the far field Kerker harmonics share the same polar-angle dependence. This polar-angle invariance is a key feature of the Kerker harmonics and allows us to focus on X^{t}_{nm} in order to understand directional properties. In contrast, the Mie expansion has a different polar-angle expansion for each vector component.

Figure 3.3.1 plots both the Kerker (X^{t}_{nm}) and Mie ($\tau^{m}_{n}, m\pi^{m}_{n}$, upper quadrant) polar angle functions up to the quantum numbers $n = 4$ and $m = 4$. From this figure we note three features of X^{t}_{nm}, designed for convenience when studying directional systems:

(1) X^{t}_{nm} has a simple relation between the two types: the backward Kerker functions are the forward Kerker functions rotated $180°$. (I.e., $X^{t}_{nm}(\theta) = X^{1-t}_{nm}(\pi - \theta)$.) This is not just convenient to conceptualize, but also allows only one type to be calculated and stored in memory. In contrast, the Mie polar angle functions are not related through a rotation and have completely different shapes. This is because π^{m}_{n} is related to the associated Legendre polynomial and τ^{m}_{n} is related to the derivative of the associated Legendre polynomial. Furthermore, $180°$ rotations of the Mie polar functions lead to different inversion parity relations that are dependent on the quantum polar numbers. I.e., $\tau^{m}_{n}(\pi - \theta) = (-1)^{n-m+1}\tau^{m}_{n}(\theta)$ and $\pi^{m}_{n}(\pi - \theta) =$

$(-1)^{n-m}\pi_n^m(\theta)$. This further complicates deriving intuitive interference relations for the Mie harmonics because the sign of the lobes alters as a function of polar number and harmonic type. The Kerker functions need no such sign relation.

(2) The Kerker polar functions are highly directional and have the clear notion of primary and side lobes. Therefore, the functions can easily represent directional fields. This is unlike the Mie counterpart, where there is no clear definition of side lobes. For each Kerker harmonic, the total number of lobes is given simply by $n - m + 1$ and the proportion of the side lobes in the nondominant hemisphere is given by $ceil\left(\frac{n-m}{2}\right)$.[§1] Furthermore, harmonics with larger polar quantum numbers have narrower beam widths for all lobes. Therefore, from knowing just the quantum numbers of a Kerker harmonic you can infer far field directionality, relative beam widths, and side lobes, including the side lobe concentration in both the forward and backward hemispheres for each harmonic. The Mie polar functions provide no such intuition, as they are not designed for this purpose. For example, contrast the field profiles of τ_3^1 and π_3^1. The number of lobes, amplitude of lobes, width of lobes, and sign of the lobes from these Mie polar functions are all different.

(3) The Mie polar functions are neither mutually orthogonal nor orthogonal to each other. In contrast, the Kerker polar functions of the same type and azimuthal number are orthogonal over the domain $\int_0^\pi \partial\theta \sin(\theta) X_{nm}^t(\theta) X_{n'm}^t(\theta)$.

Like Mie theory, the $m = 1$ column in figure 3.3.1 (circled in dashed blue) is the only column to have a nonzero exact forward or backward field. This column is particularly important and usually predominant on physical grounds. For example, symmetries of the scattering/emitting object, such as being of spherical shape, can preclude $m \neq 1$. In the Kerker basis the primary lobes of the $m = 1$ column are exactly centered in either the forward ($\theta = 0$) or backward ($\theta = \pi$) direction, with exactly no field in the opposite direction. We will show later this attribute simplifies the analytic expression for calculating forward-to-backward ratios. With that said, the Kerker basis is a directional expansion for all $m \geq 1$, as evident in figure 3.3.1. It can describe any arbitrary scattering/emissive system as an expansion of directional harmonics, given that the fields can be represented by a spherical harmonic expansion.[§2]

[§1] Note that the domain of the polar angle functions is $\theta \in [0, \pi]$ and lobes are counted within this angular region.

[§2] Just like the Mie harmonics, the Kerker harmonics are defined with respect to a global coordinate system. To efficiently represent a directional beam that is off-axis to the globally defined forward/backward direction, either the system can be solved under a new global coordinate system that aligns with the direction of interest or the rotation theorem for vector spherical harmonics, based on the Wigner-d functions, can be used.

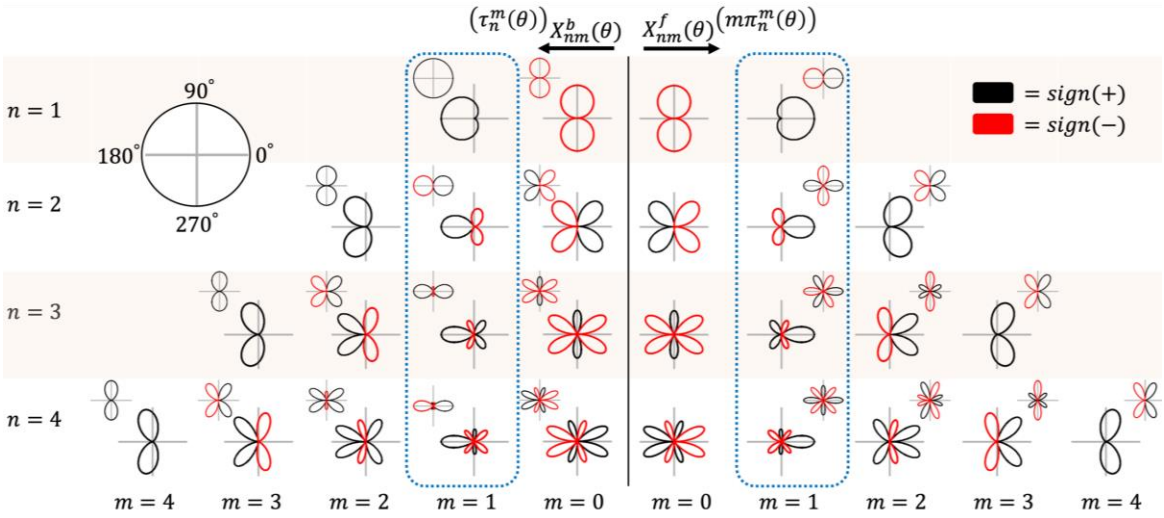

Figure 3.3.1. Table of the Kerker and Mie (upper corner) polar angle functions. Rows and columns designate polar and azimuthal quantum numbers, respectively. Forward and backward-type functions and corresponding $m\pi_n^m$ and τ_n^m functions are on the right and left-hand side, respectively. The functions are plotted in polar coordinates where the polar angle is given by the key in the upper left. Positive and negative values of the radius are denoted by black and red lines, respectively. The columns encircled by dashed blue lines contain the polar functions that have nonzero values in the exact forward or backward direction.

From the surface equivalence principle, the scattered/emitted field can also be represented as electric $(\boldsymbol{J} = \hat{\boldsymbol{e}}_r \times \boldsymbol{E})$ and magnetic $(\boldsymbol{M} = -\hat{\boldsymbol{e}}_r \times \boldsymbol{H})$ current densities. Such relations are of interest in applications such as near-to-far transformation. The Kerker basis is paired to a corresponding basis of forward $(\boldsymbol{j}_{nmp}^f)$ and backward-driving $(\boldsymbol{j}_{nmp}^b)$ current densities, where $\boldsymbol{j}_{nmp}^t(\boldsymbol{r}, k) = \hat{\boldsymbol{e}}_r \times \boldsymbol{\Upsilon}_{nmp}^t(\boldsymbol{r}, k)$. Given that

$$\boldsymbol{j}_{far,nmp}^t(\boldsymbol{r}, k) = i\frac{e^{ikr}}{kr} X_{nm}^t(\theta) \begin{bmatrix} 0\,\hat{\boldsymbol{e}}_r \\ -cos\left(m\phi - p\frac{\pi}{2}\right)\hat{\boldsymbol{e}}_\theta \\ sin\left(m\phi - p\frac{\pi}{2} + t\pi\right)\hat{\boldsymbol{e}}_\phi \end{bmatrix} + O\left\{\frac{1}{(kr)^2}\right\}, \qquad 3.3.3$$

we find that all beneficial properties of the Kerker far field harmonics also equally apply to the Kerker far field current densities. In particular, the X_{nm}^t dependence is unchanged. This provides a method to understand what current distributions give rise to directional scattering in the far field.

Using the far field Kerker basis, the time-averaged far field Poynting vector is

$$\langle \boldsymbol{S}_{far} \rangle = \frac{1}{2}\frac{1}{\mu\omega k r^2}\left(\|A(\phi,\theta)\|^2 + \|B(\phi,\theta)\|^2\right)\hat{\boldsymbol{e}}_r, \qquad 3.3.4$$

where

$$\begin{aligned} A(\theta,\phi) &= \sum_{nmp} cos\left(m\phi - p\frac{\pi}{2}\right)\left(c^f_{nmp}X^f_{nm}(\theta) + c^b_{nmp}X^b_{nm}(\theta)\right) \\ B(\theta,\phi) &= \sum_{nmp} sin\left(m\phi - p\frac{\pi}{2}\right)\left(c^f_{nmp}X^f_{nm}(\theta) - c^b_{nmp}X^b_{nm}(\theta)\right). \end{aligned} \qquad 3.3.5$$

The $\left(c^f_{nmp}X^f_{nm}(\theta) \pm c^b_{nmp}X^b_{nm}(\theta)\right)$ terms in equation 3.3.5 shows that it is instructive to understand how the forward and backward polar angle functions interfere with each other. Luckily, the polar angle functions are designed to concentrate energy in their respective dominant hemisphere. Therefore, interference between forward and backward harmonics is weak. Alternatively stated, primary lobes of one type (forward/backward) interact only with side lobes of the other type (backward/forward). Figure 3.3.2 illustrates this concept. From this figure we see that weak interaction enables a convenient method to intuit the interference between modes of different type. They can be viewed as *approximately* noninteracting in their respective dominant hemisphere.[§3] This provides a rule-of-thumb for approximating harmonic interference in complicated systems. In contrast, the Mie harmonics have strong interreference between the electric and magnetic-types and the resulting scattering/emission lobes have no rule-of-thumb behavior.

The right most example in figure 3.3.2 shows the most general form of interference between polar angle functions of different type and quantum numbers. The left and center examples in figure 3.3.2 show interference of opposite type polar angle functions with the same quantum numbers. These two cases are important because they represent the inverse transform that recovers the Mie angular functions. This result can be seen by rearranging equation 3.3.2 to show that $X^f_{nm}(\theta) + (-1)^{n+m+1}X^b_{nm}(\theta) = 2\tau_n^{|m|}(cos\,\theta)$ and $X^f_{nm}(\theta) - (-1)^{n+m+1}X^b_{nm}(\theta) = 2m\pi_n^{|m|}(\cos\theta)$. More generally, atom-like fields are achieved in the Kerker basis through interference that gives rise to the inverse Kerker transform:

[§3] Since side lobes are concentrated closer to the horizontal ($\theta = \pi/2$), interactions between forward and backward harmonics are more pronounced near this angular region.

$$\boldsymbol{\Psi}^{\mathrm{t}}_{nmp}(\boldsymbol{r}) = (-1)^{t(1-p)} i^{-(n+t)} \frac{1}{2} \boldsymbol{\Upsilon}^{f}_{nmt-p}(\boldsymbol{r}) - (-1)^{n+m+t} \boldsymbol{\Upsilon}^{b}_{nmt-p}(\boldsymbol{r}) \qquad 3.3.6$$

where, again, $\boldsymbol{\Psi}^{\mathrm{t}}_{nmp}(\boldsymbol{r})$ are the Mie vector harmonics with $t = 0 = M$ and $t = 1 = E$. Equation 3.3.6 and equation 3.2.3 formalize our italicized summary in the introduction. Directional fields require complicated interference in the Mie expansion and atom-like fields require complicated interference in the Kerker expansion.

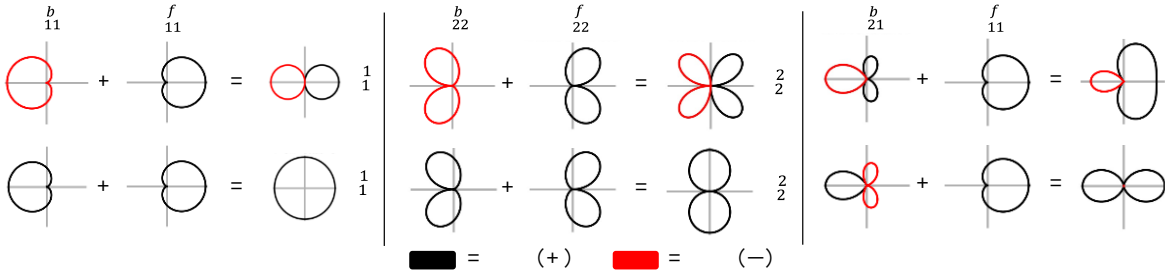

Figure 3.3.2. Examples of interference between opposite type Kerker polar angle functions. The color convention and angle orientation follow the definition from figure 3.3.1. Therefore, the top and bottom row correspond to $X^{f}_{nm} - X^{b}_{nm}$ and $X^{f}_{nm} + X^{b}_{nm}$ interference, respectively. The shaded region highlights the non-dominant hemisphere for each function. The left and middle example show how the Mie functions can be recovered, while the right example is a more general interference between different polar quantum numbers. The functions are plotted in polar coordinates where the polar angle is given by the key in the upper left. Positive and negative values of the radius are denoted by black and red lines, respectively.

From the far field Poynting vector, the far field intensity is defined as $I(\theta, \phi) = \langle \boldsymbol{S}_{far} \rangle \cdot r^2 \hat{\boldsymbol{e}}_r$. Integrating this intensity over the azimuthal direction gives

$$I(\theta) = I^{f}_{0} + I^{f}_{1} + I^{b}_{0} + I^{b}_{1} = \frac{\pi}{\mu\omega k} \sum_{tmp} (1 + \delta_{m0}) \left\| \sum_{n} c^{t}_{nmp} \, X^{t}_{nm}(\theta) \right\|^2, \qquad 3.3.6$$

where the $(1 + \delta_{m0})$ term comes from the fact that $c^{M}_{n01} = c^{E}_{n01} = 0$. Interestingly equation 3.3.6 shows that the azimuthally integrated intensity is truly not dependent on interference between the forward and backward harmonics or interference between different parity. This is, again, another useful feature of the Kerker harmonics. The total azimuthally integrated intensity can be viewed as resulting from four noninteracting partial fields, each with intensity $I^{t}_{p}(\theta) = \frac{\pi}{\mu\omega k} \sum_{m} (1 + \delta_{m0}) \left\| \sum_{n} c^{t}_{nmp} \, X^{t}_{nm}(\theta) \right\|^2$. For any given polar angle, these partial intensities have the geometric interpretation as being the sum of the distances from the origin occurring from the tip-to-tail coherent addition of $\sum_{n} c^{t}_{nmp} X^{t}_{nm}(\theta)$. This result allows for an intuitive geometric interpretation of directional scattering, which will become more evident later in this section. It

is also worth noting that four partial fields represent the most general form. In systems with symmetry, such as plane wave or dipole excitation of a sphere, one forward and one backward partial field completely describes the system. Furthermore, it is often the case that only the $m = 1$ terms are appreciable. Therefore, it is common that multiple simplifications to equation 3.3.6 are applicable.

Equations 3.3.4 and 3.3.6 highlight the importance of understanding interference between Kerker polar angle functions of the same type. Figure 3.3.3 defines this relationship for the forward polar angle functions. We omit examples of the backward functions because, unlike the Mie harmonics, the inversion symmetry implies the results are the same just rotated $180°$. Figure 3.3.3 shows that constructive interference of same type harmonics results in an increased primary lobe and an overall more directive far field. Likewise, destructive interference decreases the primary lobe and reduces directivity. This provides an intuitive interference relationship to identify directive systems. Adding coefficients of the same type increases directivity. Subtraction reduces directivity. This condition can be easily generalized to complex valued coefficients giving an intuitive geometric interpretation based on coefficients as vectors in the complex plane. From this picture, same type Kerker coefficients pointing in a similar direction will increase directivity. Coefficients pointing in opposite directions will decrease the directivity.

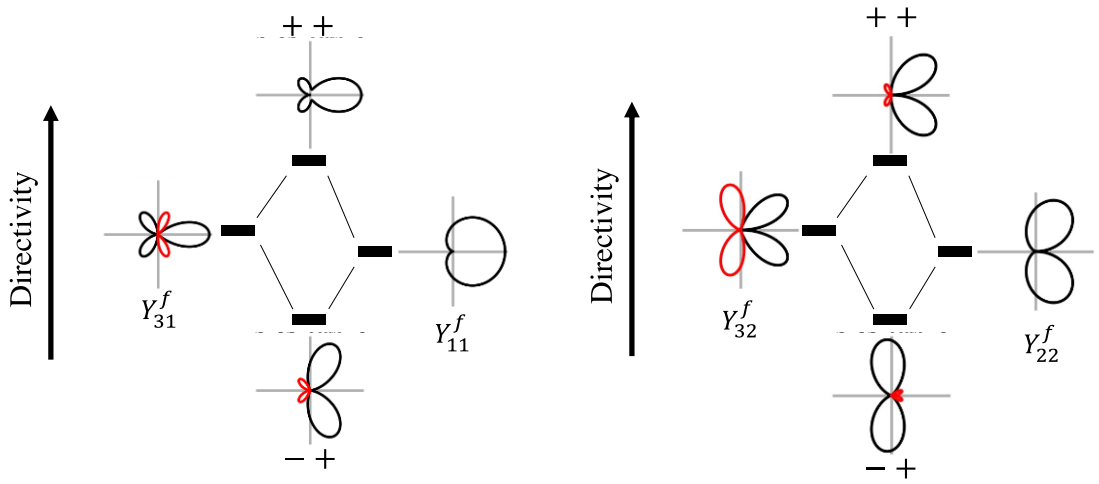

Figure 3.3.3. Examples of interference between same type Kerker polar angle functions. The left example is a combination of same parity polar numbers when $m = 1$. The right example is a combination of opposite parity polar numbers for azimuthal numbers that do not have exact forward scattering/emission ($m \neq 1$).

In the exact forward and backward directions, the Kerker polar angle functions are designed to take the simple form

$$X_{nm}^{f}(\theta = 0) = \frac{1}{2}K_n\delta_{m1} \quad X_{nm}^{f}(\theta = \pi) = 0$$
$$X_{nm}^{b}(\theta = 0) = 0 \quad X_{nm}^{b}(\theta = \pi) = \frac{1}{2}K_n\delta_{m1}, \qquad 3.3.7$$

where $K_n = \sqrt{(2n+1)}$. Equation 12 formalizes a property of the Kerker harmonics that can be inferred from figure 3.3.1. The Kerker harmonics have an exact forward or backward lobe only for the $m = 1$ quantum number. Furthermore, these functions have exactly zero field in the opposite direction. Therefore, there is always complete noninteraction between forward and backward harmonics in the exact forward and backward directions. This property enables a simplified and geometrically intuitive expression for calculating exact forward and backward intensities and forward-to-backward ratios.

The far field intensity in the exact forward and backward directions is

$$I(\theta = 0) = \frac{\pi}{2\mu k\omega}\left(\sum_p \left\|\sum_n K_n c_{n1p}^{f}\right\|^2\right)$$
$$I(\theta = \pi) = \frac{\pi}{2\mu k\omega}\left(\sum_p \left\|\sum_n K_n c_{n1p}^{b}\right\|^2\right). \qquad 3.3.8$$

Equation 3.3.8 shows the exact forward and backward intensity can be understood geometrically as the magnitude of the vector that results from coherently adding scaled forward and backward coefficients in the complex plane, $\sum_n K_n c_{n1p}^{t}$. The forward-to-backward ratio is then the ratio of the lengths of these vectors. This provides a useful geometric connection between the Kerker coefficients and the resulting forward and backward intensity. When vectors added together approach a closed loop, there is weak scattering/emission in that direction. Equation 3.3.8 is a specific example of equation 3.3.6, for the important case where $\theta = 0$ or π. Under this condition, the scaling factor X_{nm}^{t} takes the simplified form given by equation 3.3.7. For an arbitrary direction, the same vector addition rules apply but the scaling factors are based on equation 3.3.6.

Equation 3.3.8 provides intuitive geometric conditions to understand the Kerker effects. Forward or backward Kerker scattering can now be viewed as the special case when either all $c_{n1\mathrm{p}}^{b}$'s or $c_{n1\mathrm{p}}^{f}$'s are zero, respectively. E.g., a forward Kerker scattering object will have no backward Kerker coefficients, $c_{n1\mathrm{p}}^{b}$. This property is why the coefficients are termed "Kerker coefficients." Generalized forward or backward Kerker scattering can also be understood as occurring when either $\sum_n K_n c_{n1p}^{b}$or $\sum_n K_n c_{n1p}^{f}$ are zero, respectively. This corresponds to vectors of one type that, when added head-to-tail, form a closed loop in the complex plane. The

transverse Kerker effect occurs when both vectors of both types form a closed loop. I.e., $\sum_n K_n c^b_{n1p}$and $\sum_n K_n c^f_{n1p}$ are zero. Forms of directional scattering which do not obtain identically zero forward or backward fields are identified by comparing the length of the coherently added forward vectors versus the backward vectors. I.e., the forward-to-backward ratio is then the ratio of the length to the total forward to the total backward vectors. Note that these conditions apply for all relevant parities used to describe the field. Figure 3.3.4 gives a schematic of the geometric representations of different types of directional scattering based on the Kerker coefficients. These are substantially easier interpretations compared to the complex modal interference relationships necessary to satisfy these conditions in the Mie framework. This will be further discussed through examples in the next section.

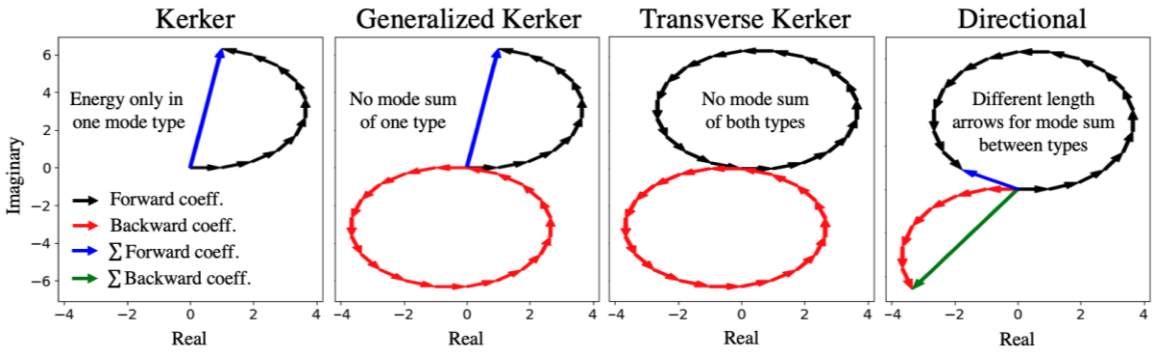

Figure 3.3.4. Schematics of different types of directional scattering/emission represented as closed and open-loop paths in the complex plane. Individual forward and backward modes are given by black and red arrows, respectively. Modes of the same type are connected head-to-tail and progressively increment from $n = 1$ (tail at the origin) to $n = n_{max}$. The coherent sum of the forward and backward modes is designated by blue and green arrows, respectively. These arrows start at the origin and connect to the tip of the max polar number vector. The left most schematic is an example of forward Kerker behavior, where no backward modes are present. The left middle example is a forward generalized Kerker effect where backward modes coherently cancel in the exact backward direction. The right middle example shows the transverse Kerker effect where both modes coherently cancel the exact forward and backward direction leaving only transverse (side lobe) scattering/emission. The right most schematic is an example of general backward preferential scattering/emission.

Finally, it is instructive to consider the expression for total power flow and directivity under the Kerker expansion. Like the vector spherical harmonics, the Kerker harmonics are orthogonal on the sphere. Therefore, the total scattered/emitted power is

$$W_{scatter/emit} = W_0^f + W_1^f + W_0^b + W_1^b = \frac{\pi}{2\mu\omega k}\sum_{tnmp}(1+\delta_{m0})\left\|c^t_{nmp}\right\|^2, \qquad 3.3.9$$

where the total power is composed of the forward or backward partial powers, $W_p^t = \frac{\pi}{2\mu\omega k}\sum_{nm}(1+\delta_{m0})\left\|c_{nmp}^t\right\|^2$. Unlike the Mie harmonics which distribute the total power into electric and magnetic-type excitations, equation 3.3.9 shows the Kerker harmonics distribute power into forward and backward-type excitations. This helps give intuition on the fraction of the total power concentrated into a particular hemisphere. This fraction can also be understood geometrically, where each partial power (and therefore the total power) is given by the arclength of the scattering coefficients added head-to-tail in the complex plane. I.e., a longer arclength means a larger proportion of the total power is concentrated into that harmonic type. Dividing the origin-to-tip vector length of equation 3.3.8 by the arclength of equation 3.3.9 then gives an intuitive definition of forward or backward directivity as

$$D^{t'} = 4\pi\frac{\sum_p\left\|\sum_n K_n c_{n1p}^{t'}\right\|^2}{\sum_{tnmp}(1+\delta_{m0})\left\|c_{nmp}^t\right\|^2}, \qquad 3.3.10$$

where $D^f = D(\theta = 0)$ and $D^b = D(\theta = \pi)$. Equation 3.3.10 formalizes the argument of directivity presented in figure 3.3.3 and directly connects directivity to the behavior of Kerker coefficients in the complex plane. Directivity is proportional to origin-to-tip length and inversely proportional to arclength. From this framework we can rigorously derive the conditions to maximize directivity and relate these conditions to intuitive curves in the complex plane.

As more complex coefficients of the same type (each represented as a vector in the complex plane) point in a similar direction in the complex plane the numerator of equation 3.3.10 increases while the arclength remains unchanged. The triangle inequality enforces that the numerator of equation 3.3.10 is maximized when all vectors of the same type point in the exact same direction, $\sum_p\left\|\sum_n K_n c_{n1p}^{t'}\right\|^2 = \sum_{np}\left\|K_n c_{n1p}^{t'}\right\|^2$. I.e., the curve formed by head-to-tail addition of the coefficients forms a straight line. The geometric representation of all vectors pointing in the same direction is the condition of perfect constructive interference. Though, to maximize directivity, the denominator of equation 3.3.10 should also be minimized. To achieve this, all coefficients in the denominator that are not present in the numerator should be zero. Since $K_n > 1$, we can conclude that:

The theoretically maximal directivity for a system with n_{max} harmonic orders occurs when you satisfy Kerker's condition and all Kerker coefficients constructively interfere.

Therefore, Kerker scattering is a necessary but not sufficient condition to achieve the theoretical maximum directivity. Furthermore, generalized Kerker can never achieve the theoretically maximal directivity because though the origin-to-tip length in the unwanted direction is zero, the arclength for that direction is not zero.

3.4 FEATURES OF THE KERKER TRANSFORM

To highlight the usefulness of the Kerker transform, we give four instructive examples of directional scattering and study their results under the Kerker and Mie expansions. The goal in this section is to provide examples of when it can be useful to switch from the Mie to the Kerker framework. In order to highlight the generality of the Kerker expansion, we study both nearfield and far-field excitations of sub-wavelength and larger than wavelength particles. All examples are summarized in figure 3.4.1.

The first and second row of figure 3.4.1 shows a schematic of each system and their corresponding azimuthally integrated far field polar intensity profile, respectively. The left example is the scattering response of a sphere with the material properties initially proposed by Milton Kerker to explain Kerker scattering; the case where $\epsilon = \mu$. The response has exactly no backward field and Kerker's condition is satisfied for all quantum numbers supported by the sphere. The middle-left example is of generalized backward Kerker emission, where near complete suppression of the forward intensity is achieved. The system achieving this emission is composed of the combined response from a 374nm wavelength emitter near-field coupled 90nm below a 164nm TiO_2 sphere ($\eta = \sqrt{\epsilon_r \mu_r} = 2.42$)[75]. The middle-right example is of transverse Kerker scattering from a 120nm Si sphere ($\eta = 3.92 + i2.49E^{-2}$)[76], achieved by coupling two 609nm wavelength emitters to the sphere. One emitter is located 204nm above and below the sphere, respectively. The right most example is of highly directional forward scattering by creating a photonic nanojet. This scattering is achieved by illuminating a 1200nm SiO_2 sphere ($\eta = 1.43 + i2.52E^{-3}$)[77] with a 400nm plane wave. In all cases, the background medium is assumed to be air. The solution to the scattering by a sphere illuminated by a plane wave or a dipole emitter can be found in citations 53 and 78, respectively.

The third and fourth row of figure 3.4.1 plots the K_n-scaled Kerker (upper row) and Mie (lower row) coefficients, respectively, as vectors in the complex plane. This plotting method is commonly used as it describes both amplitude and phase, which is necessary to understand directional scattering [68,79]. The left example clearly shows forward Kerker scattering as the backward coefficients (red arrows) satisfy the Kerker condition that all c_{n10}^{b}'s are zero. The forward coefficients (black arrows) constructively interfere leading to a nonzero total forward intensity (blue arrow). Alternatively, determining Kerker's forward condition using the Mie coefficients requires a systematic comparison of both the angle and phase relationship between each pair of electric and magnetic-type harmonics. Though this is a tractable task for $n_{max} \approx 3$, it is still hard to say for certain that the system is exactly satisfying the Kerker forward condition without using a ruler and protractor.

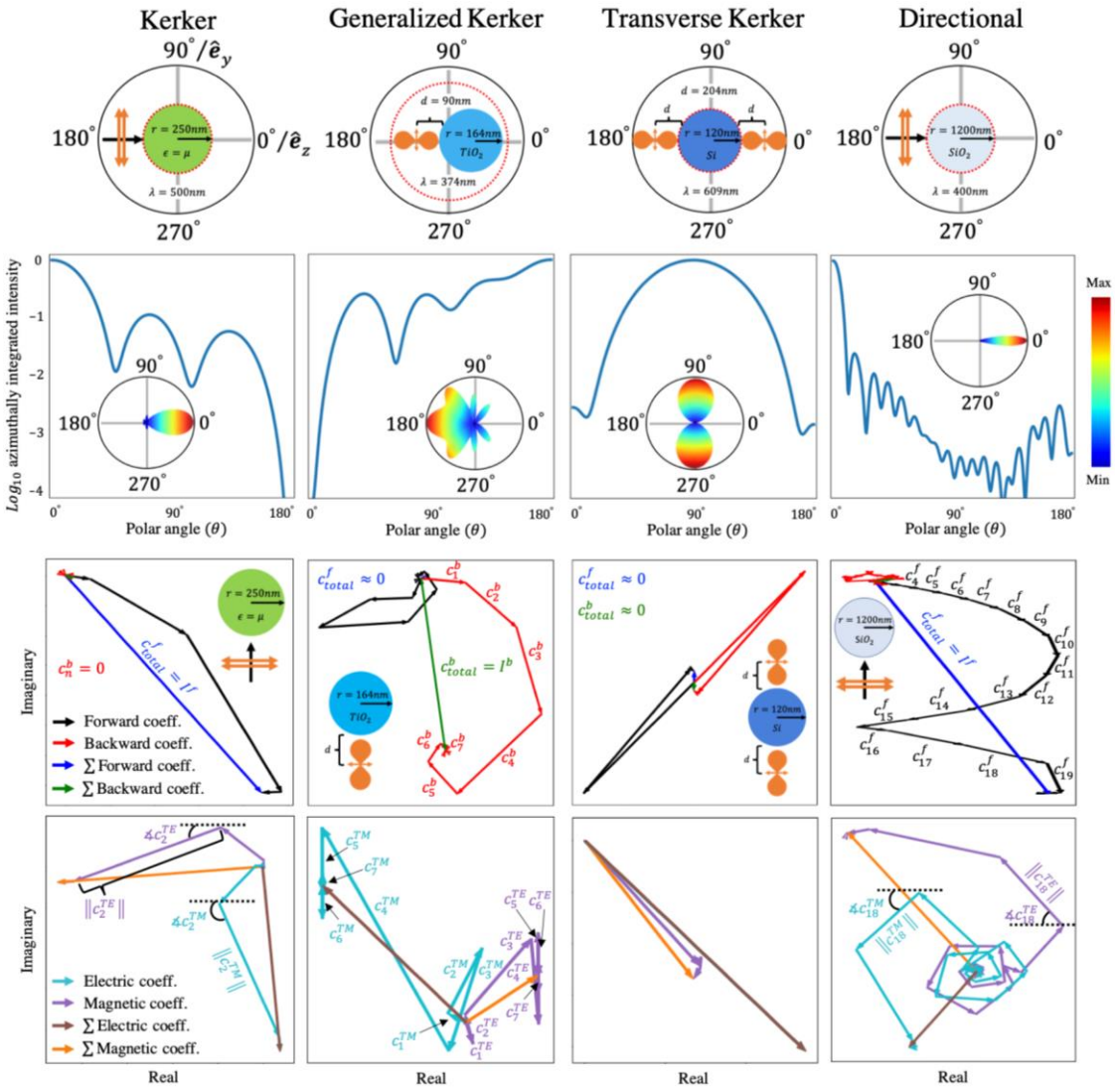

Figure 3.4.1. Schematics of highly directional scattering/emission (row 1), log base 10 normalized azimuthally integrated far field polar intensity plots (row 2), and corresponding K_n-scaled Kerker (row 3) and Mie (row 4) coefficients as vectors in the complex plane. The first example (column 1) is of an exact Kerker scattering system composed of a 250nm radius magnetic sphere ($\epsilon = \mu$) excited by a 500nm wavelength plane wave. The second example (column 2) shows generalized backward Kerker emission achieved by near field coupling a 164nm TiO_2 sphere to a dipole emitting at 374nm. The dipole is located 90nm below the bottom of the sphere and has a moment in the $\hat{\boldsymbol{e}}_y$ direction. The third example (column 3) is of transverse Kerker scattering achieved in a 120nm Si sphere excited simultaneously by two dipoles, both emitting at 609nm. The dipoles are 204nm above and below the sphere, respectively. Both dipoles have moments in the $\hat{\boldsymbol{e}}_y$ direction. The final example (column 4) is of highly directional scattering from a photonic nanojet made from a 1200nm SiO_2 sphere excited by a plane wave with a 426nm wavelength. In all cases the sphere is centered at the origin and the region outside of the red dashed circle defines the domain of validity for the expansion. Coefficients of

the same type are connected head-to-tail and progressively increment from $n = 1$ (tail at the origin) to $n = n_{max}$.

The Kerker coefficients in the middle-left example show generalized backward Kerker behavior. This is evident by the coherent sum of the forward coefficients forming a closed loop, $\sum_n K_n c_{n10}^f \approx 0$, and the coherent sum of the backward coefficients producing a nonzero open loop for the total backward intensity (green arrow). The arc in the path length of the backward coefficients as well as the loop of the forward coefficients indicate the presence of excess side lobes since the vectors are not strictly in the same direction. These side lobes are evident in the azimuthally integrated intensity. The Mie coefficients traverse a sporadic pattern in the complex plane. With $n_{max} \approx 7$ and no easily discernable interference relationship, these coefficients do not illuminate directional emission or properties of side lobes. Clearly the Mie coefficients are not the appropriate tool for this problem.

The middle-right example shows transverse Kerker behavior as evident by both the forward and backward Kerker coefficients traversing a closed loop, $\sum_n K_n c_{n10}^f \approx 0$ and $\sum_n K_n c_{n10}^b \approx 0$. Though the Mie coefficients do not follow a complicated pattern, it is not immediately evident that the coefficients lead to transverse Kerker behavior, compared to the Kerker coefficients.

Finally, the right example shows highly forward directional scattering from the photonic nanojet, as evident by the open contours in the Kerker coefficients. Directionality is achieved through the interference of around 20 appreciable harmonics in each basis system. In the Kerker basis, the total forward arrow is substantially larger compared to the total backward arrow, indicating a strong preference for forward scattering. Furthermore, each coefficient has a similar magnitude. Therefore, there is no single harmonic dominating the side lobes. This is evident by the many similar sized side lobes seen in in the azimuthally integrated intensity. The electric and magnetic Mie coefficients follow a spiral pattern which indicates similar phase and magnitude behavior between the electric and magnetic-type coefficients. This pattern *almost* appears to satisfy Kerker's condition. Though, as evident by the nonzero backward Kerker coefficients, this system is not Kerker scattering. Furthermore, discrepancies between the electric and magnetic-type coefficients eventually cause the arrows of the two types to become out of synch. This makes the overall directionality harder to gauge. Finally, the Mie coefficients do nothing to illuminate the nature of side lobes.

Besides viewing coefficients in the complex plane, intuition can also be developed by studying the analytic form of directional fields in the Kerker basis based on the properties defined in

section two. For example, equip with the Kerker basis, the two systems in the introduction can now be rewritten as

$$\begin{aligned} &System\ 1\text{:} \quad a\boldsymbol{\Upsilon}^{f}_{111} + b\boldsymbol{\Upsilon}^{f}_{210} + c\boldsymbol{\Upsilon}^{f}_{311} + a\boldsymbol{\Upsilon}^{b}_{111} - b\boldsymbol{\Upsilon}^{b}_{210} \\ &System\ 2\text{:} \quad a\boldsymbol{\Upsilon}^{f}_{111} + b\boldsymbol{\Upsilon}^{f}_{210} + c\boldsymbol{\Upsilon}^{f}_{311} + a\boldsymbol{\Upsilon}^{b}_{111} + b\boldsymbol{\Upsilon}^{b}_{210}, \end{aligned}$$

where $a, b, c \in \mathbb{Z}^{+} \ll \infty$. Completely by inspection, the following can be concluded about the two systems: First, both systems are always forward dominant, regardless of the choice of $a, b,$ or c. The forward-to-backward ratios are proportional to $\frac{\|a+b+c\|^2}{\|a-b\|^2}$ and $\frac{\|a+b+c\|^2}{\|a+b\|^2}$, respectively. Therefore, system 1 will always have the larger forward-to-backward ratio. Assuming $a,\ b,$ and c have a similar value, three lobes in the range $\theta \in [0, \pi]$ or less are expected for both systems (two lobes in the forward hemisphere and the other lobe in the backward hemisphere). System 2 has constructive backward interference, $a + b$, which favors lobes near the exact backward direction. Alternatively, system 1 has destructive backward interference, $a - b$, which favors pushing power away from $\theta = \pi$ and into the sides. If either $a,\ b,$ or c are strongly dominant, then the system degenerates to more closely mimic the corresponding dominant Kerker harmonic. Side lobe predictions will change accordingly. Finally, a forward Kerker condition is clearly observed in both systems because $\boldsymbol{\Upsilon}^{b}_{311} = 0$, regardless of the choice of $a, b,$ or c. Though, neither system is fully forward Kerker as $\boldsymbol{\Upsilon}^{b}_{111}$ and $\boldsymbol{\Upsilon}^{b}_{210}$ are nonzero. System 1 has the potential to be generalized Kerker if $a = b$ (suitably normalized). System 2 can only be generalized directional since a and b are constrained to the positive integers. We encourage the reader to return to the introduction and attempt to formulate these conclusions from the Mie framework. Examples of the two systems for different values of $a,\ b,$ and c are presented in the supplementary information.

3.5 CONCLUSION

We propose a linear transform to convert the atom-like vector spherical harmonics found in Mie theory to forward and backward directional vector harmonics and show the use of this method to understand directional scattering/emissive systems. The directional harmonics, termed the Kerker harmonics, have a simple far field expression governed primarily by the Kerker polar angle functions. These functions have a clear notion of primary and side lobes, weak coupling between forward and backward types, and coupling between same type harmonics controls directivity. The resulting azimuthally integrated and exact forward or backward intensity both have a simple analytic form which leads to intuitive definitions of Kerker, generalized Kerker, transverse Kerker, and highly directional scattering /emission as open and closed loop contours of Kerker coefficients in the complex plane. Total power flow is related to the arc length of these coefficients. This provides a simple definition for the condition of theoretically maximal directivity. Examples of a Kerker, generalized Kerker, transverse Kerker, and highly directional system are shown to be more conceptually intuitive in the Kerker basis compared to the Mie basis when viewed in the complex plane. These examples explore the use of this transform in both scattering and emissive systems ranging from sub-wavelength to larger-than-wavelength size regimes (e.g., 20 appreciable harmonics).

3.6 APPENDIX A: EVEN AND ODD MIE VECTOR HARMONICS

The Kerker transform relies on an interference between Mie harmonics with an explicit even and odd azimuthal dependence. This relationship is obscured in the Mie harmonics which rely on the complex exponential form of azimuthal dependence. The even and odd Mie harmonics are

$$\boldsymbol{\Psi}^{M}_{nm\,o}{}^{e} = \frac{1}{\sqrt{n(n+1)}}\frac{1}{kr}\boldsymbol{\mathcal{R}}(kr)\begin{pmatrix} -sin(m\phi) \\ cos(m\phi) \\ -cos(m\phi) \\ -sin(m\phi) \end{pmatrix} m\pi_n^{|m|}(cos\,\theta)\hat{\boldsymbol{e}}_\theta \\ \tau_n^{|m|}(cos\,\theta)\hat{\boldsymbol{e}}_\phi \qquad (3.6.1a)$$

$$\boldsymbol{\Psi}^{E}_{nm\,o}{}^{e} = \frac{1}{\sqrt{n(n+1)}}\frac{1}{kr}$$

$$\begin{pmatrix} cos(m\phi) \\ sin(m\phi) \end{pmatrix} n(n+1)h_n^1(kr)P_n^{|m|}(cos\,\theta)\hat{\boldsymbol{e}}_r \\ +\dot{\boldsymbol{\mathcal{R}}}(kr)\begin{pmatrix} cos(m\phi) \\ sin(m\phi) \\ -sin(m\phi) \\ cos(m\phi) \end{pmatrix} \tau_n^{|m|}(cos\,\theta)\hat{\boldsymbol{e}}_\theta \\ + m\pi_n^{|m|}(cos\,\theta)\hat{\boldsymbol{e}}_\phi \qquad (3.6.1b)$$

where $m \in [0, n]$ and the index subscript $0 = e = even$ and $1 = o = odd$ is used for convenience when using a compact summation notation. The even and odd harmonics can be found from the complex exponential notation using the transform,

$$\boldsymbol{\Psi}^{M}_{nm\,o}{}^{e} = \sqrt{2}\ \boldsymbol{\mathcal{R}}(kr)\begin{matrix}\Re[\boldsymbol{\psi}^{far}_{nm}] \\ \Im[\boldsymbol{\psi}^{far}_{nm}]\end{matrix} \qquad (3.6.2a)$$

$$\boldsymbol{\Psi}^{E}_{nm\,o}{}^{e} = \sqrt{2}\,\nabla \times h_n^1(kr)\begin{matrix}\Re[\boldsymbol{\psi}^{far}_{nm}] \\ \Im[\boldsymbol{\psi}^{far}_{nm}],\end{matrix} \qquad (3.6.2b)$$

where the regular harmonics are found simply by replacing the radial dependence. Again,

$$\begin{matrix}\boldsymbol{\mathcal{R}}(kr) \\ \mathrm{Rg}\boldsymbol{\mathcal{R}}(kr)\end{matrix} = kr\begin{matrix}h_n^1(kr) \\ j_n(kr)\end{matrix}, \quad \begin{matrix}\dot{\boldsymbol{\mathcal{R}}}(kr) \\ \mathrm{Rg}\dot{\boldsymbol{\mathcal{R}}}(kr)\end{matrix} = \frac{d}{d(kr)}\left(kr\begin{matrix}h_n^1(kr) \\ j_n(kr)\end{matrix}\right).$$

Chapter 4

RANDOM PARTICLE FILMS AS OPTICAL FILTERS

Wray, P. R.; Paul, E. H.; Atwater, H. A., Optical Filters Made from Random Metasurfaces using Bayesian Optimization, *Nanophotonics* 2023. (accepted)

ABSTRACT

We theoretically investigate the ability to design optical filters from a single material and a single layer of randomly dispersed resonant dielectric particles, defining a random metasurface. Using a Bayesian and generalized Mie inverse-design approach, we design particle radii distributions based on Gaussian kernels that give rise to longpass, shortpass, bandpass, and bandstop spectral bands in the infrared. The optical response is shown to be directly related to electric and magnetic multipole scattering of the constituent particles and near field coupling. We discuss the effect of the particle size distribution and particle-particle coupling on filter design in uniformly random spatially dispersed systems lacking long-range order.

4.1 INTRODUCTION

Filters designed from disordered metasurfaces may offer a platform to circumvent the Achilles heel of meticulous fabrication. This is because the approach is inherently tolerant to manufacturing error, leading to an increase in throughput and/or a reduced fabrication cost. Furthermore, disordered metasurfaces do not need to rely on multiple materials to achieve a filter response. This benefits applications operating in harsh environments, where issues of different thermal expansion coefficients, chemical stability, miscibility, compliance to mechanical stress, and different resistance to ionizing radiation between materials increases the complexity of filter design[80–92]. Engineered randomness has a long history of producing emergent phenomena. Historical examples include sub-wavelength scatterers, which catalyzed the field of metamaterials by producing effective media with constitutive parameters not seen in the bulk constituents[18,93,94]. Another example is resonant particle absorption and disorder-induced light trapping (e.g., Anderson localization) that has also shown to produce record-breaking broad-band, angle, and polarization-invariant near-black-body absorbers. Furthermore, these systems are shown to be scalable and cost effective compared to ordered photonic counterparts[95–99].

Though the discussion above highlights a case for random metasurfaces, the study of disorder in the field is still an open subject of research. A primary difficulty is that strong light-matter interactions are often necessary in metasurfaces, and this can produce unruly particle-particle coupling effects when the spatial position of particles is not well controlled. It is also important to note that the systems proposed do not fall into the category of effective medium theories. In particular, low harmonic order (electric dipole), non-resonant, and negligible particle-particle coupling are all invalid assumptions in the proposed regime. In fact, it is exactly by leveraging higher harmonics, resonances, and particle-particle coupling that spectral filtering is achieved. A random metasurface therefore requires a robustness to (or appropriate tailoring by) random coupling effects of strongly interacting particles. Otherwise, there would be no emergent collective giving rise to meaningful reflection/transmission bands.

In this manuscript we explore how longpass, shortpass, bandpass, and bandstop spectral features can emerge using only a single layer of completely randomly positioned and randomly sized particles that are all made from the same material. This represents an extreme of filter design where multiple material compatibilities and fabrication sensitivity are no longer a primary concern. This also represents a separation in the philosophy of traditional filters. Spectral properties are entirely controlled by probability distributions. For example, instead of optimizing the number of layers, materials, and thickness in a thin film, you optimize a particle distribution and packing fraction in a single layer. The parameters are found using Bayesian inverse design

and the results are studied theoretically to pinpoint the governing physics giving rise to the desired spectral response. Our framework, based on generalized multi-particle Mie theory, provides explicit information about the coupling between particles, which is often obscured in inverse design. Furthermore, the optimizer produces fabrication feasible systems that are motivated by well-known massively large-scale and cost-effective synthesis and deposition techniques.

The primary goal of the manuscript is two-fold: (1) to present the feasibility of random metasurfaces (e.g., a single layer of randomly distributed particles) in designing optical filters and (2) to present a framework and analysis of the underlying physics giving rise to the filter response in order to motivate future directions and designs.

The first section outlines the theoretical framework and inverse design approach used to derive the transmission, reflection, and absorption from the random metasurface. For brevity, we focus on the main concepts. Detailed derivations are in the supplementary information. The second section presents the result of the optimizer, showing the possibility to design the four canonical filter types: longpass, shortpass, bandpass, and bandstop all made from a single layer of particles and of the same material. From this, we outline how the theoretical approach provides insight into the role of the particle shape distribution and the effects of random particle coupling in the final filter response. We conclude with a summary of the results.

4.2 INVERSE DESIGN THROUGH BAYESIAN OPTIMIZATION

The random metasurface problem is formalized as a single layer of randomly shaped scattering elements that are randomly dispersed in the x-y plane. The film is characterized by a particle shape distribution, $P(s)$, and the particles occupy the cross-sectional area filling fraction, ff, in the plane. The optimization problem is

$$\begin{aligned} \min_{\Omega=\{P(s),ff\}} \; & \|T_{ideal}(\lambda) - T(\lambda)\|^2 + \|R_{ideal}(\lambda) - R(\lambda)\|^2 \\ & s.t., \\ & 0 \le P(s) \le 1, \\ & \int P(s)ds = 1, \\ & s_{min} \le s \le s_{max}, \\ & 0 \le ff \le ff_{max}, \end{aligned} \tag{4.2.1}$$

where T_{ideal} and R_{ideal} are the ideal (user defined) transmission and reflection response, respectively. ff_{max} is the upper bound of the particle area filling fraction. s_{min} and s_{max} are the lower and upper bound of the possible particle radii, respectively. λ is the free space wavelength of the incident plane wave excitation. The first two constraints in equation 4.2.1 enforce the definition of a probability distribution over particle radii. The third and fourth constraints serve to provide practical bounds on the search space. The minimum and maximum possible particle radii is set based on the particle size parameter, $ks = (2\pi/\lambda)s$, which nominally determines the set of possible modes supported in a particle. s_{min} and s_{max} are constrained such that $0.1 \le ks \le 3$. The maximum allowed filling fraction is $ff_{max} = 60\%$, since higher filling fractions approach lattice packing, and we are concerned with random spatial distributions that do not exhibit long-range order. Otherwise, the only other constraint is that particles cannot overlap and must remain within a single layer. I.e., particles do not sit on top, above, or below of one another and cannot fuse together. Particles can (and often do) touch side to side and particle-particle coupling effects can be significant.

Calculating the total transmission, T, reflection, R, and absorption, A, response of the random metasurface relies on three cornerstones that are expanded upon in the supplementary information. First, the scattered field formalism is used to explicitly describe how nanoscopic interactions construct emergent macroscopic (film-level) behavior. Second, each particle in the film is expanded into a generalized Mie basis. This allows the effect of particle shape and particle-particle coupling to be represented as a tangible set of atom-like interactions. The third

cornerstone is to use Monte Carlo integration to solve the statistical nature of the more general infinite random film problem.

In matrix notation, the Mie expansion of an arbitrary electric field is $\boldsymbol{E} = \boldsymbol{\Psi} c$, where $\boldsymbol{\Psi} \in \mathbb{C}^{3\times|l|}$ is a complex-valued matrix of Mie harmonics and $c \in \mathbb{C}^{|l|}$ is a vector of the basis (scattering) coefficients. $l = t, n, m, p$ is a unique index defined by the harmonic's quantum polar, $n \in \mathbb{Z}^+$, and azimuthal number, $m \in [0, n] \cup \mathbb{Z}^+$, as well as the harmonic type, t ($0 =$ electric-type, $1 =$ magnetic-type), and parity, p ($0 =$ even, $1 =$ odd). Correspondingly, $|l|$ is the size of the dimension of all possible harmonic orders necessary to describe the electromagnetic field. Using this method, the governing interaction equation for an arbitrary particle, a, embedded in a film of J particles is

$$c_a - \mathbb{T}_a(s) \sum_{b\neq a}^{J} \mathbb{H}^{ab}(\boldsymbol{d}_{ab}) c_b = \mathbb{T}_a(s) \mathbb{J}^{a0}(\boldsymbol{d}_{a0}) c_{inc}. \qquad 4.2.2$$

$\mathbb{T} \in \mathbb{C}^{|l|\times|l|}$ provides a mapping from the local field a particle experiences to the resulting scattered field the particle emits, $c = \mathbb{T} c_{loc}$. The scattered field is a result of the current distribution within the particle, that is responding to the external local field. $\mathbb{T}$ encapsulates how particle properties such as size, shape, and material define scattering as a response to an arbitrary excitation. $\mathbb{H} \in \mathbb{C}^{|l|\times|l|}$ is a translation operator that describes how a scattered field from particle b contributes to the local field onto particle a. $\mathbb{J} \in \mathbb{C}^{|l|\times|l|}$ is a similar operator translating the incident plane wave from the origin to the location of particle a. Both of these operators are a function of the relative vector distance between particles, $\boldsymbol{d}_{ab} \in \mathbb{R}^3$, or the particle's distance to the origin, $\boldsymbol{d}_{a0} \in \mathbb{R}^3$. The exact solution to the J – particle coupling problem is found by writing equation 4.2.2 for every particle, then solving the system of J coupled equations. Repeating this process for different particle configurations constitutes the Monte Carlo scheme.

In principle there is no closed form solution for the infinite random film problem, given an arbitrary joint shape and spatial distribution[100–102]. Hence, operations on random variables are solved through Monte Carlo. This allows generalized distributions to be studied by realizing them through computer generation. At each iteration of our algorithm, we first generate N instances of a random film of nonoverlapping particles for each s in $P(s)$. This is done using a custom event-driven particle dynamics algorithm that packs particles to the specified fill fraction, then moves them randomly to remove artificial correlations as a result of the initial packing. The algorithm is designed to mimic the random motion of uncharged hard particles in a Langmuir-Blodgett trough, which is a practical deposition tool to realizing such a film and holds potential

as a large-scale deposition technique[103,104]. Each iteration of the optimizer involves $S \times N \times \Lambda$ generalized Mie simulations. Here, S is the discretization size of the shape distribution. N is the number of sampled unique local fields a particle experiences. I.e., for each sampled particle with shape s, there are N realizations of a unique photonic environment of neighboring particles. Λ is the total number of wavelengths considered. Simulations are in frequency-domain. The generalized Mie simulations are performed using a custom-built code, derived from SMUTHI[105], for increased computation speed. It is also important to note that the method is complete and converges to an exact solution as the multipole order and the number and size of Monte Carlo samples increases. In particular, this approach captures the reflection and transmission from both the coherent and incoherent field. The latter is generally substantially harder to describe analytically and cannot be described by an effective medium theory.

By recasting the random film problem to leverage the orthogonality of the Mie functions, it is possible to substantially increase the speed of electromagnetic calculations. For the optimizer, transmission, reflection, and absorption are defined as

$$\begin{aligned} T(\lambda) &= 1 - R(\lambda) - A(\lambda) \\ R(\lambda) &= \frac{ff\ \mathbb{E}[\sigma_{sca}(\lambda,r,s)]}{1+FBR_A} \\ A(\lambda) &= ff\ \mathbb{E}[\sigma_{abs}(\lambda,r,s)]. \end{aligned} \qquad 4.2.3$$

$\mathbb{E}$ is the expectation operator over the joint particle shape and position distribution. $\mathbb{E}[\sigma_{sca}(\lambda,r,s)]$ and $\mathbb{E}[\sigma_{abs}(\lambda,r,s)]$ are the expected scattering and absorption efficiency of a particle within the film. $FBR_A(\lambda) \approx \frac{\mathbb{E}[\sigma_{sca}(\theta=0°,\lambda,r,s)]}{\mathbb{E}[\sigma_{sca}(\theta=90°,\lambda,r,s)]}$ is the ratio of the expected scattering in the forward, $\theta = 0°$, and backward, $\theta = 90°$, directions. This ratio leverages the degeneracy of the Mie harmonics at the poles. The advantage of equation 3 is computational speed. In particular, the FBR_A reduces two lengthy hemispherical integrations over $O(l!)$ different multipole permutations to a calculation of $O(n^2)$ that does not require a single numerical integration[106]. This change provides a considerable reduction in computational effort. The power balance relation for the random film is $\mathbb{E}[\sigma_{ext}] = \mathbb{E}[\sigma_{abs}] + \mathbb{E}[\sigma_{sca}]$, where $\mathbb{E}[\sigma_{ext}]$ is the measure of the power removed from the incident plane wave as a result of interference with the collective scattered field emanating from the random metasurface. Unlike isolated particle Mie theory, it is necessary to account for the interference between each particle's scattered field. This is encapsulated in the scattering efficiency for each particle, $\sigma_{sca} = \sigma_{sca-i} + \sigma_{sca-d}$. $\sigma_{sca-i} \propto c^\dagger c$ is a measure of the power scattered by each particle and $\sigma_{sca-d} \propto c_a^\dagger \sum \mathbb{H}^{ab} c_b$ accounts for

the interference between scattered fields. † denotes the conjugate transpose operation. For historical reasons, σ_{sca-i} and σ_{sca-d} are termed the "independent" and "dependent" scattering efficiency.

The key insight of equations 4.2.1 – 4.2.3, is that the film's total reflection, transmission, and absorption is governed by the ensemble average of the directional scattering and the absorption efficiencies of the individual particles making up the film. These expected values are controlled by the particle shape, $P(s)$, and spatial position distribution, $P(\boldsymbol{r})$. The former nominally dictates the scattering modes a particle will support and is primarily controlled through $\mathbb{T}$. The latter defines the effect of spatial correlation in particle-particle coupling dynamics, which it primarily controlled through $\mathbb{H}$. Note that these two distributions are not uncorrelated as the shape distribution limits the possible particle spatial configurations since particles cannot overlap.

Even with the computational benefits inherent to generalized Mie theory and equation 4.2.3, this method poses a computational challenge due to the many simulations necessary to reach convergence in both Monte Carlo and in optimization. To accelerate performance the Monte Carlo process (both the event-driven particle dynamics and electromagnetic calculation) is massively parallelized through a distributed programming scheme using Dask[107]. A graphical image of nanoparticle coupling giving rise to different far field scattering distributions of each particle and the optimization pipeline is shown in figure 4.2.1. All computationally heavy calculations are written in C to maximize computation speed.

Besides analytic, algorithmic, and parallelization optimizations of the electromagnetic solver, it is also critical to minimize the number of function calls necessary for the optimizer to reach a satisfying filter performance. Bayesian optimization is a well-suited solution for this problem and the framework we adopt.

Bayesian optimization is a global optimization technique that can minimize the number of evaluations of costly nondifferentiable and noisy objective functions with mixed constraints at moderate dimensions[108]. We use Bayesian optimization based on BoTorch[109] with a Gaussian process prior and the expected improvement acquisition function. This combination gives cheap-to-evaluate surrogates, an analytic form of the acquisition function, and inherently provides a tradeoff between exploitation and exploration of the parameter space[108]. To enable a more efficient reuse of samples, the reflection and transmission curve of each evaluated filter is saved in a global dataset and the next sample is based on the totality of the shared data. This is because $P(s)$ and ff uniquely define the filter, which, for example, cannot simultaneously be a

good shortpass and longpass filter. Therefore, for example, the results from the longpass filter optimization helps increase the information available to the Bayesian prior for the shortpass optimizer. Each optimization utilizes its own objective but shares information about the evaluation points of all other running and past run results.

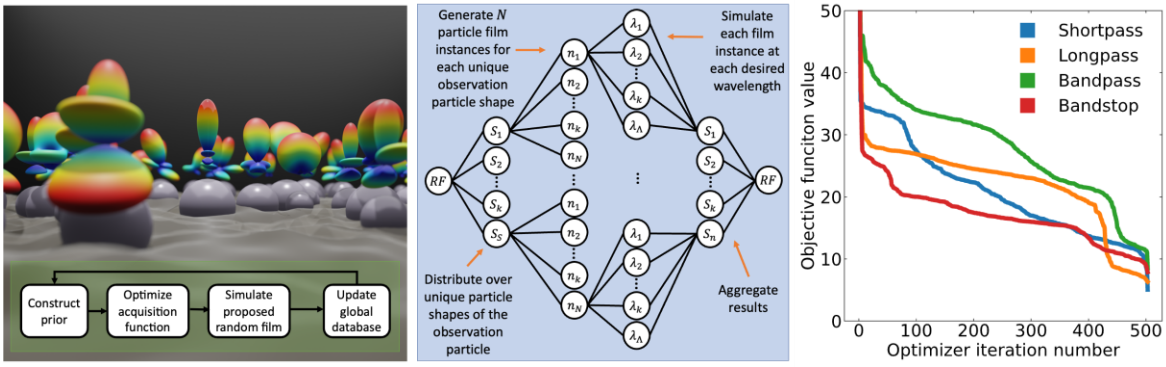

Figure 4.2.1. Bayesian optimization procedure. (Left) Schematic of the distributed network used to simulate a random film and compute equations 7-12. The random film (RF) is characterized by a discretized size distribution and area fill fraction. The program first distributes the calculation for each unique particle size (S) and, for each of those, distributes the task of generating unique spatial distribution samples (n). Each spatial distribution then distributes the task of solving the electromagnetic problem of that sample for each desired wavelength. The results are then compiled. (Middle) Flow diagram of the Bayesian optimizer. Seed particle distributions and fill fractions are first simulated to construct a prior. From this, the optimal solution to the expected improvement function picks the next proposed sample point. Each sample is a discrete probability distribution of particle sizes and an area fill fraction. The sample is then simulated and the reflection and transmission result is stored in a global database. The optimizer then compiles all data in the global database and uses the totality of the data to update the prior. The process then iterates by again choosing the next sample point through the acquisition function on the updated prior. (Right) Best (minimum) objective function for the longpass (orange), shortpass (blue), bandpass (green), and bandstop (red) filter as a function of Bayesian optimizer iterations.

4.3 SINGLE LAYER PARTICLE FILTERS

Figure 4.3.1 shows the resulting design of bandstop, longpass, shortpass, and bandpass spectral features in the infrared, using the approach outlined in section 4.2. Overall, low absorption loss filters can be achieved with stopbands ranging from 50% to over 90% and passbands from 40% to over 80%. In all cases, our result is compared to full-wave finite-difference time-domain (FDTD, dotted lines) simulations to highlight the accuracy of our framework. Both methods show excellent agreement, further validating the use of this method to property represent complex interparticle coupling dynamics in random systems.

The filters are made completely out of a single layer of randomly placed germanium particles with optimized radii distributions (black dashed overlay line), and unique packing fractions, shown in the top right. In all cases the optimal radii distributions can be constructed from the sum of simple Gaussian distributions (colored solid lines). This supports the feasibility of designing such filters in experiment. The Gaussian distribution is the common default distribution found in many particle synthesis and size-filtering techniques[110–113], so one can simply mix different batches of synthesized particles at the proper weight fraction to produce the optimal distribution.

The spectral range was chosen so that the refractive index of germanium is approximately constant ($\eta = 4.17 + i5 \times 10^{-3}$). By choosing a region of high dielectric index and low material loss we show that each filter's stopband is not a result of absorption, but instead a result of strong multiple scattering and interference effects. This is a fundamentally different approach compared to the small particle systems that are well described by effective media. For example, section 4.6 gives a comparison to the Maxwell-Garnett and Bruggeman mixing formulas, which show poor modeling performance.

Since the framework utilizes the scattered field formalism, it is possible to decompose the filter response based on particle size in order to study the effect of the particle size distribution. Clearly, such an analysis is not possible in full-wave techniques that only record the total field. Figure 4.3.2 decomposes each filter's reflection and transmission spectra based on the underlying Gaussian size distributions in figure 4.3.1. Figure 4.3.2 shows that the primary (largest, light blue) Gaussian is also the primary contribution to the overall filter response. This is sensible as our analytic derivation in the supplementals shows the filter response is linearly proportional to the shape distribution. The remaining Gaussian distributions, clustering close to the primary distribution, then act as higher order correction terms chosen by the optimizer to broaden and flatten pass/stopbands.

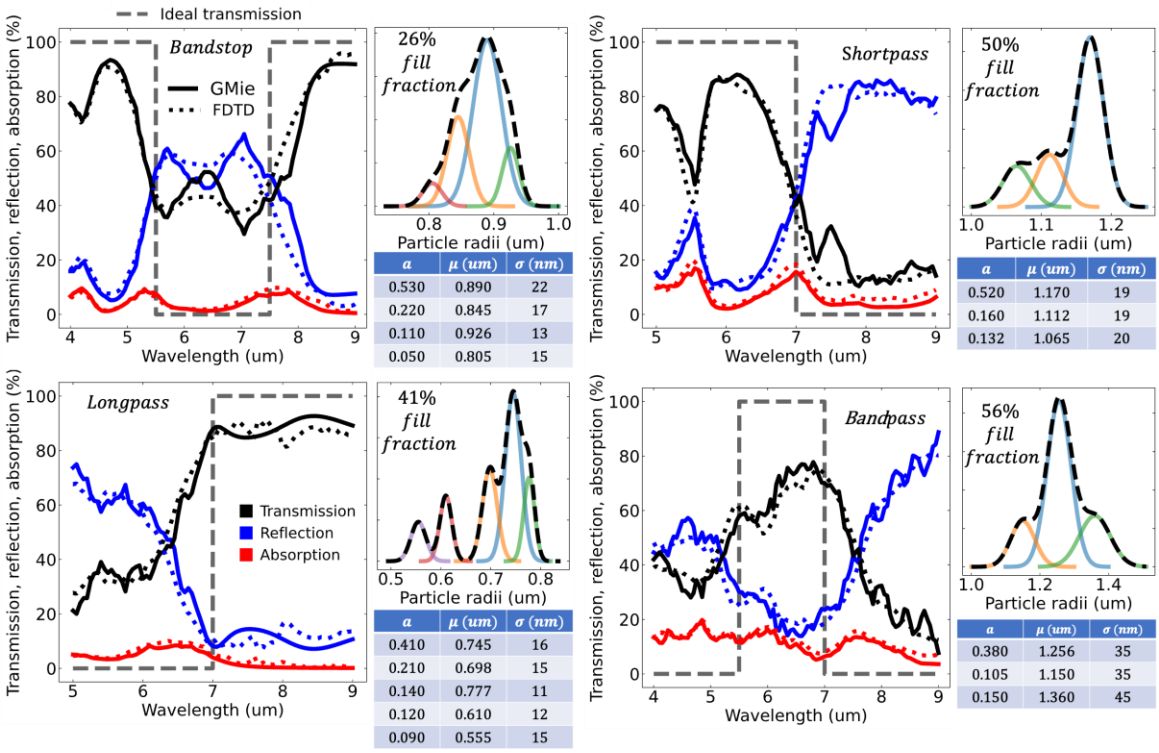

a	μ (um)	σ (nm)
0.530	0.890	22
0.220	0.845	17
0.110	0.926	13
0.050	0.805	15

a	μ (um)	σ (nm)
0.520	1.170	19
0.160	1.112	19
0.132	1.065	20

a	μ (um)	σ (nm)
0.410	0.745	16
0.210	0.698	15
0.140	0.777	11
0.120	0.610	12
0.090	0.555	15

a	μ (um)	σ (nm)
0.380	1.256	35
0.105	1.150	35
0.150	1.360	45

Figure 4.3.1. Transmission (black), reflection (blue), and absorption (red) response for the four particle filters. Solid lines are calculated using the generalized Mie method. Dotted lines are calculated using finite-difference time-domain (FDTD). The ideal transmission is in dashed shaded black. For each filter, the upper right figure is the film's particle size probability distribution and area fill fraction. The size distribution is decomposed into Gaussian distributions and the table for the Gaussian amplitudes (a), mean value (μ), and standard deviation (σ) are shown in the corresponding table below the figure.

Figure 4.3.2 also compares the filter response if particle-particle coupling effects were removed (dashed lines). The purpose of comparing to a non-physical scenario of filters made from noninteracting particles is to contrast how coupling alters the overall spectral response. This also highlights a benefit to the theoretical construction. Simulations assuming no particle coupling can easily be derived by eliminating the particle coupling operator, $\mathbb{H} = 0$, between particle pairs. Therefore, you can "turn on" and "turn off" particle coupling effects at will by including or removing the $\mathbb{H}$ term, respectively. In figure 4.3.2, the uncoupled system produces a non-physical total reflection and transmission spectra. This is expected as the $\mathbb{H} = 0$ assumption does not define a proper power balance relationship. The inaccuracy is best seen near particle resonances, where the electrical cross sections of individual particles are more likely to overlap. Recall, that physical particles cannot overlap. But nothing prevents electrical (e.g., scattering and

absorption) cross sections from overlapping. When coupling is not accounted for in the bookkeeping, then it is possible that the sum of all electrical cross sections from all particles becomes larger than the extent of the x – y plane. Clearly this is nonphysical as the extinction theorem outlines that the total particle system cannot extinguish more power than what is supplied by the incident plane wave. Correspondingly, these nonphysical regions in the uncoupled spectra highlight where net quenching must occur in order to maintain power balance. The quenching is a direct result of particle-particle coupling effects. Further detail on the role of particle coupling versus particle size can be found in section 4.5.

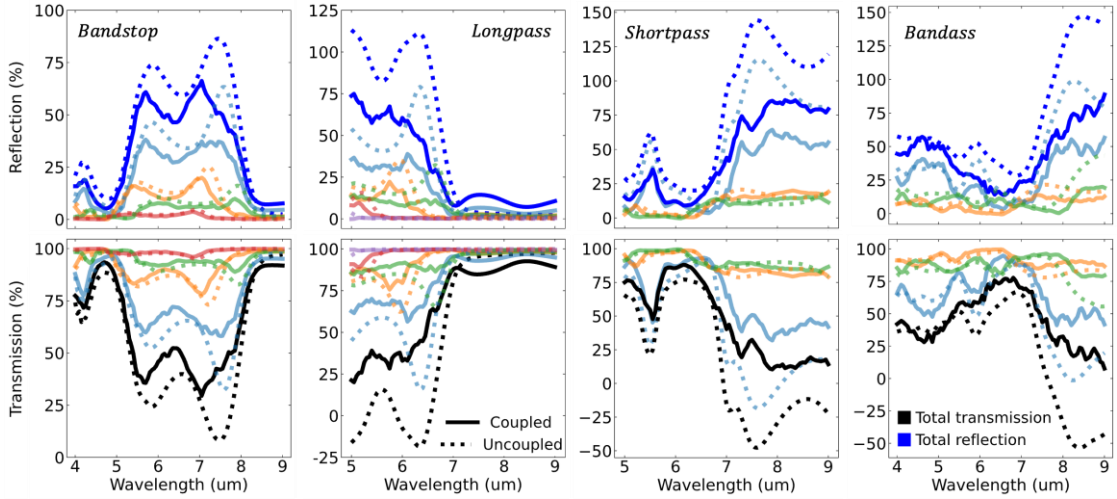

Figure 4.3.2. Reflection (blue) and transmission (black) response of each particle filter decomposed to resolve the contributions from each Gaussian distribution making up the particle film. The Gaussian-resolved reflection and transmission are color coded according to the colors of the Gaussian fit in figure 4.3.1. Solid line curves are calculated using generalized Mie theory accounting for particle coupling. Dotted line curves are calculated assuming no particle coupling.

Strictly speaking, the uncoupled assumption is accurate only in the limit of vanishing electrical cross sections and/or vanishing fill fraction. This is a common stipulation in effective medium theories that clearly does not apply in our case. With that said, even though the uncoupled predictions are not physical, they still predict well the spectral location of stopbands and passbands. This may provide valuable insight to future work in random metasurface optimization. First, uncoupled calculations are exceptionally faster and more memory efficient to calculate compared to coupled calculations. This is because particle coupling forms a large set of coupled linear equations that must be constructed and then solved. In future works, the optimizer could first use the uncoupled model to quickly rule out areas of the search space that clearly do not match the objective function. Bayesian optimization provides a clear theoretical interpretation of such a low-fidelity simulation as adding additional information to the Bayesian

prior. Furthermore, the nonphysical regions in the uncoupled spectra could be penalized, weighted, or smoothed to mimic the necessary net reduction in particle cross sections. This then gives a low fidelity surrogate model for coupling effects.

Uncoupled simulations correctly predicting the location of passbands and stopbands implies a dominance in $\mathbb{E}[\sigma_{sca-i}]$ over $\mathbb{E}[\sigma_{sca-d}]$ in defining the spectral shape. This is sensible when the structure factor of the film lacks a strong coherence effect. Then $\mathbb{T}$ can dominate over the role of $\mathbb{H}$. With that said, though the structure factor is not strongly coherent, particle coupling still plays an important role to maintain global power balance. To study how particle coupling is dependent on the film's structure factor, figure 4.3.3 plots the statistics of σ_{sca-d} as a function of the radial distance, ρ, between particles. Recall that σ_{sca-d} is the portion of a particle's scattering efficiency accounting for the interference with other scattered fields. The solid black lines in figure 4.3.3 plot the expectation of the dependent scattering efficiency, $\mathbb{E}[\sigma_{sca-d}]$. The shaded region gives the standard deviation. The statistics of σ_{sca-d} are shown at four representative spectral locations. Two locations are in the passband and two are in the stopband of each filter. In figure 4.3.3, the particle – particle pair correlation function, $g(\rho)$, for each filter is also shown in the upper right of each plot. This gives reference to the spatial structure factor of the film. In all cases, the radial distribution function resembles the Percus-Yevick equation for hard spheres. There is clear short-range order and correlation increases with increasing filling fraction. No long-range order exists. At large interparticle distances ($k\rho \geq 10$), $\mathbb{E}[\sigma_{sca-d}]$ decays with a spherical Bessel-like oscillation. This indicates uncorrelated interactions consistent with a lack of long-range order.

In almost all cases the short-range dependent scattering efficiency has an overall deleterious effect evident by the dip near the minimal distance. This is consistent with the idea that power balance is maintained primarily by nearest neighbor energy stealing. For an individual particle, the local photonic environment can strongly vary, primarily due to the behavior of nearest neighbor particles. This is evident by the large standard deviations in power transfer at short distances. In all cases, when $\mathbb{T}$ is resonant nearest neighbor coupling interactions are stronger and more varying. This supports our geometric interpretation. Quenching is a result of scattering cross sections (when larger than geometric cross sections) have a greater degree of mutual overlap at wavelengths satisfying resonant scattering conditions.

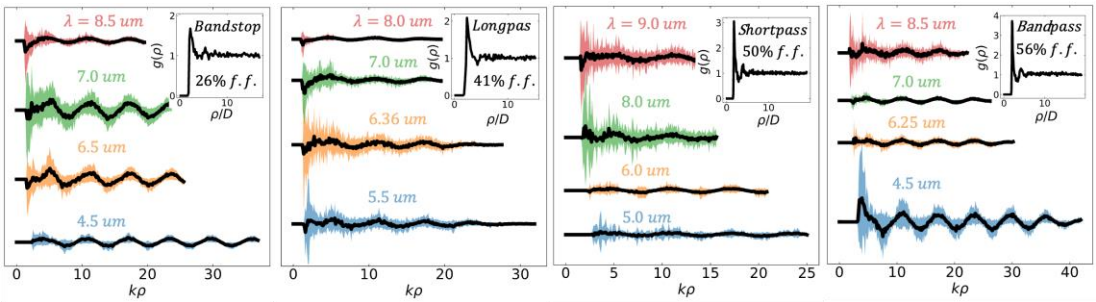

Figure 4.3.3. Average (black) contribution of the dependent scattering efficiency as a function of wavelength-normalized distance from the observation particle. For each filter, the distance-resolved efficiency at four wavelengths are shown. Each wavelength is color coded and the color shaded region around the mean values gives the area within one standard deviation from the mean dependent scattering efficiency. In each figure, two wavelengths are in the passband and two are in the stopband. The upper right quadrant of each figure plots an example radial distribution function of the particle film based on the size distribution function and area fill fraction from figure 4.3.1.

To study further the role $\mathbb{T}$ plays in defining the filter response, figure 4.3.4 plots the independent scattering efficiency, $\sigma_{sca-i} \propto \mathbb{T}^{\dagger}\mathbb{T}$. This defines the scattered power emanating directly from individual particles within the film. Since the Mie scattering harmonics represent fields as atom-like electric and magnetic-type multipoles, we decompose σ_{sca-i} into its various Mie harmonic contributions to further illuminate the contribution from each harmonic (left column). Furthermore, we also transform from the Mie harmonics into a Kerker harmonic basis and perform the same harmonic decomposition of σ_{sca-i} in terms of Kerker harmonics as well. Like figure 4.3.2, we also plot the result from filters made of uncoupled particles (dashed lines) so that we can contrast the two.

The left column of figure 4.3.4 plots $\sigma^{t}_{sca-i,np}$, where n is the polar quantum number, p is the parity, and t denotes an electric or magnetic-type multipole under the Mie basis. The sum over all quantum azimuthal numbers, $m \in [0, n]$, is performed since we are not concerned with azimuthal variations. Due to the azimuthal symmetry $m = 1$ for the uncoupled approximation. In the coupled system, all integer values of m can be populated due to particle coupling. Therefore, the m summation is necessary and corresponds to an azimuthal integration of the scattering response. Multiple scattering also induces electric and magnetic-type multipoles of opposite parity to those expected by the polarization state of the external plane wave excitation. Therefore, cross-polarized scattering is another feature not seen in the uncoupled approximation (or in planar-film filters). To clarify the cross polarized terms have a $\times$ superscript in the legend and are represented by dotted lines.

For all filters, the electric and magnetic-type dipoles are the primary harmonics driving the filter response. Strong reflections are then a result of strong backward scattering near the middle electric and magnetic dipole crossing point. This is analogous to the backward Kerker effect for random film systems[106]. The contribution of higher order harmonics is presented in the supplementary information.

On average the coupled system's scattering harmonics have the same spectral shape and location compared to uncoupled predictions. This again substantiates the result of figure 4.3.2 and indicates the role of $\mathbb{T}$ in defining the scattering spectra for these systems. Resonant peaks are reduced as a result of interparticle coupling. The reduction of resonant peaks is clearly more pronounced when particles are packed at a higher fill fraction. The electric dipole resonance is shown to be more affected by interparticle coupling compared to the magnetic dipole resonance. This is sensible as the latter comes from a strong closed loop oscillation of weakly damped bound charges, which can be seen deep into the core of the particle. In contrast, the charge distribution of the electric dipole is instead distributed on the outer edges of the particle, making it more susceptible to changes by the external environment.

In the shortpass and bandpass filter, the electric dipole resonance is reduced by more than half, lacks a well-defined peak, and the cross polarized harmonics are of near equal magnitude to the same-polarized harmonics. Such deviation of the scattering behavior compared to an uncoupled particle brings the question: If mode profile dictates the direction of scattered photons and the shortpass and bandpass coupled system are strongly different to their uncoupled analogy, why does figure 4.3.2 show they have similar spectral behavior?

Though the Mie harmonics provide insight into the difference in robustness of electric and magnetic-type resonances as a result of particle coupling, these harmonics do not provide insight into the directionality of scattering. For sufficiently high-index and low-loss dielectrics, in the Mie size regime, directional scattering can be found at crossing points of the magnetic and electric harmonics. This effect, termed the Kerker effect, is strongly dependent on both the relative amplitude and phase of the interfering harmonics. Furthermore, cross polarization terms must also be considered in random systems[106]. Strictly speaking, directional scattering is the result of coupling between $O(nmp!)$ harmonic pairs because the orthogonality conditions of the Mie harmonics cannot be leveraged on the hemisphere. Furthermore, the analysis is of both amplitude and phase is necessary as directionality is a coherent interference phenomenon.

The Kerker harmonics are a basis of highly directional forward and backward-type multipoles which are designed to better elucidate features related to the directionality of such scattering.

These harmonics can be constructed from a linear transform of the outward propagating (Hankel) Mie harmonics as,

$$\begin{aligned}\boldsymbol{\Upsilon}^{f}_{nmp}(\boldsymbol{r}) &= (i)^n\left(\boldsymbol{\Psi}^{M}_{nmp}(\boldsymbol{r}) + (-1)^p i\boldsymbol{\Psi}^{E}_{nm1-p}(\boldsymbol{r})\right)\\ \boldsymbol{\Upsilon}^{b}_{nmp}(\boldsymbol{r}) &= (-1)^{(n+m+1)}(i)^n\left(\boldsymbol{\Psi}^{M}_{nmp}(\boldsymbol{r}) + (-1)^{1-p} i\boldsymbol{\Psi}^{E}_{nm1-p}(\boldsymbol{r})\right),\end{aligned} \qquad 4.3.1$$

where f and b denote the basis of forward and backward-type directional Kerker harmonics, respectively. E and M denote electric and magnetic-type Mie harmonics, respectively. Correspondingly, the Kerker scattering coefficients are related to the Mie coefficients through the transform,

$$c^{t}_{nmp} = \frac{1}{2}(-1)^{t(n-m-1)}(-i)^n\left(c^{M}_{nmp} + (-1)^{1-t-p} i c^{E}_{nm1-p}\right), \qquad 4.3.2$$

where $t \in \{f = 0, b = 1\}$ denotes a forward or backward-type multipole, respectively. We append the E and M superscript to the electric and magnetic-type Mie coefficients to distinguish them from the Kerker coefficients. Equations 4.3.1 and 4.3.2 define an element-wise transform where $\boldsymbol{\Psi}^{t}_{nmp} c^{t}_{nmp} \in \mathbb{C}^3$.

A primary benefit of the Kerker basis relevant to our analysis is that directional scattering can be inferred from the forward and backward decomposition of the total scattering efficiency. I.e., $\sigma_{sca-i} = \sigma^{f}_{sca-i} + \sigma^{b}_{sca-i}$. This leverages the properties of the Kerker harmonics to simplify analysis regarding photon redirection.

The right column of figure 4.3.4 plots the independent scattering efficiency decomposed into Kerker harmonics. Again, the sum over all azimuthal numbers is performed and cross polarization is referenced to the polarization of the external plane wave. Under the Kerker basis, both the first order forward and backward directional harmonic are predominant for all four filters. This is a result of the dominance of the dipole modes in the Mie basis. In all cases, the Kerker backward harmonic shows a strong contribution in each filter's respective stopband. This is also the middle crossing point between the electric and magnetic dipole mode. In the stopband of the bandstop filter, the backward Kerker harmonic is dominant compared to the forward Kerker harmonic. This indicates preferential backward-dominant scattering in that region. Furthermore, both the bandstop and longpass filter have forward dominant scatting in their long-wavelength passbands.

Though, anomalous directional scatting is present in some filters, it is not the predominant factor in defining each filters performance. In fact, the stopband of the longpass, shortpass, and bandstop filter are all characterized by forward and backward harmonics having approximately the same scattering efficiency. No anomalous directional scattering is occurring in the stopband regions. This strongly contrasts the prediction of uncoupled particles, which attribute all stopbands to highly directional backward-dominant scattering. The question is then, why does the coupled system still have a stopband despite lacking appreciable backward dominated scattering? Furthermore, why does the uncoupled particle approximation still show a similar overall shape in figure 4.3.2, despite predicting strong directional scattering not seen in the coupled counterpart?

They key insight is that the reflection is driven solely by backward particle scattering, which is proportional to σ_{sca-i}^{b}. Therefore, from the point of view of the optimizer, it is not necessary to simultaneously tune σ_{sca-i}^{f} as an independent parameter. Instead, it is only necessary to ensure a strong backward harmonic in the stopband and a weak backward harmonic in the passband. The behavior of the forward scattering Kerker harmonic is taken care of by energy conservation. I.e., the extinction terms will suppress scattering in the transmission region when necessary. Therefore, thought the ratio between forward and backward harmonics is not preserved for all filters between the coupled and uncoupled systems, the location of increased/decreased backward scattering is preserved and this is the defining parameter. Thus, both systems predict a similar filter type.

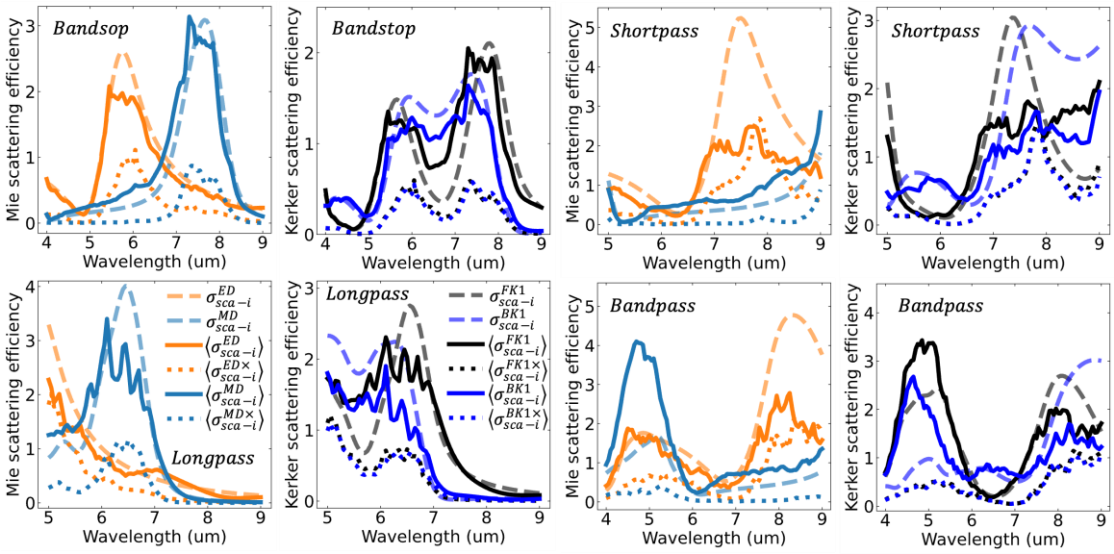

Figure 4.3.4. Independent scattering efficiency of all four designed filters. The left column shows the contribution of the electric (orange) and magnetic (light blue) dipole harmonics to the scattering efficiency. The first order forward (black) and backward (blue) Kerker representation is shown in the corresponding figure to the right. In all cases solid lines denote to the independent efficiency arising from harmonics with parity aligned with the expected orientation according to the plane wave polarization. E.g., given a linearly polarized incident plane wave, the expected orientation is electric dipoles aligned with the incident electric field and magnetic dipoles are aligned with the incident magnetic field. Dotted lines are the contributions of harmonics excited in the cross-polarization orientation. E.g., electric dipoles aligned with the incident magnetic field and magnetic dipoles aligned with the incident electric field. Dashed lines plot the independent scattering efficiency assuming no multiple scattering contribution to the local field. I.e., uncoupled particles. Since the cross-polarization term is a direct result of the multiply scattered field, the uncoupled system has no cross-polarization harmonics. For readability, the legend uses $\langle\cdot\rangle$ $(= E[E[\cdot]|s])$ to denote film-level efficiencies that incorporate particle coupling. This allows unbracketed terms to denote uncoupled film-level efficiencies.

4.4 CONCLUSION

We outline a massively parallelizable Monte Carlo integration technique to solve the total transmission, reflection, and absorption response arising from a monolayer of randomly distributed and arbitrarily shaped particles at packing fractions which lack long range order. This method is based on the generalized Mie technique and fully accounts for multiparticle coupling, including nearfield interactions of highly Mie resonant particles supporting both electric and magnetic-type resonances. The approach shows great agreement with (massively large) random film simulations using finite-difference time-domain using a fraction of the corresponding computational time and resources. The method also provides unique insights into how the collective film response is driven by the statistical properties of the constituent particles within the film. This provides a link between global film response and parameters such as particle size distribution, which can be designed using an appropriate fabrication method.

Using Bayesian optimization, we inversely design particle size probability distributions and packing fractions which give rise to the four fundamental filters (bandpass, shortpass, longpass, and bandstop) in the infrared. Furthermore, these filters are made from a *single material* and a *single monolayer* of randomly distributed Mie resonant particles, where the key design parameters are given by probability distributions. This represents a uniquely different approach to filter design compared to traditional methods such as thin films, metasurfaces, photonic crystals, or small particle mixtures relying on material differences between the host and inclusions.

Given the well-defined theoretical framework our technique provides, we study the effect of both the particle distribution and packing fraction on individual particle scattering behavior, interparticle coupling, and how these parameters give rise to the overall filter response. We directly show that the multiply scattered field is appreciable only at nearest-neighbor distances where the particle radial distribution function is highly correlated. Particle-particle coupling is shown to primarily cause energy stealing between particles on average in order to obey energy conservation, even though individual particle clusters can vary greatly. Energy stealing is more pronounced when particles are at a scattering resonance and there is more mutual overlap in scattering cross sections. Despite strong interparticle coupling, uncoupled simulations give good predictions to the spectral location of the pass and stopbands. From a harmonic analysis we show that even though these systems predict different behavior on the nanoscopic (individual particle) level, resulting macroscopic behavior is similar enough to warrant use in the optimization procedure as a low-fidelity surrogate and that this approximation can be substantiated by theory.

4.5 ISOLATED VERSUS COUPLED ELECTRICAL CROSS SECTIONS

Figures 4.3.2 – 4.3.4 in the main text highlight the role individual scattering of particles plays in filter design. This section expands on the analysis of the main text in this regard. Figures 4.5.1 – 4.5.4 plot the absorption and scattering profile of isolated particles and compares this to particles embedded in a random film, where the size distributions and correlation function is the same as the main text. The goal of this comparison is to see how random coupling alters the overall scattering and absorption efficiency of the particles within the film.

The plots are both wavelength and particle size resolved and the color bar is normalized so that summing over all unique particle radii will return the total absorption and scattering efficiency of the film. To conceptually understand this normalization, recall that the total scattering and absorption efficiency of the film is the expected value of the efficiencies of the particles within the film. By the law of total expectation, the discretized expected efficiency can be written generically as $\mathbb{E}[\sigma] = \sum \sigma(s)P(s)$, where s is the unique particle shape, $\sigma(s)$ is the expected efficiency for that particle shape (averaged over all positions), and $P(s)$ is the probability of observing shape s. The color bar is $\sigma(s)P(s)$.

Figures 4.5.1 – 4.5.4 show that a primary role of particle coupling is to smooth/blur the scattering resonance peaks of isolated particles in order to flatten and broaden the passband/stopbands. For example, in the shortpass filter, particle coupling smooths takes the isolated scattering peak near 7.3 um and smooths it across the 7 – 9 um spectral window. This creates the reliable and relatively flat stopband from 7.3 – 9 um seen in the figure 2 of the main text. The results of figure 4.5.1 further support the idea that the optimizer uses particle coupling as a tool to broaden/smooth otherwise narrowband isolated scattering resonances across the spectral regions of interest.

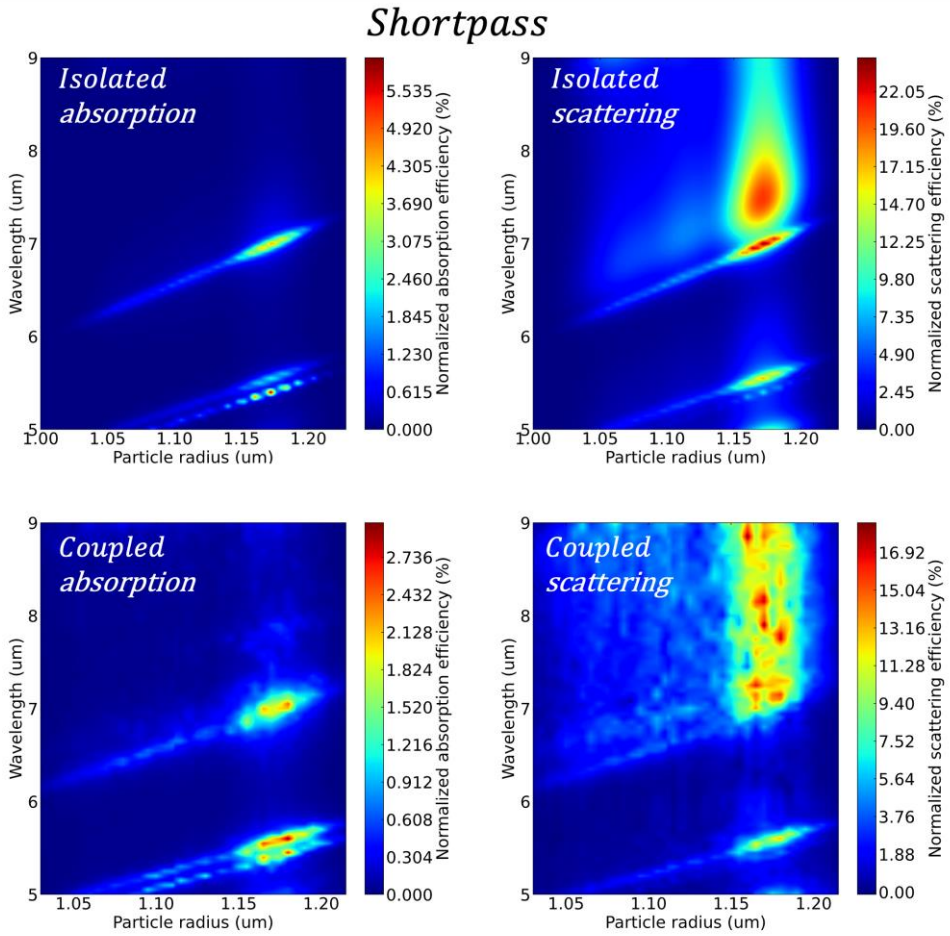

Figure 4.5.1. Contribution of a random film's total absorption (left column) and scattering (right column) efficiency as a function of the radius of particles within the film. The top row is calculated using uncoupled particles. Therefore, the sum of all particles can produce a total (film level) scattering and absorption efficiency that is not physical. Nonetheless, this row provides insight into the scattering and absorption behavior of the embedded particles when in a homogeneous environment. The bottom row gives the values when particles are coupled. This the sum of all particles efficiencies for this row does define a proper power balance relation.

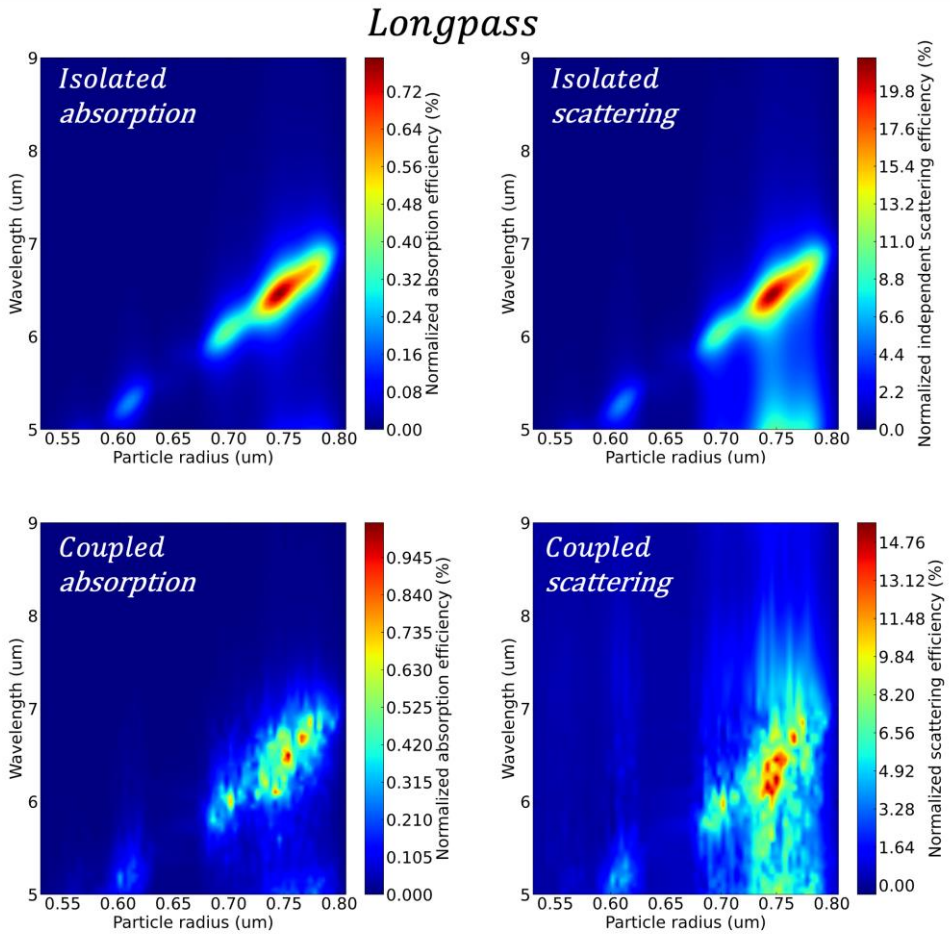

Figure 4.5.2. Contribution of a random film's total absorption (left column) and scattering (right column) efficiency as a function of the radius of particles within the film. The top row is calculated using uncoupled particles. Therefore, the sum of all particles can produce a total (film level) scattering and absorption efficiency that is not physical. Nonetheless, this row provides insight into the scattering and absorption behavior of the embedded particles when in a homogeneous environment. The bottom row gives the values when particles are coupled. This the sum of all particles efficiencies for this row does define a proper power balance relation.

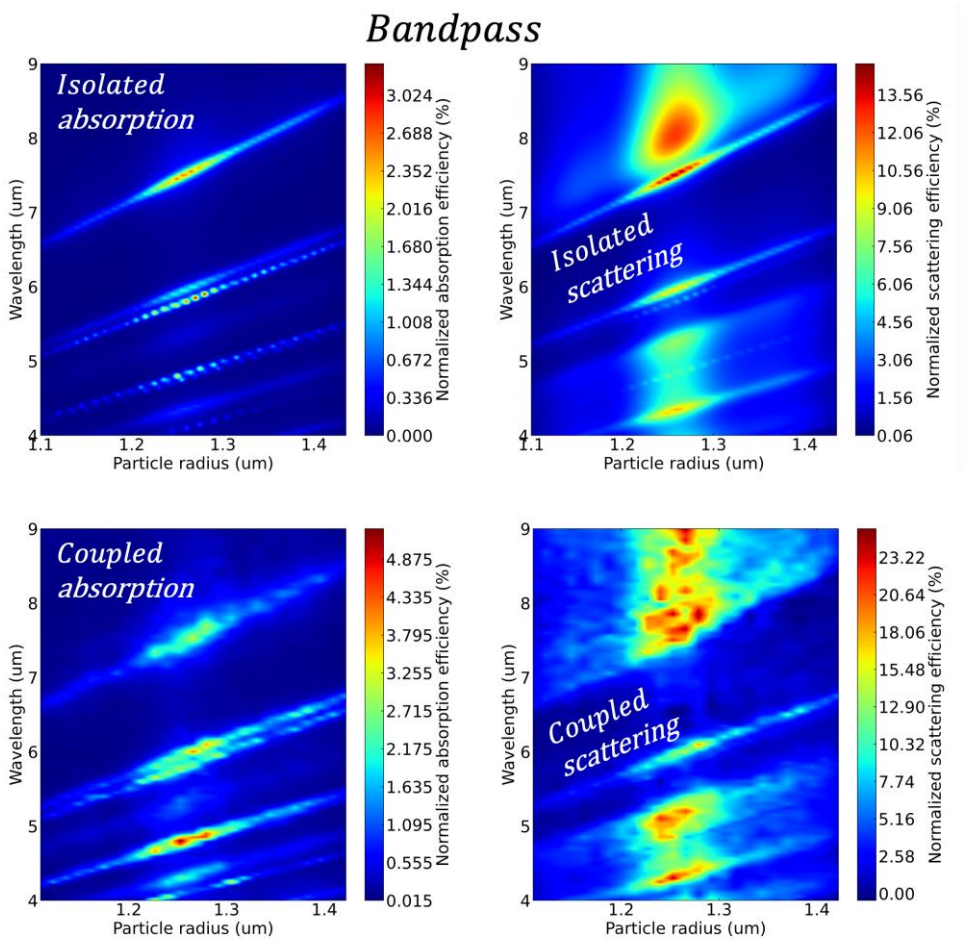

Figure 4.5.3. Contribution of a random film's total absorption (left column) and scattering (right column) efficiency as a function of the radius of particles within the film. The top row is calculated using uncoupled particles. Therefore, the sum of all particles can produce a total (film level) scattering and absorption efficiency that is not physical. Nonetheless, this row provides insight into the scattering and absorption behavior of the embedded particles when in a homogeneous environment. The bottom row gives the values when particles are coupled. This the sum of all particles efficiencies for this row does define a proper power balance relation.

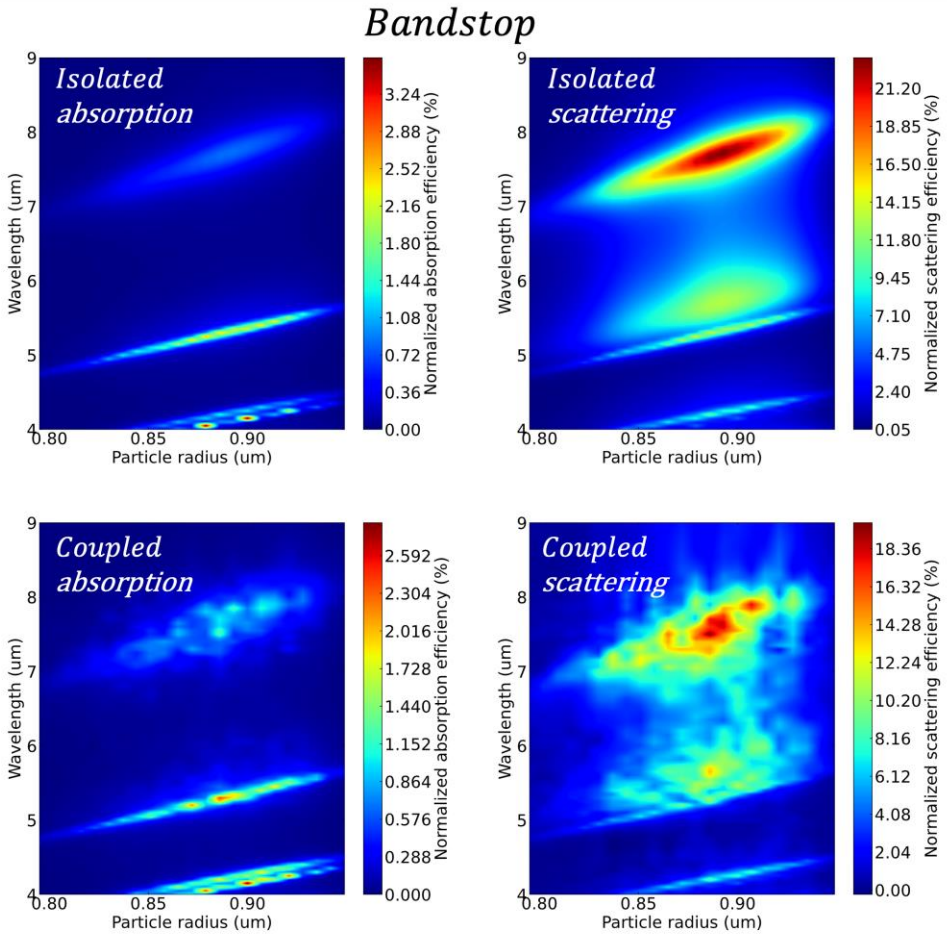

Figure 4.5.4. Contribution of a random film's total absorption (left column) and scattering (right column) efficiency as a function of the radius of particles within the film. The top row is calculated using uncoupled particles. Therefore, the sum of all particles can produce a total (film level) scattering and absorption efficiency that is not physical. Nonetheless, this row provides insight into the scattering and absorption behavior of the embedded particles when in a homogeneous environment. The bottom row gives the values when particles are coupled. This the sum of all particles efficiencies for this row does define a proper power balance relation.

4.6 COMPARISON TO QUASI-STATIC EFFECTIVE MEDIUMS

Given the computational complexity of the method outlined, it is prudent to discuss how this method compares to simpler models. Figure 4.6.1 compares the spectra of the random film's generated in the main text to their Maxwell-Garnett and Bruggeman counterparts. Thin film transmission matrix calculations are used to calculate the spectra of all effective media simulations. In this case, the film thickness for each effective medium calculation was defined by the mode diameter of the particle radii distribution. In all cases the mode (most likely) particle diameter is close to both the maximum and mean particle diameter. Changing the thickness between these three parameters did not have a significant effect on the resulting spectra. Filling fractions are chosen to be the same as the optimized filling fraction of the main text. It is clear from figure 4.6.1 that the Maxwell-Garnett and Bruggeman effective media do not accurately predict the true spectra of the particle filters. I.e., these models do not match the full-wave finite-difference time-domain results or the Monte Carlo generalized Mie results. Furthermore, by comparison, the effective media predict much lower quality filters. In multiple cases the reflection and transmission spectra is predominantly flat throughout the spectral range. In these cases, there is no transition from a dominant reflection region to a dominant transmission region at all.

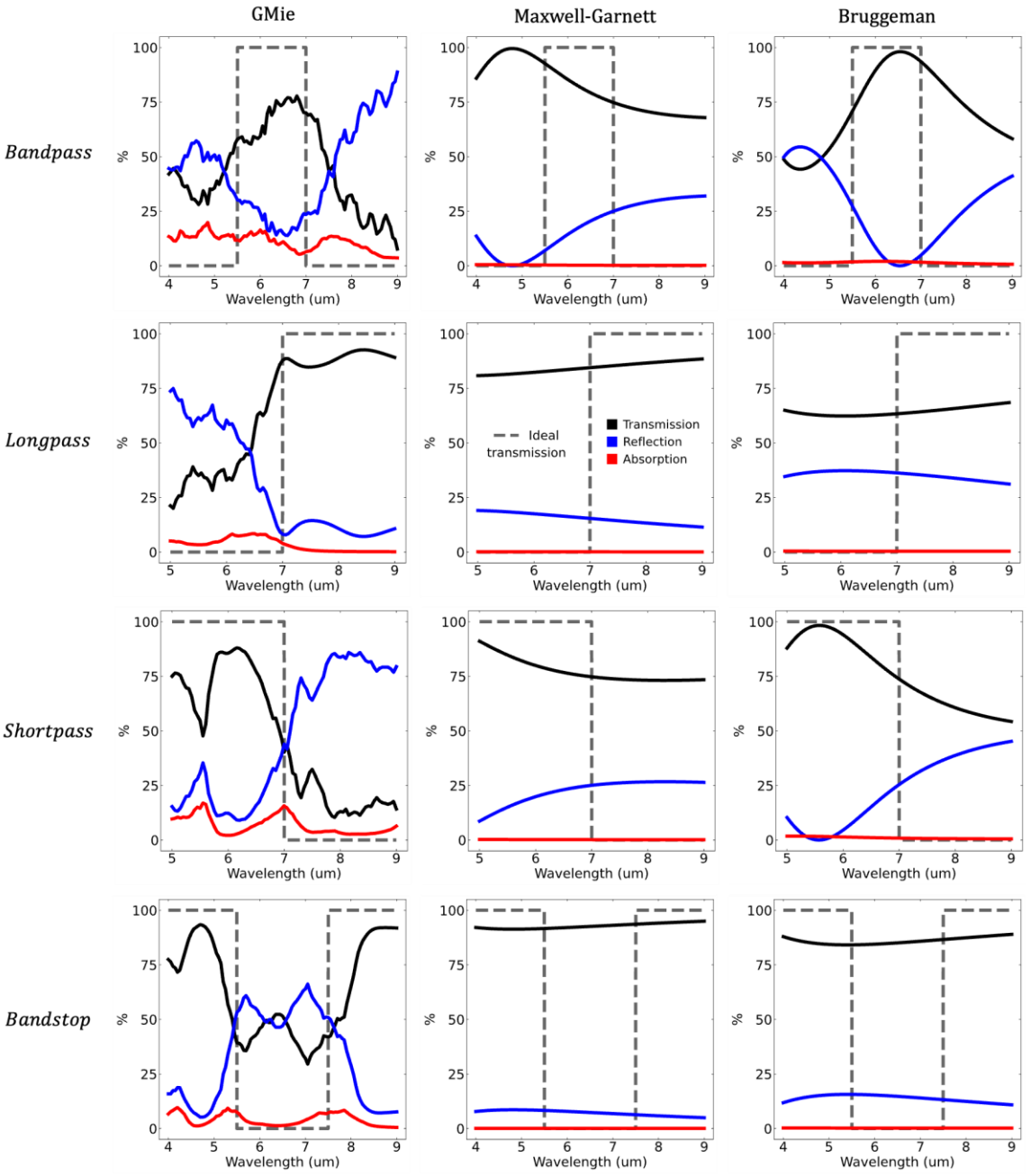

Figure 4.6.1. Comparison of particle filters made from randomly distributed Mie resonant particles confined to a single layer and filters made from analogous effective media based on the Maxwell-Garnett and Bruggeman approximations. The thickness and filling fraction of the effective medium models are determined by the optimizer distribution. The input parameters are: bandpass (thickness = 1256 nm, filling fraction = 56%), longpass (thickness = 745 nm, filling fraction = 41%), shortpass (thickness = 1170 nm, filling fraction = 50%), bandstop (thickness = 890 nm, filling fraction = 26%).

SECTION 2

EFFECTIVE MEDIUMS:

CLASSICAL THEORIES AND BEYOND

Chapter 5

THEORY OF EFFECTIVE MEDIUMS

5.1 INTRODUCTION

Though all matter consists of hierarchical levels of discrete objects, i.e., particle, molecule, atom, electron, nucleon, et cetera; the effective medium provides a method to describe the perceived continuum we experience. The process of blurring the discrete into the continuum is called homogenization. Once the interactions of a complex collective are homogenized, underlying rules need to be set that outline how the homogenized collective responds to external fields, forces, or other stimuli. These governing rules are called constitutive relations. Some are derived empirically through experiment; others can be derived from first principles. Clearly the theory of constitutive relations is of great importance. In may cases it provides the connection between the macro and nanoscopic. For example, in electromagnetism, constitutive relations can define how matter interacts with both fields and intensities, given the degree of disorder in the system. Following a common nomenclature in the electromagnetics community, constitutive relations for electromagnetic *fields* define an "effective medium." In situations where the nanoscopic cannot be directly observed, homogenization offer a model to infer the nanoscopic governing dynamics. When the nanoscopic can be directly observed and even controlled, then homogenization give a recipe to create emergent macroscopic behavior.

In electromagnetism, effective mediums of a disordered system were one of the first frameworks to explore metamaterials. In this context, the "material" observed was a homogenized representation of a more complex many-body interaction under the hood, where the incoherent intensity was negligible. Correspondingly, through proper design of nanoscopic dynamics homogenized "materials" were designed with coherent properties unseen in nature. Of course, in reality, all interactions at the nanoscopic scale uphold known physical principles. It is just that we cannot directly observe the minute details, so we observe the emergent collective. Examples of coherent metamaterial-induced anomalous macroscopic behavior include gradient impedance and refractive indices[114–119], optically induced magnetism[38,120–123], a negative index of refraction[124–130], tailored anisotropy and hyperbolicity[131–136], and more. Of course, metamaterials are not, to the best of my knowledge, a complete panacea for all physical restrictions. For example, governing properties such as conservation relations and causality cause overarching restrictions

onto the mathematical forms an effective media can take[127,137–147]. Variational bounds pose limits on the behavior of effective media given the extremes in spatial configurations[148–151]. This will be discussed in detail in section 5.4.

Part one of this dissertation discussed homogenization of both the coherent and incoherent field in the context of random metasurfaces. Starting from Lipmann-Schwinger, both the coherent field and intensity relations are derived for complex distributions of particle disorder through a Monte Carlo scheme. Applications of this approach were then presented as case studies exploring anomalous behavior.

In part two, homogenization is discussed beyond the confinement to two dimensions. Allowing randomness to now exist in a third dimension transitions the discussion from metasurfaces to metamaterials. This also brings considerably more complexity to rigorous analysis. Hence, part two places a strong emphasis on calculatable approximate theories ("mixing rules") and their applications. Furthermore, emphasis is placed on systems that are primarily coherent. Incoherent theories can be studied from the starting point of the Bethe-Salpeter equations, but this is beyond scope. Similar to part one, the theory of coherent metamaterials will be outlined, including a Monte Carlo scheme that can be used to model beyond the other discussed regimes. Applications of these models are then presented as case studies exploring anomalous behavior and their applications.

5.2 DYSON AND THE SELF-ENERGY

"In complexity, it is only simplicity that can be interesting."

- Steven Weinberg, Lake Views, 2012

As discussed in section 1.8, the concept of order of scattering can play an important role in understanding the assumptions of effective medium theories. In this vein, Feynman diagrams, the Dyson equation, and the concept of self-energy provides an elegant and thorough *ab initio* derivation that connects all effective medium theories to approximations of order of scattering.

Recall from section 1.8 the mean field is defined as the solution to equation 1.8.2,

$$\int_{\mathcal{V}} dP_U \left(\nabla \times \nabla \times \widetilde{\boldsymbol{E}} - k^2 \widetilde{\boldsymbol{E}} = \widetilde{U}\widetilde{\boldsymbol{E}}\right).$$

The primary difficulty of this problem is that $\mathbb{E}\left[\widetilde{U}\widetilde{\boldsymbol{E}}\right] \neq \mathbb{E}\left[\widetilde{U}\right]\mathbb{E}\left[\widetilde{\boldsymbol{E}}\right]$. The subject of effective medium theories is in defining an effective potential, $\overline{\overline{\boldsymbol{U}}}_{eff}(\boldsymbol{r}, \boldsymbol{r}')$, such that

$$\mathbb{E}\left[\widetilde{U}\widetilde{\boldsymbol{E}}\right](\boldsymbol{r}) \approx \int d\boldsymbol{r}' \overline{\overline{\boldsymbol{U}}}_{eff}(\boldsymbol{r}, \boldsymbol{r}')\, \mathbb{E}\left[\widetilde{\boldsymbol{E}}\right](\boldsymbol{r}') = \mathbb{U}_{eff}\mathbb{E}\left[\widetilde{\boldsymbol{E}}\right]. \qquad 5.2.1$$

Equation 5.2.1 introduces the non-local tensor, $\overline{\overline{\boldsymbol{U}}}_{eff}(\boldsymbol{r}, \boldsymbol{r}')$, which is commonly known as the "self-energy" or "mass operator" in many-body scattering theory. Note that, given the statistical properties of the true underlying potential as outlined in section 1.8, the effective potential will be translational invariant, $\overline{\overline{\boldsymbol{U}}}_{eff}(\boldsymbol{r}, \boldsymbol{r}') = \overline{\overline{\boldsymbol{U}}}_{eff}(\boldsymbol{r} - \boldsymbol{r}')$. Again, a double struck notation is used for operators of the form $\mathbb{A}(\boldsymbol{x}, \boldsymbol{x}') = \int d\boldsymbol{x}'\, \overline{\overline{\boldsymbol{A}}}(\boldsymbol{x}, \boldsymbol{x}')$. Brackets are used when necessary for clarity.

Recall from section 1.3 that the electric field Green's dyadic of a realized inhomogeneous potential, $\overline{\overline{\boldsymbol{G}}}_e$, is defined as

$$\nabla \times \nabla \times \overline{\overline{\boldsymbol{G}}}_e(\boldsymbol{r}, \boldsymbol{r}') - k^2 \overline{\overline{\boldsymbol{G}}}_e(\boldsymbol{r}, \boldsymbol{r}') = \delta(\boldsymbol{r} - \boldsymbol{r}') + U(\boldsymbol{r})\overline{\overline{\boldsymbol{G}}}_e(\boldsymbol{r}, \boldsymbol{r}'),$$

and $\overline{\overline{\boldsymbol{G}}}_{eo}$ is the electric dyadic to the homogenous system, $U = 0$. The explicit form of this operator is defined in section 1.3, though it is beneficial to define it here as

$$\overline{\overline{\boldsymbol{G}}}_{eo}(\boldsymbol{r}-\boldsymbol{r}') = PV\overline{\overline{\boldsymbol{G}}}_{eo}(\boldsymbol{r}-\boldsymbol{r}') + \overline{\overline{\boldsymbol{D}}}\delta(\|\boldsymbol{r}-\boldsymbol{r}'\|), \tag{5.2.2}$$

where $PV\overline{\overline{\boldsymbol{G}}}_{eo}$is the principal value of the operator excluding an infinitesimal region centered at $\|\boldsymbol{r}-\boldsymbol{r}'\| = 0$. $\overline{\overline{\boldsymbol{D}}}$ is the depolarization dyadic defined by the form of the removed region. The Green's solution to the inhomogeneous wave equation is,

$$\mathbb{G}_e = \mathbb{G}_{eo} + \mathbb{G}_{eo}\mathbb{U}\mathbb{G}_e. \tag{5.2.3}$$

Through introducing the transition operator, equation 5.2.3 can be written in Lippmann-Schwinger form,

$$\mathbb{G}_e = \mathbb{G}_{eo} + \mathbb{G}_{eo}\mathbb{T}\mathbb{G}_{eo} \tag{5.2.4(a)}$$
$$\mathbb{T} = \mathbb{U}(\mathbb{I} - \mathbb{G}_{eo}\mathbb{U})^{-1}, \tag{5.2.4(b)}$$

where the transition operator, $\mathbb{T}$, is of the entire cluster. This is an important step for calculating the coherent field as it isolates all randomness to $\mathbb{T}$. The propagator on the right-hand side of $\mathbb{T}$ propagates the incident field to a deterministic anchor point in space. The transition matrix $\mathbb{T}$ then defines an incident-to-scattered field conversion that allows all multiple scattering in space to be accounted for and referenced to the anchor point. The propagator on the left-hand side of $\mathbb{T}$ then propagates this scattered field from the known anchor point to the desired location of evaluation. Correspondingly, the Green's operator for the coherent field can be found by taking the expectation of the total Green's solution,

$$\mathbb{E}[\mathbb{G}_e] = (\mathbb{I} + \mathbb{G}_{eo}\mathbb{E}[\mathbb{T}])\mathbb{G}_{eo}, \tag{5.2.5}$$

where the right-hand side need only the expectation of $\mathbb{T}$, which is an ensemble expectation of possible particle positions and types.

Recall from section 1.3 that for discrete inhomogeneities it is meaningful to apply the Lippmann-Schwinger procedure on a per particle basis. Correspondingly, the Lippmann-Schwinger solution can be repackaged in Foldy-Lax form,

$$\mathbb{G}_e = \mathbb{G}_{eo} + \mathbb{G}_{eo} \sum_a^N \mathbb{T}_a \mathbb{G}_{ea} \quad 5.2.6(a)$$

$$\mathbb{G}_{ea} = \mathbb{G}_{eo} + \mathbb{G}_{eo} \sum_{b\neq a}^N \mathbb{T}_b \mathbb{G}_{eb} \quad 5.2.6(b)$$

$$\mathbb{T}_a = \mathbb{U}_a (\mathbb{I} - \mathbb{G}_{eo} \mathbb{U}_a)^{-1}, \quad 5.2.6(c)$$

where, $\mathbb{T}_a$ and $\mathbb{G}_{ea}$ are the particle-specific transition and Green's operator, respectively. The benefit of the Foldy-Lax form is that the transition operators for individual particles can be found separately, either through the extended boundary technique, full-wave simulations, or another method. The coherent field in Foldy-Lax form is

$$\mathbb{E}[\mathbb{G}_e] = \mathbb{G}_{eo} + \mathbb{G}_{eo} \sum_a^N \mathbb{E}[\mathbb{T}_a \mathbb{G}_{ea}] = \mathbb{G}_{eo} + \mathbb{G}_{eo} N \mathbb{E}\big[\mathbb{T}_a \mathbb{E}[\mathbb{G}_{ea}|a]\big] \quad 5.2.7(a)$$

$$\mathbb{E}[\mathbb{G}_{ea}] = \mathbb{G}_{eo} + \mathbb{G}_{eo} \sum_{b\neq a}^N \mathbb{E}[\mathbb{T}_b \mathbb{G}_{eb}] = \mathbb{G}_{eo} + \mathbb{G}_{eo}(N-1)\mathbb{E}\big[\mathbb{T}_b \mathbb{E}[\mathbb{G}_{eb}|a,b]\big]. \quad 5.2.7(b)$$

As discussed in section 1.8 and section 1.9, equation 5.2.7 produces an infinite hierarchy of conditional expectations, where $\mathbb{E}\big[\mathbb{T}_a \mathbb{E}[\mathbb{G}_{ea}|a]\big]$ is calculated from $\mathbb{E}\big[\mathbb{T}_b \mathbb{E}[\mathbb{G}_{eb}|a,b]\big]$, which is calculated from $\mathbb{E}\big[\mathbb{T}_c \mathbb{E}[\mathbb{G}_{ec}|a,b,c]\big]$, et cetera. Applying the same analysis as outlined in section 1.3, the cluster-level transition operator can be written as an order of scattering expansion of particle-level operators. This outlines how to construct $\mathbb{T}$ as a process of multiple order of scattering events. The cluster-level transition operator for the coherent field is,

$$\mathbb{E}[\mathbb{T}] = \mathbb{E}[\textstyle\sum_a^N \mathbb{T}_a] + \mathbb{E}[\sum_a^N \sum_{b\neq a}^N \mathbb{T}_a \mathbb{G}_{eo} \mathbb{T}_b] + \cdots \quad 5.2.8$$

Rewriting equation 5.2.5 to the mathematical form of equation 5.2.3, the Green's operator for the coherent field takes the well-known form of a Dyson equation,

$$\mathbb{E}[\mathbb{G}_e] = \mathbb{G}_{eo} + \mathbb{G}_{eo} \mathbb{U}_{eff} \mathbb{E}[\mathbb{G}_e] \quad 5.2.9(a)$$

$$\mathbb{U}_{eff} = \mathbb{E}[\mathbb{T}](\mathbb{I} + \mathbb{G}_{eo} \mathbb{E}[\mathbb{T}])^{-1}. \quad 5.2.9(b)$$

Comparing equation 5.2.9(a) to equation 5.2.3 it is clear that $\mathbb{U}_{eff}$, defined by equation 5.2.9(b), is the procedure necessary to formally uphold $\mathbb{E}\big[\widetilde{U}\widetilde{\boldsymbol{E}}\big](\boldsymbol{r}) = \int d\boldsymbol{r}' \overline{\overline{\boldsymbol{U}}}_{eff}(\boldsymbol{r},\boldsymbol{r}')\, \mathbb{E}\big[\widetilde{\boldsymbol{E}}\big](\boldsymbol{r}')$, hence

the $\mathbb{E}\left[\widetilde{U}\widetilde{E}\right] = \mathbb{U}_{eff}\mathbb{E}\left[\widetilde{E}\right]$ problem is formally solved. Throughout this dissertation, it is assumed that operators defined by a Neumann series are convergent in the operator norm so that the inverse is defined as,

$$\sum_{j}^{\infty} \mathbb{A}^{j} = (\mathbb{I} - \mathbb{A})^{-1}.$$

Now that the effective potential (self-energy) is properly defined, the inhomogeneous wave equation for the coherent field is

$$\nabla \times \nabla \times \mathbb{E}[\overline{\overline{\boldsymbol{G}}}_e] - k^2\mathbb{E}[\overline{\overline{\boldsymbol{G}}}_e] = \delta(\boldsymbol{r} - \boldsymbol{r}') + \int d\boldsymbol{r}'\overline{\overline{\boldsymbol{U}}}_{eff}\,\mathbb{E}\left[\overline{\overline{\boldsymbol{G}}}_e\right].$$

At this stage it is useful to work in momentum space to avoid spatial convolutions with the nonlocal self-energy. The operators in their Fourier transformed form, $\boldsymbol{r} \to \boldsymbol{p}$ and $\boldsymbol{r}' \to \boldsymbol{p}'$, are

$$\mathcal{F}_{\boldsymbol{r}}\left[\mathcal{F}_{\boldsymbol{r}'}\left[\mathbb{U}_{eff}(\boldsymbol{r},\boldsymbol{r}')\right]\right] = \mathbb{U}_{eff}(\boldsymbol{p},\boldsymbol{p}')$$
$$\mathcal{F}_{\boldsymbol{r}}\left[\mathcal{F}_{\boldsymbol{r}'}[\mathbb{E}[\mathbb{G}_e](\boldsymbol{r},\boldsymbol{r}')]\right] = \mathbb{E}[\mathbb{G}_e](\boldsymbol{p},\boldsymbol{p}').$$

Since the systems under study are translationally invariant, the momentum is a conserved quantity,

$$\mathbb{U}_{eff}(\boldsymbol{r},\boldsymbol{r}') = \mathbb{U}_{eff}(\boldsymbol{r}-\boldsymbol{r}') \Leftrightarrow \mathbb{U}_{eff}(\boldsymbol{p},\boldsymbol{p}')\delta(\boldsymbol{p}-\boldsymbol{p}') = \overline{\overline{\boldsymbol{U}}}_{eff}(\boldsymbol{p})$$
$$\mathbb{E}[\mathbb{G}_e](\boldsymbol{r},\boldsymbol{r}') = \mathbb{E}[\mathbb{G}_e](\boldsymbol{r}-\boldsymbol{r}') \Leftrightarrow \mathbb{E}[\mathbb{G}_e](\boldsymbol{p},\boldsymbol{p}')\delta(\boldsymbol{p}-\boldsymbol{p}') = \mathbb{E}\left[\overline{\overline{\boldsymbol{G}}}_e\right](\boldsymbol{p}),$$

and the Green's function solution for the coherent field is,

$$\mathbb{E}\left[\overline{\overline{\boldsymbol{G}}}_e\right](\boldsymbol{p})$$
$$= \overline{\overline{\boldsymbol{G}}}_{eo}(\boldsymbol{p})\left(\overline{\overline{\boldsymbol{I}}} - \overline{\overline{\boldsymbol{G}}}_{eo}(\boldsymbol{p})\overline{\overline{\boldsymbol{U}}}_{eff}(\boldsymbol{p})\right)^{-1} \qquad 5.2.10(a)$$
$$= \left(p^2\left(\overline{\overline{\boldsymbol{I}}} - \hat{\boldsymbol{e}}_p\otimes\hat{\boldsymbol{e}}_p\right) - k^2\overline{\overline{\boldsymbol{I}}} - \overline{\overline{\boldsymbol{U}}}_{eff}(\boldsymbol{p})\right)^{-1}. \qquad 5.2.10(b)$$

Equation 5.2.10 brings a rich set of information about the coherent field, including a statistical generalization of band diagrams, density of states, coherence length, and the form of the coherent field in real space. Radiation modes of the system are determined by $\det[\mathbb{E}\left[\overline{\overline{\boldsymbol{G}}}_e\right]^{-1}] =$

0. This comes from the general definition, $\overline{\overline{\boldsymbol{G}}}_e^{-1}\boldsymbol{E} = \boldsymbol{J}$, then finding the non-trivial solutions to the homogeneous equation, $\boldsymbol{J} = \boldsymbol{0} \rightarrow \det\left[\overline{\overline{\boldsymbol{G}}}_e^{-1}\right] = 0$. Inserting the homogeneous Green's function,

$$\overline{\overline{\boldsymbol{G}}}_{eo}(\boldsymbol{p}) = \left(p^2\left(\overline{\overline{\boldsymbol{I}}} - \hat{\boldsymbol{e}}_p \otimes \hat{\boldsymbol{e}}_p\right) - k^2\overline{\overline{\boldsymbol{I}}}\right)^{-1}, \tag{5.2.11}$$

into equation 5.2.10(a) gives 5.2.10(b). Furthermore, comparing the homogeneous Green's function to the Green's function of the coherent field makes clear the relation of the effective propagation constant and the self-energy. Disregarding rigor, the effective permittivity has the form,

$$\overline{\overline{\boldsymbol{\varepsilon}}}_{eff}(\boldsymbol{p}) = \overline{\overline{\boldsymbol{I}}} + \overline{\overline{\boldsymbol{U}}}_{eff}(\boldsymbol{p})/k^2. \tag{5.2.12}$$

Again, the proper solution is found through the eigenvalue equation given by $\det[\mathbb{E}\left[\overline{\overline{\boldsymbol{G}}}_e\right]^{-1}] = 0$. It can now be rigorously stated that the complexity of the problem relies on how to estimate the expected multiple scattering behavior given by equations 5.2.9(b) and 5.2.8. Equation 5.2.10 shows that the dispersion is generally different for parallel and perpendicular components as well as the direction of propagation. Clearly this allows for a diverse set of behaviors that are not represented in most effective medium theories. In fact, given that $\det[\mathbb{E}\left[\overline{\overline{\boldsymbol{G}}}_e\right]^{-1}] = 0$ is exact, there is no guarantee that it admits solutions, $\overline{\overline{\boldsymbol{k}}}_{eff}$, that are meaningfully consistent with a homogenized medium. Correspondingly, the self-energy not only describes the form of the coherent field propagator, but also the properties of the underlying material distribution necessary for an effective medium description to be meaningful.

Clearly, the multiple scattering of causal components creates a causal effective medium response. Among the most important properties of the coherent Green's function is its spectral function, $-\Im\left[\mathbb{E}\left[\overline{\overline{\boldsymbol{G}}}_e\right]\right]$, which is proportional to the density of states and should be non-negative. The solutions of $\overline{\overline{\boldsymbol{k}}}_{eff}$ should then properly decay (possibly infinitesimally small) with propagation. The decay of the coherent field comes exclusively from $\Im[\overline{\overline{\boldsymbol{U}}}_{eff}]$, and occurs from both absorption and scattering. This gives the notion of a coherence length, $\ell_{ext}^{-1} = \ell_{sca}^{-1} + \ell_{abs}^{-1}$, which is finite (possibly approaching infinity) even when all inhomogeneities are lossless. The coherence length is a characteristic distance for a random system and dictates the length scales where an effective medium description is meaningful. For example, in a scattering dominate

system, $\ell_{ext} \approx \ell_{sca}$, the coherence length is the distance where the coherent state depletes to the incoherent state. In three dimensions, $k\ell_{sca} \leq 1$ is a marker for the transition to localization according to the Ioffe-Regel criterion. Clearly finite coherence lengths mean the eigenmodes are at best quasi-radiation modes. The delta functions in the spectral function become broadened peaks. In this regard, suitable solutions can be found from the spectral function.

The self-energy provides a formal solution to the effective medium problem. From the self-energy and the corresponding Green's solution all properties of the coherent field can be defined.

5.3 A CLASS OF MIXING RULES: GARNETT, BRUGGEMAN, AND OTHERS

> "Craftsmen, as well as engineers, recognized that any averaging depended on what process or property was involved. People who worked with wood had no doubt that the fibrous grain structure was important."
>
> - Marshall Stoneham, Forward to Effective Medium Theory, 1999

The most established class of effective mediums are those that assume the effective medium is passive, linear, homogeneous, and isotropic. Furthermore, the scattering response is traditionally assumed to be electric dipole dominant, though generalizations will be discussed. This section outlines the assumptions imposed on the self-energy to derive the well-known approximations of individual scattering, Lorentz-Lorentz/Maxwell-Garnett[152], Bruggeman[18,153,154], and Gyorffy, Korringa, and Mills[18,153,154]. General assumptions for the self-energy applicable to all theories are discussed first. Then, the subtleties underpinning each approximation are outlined. In particular, the connection to the self-energy is used to show how the discussed approximations are special cases of more general approximations in condensed matter research. Namely, the Lorentz-Lorentz/Maxwell-Garnett mixing rule is the first order term in the quasi-crystalline approximation[18,153,154]. Bruggeman's work is an application of the individual scattering approximation under the coherent potential framework[18,153,154]. Gyorffy, Korringa, and Mills is an application of the quasi-crystalline approximation under the coherent potential framework[153,154]. The section finishes by showing that all of the discussed approximations are connected aa broader class, which can be described through a single equation[153]. This result is used extensively in the next chapter.

A common hypothesis underpinning all mixing rules in this section is that the random media is statistically isotropic and that field variations are on scales larger than the size of the scatterers and their correlation lengths. Given the requirement of small scatterers, it is also generally assumed that scattering is electric dipole dominant. Inductive fields are negligible, and the effective medium does not have an effective magnetic component, $\mu_{eff} = 1$. Given these conditions, the self-energy is local (no $\boldsymbol{p}$-dependence, as spatial dispersion implies nonlocality) and isotropic and

$$\bar{\bar{\boldsymbol{U}}}_{eff} = (\varepsilon_{eff} - 1)k^2\bar{\bar{\boldsymbol{I}}}, \tag{5.3.1}$$

where ε_{eff} is the effective refractive index[154,155]. In this case, the coherent Green's function is,

$$\mathbb{E}[\bar{\bar{\boldsymbol{G}}}_e] = \left(\bar{\bar{\boldsymbol{I}}} + \frac{1}{k_{eff}^2}\nabla \otimes \nabla\right)\frac{e^{ik_{eff}|\boldsymbol{r}-\boldsymbol{r}'|}}{4\pi|\boldsymbol{r}-\boldsymbol{r}'|}, \tag{5.3.2}$$

which exactly recovers the solution to a passive, linear, homogeneous, and isotropic medium of k_{eff}.

The electric dipole assumption is not ill founded when viewing the particle as a cavity. The quasistatic restriction limits $\mathbb{T}$ to appreciably support only the lowest order (electric dipole) harmonic as is easily shown through Mie theory, which is applicable to particles of any shape in the vanishing size regime. As long as the local density of electromagnetic states does not contain strong high order harmonics that disproportionately outweigh the particle's natural suppression of these excitations, on average, then all multiple scattering reduces to dipole-dipole coupling. This dramatically narrows the state space of multiple scattering. Note, as discussed in section 1.9, a particular particle can experience high-order harmonic scattering. This is ok, as the condition is concerned only with the average behavior.

For explicit detail on the derivations of the individual scattering, Lorentz-Lorentz/Maxwell-Garnett, Bruggeman, and Gyorffy, Korringa, and Mills approximations, I recommend the book "Theory of microwave remote sensing," by Tsang, Kong, and Shin. A forewarning, the system of numbering equations is absolutely maddening.

Individual scattering approximation (ISA)

The simplest effective medium is called the individual scattering approximation, which proposes to stop the cascade infinite conditional expectations through the assumption,

$$\mathbb{E}[\mathbb{G}_{ea}|a] \approx \mathbb{E}[\mathbb{G}_e]. \tag{5.3.3}$$

Physically this assumption means that that it does not matter the placement of other particles, the expected Green's solution for each individual particle is the same. One simple example where this assumption can hold is in very sparse distributions. Then the local field of every particle is dominated by the incident field no matter the permutations in particle configurations. The ISA

is attributed to Foldy and is sometimes called Foldy's approximation[154]. This terminology is avoided to ward off confusion with the Foldy-Lax form of multiple scattering. (What a good problem for Foldy to have!)

If the particle's type is not dependent on position, which is the assumption used throughout this dissertation, then under the ISA,

$$\mathbb{E}\left[\mathbb{T}_a \mathbb{E}[\mathbb{G}_{ea}|a]\right] \approx \frac{1}{V}\mathbb{E}[\mathbb{T}_a|\boldsymbol{r}_a = \mathbf{0}]\mathbb{E}[\mathbb{G}_e], \tag{5.3.4}$$

where $\mathbb{E}[\mathbb{T}_a|\boldsymbol{r}_a = \mathbf{0}]$ is an expectation only of particle types assuming the particle is at the origin (more generally, the anchor point). Hence, $\mathbb{E}[\mathbb{T}_a|\boldsymbol{r}_a = \mathbf{0}]$ can be well calculated from a library of possible particle types. Equations 5.3.4 is the spirit of the result seen in section 1.9. The Foldy-Lax interpretation under the ISA is

$$\mathbb{E}[\mathbb{G}_e] = \mathbb{G}_{eo} + \frac{N}{V}\mathbb{G}_{eo}\mathbb{E}[\mathbb{T}_a|\boldsymbol{r}_a = \mathbf{0}]\mathbb{E}[\mathbb{G}_e], \tag{5.3.5}$$

which gives exactly the Dyson equation with self-energy,

$$\mathbb{U}_{eff}^{ISA} = \frac{N}{V}\mathbb{E}[\mathbb{T}_a|\boldsymbol{r}_a = \mathbf{0}]. \tag{5.3.6}$$

Propagating solutions are then found from the eigenvalue problem,

$$\det\left[p^2\left(\overline{\overline{\boldsymbol{I}}} - \hat{\boldsymbol{e}}_p \otimes \hat{\boldsymbol{e}}_p\right) - k^2\overline{\overline{\boldsymbol{I}}} + \frac{N}{V}\mathbb{E}\left[\overline{\overline{\boldsymbol{T}}}_a|\boldsymbol{r}_a = \mathbf{0}\right]\right] = 0. \tag{5.3.7}$$

The assumptions discussed at the beginning of this section, imply the particle transition operator needs to be diagonal and "on-shell," $\boldsymbol{p} \approx k\hat{\boldsymbol{p}}$. For small enough particle, shape and material anisotropy can be ignored. Infinitesimally small particles behave like an infinitesimally small sphere. For such particles, the transition matrix is diagonal, on shell, and dominated by the Mie electric dipole harmonic as show by a power series expansion of the Mie solution,

$$a_1 = -i\left(\frac{2}{3}\right)\left(\frac{\varepsilon_s-\varepsilon_h}{\varepsilon_s+2\varepsilon_h}\right)(k_oR)^3 + O((k_oR)^5), \quad 5.3.8$$

where R is the circumscribing radius of the particle and $\varepsilon_r = \varepsilon_s/\varepsilon_h$ is the ratio between the permittivity of the sphere, ε_s, and the embedding host media, ε_h. Under the electric dipole approximation, $\mathbb{T}_a \approx \bar{\bar{\boldsymbol{D}}}^{-1}\int d\boldsymbol{r}'\alpha_a\delta(\boldsymbol{r}-\boldsymbol{r}')$, where α_a is the electric dipole polarizability and for a sphere $\bar{\bar{\boldsymbol{D}}}^{-1} = 3k^2\bar{\bar{\boldsymbol{I}}}$. The spherical cavity is explicitly chosen to maintain isotropy, assuming that the singular term would be dominant post integration. The conversion from the Mie harmonic coefficient to polarizability is $\alpha_e = 6\pi i a_1/k_0^3$. This allows a connection between the physical properties of the particle and the moment of the effective dipole it would produce. Clearly grace is being given between the conflict of "infinitesimally small" and remaining in the classical regime. Truly infinitesimally small means a quantum mechanical description of the dipole moment. Importantly, equation 5.3.8 and the spherical cavity satisfies the overarching requirements for the potential as outlined initially in this section. For very small particles the ISA effective permittivity is

$$\varepsilon_{eff}^{ISA} \approx \varepsilon_h\left(1 + \sum_{\mathcal{T}} f f_{\mathcal{T}}\left(\frac{\varepsilon_{\mathcal{T}}-\varepsilon_h}{\varepsilon_{\mathcal{T}}+2\varepsilon_h}\right)\right). \quad 5.3.9$$

Uses of the individual scattering approximation can be found in the well-known books "absorption and scattering of light by small particles," by Bohren and Huffman, and in "light scattering by small particles," by van de Hulst. It is clear that equation 5.3.7 can extended beyond equation 5.3.9. Though, this could evoke $\varepsilon_{eff} \to \bar{\bar{\boldsymbol{\varepsilon}}}_{eff}(\boldsymbol{p})$. For example, as discussed by Bohren, Huffman, and van de Hulst, higher order harmonics can create asymmetry of forward and backward scattering. Strong inductive currents found in optically induced magnetic resonances require either a direction-dependent refractive index or a reinterpretation of the effect using an effective permeability.

Lorentz-Lorentz approximation (LLA)

Lorentz improved the ISA in proper circumstances by instead evoking the quasi-crystalline approximation (QCA) and retaining the leading term. The key to the QCA is to approximate all correlations as products of pair-wise correlations, $g_2(\boldsymbol{r}_1,\boldsymbol{r}_2)$. E.g., $g_3(\boldsymbol{r}_1,\boldsymbol{r}_2,\boldsymbol{r}_3) \approx g_2(\boldsymbol{r}_1,\boldsymbol{r}_2)g_2(\boldsymbol{r}_1,\boldsymbol{r}_3)g_2(\boldsymbol{r}_2,\boldsymbol{r}_3)$ and so forth. The Dyson equation is then easily understood from the Feynman diagram.

Under the assumptions posed at the beginning of this section, the self-energy of the QCA is

$$U_{eff}^{QC}\bar{\bar{\boldsymbol{I}}} = \frac{\frac{N}{V}3k^2\bar{\bar{\boldsymbol{I}}}\mathbb{E}[\alpha_a]}{\bar{\bar{\boldsymbol{I}}}-\frac{N}{V}\mathbb{E}[\alpha_a](\bar{\bar{\boldsymbol{I}}}+3k^2\bar{\bar{\boldsymbol{I}}}\int d\boldsymbol{r}PV\bar{\bar{\boldsymbol{G}}}_{eo}(1-g_2(\boldsymbol{r}_1-\boldsymbol{r}_2)))}, \tag{5.3.10}$$

where, the spherical cavity is again assumed on symmetry arguments. Taking the further assumption that the integral term is negligible recovers the Lorentz-Lorentz (LL) approximation of the self-energy,

$$U_{eff}^{LL} = \frac{\frac{N}{V}3k^2\mathbb{E}[\alpha_a]}{1-\frac{N}{V}\mathbb{E}[\alpha_a]}, \tag{5.3.11}$$

from the self-energy the Lorentz-Lorentz effective permittivity is

$$\frac{\varepsilon_{eff}^{LL}-1}{\varepsilon_{eff}^{LL}+2} \approx \mathbb{E}\left[ff_a\left(\frac{\varepsilon_a-\varepsilon_h}{\varepsilon_a+2\varepsilon_h}\right)\right]. \tag{5.3.12}$$

Interestingly the Lorentz-Lorentz approximation can be derived directly from equation 5.2.8, under suitable assumption of packed electric dipoles. The key to this interpretation is to construct a system such that the transition operator and Green's propagator have the same value at all sites. Then the Lorentz-Lorentz approximation actually incorporates all order of scattering terms under the dipole approximation as long as the dipoles are sufficiently close. At distances much smaller than the wavelength, the dominant term in the integral of the homogeneous Green's function shown in equation 5.2.2 is $\approx \bar{\bar{\boldsymbol{D}}}\delta(\|\boldsymbol{r}-\boldsymbol{r}'\|)$. For a system of packed identical electric dipoles, the order of scattering is

$$\begin{aligned}&\mathbb{E}[\textstyle\sum_a^N \mathbb{T}_a] + \mathbb{E}[\sum_a^N \sum_{b\neq a}^N \mathbb{T}_a\mathbb{G}_{eo}\,\mathbb{T}_b] + \mathbb{E}\left[\sum_a^N \sum_{b\neq a}^N \sum_{\substack{c\neq a\\ c\neq b}}^N \mathbb{T}_a\mathbb{G}_{eo}\,\mathbb{T}_b\mathbb{G}_{eo}\mathbb{T}_c\right]\cdots\\ &\approx \frac{N}{V}\alpha\bar{\bar{\boldsymbol{D}}}^{-1}\left(1+\frac{N}{V}\alpha+\left(\frac{N}{V}\alpha\right)^2+\left(\frac{N}{V}\alpha\right)^3+\cdots\right).\end{aligned} \tag{5.3.13}$$

Equation 5.3.13 is a geometric series,

$$\frac{N}{V}\alpha\bar{\bar{\boldsymbol{D}}}^{-1}\sum_j^N\left(\frac{N}{V}\alpha\right)^j = \frac{N}{V}\alpha\bar{\bar{\boldsymbol{D}}}^{-1}\frac{1-\left(\frac{N}{V}\alpha\right)^N}{1-\left(\frac{N}{V}\alpha\right)} \xrightarrow[\alpha<V/N]{N\to\infty} \frac{\frac{N}{V}\alpha}{1-\frac{N}{V}\alpha}\bar{\bar{\boldsymbol{D}}}^{-1} = \mathbb{U}_{eff}^{LL}. \tag{5.3.14}$$

Clearly this condition does not hold in general. The equivalence of the operators per particle means that every particle experiences the same local field, on ensemble average. Correspondingly, the accumulated effect of all order of scattering terms for this system is to completely smooth the local field across the sample. The accuracy of the Lorentz-Lorentz approximation is now understood as being dependent on how well the system upholds the geometric series representation. As particle-particle interactions deviate the error (Δ) in the j'th multiple scattering term is $O(\Delta^j)$.

Furthermore, recall that convergence of the geometric series requires $\alpha < V/N$. Correspondingly, two length scale conditions must be upheld in this interpretation. First, the distances between neighboring dipoles must be electrically small (the Green's condition). Second, the distance between dipoles must be sufficiently large relative to the displacement distance of the charges forming the dipole moment (the geometric series condition). These seemingly competing conditions are reconciled by stating that the dipole volume should shrink faster than the packing density. For actual atoms in a material, these conditions are simultaneously satisfied. Neighboring atoms are certainly closer than the wavelength, though the actual filling fraction of the atoms is still primarily vacuum. Interestingly, the initial proposal of the Lorentz-Lorentz relation was in deriving the self-energy for an ideal cubic array of electric dipoles. Correspondingly, equation 5.3.14 works equally well for a packed array.

Maxwell-Garnett approximation (MGA)

In the current presentation there is no functional difference between the Maxwell-Garnett (MG) and Lorentz-Lorentz solutions. Though, traditionally the Lorentz-Lorentz picture is attributed up to the local field correction and Maxwell-Garnett then define the transition operator from the quasistatic Mie solution. At more moderate sizes still within the dipole regime, particle size/shape can contribute to the effective dipole moment. If correlations can still be assumed weak in the quasi-crystalline self-energy, then only the transition operator terms need to be modified. For a sphere, this is completely described by Mie's result of the first electric harmonic coefficient, re equation 1.4.9(a),

$$a_1 = \frac{j_1(kR)d_{k_sR}\left(k_sRj_1(k_sR)\right) - j_1(k_sR)d_{kR}\left(kRj_1(kR)\right)}{j_n(k_sR)d_{kR}\left(kRh_1(kR)\right) - h_1(kR)d_{k_sR}\left(k_sRj_1(k_sR)\right)}.$$

Correspondingly an effective dipole permeability can be similarly calculated using equation 1.4.9(b),

$$b_1 = \frac{k^2 j_n(kR) d_{k_s R}\left(k_s R j_n(k_s R)\right) - k_s^2 j_n(k_s R) d_{kR}\left(kR j_n(kR)\right)}{k_s^2 j_n(k_s R) d_{kR}\left(kR h_n(kR)\right) - k^2 h_n(kR) d_{k_s R}\left(k_s R j_n(k_s R)\right)}.$$

For non-spherical particles in the dipole regime, an additional orientation dependence can exist requiring a more general dyadic scattering and $\overline{\overline{\boldsymbol{D}}}^{-1}$ representation. For example, ellipsoidal particles have a different polarizability depending on the orientation of the exciting field relative to the principal axes of the ellipse. Such generalizations for simple geometric shapes have well-known analytic forms and can be easily incorporated.

Bruggeman approximation (BGA)

The Bruggeman approximation takes a fundamentally different approach to defining the self-energy. Instead of the background of space being the host, ϵ, and using the true permittivity potential, U, you assume the background is ε_{eff} (unknown) and ϵ is instead part of the potential. This is the coherent potential approximation. The new system will henceforth be called the "effective background system." The homogeneous Green's operator of the effective background system is $\mathbb{G}_{eff,o}$ and the expected inhomogeneous Green's solution is

$$\mathbb{E}[\breve{\mathbb{G}}] = \mathbb{G}_{eff,o} + \mathbb{G}_{eff,o}\mathbb{E}[\breve{\mathbb{T}}]\mathbb{G}_{eff,o}, \qquad 5.3.15$$

where $\breve{\mathbb{T}}$ is the cluster transition matrix in the effective medium. Recall, the solution of interest is $\mathbb{E}[\mathbb{G}] = \mathbb{G}_{eff}$. Correspondingly the solution to the actual system can be found from the solution of the effective system by finding the condition where

$$\mathbb{E}[\breve{\mathbb{T}}] = 0. \qquad 5.3.16$$

In the field of condensed matter, this is called the coherent potential approximation as the homogeneous Greens function explicitly includes the true effective potential, $\mathbb{U}_{eff}$ (the potential of the coherent field). Note that $\mathbb{U}_{eff}$ is not the self-energy of the effective background system. The effective system is defined by $\mathbb{E}[\breve{\mathbb{T}}]$, not $\mathbb{E}[\mathbb{T}]$.

At first glance equation 5.3.16 does not appear to provide much insight as the problem. $\mathbb{G}_{eff}$ is still unknown and in fact adds complication as the effective embedding is not necessarily lossless. Also, $\mathbb{E}[\breve{\mathbb{T}}]$ is still dictated by all order of scattering terms,

$$\mathbb{E}\left[\sum_a^N \breve{\mathbb{T}}_a\right] + \mathbb{E}\left[\sum_a^N \sum_{b\neq a}^N \breve{\mathbb{T}}_a \mathbb{G}_{eff}\, \breve{\mathbb{T}}_b\right] + \mathbb{E}\left[\sum_a^N \sum_{b\neq a}^N \sum_{\substack{c\neq a \\ c\neq b}}^N \breve{\mathbb{T}}_a \mathbb{G}_{eff}\, \breve{\mathbb{T}}_b \mathbb{G}_{eff}\, \breve{\mathbb{T}}_c\right] \ldots = 0, \tag{5.3.17}$$

now of the effective transition matrix for each particle, $\breve{\mathbb{T}}_a$. The key is in the null requirement, which allows you to avoid solving equation 5.3.15, under proper conditions. It is possible that all multiple scattering terms in equation 5.3.17 are non-negligible yet still perfectly canceling. Though, from physical grounds, it is likely that the permittivity contrast between the inhomogeneities and the effective medium is small. Correspondingly, it is likely that the particles are weakly scattering in the effective system and multiple scattering terms are negligible. If this is true, then it is reasonable to evoke the individual scattering approximation for the effective background system. Correspondingly,

$$\mathbb{E}[\breve{\mathbb{T}}] \approx \mathbb{E}\left[\sum_a^N \breve{\mathbb{T}}_a\right] = 0. \tag{5.3.18}$$

Equation 5.3.18 is the primary result of the Bruggeman (coherent potential + individual scattering) approximation. The core idea is to map the initial problem to an analogous one where the individual scattering approximation is more acceptable to be evoked.

Note that equation 5.2.12, which explicitly relates an effective permittivity to the self-energy is not useful as the self-energy of the effective background system is enforced to be zero. With that said, the effective permittivity can be found directly through equation 5.3.18. Using the Mie solution for the dipole polarizability of small sphere embedded in the effective medium the effective permittivity is

$$\mathbb{E}\left[\sum_a^N \breve{\mathbb{T}}_a\right] \approx \sum_{\mathcal{T}} f f_{\mathcal{T}} \frac{\varepsilon_{\mathcal{T}} - \varepsilon_{eff}}{\varepsilon_{\mathcal{T}} + 2\varepsilon_{eff}} = 0, \tag{5.3.19}$$

where the sum is over all material types, $\mathcal{T}$, including the true background material, ϵ. Similar to the individual scattering approximation, the mathematical form of the Bruggeman approximation is readily extendable to include higher order corrections to the dipole moment as well as higher order harmonic terms. Though, care should be taken as the individual scattering

approximation was evoked under the pretense of weak scattering, which should not hold when scattering includes many high order harmonics. With that said, other physical characteristics such as a sparse distribution can make the individual scattering approximation valid. So, the applicability of the theory when including multipoles depends on the underlying structure of the system. In general, the breakdown of this theory depends on the breakdown of the individual scattering approximation. Since the background is the unknown, ε_{eff}, this poses a problem for the model when discussing resonances in ε_{eff}. If the effective media contains strong resonances that are spectrally separated from the resonances of the constituent inclusions, a large permittivity contrast can occur, and weak multiple scattering may not be a valid assumption unless particles are well separated. Correspondingly, the Bruggeman approximation for dense particle systems is most likely to work well outside of resonant regimes where large permittivity fluctuations are not observed.

Finally, it should be emphasized that the coherent potential is a general concept that can be applied in conjunction with a closure relation. The core idea of the coherent potential is that if the homogeneous background is changed, the scattering potential changes accordingly. The background is a free parameter to help solve the problem. From the general solution of the Dyson equation

$$\mathbb{E}\left[\overline{\overline{\boldsymbol{G}}}_e\right](\boldsymbol{p}) = \left(\overline{\overline{\boldsymbol{G}}}_{eo}^{-1}(\boldsymbol{p}) - \overline{\overline{\boldsymbol{U}}}_{eff}(\boldsymbol{p})\right)^{-1}, \tag{5.3.20}$$

where, in general, the background defining $\overline{\overline{\boldsymbol{G}}}_{eo}$ is arbitrarily defined. A good solution is $\overline{\overline{\boldsymbol{G}}}_{eo} = \mathbb{E}\left[\overline{\overline{\boldsymbol{G}}}_e\right]$ because this implies, $\overline{\overline{\boldsymbol{U}}}_{eff}(\boldsymbol{p}) = 0$. The closure relations on $\overline{\overline{\boldsymbol{U}}}_{eff}$ is then whatever approximation best fits the problem. In the case of Bruggeman, $\overline{\overline{\boldsymbol{U}}}_{eff}^{BG} = \frac{N}{V}\mathbb{E}\left[\overline{\overline{\boldsymbol{T}}}_a | \boldsymbol{r}_a = \boldsymbol{0}\right]$, which is the ISA closure.

Gyorffy, Korringa, and Mills approximation (GKMA)

Gyorffy, Korringa, and Mills use the coherent potential approach to find and effective background where the quasi-crystalline approximation is more acceptable to be evoked. The coherent potential + quasi-crystalline potential Greens function is,

$$\mathbb{E}[\overline{\overline{\boldsymbol{G}}}_e](\boldsymbol{p}) = \left(\overline{\overline{\breve{\boldsymbol{G}}}}_{eo}^{-1}(\boldsymbol{p}) - \overline{\overline{\boldsymbol{U}}}_{eff}^{QC}(\boldsymbol{p})\right)^{-1}, \quad 5.3.21$$

where $\overline{\overline{\boldsymbol{G}}}_{e,eff}$ is the homogeneous Green's solution to the effective background system. After algebra and quasistatic assumptions[154,156], the GKM effective medium for a two-phase mixture is

$$\varepsilon_{eff}^{GMK} = \varepsilon_h + \frac{3ff(\varepsilon_a - \varepsilon_h)\varepsilon_{eff}^{GMK}}{3\varepsilon_{eff}^{GMK} + (\varepsilon_a - \varepsilon_h)(1-ff)}. \quad 5.3.22$$

The derivation and generalization of equation 5.3.23 can be found in [154] and [156], including extensions to multiphase mixtures. Replacing $\varepsilon_{eff}^{GMK} \to \varepsilon_h$ on the right-hand side recovers the Lorentz-Lorentz/Maxwell-Garnett relations. Correspondingly, the nonlinearity of 5.3.22 with respect to ε_{eff}^{GMK} is a distinctive feature of the coherent potential framework.

Unifying the class of mixing rules

The mixing rules discussed above provide 5 distinctly different ansatz for the behavior of the average local field. With these different assumptions at hand a large range of possible particle configurations can be modeled. The overarching requirement consistent to all 5 theories is that the coherent Green's function takes the same form as the homogeneous Green's function in a passive, linear, homogeneous, and isotropic medium of k_{eff}. Correspondingly, if there is good reason to believe this is true, then it is a good bet that one of the 5 discussed ansatz can model the effective medium well enough for practical applications. The goal is then to pick the right approximation for the job.

Ari Sihvola showed that, for two-phase mixtures, the common quasistatic effective medium approximations are part of a unified class defined by the equation[153],

$$\frac{\varepsilon_{eff} - \varepsilon_h}{\varepsilon_{eff} + 2\varepsilon_h + \nu(\varepsilon_{eff} - \varepsilon_h)} = ff\,\frac{\varepsilon_i - \varepsilon_h}{\varepsilon_i + 2\varepsilon_h + \nu(\varepsilon_{eff} - \varepsilon_h)}. \quad 5.3.23$$

The dimensionless unification parameter $\nu \in \mathbb{R} \cap [0,3]$, encapsulates how each approximation alters the self-energy. $\nu = 0$ recovers the Maxwell-Garnett rule, $\nu = 1$ recovers the Bruggeman rule, and $\nu = 3$ recovers the Gyorffy, Korringa, and Mills rule. For dilute mixtures, there is little

difference in the chosen value of ν and all theories converge to the individual scattering approximation. The equivalence of the mixing rules for dilute mixtures is easily seen from a perturbation expansion of equation 5.3.24 with respect to the filling fraction,

$$\varepsilon_{eff} = \varepsilon_h + 3\varepsilon_h\left(\frac{\varepsilon_i-\varepsilon_h}{\varepsilon_i+2\varepsilon_h}\right)ff + 3\varepsilon_h\left(\frac{\varepsilon_i-\varepsilon_h}{\varepsilon_i+2\varepsilon_h}\right)^2\left(1+\nu\frac{\varepsilon_i-\varepsilon_h}{\varepsilon_i+2\varepsilon_h}\right)ff^2 + \cdots. \quad 5.3.24$$

In equation 5.3.24, the dependence on the mixing rule, ν, appears first $O(ff^2)$ and in all higher order terms after. This perturbation expansion makes clear that all the mixing rules are assumptions aimed at predicting higher-order corrections on the individual scattering approximation when the filling fraction increases. This is sensible as the contribution to multiple scattering becomes more predominant at larger filling fractions, hence the other order of scattering terms beyond single site scattering should be considered. This unified equation also allows for a way to model particle configurations that straddle between to approximations. $\nu = 1.5$ can be understood as a local field behavior somewhere between Maxwell-Garnett and Bruggeman, for example. Though non-integer values of ν are not rigorously derived from an underlying assumption, the power series of equation 5.3.24 makes clear the effect of this now continuous transition from $\nu = 0 \rightarrow 1 \rightarrow 2 \rightarrow 3$. Correspondingly, equation 5.3.23 provides a powerful framework for modeling and design. This is especially true when pairing equation 5.3.23 to the theoretical limits on the properties an effective medium may take.

Five of the most established mixing rules are connected as being part of a broader class. Connected through their common assumption on the self-energy, each mixing rule provides a different correction to higher order expansion terms for the local field. These corrections delegate each mixing rule as preferred given the context of the system.

5.4 VARIATIONAL BOUNDS

The subject of effective mediums is vast. This is well expected given the degrees of freedom in light-matter interactions, the possible material arrangements, and the desire to produce more stringent and informative predictions. In the last section a unifying formula is discussed that can help define what effective medium is best suited for a system that exist in a grey area between different models. In this regard, it is also important to understand the theoretical bounds on the form an effective medium may take. This defines the upper and lower limit of the effective constitutive parameters based on general conservation principles and variational calculus. The bounds discussed in this section are those with direct application to works in this dissertation which involve the electric dipole regime and two-phase mixtures, {host = ε_h, inclusion= ε_i}. To the best of my knowledge, the subject of bounds for more extended systems are still a debated subject of research and will be ignored.

It is tempting to assume the effective permittivity is bounded by the limiting behavior of the underlying materials. Interestingly, this is not generally true,

$$\begin{aligned} min\{\Re[\varepsilon_h], \Re[\varepsilon_i]\} \not\leq\ & \Re\left[\varepsilon_{eff}\right] \not\leq max\{\Re[\varepsilon_h], \Re[\varepsilon_i]\} \\ min\{\Im[\varepsilon_h], \Im[\varepsilon_i]\} \not\leq\ & \Im\left[\varepsilon_{eff}\right] \not\leq max\{\Im[\varepsilon_h], \Im[\varepsilon_i]\}. \end{aligned} \qquad 5.4.1$$

The lack of bounds in equation 5.4.1 can be best understood from the necessity to uphold causality. For lossy materials, the expected value of multiple scattering can increase the overall absorption in the effective medium beyond that of any homogeneous bulk constituent. The increase in absorption also necessitates a stronger change in the real part of the effective permittivity to remain Kramers-Kronig consistent. From the behavior of the Hilbert transform, it becomes clear that upholding equation 5.4.1 would break causality under the correct circumstances. In a mixture of lossless materials equation 5.4.1 will hold, as long as the incoherent field is negligible. This is because there is no change in one-way power transfer.

For lossy materials, absolute bounds for the effective permittivity were derived independently by both Bergman[148] and Milton[149] in 1980. The result is a generalization of the Wiener bounds[157] (introduced in 1912) to the complex plane and follows the same concept of bounds derived from series and parallel impedance networks. The Bergman-Milton (BM) bounds restrict all "traditional" effective mediums to have permittivity values which exist in the interior region enclosed by the two parametric curves,

$$\zeta(ff;\varepsilon_i,\varepsilon_h) = \left({ff}/{\varepsilon_i} + {(1-ff)}/{\varepsilon_h}\right)^{-1} \quad \text{5.4.2a}$$

$$\xi(ff;\varepsilon_i,\varepsilon_h) = ff\varepsilon_i + (1-ff)\varepsilon_h, \quad \text{5.4.2b}$$

in the complex plane. Equation 5.4.2a defines a circle in the complex plane which includes the origin. Equation 5.4.2b defines a line in the complex plane. Both are parameterized by the real-valued filling factor, $ff \in [0,1]$, of the inclusion. Importantly, the domain of validity, Ω, is the domain enclosed by the two curves that does not include the origin. Clearly this is sensible as $\varepsilon = 0$ is nonphysical. Figure 5.4.1 gives examples of the BM bounds viewed as curves in the complex plane for composites of metallic and non-metallic mixtures. Figure 5.4.1 makes clear that any vector starting from the origin must cross the line before touching the arc. Correspondingly, the minima and maxima for the absolute value of the effective permittivity lie on the line and arc, respectively.

From the work of Wiener, it is clear that equation 5.4.2 is analogous to the effective permittivity of a laminate thin film composed of sub-wavelength periodic repetitions of ε_i and ε_h layers. Relative thicknesses of the layers are defined by the filling fraction. Note that in this case, expectations are taken over space as there is no notion of a distribution in this context. An incident electric field impinging normal or parallel to the layer surface then defines equation 5.4.2a and b, respectively. This represents two diametrical extremes of material configurations with respect to the indecent field. Given the sub-wavelength nature of the layers (relative thicknesses defined by the filling fraction), the layer interactions can be viewed from a quasi-static effective circuit analogy. Here each layer is given an associated resistance in series with a capacitance, termed an RC element. When the electric field is propagating normal to the layers the configuration is analogous to a series network of RC elements. An electric field propagating parallel to the layers is analogous to a network in parallel. For lossless permittivity, the networks are purely of capacitors. This analogy makes clear why inductances must be assumed negligible. Otherwise, in a lossless system, a capacitor and inductor network can define a resonance condition.

A more stringent bound is set by Hashin and Shtrikman in 1962[153,158], which has applications to random mixtures of spheres. The key concept of the Hashin-Shtrikman bound is that there should be no extinction of the coherent field when a coated spherical inclusion with core, $\boldsymbol{\varepsilon_i}$, and shell, $\boldsymbol{\varepsilon_h}$, is embedded in a homogeneous material, $\boldsymbol{\varepsilon_{eff}}$. The condition of invisibility is independent of sphere size as long as the size is such that $\boldsymbol{O\left((kb)^5\right)}$ is negligible, where $\boldsymbol{b}$ is the radius of the outer coating. Correspondingly, Hashin and Shtrikman show through rigorous derivation that the entire domain of homogeneous material, $\boldsymbol{\varepsilon_{eff}}$, can be replaced by a jam

packing of spheres of shrinking size to all gaps. Since each sphere is inviable to the coherent field, the entire space is replaced by an inhomogeneous mixture of cores embedded in host shells without perturbing the coherent field. A schematic of the Hashin and Shtrikman thought experiment is shown in figure 5.4.1.

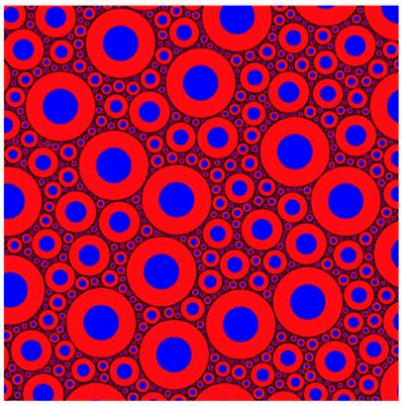

Figure 5.4.1. Example of the Hashin and Shtrikman thought experiment. An effective medium is entirely replaced with coated particles. The particles varying in size to fill the entire space. Each particle satisfies the invisibility condition in the effective medium. Correspondingly, the media replaced by spheres should behave the same as the effective media. [Reprint with permission from Phys. Rev. E 99, 052141 (2019).]

The result is exactly the Maxwell-Garnett formula, and the bounds are given by interchanging of the role of host and inclusion,

$$\varepsilon_{MG}(ff;\varepsilon_a,\varepsilon_b) \leq \varepsilon_{eff} \leq \varepsilon_{MG}(ff;\varepsilon_b,\varepsilon_a). \qquad 5.4.3$$

Here ε_{MG} is the Maxwell-Garnett effective permittivity. The lower bound is given when the larger permittivity is assumed to be the shell. The upper bound is when the larger permittivity is assumed to be the core. The Hashin-Shtrikman bound makes use of the asymmetry in the Maxwell-Garnett mixing rule to pose limits for spherical-type inclusions. Correspondingly, the Bruggeman mixing rule lies within the Hashin-Shtrikman bound. Formally equation 5.4.3 is derived given a variational approach in the quasi-static regime. Correspondingly, it is unclear to me if the bounds hold for higher order extensions of Maxwell-Garnett's mixing rule. Nonetheless the result is a powerful tool for sufficiently sub-wavelength inclusions.

Given limited information about the system, the variational bounds confine the behavior of an effective medium. When applicable, they provide a powerful tool to understand the range of behavior that may be observed in measurement.

5.5 BEYOND QUASISTATIC

The self-energy brought a rigorous framework to understand the most widely used effective medium theories. From this the form each mixing rule can be mapped to assumptions on the order of scattering behavior of the system or an analogous system. Given the coherent Green's functions takes the form of a passive, linear, homogeneous, and isotropic media, well-defined approximations can be understood in terms of measurable variables such as particle size and filling fraction. With that said, higher order generalizations can be available given the overarching self-energy picture. In this section, an intuitive picture of the impact of extending the individual scattering, Maxwell-Garnett, and Bruggeman approximations to higher order multipole terms is discussed. In particular, this section views the generalizations from the framework of satisfying the extinction theorem. This provides intuition to the underlying assumptions of the mixing rules beyond the quasistatic regime.

Consider an inhomogeneous volume that supports a propagating coherent field in the form of a plane wave. Let this inhomogeneous volume be replaced by its effective medium counterpart, except within a ball of radius b at the origin, which still contains the inhomogeneities inside it. From the point of view of the coherent field propagating in this media, the ball should appear invisible in an ensemble average sense. Correspondingly, the expected extinction cross section of the ball of particles inside the effective medium must be

$$\mathbb{E}[C_{ext}] = 0. \tag{5.5.1}$$

Equation 5.5.1 is the core condition of an effective medium viewed in the embedded particle framework. Since the inclusion was chosen to be spherical, the scattered field of the inhomogeneous ball can be expanded in a basis of Mie vector harmonics. It is useful to connect the extinction condition to the transition operator, $\mathbb{T}$, through the scattering dyadic. Recall,

$$\boldsymbol{E}_{sca} = \mathbb{G}_{eo}\mathbb{T}\boldsymbol{E}_{inc}.$$

Performing the operator integrations, the scattered field in the far field limit is

$$\boldsymbol{E}_{sca} = \frac{e^{ikr}}{r}\,\boldsymbol{E}^{\infty}_{sca}\left(k\widehat{\boldsymbol{\beta}}\right) = \left(\mathbb{I} - \hat{\boldsymbol{e}}_p \otimes \hat{\boldsymbol{e}}_p\right)\frac{e^{ikr}}{4\pi r}\,\overline{\overline{\boldsymbol{T}}}(k\widehat{\boldsymbol{p}}, k\widehat{\boldsymbol{k}}_{inc}) \cdot \boldsymbol{E}_{inc}, \tag{5.5.2}$$

where $\widehat{\boldsymbol{\beta}}$ is the angle subtended by $\widehat{\boldsymbol{k}}_{inc}$ and $\widehat{\boldsymbol{p}}$. Correspondingly, the far field transition dyadic outlined in Chapter 1 is related to the more general transition operator by

$$\boldsymbol{E}_{sca}^{\infty}(k\widehat{\boldsymbol{\beta}})\cdot\hat{\boldsymbol{e}}_{inc}(\widehat{\boldsymbol{k}}_{\boldsymbol{inc}})=\frac{\|\boldsymbol{E}_{inc}\|}{4\pi}(\mathbb{I}-\hat{\boldsymbol{e}}_{p}\otimes\hat{\boldsymbol{e}}_{p})\overline{\overline{\boldsymbol{T}}}(k\widehat{\boldsymbol{p}},k\widehat{\boldsymbol{k}}_{\boldsymbol{inc}})\cdot\hat{\boldsymbol{e}}_{inc}(\widehat{\boldsymbol{k}}_{\boldsymbol{inc}}),\qquad 5.5.3$$

where, from Chapter 1, $\boldsymbol{E}_{sca}^{\infty}(\hat{\boldsymbol{r}})=\frac{1}{k}\boldsymbol{\Psi}^{far}\boldsymbol{c}$. It is important to note that equation 5.5.3 is an on-shell approximation, where both $\boldsymbol{p}$ and $\boldsymbol{k}_{inc}$ are of the same magnitude. Furthermore, equation 5.5.3 assumes the validity of a far field representation in a background media defined by the effective media. Clearly this is not rigorously correct as the background can have loss. Though, usually there the effective medium representation is evoked when coherence lengths are sufficiently long. This is a justification behind the far field representation. Correspondingly, the condition for invisibility is

$$\mathbb{E}[\boldsymbol{E}_{sca}^{\infty}\cdot\hat{\boldsymbol{e}}_{inc}](\theta=0)=\sum_{n}\sqrt{2n+1}\mathbb{E}\left[c_{n}^{f}\right]=0,\qquad 5.5.4$$

where the forward direction is governed by the forward Kerker coefficient, c_n^f. It is then the job of the effective medium theory to provide a model for $\mathbb{E}[\boldsymbol{E}_{sca}^{\infty}\cdot\hat{\boldsymbol{e}}_{inc}]$. By construction, all models of this form will satisfy equation 5.5.4. It is the behavior of the terms inside $\mathbb{E}[\boldsymbol{E}_{sca}^{\infty}\cdot\hat{\boldsymbol{e}}_{inc}]$ that dictate model accuracy.

In the case of Bruggeman, the ball is filled with particles of material 1 with probability P_1, material 2 with probability P_2, and so forth. The probability of each material is a measurable quantity dictated by the filling factor, ff, for that material. This is the same grouping procedure for calculating total expectation over particle types as found in section 1.8. The Bruggeman mixing rule then takes a generalized form,

$$\sum_{\mathcal{T}}ff_{\mathcal{T}}\,\mathbb{E}\left[\boldsymbol{E}_{sca,\mathcal{T}}^{\infty}\cdot\hat{\boldsymbol{e}}_{inc}\right](\theta=0|\varepsilon_{eff})=0,\qquad 5.5.5$$

where $\mathbb{E}\left[\boldsymbol{E}_{sca,\mathcal{T}}^{\infty}\cdot\hat{\boldsymbol{e}}_{inc}\right](\theta=0|\varepsilon_{eff})$ is the forward scattering of a particle of type $\mathcal{T}$ embedded in the effective medium under plane wave excitation. Equation 5.5.5 is a primary characteristic of Bruggeman's theory beyond the quasistatic regime and has essentially the same form as equation 5.3.17, for the forward direction. In the limit of a vanishingly small and non-resonant inclusion, then

$$\mathbb{E}\left[\boldsymbol{E}_{sca,\mathcal{T}}^{\infty} \cdot \hat{\boldsymbol{e}}_{inc}\right]\left(\theta = 0|\varepsilon_{eff}\right) \approx -i(kb)^3 \frac{\varepsilon_{\mathcal{T}} - \varepsilon_{eff}}{\varepsilon_{\mathcal{T}} + 2\varepsilon_{eff}} + O((kb)^5). \quad 5.5.6$$

Correspondingly, the traditional form of Bruggeman's mixing rule is recovered,

$$\sum_{\mathcal{T}} ff_{\mathcal{T}} \frac{\varepsilon_{\mathcal{T}} - \varepsilon_{eff}}{\varepsilon_{\mathcal{T}} + 2\varepsilon_{eff}} = 0. \quad 5.5.7$$

The assumption underlying Maxwell-Garnett's theory is less straightforward. Garnett presumes a well-defined hierarchy of inclusion embedded in host. For a singly type inclusion, this hierarchy is enforced as a coated sphere embedded in the effective medium. The expected scattering amplitude in the forward direction takes the form of that from a coated sphere (CS) with a core filled with inclusion and an outer shell filled with the host medium. The filling factor, $ff = (a/b)^3$, of the inclusions define the ratio between the core radius, a, and outer shell radius, b. In the small sphere limit,

$$\begin{aligned}&\mathbb{E}\left[\boldsymbol{E}_{sca,\mathcal{T}}^{\infty,CS} \cdot \hat{\boldsymbol{e}}_{inc}\right]\left(\theta = 0|\varepsilon_{eff}\right) \\ &= i(kb)^3 \frac{(\varepsilon_h - \varepsilon_{eff})(\varepsilon_a + 2\varepsilon_h) + ff(\varepsilon_a - \varepsilon_h)(\varepsilon_{eff} + 2\varepsilon_h)}{(\varepsilon_h + 2\varepsilon_{eff})(\varepsilon_a + 2\varepsilon_h) + ff(2\varepsilon_h - \varepsilon_{eff})(\varepsilon_a - 2\varepsilon_h)} + O((kb)^5)\end{aligned} \quad 5.5.8$$

where ε_{a} and ε_{h} are the permittivity of the inclusion and host, respectively. Correspondingly, the traditional form of Maxwell-Garnett's theory is recovered as a null condition of the numerator,

$$\frac{\varepsilon_{eff} - \varepsilon_h}{\varepsilon_{eff} - 2\varepsilon_h} = ff \frac{\varepsilon_a - \varepsilon_h}{\varepsilon_a + 2\varepsilon_h}. \quad 5.5.9$$

The core-shell framework makes clear the well-known asymmetry in the role of host and inclusion that plagues Maxwell-Garnett's theory. Clearly, even when $ff = 0.5$ switching the core and shell materials can still result in substantially different scattering properties. For more than one inclusion, it is not clear that the core-shell interpretation can be extended, though the asymmetry problem still remains. For an arbitrary number of inclusions, a similar procedure of assigning probabilities to inclusions and summing to calculate expectation can be used. In this case the scattered far field is with respect to the host and the effective permittivity is an "inclusion" with probability 1 that explicitly cancels the inclusion contributions,

$$\mathbb{E}\left[\boldsymbol{E}^{\infty}_{sca,eff}\cdot\hat{\boldsymbol{e}}_{inc}\right](\theta=0|\varepsilon_h)+\sum_{\mathcal{T}} f f_{\mathcal{T}}\,\mathbb{E}\left[\boldsymbol{E}^{\infty}_{sca,\mathcal{T}}\cdot\hat{\boldsymbol{e}}_{inc}\right](\theta=0|\varepsilon_h)=0. \qquad 5.5.10$$

For scattering just outside of the quasistatic regime, where the coherent Green's function is still expected to resemble the homogeneous solution, the extinction theorem provides an intuitive framework to define mixing rules. In particular the Bruggeman (coherent potential) and the Maxwell-Garnett (average transition matrix) assumptions can be readily generalized.

5.6 BEYOND THE KNOWN: COUPLING, RESONANCE, AND STRUCTURE

Though section 5.5 shows that the canonical mixing rules can be generalized for higher order harmonic scattering, these generalizations still do not encompass the full space of the self-energy in generalized form, $\overline{\overline{\boldsymbol{U}}}_{eff}(\boldsymbol{p})$. Particle distributions that are beyond the scope previously discussed are, of course, quite complicated to model. For example, section 1.8 discusses how correlation functions beyond pairwise are often not analytically defined. Though, just because these systems are hard to analytically describe does not mean they do not readily exist. For example, films/clusters characterized as a random fractal are natures go-to distribution when deposition/clustering kinetics are dominated by Brownian motion. This distribution represents an interesting system of study as the space filled with particles can be quite sparse. Nonetheless, the scale invariance property of the distribution and the fact that particles are guaranteed connected to at least one neighbor means application of the traditional theories are unlikely to hold. To address such systems, this dissertation again utilizes the power of the Monte Carlo approach to offload the complexity of accounting for resonances, strong particle-particle interactions, and non-trivial correlation functions. This is analogous to the procedure outlined in section 1.9, tailored now to the three-dimensional effective medium framework.

The derivation of this effective medium theory starts from the fundamentals, namely the Monte Carlo expression of the coherent field outlined in equations 1.91-1.95. In particular the primary condition of importance is

$$\mathbb{E}\left[\widetilde{\boldsymbol{E}}_{sca,a}\right] \approx \mathbb{E}\left[\boldsymbol{\Psi}(\boldsymbol{r}-\boldsymbol{r}_a)e^{i\boldsymbol{k}_{inc}\cdot\boldsymbol{r}_a}\right]\mathbb{E}\left[\overline{c_a^{MC}}(\mathcal{T}_a)\right]. \tag{5.6.1}$$

Note that unlike the system studied in section 1.9, particles now stack on top one another. Correspondingly, the particle center is not confined to the $x-y$ plane and $\boldsymbol{\rho}_a \to \boldsymbol{r}_a$. To evaluate $\mathbb{E}\left[\boldsymbol{\Psi}(\boldsymbol{r}-\boldsymbol{r}_a)e^{i\boldsymbol{k}_{inc}\cdot\boldsymbol{r}_a}\right]$ the Mie harmonics are expanded into a basis of plane waves, as outlined in section 1.9. Given that there is no bias in the potential to place particle a at a particular location, the probability of finding particle a in any location is uniform over the volume comprising the particle film, $P(\boldsymbol{r}_a) = 1/\int d^2\boldsymbol{r}$. The condition of no bias takes some care in interpretation and does inherently limit the possible distributions for which this theory is valid. This will be further discussed in the next section. Similar to section 1.9 the expectation of the location of particle a gives,

$$\mathbb{E}\left[\boldsymbol{\Psi}(\boldsymbol{r}-\boldsymbol{r}_a)e^{i\boldsymbol{k}_{inc}\cdot\boldsymbol{r}_a}\right] \to \mathcal{F}^{\pm}\left[P(\boldsymbol{r}_a)e^{i\boldsymbol{k}_{inc}\cdot\boldsymbol{r}_a}\right] = \frac{\delta(\boldsymbol{k}_{\parallel}-\boldsymbol{k}_{inc,\parallel})}{\int d^2\boldsymbol{r}}\begin{cases} d & + \\ \frac{sin(|k_z|d)}{|k_z|} & - \end{cases} \tag{5.6.2}$$

where d is the film thickness. Usually, the setup for the derivation of an effective medium assumes an infinite space. In this case the goal is opposite, and this will become clear throughout the derivation. Equation 5.6.2 shows that the translation invariance in the $x-y$ plane enforces a momentum match between the component of the wave vector from the coherent field and incident field on the particle plane. The second term is a result of the finite thickness of the film,

which takes a different form when considering the coherent scattered field propagating in the transmission, $+$, and reflection, $-$, hemispheres. Correspondingly the coherent field is

$$\mathbb{E}\left[\widetilde{\boldsymbol{E}}_{sca,a}\right] \approx \frac{1}{\int d^2\boldsymbol{r}}\frac{1}{\cos\theta_{inc}}\sum_q E^{\pm}_{coh,a}\hat{\boldsymbol{e}}_q\left(\hat{\boldsymbol{k}}^{\pm}_{inc}\right)e^{i\boldsymbol{k}^{\pm}_{inc}\cdot\boldsymbol{r}}\begin{cases} d & + \\ \frac{sin(|k_z|d)}{|k_z|} & - \end{cases} \tag{5.6.3}$$

where $\boldsymbol{k}^{\pm}_{inc} = \boldsymbol{k}_{inc,\parallel} \pm k_z$ and

$$E^{\pm}_{coh,a,q} = \frac{2\pi}{k^2}\left(\boldsymbol{\Psi}^{far}\left(\hat{\boldsymbol{k}}^{\pm}_{inc}\right)\cdot\hat{\boldsymbol{e}}_q\left(\hat{\boldsymbol{k}}^{\pm}_{inc}\right)\right)\overline{c^{MC}_a}(\mathcal{T}_a)\begin{cases} d & + \\ \frac{sin(|k_z|d)}{|k_z|} & - \end{cases}. \tag{5.6.4}$$

In analogy to section 1.6 the sum of all particles can be grouped by type then the number of particles of that type in order to write equation 5.6.4 in terms of experimentally measurable quantities such as fill fraction.

$$\mathbb{E}\left[\widetilde{\boldsymbol{E}}_{sca}\right] \approx \frac{kd}{\cos\theta_{inc}}\sum_q E^{\pm}_{coh,q}\hat{\boldsymbol{e}}_q\left(\hat{\boldsymbol{k}}^{\pm}_{inc}\right)e^{i\boldsymbol{k}^{\pm}_{inc}\cdot\boldsymbol{r}} \tag{5.6.5}$$

where the coherent amplitude is

$$\begin{aligned} E^{\pm}_{coh,q} &= \sum_a^N E^{\pm}_{coh,a,q} \\ &= \left(\boldsymbol{\Psi}^{far}\left(\hat{\boldsymbol{k}}^{\pm}_{inc}\right)\cdot\hat{\boldsymbol{e}}_q\left(\hat{\boldsymbol{k}}^{\pm}_{inc}\right)\right)\left(\sum^{|\mathcal{T}|}\gamma_{\mathcal{T}_a}\overline{c^{MC}_a}(\mathcal{T}_a)\right)\begin{cases} 1 & + \\ sinc(|k_z|d) & - \end{cases}. \end{aligned} \tag{5.6.6}$$

Equation 5.6.6 replaces the area weight factor, $w_{\mathcal{T}_a}$, used in section 1.9 with a volumetric weight factor, $\gamma_{\mathcal{T}_a} = \frac{2\pi}{k^3}\frac{ff_{\mathcal{T}_a}}{V_{\mathcal{T}_a}}$, where $ff_{\mathcal{T}_a}$ and $V_{\mathcal{T}_a}$ are the total filling factor and volume of type $\mathcal{T}_a$ particles. Equation 5.6.6 can be written in terms of the incident field as

$$\begin{bmatrix} E^{TE\pm}_{sca} \\ E^{TM\pm}_{sca} \end{bmatrix} = \frac{kd}{\cos\theta_{inc}}\begin{bmatrix} E^{\pm}_{coh,TE} & E^{\pm}_{coh,TE} \\ E^{\pm}_{coh,TM} & E^{\pm}_{coh,TM} \end{bmatrix}\begin{bmatrix} E^{TE}_{inc} \\ E^{TM}_{inc} \end{bmatrix}. \tag{5.6.7}$$

To form an effective medium the problem now needs to be recast in terms of effective constitutive parameters. Following a similar framework to Bohren[159], recall that the transmission through a slab at normal incidence is related to the incident field, $E_t = tE_{inc}$, through the amplitude transmission coefficient,

$$t \approx e^{ik(\eta_{eff}-1)d} = 1 + ik\left(\eta_{eff}-1\right)d - O\left((kd)^2\left(\eta_{eff}-1\right)^2\right). \tag{5.6.8}$$

The second equality in equation 5.6.8 being the Taylor series of the exponential to first order. Focusing on TE polarization at the transmission side of the slab interface the field equality would be

$$1 + kdE^{+}_{coh,TE} = 1 + ik\left(\eta_{eff} - 1\right)d - O\left((kd)^2\left(\eta_{eff} - 1\right)^2\right). \quad 5.6.9$$

The effective refractive index is then related to the coherent field amplitude as,

$$1 - \eta_{eff} = iE^{+}_{coh,TE} + O\left(i(kd)\left(\eta_{eff} - 1\right)^2\right). \quad 5.6.10$$

A similar procedure can be performed for the polarization conversion term. Furthermore, as outlined by Bohren and Huffman[1], an effective refractive index relating $E^{-}_{coh,TE}$ can be derived at the interface of the film and the reflection hemisphere. Unfortunately, the two refractive indices at the transmission and reflection interface are not equal unless $E^{-}_{coh,TE} = E^{+}_{coh,TE}$. This exposes the primary flaw of the procedure defined by equations 5.6.8 – 5.6.10. It does not produce a single unified set of constitutive parameters to define both the upper and lower interface of the film. Indeed, this led Bohren to propose the necessity of two different independent quantities: an effective permittivity and an effective permeability. Including both terms, the asymmetry can be properly accounted for. Therefore, equations 5.6.8 – 5.6.10 serve only as an example as they are still instructive to show, to first order, that the effective refractive index at any depth in the film is $\propto E^{\pm}_{coh}$. When $k_z d \ll 1$, then $sinc(k_z d) \approx 1$ and $E^{\pm}_{coh}$ has no d-dependence. Importantly this identifies that, to first order, effective constitutive parameters do not change with thickness and the effective medium problem, $\varepsilon_{eff}, \mu_{eff}$, can be transformed into an equivalent surface sheet problem, $\varepsilon_{eff,\|}, \mu_{eff,\|}$. Recovery of the bulk is then simply found from the relation $\varepsilon_{eff,\|} \to \varepsilon_{eff}/d$ and $\mu_{eff,\|} \to \mu_{eff}/d$.

At this stage the derivation follows exactly the work of Barrera and Garcia-Valenzuela[161]. The core concept is that, in the limit that the effective medium is a sheet, the asymmetry between the transmitted and reflected scattered field relies on the introduction of an effective current density, $\boldsymbol{J}_{eff}$, and magnetization, $\boldsymbol{M}_{eff}$, on the surface. Equating the effective currents to the corresponding fields, again as outlined in Barrera and Garcia-Valenzuela[161], gives the effective permittivity and permeability,

$$\epsilon^{TE}_{eff}(\theta_i) = 1 + i(\mathbb{E}[\tilde{\chi}^{+}_{TE}(\theta_i)] - \tan^2(\theta_i)\,\mathbb{E}[\tilde{\chi}^{-}_{TE}(\theta_i)]) \quad 5.6.11(a)$$

$$\epsilon^{TM}_{eff}(\theta_i) = 1 + \frac{i}{\cos^2(\theta_i)}\,\mathbb{E}[\tilde{\chi}^{-}_{TM}(\theta_i)] \quad 5.6.11(b)$$

$$\mu^{TE}_{eff}(\theta_i) = 1 + \frac{i}{\cos^2(\theta_i)}\,\mathbb{E}[\tilde{\chi}^{-}_{TE}(\theta_i)] \quad 5.6.11(c)$$

$$\mu^{TM}_{eff}(\theta_i) = 1 + i(\mathbb{E}[\tilde{\chi}^{+}_{TM}(\theta_i)] - \tan^2(\theta_i)\,\mathbb{E}[\tilde{\chi}^{-}_{TM}(\theta_i)]), \quad 5.6.11(d)$$

where

$$\mathbb{E}\left[\underset{TE}{\tilde{\chi}_{TM}^{\pm}}(\theta_i)\right] \approx \begin{cases} \sum_{\mathcal{T}_a=1}^{|\mathcal{T}|} \sum_{n=1}^{N} \sum_{m=0}^{n} \sum_{p=0}^{1} \gamma_{\mathcal{T}_a} \overline{c_{sca,nmp}^{MC,TM}}(\mathcal{T}_a) \mathcal{S}_{nm(1-p)}^{\pm}(\theta_i) \\ \sum_{\mathcal{T}_a=1}^{|\mathcal{T}|} \sum_{n=1}^{N} \sum_{m=0}^{n} \sum_{p=0}^{1} \gamma_{\mathcal{T}_a} \overline{c_{sca,nmp}^{MC,TE}}(\mathcal{T}_a) \mathcal{S}_{nmp}^{\pm}(\theta_i) \end{cases} \quad 5.6.12$$

and

$$\mathcal{S}_{nmp}^{\pm}(\theta_i) = \tau_{nmp}(0) \pm \tau_{nmp}(\pi - 2\theta_i). \quad 5.6.13$$

Equation 5.6.11 describes the effective permittivity and permeability in terms of expected susceptibilities that are incident angle and polarization resolved. For example, the effective electric susceptibility in TE is $\tilde{\chi}_{eff,e}^{TE} = i(\mathbb{E}[\tilde{\chi}_{TE}^{+}(\theta_i)] - \tan^2(\theta_i)\, \mathbb{E}[\tilde{\chi}_{TE}^{-}(\theta_i)])$. All four of the effective susceptibilities are related to the Monte Carlo-derived properties of the underlying film through equation 5.6.12. The polar angle dependence, $\mathcal{S}_{nmp}^{\pm}(\theta_i)$, is essential the Kerker forward and backward polar scattering function, without the additional phase terms. The task is now to find a suitable sampling scheme to achieve meaningful Monte Carlo estimates.

Equation 5.6.11 can be written and a sample, order, and type resolved form,

$$\epsilon_{eff,np}^{TM}(\theta_i; \mathcal{T}_a) = \frac{1}{2LN} + \frac{i\gamma_{\mathcal{T}_a}}{L} \sum_{m=0}^{n} \overline{c_{sca,nmp}^{MC,TM}}(\mathcal{T}_a) \frac{\mathbb{t}_{nm(1-p)}^{-}(\theta_i)}{\cos^2(\theta_i)}$$

$$\mu_{eff,np}^{TE}(\theta_i; \mathcal{T}_a) = \frac{1}{2LN} + \frac{i\gamma_l}{L} \sum_{m=0}^{n} \overline{c_{sca,nmp}^{MC,TE}}(\mathcal{T}_a) \frac{\mathbb{t}_{nmp}^{-}(\theta_i)}{\cos^2(\theta_i)}$$

$$\mu_{eff,np}^{TM}(\theta_i; \mathcal{T}_a)$$

$$= \frac{1}{2LN} + \frac{i\gamma_{\mathcal{T}_a}}{L} \sum_{m=0}^{n} \overline{c_{sca,nmp}^{MC,TM}}(\mathcal{T}_a) \left(\mathbb{t}_{nm(1-p)}^{+}(\theta_i) - \tan^2(\theta_i)\, \mathbb{t}_{nm(1-p)}^{-}(\theta_i)\right)$$

$$\epsilon_{eff,np}^{TE}(\theta_i; \mathcal{T}_a)$$

$$= \frac{1}{2LN} + \frac{i\gamma_{\mathcal{T}_a}}{L} \sum_{m=0}^{n} \overline{c_{sca,nmp}^{MC,TE}}(\mathcal{T}_a) \left(\mathbb{t}_{nmp}^{+}(\theta_i) - \tan^2(\theta_i)\, \mathbb{t}_{nmp}^{-}(\theta_i)\right),$$

where the total value of the permittivity and permeability can be found through coherent summation.

For systems that are not amenable to giving a well-defined analytic form of the self-energy, a Monte-Carlo approach can be used. This opens the space of possible systems where effective medium properties can be discussed and encapsulate aspects of such systems, such as non-locality.

5.7 A SAMPLING STRATEGY

Similar to the Monte Carlo approach for modeling random metasurfaces, the validity of a Monte Carlo-based effective medium theory relies, in part, on the accuracy of simulating the behavior of the film distribution. For three dimensional films, the space of possible particle configurations is large. The work in this dissertation is focused on using equation 5.6.11 to model random fractal films. This is because the motivating technology, the nonthermal equilibrium dusty plasma synthesis method, can create fractal films under proper deposition conditions and these films are well-known to manifest emergent properties not achievable in other systems. In particular, optical phenomena can emerge that will not be observed in quasi-static effective mediums or in bulk material counterparts. In this regard, it is important to understand the governing properties of random fractals that make them amenable to a Monte Carlo-based effective medium theory and why such systems manifest emergent behavior.

A Short Interlude on Random Fractals

Fractal is the commonly used terminology for a set which, in some sense, has a self-similar structure. Self-similar meaning the whole has the same shape as one or more of the parts. Though this definition is broad, this dissertation is concerned with scale invariant self-similarity, meaning properties that do not change as you scale to smaller or larger size. Plainly speaking, something has a scale invariant property if you can cut off a part, zoom in, and you recover the property you started with. A common example of a scale invariant structure is a Koch snowflake. In a computer animation, you can infinitely zoom into any edge of the snowflake, and it will appear as if you are looping back to the start. Fractals are not relegated to purely mathematical objects. Figure 5.7.1 shows a close-up of Romanesco broccoli, which gives an example of scale invariance occurring in nature. Indeed, scale-invariant fractals are in fact all around us!

Though fractals are easiest to understand in an ordered example, scale invariance can also be a property of the statistics of the system. In this case, when you zoom into a small part of a larger random system the statistical properties do not change. The underlying shape may be different from realization to realization, but the statistics are scale invariant. Interestingly, random fractals occur often in nature. An important example of random scale invariance is a stochastic Wiener process[162,163]. The first governing feature of this process is that the increment from state a to state b is independent of any knowledge of past decisions. I.e., the motion has no notion of a history propelling/biasing it to a particular next transition. Second, the governing statistics determining the transition from state a to state b is given by a Gaussian increment. I.e., the governing dynamics of the state change can be described by a collection of independent random

actions. Finally, the properties above should hold no matter how small or large the state increment is. These three governing properties constitute a recipe for self-similarity. Such a process may appear farcical to appear in nature, but this is not the case! Thanks to the law of large numbers, Gaussian behavior is dominant in many systems that have a large number of competing forces[164]. Take, for example, a snowflake falling from the sky. Gravity is propelling the snowflake downward. For clarity, assume the downward direction is the z axis. In the $x-y$ directions the snowflake tumbles seemingly randomly. This is because the lateral movement is governed by a large and chaotic set of fluctuations from the wind, temperature variations, collisions with other snowflakes, and the seemingly random rotations of the snowflake that push it like a small kite. This chaotic $x-y$ movement can be well approximated as a Gaussian random walk and, correspondingly, a Wiener-like process[162,164,165]. Another well-known and similar example is atoms/molecules moving in the atmosphere. Atoms such as carbon are so small that they float around in the atmosphere. Though strong winds may push them in a governing direction for some time, the remainder of their motion is primarily random and memoryless. Tiny fluctuations in local temperatures, air currents, and bouncing (or sticking) to other particles provides a seemingly statistically independent competition of external forces. When objects agglomerate by a Wiener-like process they form a scale invariant cluster. The dynamics of the motion dictates the statistical properties. It is important to note that the dynamics of the carbon atom and the snowflake are meaningfully different. This is because the snowflake has a deterministic downward motion (assuming it is heavy enough) whereas the carbon atom undergoes a true three-dimensional random walk. These differences manifest in the geometric structure of the cluster growth.

Figure 5.7.1. Picture of Romanesco broccoli (during a particularly fun visit to Paris, France) as an example of scale-invariance. The entire broccoli (left) is made of spirally nodules. Each nodule (right) is made of spirally nodules. Each nodule of a nodule is also made of spirally nodules.

Interestingly, fractal clusters of compounds in the atmosphere plays an important role in estimating the effects of climate change. To understand this, as well as the motivations behind random fractals in this dissertation, the connection between scale invariance of the system and scale invariance of Maxwell's equations needs to be discussed. In general, scale invariance has important implications in field theories as it describes characteristic properties of wave motion that can be witnessed at any length scale. In a homogeneous system, the wave equation for electromagnetism is scale invariant as long as the material properties do not change within the length scale. This is easily seen by replacing $\boldsymbol{r} \rightarrow \xi \boldsymbol{r}$ and $t \rightarrow \xi t$ and showing it creates no change in the underlying equation,

$$\nabla^2 \boldsymbol{E}(\boldsymbol{r}, t) = \frac{1}{v^2} \frac{\partial^2 \boldsymbol{E}(\boldsymbol{r}, t)}{\partial t^2}.$$

Maxwell's equations are inherently scale-invariant. It is the underlying material properties, the size and shape-dependent configuration of materials and their wavelength-dependent response that breaks scale invariance. Correspondingly, if the material response does not change within a range of wavelengths and the material is organized in a scale invariant way, then within the range applicable to the wavelength range the system is scale invariant. Such a property can then be the catalyst for emergent phenomena as long as the scale invariance is of an interesting form.

As a motivating example, let us return back to the case study of atmospheric carbon. Carbon has a broadband absorption spectrum across the entire visible regime. When carbon atoms conglomerate in the atmosphere, they form of a scale invariant random fractal. When the random fractal is large enough it is no longer approximated as a dipole to the incoming light and instead has a shape-dependent light-matter interaction[166]. Scale invariance implies that if there is a strong absorption resonance at high energy, e.g., $\lambda = 200$ nm, then a strong absorption resonance will be statistically guaranteed at all lower energies, e.g., $\lambda = 200 - 800$ nm, up to the length where scale invariance is broken (the cluster size)[167]. There is great importance in this statistical implication. A collection of carbon atoms will have substantially stronger absorption in a random fractal configuration when compared to a non-scale invariant configuration! This is because a strong resonance in one region implies it everywhere! The power of this property in design is that one needs only to satisfy their desired condition in an isolated part and the whole will follow. Correspondingly, three-dimensional random fractals, which have both scale and rotational invariance can be used to make broadband, polarization, and angle invariant absorbers[113,131,168].

The emergent absorption spectra seen in random fractals of carbon is not an arbitrary example. It was the inspiration for Chapter 7 of this dissertation. When atmospheric scientist sought to model light absorption in the atmosphere, the Bruggeman, Maxwell-Garnett, and similar approximations were compared to measurement. It was found that this class of effective mediums dramatically under predicted the measured absorption in the atmosphere to an unacceptable degree. From initial thought, this inaccuracy is perplexing. The atmosphere is sparsely filled with absorbing atoms/molecules in the wavelength range and surely each molecule/atom should behave like a point dipole. Under this reasoning, at face value, the atmosphere appears to be a perfect system to adhere to the mixing rules detailed in section 5.3. They key to the inaccuracy relies on the relative configuration of the constituents. Indeed, random fractals highlight the danger of translating assumptions of the local field to assumptions of the underlying distribution. This is because random fractals have an unusual collection of properties. They have an inherently low filling fraction, they do not have long-range correlation, and they can be composed of point-like electric dipoles[162,167]. Nonetheless, they can have strong particle-particle interactions due to large short-range correlation[162,167]. It is this unusual collection of properties that makes all the difference. Local clusters within the larger aggregate can support large topologically disconnected electromagnetic densities[167,169,170]. These large spatial fluctuations in the local field give rise to a terminology of "hot" (strong field) and "cold" (weak field) spots[167,169,170]. Clearly such a system does not actually uphold the true nature of the local field assumed by the Bruggeman, Maxwell-Garnett, and similar. With that said, the topological disconnectedness does enable an effective medium picture[131,168,171,172]. The key in this regard is to attempt to model the distinct local regions of similar behavior by an effective particle that then weakly interacts with its neighbor. Then the generalized individual scattering approximation can be evoked on the effective particles.

Making Effective Particles

In the context of particle deposition from a nonthermal equilibrium dusty plasma reactor, the random fractal structure can occur through agglomeration when particles are suspended in the plasma or at the time of deposition onto the substrate[173,174]. As discussed in the snowflake example, the kinetics inherent to both processes can be governed by memoryless random motion, but the ultimate fractal structure is different. This is because agglomeration inside the reactor allows for cluster growth in all three dimensions. Agglomeration upon deposition to the substrate grows the particle film strictly in height. An example of the underlying difference between the structure of such random fractals is shown in figure 5.7.2 and figure 5.7.3.

Exact modeling of the particle kinetics in the dusty plasma pipeline requires a complicated understanding of fluid dynamics and the role of characteristics parameters such as flow rate, plasma power, particle trapping mechanisms, et cetera. Such understandings are an active subject of research in the plasma physics community, necessitating large computer models, and beyond the scope of this dissertation. With that said, a sufficient history of work has shown that simple diffusion-limited aggregation (DLA) models based on Newtonian-like ballistics and Gaussian random motion can accurately describe the underlying fractal structure in simulation. Correspondingly, this dissertation adopts a simple diffusion-limited aggregation scheme based on particle kinetics of the form,

$$\Delta \boldsymbol{r} = \boldsymbol{v}\Delta t + \boldsymbol{N}(0, \sigma^2 \Delta t) \tag{5.7.1}$$

where $\Delta \boldsymbol{r} = \boldsymbol{r}(t_{n+1}) - \boldsymbol{r}(t_n)$ is the movement of the particle from $\boldsymbol{r}(t_n)$ to $\boldsymbol{r}(t_{n+1})$ over the time interval, $\Delta t = t_{n+1} - t_n$, and $n \in \mathbb{Z} \cup [0, \infty)$ is the simulation step number. $\boldsymbol{v}$ is a free parameter ballistic velocity term proportional to the net drag force, according to Stokes law, as well as any other consistent bias force, such as gravity. All other local forces have no net average contribution are modeled as a zero mean Gaussian random vector, $\boldsymbol{N} \in \mathbb{R}^3$. The variance of the Gaussian, σ^2, is another free parameter that controls the ratio of randomness to ballistic motion. When particles collide, the collision is either completely inelastic or elastic. This decision is determined by a stick probability,

$$P_{stick} = \gamma cos(\theta) + \beta. \tag{5.7.2}$$

γ is a free parameter determining the stick probability as a function of the angle of collision, θ. This parameter is most important when $\boldsymbol{v}$ is nonnegligible such as in simulations of particles depositing on substrates. If there is a net downward bias and particles hit at a grazing incidence, they would be unlikely to stick. This parameter prevents fractal film growth with unnatural looking 90-degree connections that would likely collapse to a more energy favorable orientation. β is another free parameter more important in three-dimensional clustering within the reactor. From the viewpoint of the particle all directions are closer to equivalent. Equation 5.7.1 and 5.7.2 constitute the growth model. A particle is moved based on the ballistics and random motion component. The particle is then checked for a collision. If a collision occurs, a random number weighed by equation 5.7.2 determines bounce or agglomerate. The process then repeats. Figure 5.7.2 gives an example of particles deposited on a substrate. The free parameters are tuned until experimentally measured parameters such as filling fraction and surface roughness

sufficiently match measurement. In this regard, particle generation is not completely a predictive technique as the free parameters need to be set by experimental input.

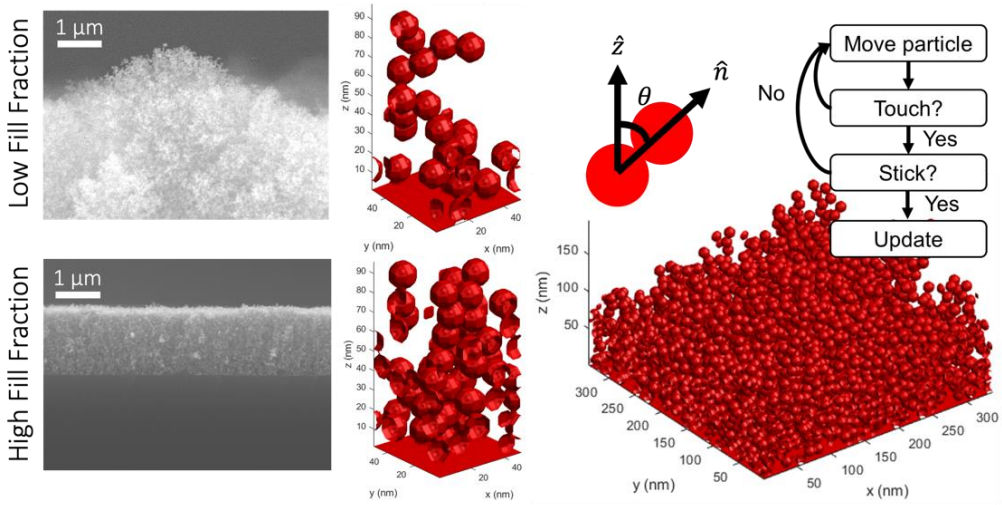

Figure 5.7.2. Example of scale invariant fractal growth on a substrate from dusty plasma synthesis deposition (left) and equivalent particle deposition model (right) using diffusion-limited aggregation. The upper left image shows low fill fraction, fractal-like, particle growth from diffusion dominated deposition of GaN particles. The lower left image shows a high filling fraction compact film deposited by ballistic dominated motion. Beside each image is a cross section of simulated particle deposition showing the ability to capture fractal-like and packed sphere configurations through tuning the free parameters in equations 5.7.1 and 5.7.2. The figure on the far right shows the collision angle defined in equation 5.7.2 as well as the flow diagram of the deposition algorithm.

Fractal films grown through substrate deposition does not resemble a statistical spherical symmetry, so it is hard to determine how to partition the cluster into effective particles. In contrast, particle agglomeration dominated by three-dimensional clustering within the reactor at the time of growth offers a more amenable system to the effective particle framework. For example, the three-dimensional cluster has a well-defined minimally circumscribing ball and, correspondingly, a single collective transition matrix. Upon sufficient discussion and experimentation with collaborators it was found that a strong exit pressure from the plasma reactor can create near ballistic motion onto the substrate. Correspondingly, the scale-invariant properties are governed primarily by three-dimensional clustering within the reactor. Thought the particle deposition algorithm can model particles on substrates, the sampling of effective particles formed by three-dimensional clustering within the reactor is used exclusively in Chapter 7.

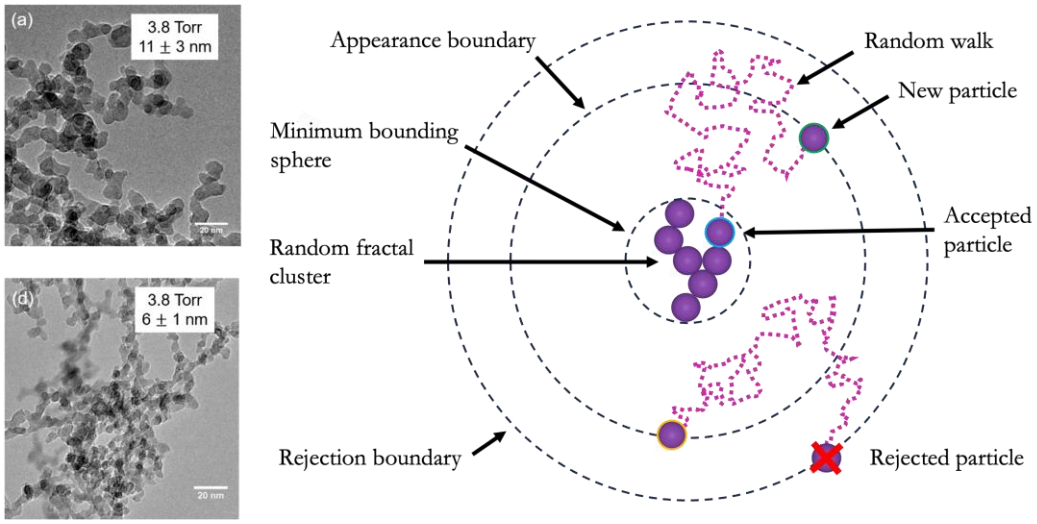

Figure 5.7.3. Example of particle growth and model from inside a plasma reactor based on diffusion-limited aggregation. (Upper left) Closeup of an edge of large fractal cluster. (Lower left) Large fractal cluster. Both images are taken from Chapter 10 of this dissertation. Further detail can be found in [Li. Z., Wray P. R., et. al., *ACS Omega* **2020**, *5* (38), 24754–24761]. (Right) Schematic of the particle growth model for mimicking three-dimensional fractal growth in a plasma reactor. Particles appear randomly on the appearance boundary. They then move by random three-dimensional motion based on equation 5.7.1. If the particle crossed the rejection boundary it is assumed to have left the region never to appear again. Otherwise, the particle simulation continues until aggregation occurs within the minimum bonding sphere. The minimum bounding sphere and particle number help to enforce filling fraction in a statistical sense.

The process of making effective particles makes clear the importance of being experiment informed. When clustering occurs in the reactor, each deposited cluster can be composed of 2, 3, 4, or more particles. Correspondingly, sparse samples should be made where individual clusters can be imaged, and statistics can be formed. Though in a film, clusters can still stack on top one another. Measuring the film's height, filling fraction, and roughness help to dictate the average compactness of the particle clusters and likelihood of stacking. This is especially important as measurement of isolated clusters may not be as accurate to particle packing once particles stack. In reality the free parameters are most likely accurate up to a range of values. The goal of direct measurement is to minimize the range. In this regard, the effective particle framework can be viewed as a predictive or characterization scheme. From the predictive viewpoint, the free parameters are estimated as single values, the model is run, and the effective medium model is formed. Simulating over a range of free parameters can then be used to inform error bounds on predictions. From the viewpoint of characterization, the same process is performed in a feedback loop where the free parameters are instead tuned to find the best match with experimental data. The gold standard in this regard is angle and polarization resolved reflection, transmission, and absorption measurements of both the coherent and incoherent

field. If the match is satisfying, then the value in the characterization approach is similar to that of ellipsometry for thin films. You can fine-tune values obtained through direct measurement techniques such as filling fraction as well as provide a discussion of the underlying electromagnetic behavior in the system giving rise to observed emergent behavior.

Through a proper cluster growth model, effective particles exhibiting fractal-like behavior can be incorporated into an effective medium framework.

Chapter 6

PARTICLE FILMS FOR OPTIMAL RADIATIVE COOLING

Wray, P.; Su, M.; Atwater, H. Design of Efficient Radiative Emission and Daytime Cooling Structures with Si3N4 and SiO2 Nanoparticle Laminate Films. *Opt. Express* **2020**. https://doi.org/10.1364/OE.408845.

ABSTRACT

Research on radiative cooling has attracted recent widespread interest owing to the potential for low-cost passive structures to enable large-scale thermal energy management. Using a generalized effective medium theory, we theoretically show that two-layer films comprised of SiO_2 and Si_3N_4 nanoparticle layers on an Ag back reflector exhibit superior radiative cooling compared to single-layer or two-layer dense solid films and can outperform other reported designs. The performance enhancement is a result of the ability to tune the nanoparticle fill fraction, which improves the spectral match between emissivity of this structure and the atmospheric transmission window. We also propose a standardized method for comparing the performance of radiative cooling structures reported by the research community.

6.1 INTRODUCTION

Approximately forty percent of the world population lives in consistently hot regions, many of which have homes lacking air conditioning[175–177]. Rising standards of living and growing demand for improved public health and comfortable living conditions is projected to lead to a 450% increase in air conditioning from 2010 to 2050 worldwide, representing one of the largest contributors to worldwide energy consumption[178–180]. Furthermore, current air conditioning systems account for almost 700 million metric tons of CO_2-equivalent emissions per year[176]. Seventy-four percent of these emissions are from electricity generation and approximately nineteen percent from refrigerant based hydrochlorofluorocarbons (HCFCs) which have a disproportionately large global warming impact relative to their mass[176]. These predictions highlight the importance of developing improved sustainable and environmentally friendly cooling technologies. Furthermore, a low cost and easily implemented passive cooling technology can promote early adoption in developing countries, reduce overall energy use, and lower greenhouse gas emissions.

Cooling by radiative heat transfer from a terrestrial ambient to the cold ambient of space is a passive, sustainable solid-state technique to provide cooling without the need for external power or additional operating costs. Photonic structures which are both highly reflective in the solar spectrum (below 2.5 μm) and highly emissive in the infrared atmospheric transmission window (8 – 14 μm) can suppress solar heating and remove heat through infrared (IR) radiation to cool throughout the diurnal cycle. Radiative cooling structures are particularly applicable in regions with low humidity, where the atmosphere is most transparent, such as Mexico, northern and southern Africa, the Middle East, Australia, India, parts of North and South America, and areas of northern Asia[176,181]. The primary requirement of a radiative cooler is to provide enough cooling power at a specified temperature to more than offset its own parasitic heating, thus providing net cooling, and is constrained by the limited bandwidth of the infrared atmospheric transmission window and stringent reflectivity requirements in the solar spectrum. Recent designs for daytime radiative cooling structures to improve cooling performance include structures with glass nanoparticles embedded into a polymer film, layered thin films on back reflectors, and complex lithographically patterned structures such as many-layered nanoarrays [182–193]. Other passive cooling techniques – such as earth to air heat exchangers, evaporative coolers, and nocturnal convective coolers – focus on removing heat through a heat sink (ground, water, or, air respectively), but suffer from high initial costs, continual operating costs, and/or external power requirements[194,195].

Films composed of Rayleigh scattering nanoparticles can provide simple photonic designs for improving daytime cooling performance and are amenable to scalable manufacturing [196,197]. By

tuning the nanoparticle fill fraction, air-material composites of this type can provide broadband impedance matching to free space and the ability to spectrally tune absorption resonances by changing the local (Lorentz) field[18,152,198]. Conversely, layered structures synthesized by thin film deposition can enable improved impedance matching to free space and resonance shifts through either graded index stacks, periodic layered structures, or intricate patterning[199–202]. For graded index and periodic structures, impedance matching is limited by the minimum practically achievable refractive index in the low index layers and the number of layers in the stack[199]. Furthermore, graded index and periodic layered structures are constrained by the limited portfolio of materials that can be used to achieve the stringent broadband reflection and emission requirements of a daytime radiative cooler [203]. Use of patterned subwavelength-scale resonant or wavelength-scale diffractive photonic structures represents another approach to tune photonic properties but is limited by fabrication complexity for large-area low-cost structures[203]. In this paper, we theoretically show that nanoparticle films can circumvent the impedance matching and materials limits which constrain layered structures. Two-layer nanoparticle films can achieve radiative cooling performance comparable to or greater than others reported to date, based solely on tuning nanoparticle fill fraction and film thickness.

Using a generalized effective medium theory, we show that simple two-layer nanoparticle films composed of separate layers of SiO_2 and Si_3N_4 particles on a silver back reflector can outperform all dense solid laminate thin films and provide a cooling performance superior to those reported previously[182–193]. Using consistent solar, atmospheric, convective/conductive, and ambient temperature conditions across comparisons, we find that the radiative cooling performance of two-layer nanoparticle film designs exceeds many reports of radiative cooling designs in literature by up to 20 W/m^2 and 25 W/m^2 at operating temperatures of 290 K and 280 K, respectively. Furthermore, optimized two-layer nanoparticle film designs have higher cooling power than optimized dense solid laminate thin films, regardless of which structure or composition is chosen. These results support the idea that random nanoparticle laminate films could provide a feasible alternative to dense solid thin film or patterned designs, provided scalable synthesis techniques can be identified. In this regard, plasma synthesis or ball milling could be considered as possible scalable deposition methods[196,204].

6.2 DEFINING AN OPTIMAL RADIATIVE COOLER

There are three important factors to consider when designing a daytime radiative cooling structure, which can be inferred from equation 6.5.1 – 6.5.6. First, the criterion for defining an optimal radiative cooling structure should be to maximize the structure's net cooling power at a desired target operating temperature, called the "optimization temperature." Second, the performance of a radiative cooling structure is fundamentally limited by the atmospheric emission spectrum. As such, the atmospheric emission spectrum of the target operating environment needs to be carefully considered. Third, to achieve cooling below ambient temperature, solar absorption and other forms of parasitic heating must be kept below a critical threshold.

We can define the theoretical spectral emission of an optimal radiative cooling structure as

$$e_r(\lambda, T_r, T_a, \theta, \alpha) = \begin{cases} 1, & I_B(\lambda, T_r) > I_B(\lambda, T_a) e_a(\lambda, \theta, \alpha) \\ 0, & else \end{cases} \quad 6.2.1$$

where e_r is the emissivity of the structure, e_a is the emissivity of the atmosphere, λ is the free space wavelength, T_r is the structure's temperature, T_a is the ambient temperature, θ is the angle of emission, and a is a variable encapsulating the conditions relating to the composition of the atmosphere[205]. I_B is defined as the blackbody spectral radiance

$$I_B = \frac{2hc^2}{\lambda^5} \frac{1}{e^{\frac{hc}{\lambda k_B T}} - 1} \quad 6.2.2$$

where h is Plank's constant, $k_B$is the Boltzmann constant, and c is the speed of light. Equation 6.2.1 shows that the theoretical optimal cooling performance is a function of the temperature of the radiative cooling structure, ambient temperature, emission angle, and atmospheric composition.

In regard to choosing the appropriate atmospheric emission spectrum, figure 6.2.1(a) shows the atmospheric transmission windows from the Gemini Observatory (low humidity level) and from the 1976 United States Standard (average humidity level)[205]. The spectra at the Gemini Observatory represents near ideal conditions where a radiative cooler with high emissivity in both the first (8 – 14 μm) and second (16 – 24 μm) atmospheric transmission windows could achieve the highest possible cooling power. However, it is shown in figure 6.2.1(a) that while two atmospheric transmission windows exist at very low humidity levels, the prevalence of

water molecules in the atmosphere greatly diminishes the contribution of the second atmospheric transmission window towards radiative cooling for most areas of the world [206]. Consequently, practical radiative coolers in terrestrial applications should optimize emission only in the first atmospheric transmission window and over all angles. The 1976 United States Standard atmospheric emission spectrum was modeled using LOWTRAN7, an open-source software comparable to MODTRAN[207–209]. Figure 6.2.1(b) shows the 1976 United States Standard atmospheric emission spectra at 300 K with blackbodies of 300 K, 280 K, 260 K, and 240 K overlaid in the background[206]. From figure 6.2.1(b), we see that the optimal emission window as described in equation 6.2.1 for achieving maximum cooling power is denoted by the area of each blackbody that is not overlapped by the atmospheric emittance. This demonstrates the dependence of the optimal spectral emission window on the operating temperature. Figure 6.2.1(c) illustrates the radiative cooling power (P_r) to operating temperature relationship for ideal radiative coolers as defined by Equation (1). Each solid curve is the radiative cooling power based on spectral emission windows optimized for 300 K, 280 K, 260 K, and 240 K blackbodies minus the atmospheric heating (P_a), at an ambient temperature of 300 K. From the solid curves in figure 6.2.1(c), we see that each optimal spectral emission window achieves a superior cooling power compared to its peers when operating at or near its optimization temperature. The dashed horizontal lines show the net-zero power curves ($P_{net} = 0$) for different percentages of solar absorption (P_{sun}). From these dashed lines, we find that radiative cooling while operating below the ambient temperature of 300 K is effectively impossible if parasitic solar absorption is higher than 10%. The dashed sloped lines show $P_{net} = 0$ when considering different non-radiative heat transfer coefficients (q), which account for convective and conductive heat transfer (P_{other}). The overall $P_{net} = 0$ line is determined by a linear combination of the solar absorption and non-radiative heat transfer effects.

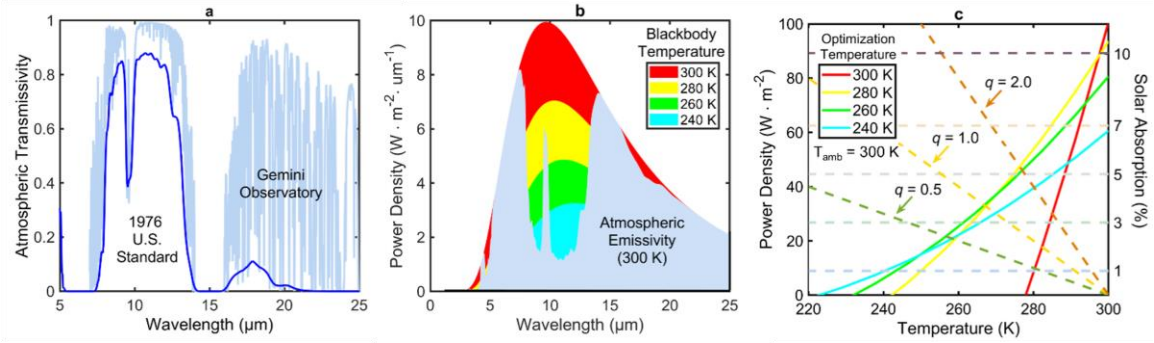

Figure 6.2.1. Conditions of optimal radiative cooling. (a) Atmospheric transmission spectra at low humidity taken from the Gemini Observatory and at average humidity taken from the 1976 U.S. Standard; (b) blackbody spectra at various temperatures (300 K, 280 K, 260 K, and 240 K) overlaid on the atmospheric emission spectrum from 1976 U.S. Standard at 300 K; (c) radiative cooling power density versus operating temperature relationship for the four theoretically optimal radiative cooling spectral emission windows defined from (b), each is optimized to provide superior cooling power at a specific optimization temperature under ambient conditions (300 K). The solid lines show radiative cooling power (P_r) minus atmospheric heating (P_a) versus operating temperature for each of the optimal radiative coolers. Solar absorption percent is given by the horizontal dashed lines. Losses from conduction and convection for various non-radiative heat transfer coefficients (q), are marked with sloping dashed lines. The total net zero cooling power line is represented by a linear combination of the solar absorption line and non-radiative heat transfer coefficient line.

6.3 RADIATIVE COOLING IN NANOPARTICLE LAMINATE FILMS

Using a generalized effective medium theory, we design different radiative cooling structures comprised of separate layers of SiO_2 and Si_3N_4 nanoparticle films with air as the matrix medium. We find that two-layer nanoparticle films always outperform dense solid laminate thin films and are sufficient to achieve cooling performances greater than or similar to previously reported structures[182–193]. In our designs, SiO_2 and Si_3N_4 were chosen as the emissive materials because of their strongly peaked absorption within the atmospheric transmission window. Specifically, in-phase and out-of-phase stretching of the Si–O bond is responsible for the strong absorption peak in SiO_2 from 8 – 10 μm, and Si–N bond stretching is responsible for the broad absorption peak in Si_3N_4 from 9 – 15 μm[210–213]. In both cases the absorption coefficient for wavelengths between 0.25 – 5 μm can be made negligibly small. The generalized effective medium permittivity, considering a single type of inclusion, is given by:

$$\frac{\varepsilon_{eff}-\varepsilon_e}{2\varepsilon_e+\varepsilon_{eff}+v(\varepsilon_{eff}-\varepsilon_e)} = ff\,\frac{\varepsilon_i-\varepsilon_e}{2\varepsilon_e+\varepsilon_i+v(\varepsilon_{eff}-\varepsilon_e)} \qquad 6.3.1$$

where ε_e is the host permittivity (free space in this case), ε_i is the inclusion permittivity (SiO_2 or Si_3N_4), ff is the inclusion fill fraction, ε_{eff} is the resulting effective permittivity, and v is a continuous variable which encapsulates how the inclusion responds to the internal field. Using this framework, the Maxwell Garnett (MG) formula is recovered at $v = 0$, Bruggeman at $v = 2$, and coherent potential (CP) at $v = 3$[214]. Therefore, this generalized formula spans a set of effective medium theories and values of v between the common theories can be viewed as a hybrid response in the internal field. For each structure designed, we span v to compare the structure's cooling performance under each effective medium formula and hybrid parameters. As a representative example figure 6.3.1(a) – 6.3.1(e) show the real (n) and complex (k) refractive index for bulk SiO_2 and Si_3N_4 as well as the effective n_{eff} and k_{eff} for laminate nanoparticle films of SiO_2 or Si_3N_4 as a function of fill fraction under the Bruggeman formula[214,215]. Figure 6.3.1(a) – (b), (d) – (e) show that by tuning the nanoparticle fill fraction, we can reduce impedance mismatch between the nanoparticle film and free space. We can also spectrally shift the location of maximum k_{eff} of the material composite as a result of coupling between phonons and the internal field[18,152,198]. Figure 6.3.1(c) and (f) emphasize the effect of spectral shifting by normalizing the amplitude of k_{eff} for SiO_2 and Si_3N_4 laminate nanoparticle films within the atmospheric transmission window, respectively. Both increased impedance matching, and spectral absorption resonance shifting are found to be consistent features no matter the choice of v. We note that SiO_2 and Si_3N_4 nanoparticles with diameters of 50 nm or less satisfy the condition of Rayleigh scattering throughout the visible and IR wavelength

regime[53]. Under this condition, the effective medium theory given by equation 6.3.1 is valid[18,152,198,216–220]. Synthesis of nanoparticle films composed of nanoparticles of this size and smaller, and with sufficiently narrow size distributions and high uniformity, can be done via both dusty plasma synthesis and ball milling[204,221–224]. We set a 60% fill fraction as a realistic upper limit due to the theoretical limit of random sphere packing (62 – 64%)[225,226].

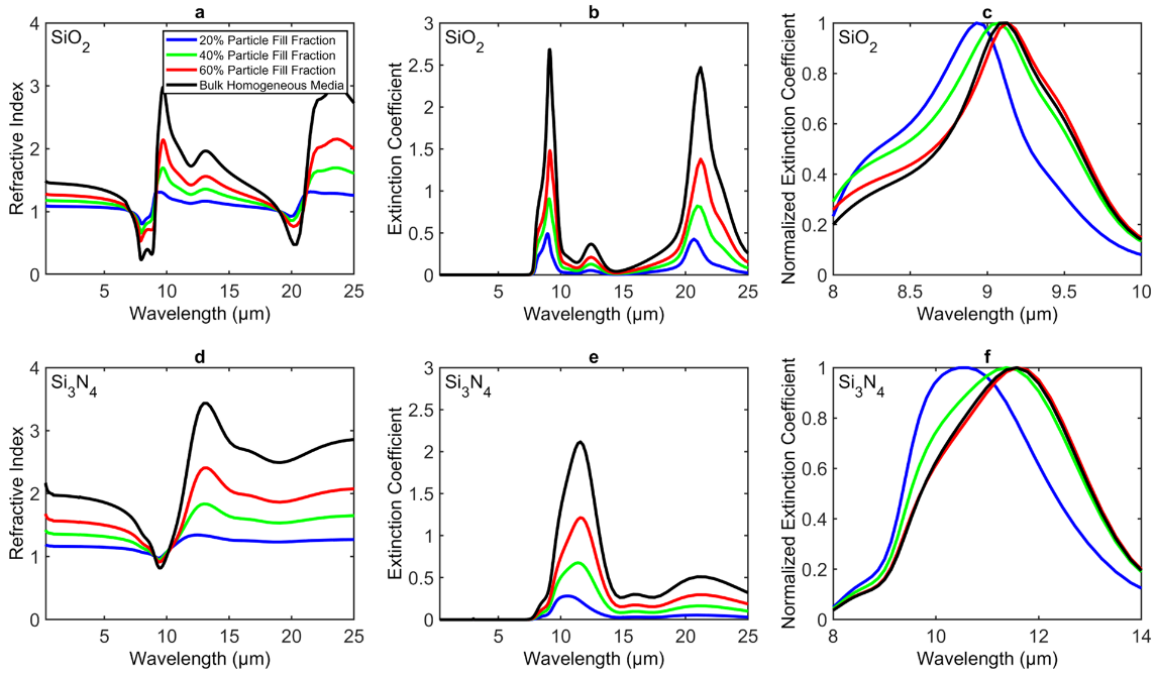

Figure 6.3.1. Effective permittivity versus inclusion filling fraction. (a), (b) n_{eff} and k_{eff} for SiO_2 at various fill fractions with air as the matrix medium; (c) normalized k_{eff} for SiO_2 within atmospheric transmission window demonstrating spectral shifting as a function of fill fraction; (d), (e) n_{eff} and k_{eff} for Si_3N_4 at various fill fractions with air as the matrix medium; (f) normalized k_{eff} for Si_3N_4 within the atmospheric transmission window demonstrating spectral shifting as a function of fill fraction.

We also study the limits an effective permittivity for a random particle film can be, which is determined from the Hashin-Shtrikman (HK) bounds:

$$\varepsilon_{MG} \leq \varepsilon_{eff} \leq \varepsilon_{MG-Comp} \qquad 6.3.2$$

where the lower limit is given by the MG formula and the upper limit by the MG formula of the complementary structure in which the host and medium materials are transposed. Thus, equation 6.3.2 gives an estimate on the permittivity extrema we may encounter for nanoparticle

laminate films, and equation 6.3.2 provides the framework to model the behavior of these films under an entire class of effective medium theories within the HK bounds. From this framework, we can compare two-layer SiO_2 and Si_3N_4 laminate nanoparticle films to dense solid thin film equivalents.

Using transfer matrix calculations, we determine each structure's wavelength, angle, and polarization-resolved absorption/emission profile, then calculate its net radiative cooling power (P_{net}) as a function of operating temperature[227,228]. Optimal designs for each temperature regime were found by systematically varying each laminate nanoparticle layer thickness, fill fraction, material orientation (alternating the material of the top and bottom layers), and film type (laminate nanoparticle film or dense solid thin film) for all permutations of two-layer structures of SiO_2 and Si_3N_4 on an Ag back reflector. As such, a total of 32 two-layer radiative cooling structures were optimized. At each of four optimization temperature (300 K, 290 K, 280 K, 270 K), we optimized eight unique two-layer structures on a silver back reflector based on material order (SiO_2 on Si_3N_4 or Si_3N_4 on SiO_2) and film type (two thin film layers, thin film on laminate nanoparticle film, laminate nanoparticle film on thin film, and two laminate nanoparticle films). Figure 6.3.2(a) shows an example schematic of a radiative cooling structure comprised of two layers of laminate nanoparticle films on a silver back reflector. The specific design parameters (layer thickness, fill fraction) and radiative cooling powers for all 32 optimized radiative cooling structures can be found in tables 6.6.1 – 6.6.18.

Figure 6.3.2(b) shows the radiative cooling power of each of the 32 optimized two-layer radiative cooling structures under the Bruggeman mixing rule ($v = 2$). Each structure is shown at the operating temperature where their spectra has been optimized to give the most cooling power (optimization temperature). We assume an ambient of 300 K and account for solar absorption. No conduction or convection losses ($q = 0$) are shown as they would be common to each structure and are not an aspect of the photonic design. From figure 6.3.2(b), we see that optimized two-layer laminate nanoparticle films on a silver back reflector outperform optimized two-layer dense solid thin films at all optimization temperatures. The best performing two-layer laminate nanoparticle film structures show a 40% to 120% increase in radiative cooling power compared to the best performing two-layer dense solid thin film structures. The laminate nanoparticle films also demonstrate cooling at 270 K, which is unachievable in a dense solid thin film structure. Figure 6.3.2(c) shows the radiative cooling power of each of 32 optimized two-layer radiative cooling structures under the Maxwell Garnett mixing rule. From figure 6.3.2(c), we see that optimized two-layer laminate nanoparticle films on silver back reflector are still predicted to outperform optimized two-layer dense solid thin films at all target temperatures, with increases of 30% and 109% in

radiative cooling power when using the Maxwell Garnett mixing rule. Using the design parameters for the best performing two-layer laminate nanoparticle film and its two-layer thin film analog at each optimization temperature, we show in figure 6.3.2(d) the radiative cooling power of the laminate nanoparticle films when calculated using different effective medium formulas (v = 0, 1, 2, 3). Results from the HK bounds and the optimal thin film design are also plotted. From figure 6.3.2(d) we see that laminate nanoparticle films have higher predicted radiative cooling powers than two-layer thin film structures of the same material at all operating temperatures regardless of the effective medium theory used. In all cases, the AM1.5 solar spectrum was used, and the atmospheric transmittance data was taken from the 1976 U.S. Standard using LOWTRAN7[229], integrated over angle and wavelength for both polarizations, and the ambient temperature was 300 K. Non-radiative heat losses were not considered since these losses would be common since film thicknesses are negligible for heat capacitance, the losses can be and often are controlled by the design of an external box, and are not inherent to the photonic aspects of the design. This does not detract from the comparison. The angular, spectral, and polarization-resolved emissivity profiles for all two-layer laminate nanoparticle film structures as calculated by both Bruggeman and Maxwell Garnett effective medium formulas can be found in figure 6.7.1 – 6.7.8.

Figure 6.3.3 compares the cooling performance of the optimal two-layer laminate nanoparticle films from figure 6.3.2(a) under the Bruggeman mixing rule to structures that have been previously reported[182–185,192]. In order to provide a direct comparison, absorptivity/emissivity curves from previous reports are digitized and the radiative cooling performance is compared using the same AM1.5 solar spectrum and atmospheric absorption spectrum (the 1976 U.S. Standard)[205]. Furthermore, all calculations use an ambient of 300 K, and no non-radiative heat losses were considered. Therefore, the results should be interpreted as the relative average performance based on United States standards. Since multiple papers only report emissivity curves at normal incidence, all calculations assume the structure emits as a Lambertian surface [182–185,192]. We then perform the angular integration found in equation 6.5.2 – 6.5.4 under this assumption, allowing us to account for the angular dependence of the 1976 U.S. Standard atmospheric spectra. While the lack of angular information will alter the achievable cooling power, applying the approximation of Lambertian emittance allows for a consistent comparison between curves. Non-radiative heat losses were not considered since these losses are or can be controlled by the design of an external box and are not inherent to the photonic aspects of the design. Solar absorption is considered since it is part of the photonic design for daytime cooling. The results suggest that laminate nanoparticle film structures can provide cooling performance superior to other reported radiative cooling structures at temperatures below a 300 K ambient, many of which are achieved only through complex photonic designs.

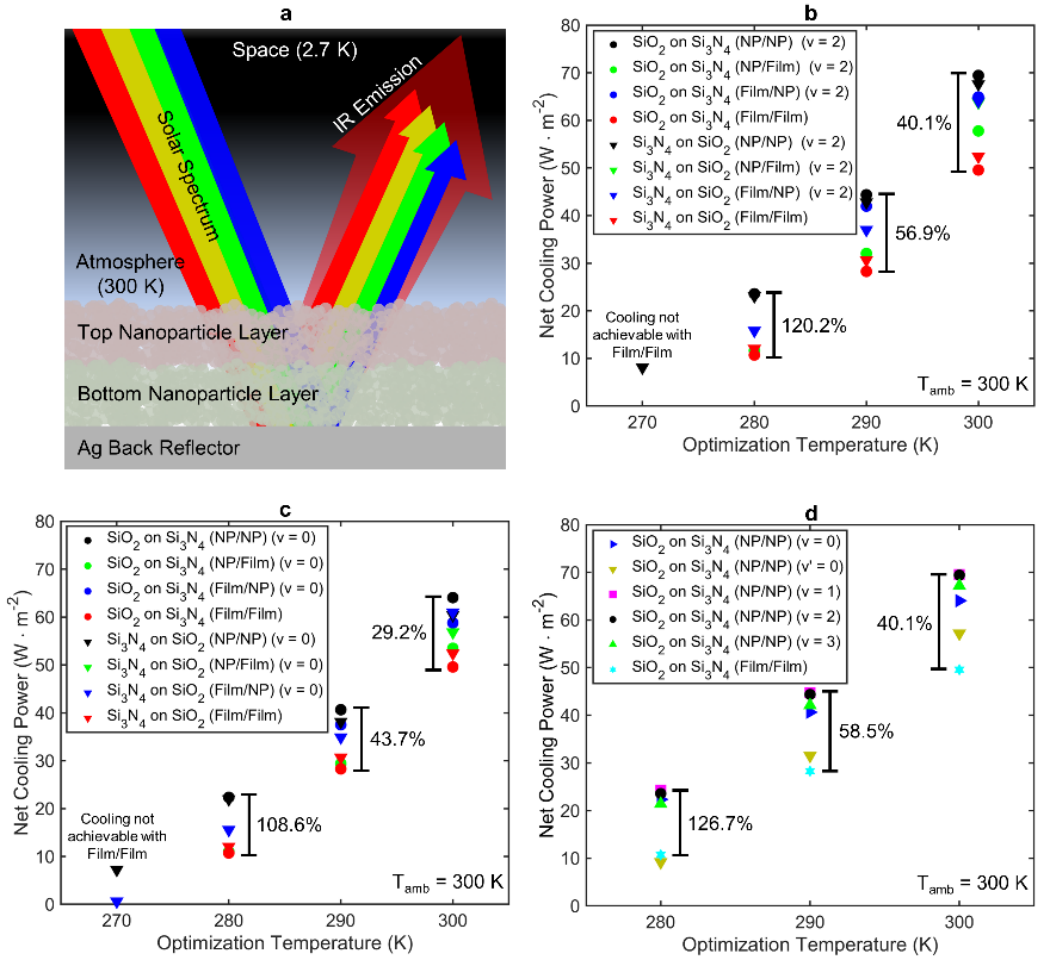

Figure 6.3.2. Summary of radiative cooling performance. (a) Schematic of radiative cooler comprised of two layers of laminate nanoparticle films on a silver back reflector; (b) net radiative cooling power of all 32 optimal two-layer nanoparticle film, thin film, or nanoparticle and thin film composite structures of SiO_2 and Si_3N_4 operating at their optimization temperature calculated using the Bruggeman effective medium formula ($v = 2$); (c) net radiative cooling power of all 32 optimal two-layer nanoparticle film, thin film, or nanoparticle and thin film composite structures of SiO_2 and Si_3N4 operating at their optimization temperature calculated using the Maxwell Garnett effective medium formula ($v = 0$); (d) net radiative cooling power versus optimization temperature for the optimal two-layer nanoparticle films calculated using different effective medium theories. The nanoparticle film structure performance is compared to the two-layer thin-film analog to demonstrate that superior radiative cooling power is predicted regardless of which effective medium formula is used. All figures assume an ambient temperature of 300 K and no conduction or convection losses ($q = 0$).

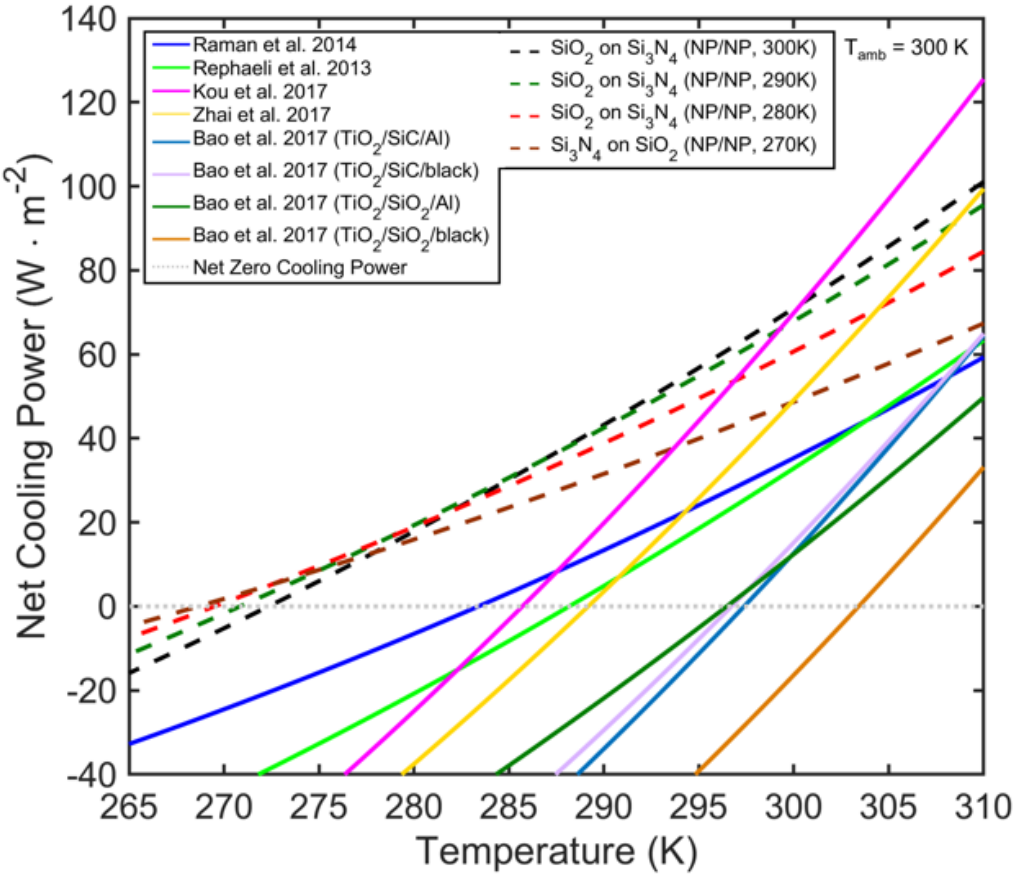

Figure 6.3.3. Comparison between various radiative structure performances from literature (solid) and proposed two-layer radiative cooling structures composed of SiO_2 and Si_3N_4 laminate nanoparticle films on silver back reflector (dashed). Each dashed curve represents a unique two-layer radiative cooler optimized for a different operating temperature. Literature curves are obtained through digitization of published emissivity data at normal incidence, and it is assumed the emissivity is angle independent. This figure serves purely as a guide for visualizing the relative benefit of nanoparticle films in radiative cooling.

6.4 CONCLUSION

We have demonstrated that SiO_2 and Si_3N_4 two-layer nanoparticle laminate films can give rise to radiative cooling powers that are higher than the best dense solid thin film laminate designs using the same materials. This result is robust with respect to the effective medium theory employed for optimization. Furthermore, we show that simple two-layer nanoparticle structures are sufficient to achieve cooling performances exceeding that of previously reported designs. Cooling performance improvements ranging from 20 W/m^2 to 25 W/m^2 over previously reported designs are possible with two-layer laminate nanoparticle films at operating temperatures of 290 K and 280 K, respectively, and two-layer laminate nanoparticle films remain competitive with previously reported designs at 300 K. This work suggests that nanoparticle laminate films are a promising component for future simple, scalable, and effective daytime radiative cooling structures.

6.5 RADIATIVE COOLING THEORY

Radiative cooling structures are designed to selectively emit radiation within the atmospheric transmission window, reflect the solar spectrum, and minimize conductive or convective heating losses. Formally this is expressed as a power balance

$$P_{net} = P_r - P_a - P_{sun} - P_{other}, \quad 6.5.1$$

where P_{net} is the net power leaving the structure, P_r is the thermal power the structure emits, P_a is the thermal power emitted from the atmosphere that is absorbed by the radiative cooler, P_{sun} is the solar power absorbed by the radiative cooler, and P_{other} accounts for heating due to conduction or convection. To cool below room temperature, the structure must reflect the solar spectrum to prevent heat buildup and emit within the atmospheric transmission window to radiate its heat into outer space. The cooling power of a radiative cooler is defined by the amount of thermal radiation it emits per unit time and can be expressed as

$$P_r(T) = 2\pi A \int_0^{\frac{\pi}{2}} \int_0^{\infty} I_B(\lambda, T_r) e_r(\lambda, \theta) \sin\theta \cos\theta \, d\lambda d\theta, \quad 6.5.2$$

where A is the structure area, e_r is the emissivity of the radiative cooler and I_B is the blackbody spectral radiance of the radiative cooler

$$I_B(\lambda, T) = \frac{2hc^2}{\lambda^5} \frac{1}{e^{\frac{hc}{\lambda k_B T}} - 1}, \quad 6.5.3$$

where T_r is the structure's temperature and λ is the emission wavelength.

Under thermodynamic equilibrium, emissivity and absorptivity can be interchanged based on Kirchhoff's law of radiation. Heating of the structure by absorbed atmospheric radiation is expressed as

$$P_a(T) = 2\pi A \int_0^{\pi/2} \int_0^{\infty} I_B(\lambda, T_a) e_r(\lambda, \theta) e_a(\lambda, \theta, \alpha) \sin\theta \cos\theta \, d\lambda d\theta, \quad 6.5.4$$

where e_a is the emissivity of the atmosphere, $I_B(\lambda, T_a)$ is the blackbody spectral radiance of the atmosphere at ambient temperature T_a, and α is a variable encapsulating the conditions relating to the composition of the atmosphere [S. Jeon and J. Shin, Scientific Reports 10(1), 1-7 (2020)]. The power absorption from direct solar radiation can be expressed as

$$P_{sun} = A \int_0^\infty I_{solar} e_r d\lambda, \quad 6.5.5$$

where I_{solar} is the AM1.5 solar spectrum. Finally, heating due to conduction and convection can be collectively expressed as

$$P_{other} = qA(T_a - T_r), \quad 6.5.6$$

where T_a is the ambient temperature, T_r is the temperature of the radiative cooler, and q is the non-radiative heat coefficient from conductive and convective heat transfer through the air and surfaces in contact with the radiative cooler.

Equations 6.5.1 – 6.5.6 outline three important facts for radiative cooling structure design. First, the criterion for an optimal cooling structure should be defined by its cooling power at a given operating temperature. This is because as the structure cools below the ambient temperature, the optimal spectral window to achieve maximum cooling power becomes a subset of the atmospheric window. Second, the performance limit for a cooling structure is fundamentally limited by the atmospheric emission spectrum. Third, to achieve net cooling performance, solar absorption and other forms of parasitic heating must be below a critical threshold.

6.6 TABLES OF COOLING POWER VERSUS TEMPERATURE

T (K)	P (W/m^2)	Si_3N_4 Thickness (nm)	SiO_2 Thickness (nm)
300	52.39	200	1200
290	30.65	100	1300
280	12.02	100	1100
270	-1.57	600	25

Table 6.6.1. Cooling power versus temperature for Si_3N_4 on SiO_2 (Film/Film) on Ag back reflector

T (K)	P (W/m^2)	Si_3N_4 Thickness (nm)	Si_3N_4 Fill Fraction (%)	SiO_2 Thickness (nm)
300	63.76	3000	25	200
290	41.25	2750	25	0
280	22.83	2500	25	0
270	8.01	2500	20	0

Table 6.6.2. Cooling power versus temperature for Si3N4 on SiO2 (NP/Film) on Ag back reflector using the Bruggeman formula ($v = 2$)

T (K)	P (W/m^2)	Si_3N_4 Thickness (nm)	SiO_2 Thickness (nm)	SiO_2 Fill Fraction (%)
300	64.00	200	2500	20
290	37.01	100	2250	30
280	15.82	100	2000	25
270	-0.09	100	1700	20

Table 6.6.3. Cooling power versus temperature for Si3N4 on SiO2 (Film/NP) on Ag back reflector using the Bruggeman formula ($v = 2$)

T (K)	P (W/m^2)	Si_3N_4 Thickness (nm)	Si_3N_4 Fill Fraction (%)	SiO_2 Thickness (nm)	SiO_2 Fill Fraction (%)
300	67.60	1100	35	1800	25
290	42.79	1600	25	1400	20
280	23.10	2500	25	50	20
270	8.10	2500	20	25	20

Table 6.6.4. Cooling power versus temperature for Si3N4 on SiO2 (NP/NP) on Ag back reflector using the Bruggeman formula ($v = 2$)

T (K)	P (W/m^2)	SiO_2 Thickness (nm)	Si_3N_4 Thickness (nm)
300	49.57	700	800
290	28.28	800	600
280	10.71	700	600
270	-1.64	0	600

Table 6.6.5. Cooling power versus temperature for SiO_2 on Si_3N_4 (Film/Film) on Ag back reflector

T (K)	P (W/m^2)	SiO_2 Thickness (nm)	SiO_2 Fill Fraction (%)	Si_3N_4 Thickness (nm)
300	57.78	1700	35	900
290	32.05	1600	35	800
280	11.64	1400	25	700
270	-1.64	0	-	600

Table 6.6.?. (No spookiness!) Cooling power versus temperature for SiO2 on Si3N4 (NP/Film) on Ag back reflector using the Bruggeman formula ($v = 2$)

T (K)	P (W/m^2)	SiO_2 Thickness (nm)	Si_3N_4 Thickness (nm)	Si_3N_4 Fill Fraction (%)
300	64.91	50	2750	30
290	41.97	25	2750	25
280	22.83	0	2500	25
270	8.01	0	2500	20

Table 6.6.7. Cooling power versus temperature for SiO_2 on Si_3N_4 (Film/NP) on Ag back reflector using the Bruggeman formula ($\boldsymbol{v}$ = 2)

T (K)	P (W/m^2)	SiO_2 Thickness (nm)	SiO_2 Fill Fraction (%)	Si_3N_4 Thickness (nm)	Si_3N_4 Fill Fraction (%)
300	69.43	900	20	2250	35
290	44.38	700	20	2250	30
280	23.58	200	20	2500	25
270	8.01	0	-	2500	20

Table 6.6.8. Cooling power versus temperature for SiO_2 on Si_3N_4 (NP/NP) on Ag back reflector using the Bruggeman formula (v = 2)

T (K)	P (W/m^2)	Si_3N_4 Thickness (nm)	Si_3N_4 Fill Fraction (%)	SiO_2 Thickness (nm)
300	56.82	3000	25	200
290	37.89	2750	25	0
280	21.33	2500	25	0
270	8.38	2500	20	0

Table 6.6.9. Cooling power versus temperature for Si3N4 on SiO2 (NP/Film) on Ag back reflector using Maxwell Garnett formula (v = 0)

T (K)	P (W/m^2)	Si_3N_4 Thickness (nm)	SiO_2 Thickness (nm)	SiO_2 Fill Fraction (%)
300	60.94	200	2500	20
290	34.88	100	2250	30
280	15.54	100	2000	25
270	0.59	100	1700	20

Table 6.6.10. Cooling power versus temperature for Si3N4 on SiO2 (Film/NP) on Ag back reflector using Maxwell Garnett formula ($v = 0$)

T (K)	P (W/m^2)	Si_3N_4 Thickness (nm)	Si_3N_4 Fill Fraction (%)	SiO_2 Thickness (nm)	SiO_2 Fill Fraction (%)
300	60.41	1100	35	1800	25
290	38.12	1600	25	1400	20
280	21.95	2500	25	50	20
270	7.22	2500	20	25	20

Table 6.6.11. Cooling power versus optimization temperature for Si3N4 on SiO2 (NP/NP) on Ag back reflector using Maxwell Garnett formula ($v = 0$)

T (K)	P (W/m^2)	SiO_2 Thickness (nm)	SiO_2 Fill Fraction (%)	Si_3N_4 Thickness (nm)
300	53.47	1700	35	900
290	29.39	1600	35	800
280	10.99	1400	25	700
270	-1.64	0	-	600

Table 6.6.12. Cooling power versus temperature for SiO2 on Si3N4 (NP/Film) on Ag back reflector using Maxwell Garnett formula ($v = 0$)

T (K)	P (W/m^2)	SiO_2 Thickness (nm)	Si_3N_4 Thickness (nm)	Si_3N_4 Fill Fraction (%)
300	58.78	50	2750	30
290	37.49	25	2750	25
280	21.33	0	2500	25
270	6.99	0	2500	20

Table 6.6.13. Cooling power versus temperature for SiO2 on Si3N4 (Film/NP) on Ag back reflector using Maxwell Garnett formula ($\boldsymbol{v}$ = 0)

T (K)	P (W/m^2)	SiO_2 Thickness (nm)	SiO_2 Fill Fraction (%)	Si_3N_4 Thickness (nm)	Si_3N_4 Fill Fraction (%)
300	64.05	900	20	2250	35
290	40.64	700	20	2250	30
280	22.34	200	20	2500	25
270	6.99	0	-	2500	20

Table 6.6.14. Cooling power versus temperature for SiO2 on Si3N4 (NP/NP) on Ag back reflector using Maxwell Garnett formula (v = 0)

T (K)	P (W/m^2)	SiO_2 Thickness (nm)	SiO_2 Fill Fraction (%)	Si_3N_4 Thickness (nm)	Si_3N_4 Fill Fraction (%)
300	57.17	900	20	2250	35
290	31.51	700	20	2250	30
280	9.18	200	20	2500	25

Table 6.6.15. Cooling power versus temperature for SiO2 on Si3N4 (NP/NP) on Ag back reflector using complementary Maxwell Garnett formula (v = 0)

T (K)	P (W/m^2)	SiO_2 Thickness (nm)	SiO_2 Fill Fraction (%)	Si_3N_4 Thickness (nm)	Si_3N_4 Fill Fraction (%)
300	69.55	900	20	2250	35
290	44.81	700	20	2250	30
280	24.28	200	20	2500	25

Table 6.6.16. Cooling power versus temperature for SiO2 on Si3N4 (NP/NP) on Ag back reflector using a generalized formula (v = 1)

T (K)	P (W/m^2)	SiO_2 Thickness (nm)	SiO_2 Fill Fraction (%)	Si_3N_4 Thickness (nm)	Si_3N_4 Fill Fraction (%)
300	67.18	900	20	2250	35
290	42.11	700	20	2250	30
280	21.42	200	20	2500	25

Table 6.6.17. Cooling power versus temperature for SiO2 on Si3N4 (NP/NP) on Ag back reflector using Coherent Potential formula (v = 3)

v	P (W/m^2)	Si_3N_4 Thickness (nm)	Si_3N_4 Fill Fraction (%)	SiO_2 Thickness (nm)	SiO_2 Fill Fraction (%)
0	7.22	2500	20	25	20
0 (complement)	-5.45	2500	20	25	20
1	8.35	2500	20	25	20
3	6.86	2500	20	25	20

Table 6.6.18. Cooling power at T = 270 K for Si3N4 on SiO2 (NP/NP) on Ag back reflector using different effective medium formulas

6.7 ANGLE AND POLARIZATION RESOLVED EMISSIVITY

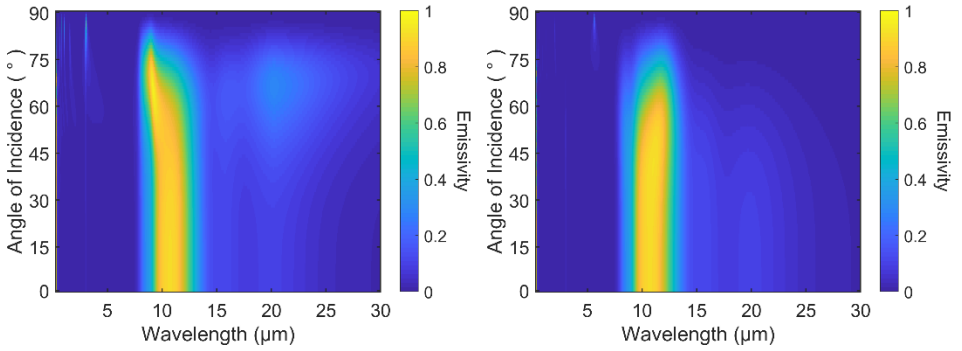

Figure 6.7.1. Spectral and angular resolved p-polarization (left) and s-polarization (right) emissivity profile for 2-layer laminate nanoparticle film radiative cooling structure optimized for 270 K at an ambient temperature of 300 K. Radiative cooling structure composed of Si_3N_4 (NP) on SiO_2 (NP) on Ag back reflector.

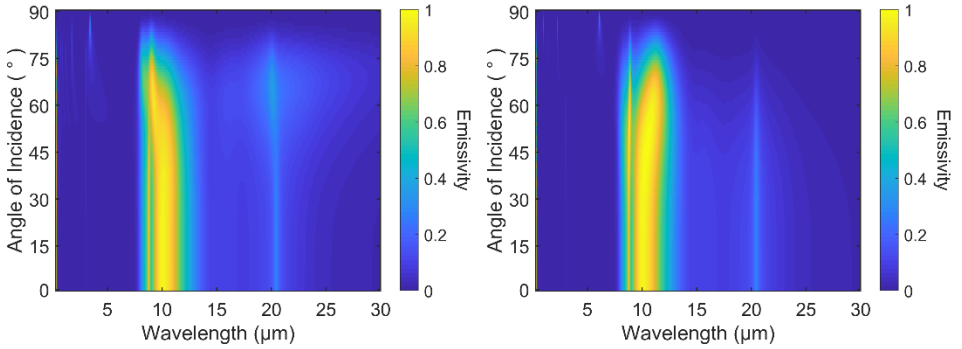

Figure 6.7.2. Spectral and angular resolved p-polarization (left) and s-polarization (right) emissivity profile for 2-layer laminate nanoparticle film radiative cooling structure optimized for 280 K at an ambient temperature of 300 K. Radiative cooling structure composed of SiO2 (NP) on Si3N4 (NP) on Ag back reflector.

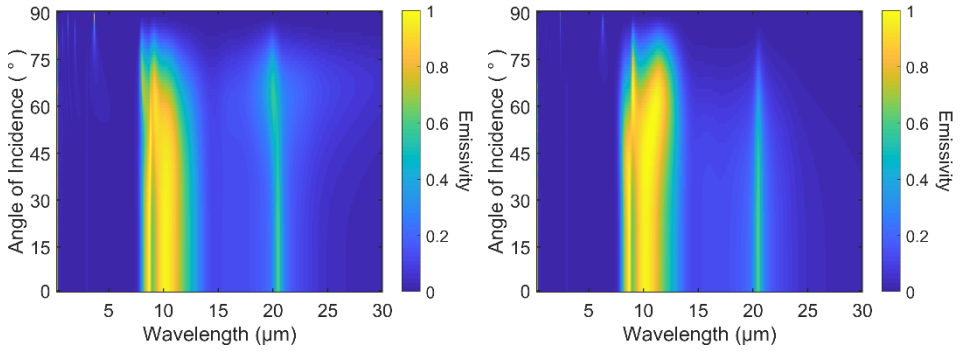

Figure 6.7.3. Spectral and angular resolved p-polarization (left) and s-polarization (right) emissivity profile for 2-layer laminate nanoparticle film radiative cooling structure optimized for 290 K at an ambient temperature of 300 K. Radiative cooling structure composed of SiO2 (NP) on Si3N4 (NP) on Ag back reflector.

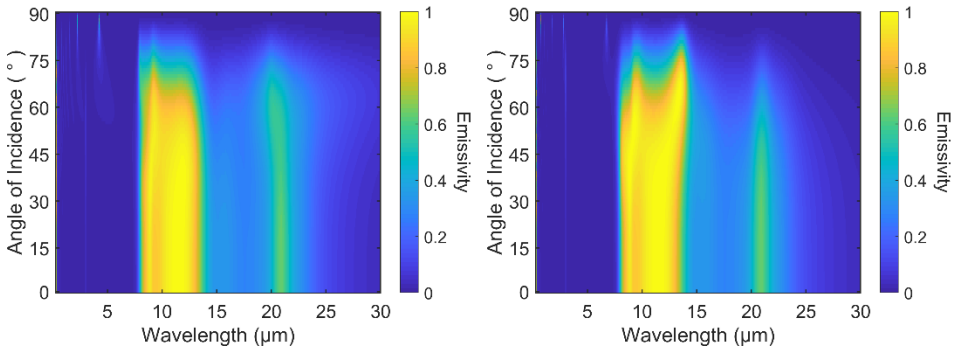

Figure 6.7.4. Spectral and angular resolved p-polarization (left) and s-polarization (right) emissivity profile for 2-layer laminate nanoparticle film radiative cooling structure optimized for 300 K at an ambient temperature of 300 K. Radiative cooling structure composed of SiO_2 (NP) on Si_3N_4 (NP) on Ag back reflector.

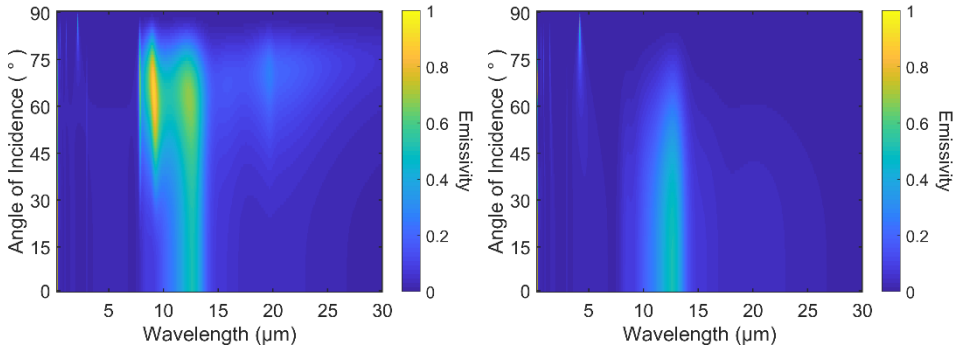

Figure 6.7.5. Spectral and angular resolved p-polarization (left) and s-polarization (right) emissivity profile for 2-layer dense solid thin film radiative cooling structure optimized for 270 K at an ambient temperature of 300 K. Radiative cooling structure composed of Si_3N_4 (Film) on SiO_2 (Film) on Ag back reflector.

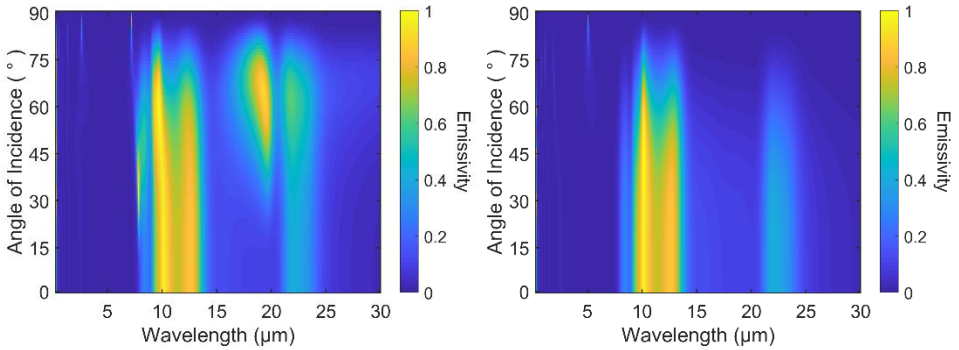

Figure 6.7.6. Spectral and angular resolved p-polarization (left) and s-polarization (right) emissivity profile for 2-layer dense solid thin film radiative cooling structure optimized for 280 K at an ambient temperature of 300 K. Radiative cooling structure composed of Si_3N_4 (Film) on SiO_2 (Film) on Ag back reflector.

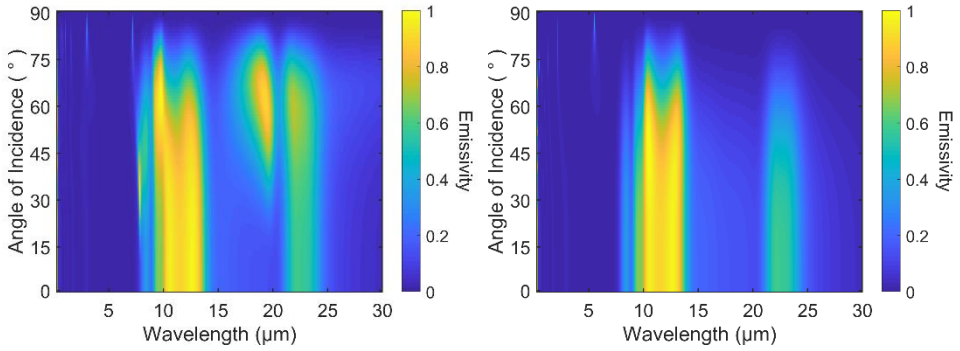

Figure 6.7.7. Spectral and angular resolved p-polarization (left) and s-polarization (right) emissivity profile for 2-layer dense solid thin film radiative cooling structure optimized for 290 K at an ambient temperature of 300 K. Radiative cooling structure composed of Si_3N_4 (Film) on SiO_2 (Film) on Ag back reflector.

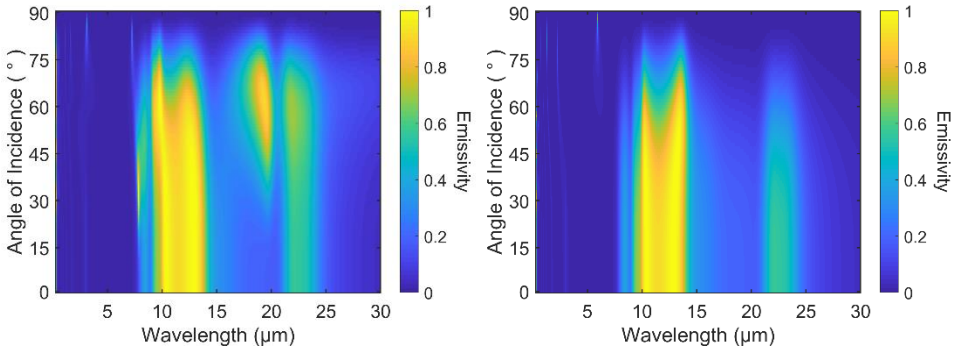

Figure 6.7.8. Spectral and angular resolved p-polarization (left) and s-polarization (right) emissivity profile for 2-layer dense solid thin film radiative cooling structure optimized for 300 K at an ambient temperature of 300 K. Radiative cooling structure composed of Si_3N_4 (Film) on SiO_2 (Film) on Ag back reflector.

6.8 EMISSIVITY FROM RELEVANT LITERATURE REPORTS

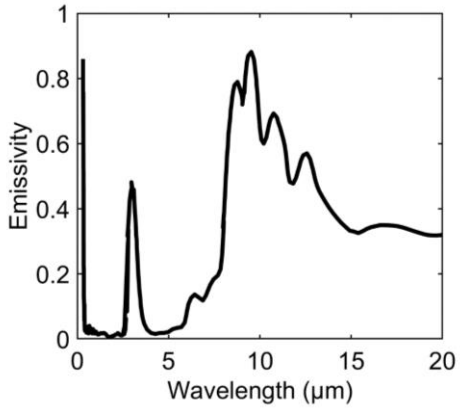

Figure 6.8.1. Digitized emissivity curve from a multilayer radiative cooler composed of seven alternating layers of HfO2 and SiO2. [From Raman *et al.*, Nature **515**(7528), 540 (2014).]

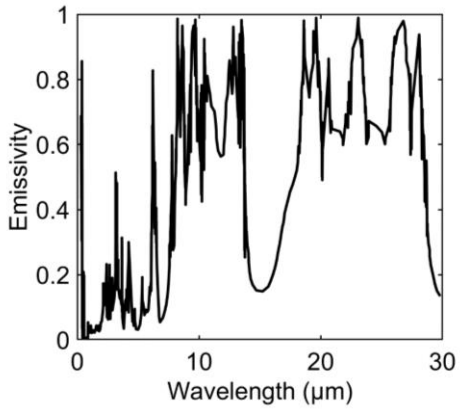

Figure 6.8.2. Digitized emissivity curve from a 2-layer 2D photonic crystal of SiC and quartz. [From Rephaeli *et al.*, Nano Letters **13**(4), 1457-1461 (2013).]

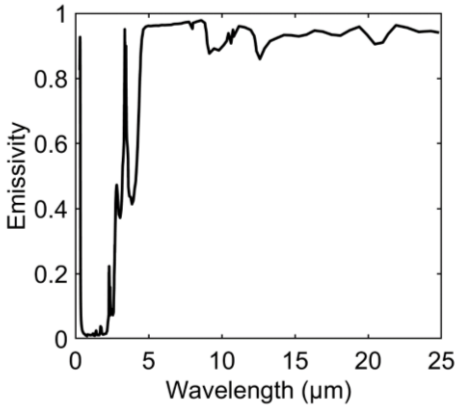

Figure 6.8.3. Digitized emissivity curve from a polymer-coated fused silica mirror. [From Kou *et al.*, ACS Photonics **4**(3), 626-630 (2017).]

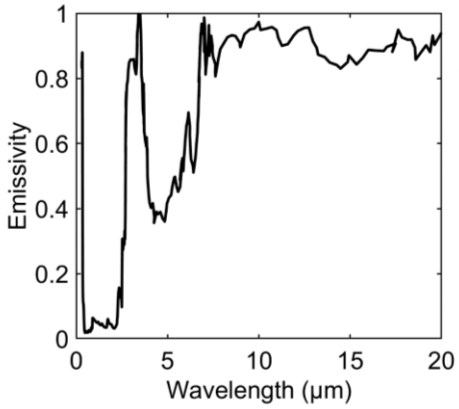

Figure 6.8.4. Digitized emissivity curve from a glass-polymer hybrid metamaterial. [From Zhai *et al.*, Science **355**(6329), 1062-1066 (2017).]

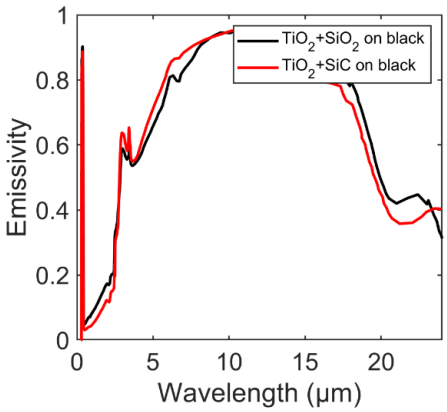

Figure 6.8.5. Digitized emissivity curve from nanoparticle-based double layer cooling structure on a black substrate. [From Bao *et al.*, Solar Energy Materials and Solar Cells **168**, 78-84 (2017).]

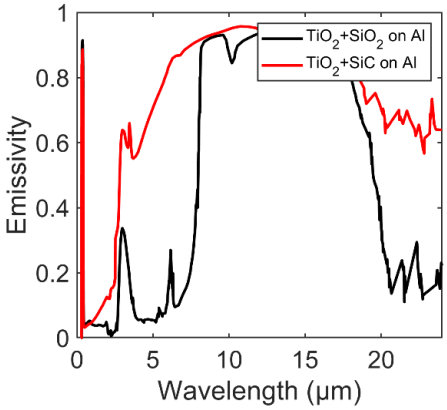

Figure 6.8.6. Digitized emissivity curve from nanoparticle-based double layer cooling structure on an aluminum substrate. [From Bao *et al.*, Solar Energy Materials and Solar Cells **168**, 78-84 (2017).]

Chapter 7

BROADBAND, OMNIDIRECTIONAL, AND POLARIZATION INVARIANT ABSORBERS

Wray, P. R.[†]; Eslamisaray, M. A.[†]; Nelson, G. M.; Ilic, O.; Kortshagen, U. R.; Atwater, H. A. Broadband, Angle- and Polarization-Invariant Antireflective and Absorbing Films by a Scalable Synthesis of Monodisperse Silicon Nanoparticles. *ACS Appl. Mater. Interfaces* 2022, 14 (20), 23624–23636. https://pubs.acs.org/doi/10.1021/acsami.2c03263

([†]P.R.W. and M.A.E. contributed equally)

ABSTRACT

Optically-induced magnetic resonances (OMRs) are highly tunable scattering states that cannot be reproduced in systems which only support electric resonances; such as in metals, lossy, or low-index materials. Despite offering unique scattering and coupling behavior, the study of OMRs in thin films has been limited by synthesis and simulation constraints. We report on the absorption and scattering response of OMR-based thin films composed of monodisperse crystalline silicon nanoparticles synthesized using a scalable nonthermal plasma growth technique and tractable simulation framework. The synthesis is solvent and ligand free, ensuring minimal contamination, and crystalline particles form with high yield and a narrow size distribution at close to room temperature. Using a scalable high throughput deposition method, we deposit random particle films, without the need of a solid host matrix, showing near complete blackbody absorption at the collective OMR. This is achieved using 70% less material than an optimized antireflective-coated crystalline silicon thin film. The film exhibits strongly directional forward scattering with very low reflectivity, thus giving rise to angle- and polarization-insensitive antireflection properties across the visible spectrum. We find that while commonly used effective medium models cannot capture the optical response, a modified effective medium accounting for multipole resonances and interparticle coupling shows excellent agreement with experiment. The effective permittivity and permeability are written in a mode and cluster resolved form, providing useful insight into how individual resonances and nanoparticle clusters affect the overall film response. Electric and magnetic-mode coupling show dramatically different behavior, resulting in uniquely different spectral broadening.

7.1 INTRODUCTION

The Maxwell-Garnett and Bruggeman theories show that through the proper mixture of vanishingly small uncoupled particles, an inhomogeneous medium could give rise to optical phenomena not seen in homogeneous single-phase media[230]. Particle mixtures of this type spawned some of the first examples of metamaterials[231], whose paradigm envision subwavelength, resonant -but independent and uncoupled-scatterers. For densely packed nanoparticles, there is a much broader set of emergent phenomena that occurs in *coupled Mie resonant* particles. Multiple works have shown that designing in this boarder space is indeed fruitful[182,232–234]. For example, optically-induced *electric* resonances (OERs) excited by localized surface plasmons have shown rich resonant and coupling behavior in deeply sub-wavelength metallic particles[235,236]. The resulting confined local fields and sensitivity to particle size and shape further broadened the scope of applications, such as in the fields of energy, sensing, and more[237–240]. More recently, researchers have recognized the potential of optically-induced *magnetic* resonances (OMRs), which are supported in sub-wavelength low-loss and high-index dielectric particles that enable access to scattering and absorption states not achievable in other particles, such as metals or low-index materials[241,29,27,106,47,242,243,23]. Correspondingly, crystalline semiconductors are target materials for producing OMRs in the visible and in particular, crystalline silicon (c-Si). The OMR arises from the creation of a strong circulating field *within the core* of the particle and can have a large quality factor. This resonance is spectrally tunable by particle size, exists in low-loss spectral regions, and has distinctly different behavior compared to OERs[244–260]. Therefore, OMRs offer the potential to further the applications of particle mixtures by expanding the state space and material library for achieving emergent phenomena. Despite the unique properties, most experimental research on OMR particles has been limited to single particle characterization or nanostructures synthesized by top-down lithographic techniques[249–253]. This is due to a synthesis bottleneck arising from constraints in synthesizing crystalline semiconductor nanoparticles in the OMR regime (around 80 nm diameter). Furthermore, theoretical considerations of particle mixtures have largely neglected the existence of OMRs, which causes non-negligible inaccuracies in previously reported theories due to the strong resonant features and unique coupling behavior of the OMR[152,214,230,261,262].

To explore further the potential of nanoparticle based effective media, we must advance our conceptual framework for the scattering and absorption response of nanoparticle films to allow for the features of OMRs. To address this, we report the synthesis and optical scattering and absorption characteristics of an angle and polarization-invariant resonant nanoparticle-based film reliant on the OMRs found in appropriately sized c-Si nanoparticles. The nanoparticles are fabricated using a dusty plasma synthesis technique capable of making highly monodispersed c-Si particles. By coupling a simple and scalable spray deposition method to the plasma

nanoparticle synthesis, a fractal-like random film is formed in an air host matrix, which is particularly suited for making strong absorbers using little material[131,167,169,171,263,264]. To understand the resulting emergent behavior, we develop an effective medium theory which accounts for both the fractal-like film deposition and a complete representation of the coupled particle resonance characteristics. The OMR nanoparticle film scattering properties are shown to be dramatically different compared to both conventional planar film counterparts and predictions from classical effective medium theories.

Nonthermal plasmas are widely used for synthesis of covalently bonded groups IV and III-V semiconducting nanocrystals owing to their nonequilibrium environment which enables the nucleation, growth, and crystallization of high melting point materials from gas phase precursors at room temperature[197,265–269]. While in the plasma, particles above a certain minimum size are negatively charged[270–272], which suppresses particle agglomeration[273,274]. Upon exiting the plasma, particles can be accelerated through a nozzle to form thin films via impaction onto a substrate[275,276]. The scalability of this single step, ligand-free, and high yield deposition technique has recently been demonstrated by Firth et al[277]. Nevertheless, the application of dusty plasmas has been limited to synthesis of small nanocrystals (mostly in a size range of 2 to 10 nm diameter), owing to the short residence time of particles in the plasma discharges. Bapat et al[278]. were the first to report the possibility of producing monodispersed Si nanocrystals of ~ 35 nm by operating the synthesis plasma in a regime where the particle residence time in the plasma is extended through electrostatic particle trapping. Once particles leave the trap, they travel through a plasma zone in which the plasma is filamentary constricted. We expand this work to a new size regime using the same discharge concept to produce resonant Si nanocrystals of over 80 nm in diameter by the trapping mechanism and residence time.

The impaction deposition method produces random fractal-like films where each particle is connected to *at least one nearest neighbor* in an air host matrix[131,167,169,171,263,264]. Particle clusters can exhibit strong near-field coupling, leading to substantially increased absorption and anti-reflection, even in the limit of vanishing inclusion fill fraction[131,167,169–171,263,264]. Absorption at longer wavelengths comes as an added benefit to the creation of the shorter wavelength unit cell as long as the material and spatial statistical properties remain unchanged[167]. Therefore, the upper and lower spectral absorption limit is dictated by the inclusion (i.e., particle design) and cluster size, highlighting the desire to control both[167].

In defining a homogenization scheme for such a film, it is important to account for particle effects traditionally assumed to be negligible, such as OMRs, and general higher-order excitations. Furthermore, the theory must account for properties unique to the fractal-like clusters which exhibit strong near-field coupling even at low fill fractions and lack long range

order[171,172,219,279–282]. This is exacerbated by the fact that OMR coupling is distinctly different from electric dipole coupling. Finally, it is also important to develop a theory which gives rise to a physical understanding of how these features shape the overall electromagnetic response. Parameter retrieval methods, such as S-parameter retrieval, can accurately model measured data but otherwise provides little physical insight[283]. We attempt to address these issues by formulating a parameter retrieval method based on the known physics of the constituent particles and deposition methods. The theory is built upon previous research relating particle multipoles to film-level effective induced electric and magnetic current densities[284]. However, their theory does not account for the coupling between OER particles, OMR particles, or between OERs and OMRs. Our primary contribution to expanding the homogenization approach is to propose a method to address this for the system stated above.

7.2 RESULTS AND DISCUSSION

Si nanocrystals that support OMRs were synthesized with an average size of 81.6 nm and a standard deviation of 1.2 nm via a nonthermal plasma process as described in detail elsewhere[278,285]. A schematic of the flow-through reactor used in this study is shown in figure 7.2.1a. The primary gas feed, a mixture of silane and argon, enters through the top of the 38 mm-outer diameter glass reactor tube. A plasma is generated in the reactor tube by applying 200 W of radio frequency (RF) power at 13.56 MHz through a copper ring electrode. At low silane flow rates and high RF powers, the plasma operates in a regime where the discharge is constricted. In this regime, the plasma consists of two regions: a diffuse region that extends a few centimeters upstream of the RF electrode, and a striated, high-luminosity plasma filament that rotates close to the wall of the tube between the RF electrode and the lower grounded metal flange. Previous laser scattering studies[278] have shown that the particle formation begins in the diffuse plasma and particles are trapped in electrostatic potential traps formed upstream of the powered electrode. This trapping mechanism enables the growth of the initial amorphous nanoparticles to sizes as large as a few hundred nanometers. The filamentary plasma provides a significantly higher plasma density and thus sinters the particles by annealing them to temperatures much higher than the gas temperature resulting in formation of single crystals. Figure 7.2.1b shows a representative bright-field transmission electron microscope (TEM) image of a particle collected in the deposition chamber. The nanoparticle is nearly spherical, as suggested by the thickness fringes and can be verified by tilting the particles to different orientations. The particle is a single crystal as verified by the selected area diffraction pattern (figure 7.2.1c). Figure 7.2.1d represents the nanoparticles highly monodisperse size distribution, obtained by image analysis of over 500 nanoparticles collected on TEM grids. The average particle size could be adjusted via changing the argon flow rate and therefore the particle residence time in the plasma reactor. The particle diameters in this study (between 79 to 86 nm) correspond to OMR spectral peaks from 417 to 433 nm, respectively. The particle size averaged OMR spectral peak is 420 nm, according to Mie theory. The spectral deviation of the OMRs as a function of particle size is considered negligible with respect to the spectral broadening effects of particle coupling (more detail below). Therefore, particles from this reactor can be regarded as supporting comparatively the same OMR. Random films of OMR-supporting particles are formed immediately downstream of the synthesis reactor via impaction of the nanocrystals onto the substrate[276,277]. Using this technique, we deposited an approximately 550 nm thick, random film with a 30% volume fill fraction on a 1 mm thick soda-lime glass substrate for optical characterization. The deposition parameters provide an optical thickness that exhibits near blackbody behavior at the OMR, discussed below, without losing characteristic spectral features from an overly large optical depth. This is necessary for understanding the physics behind the nanoparticle film scattering response. Figure 7.2.1e shows a representative top-view (left) and

cross-sectional (right) scanning electron microscope (SEM) image of the film, showing a uniform coverage of particle clusters.

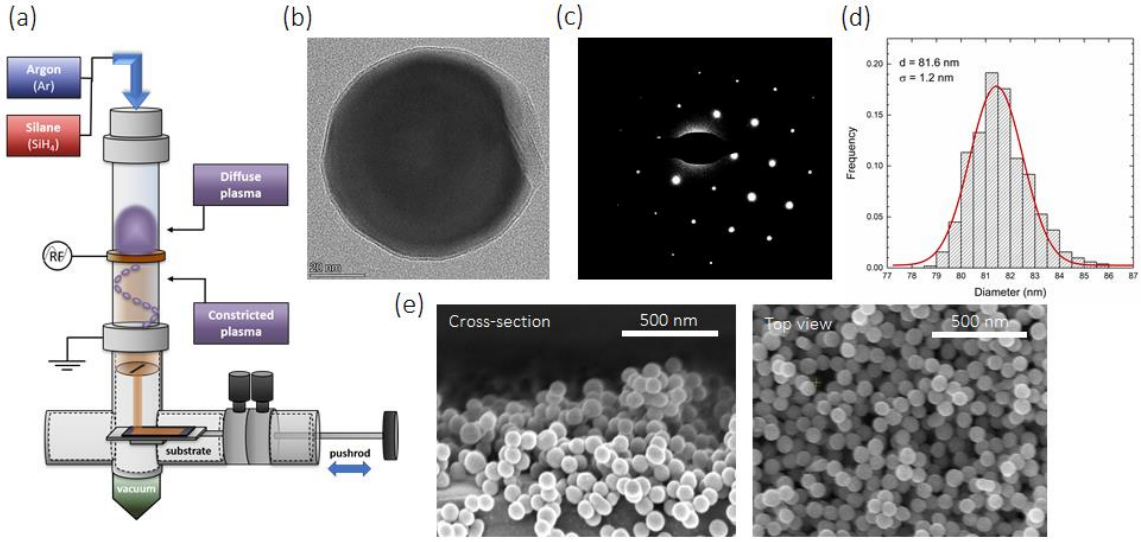

Figure 7.2.1. Particle characteristics from the plasma reactor. (a) Schematic of the flow-through nonthermal plasma reactor showing the diffuse and filamentary discharge regions. (b) Representative bright-field TEM image of a single nanocrystal synthesized in the reactor. (c) Electron diffraction pattern of a silicon nanocrystal aligned with the electron beam. (d) Size distribution of OMR supporting nanocrystals, showing an average diameter of 81.6 nm with a standard deviation of 1.2 nm. (e) Cross-sectional and top-down SEM image of the nanocrystal film deposited on glass with a fractal-like structure and an average thickness of 550 nm.

To study the absorption and scattering response of this film, angle, polarization, and wavelength resolved reflection and transmission measurements of the film were taken using an Agilent Cary 5000 UV-Vis-Nir with a Universal Measuring Attachment (UMA). Diffuse scattering was shown to be negligible (see the supplementary information for more detail), so absorption was calculated as $A = 1 - R - T$, where R, T are the reflection and the transmission of the film, respectively. Figure 7.2.2a shows the film polarization averaged transmission (black), reflection (blue), and absorption (red) spectra near normal incidence (6 degrees). The film shows a clear absorption peak of 96% at the size distribution averaged particle OMR (420 nm) accompanied by a broadened absorption tail emanating from the OMR and progressing out to longer wavelengths. Interestingly, the absorption broadening is almost exclusively due to interparticle coupling altering the behavior of electric dipoles while the magnetic dipoles remain comparatively unchanged. This effect is discussed in detail later in this section. For now, we compare the absorption response of the film to uncoupled particles simulated using the Mie solution for a particle suspended in free space. Simulated nanoparticle sizes are based on the size

distribution from figure 7.2.1d and the size distribution averaged absorption efficiency is then overlaid as a reference (dashed green). The uncoupled particle absorption is clearly peaked at the OMR which is also consistent with the film's overall absorption peak. This supports the concept that the OMR remains intact in the particle film. The uncoupled particle absorption also shows substantially less spectral broadening at longer wavelengths with respect to the film. This supports the propensity for clusters to broaden absorption, which we later show is primarily an electric dipole effect. The film also has strikingly broadband antireflection everywhere below 2.2% at near normal incidence. This indicates almost complete coupling of the incident field leading to absorption limited by optical depth. Interestingly the antireflection is achieved despite the strong interactions between particles and the incident field. This is in direct contrast to the predictions of the Maxwell-Garnett and Bruggeman formulas, which predict antireflection, due to a weak a interaction with the incident field. These results are further discussed when introducing the effective medium model later in this section.

To understand how this film compares to an optimized thin film equivalent, figure 7.2.2b compares the absorption response of the measured particle film at normal incidence to that of a simulated dense homogeneous thin film stack that has been optimized using an antireflection (AR) layer to maximize absorption centered at 420nm. The thin film stack is composed of 152nm thick silicon nitride (SiN) on top of 550nm c-Si on a 1mm glass substrate. We find that though the thin film stack can be optimized to mimic the absorption peak at 420nm, it cannot mimic the spectral broadening in absorption. Furthermore, the antireflection of the thin film stack is less broadband and overall, around 10x worse compared to the particle film when averaged over the measured spectral range. Figure 7.2.2c integrates the angle and polarization absorption response of both the measured particle film (solid red) and optimized thin film stack (dotted red). The overall absorption is then normalized to that of an ideal blackbody. Comparing the entire polarization, angle, and specular range, the particle film is over 38% more absorbing than a c-Si slab of the same thickness; even after enhancing the c-Si slab absorption by adding an optimized SiN coating on top. Furthermore, the enhanced performance in absorption of the particle film is accomplished using 70% less Si than the thin-film counterpart, does not require a top coating, and is overall 78% lighter compared to the thin film stack.

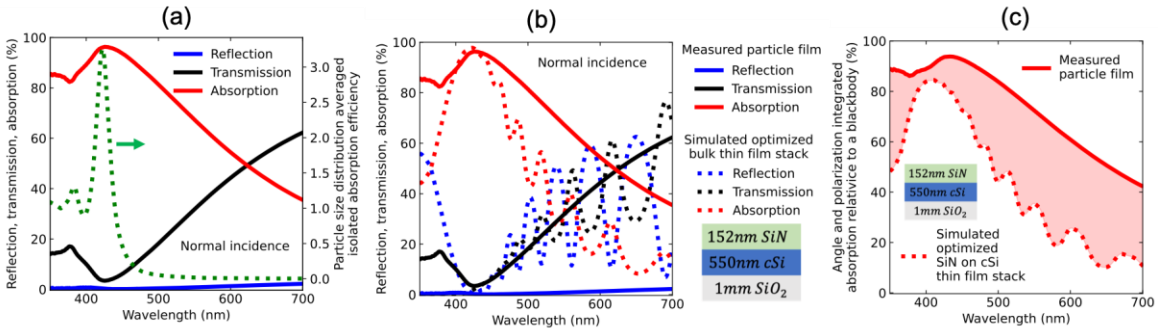

Figure 7.2.2. Comparison of the measured resonant nanoparticle film to an optimized homogeneous bulk thin film stack. (a) Measured transmission (black), reflection (blue), and absorption (red) response at normal incidence from a 550 nm thick particle film with a 30% volume fill fraction on 1 mm of soda-lime glass. The response is polarization averaged at an incident angle of 6 degrees. The green dashed curve and right y-axis plots the particle size averaged absorption efficiency of isolated c-Si particles in free-space, calculated using Mie theory. The average was weighted based on the particle size distribution given in figure 7.2.1d. (b) Comparison of the transmission (black), reflection (blue), and absorption (red) response at normal incidence from the measured particle film (solid lines) to a simulated bulk homogeneous thin film stack of 152nm SiN on 550nm cSi on 1mm of glass (botted lines). The bulk thin film stack was optimized to maximize absorption at 420nm. (c) Angle and polarization integrated absorption relative to a perfect absorbing blackbody of the measured particle film (solid, red) and the simulated optimized bulk homogeneous thin film stack (red, dashed). The red shaded area highlights the absorption enhancement achieved when transitioning from a thin film to resonant particle-based absorber.

To understand the effect of polarization and angle dependence, figure 7.2.3 plots the measured angle, polarization, and wavelength resolved absorption, reflection, and transmission response of the particle film. Similar to a blackbody, figure 7.2.3a shows near complete absorption at the OMR with strong angle insensitivity up to angles of incidence as steep as 70 degrees and almost no change in behavior as a function of incident polarization. The top two plots in figure 7.2.3a show the angle integrated absorption of the nanoparticle film relative to a black body over the same angular and spectral range. At the OMR, the nanoparticle film absorption reaches 96% of the absorption of an ideal blackbody. Figure 7.2.3b shows the particle film has antireflective properties for both polarizations. The film also shows no well-defined Brewster angle and only slight polarization splitting at large incident angles. The particle film's absorption is optical depth-limited throughout the measured spectral range, as evident by the fact that $T \approx 1 - A$ (figure 7.2.2c).

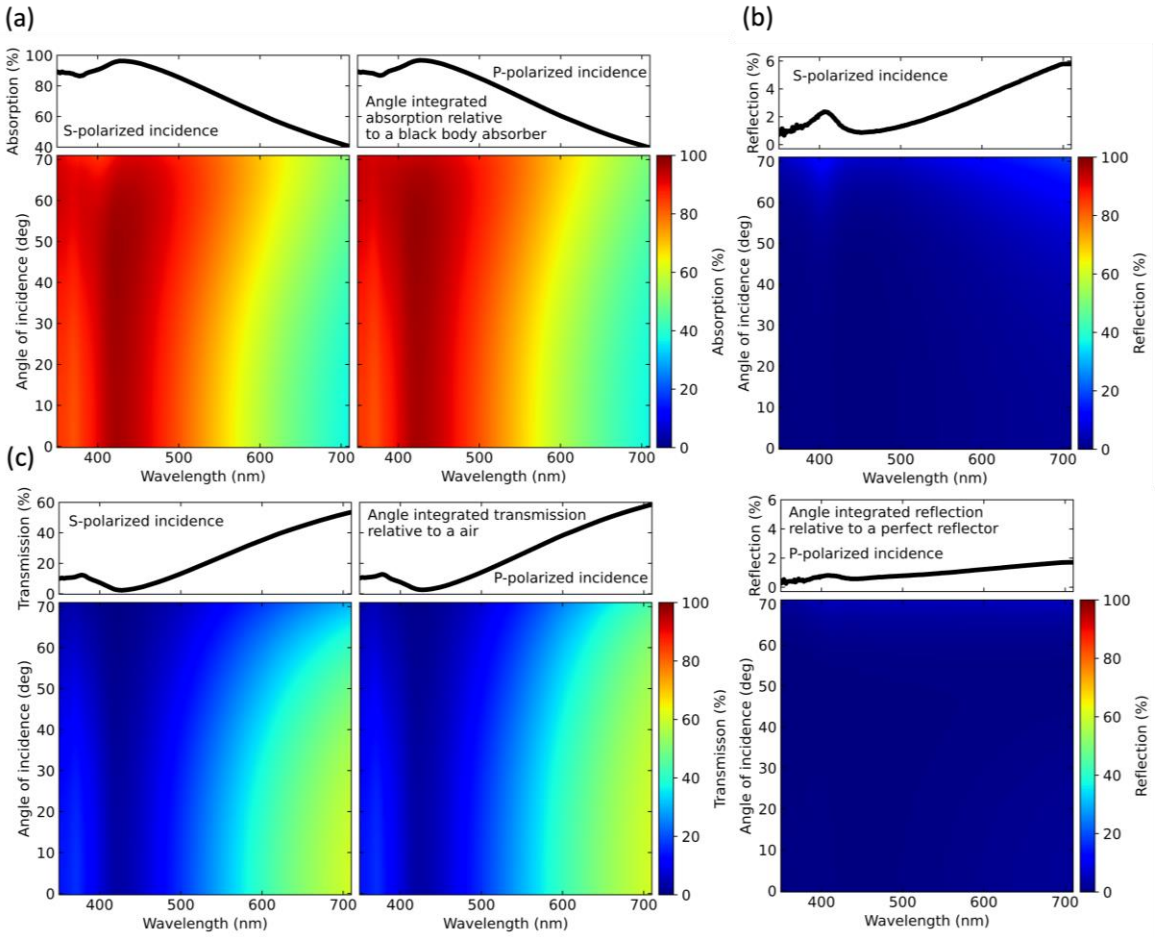

Figure 7.2.3. Angle, wavelength, and polarization resolved absorption, reflection, and transmission response of a 550 nm thick c-Si OMR supporting particle film on top of a 1 mm thick soda-lime glass substrate. (a) The bottom color maps show the film's absorption response as a function of wavelength (x-axis), angle of incidence (y-axis) and s- (left) and p-polarization (right). The corresponding top figures are the angle integrated absorption of the respective bottom color map, normalized to an ideal black body. (b) The reflection response of the particle film for s- (top) and p-polarization (bottom). In both cases the angle integrated reflection relative to a perfect reflection is shown above the corresponding color map. (c) The film's transmission response for s- (left) and p-polarization (right) with the angle integrated transmission relative to air shown above the respective color map.

Given negligible scattering pathways, the film's response can be described by a homogenized field coherent to the specular direction. Thus, a properly chosen effective medium can be used to generate a valid description of the optical response through the transfer-matrix method. The goal of our proposed effective medium method is to accurately model the experimental data in figure 7.2.3 using known film properties from figure 7.2.1. Furthermore, the method is intended to provide insight into how particle coupling behavior dictates the film's optical behavior. This

includes the effect of variations in local particle density, interparticle coupling, and the differences between electric and magnetic-type multipole coupling. Our approach generalizes the framework previously outlined[284] to account for particle coupling and leverages the result that coupling effects in a fractal-like film are localized to clusters that are otherwise electromagnetically topologically disconnected[167,263,264]. Our overall concept is that coupled particles create effective particles, which then create effective media. Cluster distributions are first simulated using a Monte Carlo event-driven 3D particle aggregation model. The goal of this model is to accurately represent the particle packing behavior that characterizes the fractal-like aggregates generated using the spray method described above. This approach has been well studied for accurately modeling films of this type[162,173,286]. The particle sticking coefficient, which scales the probability a particle will stick to another particle when coming into contact, was determined by ensuring the average volume fill fraction of 100 sampled clusters, with the same radii distribution as shown in figure 7.2.1d, matched the experimental value of 30%. We found cluster sizes varying from 4 to 20 particles with equal probability provided a good fit to the experimental data and use the sampled cluster distribution to study how local variations in packing fraction and cluster size impacts the overall film response. Consistent with the definition that a homogenized field is the particle orientation averaged electromagnetic response of the film, our effective medium is ultimately determined by the Monte Carlo integration of samples to find the average of the electromagnetic response from each cluster. Therefore, the dependence on sample number can be quantified by the uncertainty in the sample mean and convergence to the true homogenized film is guaranteed. The supplementary information shows 100 samples was sufficient to accurately reproduce the data in figure 7.2.3. Once clusters are generated, their electromagnetic response is simulated under plane wave excitation using the extended boundary technique; also known as the null-field method or generalized Mie theory[105,259,287–289]. Plane wave excitation is consistent with particle clusters being uncoupled[284] and is analogous to clusters interacting only with the incident excitation under the scattered field formalism. Using generalized Mie theory to solve the coupling problem allows for an exact solution, meaning all coupling effects within the cluster are properly represented[287]. This approach is analytical, provides an intuitive definition of particle-driven electromagnetic behavior as atom-like multipoles, and can be between one to two orders of magnitude computationally faster compared to full-wave techniques[259,287,290–292]. The overall electromagnetic response of a cluster is then transformed into a single expansion of multipoles that completely accounts for the collective behavior of all particles within the cluster, including interparticle coupling. Once transformed into a single expansion, the collective response can be viewed as coming from an "effective particle." This provides a method of studying the overall cluster's electromagnetic properties in terms of multipoles which are driven by the collective as opposed to single particle multipoles inside of the collective. Under this framework, we can study how individual particle resonances dictate the resulting collective behavior. The transform is done by

re-expanding the multipole solution of each individual particle in a cluster about the cluster center, using the addition theorem for spherical harmonics[287,293]. After each sampled cluster is written as an effective particle, the effective permittivity and permeability can be written, in terms of the effective particles, in a form that is parameterized by incident polarization (ν), cluster sample number (l), cluster multipole order (n), and cluster multipole type (magnetic, $p = 0$, or electric, $p = 1$). This is expressed in compact notation as

$$\begin{aligned}
\epsilon^{TE}_{eff,lnp}(\theta_i) &= \frac{1}{2LN} + \frac{i\gamma_l}{L}\sum_{m=0}^{n} c^{TE}_{sca,l,nmp}\left(\mathbb{t}^{+}_{nmp}(\theta_i) - \tan^2(\theta_i)\,\mathbb{t}^{-}_{nmp}(\theta_i)\right)\\
\epsilon^{TM}_{eff,lnp}(\theta_i) &= \frac{1}{2LN} + \frac{i\gamma_l}{L}\sum_{m=0}^{n} c^{TM}_{sca,l,nmp}\,\frac{\mathbb{t}^{-}_{nm(1-p)}(\theta_i)}{\cos^2(\theta_i)}\\
\mu^{TE}_{eff,lnp}(\theta_i) &= \frac{1}{2LN} + \frac{i\gamma_l}{L}\sum_{m=0}^{n} c^{TE}_{sca,l,nmp}\,\frac{\mathbb{t}^{-}_{nmp}(\theta_i)}{\cos^2(\theta_i)}\\
\mu^{TM}_{eff,lnp}(\theta_i) &= \frac{1}{2LN} + \frac{i\gamma_l}{L}\sum_{m=0}^{n} c^{TM}_{sca,l,nmp}\left(\mathbb{t}^{+}_{nm(1-p)}(\theta_i) - \tan^2(\theta_i)\,\mathbb{t}^{-}_{nm(1-p)}(\theta_i)\right)
\end{aligned} \qquad 7.2.1$$

where $c^{\nu}_{sca,nmp}$ is the effective particle's complex scattering coefficient, L is the total number of samples, and N is the largest multipole supported by the cluster. The incident field's polarization is written explicitly where $\nu = TE$ denotes transverse-electric polarization and $\nu = TM$ denotes transverse-magnetic polarization. The angle of incidence is θ_i. $\gamma_l = 3ff_l/2x_l^3$ is weight factor for the l'th effective particle, that is based on that cluster's inclusion volume fill fraction (ff_l) and size parameter ($x_l = kr_l$). Here, r_l is the radius of the smallest circumscribing sphere encapsulating all particles in the cluster and $k = \frac{2\pi}{\lambda}$ is the free space wavenumber. Therefore, the weight factor can be used as a measure of a cluster's geometric properties that also has relevance to the cluster electromagnetic response. The basis function, $\mathbb{t}^{\pm}_{nmp}(\theta_i) = \tau_{nmp}(0) \pm \tau_{nmp}(\pi - 2\theta_i)$, is a superposition of the Mie polar angle functions, $\tau_{nmp}(\theta_i)$, and describes the angular dependence of the film permittivity and permeability based on an effective particle multipole mode order and type. The total effective permittivity and permeability can then be written by superposition as $\epsilon^{\nu}_{eff} = \sum_l \sum_n \sum_p \epsilon^{\nu}_{eff,\,lnp}$ and $\mu^{\nu}_{eff} = \sum_l \sum_n \sum_p \mu^{\nu}_{eff,\,lnp}$. Further detail about deriving the generalized Mie solution and the effective medium approach described above can be found in the supplementary information. The ability to linearly decompose the permittivity and permeability into components associated with cluster type, mode order, and mode type is a notable benefit of this method, providing a tractable approach for describing and understanding how these variables give rise to the overall response. Finally, the effective medium is used to simulate the particle film's reflection, transmission, and absorption response using the transfer matrix method; accounting for non-unity permeability.[294]

A schematic of how the effective medium is formed based on the method described above is shown in figure 7.2.4a. The modeled effective medium film was 550 nm thick on a 1 mm glass substrate. Thickness was determined from cross-sectional SEM images of the measured particle film. Figure 7.2.4b shows the angle, polarization, and wavelength resolved absorption of the simulated film. Comparing this to the measured data in figure 7.2.3a, strong agreement is seen indicating the ability to represent the response of the measured film under all input excitations. Corresponding plots for reflection and transmission are shown in the supplementary information and show agreement with experimental data in figures 7.2.3b and 7.2.3c, respectively. Figure 7.2.4c shows the resulting polarization averaged reflection, transmission, and absorption response from simulation (dashed) compared to the measured data (solid) at 6 degrees incidence. We see good agreement throughout the entire spectral range showing the ability to properly represent both the OMR spectral peak and the resulting broadening emanating from that resonance. Reflection and transmission curves confirm an optical depth limited system. Figure 7.2.4d is a Brewster plot at the OMR demonstrating that the effective medium agrees with measurements, including the lack of a well-defined Brewster effect and minimal polarization splitting.

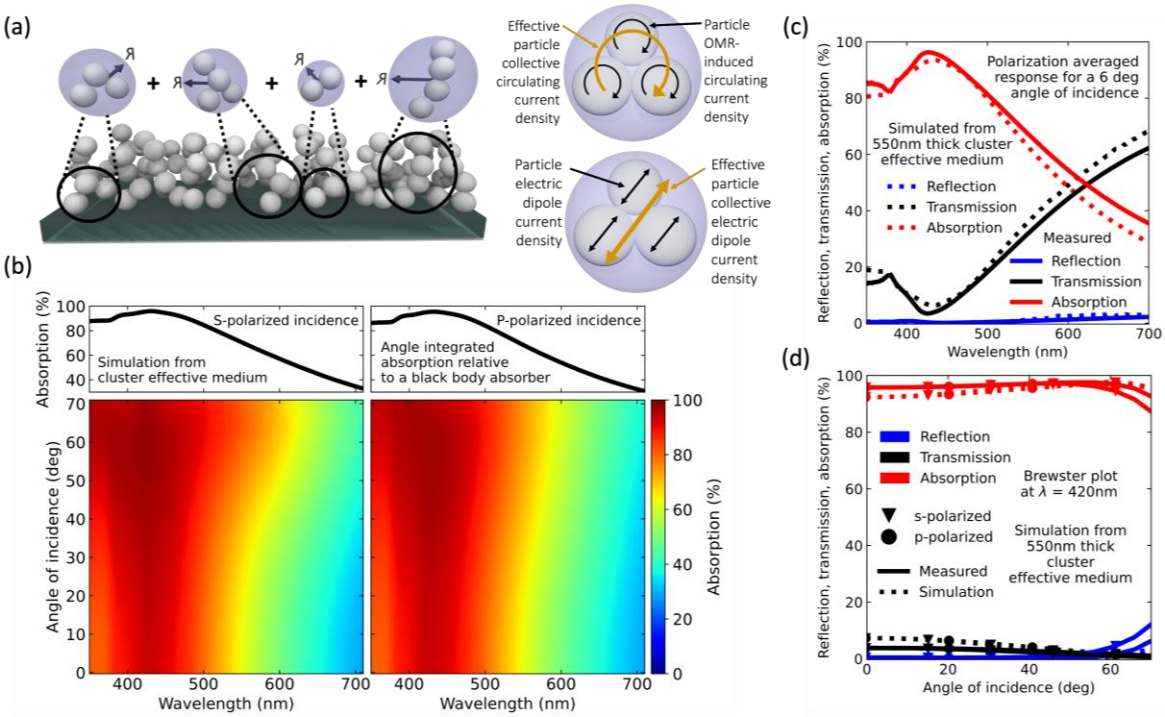

Figure 7.2.4. Comparison of the measured absorption, reflection, and transmission from figure 7.2.2 to the calculated response from the transfer matrix method, using the proposed cluster-based effective medium. (a) Pictorial description for calculating the effective medium by simulating particle clusters, then representing them as effective uncoupled particles in a random film. (b) An analogous color map to the one shown in figure 7.2.2a, but for the simulated film's response. (c) Polarization averaged absorption (red), reflection (blue), and transmission (black) spectral response at 6 degrees incidence of the simulated film (dashed) and measurement (solid). (d) Brewster plot of the absorption (red), reflection (blue), and transmission (black) response at the OMR resonance (λ = 420 nm) for the simulated film (dashed) and measurement (solid). S- and p-polarization are denoted with a downward triangle and circle marker, respectively.

To further understand how particle resonances and interparticle coupling dictate the effective medium response, figure 7.2.5 plots the effective permittivity and permeability at normal incidence. The constitutive parameters are then decomposed in terms of mode order and cluster weight. figure 7.2.5a shows that the particle film's effective permittivity (blue) is primarily a result of the first-order electric dipole (ED) mode (orange) present in the effective particles, with a small contribution from all other terms (green). The spectral shape of the collective ED clearly shows that its spectra is sensitive to interparticle coupling. To show how the response is different compared to a uniform dispersion of uncoupled particles, we overlay the effective permittivity according to the original method (dashed black), which does not account for particle coupling.[284] The full width at half maximum of the imaginary part of the cluster-based effective permittivity encompasses 65% of the spectral range whereas the uniformly dispersed and uncoupled particle

case encompasses only 16% of the spectral range. The peak of the imaginary part in the cluster-based effective permittivity is also approximately half of the uncoupled counterpart, leading to broadband antireflection. This reduction is a direct consequence of energy balance. When coupling is neglected, the energy extracted from the incident field is non-physical and overcounted due to the assumption of nonoverlapping cross sections between particles. In reality the clustered film has significant overlapping cross sections and near-field coupling transfers the energy between particles[259,295]. Figure 7.2.5b shows that the particle film's effective permeability (blue) is composed primarily of the first-order magnetic dipole (orange) with the contribution from other terms shown in green. The first-order magnetic dipole is an OMR excited *in the sampled effective particles*. This means the individual excitations of coherently-coupled particles within a cluster are working together to create a strong *collective* OMR. An illustration of this effect is shown on the right-hand side of figure 7.2.4a. We can interpret the circulating fields from the effective particles' OMR as a circulating current density in the film creating an induced magnetization[257,284]. The permeability of uncoupled OMR particles is shown as a reference (dotted, black). Interparticle coupling creates a staggering 6-fold reduction in the peak imaginary permeability, compared to the uncoupled counterpart. This is primarily because the uncoupled particle has an OMR with an optical cross-section that is much larger than the particle's geometric cross-section. To understand better how the collective ED is shaped through interparticle coupling, figure 7.2.5c decomposes the effective permittivity based on cluster weight factor. Three distinct regimes of spectral broadening are identified and shown to be associated with cluster size. The regimes are large clusters of 15 to 20 particles ($\gamma_l \leq 4$, orange), to mid-size clusters of 10 to 15 particles ($4 < \gamma_l \leq 7$, green), to smaller clusters of 4 to 9 particles ($\gamma_l > 7$, red). The small dense clusters most closely maintain the spectral features of uncoupled particles. Progressing to larger particle chains leads to absorption broadening and red shifting of the absorption resonance, as shown by the dashed black arrow. Figure 7.2.5d decomposes the effective permeability based on cluster weight factor, using the same three regimes as figure 7.2.5c. We see the same trend of a reduced amplitude and red-shifted resonance with increasing cluster weight; though the effect is substantially less pronounced. This further affirms that OMR for each nanoparticle is robust to coupling-induced changes in spectral features.

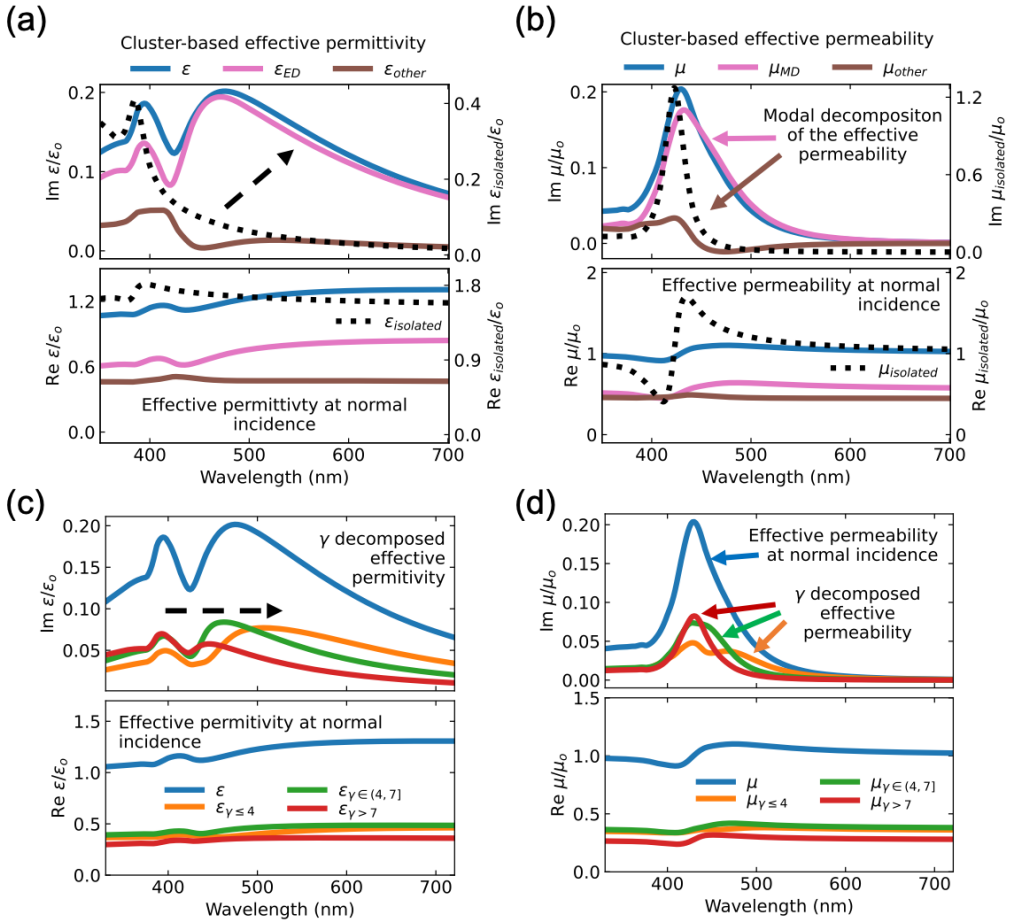

Figure 7.2.5. Analysis of the simulated cluster-based effective relative permittivity and permeability as a function of mode order, n, and scale parameter, γ. (a) Decomposition of the film's effective permittivity (blue) into the contribution from the electric-dipole mode (pink) and all other modes (brown). The effective permittivity assuming uncoupled particles that are homogeneously dispersed in air (dotted, black) is overlaid for references. The black dashed arrow highlights spectral broadening when transitioning from an uncoupled particle film to a clustered film. (b) Decomposition of the film's effective permeability (blue) into the contribution from the magnetic-dipole mode (pink) and all other modes (brown). The effective permeability assuming uncoupled particles (dotted, black) is overlaid for references. In both (a) and (b) cluster-based values are measured based on the left y-axis and uncoupled values are measured according to the right y-axis. The respective scales are different to compare spectral shape more clearly. (c) Decomposition of the film's effective permittivity (blue) into the response from clusters with scale parameters above 7 (red), between 4 to 7 (green), and below 4 (orange). The black dashed arrow outlines the trend of absorption broadening and red-shifting as a function of decreasing scale parameter. (d) Decomposition of the film's effective permeability based on the same scale parameter ranges as (c). In all cases, the imaginary part of the complex relative permittivity or permeability is the top figure. The real part is the bottom figure.

Next, we study how interparticle coupling alters the modal response of individual particles within the effective particles that make up the particle film. Figure 7.2.6 compares the magnitude of the magnetic and electric dipole modes of uncoupled particles (top left and right, respectively) to that of particles within the sampled clusters (bottom left and right, respectively). The modal response for an individual uncoupled particle was calculated using the Mie solution to a single particle suspended in free space and far away from any other inhomogeneity. As detailed above, the modal response of a particle in a sampled cluster is found using generalized Mie theory. The solution for each particle is then expanded about the cluster's origin. This technique allows for an effective particle modal response to be described by the coherent superposition of the modes from the re-expanded individual particles making up the cluster. This enables a direct study on how each individual particle affects the effective particle response. In all cases, the mode magnitudes are shown as a function of wavelength on the x-axis and are ordered according to particle size on the y-axis. The color scale plots the mode magnitude normalized to the particle's size parameter. The magnetic dipole mode in each coupled particle clearly maintains a similar spectral shape to the uncoupled counterpart with the same radius. When comparing the coupled and uncoupled responses, a similar trend can be seen in terms of spectral shift and average magnitude with increasing particle size. On the other hand, the electric dipole mode of each coupled particle is substantially altered by the effect of interparticle coupling on the single particle level. The spectral shape of the coupled electric dipole mode is substantially broadened with little resemblance to the uncoupled counterpart; showing no clear spectral trend as a function of particle size. The drastic difference between the electric and magnetic dipole modes as a result of interparticle coupling clearly shows models which only consider the film from the viewpoint of pure dipole expansion neglect how the dipoles are generated in the first place.

In order to emphasize the accuracy of this model compared to other techniques, figure 7.2.7 presents the effective medium calculations from the commonly used Maxwell-Garnett and Bruggeman effective medium theories. Figures 7.2.7a and 7.2.7c present the polarization, angle, and wavelength resolved absorption of the particle film calculated from the Maxwell-Garnett and Bruggeman effective medium theories, respectively. Though our experimental film invalidates the stated assumptions of these two theories (i.e., there is strong interparticle coupling of multipole resonant particles in the experimental film), their ease of use, prevalence in literature, and consistent track record of accurately modeling data warrants a comparison to justify the admittedly more complicated approach proposed in this manuscript. As evident in the figures 7.2.7a and 7.2.7c, instead of blackbody-like behavior as seen in the measurement results, the Bruggeman and Maxwell-Garnett theories predict little absorption and are instead mostly transparent (see the supplementary information). This is because these theories do not account for resonant behavior such as a strong OMR or interparticle coupling. This is further evident in the fact that neither theory accounts for a change in relative permeability that is

necessarily generated by an optically-induced magnetic response. Comparing the models to experiment, the relative difference in absorption is 180% (Bruggeman) and 680% (Maxwell-Garnett), when considering all angles, polarization, and wavelengths. This is in stark contrast to the cluster-based method, which has a 6% relative difference in absorption when comparing to the experimental data. The relative difference is calculated using the formula, (experimental – simulation)/simulation. The Bruggeman and Maxwell-Garnett theories show no OMR absorption peak. Furthermore, both theories predict polarization splitting and a well-defined Brewster's angle where the OMR should exist, despite neither phenomenon present in experiment at that wavelength (λ = 420 nm). The polarization and angle dependence of the Maxwell-Garnett and Bruggeman theories are shown in the figures 7.2.7b and 7.2.7d, respectively.

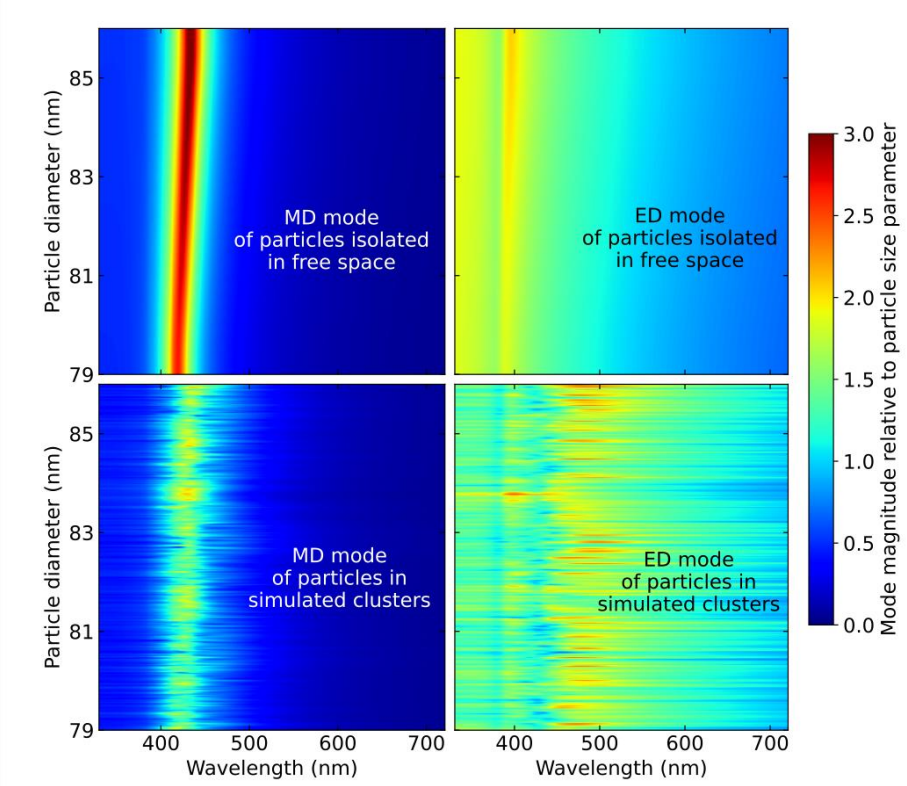

Figure 7.2.6. Comparison of uncoupled particles isolated in free space (top) magnetic-dipole (MD, left) and electric-dipole (ED, right) modes versus the same modes for particles in the simulated clusters (bottom), which are altered by interparticle coupling. In all cases, the x-axis is wavelength and the y-axis is particle diameter.

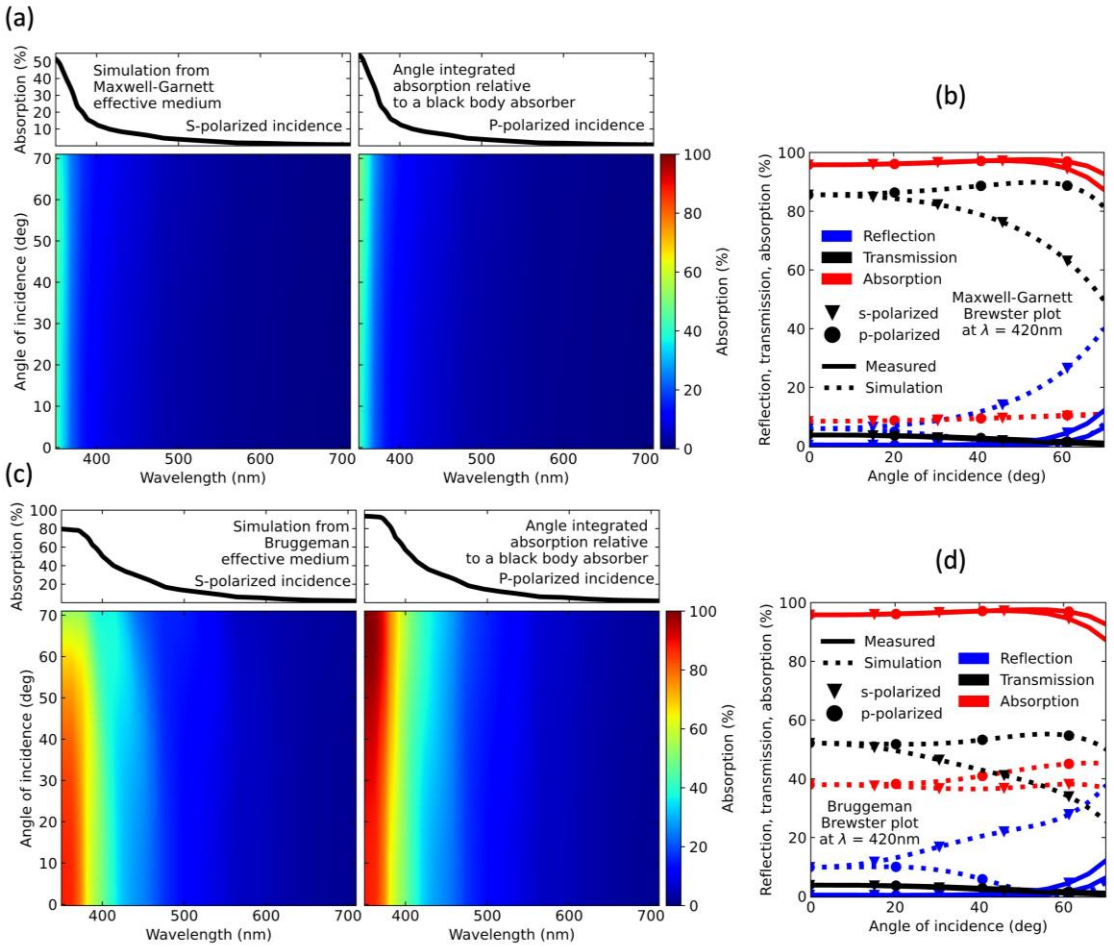

Figure 7.2.7. Angle, wavelength, and polarization resolved absorption response from a 550 nm thick effective medium on 1 mm soda-lime glass, calculated using the transfer matrix method. (a) Absorption response based on the particle film represented through the Maxwell-Garnett effective medium approach. (b) Brewster angle plot at λ = 420 nm of the measured reflection (solid blue), transmission (solid black) and absorption (solid red) response compared to the Maxwell-Garnett reflection (dashed blue), transmission (dashed black), and absorption (dashed red) response. The downward triangle and circle denote s- and p-polarization, respectively, (c) Absorption response based on the particle film represented through the Bruggeman effective medium approach. (d) Brewster angle plot at λ = 420 nm of the measured data compared to the Bruggeman effective medium. In both cases of the color maps, the angle (y-axis) and wavelength (x-axis) resolved absorption for s- (left) and p-polarization (right). The figure on top of each color map is the angle integrated absorption of the color map relative to an ideal black body.

7.3 CONCLUSION

We have employed a dusty-plasma synthesis technique to make highly crystalline silicon nanoparticle films comprised of OMR particles. The process uses particle trapping and subsequent annealing in a high-density filamentary plasma and achieves highly monodisperse nanocrystals in the size range required to exhibit OMR. The particle size distribution is narrow enough such that all particles exhibit an average OMR at 420 nm with a negligible deviation compared to the spectral broadening from the electric dipole mode. Particles are then directly deposited onto a substrate from the reactor using a scalable spray method. The resulting particle film shows broadband angle and polarization independent antireflection across the visible spectrum as well as strong absorption emanating from the designed OMR. Since OMRs and near field coupling are neglected in traditional effective medium theories, we develop an analytical approach which accurately models the behavior of the experimental film. The model describes the film in terms of the scattering response of individual particles, and also gives an overall resulting effective permeability and permittivity. Furthermore, the effective constitutive parameters can be resolved by mode and cluster-type. We find the individual particle OMRs give rise to a collective OMR which, from the perspective of the film, can be viewed as a true magnetic response. Therefore, the film has a non-unity relative permeability despite being composed of non-magnetic materials. The collective OMR is slightly red shifted compared to uncoupled particles in free space, but the spectral shape is virtually unchanged by near field coupling. Studying coupling effects on the particle level shows the OMR in each particle is individually robust to interparticle coupling. In contrast, the electric resonance has substantial spectral broadening to longer wavelengths and is responsible for a majority of the absorption broadening within the film. Both resonances experience a reduction in amplitude on the particle-level to satisfy energy balance, leading to broadband antireflection. Maxwell-Garnett and Bruggeman effective medium theories cannot accurately account for the film scattering response. Furthermore, accounting only for uncoupled particle resonances resulted in constitutive parameters that were roughly double the appropriate amplitude and had 49% less spectral broadening than necessary, measured by the full width at half maximum. This indicates that both near-field coupling and individual particle resonances need to be considered.

7.4 METHODS

Nanoparticle synthesis. Silicon nanocrystals are synthesized in a continuous-flow, low-pressure plasma reactor consisting of a quartz tube with an inner diameter of 3.5 cm and 20 cm long. Pure silane and argon enter through the top of the reactor with typical flow rates of 0.2 and 7.5 standard cubic centimeters per minute (sccm), respectively, leading to a gas residence time in the plasma zone of about 2 s. However, due to the electrostatic trapping of particles upstream of the ring electrode that was observed in ref. [278] the actual particle residence time in the reactor is expected to be longer. The electrostatic trapping requires that particles grow to a minimum threshold size before being removed from the trap by the gas flow, which causes a size filtering of the particles, leading to a narrow size distribution[296]. The plasma is excited by applying a nominal radiofrequency (RF) power of 200 W at 13.56 MHz to a ring electrode placed 6.5 cm upstream of the lower flange, which serves as the ground electrode. Nanocrystals are extracted by the gas flow through a 12 × 0.064 mm slit-shaped orifice and injected into the deposition chamber. The typical pressure in the plasma reactor is 1.7 Torr while the deposition chamber downstream of the extraction orifice has a pressure of 80 mTorr. The nanocrystals are collected directly onto glass substrates located 1.5 cm beneath the orifice. To form homogeneous films, substrates are mounted on a stainless-steel pushrod setup and translated back and forth for 30 minutes.

Transmission Electron Microscopy. TEM samples were collected on thin holey carbon coated Cu grids. Conventional TEM examination of the nanocrystals was carried out using an FEI Tecnai T12 operating at an accelerating voltage of 120 kV to obtain the particle distribution size. High-resolution imaging was performed using an FEI Talos F200x operating at an accelerating voltage of 200 kV.

Scanning Electron Microscopy. The nanocrystal film thickness was approximated using cross sectional scanning electron microscopy. Specifically, an FEI Helios NanoLab G4 was used with an accelerating voltage of 2 kV.

UV-Visible Spectroscopy. Angle and polarization-resolved absorption data from 350 nm to 700 nm was acquired using Agilent Cary 5000 UV-Vis-Nir with the Universal Measuring Attachment (UMA). Samples were angled from 6 – 71 degrees in 5-degree increments with respect to normal incidence from the lamp source. For specular reflection, the detector was angled at 2x the sample angle measured clockwise from the lamp source. Spectral transmission measurements required only the change of the sample angle, and the detector did not move from 180 degrees from the incident light. All measurements were performed for both S and P

polarizations. The schematic of the UV-Vis measurement process is presented in the supplementary material.

Fill fraction calculation. The mass of the sample was measured with a Cahn C-31 Microbalance. Density of the thin film was calculated using the sample area (4.5 mm × 10 mm), the measured film thickness from cross-sectional SEM (550 nm), and the mass of the nanocrystal film (17.4 micrograms). The volume fill fraction of the thin film (30%) was then determined as the ratio of the film density to bulk silicon density (2.329 g/cm^3).

7.5 SUPPLEMENTARY FIGURES

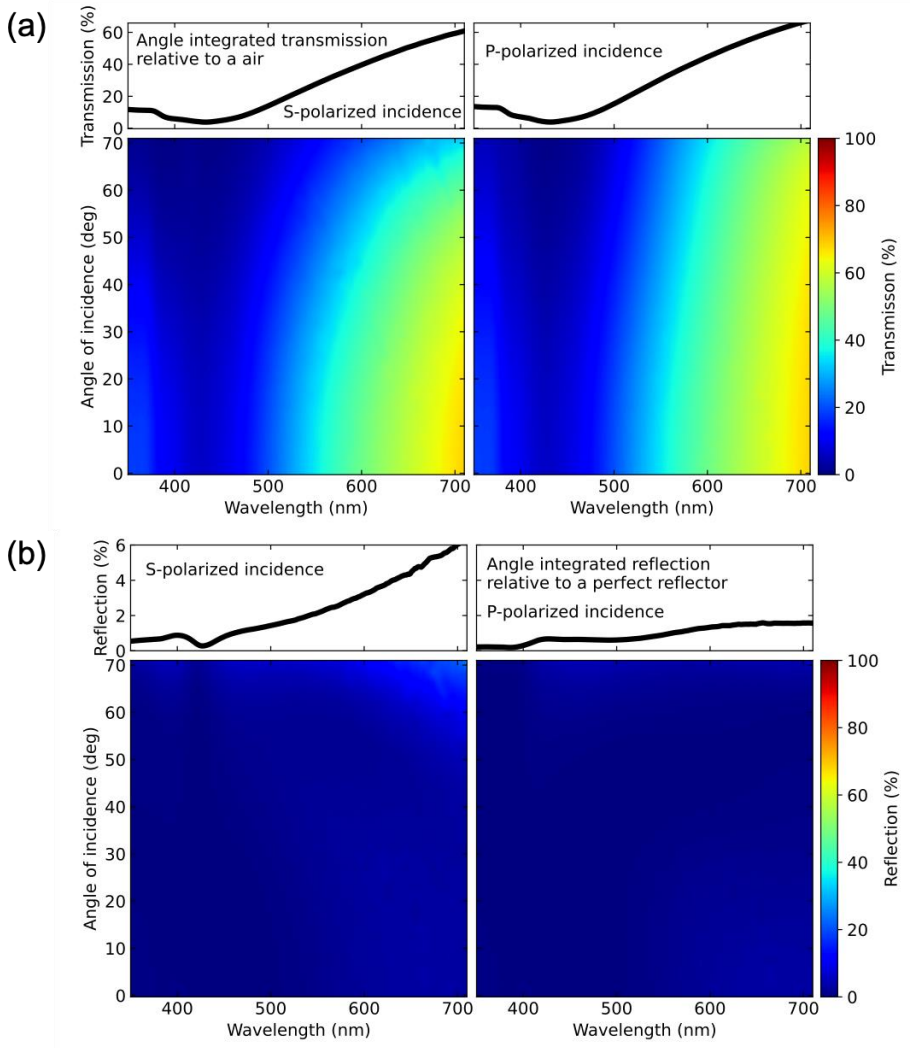

Figure 7.5.1. Angle, wavelength, and polarization resolved reflection and transmission response of a 550 nm thick c-Si particle film simulated using the cluster-based effective medium theory on top of a 1 mm soda-lime glass substrate. (a) The bottom color maps show the film's transmission response as a function of wavelength (x-axis), angle of incidence (y-axis) and s- (left) and p-polarization (right). The corresponding top figures are the angle integrated transmission relative to air. (b) The reflection response of the particle film for s- (left) and p-polarization (right). In both cases the angle integrated reflection relative to a perfect reflection is shown above the corresponding color map.

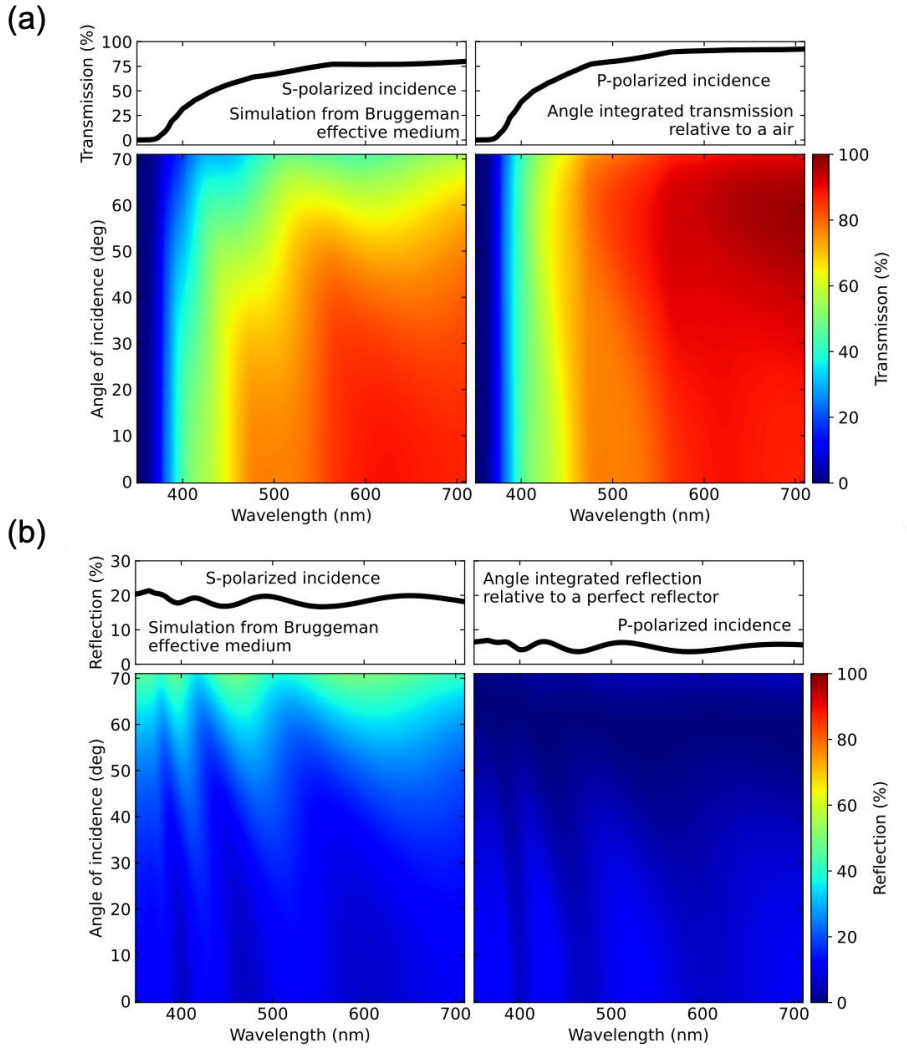

Figure 7.5.2. Angle, wavelength, and polarization resolved reflection and transmission response of a 550 nm thick c-Si particle film simulated using the Bruggeman effective medium theory on top of a 1 mm soda-lime glass substrate. (a) The bottom color maps show the film's transmission response as a function of wavelength (x-axis), angle of incidence (y-axis) and s- (left) and p-polarization (right). The corresponding top figures are the angle integrated transmission relative to air. (b) The reflection response of the particle film for s- (left) and p-polarization (right). In both cases the angle integrated reflection relative to a perfect reflection is shown above the corresponding color map.

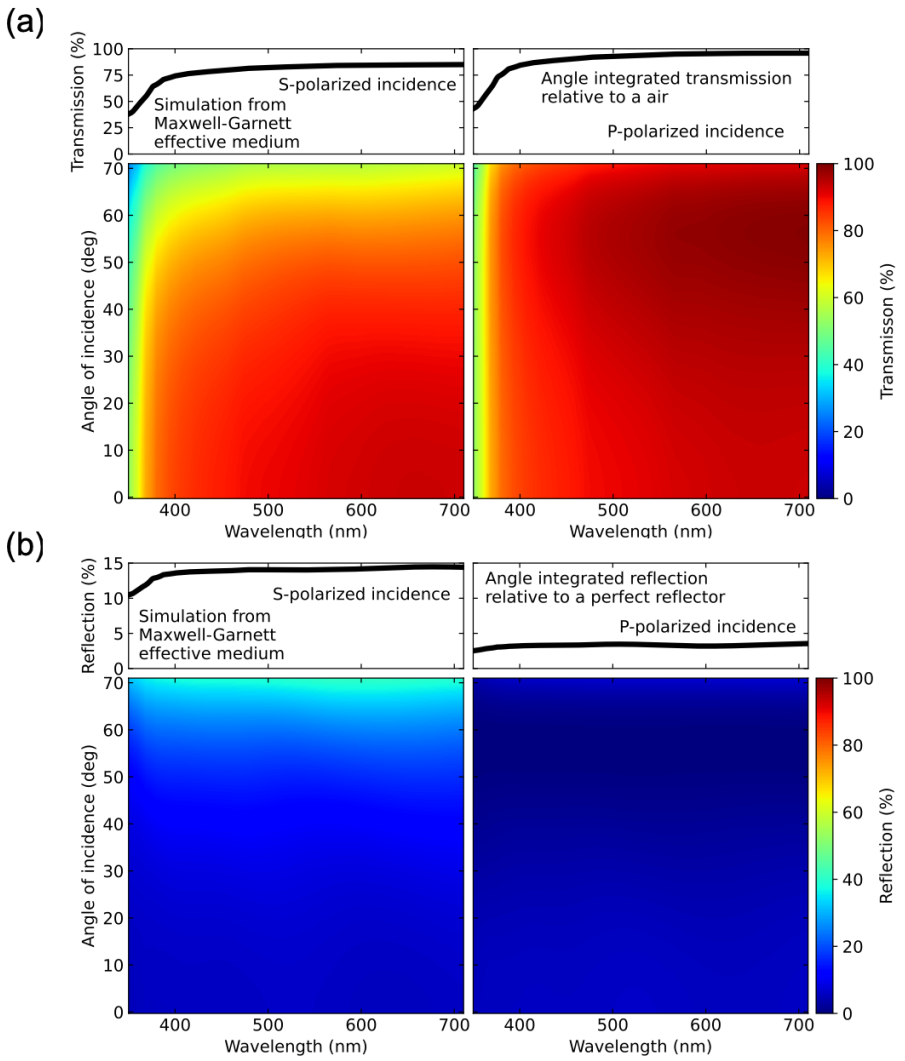

Figure 7.5.3. Angle, wavelength, and polarization resolved reflection and transmission response of a 550 nm thick c-Si particle film simulated using the Maxwell-Garnett effective medium theory on top of a 1 mm soda-lime glass substrate. (a) The bottom color maps show the film's transmission response as a function of wavelength (x-axis), angle of incidence (y-axis) and s- (left) and p-polarization (right). The corresponding top figures are the angle integrated transmission relative to air. (b) The reflection response of the particle film for s- (left) and p-polarization (right). In both cases the angle integrated reflection relative to a perfect reflection is shown above the corresponding color map.

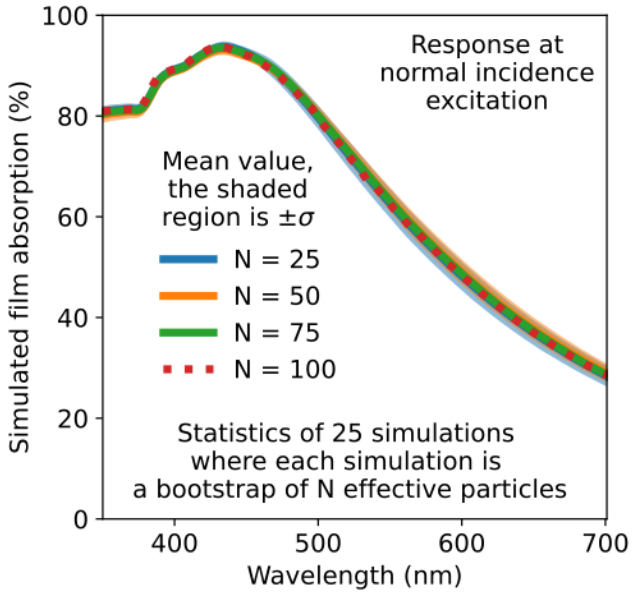

Figure 7.5.4. Sample dependence of simulated film absorption. Film absorption was simulated 25 times, where each absorption calculation was based on 25 (blue), 50 (orange), or 75 (green) random cluster samples. The mean value is given by solid lines and overlay each other. The standard deviation is given by the shaded region around the mean value. The total 100 random cluster samples is shown in dashed red for reference.

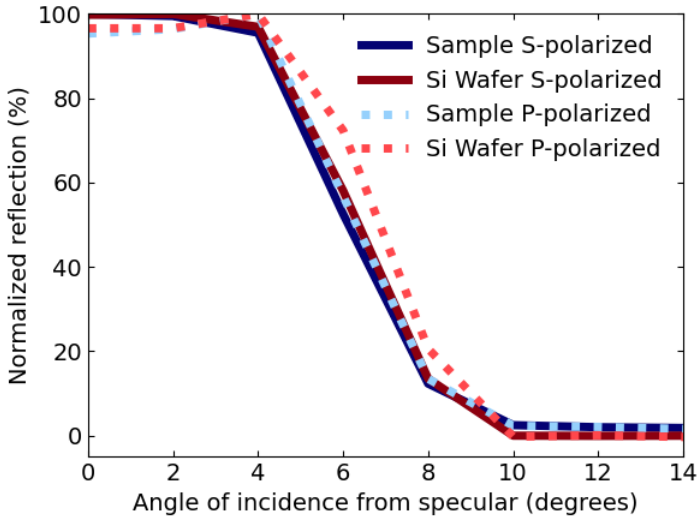

Figure 7.5.5. Diffuse normalized reflection comparison between experimental Si NC film and a clean silicon wafer, an expected specular reflection reference, showing good match at both polarizations.

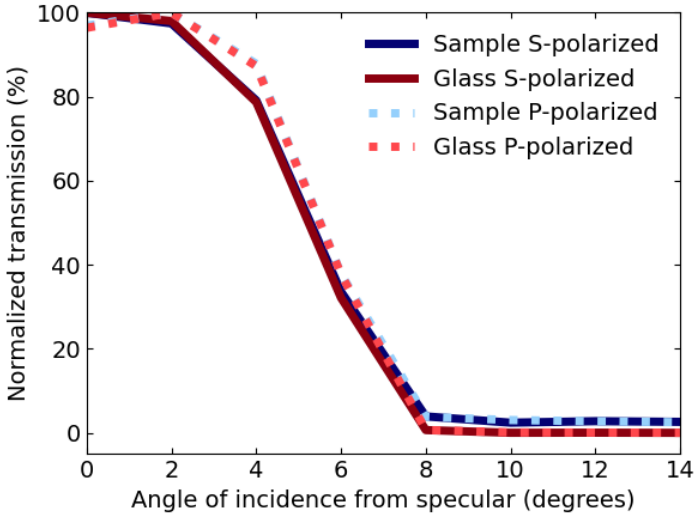

Figure 7.5.6. Diffuse Normalized Transmission comparison between experimental Si NC film and bk7 glass slide, an expected specular transmission reference, showing good match at both polarizations.

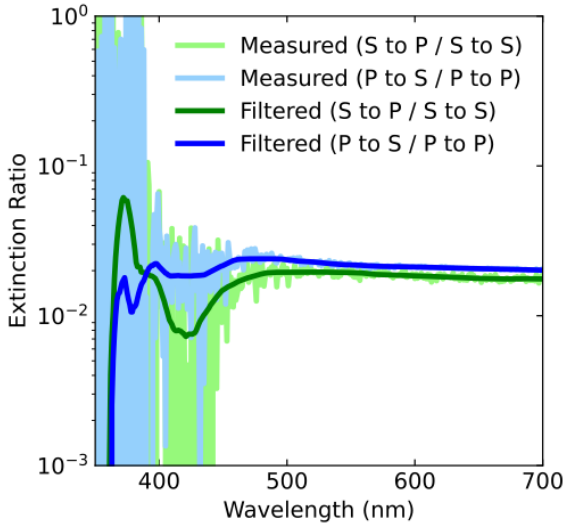

Figure 7.5.7. Transmission extinction ratio of polarization conversion in the measured sample at normal incidence. The light green and blue lines are the extinction spectra for s to p and p to s conversion, respectively. The dark green and dark blue lines are the filtered s to p and p to s spectra, respectively. Filtering was necessary because the combination of polarizer and sample absorption cause weak signals below 400nm.

SECTION 3

PARTICLE AND PARTICLE FILM

MEASUREMENT TECHNIQUES

Chapter 8

THEORY OF PARTICLE AND PARTICLE FILM MEASUREMENT

8.1 INTRODUCTION

When developing nanoparticle growth procedures, it is important to be able to characterize the product of the growth process. An inherent problem of nanoparticles and nanoparticle films is that their optical properties can be hard to accurately characterize. The transition from measured observable to governing underlying parameter(s) is usually not a simple process. Take, for example, the optical characterization of nanoparticle thin films. Constitutive parameters may be anisotropic and inhomogeneous. Absorption resonances are not a sole property of the underlying bulk material, but influenced by particle shape, multiple scattering, and the resulting local field. Characterization of the coherent and incoherent field may be necessary. In cases where effective medium theories apply, it is still important to characterize or prove negligible polarization conversion, depolarization, scattering, incident angle dependence, and resonance shifts based on particle structure and changes in the local field. In general, complex systems require careful analysis.

This section discusses how to use optical measurement to understand resonant scattering and absorption properties in single particles and how to determine bulk material, filling fraction, and surface roughness information from densely packed nanoparticle films. Section 8.2 outlines the underlying limitations on dispersion that any linear, passive, and causal permittivity must uphold. This section also describes multiple models for characterizing polariton transitions, including ionic and molecular vibrations, interband transitions (semiconductors), phonons, and other collective excitations. Section 8.3 summarizes a measurement procedure for characterizing nanoparticle thin films and how to back out bulk material properties of the nanoparticles and characteristic properties of the film. Emphasis in this section is given to aspects of measurement not commonly seen in bulk homogeneous thin film measurement. Section 8.4 gives a method of single particle measurement, where anomalous absorption and scattering properties are analyzed using Beer's law. Chapter 9 makes use of this theory to characterizes individual Huygens particles, throughout the visible spectral range. Chapter 10 uses the concepts developed for nanoparticle film measurement, to characterize the refractive index changes of α, θ and γ phase alumina nanoparticle films.

8.2 CAUSALITY, KRAMERS, KRÖNIG, SUMS, AND SPRINGS

"Every why hath a wherefore."

-William Shakespeare, The Comedy of Errors, 1594

An overarching theme in this dissertation is understanding how to design the frequency response of engineered materials. In this regard it is important to understand the frequency response of the bulk material building blocks. Though a full description of such light-matter interactions requires quantum mechanics, much about the constitutive relations can be understood through fundamental constraints and spring models. This section provides a very brief outline of how to model linear, isotropic, homogeneous, and passive bulk materials as a collection of oscillators with parameters that can be obtained either through measurement or rigorous theory. A direct application of this section is in Chapter 10, where bulk material properties are derived from measurement of particle films satisfying effective medium requirements. The indirect application is to provide a more wholistic picture on fundamental constraints of the constitutive parameters.

As outlined in Chapter 1, all bulk materials in this dissertation are

- Linear: $\boldsymbol{P} = \overline{\overline{\boldsymbol{\chi}}}(\boldsymbol{r} - \boldsymbol{r}', t - t')\boldsymbol{E}$,
- Isotropic: $\overline{\overline{\boldsymbol{\chi}}} \rightarrow \chi\overline{\overline{\boldsymbol{I}}}$,
- Homogeneous: $\chi(r - r')\delta(r - r')$,
- Passive: $\mathfrak{T}[\chi(\omega)] > 0$,
- Causal: $\chi(t \leq 0) = 0$.

Since the constitutive relations of bulk materials can be viewed as a homogenization of atoms well in the mean field regime, the underlying consequences of linearity, isotropy, and homogeneity (spatial dispersion) detailed in part II apply. These constraints place limits on the material's response to changes in the exciting field's amplitude, polarization, and propagation direction. The requirement of passivity, also detailed in part II, is a constrain that interaction necessitates loss (possibly infinitesimally small). The final property to discuss is causality, meaning that the response does not occur before the excitation.

Causality is easiest understood from a classical interpretation in the time domain. When an electromagnetic field impinges on a material the charges desire to orient themselves with respect to the field in an effort to equilibrate. This change in configuration occurs over a finite transition period. When the electromagnetic field is rapidly oscillating the charges are in a continual state

of catching up. The charges do not have information about the future, so they cannot predict the upcoming field movement to "get ahead" of the motion and meet the field exactly at time of arrival. The game of catch up is made worse given that the prior field behavior affects the current behavior of charges. Clearly if charges are being polarized in one direction and the field flips, the charges desire to flip accordingly. But they have already been set into motion in the opposite direction and covered some ground achieving that goal. This progress now needs to be undone. In this sense the charges are influenced by the past but not the future. This thought experiment also helps to understand charge behavior to fields at asymptotically high frequencies. If the field is alternating much faster than the response time, the charges have no ability to make progress in any direction. They become effectively "frozen" in place. Transparency at high energy is an important property to enable contour integrations in the complex plane. This can be formally shown to lead to the asymptotic frequency response,

$$\begin{aligned}\lim_{\omega\to\infty} \Re[\chi(\omega)] &= O\left(\frac{1}{\omega^2}\right)\\ \lim_{\omega\to\infty} \Im[\chi(\omega)] &= O\left(\frac{1}{\omega^3}\right).\end{aligned} \qquad 8.2.1$$

Equation 8.2.1 comes from an expansion of $\chi(t = 0^+)$. Correspondingly, the mathematical form of the asymptotic response depends on the derivatives of χ at $t = 0^+$. It is worth noting that absolute time is irrelevant. What is relevant is the record of the events that have occurred prior to the current state. Finally, recall that electromagnetic fields obey superposition and so does the charge response. The described system falls under the category of linear time-invariant response theory. For such materials the susceptibility can be written as a temporal convolution,

$$(\chi * \boldsymbol{E})(t) = \int_{-\infty}^{t} dt' \chi(t - t')\boldsymbol{E}(t'), \qquad 8.2.2$$

where the upper integration limit defines the lack of information of future events. Alternatively stated the susceptibility kernel is zero for negative arguments $\chi(t \leq 0) = 0$. Such a kernel can be constructed as $\chi(t) = \chi_{even}(t) + sign(t)\chi_{even}(t)$, were χ_{even} is an even function and $\chi_{odd} = sign(t)\chi_{even}$ is an odd function that exactly cancels the even function for $t \leq 0$. The Fourier transform of this decomposition is $\mathcal{F}[\chi](\omega) = \Re[\chi_{even}(\omega)] + i\Im[\chi_{even}(\omega)]$, with positive imaginary part for positive frequency, as dictated by passivity. The sign function, $sign(t)$, corresponds to a convolution of the Hilbert kernel in frequency space. The relation of the real and imaginary parts of the susceptibility are then summarized in frequency domain by the Kramers-Krönig relations,

$$\Re[\chi(\omega)] = \frac{2}{\pi} PV \int_0^\infty d\omega'\, \omega' \Im[\chi(\omega')]/(\omega'^2 - \omega^2)$$
$$\Im[\chi(\omega)] = -\frac{2\omega}{\pi} PV \int_0^\infty d\omega'\, \Re[\chi(\omega')]/(\omega'^2 - \omega^2), \quad 8.2.3$$

where the integration bounds and factor of 2 come from the fact that $\chi(t)$ is real, so $\chi(-\omega) = \chi^*(\omega^*)$. The Kramers-Krönig relations define a connection between the real and imaginary parts of a linear, passive, and causal susceptibility kernel in frequency space. Alternatively stated, $\chi(t)$ is finite for all t and represents an analytic function in the upper half of the complex frequency plane. Many sum rules can be derived by asymptotic frequency integrals of the susceptibility, the Kramers-Krönig relations, and their higher moments. These rules play an important role in further defining fundamental relations between loss and dispersion of a material system. For example, the *f*-sum rule defines a zero-sum tradeoff, where increased loss in one spectral region necessitates a decrease in loss elsewhere,

$$\frac{2}{\pi} \int_0^\infty \omega\, \Im[\chi(\omega)] d\omega = \omega_p, \quad 8.2.4$$

where ω_p is the plasma frequency. Equation 8.2.4 relates the sum of all oscillator strengths across the entire spectra to a constant, which is dictated by the material. Lists of sum rules will not be discussed, as there are multiple, and they are material specific. In particular, behavior in the static limit, such as metals versus dielectrics can be an important distinction.

In time domain the susceptibility kernel can be decomposed into a slow, χ_s, and rapid, χ_r, varying part,

$$\boldsymbol{D} = \varepsilon_o \boldsymbol{E} + (\chi_r * \boldsymbol{E})(t) + (\chi_s * \boldsymbol{E})(t) \approx \varepsilon_\infty \boldsymbol{E} + (\chi_s * \boldsymbol{E})(t), \quad 8.2.5$$

where $\varepsilon_\infty = \varepsilon_o + \int_0^\infty \chi_r(t) dt$. The introduction of the infinite permittivity, ε_∞, is valid when the time variation of the electromagnetic field is substantially slower compared to the response time of χ_r. From the viewpoint of the slow changing electromagnetic field, χ_r appears effectively as an instantaneous response. Clearly the designation of "slow" and "rapid" parts are relative to the bandwidth of the incident excitation. The important point is that material oscillators far outside of the field's bandwidth can be collectively encapsulated into a single constant. Therefore, oscillators need only be modeled explicitly if they correspond to light-matter interactions within a meaningful bandwidth encompassing the field bandwidth. It is important to note that the meaningful bandwidth is usually wider than the excitation bandwidth.

This is because oscillator tails within the bandwidth are still meaningful. Some models explicitly abstract these tails as pole terms on either side of the bandwidth.

To summarize, the susceptibility should be an analytic function in the upper half-plane with a non-negative imaginary part. This describes a Nevanlinna-Herglotz function, so any susceptibility tensor will be of Nevanlinna-Herglotz form. The Kramers-Krönig relations give the fundamental connection between the real and imaginary parts of the susceptibility. Therefore, Kramers-Krönig consistency is an important requirement in any model and can be used to derive dispersion in models that focus on only the real or imaginary part (absorption spectra is usually easier to experimentally measure). Furthermore, the Kramers-Krönig relations are important in deriving many sum rules, which further define relations between loss and dispersion. Oscillators well outside of the bandwidth converge to a static susceptibility term. Two poles outside of the bandwidth can also be used to model slowly decaying spectral tails that leak into the bandwidth of interest, when necessary. The remaining mathematical form of oscillators within the bandwidth are specific to the underlying physics of the light-matter interaction. In this regard, five models are discussed which have shown to match well with experiment, have theoretical interpretations, and have been used in this dissertation.

Lorentz and the Spring Model

Though most material models require a full quantum mechanical description, much of the underlying structure of the response function can be understood from a simple universal oscillator model. This allows for a discussion agnostic to the underlying mechanisms. Let the system under influence of the electromagnetic field be modeled as two charges connected by a spring. In a general sense, this model encapsulates the spirit of a very sub-wavelength collection of atoms that has damping and natural modes. The equation of motion is

$$\frac{d^2\boldsymbol{d}}{dt^2} + \gamma\frac{d\boldsymbol{d}}{dt} + \omega_o^2\boldsymbol{d} = -\frac{q}{m_e}\boldsymbol{E}(t) \overset{\mathcal{F}}{\rightarrow} \boldsymbol{d} = -\frac{\frac{q}{m}\boldsymbol{E}(t)}{\omega_o^2-\omega^2-i\omega\gamma}, \tag{8.2.6}$$

where $\boldsymbol{d}$ is the displacement of the charges from equilibrium, m is the mass, q is the charge, γ is the damping rate, K is the spring constant, and $\omega_o = \sqrt{K/m}$ is the natural mode of the system. In the classical framework the dipole moment is $\boldsymbol{P} = -q\boldsymbol{d}(N/V) = \varepsilon_o\chi_s\boldsymbol{E}$, where N/V is the number density of charges within the volume. Correspondingly the permittivity is,

$$\varepsilon(\omega) = \varepsilon_\infty + \varepsilon_o \frac{\omega_p^2}{\omega_o^2 - \omega^2 - i\omega\gamma}, \quad 8.2.7$$

where $\omega_p = \sqrt{Nq^2/V\varepsilon_o m}$ is usually termed the plasma frequency. Equation 8.2.7 is called the Lorentz permittivity model. Importantly, inserting the Lorentz permittivity model into the Lorentz-Lorenz self-energy predicts another Lorentz permittivity model,

$$U_{eff}^{LL} \to \varepsilon(\omega) = \varepsilon'_\infty + \frac{(\omega'_p)^2}{(\omega'_o)^2 - \omega^2 - i\gamma\omega}, \quad 8.2.8$$

where,

$$\varepsilon'_\infty = \varepsilon + ff \frac{3\varepsilon(\varepsilon_\infty - \varepsilon)}{\varepsilon_\infty + 2\varepsilon - ff(\varepsilon_\infty - \varepsilon)} \quad 8.2.9(a)$$

$$\omega'_p = \sqrt{ff} \frac{3\varepsilon\omega_p}{(1-ff)\varepsilon_\infty + (2+ff)\varepsilon} \quad 8.2.9(b)$$

$$\omega_o'^2 = \omega_o^2 + \frac{(1-ff)\omega_p^2}{(1-ff)\varepsilon_\infty/\varepsilon_o + (2+ff)\varepsilon/\varepsilon_o}. \quad 8.2.9(c)$$

This speaks generally to the pervasiveness of the Lorentz oscillator. As discussed in part II, the Lorentz-Lorenz self-energy accounts for the order of scattering series, under the proper context. This is exactly the scenario of a collection of atoms. The Lorentz model is Kramers-Krönig consistent and is quite general to the description of many bulk materials, including ionic and molecular vibrations, interband transitions (semiconductors), phonons, and other collective excitations. The governing parameters ($\omega_p^2, \omega_o^2, \gamma, \varepsilon_\infty$) can be found through measurement or rigorous theory, depending on the context of the problem.

Debye, a Special Case of Lorentz

When the Lorentz oscillator is overdamped, $\omega \ll \gamma$, it can be simplified to the Debye model,

$$\varepsilon(\omega) = \varepsilon_\infty + \varepsilon_o \frac{\omega_p^2}{\omega_o^2 - i\omega\gamma}, \quad 8.2.10$$

where convention is to assign the numerator $\Delta\varepsilon = \varepsilon(\omega = 0) - \varepsilon_\infty = \varepsilon_o\, \omega_p^2/\omega_o^2$ and normalize the loss as $\tau = \gamma/\omega_o^2$. Here, $\varepsilon_s = \varepsilon(\omega = 0)$ is the very slow varying permittivity.

Similar to the Lorentz model, the Debye model is Kramers-Krönig consistent and inserting it into the Lorentz-Lorentz self-energy returns another Debye model,

$$U_{eff}^{LL} \to \varepsilon'_{\infty} + \frac{\varepsilon'_s - \varepsilon'_{\infty}}{1+i\omega\gamma'}, \tag{8.2.11}$$

where

$$\varepsilon'_{\infty} = \varepsilon + ff\,\frac{3\varepsilon(\varepsilon_{\infty}-\varepsilon)}{\varepsilon_{\infty}+2\varepsilon-ff(\varepsilon_{\infty}-\varepsilon)} \tag{8.2.12(a)}$$

$$\varepsilon'_s = \varepsilon + ff\,\frac{3\varepsilon(\varepsilon_s-\varepsilon)}{\varepsilon_s+2\varepsilon-ff(\varepsilon_s-\varepsilon)} \tag{8.2.12(b)}$$

$$\gamma' = \gamma\,\frac{(1-ff)\varepsilon_{\infty}+(2+ff)\varepsilon}{(1-ff)\varepsilon_s+(2+ff)\varepsilon}. \tag{8.2.12(c)}$$

The Debye model is commonly used to describe the dielectric response of fluids with permanent electric dipole moment. This model is not used in this dissertation but is presented to give supporting evidence to the range of diversity of the Lorentz model.

Drude, a Special Case of Lorentz

When there is no restoring force on the charges, $K = 0$, the Lorentz model becomes the Drude model,

$$\varepsilon(\omega) = \varepsilon_{\infty} - \varepsilon_o\,\frac{\omega_p^2}{\omega^2+i\omega\gamma}. \tag{8.2.13}$$

This model is commonly used to describe the response of free charges, $\boldsymbol{J} = \sigma\boldsymbol{E}$, such as in metals. At low frequencies,

$$\nabla\times\boldsymbol{H} = -i\omega\left(\varepsilon_{\infty}+\frac{i\sigma}{\omega}\right)\boldsymbol{E} \xrightarrow{\omega\to 0} \sigma = \frac{\varepsilon_o\omega_p^2}{\gamma-i\omega}. \tag{8.2.14}$$

The Drude model is Kramers-Krönig consistent. Though, inserting the Drude model into the Lorentz-Lorentz self-energy will return a Lorenz instead of another Drude model. This is sensible given the meaning of the Drude model and the assumptions of the Lorentz local-field.

The Drude model is for a free electron sea. I.e., a continual connection of conductors. The Lorentz-Lorentz local field does not provide this low frequency divergence.

Gaussian Permittivity

In amorphous solids, Lorentzian absorption features give way to Gaussian-like absorption. The absorption spectra can then be modeled from the imaginary part of the susceptibility given by

$$\mathfrak{T}[\chi(\omega)] = Ae^{-\left(\frac{\omega-\omega_o}{\gamma}\right)^2} - Ae^{-\left(\frac{\omega+\omega_o}{\gamma}\right)^2}, \quad 8.2.15$$

where γ (the standard deviation) plays the role of the spectral broadening of the absorption resonance, which is centered at ω_o. The difference to two Gaussian functions enforces that the imaginary part is an odd function. The real part of the susceptibility is then found through the Kramers-Krönig relation.

Voigt, a Lorentz + Gaussian

In general, the degree of spectral broadening caused by Gaussian versus Lorentz features can be controlled through a Voigt function. This is a Lorentzian, L, convoluted with a Gaussian, G, in frequency space,

$$\mathfrak{T}[\chi(\omega)] = \mathfrak{T}[G(\omega;\gamma,A)] * \mathfrak{T}\left[L\left(\omega;\gamma,\omega_p\right)\right]. \quad 8.2.16$$

The Voigt function offers a method to model bundled continuums of transitions that cannot be distinctly resolved.

Superpositions of Oscillators

Since the dipole moments obey superposition, the permittivity can be decomposed into a sum of oscillators. When optical transitions are clear and discrete, summations of oscillators are used. This fits well with the quantum mechanical picture of quantized transitions in states. When many states are packed into a continuous band, it may not be meaningful to resolve each transition. In

this case, convolutions such as the Voigt function or even a Gaussian oscillator can be used. The general permittivity model can be described as

$$\varepsilon(\omega \in [\omega_{min}, \omega_{max}]) = \varepsilon_{\infty} + \varepsilon_{pole,1} + \varepsilon_{pole,2} + \sum_n \varepsilon_{osc,n}(\omega), \quad 8.2.17$$

where $\omega_{min}, \omega_{max}$ define the bandwidth of interest. The summation is over arbitrary discrete oscillators, each of which may be a convolution representing a band of oscillators. The oscillator center frequency need not be in the bandwidth of interest. Two permittivity pole terms are explicitly shown as a reminder of potential spectral leakage. Since n is a free parameter there is no restriction preventing overfitting. All oscillator parameters should have clear rationale for their values. Good practice is to first scour literature to find clear bounds of the known material transitions in the relevant bandwidth. Once these bounds are determined, the oscillator parameters can be tuned thorough an optimization problem seeking to fit the model to the experimental data. Any additional parameters used to better fit data should be on an as-needed basis, with clear justification, and used sparingly. In general, a model that can be clearly explained is better than one that is best fit.

Causality and passivity limit the functional form of the frequency dependence of permittivity. In many cases, simple oscillator models work well to describe this dependence. The Kramers-Krönig relations and corresponding sum rules for the material offer a powerful tool to establish oscillator form and bounds.

8.3 PARTICLE FILM CHARACTERIZATION

As discussed in the introduction, the optical characterization of nanoparticle thin films is certainly a harder problem compared to bulk homogeneous and isotropic thin films. This is because the characteristic parameters are meaningful in a statistical sense and may fluctuate at length scales larger than the wavelength. For example, some areas of the film can be more or less dense, resulting in different spatial correlations and local field behavior. Surface roughness can represent between 1 – 30% of the layer thickness depending on deposition parameters. In the case of dusty plasma synthesis, particle sizes are usually normal or log normal distributed. In some cases, the particles themselves may be porous and/or have varying material properties. For these reasons and others, it is necessary to characterize or prove negligible polarization conversion, depolarization, scattering, incident angle dependence, and resonance shifts based on particle structure and changes to the local field.

Your Eye is a Measurement Device

The first important step in optical characterization is your eye. In proper lighting conditions samples are surveyed for spatial consistency of deposition over a wide field of view. Spatially dependent color changes and clear diffraction fringes, sometimes best seen by tilting the sample, outline regions of strong wavelength-scale variations. Scattered color is seen upon direct illumination in an otherwise dark room. In many cases characterization by eye is all that is necessary to determine the failure of a sample. Clearly if you are attempting to make a blue filter and the film comes out red, the sample failed. If there are no regions of macroscopic consistency larger than the spot size of your measurement tool, the sample is likely a failure. With an intuition of the underlying physics and deposition conditions, quick observation of optical properties can provide a powerful feedback loop for particle growth and deposition. Even when the properties of interest are not in the visible regime, it is still worthwhile to develop an intuition of expected behavior in the visible.

Normal Incidence Spectroscopy = Quick and Informative

When the sample passes visual inspection, reflection, transmission, and absorption measurement at normal incidence provide a quick measurement of the underlying spectral features. The infrared region is able to homogenize larger scale variations, compared to the visible regime, so it can be a good spectral regime to start. Particles are more likely to behave as simple dipoles, particle films are more likely to satisfy effective medium models, and surfaces can appear less

rough. Rotation and vibration modes unique to the bulk material building block can serve as guideposts to characterize the underlying material constituents of the particles. It should be noted that all electromagnetic length scales are dependent on the refractive index. Strong phonon resonances shorten wavelengths. With that said, sub-wavelength particles in the visible are 10 – 100x smaller in the infrared. Clearly, the visible regime will interact more with smaller scale variations and material transitions that occur at higher energy. In the case of appreciable scattering, angle resolved or integrating sphere measurements can be used to decompose the scattering component. In general, structural properties obtained through infrared measurement will be more macroscopic in scale. This can help to create bounds that can then be fine-tuned from visible measurement. Underlying material behavior can also be obtained from absorption spectra with less need to decompose scattering components.

Using the Mueller Matrix

After the sample passes the eye test and has the desired spectral features at normal incidence, a full optical characterization is performed. A powerful tool in this regard is an ellipsometer, which can provide wavelength, angle, and polarization-resolved reflection and transmission spectra. With these measurements and a properly defined model, the inverse problem can be solved to backout parameters such as film thicknesses, surface roughness, and optical properties such as the complex refractive indices, including anisotropy, homogeneity, and more. An important feature of an ellipsometer is the ability to measure the sample's Mueller matrix. The Mueller matrix relates input and output stokes vectors upon interaction with the sample. The stokes vectors directly characterize the observable optical intensity. Correspondently, the Mueller matrix contains the entire optical response of any sample in terms of measurable intensity. This is in contrast to the Jones matrix and Jones vectors, that relate field quantities and are not directly amenable to measurement at infrared and optical frequencies. With that said, intensities calculated from the Jones matrix, are commonly used in homogeneous bulk thin film ellipsometry. The Jones-Mueller matrix is applicable to systems that retain fully coherent polarized light. I.e., Jones algebra does not describe light that is incoherent, depolarized, or partially polarized, which can often occur in nanoparticle films. With that said, Jones algebra is certainly important when coherent effective medium models apply. The approach taken in this dissertation is to first observe the full features of the Mueller matrix elements. From this much of the underlying behavior of the particle film can be understood, including if a Jones-Mueller representation is applicable. Spectroscopic Mueller matrix ellipsometry is covered in many textbooks. Furthermore, multiple companies exist that provide full-fledged products to measure the Mueller matrix. Therefore, this section will not repeat that detail and instead compress the knowledge relevant to how to extract information from measurement results.

The Stokes vector, $\boldsymbol{S} \in \mathbb{R}^4$, is defined as

$$\begin{bmatrix} S_0 \\ S_1 \\ S_2 \\ S_3 \end{bmatrix} \equiv \begin{bmatrix} I \\ Q \\ U \\ V \end{bmatrix} = \begin{bmatrix} I \\ I_x - I_y \\ I_{+45^\circ} - I_{-45^\circ} \\ I_R - I_L \end{bmatrix}, \tag{8.3.1}$$

where I is a measured intensity value recorded from the detector and the $x-y$ convention orients the sample's outward normal in the positive z-direction. The first element, S_0, is the total intensity. S_1 is the intensity difference between horizontal and vertically polarized intensity. S_2 is the different between 45° and -45° polarized intensity, with respect to the x-axis. Finally, S_3 is the difference between right and left circular polarization. The I, Q, U, V notation is a common convention, given for completeness. The Mueller matrix, $\mathbb{M} \in \mathbb{R}^{4\times4}$, relates input to output Stokes vectors, $\boldsymbol{S}_{out} = \mathbb{M}\boldsymbol{S}_{in}$. In general, every element of the output Stokes vector is dependent on the entire input Stokes vector and the entire corresponding row of the Mueller matrix. With that said, much about a sample can be understood from the individual Mueller matrix elements. Note that the Stokes vector and corresponding Mueller matrix can look different for reflection and transmission measurement.

$$\begin{bmatrix} S_0 \\ S_1 \\ S_2 \\ S_3 \end{bmatrix}_{out} = \mathrm{M}_{11} \begin{bmatrix} 1 & m_{12} & m_{13} & m_{14} \\ m_{21} & m_{22} & m_{23} & m_{24} \\ m_{31} & m_{32} & m_{33} & m_{34} \\ m_{41} & m_{42} & m_{43} & m_{44} \end{bmatrix} \begin{bmatrix} S_0 \\ S_1 \\ S_2 \\ S_3 \end{bmatrix}_{in}$$

Figure 8.3.1. Mueller matrix in normalized form and color coded to depict elements relevant to depolarization (grey), diattenuation (blue), polarizance (green), retardance (orange), and s-p polarization conversion (inside red dash), and same type, e.g. x-linear to y-linear, polarization conversion (inside purple dash).

Figure 8.3.1 shows the Mueller matrix grouped into categories relevant for analysis. The grey top left, M_{11}, describes the attenuation of an incident unpolarized beam after propagation (either reflection or transmission) through the sample. The remaining Mueller matrix is normalized to, M_{11}, so that all $m_{ij} \in \mathbb{R} \cup [-1,1]$. The elements in the top blue row define diattenuation. This describes the amount of attenuation of one polarization state relative to its orthogonal counterpart. For example, m_{14} describes the difference in attenuation between right and left

circular polarization. The lower left green column describes polarizance. This is a measure of how unpolarized light will become polarized upon traveling though the sample. If $\sum_{i=2}^{4} m_{i1} = 1$, then the sample will completely polarize unpolarized light. The bottom right orange section defines the nine elements related to retardance between polarization states. These indicate how phase accumulation on different axes create a conversion between polarization "types." For example, m_{24} defines how a circularly polarized input will result in a linearly polarized output. Correspondingly, the second row, $m_{2,1-4}$ defines how any indecent polarized intensity will create a linearly polarized output. m_{21} being the special case of an unpolarized input. Another special case are the diagonal terms, m_{ii}. These define polarization conversion between same type polarizations. For example, $m_{22} = 1$ means an x or y polarized input will stay x or y polarized at the output. In general, +1 diagonal terms mean polarization preservation whereas complete polarization conversion is a -1-diagonal term and a 0 diagonal is complete depolarization between the two types. For example, $m_{44} = -1$ means a left or right polarized input will result in right or left circular polarized output, respectively. $m_{44} = 0$ means there is no difference between the resulting right and left circular polarization. Another important conversion is between s- and p-polarization, defined by the upper left four elements in dashed red box.

It is often the case that the Mueller matrix has redundant information and therefore a characteristic form. In this regard are symmetries, asymmetries, and zeroes of Mueller matrix elements are telling. The reflection Mueller matrix of an isotropic sample is,

$$\mathbb{M}_r = M_{11}\begin{bmatrix} 1 & -N & 0 & 0 \\ -N & 1 & 0 & 0 \\ 0 & 0 & C & S \\ 0 & 0 & -S & C \end{bmatrix}. \qquad 8.3.2$$

For nondepolarizing samples, $N, C,$ and S are related to the standard ellipsometry amplitude, $\Psi,$ and phase, Δ, parameters of the complex p and s reflection ratio, $r_p/r_s = \tan(\Psi)\, e^{i\Delta}$, by

$$\begin{aligned} N &= cos(2\Psi), \\ C &= sin(2\Psi)\, cos(\Delta), \\ S &= sin(2\Psi)\, sin(\Delta), \end{aligned} \qquad 8.3.3$$

and $M_{11} = \frac{1}{2}\left(r_p^2 + r_s^2\right)$. For non-depolarizing samples, all Mueller matrices have a corresponding Jones matrix and hence a Jones-Mueller representation. Depolarization then removes the mapping from Jones to Mueller matrices. With that said, it is common practice to

decompose the general Mueller matrix into a Jones-Muller and depolarizing component. If the depolarization effect is not too strong, then it is still meaningful to characterize the sample from its Jones-Mueller component. From this, the sample can be characterized as a product of elementary optical elements, where the Mueller matrices are be found from Jones matrices. In the case of depolarization, the degree of polarization can be defined as $P^2 = N^2 + C^2 + S^2 \leq 1$ and the percent depolarization as $(1 - P^2) \times 100\%$. Many commercial analysis software's will extract the depolarization such that $N, C,$ and S estimate that of a non-depolarized sample,

$$\mathbb{E}[\mathbb{M}_r] = M_{11}\begin{bmatrix} 1 & -PN & 0 & 0 \\ -PN & 1 & 0 & 0 \\ 0 & 0 & PC & PS \\ 0 & 0 & -PS & PC \end{bmatrix}. \qquad 8.3.4$$

Equations 8.3.4 offers a method to use analytic material models to best fit measurement data of isotropic materials with depolarization.

The characteristic form of equation 8.3.4 can be used to help determine if a sample is isotropic. Though care should be taken. If the symmetry axes of an anisotropic material happen to be aligned parallel or perpendicular to the plane of incidence, then the anisotropic sample will have a similar block diagonal structure as equation 8.3.4. In the presence of noise and/or depolarization, it may not be obvious that the sample is in fact anisotropic. One method to rule out forms of anisotropy is to measure the sample under different orientations, as the isotropic sample will remain block diagonal.

In general, relating the Mueller matrix to constitutive parameters requires building an analytic model that reproduces the measured data. Again, the goal of this section is not to reproduce details but provide intuition. Most ellipsometry software comes with a built-in model fitting tool. The important points are that nanoparticle samples can be depolarizing, and the Mueller matrix can characterize this. It is often the case that the Mueller matrix has redundant information, resulting in symmetries, asymmetries, and zeroes that can be used to identify the expected form of the constitutive parameters. In particular, isotropic materials have a block diagonal reflection Mueller matrix, preserved upon reorientation of the incident beam. Therefore, this structure of the Mueller matrix provides evidence to the validity of using the effective medium models discussed in section 8.2. The remaining aspects are related to parameter setup and tuning.

Using all the Data

Model fitting to Mueller matrix data is a powerful but implicit method to derive parameters such as particle filling fraction, film thicknesses, roughness layers, particle material quality (from oscillator models), and an underlying estimation of the local field behavior (from the effective medium model). Upon optimization, the best fit parameters provide an analytic expression for the constitutive parameters and an estimate on the quality of the fit. Since this method is implicit, there is generally no guarantee that the parameters are indeed physically correct. In this regard, it is important to constrain the optimization problem as much as possible through measurement.

In this dissertation, the following methods were used to constrain the optimization problem. Film layer thicknesses are measured with cross sectional scanning electron microscopy (SEM). This is useful not only to determine clearly defined boundaries, but also to define regions of dense and sparse particle layers, such as a surface roughness top layer, or if a graded index is necessary. Profilometry is used to cross validate total film thickness, determine large trends in height variation such as slanted films, and to estimate surface roughness. Particle shape and material quality are statistically determined through sparse particle samples on transmission electron microscopy (TEM) grids. From bright-field TEM, particle shape and size distributions are calculated. Scanning transmission electron microscopy (STEM) in conjunction with energy-dispersive X-ray spectroscopy (EDX) gives elemental maps, useful in understanding material quality and distribution, including core-shells/oxide layers. Selected area electron diffraction (SAED) patterns are imaged to define crystalline structure in conjunction with high resolution TEM. Particle characterization help to inform the bulk material oscillator models for particles, if multiphase effective medium mixtures should be used, and if spherical, elliptical, core shell, or other effective polarizabilities are necessary. Visible and infrared normal incidence spectroscopy cross validate the consistency of explicit individual particle measurements of material quality, by looking for known absorption resonances of the constitutive elements/compounds over many particles. Slight variations of resonance peaks may also highlight changes in the local field due to particle shape and packing. Particle filling fraction is estimated by subtractive nanoparticle weight measurements. Angle-resolved scattering or integrating sphere measurements are used to quantify the percentage and behavior of the diffusely scattered field. In general, the explicit measurements discussed above are meaningful only in a statistical sense. This is, in part, why two independent measurement schemes are used when possible. E.g., SEM and profilometry, TEM and infrared spectroscopy. The explicit measurements set meaningful bounds to constrain the model fit problem. Once the bounds, the oscillator model, and effective medium model are chosen, the fill model is fit to Mueller matrix measurements across a wide range of wavelengths and angles.

8.4 SINGLE PARTICLE CHARACTERIZATION

An important step in designing metasurfaces and metamaterials with emergent optical properties is to certify that the nanoscopic constituents behave as expected. The gold standard for this is single particle measurement. But this is not always an easy task. First, the nanoparticle should be isolated and able to be found. This is easy when particles can be deterministically placed, a common feature of top-down fabrication. Though, in bottom-up processes satisfying this condition can be involved. Particle placement is not the only hurdle as fundamental signal-to-noise ratio limitations exist. First, the ratio of spot size to particle area is typically on the order of 10-0.1%. Since extinction efficiencies are limited, the percentage of incident power converted to extinction should be expected to be small. Another approach is to abandon the idea of true single particle measurement in favor of measuring a collection of particles where single particle properties can be well estimated. This removes the fundamental signal-to-noise restrictions of single particle measurement by adding more signals (particles). For bottom-up processes a gold standard in this regard is particles sparsely suspended in solution. The collective is measured, and the Beer-Lambert law is used to back out single particle properties. This section outlines the Beer-Lambert measurement approach, which is used extensively in Chapter 9 to characterize single Huygens particles.

Consider a system where particles are sparsely distributed in a liquid. Let the system be in near equilibrium so that fluctuations give rise to uniformly ergodic Brownian motion of the suspended particles. Furthermore, assume that particles do not agglomerate. Ergodic motion in three dimensions allows the ensemble distribution to be one of overlapping particles with uniform probability of occupying any volume element. Correspondingly, there are no meaningful correlations between particles and no net phase difference between scattered fields on the average. Given that particles are well separated, it can be assumed the local field is dominated by the incident field contribution. This situation is well within the regime of radiative transfer theory. If multiple scattering is weak and the thermal emission from the particles is well below the measurement wavelength, then the radiative transfer equation derives Beer's law,

$$\frac{I(L)}{I_o} = e^{-\int \partial l \, \mathbb{E}\left[C_{ext}\mathbb{E}[\rho|\mathcal{T}]\right]}, \tag{8.4.1}$$

where $\mathbb{E}[\rho|\mathcal{T}]$ is the expected number density of particles of type, $\mathcal{T}$. The outer expectation is the expected extinction cross-section over particle types, weighed by the corresponding number density for each type. In principle, $\mathbb{E}\left[C_{ext}\mathbb{E}[\rho|\mathcal{T}]\right]$ is a function of both the incident beam's pathlength, l, and cross-sectional area, A, since particles are discrete. In practice the illuminated

volume is made large enough that the addition or subtraction of edge particles does not define a substantial change in the transmittance. E.g., no binary transitions in transmittance. The variation in particles within the measurement time window is then generally small, with outer edge particles popping in and out of the volume at a near equal probability. Given a large enough spot size,

$$\mathbb{E}\left[C_{ext}\mathbb{E}[\rho|\mathcal{T}]\right] \approx ff\frac{1}{V}\int dP(\mathcal{T})C_{ext}(\mathcal{T}), \tag{8.4.2}$$

where ff is the volume filling fraction of particles in the solution and $P(\mathcal{T})$ is the probability distribution of particle types, which is a readily measurable variable using transmission electron microscopy or similar.

Incorporating Nonidealities

It is often the case that a portion of particles crash out (settle at the bottom) in the suspension. Clearly these particles should not be in the incident beam path. Therefore, crash out may cause an overestimate in volume fill fractions, when calculated from powder weight or similar prior to suspension. The primary variable of interest is type-resolved extinction. The volume filling fraction is a convenient scale factor that increases the signal-to-noise ratio. Correspondingly it would be nice to be able to normalize out filling fraction dependence upon final calculation.

As discussed, noise is an unavoidable reality of measurement. Consider three optical measurements. One in the dark, S_{dark}, one with a cuvette of solution, S_{sol}, and one with cuvette of solution and particles, S_{sam}. The model for the signal received by these samples is

$$\begin{aligned} S_{dark} &= \mathbb{E}[\tilde{Y}_{dark}] = B \\ S_{sol} &= \mathbb{E}\left[S_{sol}^{\dagger}e^{-\tilde{X}_{sol}} + \tilde{Y}_{sol}\right], \\ S_{sam} &= \mathbb{E}\left[S_{sol}^{\dagger}e^{-\left(ff\frac{L}{V}\int dP(\mathcal{T})C_{ext}(\mathcal{T})+\tilde{X}_{sam}+\tilde{X}_{sol}\right)} + \tilde{Y}_{sam}\right]. \end{aligned} \tag{8.4.3}$$

All expectations are taken over time. $\tilde{Y}\sim N(B,\sigma)$ is a normally distributed random variable to model additive white noise. $X\sim N(0,\sigma)$ is a normally distributed random variable for modeling multiplicative noise. An example of multiplicative noise in this context could be intensity fluctuations caused by floating contamination in the solution, $\ln(\tilde{X}_{sol})$, or slight changes in particle density in time, $\ln(\tilde{X}_{sam})$. The ideal signal that would be received by the detector from

an optical measurement of a single cuvette of solution is $S_{sol}^{\dagger}$. This includes cuvette reflections and any minute loss in intensity from absorption in the solution. Then

$$\frac{S_{sam}-S_{dark}}{S_{sol}-S_{dark}} = e^{-\left(\frac{\sigma_{sam}^2}{2}+ff\frac{L}{V}\int dP(\mathcal{T})C_{ext}(\mathcal{T})\right)}. \quad 8.4.4$$

If, as argued earlier, $\frac{\sigma_{sam}^2}{2} \ll ff\frac{L}{V}\int dP(\mathcal{T})C_{ext}(\mathcal{T})$, then

$$\frac{-\ln\left(\frac{S_{sam}-S_{dark}}{S_{sol}-S_{dark}}\right)}{\max_{\lambda}\left(-ln\left(\frac{S_{sam}-S_{dark}}{S_{sol}-S_{dark}}\right)\right)} = \frac{\int dP(\mathcal{T})C_{ext}(\mathcal{T})}{\max_{\lambda}(\int dP(\mathcal{T})C_{ext}(\mathcal{T}))}. \quad 8.4.5$$

Given that the particle distribution is known, equation 8.4.5 enables measurement variables to be equated explicitly to the extinction normalized by a constant scale factor, which is easy to compare with theoretical calculations.

Chapter 9

FABRICATION AND CHARACTERIZATION OF SI HUYGENS PARTICLES

Eslamisaray, M. A.[†]; Wray, P. R.[†]; Lee, Y.; Nelson, G. M.; Ilic, O.; Atwater, H. A.; Kortshagen, U. R. A Single-Step Bottom-up Approach for Synthesis of Highly Uniform Mie-Resonant Crystalline Semiconductor Particles at Visible Wavelengths. *Nano Lett.* **2023**, *23* (5), 1930–1937. https://doi.org/10.1021/acs.nanolett.2c05084.

([†]M.A.E. and P.R.W. contributed equally)

ABSTRACT

Optically Mie-resonant crystalline silicon nanoparticles are synthesized using a bottom-up nonthermal plasma process. Highly controllable particle sizes between 60 to 214 nm with standard deviations smaller than 5.4% are achieved via temporary trapping the nanoparticles inside a continuous-flow plasma reactor. The particle size is simply tuned by adjusting the precursor gas residence time. By dispersing the nanoparticles in deionized water, optical extinction measurements show stable colloidal solutions of a metafluid, supporting both strong magnetic and electric dipole resonances in the visible. The spectral overlap of these resonances is related to anomalous directional Kerker scattering. The extinction measurements show excellent agreement with Mie theory, indicating that the fabrication process is precise in maintaining a narrow deviation in size, shape, and material constraints for most samples. These particle characteristics are also independently verified via TEM analysis. This single-step gas-phase process is capable of synthesizing Mie-resonant nanoparticles of different dielectric materials and directly depositing them on desired substrates.

9.1 INTRODUCITON

Crystalline semiconductors are an important material class to study light-matter interactions from scattering particles in the visible regime. Their continuum of interband transitions separated by a clearly defined and properly sized bandgap can enable a distinctively large permittivity with comparatively little dissipative loss[297–299]. This offers material-driven benefits such as a high elastic scattering efficiency, strong field localization, and scattering states not accessible in systems of a different material[298–304]. High scattering efficiency is a direct result of inherently low absorption losses, which are particularly characteristic of indirect-gap crystalline semiconductors. Furthermore, the scattered field of dielectric particles is driven by displacement currents of bound charges. This contrasts plasmonic scattering, which is driven by conduction currents of free electrons and therefore susceptible to Ohmic losses[305–307]. The inherent lack of nonradiative loss implies the possibility of near unity radiative efficiency important in many applications, such as extracting light from quantum emitters[308]. Similar efficiency is seen in low-index and low-loss materials, such as insulators, though this is at the expense of less field confinement, a reduced mode volume, and/or increased particle size[139,298,309]. Alternatively, the notably large refractive index of semiconductors can produce a high scattering efficiency with strong field confinement, when contrasted with a low-index ambient.

Interestingly, the combination of both field confinement and low nonradiative losses can produce high quality factor (Q-factor) resonances, and this has been shown to result in unique highly directional scattering states[310–313]. For example, spherical high-index and low-loss dielectric particles can exhibit strong circulating displacement currents, which mimic magnetic multipoles, termed optically-induced magnetic resonances (OMRs). These artificial magnetic-type atoms are of interest in the metamaterial and metasurface community as they lead to a homogenized non-unity effective magnetic permeability at optical frequencies[314–316]. Furthermore, these often high-Q harmonics can interfere with broadband resonances resulting in anomalous highly directional scattering, exhibiting a Fano-like line shape, termed the Kerker effect[300,301,317]. Though magnetic multipoles exist in insulators, their Q-factors are usually too low to produce anomalous scattering, particularly backward Kerker scattering[309]. In metals, Ohmic losses damp circulating induction currents combatting the existence of magnetic-type multipoles altogether[298]. Such anomalous behavior in insulating or metallic systems therefore needs to offset the inherent shortcomings of the material. This necessitates either a precisely structured exciting field, such as particles in a cleverly designed periodic lattice, particles with multiple layers of different materials, or a properly designed particle shape, such as a metallic split-ring resonator[318–323]. In contrast, indirect bandgap crystalline semiconductors can have both strong electric and magnetic-type Mie resonances existing

simultaneously in a simple single sub-wavelength sphere, under plane-wave illumination[324–326]. Furthermore, higher-order electric and magnetic-type Mie resonances can also exist simultaneously in the sub-wavelength particle, since the large particle permittivity shrinks the effective wavelength within the particle. Clearly, crystalline semiconductors offer a platform of features desired in many fields of photonics. In that regard, spherical crystalline silicon (c-Si) particles are an ideal candidate for exploring such effects in the visible. Furthermore, c-Si particles may also integrate well with the modern Si-based technologies.

Low-cost and scalable synthesis of highly uniform crystalline high-index dielectric nanoparticles (NPs), as the building blocks of metastructures and metafluids, has been a subject of active research for over a decade, however producing ideal Si meta-atoms through bottom-up techniques still remains a challenge[327]. In the Mie-resonant regime, variations in particle size, shape, and material quality have a notable impact on the particle's overall electromagnetic response. Several fabrication methods have been developed for the synthesis of Si meta-atoms with different achievement levels over NP crystallinity, sphericity, purity, and density as well as scalability of the technique. Femtosecond laser ablation of bulk Si donor targets in air or liquid solvents[312,324,328–330] has been widely used to generate nanodroplets of molten Si that form into polydisperse spherical NPs upon solidification. A more recent method of laser-induced transfer[326,331,332] allows the direct deposition of the molten droplets onto receiver substrates with high positional accuracy necessary for the deposition of ordered metamaterials. In these methods, NP size and degree of crystallinity could be tuned by the laser energy and number of pulses with good repeatability. However, the most successful laser-induced methods require complex optical systems and inherently suffer from low throughput. Gas phase synthesis techniques enable the bottom-up production of Si meta-atoms. As one of the most promising techniques, chemical vapor deposition (CVD) can produce sub-micrometer-sized Si particles through decomposition of disilane or trisilane at elevated temperatures[333–335]. The as-synthesized particles are amorphous and porous; therefore, a post-annealing process is required to obtain polycrystalline particles. Due to the larger size of the particles, their polycrystallinity, and lack of tunability over size distribution, CVD synthesized particles have higher potential in light scattering applications for near-IR rather than the visible spectral range. Recently, colloidal synthesis of Mie-resonant Si NPs has been accomplished via grinding Si lumps with a blender into small-sized NPs[336], or thermal disproportionation of SiO powder into Si and SiO_2 before extracting the freestanding c-Si NPs by etching out the SiO_2 matrix[337,338]. The resulting colloidal solutions are highly polydisperse and therefore, require several post-synthesis centrifugation processes for size-separation of the Si NPs. Despite the scalability of this techniques, they require several post-synthesis processes, and their Si NPs lack either the ideal size/shape uniformity or purity.

9.2 PLASMA SYNTHESIS OF SIZE-CONTROLLED CRYSTALLINE SILICON NANOPARTICLES

Over the past two decades, nonthermal plasma synthesis has emerged as a competitive technology for the synthesis of nanocrystals difficult or impossible to handle with other fabrication techniques. Nanocrystals of covalently bonded group IV elements,[339–341] noble and transition metals,[342–345] and compound semiconducting materials[346–350] are among the vast library of materials successfully developed by this technology. Nonthermal plasma reactors provide a non-equilibrium environment wherein gaseous precursors, typically at room temperature, are dissociated via collisions with hot free electrons. The resulting reactive radicals and ions lead to particle nucleation, growth, and crystallization in the plasma discharge. This bottom-up process has excellent control over particle size and size distribution owing to the negative charge of the NPs immersed in the plasma preventing particle agglomeration. Compared to their liquid-phase counterparts, nonthermal plasmas also benefit from a solvent- and ligand-free process resulting in highly pure nanocrystals in which the surface passivation could be controlled via precursor selection[351] as well as in-flight functionalization.[352,353] By connecting the nonthermal plasma reactors to an extraction orifice, a pressure difference is created which accelerates nanocrystals towards the low-pressure deposition chamber where they are collected on desired substrates. This single-step deposition technique enables the scalable collection of crystalline particles in a powder form or as a thin film with tunable film thickness and porosity.[354]

Despite all the promising advances, nonthermal plasmas have been long limited to synthesis of small crystalline NPs, typically < 10 nm in diameter, due to the short residence time of NPs in plasma discharges. Bapat et al.[355] expanded this limit to c-Si NPs of 35 nm by operating the plasma in a constricted filamentary regime wherein NPs were temporarily trapped inside the reactor. NP trapping is the result of the competition of different forces acting upon negatively charged particles, including electrostatic, thermophoretic, and drag forces. Such trapping mechanism acts as a filter allowing small NPs to grow to a critical size in the trapping zone before being de-trapped and collected. Recently, Wray et al.[356] improved this process by optimizing the plasma conditions pushing the average particle diameter to 82 nm with a standard deviation of 1.2 nm. The random particle films of these NPs exhibited an OMR resonant peak at 420 nm. In this study, we expand on the previous work on nonthermal plasmas operating in the constricted filamentary regime showing that the hybrid diffuse-filamentary plasmas can produce monolithically c-Si NPs in a wide range of diameters exhibiting strong scattering resonance with extinction peaks covering the entire visible range.

Hydrogen terminated c-Si NPs supporting OMRs were synthesized via decomposition of silane (SiH_4) in a flow-through tube plasma reactor diagrammed in figure 9.2.1(a) and described in detail in the Supporting Information. The precursor dissociation and particle nucleation and growth begin in a low-density diffuse plasma region upstream of the RF electrode. In this region, NPs are temporarily trapped and grow until they reach a critical size. To verify this trapping mechanism, a laser light scattering experiment was performed by shining a sheet of laser light at $\lambda = 532$ nm through the top of the reactor, for *in situ* detection of trapped NPs. This procedure is further explained in the supporting information. Figure 9.2.1(b) shows an image of the discharge during normal operation taken by a high-speed camera. A strong green scattering signal is observed a few centimeters above the RF electrode close to the tube wall representing a high concentration of NPs at this location. We define this region as the trapping zone. Once the desired NP size is reached, which is controlled by the gas flow rates as well as other plasma conditions, NPs are de-trapped and enter the high-density filamentary region downstream of the electrode. At this stage of the reactor, NP temperature exceeds the gas temperature by several hundreds of Kelvins, mainly due to electron-ion recombination at the particle surface, resulting in crystallization of the NPs.[355,357] Finally, the now crystalline NPs travel through an extraction orifice and accelerate towards a high-vacuum deposition chamber, where they can be collected directly on the appropriate substrates for the desired application. Figure 9.2.1(c) shows a bright-field transmission electron microscope (TEM) image of a NP sample with a mean diameter of 112 nm. The NPs are highly uniform and spherical with minimal defects. The difference in apparent contrast of the NPs is due to their alignment with respect to the electron beam. Figure 9.2.1(d) shows a high-resolution image of a typical NP to better emphasize the near complete spherical shape. The crystallinity of the NPs is verified by the selected area electron diffraction (SAED) pattern shown in Figure 9.2.1(e). Even though the focus of this paper is on c-Si NPs, we also show the versatility of the nonthermal plasma technique by synthesizing germanium and silicon-germanium NPs in a similar size regime. Therefore, we show that by only changing the precursor gasses flowing into the reactor we can easily switch to synthesizing other dielectrics and even their alloys (refer to the supporting information for more details).

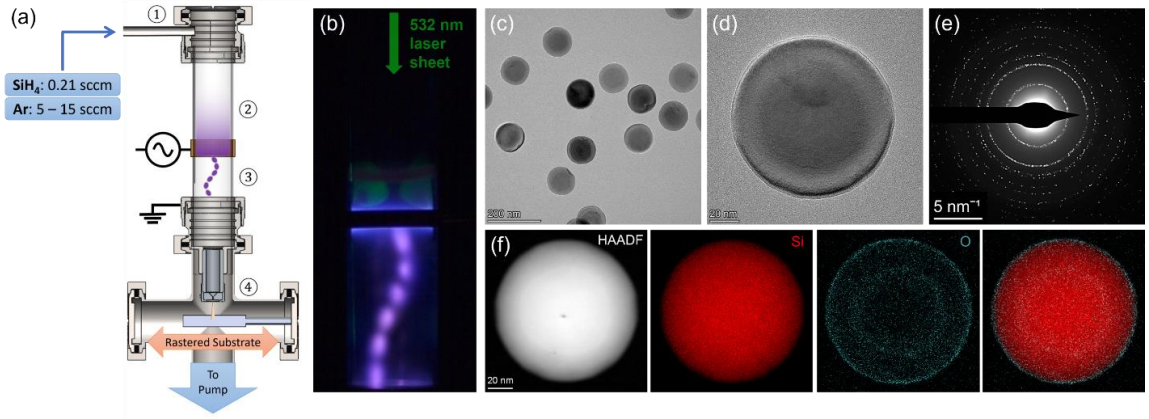

Figure 9.2.1. Particle shape and composition characteristics. (a) Schematic diagram of the flow-through nonthermal plasma reactor operating in a constricted filamentary regime. ① Precursor injection into the reactor through a side ported flange. ② Low-density diffuse region, where silane dissociation and particle nucleation begin. ③ High-density filamentary region, where size selected particles crystalize, mainly due to electron-ion recombination heating mechanism. ④ NP extraction through the orifice and injection into the deposition chamber towards the substrates. (b) High-speed camera image of the laser light scattering experiment showing the plasma discharge (violet) and particle trapping zone (green). (c, d) Representative bright-field TEM images of c-Si NPs with a mean diameter of 112 nm. (e) SAED pattern of randomly selected Si NPs showing the crystallinity of NPs. (f) Select HAADF-STEM images of a single Si NP after air exposure for one day. STEM-EDX elemental maps of Si (red) and O (dark cyan) show a Si core surrounded by a thin oxide shell.

Figure 9.2.2(a) shows six distinctly controlled c-Si NP size distributions produced using the nonthermal plasma reactor in figure 9.2.1(a). With mean diameters ranging from 60 to 214 nm, these distributions represent an over two-fold size range produced simply by varying the precursor residence time in the plasma discharge. The standard deviation of all samples is less than 5.4% of their respective mean diameters, indicating nearly monodispersed samples. Prior studies have shown that NP size correlates linearly with the particle residence time for plasma reactors operating in the diffuse regime[340]. The particle residence time includes two factors: 1. the time it takes for particles to travel the length of the reactor (i.e., the gas residence time), and 2. the time particles remain in the trapping zone. While the gas residence time can be easily determined, estimation of the particle trapping time requires intricate experimental methods capable of detecting individual particles in the reactor. Interestingly, recent Monte Carlo simulations of particle trapping for sub 10 nm NPs have shown that even though considering particle trapping in the reactor results in the synthesis of particles with larger sizes than the no trapping assumption, the average NP size is still linearly dependent on the gas residence time.[358] In figure 9.2.2(b), we experimentally validate this result by controlling the NP diameter in the constricted mode plasmas via adjusting the gas residence time. Furthermore, we show the linear relation to gas residence time holds even for particle sizes over 10x the prior studies

by Monte Carlo. Therefore, NP sizes can be simply and linearly controlled in a wide size regime, despite the complex force balance in dusty plasmas. The gas residence time is defined as $t_{res} = \frac{PA_cL_p}{P_0Q}$, where P is the pressure of the reactor, P_0 the standard pressure, Q the total gas flow rate, A_c the cross-sectional area, and L_p the length of the plasma. In figure 9.2.2(b) we tuned this time between 2.2 - 7.2 seconds by adjusting the Ar flow rate and the orifice size while all other experimental conditions, including the silane flow rate, tube size, electrode position, and RF power were fixed. All experimental conditions used in this study are summarized in supporting information table 9.5.1.

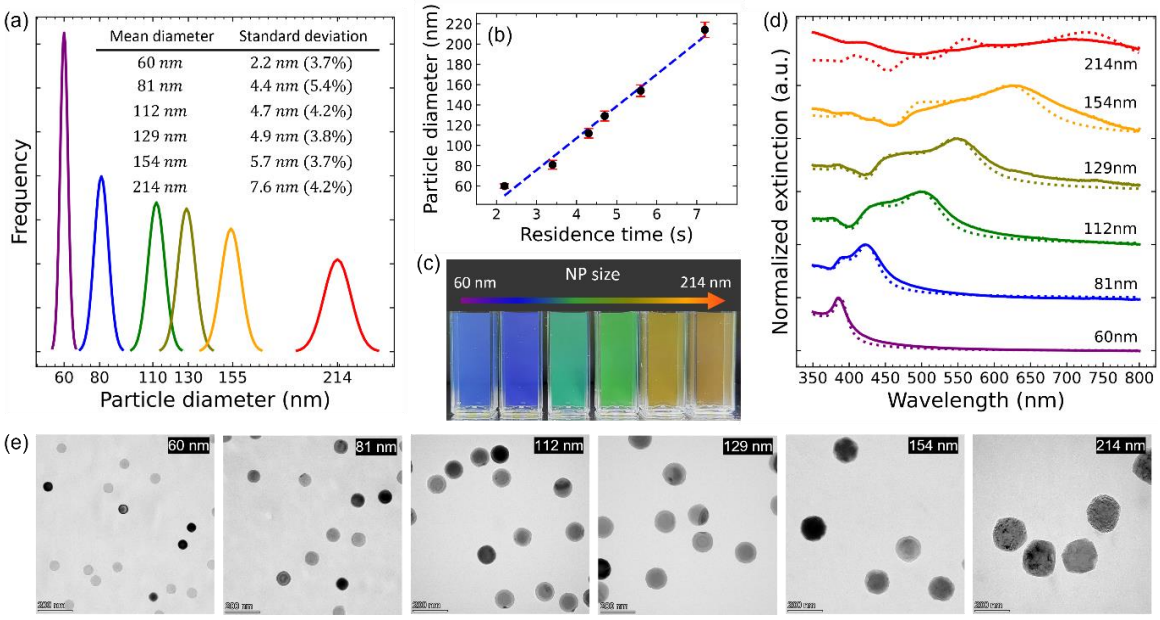

Figure 9.2.2. Particle optical characteristics. (a) Gaussian-fit particle size distributions as measured by TEM analysis of hundreds of particles for each sample. Each particle size distribution is color coded from purple (60 nm) to red (214 nm). The table shows each distribution mean particle diameter, standard deviation, and percent deviation from the mean value in parentheses, (b) Average diameters of NPs as a function of the gas residence time inside the plasma reactor. Error bars are the standard deviations obtained from the particle size distribution, (c) Photographs of colloidal dispersions of monodisperse c-Si NPs in DI water with NP size increasing from left to right. The cuvettes are illuminated with a white light from the bottom, (d) Measured (solid line) and simulated (dotted line) extinction spectra of particles suspended in DI water, (e) Representative bright-field TEM images of c-Si NPs with mean diameters ranging from 60 to 214 nm.

9.3 OPTICAL CHARACTERIZATION

The H-terminated NPs undergo a self-limiting oxidation process upon exposure to air at ambient conditions resulting in the formation of a thin (< 5 nm) oxide shell on the surface of the c-Si NPs[359,360]. This is seen in the high-angle annular-dark-field STEM (HAADF-STEM) images shown in figure 9.2.1(f). By dispersing the NPs in deionized (DI) water and sonicating the solution for 15 minutes, homogenized colloidal solutions are obtained. Figure 9.2.2(c) shows representative c-Si NPs suspended in a DI water solution under white light illumination. The samples, also referred to as metafluids, show a clear change in color across the visible spectrum, indicating that the size control is sufficient to produce strong and distinct Mie-resonant scattering throughout the visible. The oxide layer on the c-Si NPs is too small to noticeably alter the resonant modes of the NPs, especially given the low index contrast between water and SiO_2. With that said, the native oxide layer at the NP surfaces does provide a negative surface potential[336] which hinders NP agglomeration in the colloidal solution. We have found that this surface potential keeps the solution stable for many months, without the need for complex surface functionalization.

In order to better characterize the unique scattering states of these NP solutions, figure 9.2.2(d) shows the result of optical extinction measurements with simulated extinction spectra overlaid. The simulated spectra, obtained through Mie theory, are based on the measured diameter distribution in figure 9.2.2(a) and keep the same color convention, 60 nm (purple) to 214 nm (red). Apart from the 214 nm sample, we see excellent agreement between measurement and theoretical predictions in both the spectral shape and strength of the extinction. This further validates what was found in the single particle characterization in Figure 1; the nonthermal plasma process can produce, with high accuracy and specificity, pristine c-Si particles with near complete circular form. Size variations produced by this technique have standard deviations small enough that, from the electromagnetic point of view, the particle size distributions are nearly equivalent to a delta function. (a comparison to theoretical predictions based on delta function distributions is shown in the supplementary information.) All curves are normalized as $x/max(x)$ so that any potential differences in either spectral shape or oscillator strength between measurement and theory are preserved. Therefore, the striking spectral match is not simply a result of normalizing to artificially match resonance peaks, but a result of experimentally approaching near exact theoretical predictions. Both the procedure for measuring the extinction spectra and comparing measurements to simulation is described in the supplementary information.

Figure 9.2.2(e) shows representative TEM images of all samples with mean diameters ranging from 60 to 214 nm. All samples are highly monodispersed, nearly completely spherical, and,

apart from the 214 nm mean diameter sample which shows porous NPs, composed of fully dense c-Si. The reason behind the porosity of the NPs in the 214 nm sample is still not well understood; however, we believe that it could be due to smaller temperature variations in larger NPs within the plasma discharge. Such temperature variations, during both the heating and cooling processes, are necessary for the formation of single-crystalline highly dense spherical NPs[357,361]. More work is underway to improve the quality of this sample by optimizing the plasma conditions, including the RF power, reactor pressure, and plasma volume. Once dispersed in water the pores of the 214 nm NPs are filled with water, which has a lower refractive index than Si, resulting in a reduction in the effective refractive index of the NPs. Therefore, in figure 9.2.2(d) we model these water inclusions in simulation as a Bruggeman effective index and find a 20% fill fraction of water in c-Si to best fit the experimental data. All other simulated spectra assume pure c-Si particles. More detail on the 214 mean diameter sample is shown in the Supporting Information.

Given the strong agreement between measurement and simulation, figure 9.3.1 (left) takes the theoretical extinction spectra based on the measured diameter distribution and decomposes it into scattering and absorption contributions. In all cases a strong OMR is observed. In particles around 60 nm in diameter a magnetic dipole resonance occurs at a wavelength of 375 nm. This contributes primarily to an absorption dominated spectra as this wavelength is below the visible spectrum (380 - 800 nm) and within the lossy region of silicon. Though even in a region of appreciable loss, the large real refractive index of c-Si enables the existence of OMRs. As particle size increases, both the electric and magnetic-type harmonics red-shift and the extinction spectra become scattering dominated. Correspondingly, the radiative efficiency increases. Figure 9.3.1 (right) shows the radiative efficiency of each particle distribution. In each case, the average scattering efficiency for the spectral range starting from the peak of the electric dipole resonance to the end of the visible spectrum is reported with minimum and maximum values shown in parentheses. The results show efficiencies approaching 99%, even though particles are clearly strongly interacting.

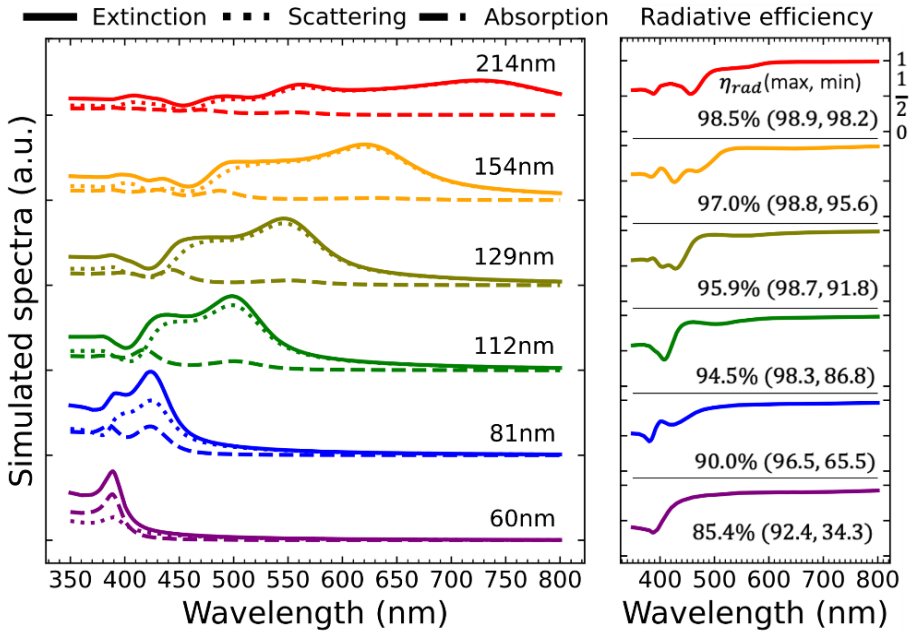

Figure 9.3.1. Comparison of measurement to simulated spectra. (Left) Simulated extinction (solid line), scattering (dotted line), and absorption (dashed line) efficiency for all particle size distributions shown in figure 9.2.2(a). (Right) Wavelength-resolved radiative efficiency for each particle size distribution. In both figures, all curves are color coded by mean particle size, according to the size convention in figure 9.2.2(a). The average, maximum, and minimum radiative efficiency for each distribution is reported directly below the respective radiative efficiency curve in the right figure. These values are calculated in the spectral window starting from the electric dipole resonance to the end of the visible spectra.

According to Mie theory, the total scattering efficiency can be decomposed into electric ($\sigma_{sca}^{E} = \frac{1}{x^2}\sum_n \|c_n^E\|^2$) and magnetic-type ($\sigma_{sca}^{M} = \frac{1}{x^2}\sum_n \|c_n^M\|^2$) partial efficiencies, where c_n^E and c_n^M are the electric and magnetic-type Mie coefficients of polar order, n, and $x = 2\pi r/\lambda$ is the size parameter of a particle with radius, r, at wavelength λ. The total efficiency is then $\sigma_{sca} = \sigma_{sca}^{E} + \sigma_{sca}^{M}$. The right column of figure 9.3.2 decomposes the scattering efficiency spectra from figure 9.3.1 into electric and magnetic type partial efficiencies to determine the fundamental atom-like oscillations that give rise to the scattering behavior. From this, we find that all particle sizes support a strong magnetic dipole resonance. Furthermore, particle sizes larger than 150 nm also support electric and magnetic quadrupoles resulting from the large and relatively lossless permittivity of c-Si. The magnetic dipole resonances are shown to spectrally intersect with the tail of the electric dipole response, a precursor to achieving Kerker scattering. To better understand the potential for anomalous directional scattering, the left column of figure 9.3.2 decomposes the scattering spectra into a basis of directional Kerker harmonics. For spherically symmetric objects under plane wave illumination the forward (c_n^f)

and backward (c_n^b) directional Kerker scattering coefficients are related to the Mie scattering coefficients through the transform, $c_n^f = \frac{(-i)^n}{2}(c_n^M - ic_n^E)$ and $c_n^b = -\frac{(i)^n}{2}(c_n^M + ic_n^E)$. The Kerker expansion maintains almost all of the properties which popularized Mie theory, while also providing a simpler analytic and conceptual framework for understanding directional scattering. Some of the advantages the Kerker expansion provides include weak coupling between forward and backward-type harmonics, clear notions of directionality and side lobes for each harmonic, and interference between same type harmonics relating to changes in directivity. Under the Kerker expansion, the scattered intensity in the exact forward direction, $I(\theta = 0) = \frac{\pi}{2Zk^2} \| \sum_n \sqrt{(2n+1)} c_n^f \|^2$, is dependent only on the forward Kerker coefficients, where Z is the impedance of the host media. Likewise, the intensity in the exact backward direction, $I(\theta = \pi) = \frac{\pi}{2Zk^2} \| \sum_n \sqrt{(2n+1)} c_n^b \|^2$, depends only on the backward Kerker coefficients. Furthermore, the total scattering efficiency can be decomposed into forward and backward partial powers, $\sigma_{sca} = \sigma_{sca}^f + \sigma_{sca}^b$, where $\sigma_{sca}^f = \frac{1}{x^2} \sum_n \| c_n^f \|^2$ and $\sigma_{sca}^b = \frac{1}{x^2} \sum_n \| c_n^f \|^2$. The left column of figure 9.3.2 shows that, in all size distributions, there exists a spectral region characterized by anomalous directional scattering. The region near the lowest energy electric and magnetic dipole crossing, shows suppressed backward coefficients and strong forward Kerker peaks. At the middle electric and magnetic crossing point shows the peak in the first order backward scattering coefficient. In both the 60 nm and 80 nm average diameter samples, we see a clear region of dominant backward Kerker coefficients, indicating anomalous backward scattering in these samples. Second order Kerker coefficients are also seen in particle sizes larger than 150 nm.

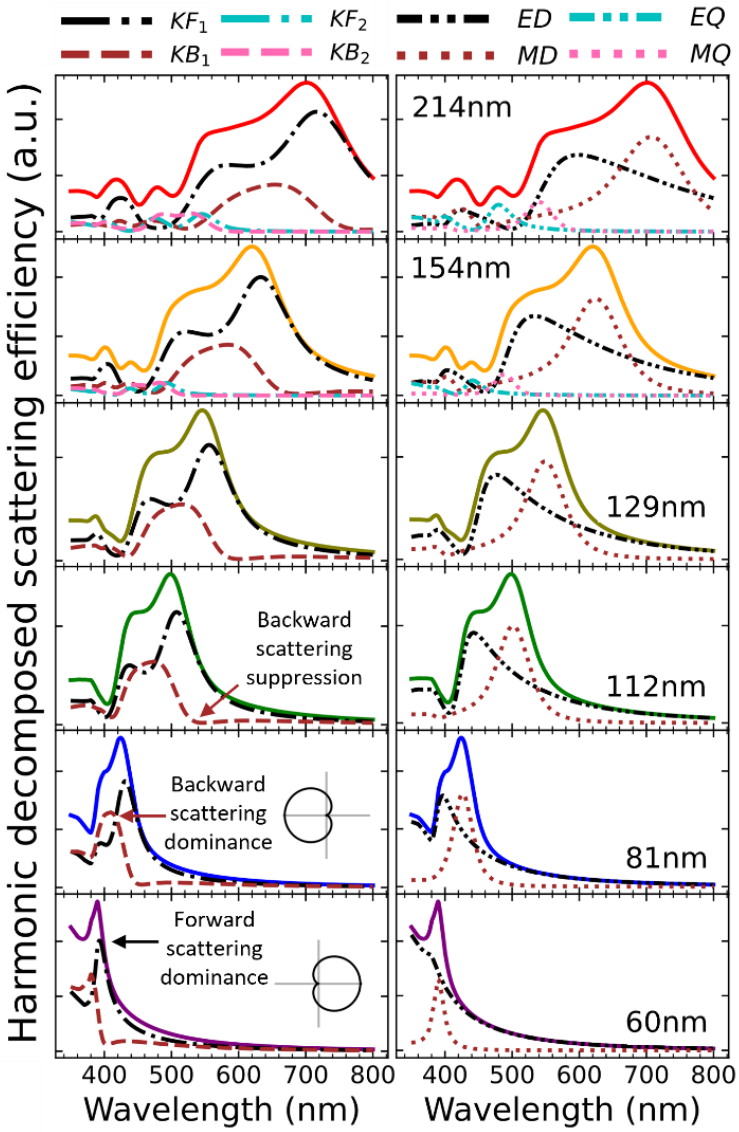

Figure 9.3.2. Harmonic decomposition of scattering efficiency. (Left) Decomposition of simulated scattering efficiency in terms of first (black) and second order (teal) forward (solid-dot line) and first (brown) and second order (pink) backward (dashed line) directional Kerker harmonics. (Right) Decomposition of simulated scattering efficiency in terms of first (black) and second order (teal) electric (solid-double dot line) and first (brown) and second order (pink) magnetic-type (dotted line) Mie harmonics. In both figures, the scattering spectra of each particle size distribution is color coded according to figure 9.2.2.

9.4 CONCLUSION

We have demonstrated the bottom-up synthesis of highly spherical pure crystalline silicon nanoparticles in the optically Mie-resonant regime, using nonthermal plasmas. Particle mean diameter is controlled between 60 to 214 nm, and all samples have shown extremely narrow size distributions of less than 5.4% of their respective mean diameters. Such control in particle size in this size regime stems from operating the plasma in a constricted filamentary regime wherein NPs are trapped in a low-density plasma region due to the balance of different forces acting upon them. This trapping mechanism acts as a filter allowing particles to grow beyond the size regime achievable in diffuse plasmas of the same reactor length. After reaching a critical size, particles are released into a high-density discharge, where they crystalize. Nanoparticle size is shown to have a linear relationship with the total gas residence time in the reactor. Optical extinction measurements of NPs in water show excellent agreement with Mie theory predictions, further verifying pristine control in particle shape and material quality. Furthermore, extinction measurements show these particles exhibit both electric and magnetic-type Mie resonances in the visible regime giving rise to anomalous highly directional Kerker scattering. A strong magnetic dipole is seen in all samples. This is only possible due to the high degree of crystallinity of the particles which allows for strong circular currents to exist within each particle. At present, particles with a 214 nm diameter or above exhibit a porous structure. We believe it is possible to improve the quality of these particles by optimizing the plasma conditions, including the RF power, reactor pressure, and plasma volume. Finally, we have demonstrated that this single-step synthesis technique could be extended to other dielectric materials by simply changing the precursor gasses flowing into the reactor.

9.5 METHODS AND SUPPLEMENTARY INFORMATION

Nanoparticle synthesis. Crystalline silicon (c-Si) nanoparticles (NPs) are synthesized using a continuous-flow nonthermal plasma reactor. The reactor consists of a 20 cm long quartz tube with an outer-diameter of 38 mm and an inner-diameter of 35 mm, connected to grounded Ultra-Torr vacuum fittings at both ends. The primary gas feed, a mixture of argon (Ar) and 0.21 standard cubic centimeters per minute (sccm) of pure silane (SiH_4), is injected into the reactor through the top sideported flange. A plasma is generated by applying 200 W of radiofrequency (RF) power at 13.56 MHz through a copper ring electrode placed on the outside of the tube, 6.5 cm above the lower grounded fitting. A slit-shaped orifice, 12 mm in length and adjustable in width, is placed at the bottom of the reactor. This adjustable orifice provides an additional mechanism for controlling the pressure of the reactor without changing the gas flow rates. It also creates a considerable pressure difference between the synthesis reactor and the deposition chamber. Therefore, upon exiting the reactor, particles are accelerated through this extraction orifice and impacted onto desired substrates. To control the NP size, the Ar flow rate was adjusted between 5.5-15 sccm and the orifice width was set between 0.03-0.1 mm to achieve reactor pressures between 1.7-3.1 Torr. All other experimental conditions, as explained in detail above, are held constant for all samples.

Laser Light Scattering. A laser light scattering (LLS) experiment was performed for *in situ* investigation of particle trapping in the reactor with a constricted capacitive discharge. A sheet of laser light was generated by passing a 500 mW, 532 nm laser beam through a plano-concave lens. The laser sheet was directed axially along the length of the discharge through a glass viewport mounted on top of the reactor tube. Scattered light was collected at ~90° to the laser sheet using a high-speed camera (Chronos 2.1 from Kron Technologies). A short exposure time of 1 ms was chosen to suppress the background emission from the diffuse plasma region and capture the fast-rotating high intensity plasma filament in the constricted plasma region.

Transmission Electron Microscopy. TEM samples were collected on thin carbon coated copper grids and analyzed using a Thermo Scientific Talos F200X scanning transmission electron microscope (STEM) equipped with a Super-X energy-dispersive X-ray (EDX) detector operating at an accelerating voltage of 200 kV. For each sample, the effective diameters of 300 particles were obtained using ImageJ in order to fit the Gaussian size distributions shown in the text. Spatially resolved STEM-EDX maps were collected with an acquisition time of 10 minutes, a dwell time of 100 μs/pixel, and drift correction after every frame. The K-edges of O, Si, and Ge were background-subtracted and integrated to produce the elemental maps.

Ultraviolet-visible (UV-Vis) Spectroscopy. The optical UV-Vis extinction spectra of different size NPs dispersed in DI water (S_{sample}) was obtained using an Agilent Cary 5000 UV-Vis-Nir spectrometer. The transmission data of the colloidal solutions in quartz cuvettes with a path length of 1 cm was recorded over the wavelength range of 350-800 nm. A cuvette filled with DI water was used as a reference (S_{ref}) and a dark measurement was used to determine instrumentation bias (S_{bias}). Transmission measurements are then defined as $T_{meas} = (S_{sample} - S_{bias})/(S_{ref} - S_{bias})$.

Numerical Modeling. Optical extinction efficiencies (σ_{ext}) of c-Si NPs in water were calculated using Mie theory according to the NP diameter distributions shown in figure 9.2.2(a). Each particle diameter distribution was converted to a discrete distribution, $P(i)$, based on 25 distinct diameters linearly spaced between $\mu \pm 3\sigma$, where μ is the distribution mean value and σ is the standard deviation. With 25 distinct sample points, the maximum diameter spacing between i and $i+1$ was less than 2 nm and 99.7% of all possible particle sizes was accounted for in each distribution. The transmittance is then $T = e^{-ff \int \partial l \sum_i w_i \sigma_{ext,i}}$, where ff is the total volume fill fraction of particles suspended in the cuvette, the integral is over the optical path length, and the summation is over the discretized particles sizes, i. $w_i = \frac{A_i P(i)}{\sum_i V_i P(i)}$ is the weight factor where A_i and V_i are the cross-sectional area and volume of particle i, respectively. Therefore, $ln(T) = -\frac{ffL}{\sum_i V_i P(i)} \sum_i A_i \sigma_{ext,i}$, where $\int \partial l = L$ under the ergodic motion assumption. To compare with measurement, we perform the normalization, $\frac{\sum_i A_i \sigma_{ext,i}}{\max(\sum_i A_i \sigma_{ext,i})} = \frac{-\ln(T_{meas})}{\max(-\ln(T_{meas}))}$, which removes uncertainty in variables such as the fill fraction, which may vary between samples.

Plasma conditions for the synthesis of size-controlled c-Si NPs. In this study, the NP size is tuned by adjusting the gas residence time via changing the flow rate of the carrier gas, Ar, as well as the orifice size, which in turn controls the reactor pressure. Table 9.5.1 summarizes the NP sizes obtained in this study and the process conditions used for their synthesis. All other synthesis conditions as well as the reactor setup are held constant for all samples and can be found in the methods.

NP diameter average ± standard deviation [nm]	Orifice width [mm]	Ar flow rate [sccm]	Reactor Pressure [Torr]	Gas residence time [s]
60 ± 2.2	0.10	15	2.2	2.2
81 ± 4.4	0.07	7.5	1.7	3.4
112 ± 4.7	0.05	8.4	2.4	4.3
129 ± 4.9	0.04	8.5	2.6	4.7
154 ± 5.7	0.03	8.5	3.1	5.6
214 ± 7.6	0.03	5.5	2.6	7.2

Table 9.5.1. Summary of the process conditions used for the synthesis of c-Si NPs with different diameters, including the orifice width, Ar flow rate, reactor pressure, and gas residence time.

Plasma synthesis of high-index NPs other than Si. Successful synthesis of optically Mie-resonant c-Si NPs in a wide range of diameters with extremely small standard deviations using nonthermal plasma processes is shown in the text. This synthesis technique is extremely versatile in producing NPs of other high-index materials. Here, we report the synthesis of germanium (Ge) and silicon-germanium (SiGe) NPs in the subwavelength size regime. The plasma conditions are similar to that of the 112 nm mean diameter c-Si sample, as presented in Table 9.5.1, except for the precursor gasses. Si, Ge, and SiGe NPs are produced using 0.21 sccm of silane, 0.21 sccm of germane, and a mixture of 0.12 sccm of silane and 0.12 sccm of germane, respectively. Figure 9.5.1 shows representative TEM and HAADF-STEM images of these particles. It is clearly seen that Ge and SiGe NPs are also nearly spherical and monodispersed. As a result of using similar recipes for their synthesis, all particles have comparable sizes with mean diameters of 112 nm, 106 nm, and 103 nm for Si, Ge, and SiGe NPs, respectively.

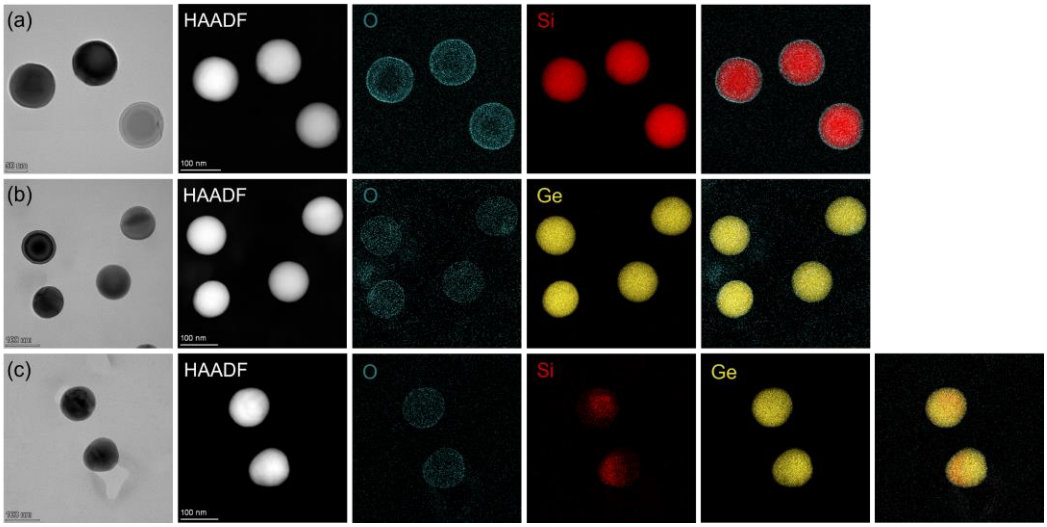

Figure 9.5.1. Representative bright-field TEM and select HAADF-STEM images of plasma synthesized (a) Si, (b) Ge, and (c) SiGe NPs, with similar average diameters, after air exposure.

Non-idealities of Si NPs of the 214 nm mean diameter sample. All NPs examined in this study are fully dense and nearly spherical with minimal defects, as shown in figure 9.2.1(e), except for the sample with average diameter of 214 nm. This sample contains NPs that are not completely spherical and contain several defects such as pores and rough surfaces, as shown in figure 9.5.1(a). The HAADF image of a typical NP (figure 9.5.1 (b)) reveals apparent contrast differences within the NP due to the porous nature of the particle. This is further verified by SEM analysis of a single NP in this size regime (figure 9.5.1(d)), clearly showing holes within the NP. Once exposed to air, the surface of such pores is oxidized, resulting in variations in the concentration of elemental O in the STEM-EDX elemental map shown in figure 9.5.1(c). As discussed in the text, the formation of such non-idealities in larger particles could be due to their smaller temperature variations during the heating and cooling processes in the plasma discharge. These defects could potentially be alleviated by further optimizing the process conditions, such as employing higher RF powers.

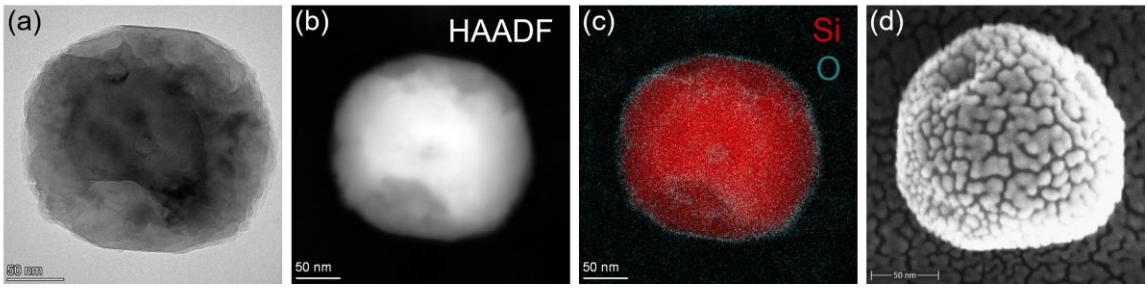

Figure 9.5.2. (a) TEM, (b) HAADF, (c) STEM-EDX elemental map, and (d) SEM images of a typical porous Si NP of the sample with average diameter of 214 nm. The SEM sample is coated with 10 nm gold before imaging, resulting in a rough texture on the surface of the NP.

Comparison of extinction measurements to extinction from a delta function distribution. To show the impact of the finite standard deviations in the particle size distribution on the optical extinction, figure 9.5.3 plots the theoretical extinction of delta function size distributions centered at the mean diameter for each sample and compares this to the results from figure 9.5.2(d) in the main text.

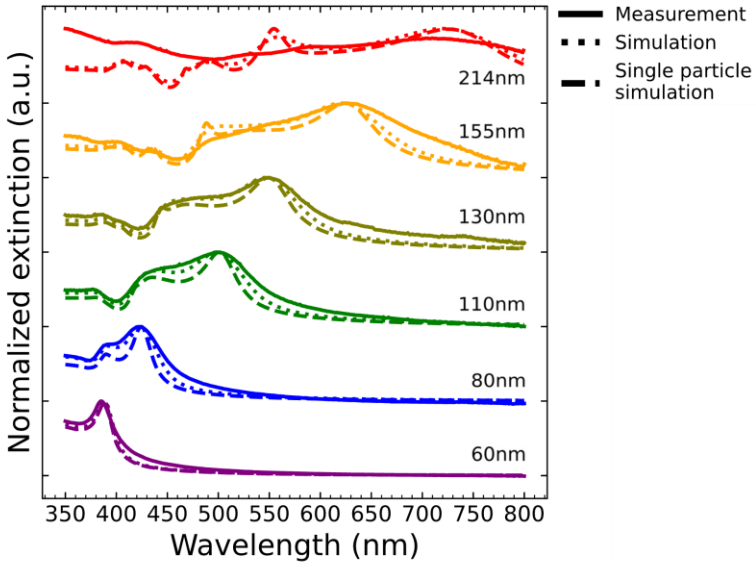

Figure 9.5.3. Extinction spectra of all samples. The measured extinction is the solid line. The simulated extinction based on the measured size distribution is the dotted line. The simulated extinction based on a single particle size (i.e., a delta function distribution at the mean value of the particle diameter) is the dashed line. All colors match the color designation to the samples in figure 9.5.2(a).

Chapter 10

CHARACTERIZATION OF ALUMINUM OXIDE NANOPARTICLE FILMS

Li, Z.; Wray, P. R.; Su, M. P.; Tu, Q.; Andaraarachchi, H. P.; Jeong, Y. J.; Atwater, H. A.; Kortshagen, U. R. Aluminum Oxide Nanoparticle Films Deposited from a Nonthermal Plasma: Synthesis, Characterization, and Crystallization. *ACS Omega* **2020**, *5* (38), 24754–24761. https://doi.org/10.1021/acsomega.0c03353.

ABSTRACT

Aluminum oxide, both in amorphous and crystalline forms, is a widely used inorganic ceramic material due to its chemical and structural properties. In this work, we synthesized amorphous aluminum oxide nanoparticles using a capacitively coupled nonthermal plasma utilizing trimethylaluminum and oxygen as precursors and studied their crystallization and phase transformation behavior through post-synthetic annealing. The use of two reactor geometries resulted in amorphous aluminum oxide nanoparticles with similar compositions but different sizes. Size tuning of these nanoparticles was achieved by varying the reactor pressure to produce amorphous aluminum oxide nanoparticles ranging from 6 nm to 22 nm. During post-synthetic annealing, amorphous nanoparticles began to crystallize at 800°C, forming crystalline θ and γ phase alumina. Their phase transformation behavior was found to be size dependent in that small 6 nm amorphous particles transformed to form phase pure α-Al_2O_3 at 1100°C, while large 11 nm particles remained in the θ and γ phases. This phenomenon is attributed to the fast rate of densification and neck formation in small amorphous aluminum oxide particles.

10.1 INTRODUCTION

Aluminum oxide (Al_2O_3), commonly known as alumina, is one of the most widely used inorganic ceramic materials due to its superior thermal, chemical, and structural properties. Alumina can exist in both amorphous and crystalline forms. Amorphous alumina is considered to be an excellent candidate for anodic materials, gate insulators in transistors, protective coatings, and catalysts[362–366]. Various methods have been employed to synthesize amorphous alumina nanoparticles, which include sol-gel processing[367,368], solution combustion[369–373], precipitation[374–376], ultrasonic treatment of porous anodic alumina membranes,[377] energetic pulsed laser ablation[378], and tragacanth gel synthesis[379].

The structure of amorphous alumina has been studied extensively and found to be comprised of a network of AlO_4 tetrahedra, AlO_5 polyhedra, and small fractions of AlO_6 octahedra[380–385]. Solid-state[386] Al nuclear magnetic resonance (NMR) studies revealed that the existence of a significant fraction of AlO_5 polyhedra, where Al^{3+} ions are penta-coordinated with oxygen ions, creates disorder and hinders the crystallization and growth of crystalline alumina phases[387]. Thus, high temperatures (~800 °C) are required for the transformation of amorphous to crystalline alumina nanoparticles[388]. This process involves a structural rearrangement reaction converting AlO_5 polyhedra into AlO_4 and AlO_6.

Phase transformation of amorphous to crystalline alumina nanoparticles can greatly depend on several parameters such as synthetic route, heating rate, grain size, and chemical composition. Crystalline alumina can exist in various metastable crystalline phases (χ, η, δ, $\varkappa$, θ, γ, ϱ)[386,389,390] and corundum or α-alumina is identified as the most thermodynamically stable phase in bulk form. The typical phase transformation sequence in crystalline alumina can be depicted as $\gamma \rightarrow \delta \rightarrow \theta \rightarrow \alpha\text{-}Al_2O_3$ [388]. The transformation of γ-Al_2O_3 (density ρ = 3.56 g/cm^{-3}) to α-Al_2O_3 (ρ = 3.98 g/cm^{-3}) is accompanied by a volume reduction of about 10% and proceeds through a meta-phase of θ-Al_2O_3[391]. Typically, the final transformation to α-Al_2O_3 requires higher annealing temperature around 1100 °C[388]. With superior hardness, low friction, unique heat transfer properties, and excellent wear resistance, α-Al_2O_3 plays a critical role in the production of advanced ceramic materials and as a core and filler material for nanocomposites[392–394]. γ-Al_2O_3 nanoparticles themselves also exhibit excellent catalytic properties due to their surface acidity and high surface area[395].

In this work, we synthesized amorphous alumina nanoparticles by a nonthermal plasma approach and studied their crystallization and phase transformation behavior during post-synthetic annealing. Nonthermal plasma synthesis has shown the potential to produce a variety of nanoparticles with high purity and narrow size distributions, and the library of nanoparticle

materials has been expanded from group-IV semiconductors to metal oxides and metal sulfides[197,224,267,348,396–398]. Furthermore, nanoparticles made by this method can be directly deposited into particle films with densities ranging from 20% to 60%[276,277]. The as-deposited aluminum oxide nanoparticles are annealed at 600 – 1100°C for the investigation of their phase transformation behavior.

10.2 SYNTHESIS OF AMORPHOUS ALUMINA NANOPARTICLES

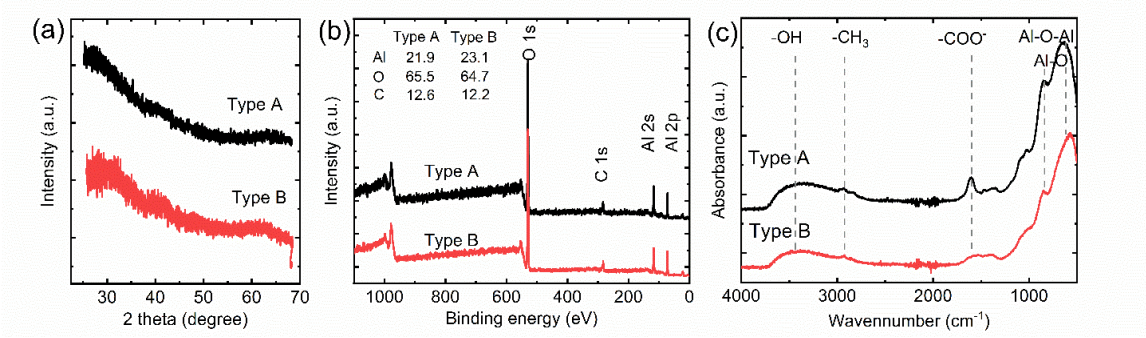

Figure 10.2.1. Characterization of AlO_x nanoparticles synthesized from type A and type B reactors at p=3.8 Torr: (a) θ–2θ mode out-of-plane XRD patterns of the as-synthesized AlO_x nanoparticles from type A and type B reactors; (b) XPS survey scan of AlO_x nanoparticles from type A and type B reactors. (c) Typical FTIR spectra of AlO_x samples from type A and type B reactors, with major absorption peaks featuring Al−O, $-COO^-$, $-CH_3$, and −OH.

Amorphous alumina (AlO_x) nanoparticles were synthesized using the two reactor geometries shown in the experimental section. Figure 10.2.1a shows the XRD spectra of as-synthesized AlO_x nanoparticle samples from both type A and B reactors at p = 3.8 Torr. The absence of definitive peaks in XRD suggests that as-synthesized AlO_x nanoparticles are amorphous. As shown in a previous study, amorphous alumina nanoparticles are thermodynamically more stable with the lowest surface energy compared to θ- and a phase polymorphs at large surface areas[399].

XPS and FTIR measurements were performed to evaluate the surface and atomic composition of AlO_x nanoparticles from both reactor configurations (figures 10.2.1b and 10.2.1c). For both samples, the main peaks in XPS correspond to O 1s, C 1s, and Al 2p at 530, 284, and 73 eV, respectively. This confirms the elemental composition in AlO_x nanoparticles. Carbon incorporation (5 – 10 at%) is commonly observed when TMA is used as the aluminum source due to strong Al−C bonds[400–402]. The carbon content can be partly due to contamination in air, as samples are shortly exposed to air during the transfer but can also originate from the methyl groups in TMA. Atomic percentage ratios of Al to O are around 1:3 for both A and B type reactor samples, with carbon percentages around 10%–15%. The atomic ratios are in general not affected by the plasma power used for synthesis (figure 10.6.1). High-resolution XPS spectra were analyzed to gain insight into the composition of both types of AlO_x nanoparticle samples (figure 10.6.2). The binding energy of the Al 2p peak at ~74.6 eV corresponds to Al−O bonding in alumina[403,404]. The O 1s peak at ~531.5 eV can be resolved into two individual peaks representing O^{2-} and OH^- [404–406]. FTIR spectra for samples from both reactor types reveal

absorption bands related to hydroxyl (−OH), alkyl (C−H), (C−O), and aluminum species (Al−O and Al−O−Al). The peak around ~670 cm^{-1} and the shoulder located around ~860 cm^{-1} correspond to the Al–O stretching vibrations in five-fold coordinated AlO_5 and four-fold coordinated AlO_4, respectively. Features from AlO_6 stretching vibrations could also be present, which according to the literature lie in the 400–650 cm^{-1} spectral range and overlap with Al–O stretching vibrations and oscillations in AlO_4 and AlO_5[400,407,408].

Statistics of AlO_x nanoparticle size was determined using transmission electron microscopy (TEM). At p = 3.8 Torr, the average size of AlO_x nanoparticles from type A and type B reactors are 11 ± 3 nm and 6 ± 1 nm, respectively. The different particle sizes can be explained by the different plasma densities at the point of TMA injection. Nanoparticle growth in plasmas proceeds through the nucleation of clusters, many of which are initially neutral[273]. These clusters quickly coagulate to form nanoparticles, leading to a reduction of the overall concentration of clusters and particles. When the cluster/nanoparticle density has dropped to the level of the ion density in the plasma, there are sufficient electrons to charge most particles negatively and suppress further coagulation[273]. In the type B reactor, the TMA precursor is injected into a higher density plasma zone compared to the type A reactor, where the precursor is injected into a less dense plasma afterglow. Coagulation in the type B reactor is therefore suppressed at smaller particle sizes, corresponding to higher particle concentrations, compared to the type A reactor. For each type of reactor, size tuning of AlO_x nanoparticles can be achieved by varying the reactor pressure. This changes the particle residence time in the plasma, and therefore tunes the time of surface growth. TEM images of as-synthesized AlO_x nanoparticles from type A and B reactors under three sets of reactor pressures are shown in figure 10.2.2. At each pressure, the type B reactor produces smaller particles than the type A reactor. For both reactor configurations, the mean particle size increases with increasing pressure. At 3.8 and 5.2 Torr, AlO_x nanoparticles from both reactors are aggregated but nearly spherical in shape and have relatively narrow size distributions (figure 10.6.3). At the relatively high pressure of 7.5 Torr, AlO_x nanoparticles exhibit a bimodal size distribution with both small and large irregular nanoparticles present.

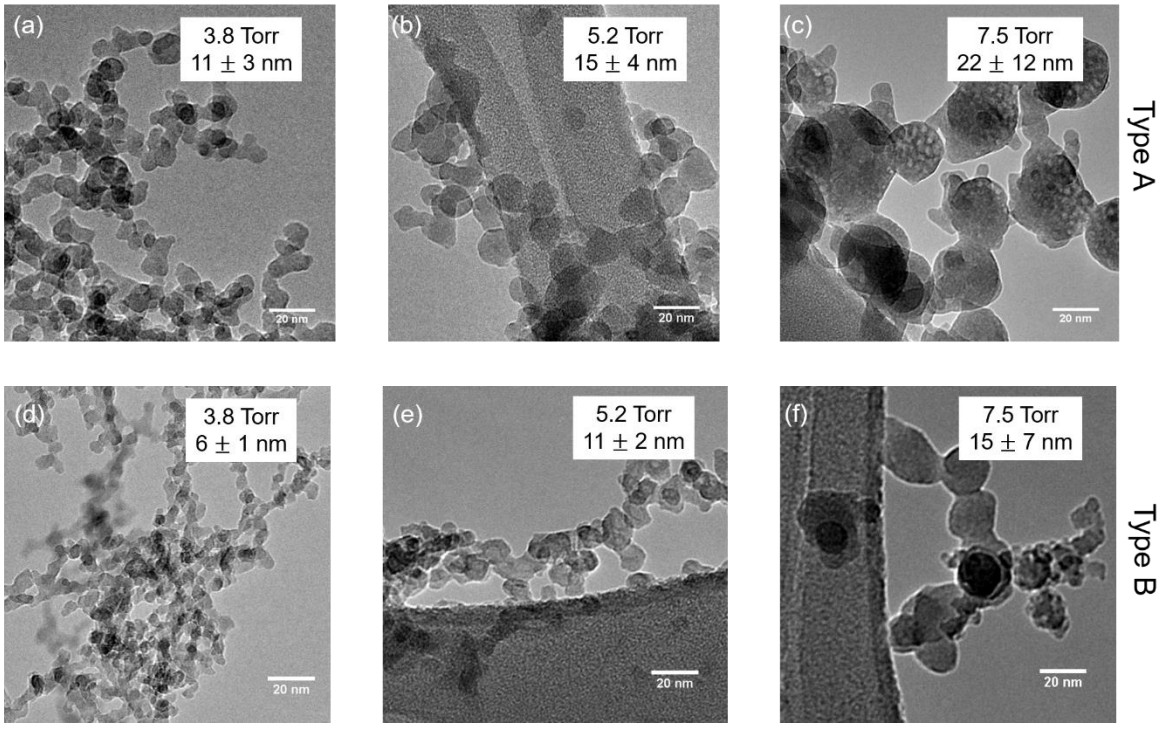

Figure 10.2.2. TEM images of AlO_x nanoparticles synthesized from type A (a)–(c) and type B (d)–(f) reactors at pressures of 3.8 Torr, 5.2 Torr and 7.5 Torr with mean sizes and standard deviations.

We estimated the process yield of each type of reactor setup by measuring the weight of the AlO_x nanoparticle powders collected at p = 3.8 Torr for 10 minutes. With a fixed substrate position, samples collected from both types of reactor setups were piles of white powders (figure 10.6.4). The sample weights from the type A and B reactor were 3.2 mg and 7.0 mg, respectively. This corresponds to yields of 19.2 mg/hour and 42.0 mg/hour. The current production rates are limited by the TMA and oxygen flow rates due to safety considerations.

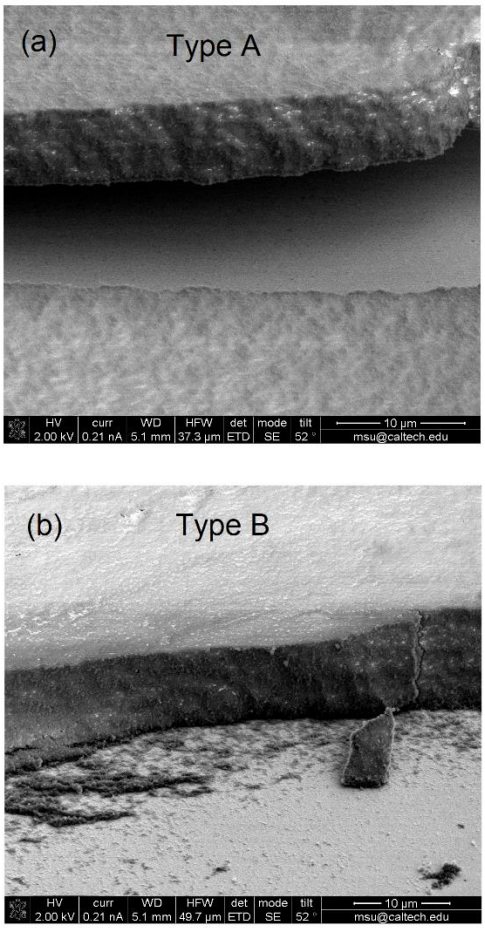

Figure 10.2.3. Cross-sectional SEM images of AlO_x nanoparticle laminate films synthesized from type A (a) and type B reactors (b). A correction factor of 1/cos(38°) is applied in the y-axis to account for the tilt of the setup with respect to the SEM Everhart-Thornley Detector (ETD).

We deposited AlO_x nanoparticle films by rastering a substrate beneath the reactor output orifice to study the optical properties of AlO_x nanoparticle films. The films were deposited with 240 raster passes and examined by scanning electron microscopy (SEM) and Mueller matrix measurements. The thickness of the AlO_x nanoparticle films were measured to be 7.1 $\pm$ 1.1 µm and 9.1$\pm$ 0.9 µm for type A and type B reactors, respectively. Characteristic cross-sectional SEM images of the nanoparticle films are shown in figure 10.2.3.

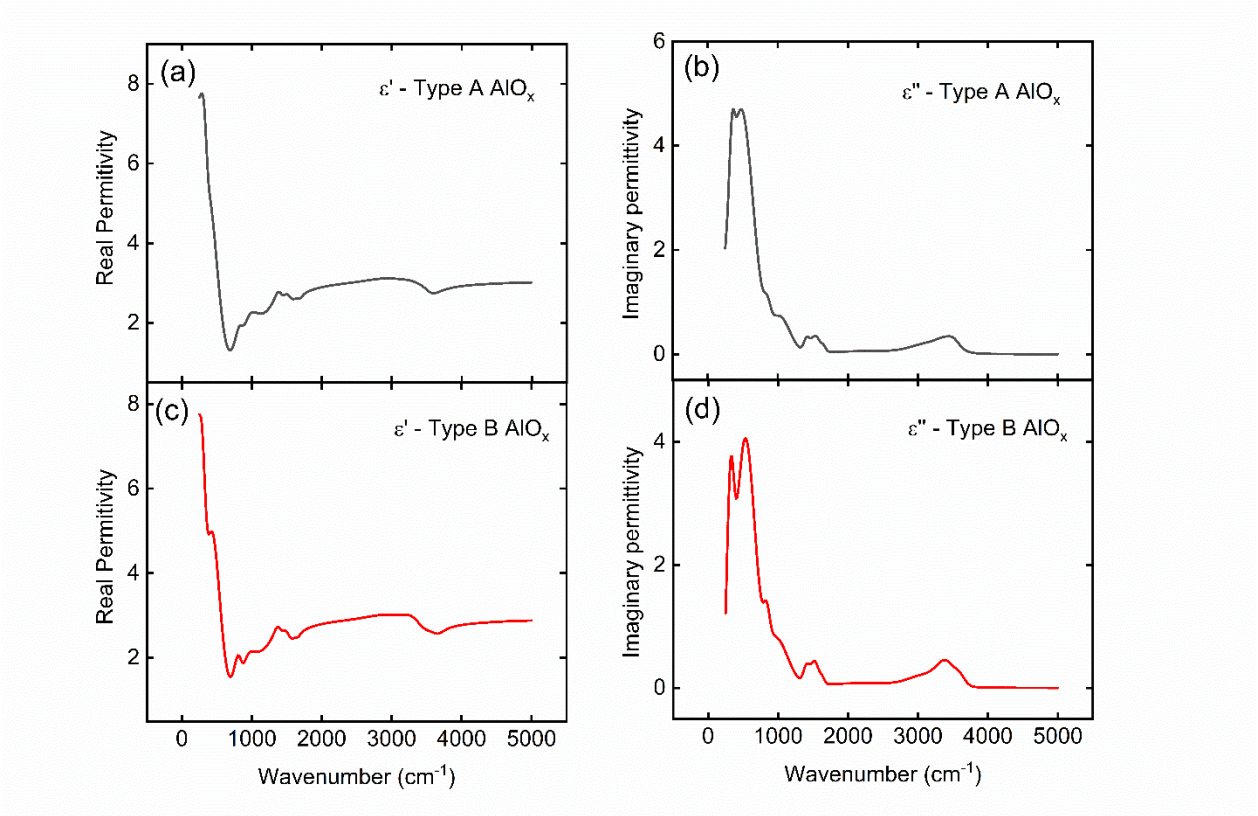

Figure 10.2.4. Real and imaginary parts of the complex AlO_x nanoparticle film's permittivity found in the type A reactor (a,b) and type B reactor (c,d), respectively.

Mueller matrix measurements, which allow for the characterization of anisotropic-depolarizing samples, including cross-polarization, were performed to extract the effective (homogenized) complex permittivity of the particle films. The measurements were also used to determine the complex permittivity of the corresponding AlO_x nanoparticles. In both type A and B films, no polarization conversion from p-polarized to s-polarized or vice versa was present. The Mueller matrix data showed only noise for elements mm_{13}, mm_{31}, mm_{22}, mm_{23}, mm_{32}, mm_{41}, and mm_{42}. Furthermore, $mm_{12} = mm_{21}$. This block diagonal structure of the Mueller matrix indicates that the type A and B samples can be treated as macroscopically isotropic[409–411]. Therefore, the effective permittivity of each sample can be represented by a wavelength dependent scalar. The nanoparticle films were best homogenized using the Bruggeman mixing formula. This formula has been shown to consistently produce an effective permittivity that accurately models nanoparticle films, including anisotropic-depolarizing effects[151,152,219,412–414]. Maxwell-Garnett and linear mixing formulas were also explored, but less accurately modeled the measured data. The permittivity of the individual nanoparticles were modeled using Gaussian oscillators, to represent amorphous phonon resonances, while satisfying the Kramers-Kronig relations. For the type A film, a sample thickness of 7.75 μm and a particle fill fraction of 22.3% provided the best fit to

the optical interference patterns in a nearly lossless region of the amorphous alumina film between 4000 – 6250 cm^{-1}. For the type B film, a thickness of 9.23 μm and fill fraction of 19.4% provided the best fit. Further detail about Bruggeman homogenization and the corresponding Gaussian oscillator model, including tables for the oscillator parameters, can be found in the supplementary information. Figure 10.2.4 shows the reconstructed imaginary part of the particle permittivity. Strong oscillators in the 300 – 700 cm^{-1} spectral range correspond to AlO_4, AlO_5 and AlO_6 stretching vibrational modes. These values corroborate our results from FTIR as well as literature[400,407,408,413]. Similar to our findings from XPS and FTIR, the reconstructed permittivity shows that the particles from both types of reactors have similar chemical composition. The depolarization constant for type A and B reactor films was 0.261 ± 0.005 and 0.407 ± 0.006, respectively. This indicates predominantly scattering of spherical like inclusions post deposition. All of the above characterizations reveal that particles from type A and type B reactors have similar compositions but different sizes.

10.3 CRYSTALLIZATION OF AMORPHOUS ALUMINA NANOPARTICLES

In a nonthermal plasma, crystallization of nanoparticles can occur through the heat generated by the recombination of electrons and ions on the nanoparticle surfaces[415,416]. Here the as-produced AlO_x nanoparticles have amorphous structures, indicating that particle heating from the nonthermal plasma is not sufficient to induce crystallization. Post-synthetic annealing of powder samples of amorphous alumina nanoparticles was explored to induce nanoparticle crystallization and subsequent phase transformation to networks of crystalline alumina nanoparticles.

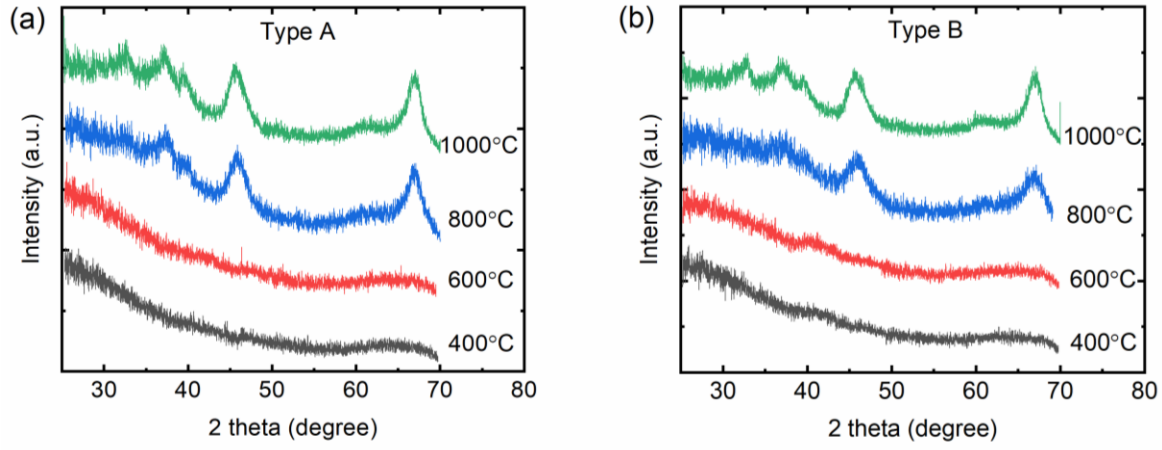

Figure 10.3.1. XRD patterns of the post-synthesis annealed AlO_x nanoparticles from (a) type A and (b) type B reactors, with annealing temperatures ranging from 400 °C to 1000 °C and an annealing time of 18 h.

To study the crystallization and phase transformation behavior of powder samples of amorphous AlO_x nanoparticles, a pile of AlO_x nanoparticles was collected and annealed in a Thermo Scientific Lindberg Blue furnace at temperatures ranging from 400–1100 °C in the atmosphere. Samples collected in this manner are expected to have porosities > 80% and consist of loose agglomerates of nanoparticles[276]. some of the agglomerates may have already been formed in the gas phase before deposition. The typical temperature ramp rate was ~50 °C/min. Since the properties of powder samples of small AlO_x nanoparticles are of primary interest, we explored the crystallization behavior of samples synthesized at 3.8 Torr from type A and B reactors, respectively. Phase transformation of amorphous alumina typically proceeds through the amorphous-to-γ and γ-to-α phase transitions[417,418], or with an additional transition to the θ-phase between the transformation from the γ- to α- phase[419], before reaching the thermodynamically stable α-phase. Our observations reveal that powder samples of AlO_x nanoparticles from both types of reactors begin to crystallize at 800 °C producing a mixture of

θ- and *γ*-phases, as shown in figure 10.3.1a and 10.3.1b. The crystallization temperature is consistent with that from the literature[370,399].

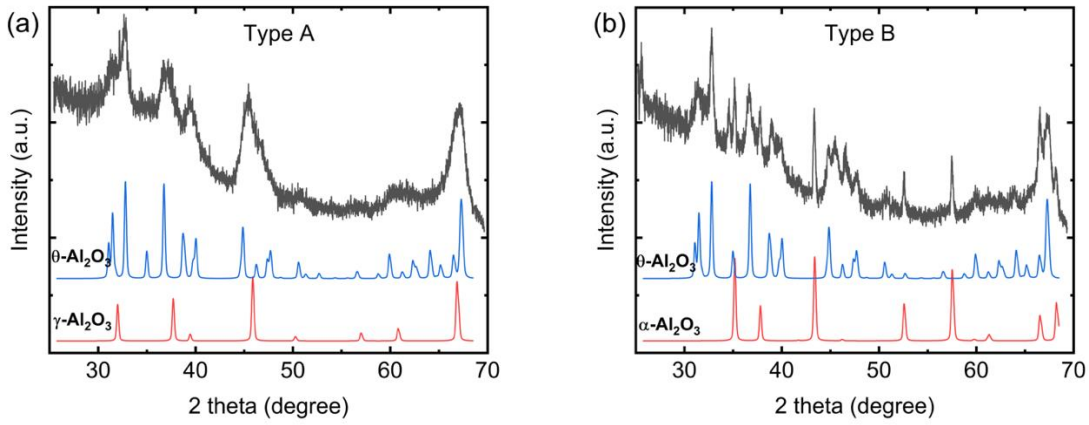

Figure 10.3.2. XRD patterns of the post-heated AlO_x nanoparticles from (a) type A and (b) type B. Both samples were annealed at 1100°C for 18 h. The bottom columns in both graphs show the reference profile of *γ*-, *θ*-, and *α*-phase aluminum oxides.

As the annealing temperature increased up to 1100 °C, we observed that the powder samples of AlO_x nanoparticles from the type A and B reactors form different crystalline phases (figure 10.3.2). The samples of larger AlO_x nanoparticles from the type A reactor form a mixture of *θ*- and *γ*-phase at 1100 °C whereas the samples of smaller AlO_x nanoparticles from the type B reactor form a mixture of *θ*- and *α*-phases. Time of post-synthetic annealing also affects phase transformation of the type B reactor AlO_x nanoparticle powders. When the annealing time increased up to 40 h, type B AlO_x nanoparticle powders form particle networks of phase pure *α*-Al_2O_3 nanocrystals (figure 10.3.3).

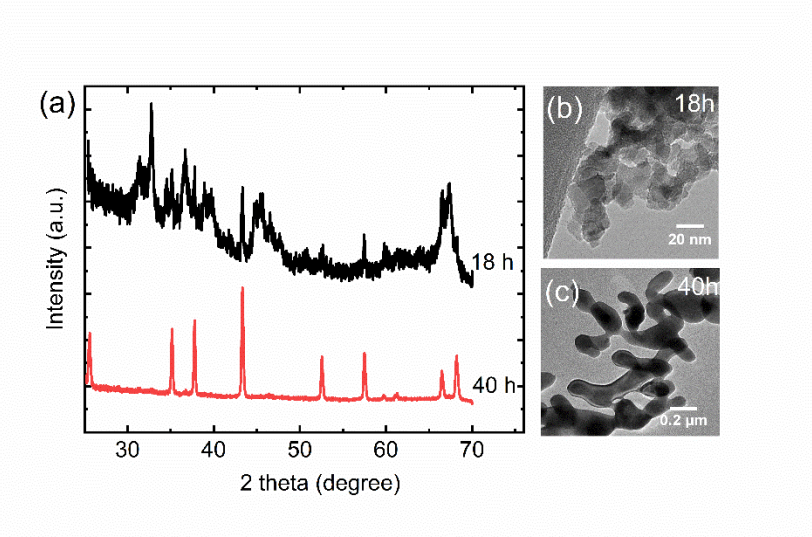

Figure 10.3.3. XRD and TEM of particles. (a) XRD pattern of type B AlO_x nanoparticles heated at 1100°C for 18 h and 40h; TEM images of (b) AlO_x nanoparticles annealed at 1100 °C for 18 h and (c) AlO_x nanoparticles annealed at 1100 °C for 40 h.

This transformation is also accompanied with a significant crystal growth. The mean crystallite sizes of crystalline alumina particles after 18 h annealing were estimated using Scherrer fittings. Annealing for 18 h of ~6 nm AlO_x nanoparticle powders at 1100 °C resulted in a particle network consisting of a mixture of ~30 nm θ-Al_2O_3 and >100 nm α-Al_2O_3 particles (figure 10.6.5). Samples of phase pure α-Al_2O_3 particles obtained after 40 h are also estimated to be comprised of nanocrystals larger than 100 nm. The crystalline grain sizes are confirmed by TEM images (figure 10.3.3b and 10.3.3c). It is interesting to observe that the powders of larger AlO_x nanoparticles from the type A reactor never exhibit α-Al_2O_3 phase even with longer annealing times.

As the powder samples of AlO_x nanoparticles from both types of reactors have similar composition, we postulated that the difference in their phase transformation behavior is likely due to the different sizes of their as-synthesized constituent particles. To test this assumption, we investigated the phase transformation behavior of powder samples of the large AlO_x particles with mean sizes around 11 and 15 nm synthesized in the type B reactor with higher reactor pressures. XRD patterns taken after 18 h of annealing time reveal that powders of smaller ~6 nm AlO_x nanoparticles form α-phase Al_2O_3 along with θ-Al_2O_3, while powders of larger ~11 and ~15 nm AlO_x nanoparticles only forms θ-Al_2O_3 and do not exhibit any α-phase features (figure 10.6.6). These observations support our assumption that powders of initially smaller size AlO_x nanoparticles have a higher tendency to transform to the α-phase after annealing.

It has been pointed out that necking and densification of particles starts to occur when annealing amorphous AlO_x nanoparticles, forming nanoporous structures before crystallization[399,420,421]. It is likely that during the annealing, the rate of densification and neck formation is faster in powder samples of smaller particles compared to larger particles, as the neck growth is dominated by mass transport and is thus enhanced in smaller size particles[422]. The fact that powder densification can be promoted by a decrease of particle sizes has also been observed in other nanoparticle systems[423]. After neck growth, the big, interconnected structures tend to transform to *a*-phase Al_2O_3 as temperature further increases, as it is the thermodynamically stable phase for bulk Al_2O_3.

10.4 CONCLUSION

Amorphous alumina nanoparticles with average sizes ranging from 6 nm to 22 nm were successfully synthesized using a nonthermal plasma approach with two different reactor geometries with typical yields of 19 mg/hour and 42 mg/hour, respectively. Infrared Mueller matrix measurements indicated the optical properties of the nanoparticle film could be modeled by a homogenized effective refractive index. The homogenized refractive index of the particle film was shown to be accurately represented using the Bruggeman effective medium model. Based on this model, particle fill fractions were estimated to be around 20% for both type A and type B reactors. Furthermore, the refractive index of the amorphous alumina nanoparticles were modeled using Gaussian oscillators, showing clear AlO_4, AlO_5, AlO_6, and Al−OH spectral peaks, matching reports in literature. Post-thermal annealing of powder samples of AlO_x particles from both types of reactors led to crystallization, forming a mixture of θ- and γ phases at 800 °C. While powder samples of small AlO_x nanoparticles with average diameters of ~ 6 nm were transformed into phase pure α-Al_2O_3 upon annealing at 1100°C. Powder samples of larger AlO_x nanoparticles never formed α-Al_2O_3.

10.5 METHODS

For the synthesis of amorphous alumina (AlO_x) nanoparticles via nonthermal plasma, trimethylaluminum (TMA) and oxygen (O_2) gas were used as precursors, with argon as the carrier gas. In the plasma region, TMA is decomposed via electron impact or radical abstraction reactions, forming reactive metal atoms or partially decomposed TMA fragments. The reactive species can subsequently react with oxygen atoms to form Al_2O_3[424]. We considered the following chemical equation to control appropriate flow rates:

$$2Al(CH_3)_3 + 12O_2 \rightarrow Al_2O_3 + 6CO_2 + 9H_2O.$$

Based on the stoichiometric molar ratio of TMA and oxygen (TMA:O_2 = 1:6), over six times more oxygen than TMA should be fed for complete oxidation of TMA to Al_2O_3 and other reaction products (CO_2 and H_2O). We chose an excess oxygen flow rate of 6 standard cubic centimeters per minute (sccm) compared with a TMA flow rate of 0.2 sccm.

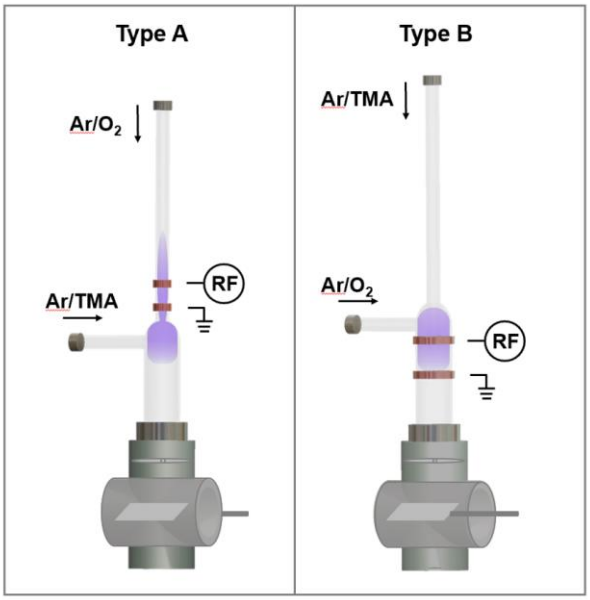

Figure 10.5.1. Schematic of the two types of nonthermal plasma reactors used for AlO_x nanoparticle synthesis and film deposition.

A schematic of the two types of reactors used in this work is shown in figure 10.5.1. AlO_x nanoparticles were synthesized in a nonthermal, low pressure flow-through reactor equipped with a 13.56 MHz radio-frequency (RF) capacitively-coupled plasma source similar to that used in refs. [348,396]. Because two precursors can spontaneously react with each other to produce uncontrolled products[425], we injected both precursor species separately into the plasma for

dissociation to occur in the plasma zone. There are two strategies that have been demonstrated before for the successful synthesis of metal oxide nanoparticles[348,396]. In the first method, denoted as type A, O_2 diluted in Ar gas was injected from the top inlet of the reactor and flowed through the region where RF power was applied. Meanwhile, 0.2 sccm of TMA vapor with 6 sccm of Ar gas was injected from a sidearm tube into the downstream region of the Ar/O_2 plasma. In this afterglow zone, AlO_x nanoparticles nucleated and grew. In the second method, denoted as type B, the TMA vapor diluted in Ar was injected through an inlet tube that extended into the main reactor chamber, while O_2 gas diluted with Ar gas was passed through a sidearm tube and into the space around the upper injection tube. The ring electrodes were placed such that plasma initiated about 1 cm above the end of the top injection tube and the discharge extended downstream of the tube end in order to dissociate TMA and O_2 precursors individually before they mix in the main reactor chamber. As-synthesized AlO_x nanoparticles in both configurations were collected on silicon wafers through a slit-shaped orifice where supersonic nanoparticle impaction produced a curtain of nanoparticles traveling at high speeds[276]. For each type of reactor, three pressure conditions were studied by using three different orifice sizes (0.3, 0.4, 0.5 mm × 8 mm) while keeping the gas flow rates constant.

For optical characterization, nanoparticle films were deposited by using the 0.5 mm × 8 mm orifice and passing a piece of Si wafer carrying a 300 nm Au film below the orifice with 240 raster passes. The gas flow rates and upstream and downstream pressures are summarized in Table 10.5.1.

	Gas	Flow rate [sccm]	P_{up} [Torr]	P_{down} [Torr]
Type A	O_2 diluted in Ar (O_2/Ar)	6 (O_2) / 60 (Ar)	3.8	0.42
	TMA vapor with Ar (TMA/Ar)	0.2 (TMA) / 6 (Ar)		
Type B	O_2 diluted in Ar (O_2/Ar)	6 (O_2) / 60 (Ar)	3.8	0.47
	TMA vapor with Ar (TMA/Ar)	0.2 (TMA) / 6 (Ar)		

Table 10.5.1. Summary of synthesis parameters used in this study.

X-ray diffraction (XRD) was performed with a Bruker D8 Discover 2D X-ray diffractometer equipped with a Co K*a* radiation point source. Instrument broadening was obtained by measuring a standard LaB_6 crystal powder sample with the same scanning parameters (figure 10.6.7). For XRD analysis, aluminum oxide nanoparticles were directly deposited onto Si wafers

to form a pile of powder. The XRD patterns were converted to the wavelength of a Cu source ($\lambda = 1.54$ Å) for data analysis.

Transmission Electron Microscope (TEM) images were taken from a Tecnai T12 microscope with an accelerating voltage of 120 kV. Nanoparticles were either directly deposited from the gas phase or drop-cast in a methanol dispersion on holey carbon TEM grids for imaging.

Fourier-transform infrared spectroscopy (FTIR) was performed with a Bruker ALPHA FT-IR spectrometer using the attenuated total reflection (ATR) module in a nitrogen-filled glovebox. AlO_x nanoparticles were dispersed in methanol and drop-cast onto the ATR crystal. Nanoparticles were allowed to dry before taking measurements.

X-ray photoelectron spectroscopy (XPS) was performed with a PHI Versa Probe III XPS and UPS system. For XPS analysis, aluminum oxide nanoparticles were deposited onto Si wafers with 30 raster passes to form a film.

Nanoparticle laminate film thicknesses were measured empirically by cross-sectioning the nanoparticle laminate films with a Ga focused ion beam (Ga-FIB) and imaging with a scanning electron microscope (FEI Nova 600 NanoLab DualBeam) at a 52° tilt. The cross-sectioning was performed in two steps: a regular cross-section (30 kV, 1 nA) approximately 2 μm in width was cut first followed by a cleaning cross-section (30 kV, 30 pA). The thickness of the cross-sections were measured with ImageJ with a correction factor of $1/\cos(38°)$ in the y-axis to account for the tilt.

To analyze the film optical properties, the first four columns of the angle- and wavelength-resolved Mueller matrix were measured in reflection mode. Mueller matrix measurements were performed using an IR-VASE Mark II ellipsometer with an AutoRetarder from the J.A. Woollam Company. The configuration was polarizer-sample-compensator-analyzer (PSCA). The measurement spectral range extended from 250 to 5000 cm^{-1} with a resolution of 7.7 cm^{-1}. The angular range was 40 to 70 degrees from the surface normal, with an angular resolution of 5 degrees. Data was averaged over 400 measurements - five days of continuous measurement per sample under ambient conditions. Once the samples were measured, an oscillator model of the film permittivity was constructed using the software WVASE32 from J.A. Woollam. Model parameters such as film thickness and particle fill fraction were initialized based on the empirical measurement averages and constrained by three times the measurement standard deviations. Initial values for the particle oscillator model were taken from literature. All model parameters were simultaneously fitted using the full angle and wavelength-resolved Mueller matrix data.

10.6 SUPPORTING FIGURES

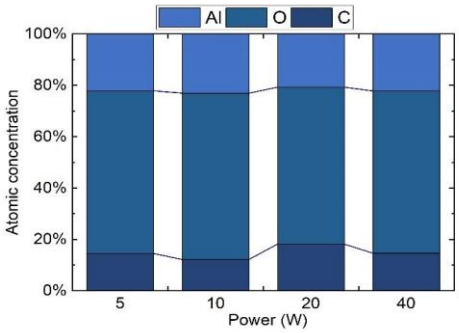

Figure 10.6.1. Atomic concentration in samples from type B reactor obtained by XPS with power varying from 5 W to 40 W.

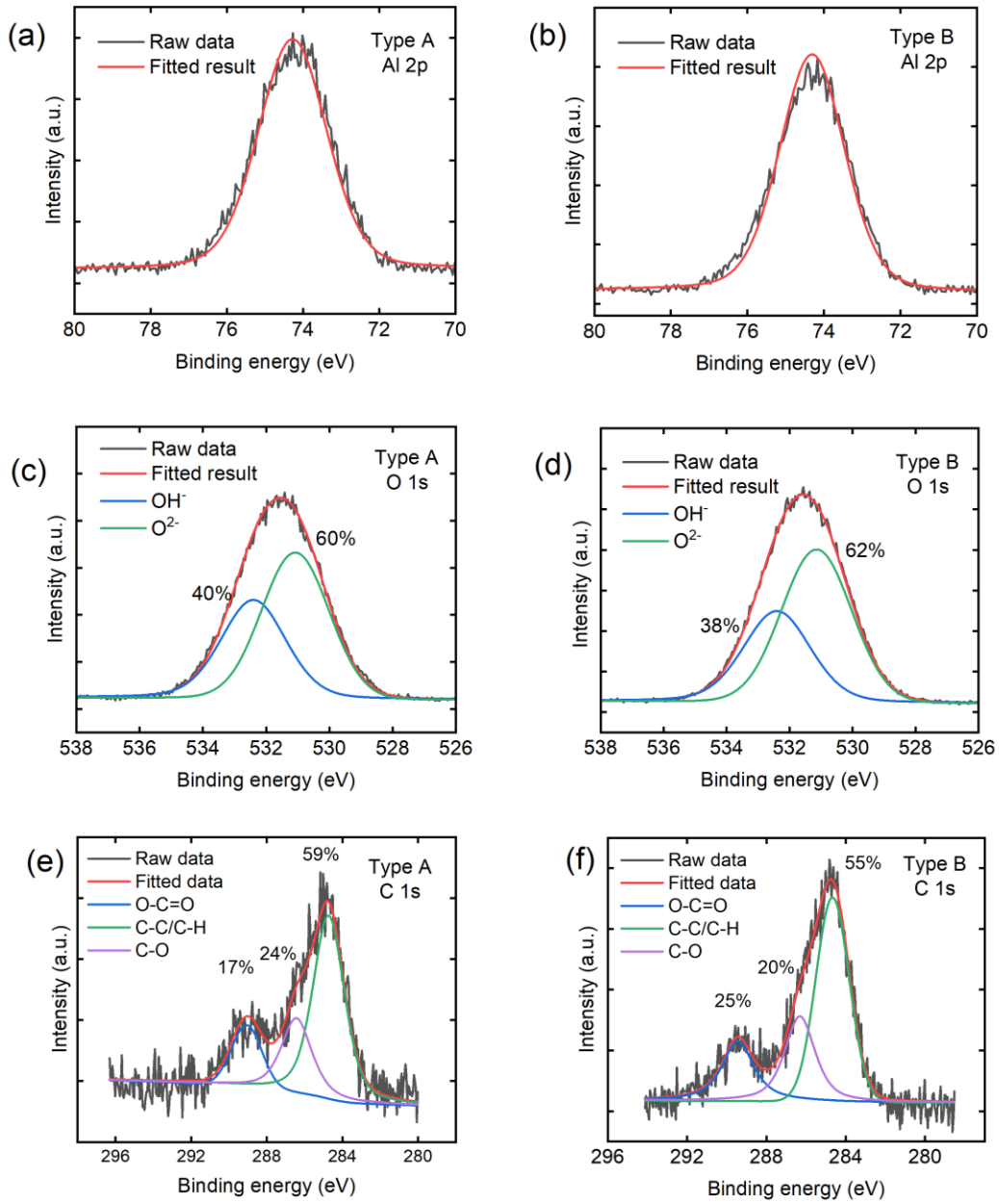

Figure 10.6.2. XPS high resolution spectra of Al 2p peak (a,b), O 1s peak (c,d) and C 1s peak (e,f) for AlO_x nanoparticle samples from type A and type B reactors. The peak corresponding to adventitious carbon is shifted to 284.8 eV as a reference.

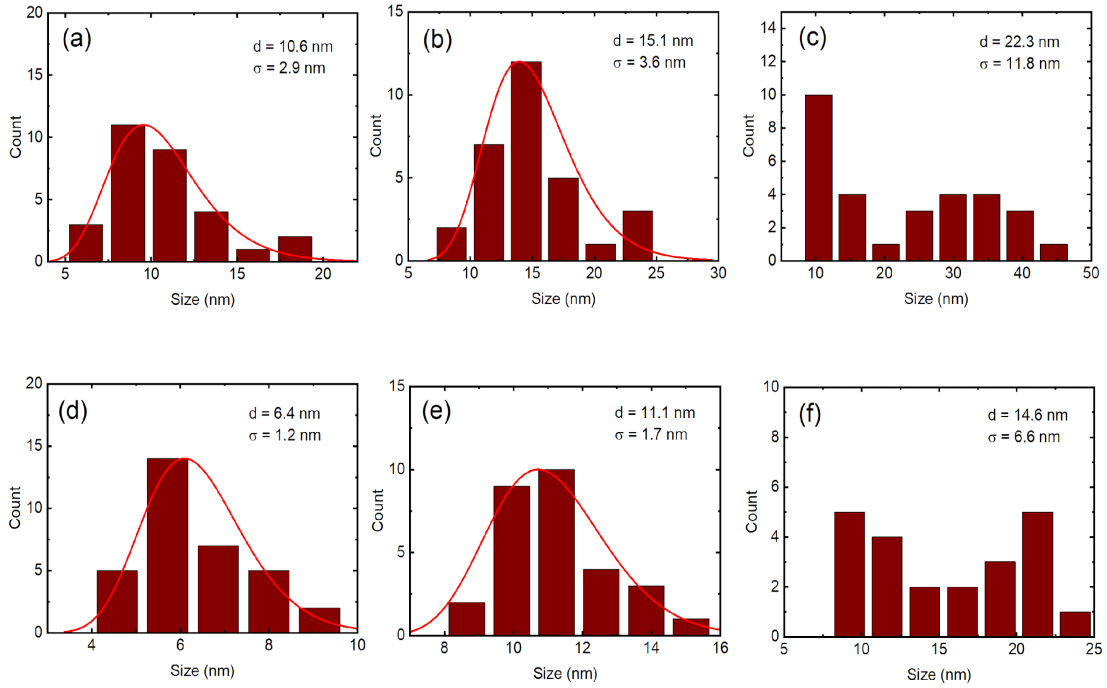

Figure 10.6.3. Size distributions corresponding to the TEM images in figures 10.2.3 (a) to (f).

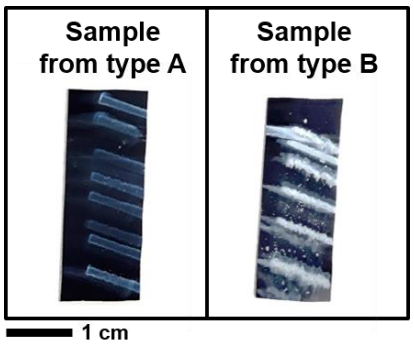

Figure 10.6.4. Photograph showing AlO_x nanoparticles deposited from type A and type B reactors for same period of time.

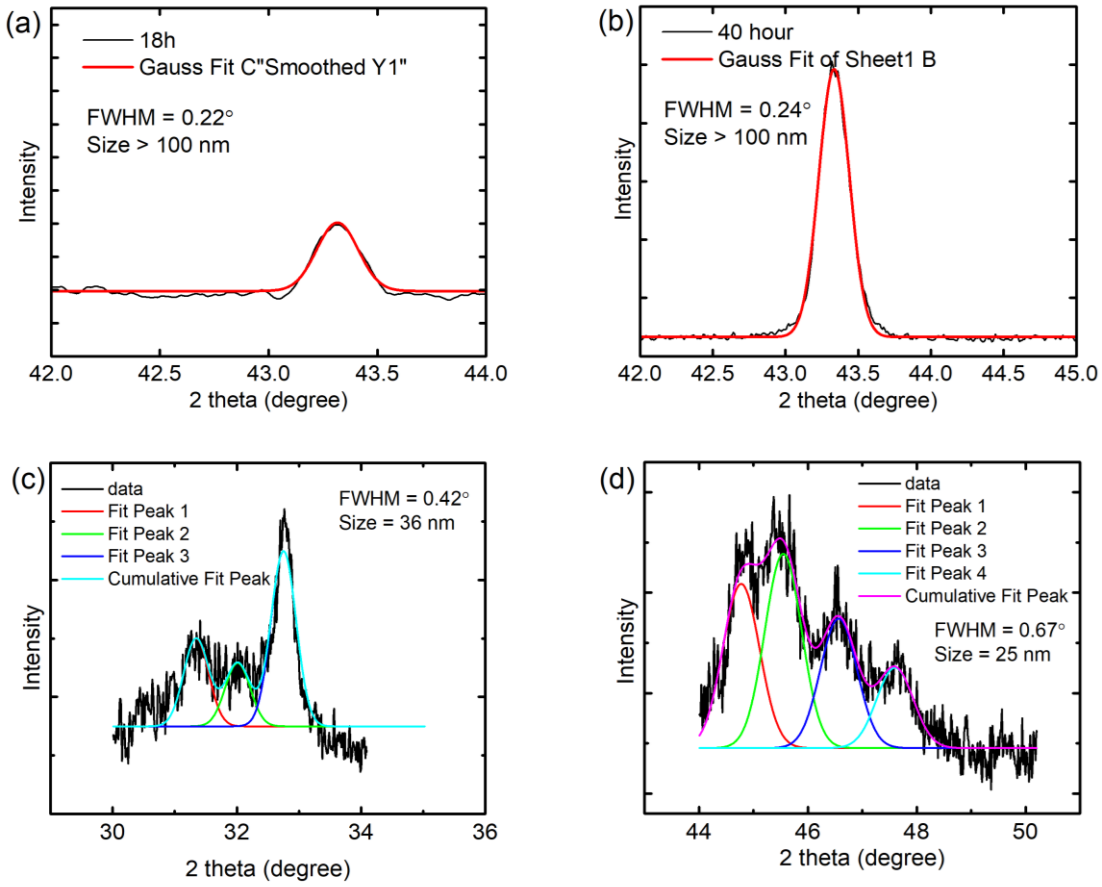

Figure 10.6.5. Scherrer fittings of XRD patterns (λ = 1.54 Å) of AlO_x nanoparticles from type B reactor after heating at 1100 °C for 18 h and for 40 h. To obtain size estimates for the α-phase and θ-phase individually, we choose non-overlapping peaks from the two phases. For the α-phase, (113) peaks were fitted (a,b). For θ-phase, peaks around 30-34° (c) and 44-50° (d) were fitted. Instrumental broadening was accounted for by subtracting the FWHM of the nearest peak of the LaB_6 standard sample, figure 10.6.1. In the Scherrer equation, a shape factor of 0.89 was used. As the widths of α-phase peaks are close to those of the LaB_6 standard sample indicating large crystallite sizes, a rough size estimate of >100 nm is quoted in the main text.

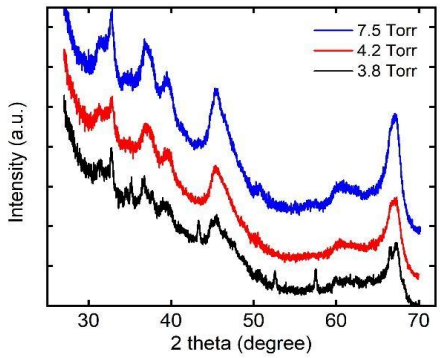

Figure 10.6.6. XRD patterns of samples from type B reactor for three nanoparticle sizes, obtained by varying the gas pressure, after annealing at 1100˚C for 18 hours. Only the smallest particles with about 6 nm size show the appearance of the α-phase.

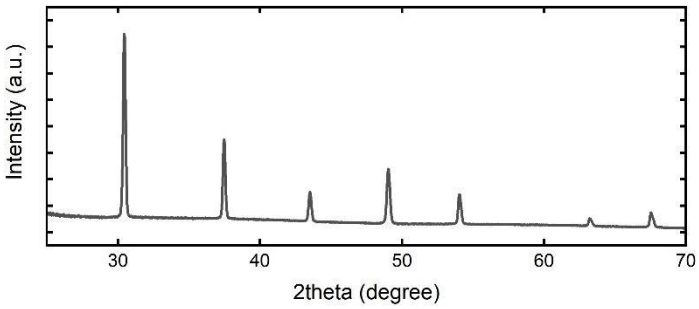

Figure 10.6.7. XRD pattern from a standard LaB_6 sample taken using a Bruker D8 Discover 2D X-ray diffractometer. This pattern is used as a reference to correct for instrument broadening.

10.7 MODELING THE PERMITTIVITY OF AlO_x NANOPARTICLE FILMS

The film's homogenized permittivity (ε_{eff}) can be represented by a wavelength dependent scalar. We model ε_{eff} using the Bruggeman mixing formula

$$f_{AlO_x}\frac{\varepsilon_{AlO_x}-\varepsilon_{eff}}{\varepsilon_{eff}+k(\varepsilon_{AlOx}-\varepsilon_{eff})}+\ \left(1-f_{AlO_x}\right)\frac{\varepsilon_{air}-\varepsilon_{eff}}{\varepsilon_{eff}+k(\varepsilon_{air}-\varepsilon_{eff})}=0, \qquad 10.7.1$$

where ε_{AlOx} and ε_{air} are the permittivity of the nanoparticles and air, respectively; f_{AlOx} $(= 22.3 \pm 0.33\%$ for type A and $19.4 \pm 0.11\%$ for type B) volume fill fraction of the AlO_x nanoparticles; and k $(= 0.261 \pm 0.005$ for type A and 0.407 ± 0.006 for type B) is the depolarizing factor. ε_{AlOx} is modeled as

$$\frac{\varepsilon_{AlO_x}(E)}{\varepsilon_o}\ =\varepsilon_\infty+\varepsilon_{pole1}+\varepsilon_{pole2}+\sum_{n=1}^{11}\varepsilon_{Gauss_n}(E), \qquad 10.7.2$$

where ε_o is the permittivity of free space and ε_∞ $(= 3.09 \pm 0.01$ for type A and 2.97 ± 0.02 for type B) is the infinite frequency permittivity. The complex part of the Gaussian oscillators $\left(\varepsilon_{Gauss_n}=\varepsilon_{1n}(E)+i\varepsilon_{2n}(E)\right)$ are given by

$$\varepsilon_{2n}(E)=A_n e^{-\left(\frac{E-E_n}{\sigma_n}\right)^2}-A_n e^{-\left(\frac{E+E_n}{\sigma_n}\right)^2},\ \sigma_n=\frac{Br_n}{2\sqrt{\ln(2)}}, \qquad 10.7.3$$

where Br_n is the full-width at half-maximum, which accounts for spectral broadening. The real part of the permittivity is given by the Kramers-Kronig relation

$$\varepsilon_{1n}(E)=\frac{2}{\pi}PV\int_0^\infty\frac{\xi\varepsilon_{2n}(\xi)}{\xi^2-E^2}d\xi, \qquad 10.7.3$$

where PV is the principle value. Table 10.7.1 and table 10.7.2 give the fit parameters of the Gaussian oscillators for the amorphous Al_2O_3 nanoparticle films from type A and type B reactors, respectively.

Type A	*Gaussian Oscillator Fit*			*Literature Values*	
Vibration	*Amplitude*	*Broadening [cm^{-1}]*	*Frequency [cm^{-1}]*	*Frequency [cm^{-1}]*	*Ref.*
AlO_6, AlO_4 Deformations	1.0340	83.221	344.27	322−326	[400,408]
AlO_6 stretching	4.6977	408.32	475.78	482−491	1
AlO_4 stretching	0.3357	107.70	851.46	902−880	[407,408,413]
Al−OH sym/asym	0.6933	341.47	1027.5	1072−1160	[408,426]
H_2O deform./vib.	0.22815	92.908	1410.6	1375	1
H−O−H bend	0.31668	159.19	1535.8	1600	[413]
$-COO^-$	0.0783	74.000	1655.8	1300−1850	[400]
	0.05905	1700.8	2355.7		
Al−OH stretching	0.19133	618.98	3207.7	3250−3600	[400,413]
O−H stretching	0.20091	278.01	3429.0	3400-3600	[400,408,426]
Al−OH stretching	0.0719	162.00	3523.7	3250−3600	[400,426]

Table 10.7.1. Gaussian oscillator parameters used to reconstruct the permittivity of nanoparticles from type A reactor. Phonon resonance type (first column), amplitude (second column), spectral broadening (third column) and resonant frequency (fourth column) of the Gaussian oscillators used to calculate the AlO_x particle permittivity from Mueller matrix data. The fifth column gives the resonant frequency range expected from previous literature reports. Citations for the expected frequency range are in the sixth column.

Type B	*Gaussian Oscillator Fit*			*Literature Values*	
Vibration	*Amplitude*	*Broadening [cm^{-1}]*	*Frequency [cm^{-1}]*	*Frequency [cm^{-1}]*	*Ref.*
AlO_6, AlO_4 Deformations	2.5049	109.52	318.72	322−326	[400,408]
AlO_6 stretching	4.0194	320.53	531.22	482−491	[408]
AlO_4 stretching	0.4802	100.47	837.05	902−880	[407,408,413]
Al−OH sym/asym	0.78315	397.17	966.53	1072−1160	
H_2O deformations/vibrations	0.26118	98.502	1403.0	1375	[400,408]
H−O−H bend	0.37889	140.14	1520.6	1600	[413]
$-COO^-$	0.0780	74.000	1635.8	1300−1850	[400]
	0.0759	1883.7	2237.9		
Al−OH stretching	0.1738	559.78	3129.3	3250−3600	[400,413]
O−H stretching	0.3324	304.69	3406.2	3400-3600	[400,408,426]
Al−OH stretching	0.1019	162.53	3607.7	3250−3600	[400,413]

Table 10.7.2. Gaussian oscillator parameters used to reconstruct the permittivity of nanoparticles from type B reactor. Phonon resonance type (first column), amplitude (second column), spectral broadening (third column) and resonant frequency (fourth column) of the Gaussian oscillators used to calculate the AlO_x particle permittivity from Mueller matrix data. The fifth column gives the resonant frequency range expected from previous literature reports. Citations for the expected frequency range are in the sixth column.

Chapter 11

CONCLUDING REMARKS

"We have not succeeded in answering all our problems. The answers we have found only serve to raise a whole set of new questions. In some ways we feel we are as confused as ever, but we believe we are confused on a higher level and about more important things."

- Bernt Øksendal, Stochastic Differential Equations, 2003

Following unprecedented advances in nanofabrication, much of modern day nanophononics is focused on the careful design of material heterogeneity to control nearly every aspect of light. Flat optics and metasurfaces push the limit of miniaturization, bringing with them a promise of compact complex lens systems in the palm of your hand. Freeform inverse design gives tantalizing claims of an unexplored and potentially fertile landscape where computer driven structures and topologies give record-breaking metrics. It is hard to tell the future of nanophotonics and where (or if) anything in this dissertation proves useful in the long run. With that said, it remains clear that there is a need for photonic devices at the scale of centimeters and at the scale of meters; and these regimes have different design constraints. The topics in this thesis have been motivated by the latter length scale. The overarching theme is to better understand the underlying mechanisms of emergent photonics behavior, when governing parameters are controlled only in the form of a probability distribution.

In general, I feel an important and under-explored area of nanophotonics is characterizing robustness to error, disorder, and nonidealities. Clearly, there are many ways to design a nanophotonic system to accomplish the same goal. Therefore, the optimal design is not necessarily a metric of efficiency, but of robustness, cost, and scalability. Understanding robustness to error/disorder is then certainly significant to narrowing the design space and choosing the best solution. This may become even more important with freeform design. An example of robustness used often in this dissertation is the optically induced magnetic resonance. As was shown in Chapters 2, 4, 7, and 9, electric type resonances in silicon easily couple between particles resulting in a notably perturbed moment given random spatial distributions. In contrast, magnetic type resonances comparatively weakly couple and maintain better their isolated particle characteristics. Correspondingly, multiple examples are shown where tuning the size distribution shifts well-defined magnetic resonance peaks across a more chaotic electric-type background.

Classifying mechanisms by their "degree of robustness" could serve as a highly useful tool as more nanophotonic concepts transition from academia to industry.

Much of this dissertation has focused on finding case examples of emergent phenomena and linking these to possible applications. In particular, examples are motivated by the features and constraints of nonthermal equilibrium dusty plasma synthesis. Though this is important for demonstrating feasibility and motivating both the photonics and plasma community, the scope is limited. For example, this dissertation places a large emphasis on particle design over correlation functions, as this directly maps to the current goals of our collaborators. Follow up academic work focusing on novel systems could explore more spatial distributions and correlation functions. Examples of disordered hyperuniformity and aperiodic tilings come to mind as interesting configurations for study. More advanced directional control of the incoherent field beyond the restriction of transmission or reflection hemispheres could also be studied. This may have an interesting impact on incoherent photonics, such as incoherent thermal and visible emitters.

In regard to the electromagnetic program, much more work can be done. It would be nice to generalize the program to support a larger set of particle shapes. At present, much of the fundamentals to support this effort already exists. Though, in practice, this support adds computational time and memory. This is because arbitrary particle shapes can require larger transition matrices and matrices of different sizes. Also, care should be taken in regard to particles with overlapping minimally circumscribing spheres. Coupling between these particles requires care in the basis conversion. Substrate interactions are of primary importance. It would also be interesting to explore approximate analytic and quasi-analytic methods and benchmark these against rigorous calculations. Simpler models are not only more amenable to the general scientific community but can offer a quick framework for optimization. For example, Bayesian optimization can use lower fidelity surrogates as a method to develop prior information. The quasi-analytic theory discussed in part I provides an interesting framework for optimization because you can explicitly access operators such as the transition and translation matrix. In this way you can define the optimization problem based on quantities not directly accessible in full-wave simulations. For example, you can explicitly define for the optimizer to maximize coupling between a magnetic-type dipole and an electric-type quadrupole. Or, for example, you can place particles at null points in the translation operator to reduce coupling effects. In general, I suspect this could offer a rich framework to design novel emergent phenomena while still maintaining an intuitive understanding of the underlying physics often lost in the optimization process.

Finally, if I have learned anything from stock market returns, it is that it is incredibly hard to predict the future. Maybe the best thing is to throw this work on a shelf, do something else, and never look back…

BIBLIOGRAPHY

(1) Novotny, L.; Hecht, B. *Principles of Nano-Optics*, 2nd ed.; Cambridge University Press, 2012. https://doi.org/10.1017/CBO9780511794193.

(2) Waterman, P. C. Matrix Formulation of Electromagnetic Scattering. *Proceedings of the IEEE* **1965**, *53* (8), 805–812. https://doi.org/10.1109/PROC.1965.4058.

(3) Waterman, P. C. Surface Fields and the T Matrix. *J. Opt. Soc. Am. A* **1999**, *16* (12), 2968. https://doi.org/10.1364/JOSAA.16.002968.

(4) Mackowski, D. The Extension of Mie Theory to Multiple Spheres. In *The Mie Theory: Basics and Applications*; Hergert, W., Wriedt, T., Eds.; Springer Series in Optical Sciences; Springer: Berlin, Heidelberg, 2012; pp 223–256. https://doi.org/10.1007/978-3-642-28738-1_8.

(5) Mishchenko, M. I.; Martin, P. A. Peter Waterman and T-Matrix Methods. *Journal of Quantitative Spectroscopy and Radiative Transfer* **2013**, *123*, 2–7. https://doi.org/10.1016/j.jqsrt.2012.10.025.

(6) Mishchenko, M. I.; Travis, L. D.; Lacis, A. A. *Multiple Scattering of Light by Particles: Radiative Transfer and Coherent Backscattering*; Cambridge University Press: Cambridge ; New York, 2006.

(7) Tsang, L.; Kong, J. A.; Ding, K.-H. *Scattering of Electromagnetic Waves: Theories and Applications*; John Wiley & Sons, Inc.: New York, USA, 2000. https://doi.org/10.1002/0471224286.

(8) Egel, A.; Theobald, D.; Donie, Y.; Lemmer, U.; Gomard, G. Light Scattering by Oblate Particles near Planar Interfaces: On the Validity of the T-Matrix Approach. *Opt. Express* **2016**, *24* (22), 25154. https://doi.org/10.1364/OE.24.025154.

(9) Theobald, D.; Egel, A.; Gomard, G.; Lemmer, U. Plane-Wave Coupling Formalism for T -Matrix Simulations of Light Scattering by Nonspherical Particles. *Phys. Rev. A* **2017**, *96* (3), 033822. https://doi.org/10.1103/PhysRevA.96.033822.

(10) Deák, A.; Bancsi, B.; Tóth, A. L.; Kovács, A. L.; Hórvölgyi, Z. Complex Langmuir–Blodgett Films from Silica Nanoparticles: An Optical Spectroscopy Study. *Colloids and Surfaces A: Physicochemical and Engineering Aspects* **2006**, *278* (1), 10–16. https://doi.org/10.1016/j.colsurfa.2005.11.070.

(11) Li, Z.; Wray, P. R.; Su, M. P.; Tu, Q.; Andaraarachchi, H. P.; Jeong, Y. J.; Atwater, H. A.; Kortshagen, U. R. Aluminum Oxide Nanoparticle Films Deposited from a Nonthermal Plasma: Synthesis, Characterization, and Crystallization. *ACS Omega* **2020**, *5* (38), 24754–24761. https://doi.org/10.1021/acsomega.0c03353.

(12) Roach, L.; Hereu, A.; Lalanne, P.; Duguet, E.; Tréguer-Delapierre, M.; Vynck, K.; Drisko, G. L. Controlling Disorder in Self-Assembled Colloidal Monolayers via Evaporative Processes. *Nanoscale* **2022**, *14* (9), 3324–3345. https://doi.org/10.1039/D1NR07814C.

(13) Eklöf, J.; Gschneidtner, T.; Lara-Avila, S.; Nygård, K.; Moth-Poulsen, K. Controlling Deposition of Nanoparticles by Tuning Surface Charge of SiO2 by Surface Modifications. *RSC Adv.* **2016**, *6* (106), 104246–104253. https://doi.org/10.1039/C6RA22412A.

(14) Adamczyk, Z.; Morga, M.; Nattich-Rak, M.; Sadowska, M. Nanoparticle and Bioparticle Deposition Kinetics. *Advances in Colloid and Interface Science* **2022**, *302*, 102630. https://doi.org/10.1016/j.cis.2022.102630.

(15) Siddique, R. H.; Gomard, G.; Hölscher, H. The Role of Random Nanostructures for the Omnidirectional Anti-Reflection Properties of the Glasswing Butterfly. *Nat Commun* **2015**, *6* (1), 6909. https://doi.org/10.1038/ncomms7909.

(16) Siddique, R. H.; Donie, Y. J.; Gomard, G.; Yalamanchili, S.; Merdzhanova, T.; Lemmer, U.; Hölscher, H. Bioinspired Phase-Separated Disordered Nanostructures for Thin Photovoltaic Absorbers. *Science Advances* **2017**, *3* (10), e1700232. https://doi.org/10.1126/sciadv.1700232.

(17) Narasimhan, V.; Siddique, R. H.; Lee, J. O.; Kumar, S.; Ndjamen, B.; Du, J.; Hong, N.; Sretavan, D.; Choo, H. Multifunctional Biophotonic Nanostructures Inspired by the Longtail Glasswing Butterfly for Medical Devices. *Nature Nanotech* **2018**, *13* (6), 512–519. https://doi.org/10.1038/s41565-018-0111-5.

(18) Choy, T. C. *Effective Medium Theory: Principles and Applications*; International series of monographs on physics; Clarendon Press, 1999.

(19) Kapitanova, P.; Odit, M.; Danaeifar, M.; Sayanskiy, A.; Belov, P.; Miroshnichenko, A.; Kivshar, Y. All-Dielectric Bianisotropic and Multimode Unidirectional Microwave Metasurfaces. In *2017 47th European Microwave Conference (EuMC)*; 2017; pp 476–479. https://doi.org/10.23919/EuMC.2017.8230893.

(20) Krasnok, A. E.; Miroshnichenko, A. E.; Belov, P. A.; Kivshar, Y. S. All-Dielectric Optical Nanoantennas. **2012**, 6.

(21) Arslan, D.; Chong, K. E.; Miroshnichenko, A. E.; Choi, D.-Y.; Neshev, D. N.; Pertsch, T.; Kivshar, Y. S.; Staude, I. Angle-Selective All-Dielectric Huygens' Metasurfaces. *Journal of Physics D: Applied Physics* **2017**, *50* (43), 434002. https://doi.org/10.1088/1361-6463/aa875c.

(22) Fu, Y. H.; Kuznetsov, A. I.; Miroshnichenko, A. E.; Yu, Y. F.; Luk'yanchuk, B. Directional Visible Light Scattering by Silicon Nanoparticles. *Nat Commun* **2013**, *4* (1), 1527. https://doi.org/10.1038/ncomms2538.

(23) Geffrin, J. M.; García-Cámara, B.; Gómez-Medina, R.; Albella, P.; Froufe-Pérez, L. S.; Eyraud, C.; Litman, A.; Vaillon, R.; González, F.; Nieto-Vesperinas, M.; Sáenz, J. J.; Moreno, F. Magnetic and Electric Coherence in Forward- and Back-Scattered Electromagnetic Waves by a Single Dielectric Subwavelength Sphere. *Nature Communications* **2012**, *3*, 1171. https://doi.org/10.1038/ncomms2167.

(24) Limonov, M. F.; Nikulin, A. V.; Li, S. V.; Samusev, K. B.; Kivshar, Y. S.; Rybin, M. V. Mie Bands in All-Dielectric High-Index Metamaterials. In *2017 Progress In Electromagnetics Research Symposium - Spring (PIERS)*; 2017; pp 2825–2827. https://doi.org/10.1109/PIERS.2017.8262234.

(25) Babicheva, V. E.; Evlyukhin, A. B. Resonant Lattice Kerker Effect in Metasurfaces With Electric and Magnetic Optical Responses. *Laser & Photonics Reviews* **2017**, *11* (6), 1700132. https://doi.org/10.1002/lpor.201700132.

(26) Kruk, S.; Kivshar, Y. Functional Meta-Optics and Nanophotonics Governed by Mie Resonances. *ACS Photonics* **2017**, *4* (11), 2638–2649. https://doi.org/10.1021/acsphotonics.7b01038.

(27) Person, S.; Jain, M.; Lapin, Z.; Sáenz, J. J.; Wicks, G.; Novotny, L. Demonstration of Zero Optical Backscattering from Single Nanoparticles. *Nano Lett.* **2013**, *13* (4), 1806–1809. https://doi.org/10.1021/nl4005018.

(28) Krasnok, A. E.; Miroshnichenko, A. E.; Belov, P. A.; Kivshar, Yu. S. Huygens Optical Elements and Yagi—Uda Nanoantennas Based on Dielectric Nanoparticles. *Jetp Lett.* **2011**, *94* (8), 593–598. https://doi.org/10.1134/S0021364011200070.

(29) Liu, W.; Kivshar, Y. S. Generalized Kerker Effects in Nanophotonics and Meta-Optics. *Optics Express* **2018**, *26* (10), 13085. https://doi.org/10.1364/OE.26.013085.

(30) Spinelli, P.; Verschuuren, M. A.; Polman, A. Broadband Omnidirectional Antireflection Coating Based on Subwavelength Surface Mie Resonators. *Nat Commun* **2012**, *3* (1), 692. https://doi.org/10.1038/ncomms1691.

(31) Vaskin, A.; Bohn, J.; Chong, K. E.; Bucher, T.; Zilk, M.; Choi, D.-Y.; Neshev, D. N.; Kivshar, Y. S.; Pertsch, T.; Staude, I. Directional and Spectral Shaping of Light Emission with Mie-Resonant Silicon Nanoantenna Arrays. *ACS Photonics* **2018**, *5* (4), 1359–1364. https://doi.org/10.1021/acsphotonics.7b01375.

(32) Chong, K. E.; Wang, L.; Staude, I.; James, A. R.; Dominguez, J.; Liu, S.; Subramania, G. S.; Decker, M.; Neshev, D. N.; Brener, I.; Kivshar, Y. S. Efficient Polarization-Insensitive Complex Wavefront Control Using Huygens' Metasurfaces Based on Dielectric Resonant Meta-Atoms. *ACS Photonics* **2016**, *3* (4), 514–519. https://doi.org/10.1021/acsphotonics.5b00678.

(33) Abdelrahman, M. I.; Saleh, H.; Fernandez-Corbaton, I.; Gralak, B.; Geffrin, J.-M.; Rockstuhl, C. Experimental Demonstration of Spectrally Broadband Huygens Sources Using Low-Index Spheres. *APL Photonics* **2019**, *4* (2), 020802. https://doi.org/10.1063/1.5080980.

(34) Shamkhi, H. K.; Sayanskiy, A.; Valero, A. C.; Kupriianov, A. S.; Kapitanova, P.; Kivshar, Y. S.; Shalin, A. S.; Tuz, V. R. Invisibility and Perfect Absorption of All-Dielectric Metasurfaces Originated from the Transverse Kerker Effect. *arXiv:1905.10538 [physics]* **2019**.

(35) Yang, Y.; Miroshnichenko, A. E.; Kostinski, S. V.; Odit, M.; Kapitanova, P.; Qiu, M.; Kivshar, Y. S. Multimode Directionality in All-Dielectric Metasurfaces. *Phys. Rev. B* **2017**, *95* (16), 165426. https://doi.org/10.1103/PhysRevB.95.165426.

(36) Born, M.; Wolf, E. *Principles of Optics: Electromagnetic Theory of Propagation, Interference and Diffraction of Light*; CUP Archive, 2000.

(37) Kerker, M.; Wang, D.-S.; Giles, C. L. Electromagnetic Scattering by Magnetic Spheres. *Journal of the Optical Society of America* **1983**, *73* (6), 765. https://doi.org/10.1364/JOSA.73.000765.

(38) Lannebère, S.; Campione, S.; Aradian, A.; Albani, M.; Capolino, F. Artificial Magnetism at Terahertz Frequencies from Three-Dimensional Lattices of TiO_2 Microspheres Accounting for Spatial Dispersion and Magnetoelectric Coupling. *Journal of the Optical Society of America B* **2014**, *31* (5), 1078. https://doi.org/10.1364/JOSAB.31.001078.

(39) Paniagua-Domínguez, R.; Yu, Y. F.; Miroshnichenko, A. E.; Krivitsky, L. A.; Fu, Y. H.; Valuckas, V.; Gonzaga, L.; Toh, Y. T.; Kay, A. Y. S.; Luk'yanchuk, B.; Kuznetsov, A. I. Generalized Brewster Effect in Dielectric Metasurfaces. *Nat Commun* **2016**, *7* (1), 10362. https://doi.org/10.1038/ncomms10362.

(40) Evlyukhin, A. B.; Novikov, S. M.; Zywietz, U.; Eriksen, R. L.; Reinhardt, C.; Bozhevolnyi, S. I.; Chichkov, B. N. Demonstration of Magnetic Dipole Resonances of Dielectric Nanospheres in the Visible Region. *Nano Letters* **2012**, *12* (7), 3749–3755. https://doi.org/10.1021/nl301594s.

(41) Ziolkowski, R. W. Using Huygens Multipole Arrays to Realize Unidirectional Needle-Like Radiation. *Physical Review X* **2017**, *7* (3). https://doi.org/10.1103/PhysRevX.7.031017.

(42) Liu, W.; Zhang, J.; Lei, B.; Ma, H.; Xie, W.; Hu, H. Ultra-Directional Forward Scattering by Individual Core-Shell Nanoparticles. *Optics Express* **2014**, *22* (13), 16178. https://doi.org/10.1364/OE.22.016178.

(43) Hopkins, B.; Filonov, D. S.; Miroshnichenko, A. E.; Monticone, F.; Alù, A.; Kivshar, Y. S. Interplay of Magnetic Responses in All-Dielectric Oligomers To Realize Magnetic Fano Resonances. *ACS Photonics* **2015**, *2* (6), 724–729. https://doi.org/10.1021/acsphotonics.5b00082.

(44) Miroshnichenko, A. E.; Kivshar, Y. S. Fano Resonances in All-Dielectric Oligomers. *Nano Lett.* **2012**, *12* (12), 6459–6463. https://doi.org/10.1021/nl303927q.

(45) Yan, J. H.; Liu, P.; Lin, Z. Y.; Wang, H.; Chen, H. J.; Wang, C. X.; Yang, G. W. Magnetically Induced Forward Scattering at Visible Wavelengths in Silicon Nanosphere Oligomers. *Nature Communications* **2015**, *6*, 7042. https://doi.org/10.1038/ncomms8042.

(46) Babicheva, V. E.; Evlyukhin, A. B. Resonant Lattice Kerker Effect in Metasurfaces With Electric and Magnetic Optical Responses. *Laser & Photonics Reviews* **2017**, *11* (6), 1700132. https://doi.org/10.1002/lpor.201700132.

(47) Babicheva, V. E.; Evlyukhin, A. B. Metasurfaces with Electric Quadrupole and Magnetic Dipole Resonant Coupling. *ACS Photonics* **2018**, *5* (5), 2022–2033. https://doi.org/10.1021/acsphotonics.7b01520.

(48) Vasilantonakis, N.; Scheuer, J.; Boag, A. Designing High-Transmission and Wide Angle All-Dielectric Flat Metasurfaces at Telecom Wavelengths. *arXiv:1711.01430 [physics]* **2017**.

(49) Yang, Y.; Kravchenko, I. I.; Briggs, D. P.; Valentine, J. All-Dielectric Metasurface Analogue of Electromagnetically Induced Transparency. *Nat Commun* **2014**, *5* (1), 5753. https://doi.org/10.1038/ncomms6753.

(50) Yang, T.; Wang, X.; Zhou, Z.; Zhou, J. Transient Characters of the Unity Reflection Phenomenon in All-Dielectric Magnetic Metamaterials. *OSA Continuum* **2018**, *1* (2), 634. https://doi.org/10.1364/OSAC.1.000634.

(51) Moitra, P.; Slovick, B. A.; li, W.; Kravchencko, I. I.; Briggs, D. P.; Krishnamurthy, S.; Valentine, J. Large-Scale All-Dielectric Metamaterial Perfect Reflectors. *ACS Photonics* **2015**, *2* (6), 692–698. https://doi.org/10.1021/acsphotonics.5b00148.

(52) Ra'di, Y.; Asadchy, V. S.; Kosulnikov, S. U.; Omelyanovich, M. M.; Morits, D.; Osipov, A. V.; Simovski, C. R.; Tretyakov, S. A. Full Light Absorption in Single Arrays of Spherical Nanoparticles. *ACS Photonics* **2015**, *2* (5), 653–660. https://doi.org/10.1021/acsphotonics.5b00073.

(53) Bohren, C. F.; Huffman, D. R. *Absorption and Scattering of Light by Small Particles*; Wiley-VCH: Weinheim, 2004.

(54) Aspnes, D. E.; Studna, A. A. Dielectric Functions and Optical Parameters of Si, Ge, GaP, GaAs, GaSb, InP, InAs, and InSb from 1.5 to 6.0 eV. *Phys. Rev. B* **1983**, *27* (2), 985–1009. https://doi.org/10.1103/PhysRevB.27.985.

(55) Kawashima, T.; Yoshikawa, H.; Adachi, S.; Fuke, S.; Ohtsuka, K. Optical Properties of Hexagonal GaN. *Journal of Applied Physics* **1997**, *82* (7), 3528–3535. https://doi.org/10.1063/1.365671.
(56) Mätzler, C. MATLAB Functions for Mie Scattering and Absorption. 19.
(57) Mackowski, D. W.; Mishchenko, M. I. Calculation of the T Matrix and the Scattering Matrix for Ensembles of Spheres. *Journal of the Optical Society of America A* **1996**, *13* (11), 2266. https://doi.org/10.1364/JOSAA.13.002266.
(58) Mackowski, D. W.; Mishchenko, M. I. A Multiple Sphere T-Matrix Fortran Code for Use on Parallel Computer Clusters. *Journal of Quantitative Spectroscopy and Radiative Transfer* **2011**, *112* (13), 2182–2192. https://doi.org/10.1016/j.jqsrt.2011.02.019.
(59) Lumerical Inc. Https://Www.Lumerical.Com/Products/.
(60) Mackowski, D. W. A Multiple Sphere T -Matrix FORTRAN Code for Use on Parallel Computer Clusters Version 3.0. 36.
(61) Jones, M. N.; Jones, M. N. *Spherical Harmonics and Tensors for Classical Field Theory*; Wiley, 1985.
(62) Varshalovich, D. A.; Moskalev, A. N.; Khersonskii, V. K. *Quantum Theory of Angular Momentum*; World Scientific Publishing Co., 1988. https://doi.org/10.1142/0270.
(63) Stratton, J. A. *Electromagnetic Theory*, First.; McGraw-Hill Book Company Inc., 1941.
(64) Bohren, C. F. Scattering of Electromagnetic Waves by an Optically Active Spherical Shell. *The Journal of Chemical Physics* **1975**, *62* (4), 1566–1571. https://doi.org/10.1063/1.430622.
(65) Fernandez-Corbaton, I. Forward and Backward Helicity Scattering Coefficients for Systems with Discrete Rotational Symmetry. *Opt. Express, OE* **2013**, *21* (24), 29885–29893. https://doi.org/10.1364/OE.21.029885.
(66) Coenen, T.; Bernal Arango, F.; Femius Koenderink, A.; Polman, A. Directional Emission from a Single Plasmonic Scatterer. *Nat Commun* **2014**, *5* (1), 3250. https://doi.org/10.1038/ncomms4250.
(67) Curto, A. G.; Volpe, G.; Taminiau, T. H.; Kreuzer, M. P.; Quidant, R.; van Hulst, N. F. Unidirectional Emission of a Quantum Dot Coupled to a Nanoantenna. *Science* **2010**, *329* (5994), 930–933. https://doi.org/10.1126/science.1191922.
(68) Cihan, A. F.; Curto, A. G.; Raza, S.; Kik, P. G.; Brongersma, M. L. Silicon Mie Resonators for Highly Directional Light Emission from Monolayer MoS2. *Nature Photon* **2018**, *12* (5), 284–290. https://doi.org/10.1038/s41566-018-0155-y.
(69) Qu, Y.; Pan, M.; Qiu, M. Directional and Spectral Control of Thermal Emission and Its Application in Radiative Cooling and Infrared Light Sources. *Phys. Rev. Applied* **2020**, *13* (6), 064052. https://doi.org/10.1103/PhysRevApplied.13.064052.
(70) Itagi, A. V.; Challener, W. A. Optics of Photonic Nanojets. *J. Opt. Soc. Am. A* **2005**, *22* (12), 2847. https://doi.org/10.1364/JOSAA.22.002847.
(71) Li, X.; Chen, Z.; Taflove, A.; Backman, V. Optical Analysis of Nanoparticles via Enhanced Backscattering Facilitated by 3-D Photonic Nanojets. *Opt. Express, OE* **2005**, *13* (2), 526–533. https://doi.org/10.1364/OPEX.13.000526.
(72) Alaee, R.; Filter, R.; Lehr, D.; Lederer, F.; Rockstuhl, C. A Generalized Kerker Condition for Highly Directive Nanoantennas. *Opt. Lett.* **2015**, *40* (11), 2645. https://doi.org/10.1364/OL.40.002645.

(73) Tzarouchis, D.; Sihvola, A. Light Scattering by a Dielectric Sphere: Perspectives on the Mie Resonances. *Applied Sciences* **2018**, *8* (2), 184. https://doi.org/10.3390/app8020184.
(74) Zambrana-Puyalto, X.; Fernandez-Corbaton, I.; Juan, M. L.; Vidal, X.; Molina-Terriza, G. Duality Symmetry and Kerker Conditions. *Opt. Lett.* **2013**, *38* (11), 1857. https://doi.org/10.1364/OL.38.001857.
(75) Sarkar, S.; Gupta, V.; Kumar, M.; Schubert, J.; Probst, P. T.; Joseph, J.; König, T. A. F. Hybridized Guided-Mode Resonances via Colloidal Plasmonic Self-Assembled Grating. *ACS Appl. Mater. Interfaces* **2019**, *11* (14), 13752–13760. https://doi.org/10.1021/acsami.8b20535.
(76) Aspnes, D. E.; Studna, A. A. Dielectric Functions and Optical Parameters of Si, Ge, GaP, GaAs, GaSb, InP, InAs, and InSb from 1.5 to 6.0 eV. *Phys. Rev. B* **1983**, *27* (2), 985–1009. https://doi.org/10.1103/PhysRevB.27.985.
(77) Marcos, L. V. R.; Larruquert, J. I.; Méndez, J. A.; Aznárez, J. A. Self-Consistent Optical Constants of SiO_2 and Ta_2O_5 Films. *Opt. Mater. Express, OME* **2016**, *6* (11), 3622–3637. https://doi.org/10.1364/OME.6.003622.
(78) Tai, C. *Dyadic Green Functions in Electromagnetic Theory*; IEEE Press, 1994.
(79) Fang, J.; Wang, M.; Yao, K.; Zhang, T.; Krasnok, A.; Jiang, T.; Choi, J.; Kahn, E.; Korgel, B. A.; Terrones, M.; Li, X.; Alù, A.; Zheng, Y. Directivity Modulation of Exciton Emission Using Single Dielectric Nanospheres. 39.
(80) *Materials Science of Thin Films - 2nd Edition*. https://www.elsevier.com/books/materials-science-of-thin-films/ohring/978-0-12-524975-1 (accessed 2022-11-13).
(81) Guler, U.; Boltasseva, A.; Shalaev, V. M. Refractory Plasmonics. *Science* **2014**, *344* (6181), 263–264. https://doi.org/10.1126/science.1252722.
(82) Becker, R. A. Optical Material Problems of Interplanetary Space. *Appl. Opt., AO* **1967**, *6* (5), 955–962. https://doi.org/10.1364/AO.6.000955.
(83) Pelizzo, M. G.; Corso, A. J.; Tessarolo, E.; Zuppella, P.; Böttger, R.; Huebner, R.; Corte, V. D.; Palumbo, P.; Taglioni, G.; Preti, G.; Foggetta, L.; Valente, P.; Rancoita, P.; Martucci, A.; Napolitani, E. Optical Components in Harsh Space Environment. In *Planetary Defense and Space Environment Applications*; SPIE, 2016; Vol. 9981, pp 150–157. https://doi.org/10.1117/12.2237966.
(84) Blue, M. D.; Roberts, D. W. Effects of Space Exposure on Optical Filters. *Appl. Opt.* **1992**, *31* (25), 5299. https://doi.org/10.1364/AO.31.005299.
(85) Grillot, P. N.; Rosenberg, W. J. Proton Radiation Damage in Optical Filter Glass. *Appl. Opt., AO* **1989**, *28* (20), 4473–4477. https://doi.org/10.1364/AO.28.004473.
(86) Nicoletta, C. A.; Eubanks, A. G. Effect of Simulated Space Radiation on Selected Optical Materials. *Appl. Opt., AO* **1972**, *11* (6), 1365–1370. https://doi.org/10.1364/AO.11.001365.
(87) Pellicori, S. F.; Russell, E. E.; Watts, L. A. Radiation Induced Transmission Loss in Optical Materials. *Appl. Opt., AO* **1979**, *18* (15), 2618–2621. https://doi.org/10.1364/AO.18.002618.
(88) Brunsting, A.; Kheiri, M. A.; Simonaitis, D. F.; Dosmann, A. J. Environmental Effects on All-Dielectric Bandpass Filters. *Appl. Opt., AO* **1986**, *25* (18), 3235–3241. https://doi.org/10.1364/AO.25.003235.

(89) Druffel, T.; Geng, K.; Grulke, E. Mechanical Comparison of a Polymer Nanocomposite to a Ceramic Thin-Film Anti-Reflective Filter. *Nanotechnology* **2006**, *17* (14), 3584–3590. https://doi.org/10.1088/0957-4484/17/14/038.

(90) Park, S.; Park, H.; Seong, S.; Chung, Y. Multilayer Substrate to Use Brittle Materials in Flexible Electronics. *Sci Rep* **2020**, *10* (1), 7660. https://doi.org/10.1038/s41598-020-64057-6.

(91) Abadias, G.; Chason, E.; Keckes, J.; Sebastiani, M.; Thompson, G. B.; Barthel, E.; Doll, G. L.; Murray, C. E.; Stoessel, C. H.; Martinu, L. Review Article: Stress in Thin Films and Coatings: Current Status, Challenges, and Prospects. *Journal of Vacuum Science & Technology A* **2018**, *36* (2), 020801. https://doi.org/10.1116/1.5011790.

(92) Takashashi, H. Temperature Stability of Thin-Film Narrow-Bandpass Filters Produced by Ion-Assisted Deposition. *Appl. Opt., AO* **1995**, *34* (4), 667–675. https://doi.org/10.1364/AO.34.000667.

(93) Schaming, D.; Remita, H. Nanotechnology: From the Ancient Time to Nowadays. *Found Chem* **2015**, *17* (3), 187–205. https://doi.org/10.1007/s10698-015-9235-y.

(94) Shaukat, A.; Noble, F.; Arif, K. M. Nanostructured Color Filters: A Review of Recent Developments. *Nanomaterials* **2020**, *10* (8), 1554. https://doi.org/10.3390/nano10081554.

(95) Cartwright, J. Fifty Shades of Black. *Phys. World* **2015**, *28* (11), 25–28. https://doi.org/10.1088/2058-7058/28/11/32.

(96) Cui, K.; Wardle, B. L. Breakdown of Native Oxide Enables Multifunctional, Free-Form Carbon Nanotube–Metal Hierarchical Architectures. *ACS Appl. Mater. Interfaces* **2019**, *11* (38), 35212–35220. https://doi.org/10.1021/acsami.9b08290.

(97) Lehman, J.; Sanders, A.; Hanssen, L.; Wilthan, B.; Zeng, J.; Jensen, C. Very Black Infrared Detector from Vertically Aligned Carbon Nanotubes and Electric-Field Poling of Lithium Tantalate. *Nano Lett.* **2010**, *10* (9), 3261–3266. https://doi.org/10.1021/nl100582j.

(98) Anderson, P. W. Absence of Diffusion in Certain Random Lattices. *Phys. Rev.* **1958**, *109* (5), 1492–1505. https://doi.org/10.1103/PhysRev.109.1492.

(99) Persky, M. J. Review of Black Surfaces for Space-Borne Infrared Systems. *Review of Scientific Instruments* **1999**, *70* (5), 2193–2217. https://doi.org/10.1063/1.1149739.

(100) de Laat, D.; Filho, F. M. de O.; Vallentin, F. Upper Bounds for Packings of Spheres of Several Radii. *Forum math. Sigma* **2014**, *2*, e23. https://doi.org/10.1017/fms.2014.24.

(101) Likos, C. N.; Henley, C. L. Complex Alloy Phases for Binary Hard-Disc Mixtures. *Philosophical Magazine B* **1993**, *68* (1), 85–113. https://doi.org/10.1080/13642819308215284.

(102) Bédaride, N.; Fernique, T. Density of Binary Disc Packings: The 9 Compact Packings. arXiv May 3, 2021. http://arxiv.org/abs/2002.07168 (accessed 2022-11-12).

(103) Barad, H.-N.; Kwon, H.; Alarcón-Correa, M.; Fischer, P. Large Area Patterning of Nanoparticles and Nanostructures: Current Status and Future Prospects. *ACS Nano* **2021**, *15* (4), 5861–5875. https://doi.org/10.1021/acsnano.0c09999.

(104) Li, X.; Gilchrist, J. F. Large-Area Nanoparticle Films by Continuous Automated Langmuir–Blodgett Assembly and Deposition. *Langmuir* **2016**, *32* (5), 1220–1226. https://doi.org/10.1021/acs.langmuir.5b03760.

(105) Egel, A.; Czajkowski, K. M.; Theobald, D.; Ladutenko, K.; Kuznetsov, A. S.; Pattelli, L. SMUTHI: A Python Package for the Simulation of Light Scattering by Multiple Particles near or between Planar Interfaces. *Journal of Quantitative Spectroscopy and Radiative Transfer* **2021**, *273*, 107846. https://doi.org/10.1016/j.jqsrt.2021.107846.
(106) Wray, P. R.; Atwater, H. A. Light–Matter Interactions in Films of Randomly Distributed Unidirectionally Scattering Dielectric Nanoparticles. *ACS Photonics* **2020**, *7* (8), 2105–2114. https://doi.org/10.1021/acsphotonics.0c00545.
(107) Rocklin, M. Dask: Parallel Computation with Blocked Algorithms and Task Scheduling; Austin, Texas, 2015; pp 126–132. https://doi.org/10.25080/Majora-7b98e3ed-013.
(108) Frazier, P. I. A Tutorial on Bayesian Optimization. arXiv July 8, 2018. http://arxiv.org/abs/1807.02811 (accessed 2022-08-18).
(109) Balandat, M.; Karrer, B.; Jiang, D. R.; Daulton, S.; Letham, B.; Wilson, A. G.; Bakshy, E. BOTORCH: A Framework for Efficient Monte-Carlo Bayesian Optimization. 15.
(110) Thanh, N. T. K.; Maclean, N.; Mahiddine, S. Mechanisms of Nucleation and Growth of Nanoparticles in Solution. *Chem. Rev.* **2014**, *114* (15), 7610–7630. https://doi.org/10.1021/cr400544s.
(111) Kim, S. C.; Harrington, M. S.; Pui, D. Y. H. Experimental Study of Nanoparticles Penetration through Commercial Filter Media. In *Nanotechnology and Occupational Health*; Maynard, A. D., Pui, D. Y. H., Eds.; Springer Netherlands: Dordrecht, 2007; pp 117–125. https://doi.org/10.1007/978-1-4020-5859-2_12.
(112) Robertson, J. D.; Rizzello, L.; Avila-Olias, M.; Gaitzsch, J.; Contini, C.; Magoń, M. S.; Renshaw, S. A.; Battaglia, G. Purification of Nanoparticles by Size and Shape. *Sci Rep* **2016**, *6* (1), 27494. https://doi.org/10.1038/srep27494.
(113) Wray, P. R.; Eslamisaray, M. A.; Nelson, G. M.; Ilic, O.; Kortshagen, U. R.; Atwater, H. A. Broadband, Angle- and Polarization-Invariant Antireflective and Absorbing Films by a Scalable Synthesis of Monodisperse Silicon Nanoparticles. *ACS Appl. Mater. Interfaces* **2022**, *14* (20), 23624–23636. https://doi.org/10.1021/acsami.2c03263.
(114) Ding, F.; Pors, A.; Bozhevolnyi, S. I. Gradient Metasurfaces: A Review of Fundamentals and Applications. *Rep. Prog. Phys.* **2018**, *81* (2), 026401. https://doi.org/10.1088/1361-6633/aa8732.
(115) Hsieh, C.-H. Design and Manufacturing of All-Dielectric Optical Metamaterial with Gradient Index of Refraction. Thesis, Massachusetts Institute of Technology, 2015. https://dspace.mit.edu/handle/1721.1/100120 (accessed 2023-09-13).
(116) Jang, J.; Badloe, T.; Yang, Y.; Lee, T.; Mun, J.; Rho, J. Spectral Modulation through the Hybridization of Mie-Scatterers and Quasi-Guided Mode Resonances: Realizing Full and Gradients of Structural Color. *ACS Nano* **2020**. https://doi.org/10.1021/acsnano.0c05656.
(117) Mohammadi Estakhri, N.; Alù, A. Wave-Front Transformation with Gradient Metasurfaces. *Phys. Rev. X* **2016**, *6* (4), 041008. https://doi.org/10.1103/PhysRevX.6.041008.
(118) Smith, D. R.; Mock, J. J.; Starr, A. F.; Schurig, D. Gradient Index Metamaterials. *Phys. Rev. E* **2005**, *71* (3), 036609. https://doi.org/10.1103/PhysRevE.71.036609.
(119) Weber, J.; Bartzsch, H.; Frach, P. Sputter Deposition of Silicon Oxynitride Gradient and Multilayer Coatings. 5.

(120) Campione, S.; Lannebère, S.; Aradian, A.; Albani, M.; Capolino, F. Complex Modes and Artificial Magnetism in Three-Dimensional Periodic Arrays of Titanium Dioxide Microspheres at Millimeter Waves. *Journal of the Optical Society of America B* **2012**, *29* (7), 1697. https://doi.org/10.1364/JOSAB.29.001697.

(121) Merlin, R. Metamaterials and the Landau–Lifshitz Permeability Argument: Large Permittivity Begets High-Frequency Magnetism. *Proceedings of the National Academy of Sciences* **2009**, *106* (6), 1693–1698. https://doi.org/10.1073/pnas.0808478106.

(122) Papadakis, G. T.; Fleischman, D.; Davoyan, A.; Yeh, P.; Atwater, H. A. Optical Magnetism in Planar Metamaterial Heterostructures. *Nat Commun* **2018**, *9* (1), 296. https://doi.org/10.1038/s41467-017-02589-8.

(123) Pendry, J. B.; Holden, A. J.; Robbins, D. J.; Stewart, W. J. Magnetism from Conductors and Enhanced Nonlinear Phenomena. *IEEE Transactions on Microwave Theory and Techniques* **1999**, *47* (11), 2075–2084. https://doi.org/10.1109/22.798002.

(124) Boltasseva, A.; Shalaev, V. M. Fabrication of Optical Negative-Index Metamaterials: Recent Advances and Outlook. *Metamaterials* **2008**, *2* (1), 1–17. https://doi.org/10.1016/j.metmat.2008.03.004.

(125) Chaumet, P. C.; Rahmani, A. Coupled-Dipole Method for Magnetic and Negative-Refraction Materials. *Journal of Quantitative Spectroscopy and Radiative Transfer* **2009**, *110* (1–2), 22–29. https://doi.org/10.1016/j.jqsrt.2008.09.004.

(126) Huang, T. C.; Wang, B. X.; Zhao, C. Y. Negative Refraction in Metamaterials Based on Dielectric Spherical Particles. *Journal of Quantitative Spectroscopy and Radiative Transfer* **2018**, *214*, 82–93. https://doi.org/10.1016/j.jqsrt.2018.04.030.

(127) Stockman, M. I. Criterion for Negative Refraction with Low Optical Losses from a Fundamental Principle of Causality. *Phys. Rev. Lett.* **2007**, *98* (17), 177404. https://doi.org/10.1103/PhysRevLett.98.177404.

(128) Shalaev, V. M. Optical Negative-Index Metamaterials. *Nature Photon* **2007**, *1* (1), 41–48. https://doi.org/10.1038/nphoton.2006.49.

(129) Wheeler, M. S.; Aitchison, J. S.; Mojahedi, M. Coated Nonmagnetic Spheres with a Negative Index of Refraction at Infrared Frequencies. *Physical Review B* **2006**, *73* (4). https://doi.org/10.1103/PhysRevB.73.045105.

(130) Smith, D. R. Metamaterials and Negative Refractive Index. *Science* **2004**, *305* (5685), 788–792. https://doi.org/10.1126/science.1096796.

(131) Karpov, S. V.; Gerasimov, V. S.; Isaev, I. L.; Markel, V. A. Local Anisotropy and Giant Enhancement of Local Electromagnetic Fields in Fractal Aggregates of Metal Nanoparticles. *Phys. Rev. B* **2005**, *72* (20), 205425. https://doi.org/10.1103/PhysRevB.72.205425.

(132) Galfsky, T.; Krishnamoorthy, H. N. S.; Newman, W. D.; Narimanov, E.; Jacob, Z.; Menon, V. M. Directional Emission from Quantum Dots in a Hyperbolic Metamaterial. In *CLEO: 2014*; OSA: San Jose, California, 2014; p FTu3C.6. https://doi.org/10.1364/CLEO_QELS.2014.FTu3C.6.

(133) Wang, L.; Li, S.; Zhang, B.; Qin, Y.; Tian, Z.; Fang, Y.; Li, Y.; Liu, Z.; Mei, Y. Asymmetrically Curved Hyperbolic Metamaterial Structure with Gradient Thicknesses for Enhanced Directional Spontaneous Emission. *ACS Appl. Mater. Interfaces* **2018**, *10* (9), 7704–7708. https://doi.org/10.1021/acsami.7b19721.

(134) Fasold, S.; Linß, S.; Kawde, T.; Falkner, M.; Decker, M.; Pertsch, T.; Staude, I. Disorder-Enabled Pure Chirality in Bilayer Plasmonic Metasurfaces. *ACS Photonics* **2018**, *5* (5), 1773–1778. https://doi.org/10.1021/acsphotonics.7b01460.

(135) Psarobas, I. E.; Stefanou, N.; Modinos, A. Photonic Crystals of Chiral Spheres. *Journal of the Optical Society of America A* **1999**, *16* (2), 343. https://doi.org/10.1364/JOSAA.16.000343.

(136) Schmidt, D.; Schubert, E.; Schubert, M. Generalized Ellipsometry Determination of Non-Reciprocity in Chiral Silicon Sculptured Thin Films. *physica status solidi (a)* **2008**, *205* (4), 748–751. https://doi.org/10.1002/pssa.200777906.

(137) Lucarini, V.; Saarinen, J. J.; Peiponen, K.-E.; Vartiainen, E. M. *Kramers-Kronig Relations in Optical Materials Research*; Springer Science & Business Media, 2005.

(138) Peiponen, K.-E.; Lucarini, V.; Vartiainen, E. M.; Saarinen, J. J. Kramers-Kronig Relations and Sum Rules of Negative Refractive Index Media. *Eur. Phys. J. B* **2004**, *41* (1), 61–65. https://doi.org/10.1140/epjb/e2004-00294-6.

(139) Shim, H.; Monticone, F.; Miller, O. D. Fundamental Limits to the Refractive Index of Transparent Optical Materials. *Advanced Materials* **2021**, *33* (43), 2103946. https://doi.org/10.1002/adma.202103946.

(140) Chao, P.; Strekha, B.; Kuate Defo, R.; Molesky, S.; Rodriguez, A. W. Physical Limits in Electromagnetism. *Nat Rev Phys* **2022**, *4* (8), 543–559. https://doi.org/10.1038/s42254-022-00468-w.

(141) Miller, O. D.; Polimeridis, A. G.; Homer Reid, M. T.; Hsu, C. W.; DeLacy, B. G.; Joannopoulos, J. D.; Soljačić, M.; Johnson, S. G. Fundamental Limits to Optical Response in Absorptive Systems. *Opt. Express* **2016**, *24* (4), 3329. https://doi.org/10.1364/OE.24.003329.

(142) Raman, A.; Yu, Z.; Fan, S. Limits on Broadband Absorption Enhancement in the Presence of Multiple Lossy Materials. *arXiv:1812.10429 [physics]* **2018**.

(143) Alù, A.; Yaghjian, A. D.; Shore, R. A.; Silveirinha, M. G. Causality Relations in the Homogenization of Metamaterials. *Phys. Rev. B* **2011**, *84* (5), 054305. https://doi.org/10.1103/PhysRevB.84.054305.

(144) Jefimenko, O. D. Presenting Electromagnetic Theory in Accordance with the Principle of Causality. *Eur. J. Phys.* **2004**, *25* (2), 287–296. https://doi.org/10.1088/0143-0807/25/2/015.

(145) Srivastava, A. Causality and Passivity: From Electromagnetism and Network Theory to Metamaterials. *Mechanics of Materials* **2021**, *154*, 103710. https://doi.org/10.1016/j.mechmat.2020.103710.

(146) Byrnes, N.; Foreman, M. R. Symmetry Constraints for Vector Scattering and Transfer Matrices Containing Evanescent Components: Energy Conservation, Reciprocity, and Time Reversal. *Phys. Rev. Research* **2021**, *3* (1), 013129. https://doi.org/10.1103/PhysRevResearch.3.013129.

(147) Dogariu, A.; Schwartz, C. Conservation of Angular Momentum of Light in Single Scattering. *Opt. Express* **2006**, *14* (18), 8425. https://doi.org/10.1364/OE.14.008425.

(148) Bergman, D. J. Rigorous Bounds for the Complex Dielectric Constant of a Two-Component Composite. *Annals of Physics* **1982**, *138* (1), 78–114. https://doi.org/10.1016/0003-4916(82)90176-2.

(149) Milton, G. W. Bounds on the Complex Dielectric Constant of a Composite Material. *Applied Physics Letters* **1980**, *37* (3), 300–302. https://doi.org/10.1063/1.91895.
(150) Kern, C.; Miller, O. D.; Milton, G. W. On the Range of Complex Effective Permittivities of Isotropic Two-Phase Composites and Related Problems. arXiv June 6, 2020. http://arxiv.org/abs/2006.03830 (accessed 2023-09-04).
(151) Sihvola, A. Mixing Rules with Complex Dielectric Coefficients. *Subsurface Sensing Technologies and Applications* **2000**, *1* (4), 393–415. https://doi.org/10.1023/A:1026511515005.
(152) Markel, V. Introduction to the Maxwell Garnett Approximation: Tutorial. *Journal of the Optical Society of America. A Optics, Image Science, and Vision* **2016**, *33* (7), 1244–1256. https://doi.org/10.1364/JOSAA.33.001244.
(153) Sihvola, A. Electromagnetic Mixing Formulas and Applications. **1999**.
(154) Tsang, L.; Kong, J. A.; Shin, R. T. Theory of Microwave Remote Sensing, 1985. https://ntrs.nasa.gov/citations/19850058641 (accessed 2023-09-13).
(155) Berginc, G. Dyson Equation for Electromagnetic Scattering of Heterogeneous Media with Spatially Disordered Particles: Properties of the Effective Medium. *J. Phys.: Conf. Ser.* **2016**, *738*, 012023. https://doi.org/10.1088/1742-6596/738/1/012023.
(156) Soubret, A.; Berginc, G. Effective Dielectric Constant for a Random Medium. arXiv December 18, 2003. http://arxiv.org/abs/physics/0312117 (accessed 2023-09-13).
(157) Peigney, B. E.; Peigney, M. Bounds for Nonlinear Composite Conductors via the Translation Method. *Journal of the Mechanics and Physics of Solids* **2017**, *101*, 93–117. https://doi.org/10.1016/j.jmps.2017.01.017.
(158) Milton, G. W. *The Theory of Composites*; Cambridge Monographs on Applied and Computational Mathematics; Cambridge University Press: Cambridge, 2002. https://doi.org/10.1017/CBO9780511613357.
(159) Bohren, C. F. Applicability of Effective-Medium Theories to Problems of Scattering and Absorption by Nonhomogeneous Atmospheric Particles. *Journal of the Atmospheric Sciences* **1986**, *43* (5), 468–475. https://doi.org/10.1175/1520-0469(1986)043<0468:AOEMTT>2.0.CO;2.
(160) Bohren and Huffman - 2004 - Absorption and Scattering of Light by Small Partic.Pdf. https://onlinelibrary.wiley.com/doi/pdf/10.1002/9783527618156 (accessed 2018-11-18).
(161) Barrera, R. G.; García-Valenzuela, A. Coherent Reflectance in a System of Random Mie Scatterers and Its Relation to the Effective-Medium Approach. *J. Opt. Soc. Am. A* **2003**, *20* (2), 296. https://doi.org/10.1364/JOSAA.20.000296.
(162) Barabási, A. L.; Stanley, H. E. *Fractal Concepts in Surface Growth*; Cambridge University Press, 1995.
(163) Kant, R. Statistics of Approximately Self-Affine Fractals: Random Corrugated Surface and Time Series. *Physical Review E* **1996**, *53* (6), 5749–5763. https://doi.org/10.1103/PhysRevE.53.5749.
(164) Peitgen, H.-O.; Jürgens, H.; Saupe, D. *Chaos and Fractals*; Springer: New York, NY, 2004. https://doi.org/10.1007/b97624.

(165) N.T.Al-Rashid, S. STUDY BROWNIAN MOTION AND SHOWING THE TRAJECTORIES OF PARTICLES USING FRACTAL GEOMETRY. *JUAPS* **2012**, *1* (2), 75–89. https://doi.org/10.37652/juaps.2007.15270.

(166) Chakrabarty, R. K.; Moosmüller, H.; Arnott, W. P.; Garro, M. A.; Slowik, J. G.; Cross, E. S.; Han, J.-H.; Davidovits, P.; Onasch, T. B.; Worsnop, D. R. Light Scattering and Absorption by Fractal-like Carbonaceous Chain Aggregates: Comparison of Theories and Experiment. *Applied Optics* **2007**, *46* (28), 6990. https://doi.org/10.1364/AO.46.006990.

(167) Shalaev, V. M. *Nonlinear Optics of Random Media: Fractal Composites and Metal-Dielectric Films*; Springer Tracts in Modern Physics; Springer Berlin Heidelberg, 2007.

(168) Liu, L.; Mishchenko, M. I.; Patrick Arnott, W. A Study of Radiative Properties of Fractal Soot Aggregates Using the Superposition T-Matrix Method. *Journal of Quantitative Spectroscopy and Radiative Transfer* **2008**, *109* (15), 2656–2663. https://doi.org/10.1016/j.jqsrt.2008.05.001.

(169) Stockman, M. I.; Pandey, L. N.; Muratov, L. S.; George, T. F. Giant Fluctuations of Local Optical Fields in Fractal Clusters. *Phys. Rev. Lett.* **1994**, *72* (15), 2486–2489. https://doi.org/10.1103/PhysRevLett.72.2486.

(170) Markel, V. A.; Shalaev, V. M.; Poliakov, E. Y.; George, T. F. Fluctuations of Light Scattered by Fractal Clusters. *J. Opt. Soc. Am. A* **1997**, *14* (1), 60. https://doi.org/10.1364/JOSAA.14.000060.

(171) Liu, F.; Smallwood, G. J. Effect of Aggregation on the Absorption Cross-Section of Fractal Soot Aggregates and Its Impact on LII Modelling. *Journal of Quantitative Spectroscopy and Radiative Transfer* **2010**, *111* (2), 302–308. https://doi.org/10.1016/j.jqsrt.2009.06.017.

(172) Botet, R.; Rannou, P.; Cabane, M. Mean-Field Approximation of Mie Scattering by Fractal Aggregates of Identical Spheres. *Appl. Opt.* **1997**, *36* (33), 8791. https://doi.org/10.1364/AO.36.008791.

(173) Dick, V. V.; Solov'yov, I. A.; Solov'yov, A. V. Nanoparticles Dynamics on a Surface: Fractal Pattern Formation and Fragmentation. *Journal of Physics: Conference Series* **2010**, *248*, 012025. https://doi.org/10.1088/1742-6596/248/1/012025.

(174) Chen, X. *Nanoparticle Dynamics in the Non-Equilibrium to Equilibrium Transition Region of Plasma Reactors*; 2019.

(175) nternational Energy Agency. The Future of Cooling, 2018.

(176) Goetzler, W.; Guernsey, M.; Young, J.; Fujrman, J.; Abdelaziz, A. *The Future of Air Conditioning for Buildings*; DOE/EE--1394, 1420235; 2016; p DOE/EE--1394, 1420235. https://doi.org/10.2172/1420235.

(177) *The future of Air Conditioning World Demand & Warming Temperature Increases*. https://www.enerdata.net/publications/executive-briefing/the-future-air-conditioning-global-demand.html (accessed 2020-02-10).

(178) Energy Information Administration. *Residential Energy Consumption Survey*. https://www.eia.gov/consumption/residential/ (accessed 2019-11-01).

(179) Santamouris, M.; Kolokotsa, D. Passive Cooling Dissipation Techniques for Buildings and Other Structures: The State of the Art. *Energy and Buildings* **2013**, *57*, 74–94. https://doi.org/10.1016/j.enbuild.2012.11.002.

(180) Seyboth, K.; Beurskens, L.; Langniss, O.; Sims, R. E. H. Recognising the Potential for Renewable Energy Heating and Cooling. *Energy Policy* **2008**, *36* (7), 2460–2463. https://doi.org/10.1016/j.enpol.2008.02.046.

(181) Fensholt, R.; Horion, S.; Tagesson, T.; Ehammer, A.; Grogan, K.; Tian, F.; Huber, S.; Verbesselt, J.; Prince, S. D.; Tucker, C. J.; Rasmussen, K. Assessment of Vegetation Trends in Drylands from Time Series of Earth Observation Data. In *Remote Sensing Time Series: Revealing Land Surface Dynamics*; Kuenzer, C., Dech, S., Wagner, W., Eds.; Remote Sensing and Digital Image Processing; Springer International Publishing: Cham, 2015; pp 159–182. https://doi.org/10.1007/978-3-319-15967-6_8.

(182) Zhai, Y.; Ma, Y.; David, S. N.; Zhao, D.; Lou, R.; Tan, G.; Yang, R.; Yin, X. Scalable-Manufactured Randomized Glass-Polymer Hybrid Metamaterial for Daytime Radiative Cooling. *Science* **2017**, *355* (6329), 1062–1066. https://doi.org/10.1126/science.aai7899.

(183) Kou, J.; Jurado, Z.; Chen, Z.; Fan, S.; Minnich, A. J. Daytime Radiative Cooling Using Near-Black Infrared Emitters. *ACS Photonics* **2017**, *4* (3), 626–630. https://doi.org/10.1021/acsphotonics.6b00991.

(184) Raman, A. P.; Anoma, M. A.; Zhu, L.; Rephaeli, E.; Fan, S. Passive Radiative Cooling below Ambient Air Temperature under Direct Sunlight. *Nature* **2014**, *515*, 540.

(185) Rephaeli, E.; Raman, A.; Fan, S. Ultrabroadband Photonic Structures To Achieve High-Performance Daytime Radiative Cooling. *Nano Lett.* **2013**, *13* (4), 1457–1461. https://doi.org/10.1021/nl4004283.

(186) Chen, Z.; Zhu, L.; Raman, A.; Fan, S. Radiative Cooling to Deep Sub-Freezing Temperatures through a 24-h Day–Night Cycle. *Nature Communications* **2016**, *7*, 13729. https://doi.org/10.1038/ncomms13729.

(187) Hossain, M. M.; Jia, B.; Gu, M. A Metamaterial Emitter for Highly Efficient Radiative Cooling. *Advanced Optical Materials* **2015**, *3* (8), 1047–1051. https://doi.org/10.1002/adom.201500119.

(188) Zhu, L.; Raman, A.; Fan, S. Color-Preserving Daytime Radiative Cooling. *Applied Physics Letters* **2013**, *103* (22), 223902. https://doi.org/10.1063/1.4835995.

(189) Huang, Z.; Ruan, X. Nanoparticle Embedded Double-Layer Coating for Daytime Radiative Cooling. *International Journal of Heat and Mass Transfer* **2017**, *104*, 890–896. https://doi.org/10.1016/j.ijheatmasstransfer.2016.08.009.

(190) Zhu, L.; Raman, A.; Wang, K. X.; Anoma, M. A.; Fan, S. Radiative Cooling of Solar Cells. *Optica, OPTICA* **2014**, *1* (1), 32–38. https://doi.org/10.1364/OPTICA.1.000032.

(191) Ao, X.; Hu, M.; Zhao, B.; Chen, N.; Pei, G.; Zou, C. Preliminary Experimental Study of a Specular and a Diffuse Surface for Daytime Radiative Cooling. *Solar Energy Materials and Solar Cells* **2019**, *191*, 290–296. https://doi.org/10.1016/j.solmat.2018.11.032.

(192) Bao, H.; Yan, C.; Wang, B.; Fang, X.; Zhao, C. Y.; Ruan, X. Double-Layer Nanoparticle-Based Coatings for Efficient Terrestrial Radiative Cooling. *Solar Energy Materials and Solar Cells* **2017**, *168*, 78–84. https://doi.org/10.1016/j.solmat.2017.04.020.

(193) Gentle, A. R.; Smith, G. B. Radiative Heat Pumping from the Earth Using Surface Phonon Resonant Nanoparticles. *Nano Lett.* **2010**, *10* (2), 373–379. https://doi.org/10.1021/nl903271d.

(194) Chan, H.-Y.; Riffat, S. B.; Zhu, J. Review of Passive Solar Heating and Cooling Technologies. *Renewable and Sustainable Energy Reviews* **2010**, *14* (2), 781–789. https://doi.org/10.1016/j.rser.2009.10.030.

(195) Kamal, M. A. An Overview of Passive Cooling Techniques in Buildings: Design Concepts and Architectural Interventions. *Acta Technica Napocensis: Civil Engineering & Architecture* **2012**, *55*, 84–97.

(196) Kortshagen, U. Nonthermal Plasma Synthesis of Semiconductor Nanocrystals. *J. Phys. D: Appl. Phys.* **2009**, *42* (11), 113001. https://doi.org/10.1088/0022-3727/42/11/113001.

(197) Mangolini, L.; Thimsen, E.; Kortshagen, U. High-Yield Plasma Synthesis of Luminescent Silicon Nanocrystals. *Nano Lett.* **2005**, *5* (4), 655–659. https://doi.org/10.1021/nl050066y.

(198) Kendrick, J.; Burnett, A. D. PDielec: The Calculation of Infrared and Terahertz Absorption for Powdered Crystals. *J Comput Chem* **2016**, *37* (16), 1491–1504. https://doi.org/10.1002/jcc.24344.

(199) Xi, J.-Q.; Schubert, M. F.; Kim, J. K.; Schubert, E. F.; Chen, M.; Lin, S.-Y.; Liu, W.; Smart, J. A. Optical Thin-Film Materials with Low Refractive Index for Broadband Elimination of Fresnel Reflection. *Nature Photonics* **2007**, *1* (3), 176–179. https://doi.org/10.1038/nphoton.2007.26.

(200) Yeh, P.; Yariv, A.; Hong, C.-S. Electromagnetic Propagation in Periodic Stratified Media I General Theory*. *Journal of the Optical Society of America* **1977**, *67* (4), 423. https://doi.org/10.1364/JOSA.67.000423.

(201) Zaitsu, S.; Jitsuno, T.; Nakatsuka, M.; Yamanaka, T.; Motokoshi, S. Optical Thin Films Consisting of Nanoscale Laminated Layers. *Applied Physics Letters* **2002**, *80* (14), 2442–2444. https://doi.org/10.1063/1.1467622.

(202) Molesky, S.; Dewalt, C. J.; Jacob, Z. High Temperature Epsilon-near-Zero and Epsilon-near-Pole Metamaterial Emitters for Thermophotovoltaics. **2012**, 15.

(203) Hossain, Md. M.; Gu, M. Radiative Cooling: Principles, Progress, and Potentials. *Adv Sci (Weinh)* **2016**, *3* (7). https://doi.org/10.1002/advs.201500360.

(204) Goya, G. F. Handling the Particle Size and Distribution of Fe3O4 Nanoparticles through Ball Milling. *Solid State Communications* **2004**, *130* (12), 783–787. https://doi.org/10.1016/j.ssc.2004.04.012.

(205) U.S. Government Printing Office. *U.S. Standard Atmosphere*; Washington, D.C., 1976. https://www.ngdc.noaa.gov/stp/space-weather/online-publications/miscellaneous/us-standard-atmosphere-1976/us-standard-atmosphere_st76-1562_noaa.pdf (accessed 2023-09-02).

(206) Granqvist, C. G.; Hjortsberg, A. Radiative Cooling to Low Temperatures: General Considerations and Application to Selectively Emitting SiO Films. *Journal of Applied Physics* **1981**, *52* (6), 4205–4220. https://doi.org/10.1063/1.329270.

(207) Wright, J. C. Accuracy of LOWTRAN 7 and MODTRAN in the 2.0-5.5-T1m Region. 5.

(208) Wright, J. Evaluation of LOWTRAN and MODTRAN for Use over High Zenith Angle/Long Path Length Viewing. 188.
(209) Abreu, L. W.; Anderson, G. P. *The MODTRAN 2/3 Report and LOWTRAN 7 MODEL*. https://web.gps.caltech.edu/~vijay/pdf/modrept.pdf (accessed 2023-09-02).
(210) Launer, P.; Arkles, B. Infrared Analysis of Organsilicon Compounds: Spectra-Structure Correlations. In *Reprinted from Silicone Compounds Register and Review*; 2008; pp 223–226.
(211) Smith, A. L. Infrared Spectra-Structure Correlations for Organosilicon Compounds. *Spectrochimica Acta* **1960**, *16* (1), 87–105. https://doi.org/10.1016/0371-1951(60)80074-4.
(212) Jayes, L.; Hard, A. P.; Séné, C.; Parker, S. F.; Jayasooriya, U. A. Vibrational Spectroscopic Analysis of Silicones: A Fourier Transform-Raman and Inelastic Neutron Scattering Investigation. *Anal. Chem.* **2003**, *75* (4), 742–746. https://doi.org/10.1021/ac026012f.
(213) *The Infrared Spectra of Complex Molecules: Volume Two Advances in Infrared Group Frequencies | SpringerLink*. https://link.springer.com/book/10.1007/978-94-011-6520-4 (accessed 2023-09-02).
(214) Shivola, A. H. Self-Consistency Aspects of Dielectric Mixing Theories. *IEEE Transactions on Geoscience and Remote Sensing* **1989**, *27* (4), 403–415. https://doi.org/10.1109/36.29560.
(215) Malitson, I. H. Interspecimen Comparison of the Refractive Index of Fused Silica*,†. *J. Opt. Soc. Am., JOSA* **1965**, *55* (10), 1205–1209. https://doi.org/10.1364/JOSA.55.001205.
(216) Chýlek, P.; Srivastava, V.; Pinnick, R. G.; Wang, R. T. Scattering of Electromagnetic Waves by Composite Spherical Particles: Experiment and Effective Medium Approximations. *Appl. Opt.* **1988**, *27* (12), 2396. https://doi.org/10.1364/AO.27.002396.
(217) Stroud, D. The Effective Medium Approximations: Some Recent Developments. *Superlattices and Microstructures* **1998**, *23* (3), 567–573. https://doi.org/10.1006/spmi.1997.0524.
(218) Karkkainen, K. K.; Sihvola, A. H.; Nikoskinen, K. I. Effective Permittivity of Mixtures: Numerical Validation by the FDTD Method. *IEEE Transactions on Geoscience and Remote Sensing* **2000**, *38* (3), 1303–1308. https://doi.org/10.1109/36.843023.
(219) Voshchinnikov, N. V.; Videen, G.; Henning, T. Effective Medium Theories for Irregular Fluffy Structures: Aggregation of Small Particles. *Appl. Opt.* **2007**, *46* (19), 4065. https://doi.org/10.1364/AO.46.004065.
(220) Bossa, J.-B.; Isokoski, K.; Paardekooper, D. M.; Bonnin, M.; van der Linden, E. P.; Triemstra, T.; Cazaux, S.; Tielens, A. G. G. M.; Linnartz, H. Porosity Measurements of Interstellar Ice Mixtures Using Optical Laser Interference and Extended Effective Medium Approximations. *A&A* **2014**, *561*, A136. https://doi.org/10.1051/0004-6361/201322549.
(221) Hülser, T.; Schnurre, S. M.; Wiggers, H.; Schulz, C. Gas-Phase Synthesis of Nanoscale Silicon as an Economical Route towards Sustainable Energy Technology. *KONA Powder and Particle Journal* **2011**, *29*, 191–207. https://doi.org/10.14356/kona.2011021.

(222) Rao, N.; Girshick, S.; Heberlein, J.; McMurry, P.; Jones, S.; Hansen, D.; Micheel, B. Nanoparticle Formation Using a Plasma Expansion Process. *Plasma Chem Plasma Process* **1995**, *15* (4), 581–606. https://doi.org/10.1007/BF01447062.

(223) Shigeta, M.; Murphy, A. B. Thermal Plasmas for Nanofabrication. *J. Phys. D: Appl. Phys.* **2011**, *44* (17), 174025. https://doi.org/10.1088/0022-3727/44/17/174025.

(224) Gresback, R.; Holman, Z.; Kortshagen, U. Nonthermal Plasma Synthesis of Size-Controlled, Monodisperse, Freestanding Germanium Nanocrystals. *Applied Physics Letters* **2007**, *91* (9), 093119. https://doi.org/10.1063/1.2778356.

(225) Donev, A.; Cisse, I.; Sachs, D.; Variano, E. A.; al, et. Improving the Density of Jammed Disordered Packings Using Ellipsoids. *Science; Washington* **2004**, *303* (5660), 990–993.

(226) *Porous Media Fluid Transport and Pore Structure - 1st Edition*. https://www.elsevier.com/books/porous-media-fluid-transport-and-pore-structure/dullien/978-0-12-223650-1 (accessed 2019-09-18).

(227) Varner, J. F.; Eldabagh, N.; Volta, D.; Eldabagh, R.; Foley, J. WPTherml: A Python Package for the Design of Materials for Harnessing Heat. ChemRxiv June 28, 2019. https://doi.org/10.26434/chemrxiv.8341046.v1.

(228) Byrnes, S. J. Multilayer Optical Calculations. *arXiv:1603.02720 [physics]* **2016**.

(229) *Users Guide to LOWTRAN 7*. https://apps.dtic.mil/sti/citations/ADA206773 (accessed 2023-09-02).

(230) Choy, T. C. *Effective Medium Theory: Principles and Applications*; International series of monographs on physics; Clarendon Press, 1999.

(231) Ziolkowski, R. W. Metamaterials: The Early Years in the USA. *EPJ Applied Metamaterials* **2014**, *1*, 5. https://doi.org/10.1051/epjam/2014004.

(232) Hsu, C. W.; Zhen, B.; Qiu, W.; Shapira, O.; DeLacy, B. G.; Joannopoulos, J. D.; Soljačić, M. Transparent Displays Enabled by Resonant Nanoparticle Scattering. *Nat Commun* **2014**, *5* (1), 3152. https://doi.org/10.1038/ncomms4152.

(233) Capretti, A.; Lesage, A.; Gregorkiewicz, T. Integrating Quantum Dots and Dielectric Mie Resonators: A Hierarchical Metamaterial Inheriting the Best of Both. *ACS Photonics* **2017**, *4* (9), 2187–2196. https://doi.org/10.1021/acsphotonics.7b00320.

(234) Kim, H.; Chang, J. H. Increased Light Penetration Due to Ultrasound-Induced Air Bubbles in Optical Scattering Media. *Sci Rep* **2017**, *7* (1), 16105. https://doi.org/10.1038/s41598-017-16444-9.

(235) KIK, P. G.; BRONGERSMA, M. L. SURFACE PLASMON NANOPHOTONICS. In *Surface Plasmon Nanophotonics*; Brongersma, M. L., Kik, P. G., Eds.; Springer Series in Optical Sciences; Springer Netherlands: Dordrecht, 2007; pp 1–9. https://doi.org/10.1007/978-1-4020-4333-8_1.

(236) Odom, T. W.; Schatz, G. C. Introduction to Plasmonics. *Chem. Rev.* **2011**, *111* (6), 3667–3668. https://doi.org/10.1021/cr2001349.

(237) Kamat, P. V.; Hartland, G. V. Plasmons for Energy Conversion. *ACS Energy Lett.* **2018**, *3* (6), 1467–1469. https://doi.org/10.1021/acsenergylett.8b00721.

(238) Butt, M. A.; Khonina, S. N.; Kazanskiy, N. L. Plasmonics: A Necessity in the Field of Sensing-A Review (Invited). *Fiber and Integrated Optics* **2021**, *40* (1), 14–47. https://doi.org/10.1080/01468030.2021.1902590.

(239) A Small World Full of Opportunities. *Nature Mater* **2010**, *9* (3), 181–181. https://doi.org/10.1038/nmat2720.

(240) Stockman, M. I.; Kneipp, K.; Bozhevolnyi, S. I.; Saha, S.; Dutta, A.; Ndukaife, J.; Kinsey, N.; Reddy, H.; Guler, U.; Shalaev, V. M.; Boltasseva, A.; Gholipour, B.; Krishnamoorthy, H. N. S.; MacDonald, K. F.; Soci, C.; Zheludev, N. I.; Savinov, V.; Singh, R.; Groß, P.; Lienau, C.; Vadai, M.; Solomon, M. L.; Barton, D. R.; Lawrence, M.; Dionne, J. A.; Boriskina, S. V.; Esteban, R.; Aizpurua, J.; Zhang, X.; Yang, S.; Wang, D.; Wang, W.; Odom, T. W.; Accanto, N.; Roque, P. M. de; Hancu, I. M.; Piatkowski, L.; Hulst, N. F. van; Kling, M. F. Roadmap on Plasmonics. *J. Opt.* **2018**, *20* (4), 043001. https://doi.org/10.1088/2040-8986/aaa114.

(241) Kuznetsov, A. I.; Miroshnichenko, A. E.; Fu, Y. H.; Zhang, J.; Luk'yanchuk, B. Magnetic Light. *Sci Rep* **2012**, *2* (1), 492. https://doi.org/10.1038/srep00492.

(242) Babicheva, V. E.; Moloney, J. V. Lattice Effect Influence on the Electric and Magnetic Dipole Resonance Overlap in a Disk Array. *Nanophotonics* **2018**, *7* (10), 1663–1668. https://doi.org/10.1515/nanoph-2018-0107.

(243) Bakker, R. M.; Permyakov, D.; Yu, Y. F.; Markovich, D.; Paniagua-Domínguez, R.; Gonzaga, L.; Samusev, A.; Kivshar, Y.; Luk'yanchuk, B.; Kuznetsov, A. I. Magnetic and Electric Hotspots with Silicon Nanodimers. *Nano Lett.* **2015**, *15* (3), 2137–2142. https://doi.org/10.1021/acs.nanolett.5b00128.

(244) Kruk, S.; Kivshar, Y. Functional Meta-Optics and Nanophotonics Governed by Mie Resonances. *ACS Photonics* **2017**, *4* (11), 2638–2649. https://doi.org/10.1021/acsphotonics.7b01038.

(245) Sautter, J.; Staude, I.; Decker, M.; Rusak, E.; Neshev, D. N.; Brener, I.; Kivshar, Y. S. Active Tuning of All-Dielectric Metasurfaces. *ACS Nano* **2015**, *9* (4), 4308–4315. https://doi.org/10.1021/acsnano.5b00723.

(246) Kivshar, Y.; Miroshnichenko, A. Optical Magnetic Responses and Subwavelength Localization of Light, Driven by Mie Resonances in High-Index Nanoparticles, Could Spur New, Breakthrough Applications for Nanoantennas, Nanolasers, Highly Efficient Metasurfaces and Ultrafast Metadevices. 8.

(247) Moitra, P.; Slovick, B. A.; li, W.; Kravchencko, I. I.; Briggs, D. P.; Krishnamurthy, S.; Valentine, J. Large-Scale All-Dielectric Metamaterial Perfect Reflectors. *ACS Photonics* **2015**, *2* (6), 692–698. https://doi.org/10.1021/acsphotonics.5b00148.

(248) Yang, C.-Y.; Yang, J.-H.; Yang, Z.-Y.; Zhou, Z.-X.; Sun, M.-G.; Babicheva, V. E.; Chen, K.-P. Nonradiating Silicon Nanoantenna Metasurfaces as Narrowband Absorbers. *ACS Photonics* **2018**, *5* (7), 2596–2601. https://doi.org/10.1021/acsphotonics.7b01186.

(249) Kuznetsov, A. I.; Miroshnichenko, A. E.; Fu, Y. H.; Zhang, J.; Luk'yanchuk, B. Magnetic Light. *Sci Rep* **2012**, *2* (1), 492. https://doi.org/10.1038/srep00492.

(250) Person, S.; Jain, M.; Lapin, Z.; Sáenz, J. J.; Wicks, G.; Novotny, L. Demonstration of Zero Optical Backscattering from Single Nanoparticles. *Nano Lett.* **2013**, *13* (4), 1806–1809. https://doi.org/10.1021/nl4005018.

(251) Spinelli, P.; Verschuuren, M. A.; Polman, A. Broadband Omnidirectional Antireflection Coating Based on Subwavelength Surface Mie Resonators. *Nat Commun* **2012**, *3* (1), 692. https://doi.org/10.1038/ncomms1691.

(252) Fu, Y. H.; Kuznetsov, A. I.; Miroshnichenko, A. E.; Yu, Y. F.; Luk'yanchuk, B. Directional Visible Light Scattering by Silicon Nanoparticles. *Nat Commun* **2013**, *4* (1), 1527. https://doi.org/10.1038/ncomms2538.

(253) Evlyukhin, A. B.; Novikov, S. M.; Zywietz, U.; Eriksen, R. L.; Reinhardt, C.; Bozhevolnyi, S. I.; Chichkov, B. N. Demonstration of Magnetic Dipole Resonances of Dielectric Nanospheres in the Visible Region. *Nano Letters* **2012**, *12* (7), 3749–3755. https://doi.org/10.1021/nl301594s.

(254) Babicheva, V. E.; Evlyukhin, A. B. Resonant Lattice Kerker Effect in Metasurfaces With Electric and Magnetic Optical Responses. *Laser & Photonics Reviews* **2017**, *11* (6), 1700132. https://doi.org/10.1002/lpor.201700132.

(255) García-Etxarri, A.; Gómez-Medina, R.; Froufe-Pérez, L. S.; López, C.; Chantada, L.; Scheffold, F.; Aizpurua, J.; Nieto-Vesperinas, M.; Sáenz, J. J. Strong Magnetic Response of Submicron Silicon Particles in the Infrared. *Opt. Express* **2011**, *19* (6), 4815. https://doi.org/10.1364/OE.19.004815.

(256) Ghadarghadr, S.; Mosallaei, H. Coupled Dielectric Nanoparticles Manipulating Metamaterials Optical Characteristics. *IEEE Transactions on Nanotechnology* **2009**, *8* (5), 582–594. https://doi.org/10.1109/TNANO.2009.2013619.

(257) Hopkins, B.; Filonov, D. S.; Miroshnichenko, A. E.; Monticone, F.; Alù, A.; Kivshar, Y. S. Interplay of Magnetic Responses in All-Dielectric Oligomers To Realize Magnetic Fano Resonances. *ACS Photonics* **2015**, *2* (6), 724–729. https://doi.org/10.1021/acsphotonics.5b00082.

(258) Miroshnichenko, A. E.; Kivshar, Y. S. Fano Resonances in All-Dielectric Oligomers. *Nano Lett.* **2012**, *12* (12), 6459–6463. https://doi.org/10.1021/nl303927q.

(259) Wray, P. R.; Atwater, H. A. Light–Matter Interactions in Films of Randomly Distributed Unidirectionally Scattering Dielectric Nanoparticles. *ACS Photonics* **2020**, *7* (8), 2105–2114. https://doi.org/10.1021/acsphotonics.0c00545.

(260) Zywietz, U.; Schmidt, M. K.; Evlyukhin, A. B.; Reinhardt, C.; Aizpurua, J.; Chichkov, B. N. Electromagnetic Resonances of Silicon Nanoparticle Dimers in the Visible. *ACS Photonics* **2015**, *2* (7), 913–920. https://doi.org/10.1021/acsphotonics.5b00105.

(261) Cross, G. H. Fundamental Limit to the Use of Effective Medium Theories in Optics. *Opt. Lett., OL* **2013**, *38* (16), 3057–3060. https://doi.org/10.1364/OL.38.003057.

(262) Niklasson, G. A.; Granqvist, C. G.; Hunderi, O. Effective Medium Models for the Optical Properties of Inhomogeneous Materials. *Applied Optics* **1981**, *20* (1), 26. https://doi.org/10.1364/AO.20.000026.

(263) Fazio, B.; Artoni, P.; Antonia Iatì, M.; D'Andrea, C.; Lo Faro, M. J.; Del Sorbo, S.; Pirotta, S.; Giuseppe Gucciardi, P.; Musumeci, P.; Salvatore Vasi, C.; Saija, R.; Galli, M.; Priolo, F.; Irrera, A. Strongly Enhanced Light Trapping in a Two-Dimensional Silicon Nanowire Random Fractal Array. *Light Sci Appl* **2016**, *5* (4), e16062–e16062. https://doi.org/10.1038/lsa.2016.62.

(264) Ball, P. Fractal Standstill. *Nature Mater* **2010**, *9* (12), 964–964. https://doi.org/10.1038/nmat2910.

(265) Kortshagen, U. R.; Sankaran, R. M.; Pereira, R. N.; Girshick, S. L.; Wu, J. J.; Aydil, E. S. Nonthermal Plasma Synthesis of Nanocrystals: Fundamental Principles, Materials, and Applications. *Chem. Rev.* **2016**, *116* (18), 11061–11127. https://doi.org/10.1021/acs.chemrev.6b00039.

(266) Kramer, N. J.; Anthony, R. J.; Mamunuru, M.; Aydil, E. S.; Kortshagen, U. R. Plasma-Induced Crystallization of Silicon Nanoparticles. *J. Phys. D: Appl. Phys.* **2014**, *47* (7), 075202. https://doi.org/10.1088/0022-3727/47/7/075202.

(267) Alvarez Barragan, A.; Ilawe, N. V.; Zhong, L.; Wong, B. M.; Mangolini, L. A Non-Thermal Plasma Route to Plasmonic TiN Nanoparticles. *J. Phys. Chem. C* **2017**, *121* (4), 2316–2322. https://doi.org/10.1021/acs.jpcc.6b08910.

(268) Ho, A.; Mandal, R.; Lunt, R. R.; Anthony, R. J. Nonthermal Plasma Synthesis of Gallium Nitride Nanoparticles: Implications for Optical and Electronic Applications. *ACS Appl. Nano Mater.* **2021**, *4* (6), 5624–5629. https://doi.org/10.1021/acsanm.1c00544.

(269) Exarhos, S.; Alvarez-Barragan, A.; Aytan, E.; Balandin, A. A.; Mangolini, L. Plasmonic Core–Shell Zirconium Nitride–Silicon Oxynitride Nanoparticles. *ACS Energy Lett.* **2018**, *3* (10), 2349–2356. https://doi.org/10.1021/acsenergylett.8b01478.

(270) Choi, S. J.; Kushner, M. J. A Particle-in-Cell Simulation of Dust Charging and Shielding in Low Pressure Glow Discharges. *IEEE Trans. Plasma Sci.* **1994**, *22* (2), 138–150. https://doi.org/10.1109/27.279017.

(271) Goree, J. Ion Trapping by a Charged Dust Grain in a Plasma. *Phys. Rev. Lett.* **1992**, *69* (2), 277–280. https://doi.org/10.1103/PhysRevLett.69.277.

(272) Matsoukas, T.; Russell, M. Particle Charging in Low-pressure Plasmas. *Journal of Applied Physics* **1995**, *77* (9), 4285–4292. https://doi.org/10.1063/1.359451.

(273) Kortshagen, U.; Bhandarkar, U. Modeling of Particulate Coagulation in Low Pressure Plasmas. *Phys. Rev. E* **1999**, *60* (1), 887–898. https://doi.org/10.1103/PhysRevE.60.887.

(274) Schweigert, V. A.; Schweigert, I. V. Coagulation in a Low-Temperature Plasma. *J. Phys. D: Appl. Phys.* **1996**, *29* (3), 655–659. https://doi.org/10.1088/0022-3727/29/3/026.

(275) Rao, N. P.; Lee, H. J.; Kelkar, M.; Hansen, D. J.; Heberlein, J. V. R.; McMurry, P. H.; Girshick, S. L. Nanostructured Materials Production by Hypersonic Plasma Particle Deposition. *Nanostructured Materials* **1997**, *9* (1–8), 129–132. https://doi.org/10.1016/S0965-9773(97)00035-4.

(276) Holman, Z. C.; Kortshagen, U. R. A Flexible Method for Depositing Dense Nanocrystal Thin Films: Impaction of Germanium Nanocrystals. *Nanotechnology* **2010**, *21* (33), 335302. https://doi.org/10.1088/0957-4484/21/33/335302.

(277) Firth, P.; Holman, Z. C. Aerosol Impaction-Driven Assembly System for the Production of Uniform Nanoparticle Thin Films with Independently Tunable Thickness and Porosity. *ACS Appl. Nano Mater.* **2018**, *1* (8), 4351–4357. https://doi.org/10.1021/acsanm.8b01334.

(278) Bapat, A.; Anderson, C.; Perrey, C. R.; Carter, C. B.; Campbell, S. A.; Kortshagen, U. Plasma Synthesis of Single-Crystal Silicon Nanoparticles for Novel Electronic Device Applications. *Plasma Phys. Control. Fusion* **2004**, *46* (12B), B97–B109. https://doi.org/10.1088/0741-3335/46/12B/009.

(279) Farias, T. L.; Köylü, Ü. Ö.; Carvalho, M. G. Range of Validity of the Rayleigh–Debye–Gans Theory for Optics of Fractal Aggregates. *Applied Optics* **1996**, *35* (33), 6560. https://doi.org/10.1364/AO.35.006560.

(280) Perrin, J.-M.; Lamy, P. L. On the Validity of Effective-Medium Theories in the Case of Light Extinction by Inhomogeneous Dust Particles. *The Astrophysical Journal* **1990**, *364*, 146. https://doi.org/10.1086/169395.

(281) Videen, G.; Chýlek, P. Scattering by a Composite Sphere with an Absorbing Inclusion and Effective Medium Approximations. *Optics Communications* **1998**, *158* (1), 1–6. https://doi.org/10.1016/S0030-4018(98)00557-4.

(282) Wang, G.; Sorensen, C. M. Experimental Test of the Rayleigh-Debye-Gans Theory for Light Scattering by Fractal Aggregates. *Applied Optics* **2002**, *41* (22), 4645. https://doi.org/10.1364/AO.41.004645.

(283) Smith, D. R.; Vier, D. C.; Koschny, Th.; Soukoulis, C. M. Electromagnetic Parameter Retrieval from Inhomogeneous Metamaterials. *Phys. Rev. E* **2005**, *71* (3), 036617. https://doi.org/10.1103/PhysRevE.71.036617.

(284) Barrera, R. G.; García-Valenzuela, A. Coherent Reflectance in a System of Random Mie Scatterers and Its Relation to the Effective-Medium Approach. *J. Opt. Soc. Am. A* **2003**, *20* (2), 296. https://doi.org/10.1364/JOSAA.20.000296.

(285) Bapat, A.; Gatti, M.; Ding, Y.-P.; Campbell, S. A.; Kortshagen, U. A Plasma Process for the Synthesis of Cubic-Shaped Silicon Nanocrystals for Nanoelectronic Devices. *J. Phys. D: Appl. Phys.* **2007**, *40* (8), 2247–2257. https://doi.org/10.1088/0022-3727/40/8/S03.

(286) Heinson, W. R. Simulation Studies on Shape and Growth Kinetics for Fractal Aggregates in Aerosol and Collodial Systems. *Doctoral dissertation* **2008**, 126.

(287) Doicu, A.; Wriedt, T.; Eremin, Y. A. *Light Scattering by Systems of Particles: Null-Field Method with Discrete Sources: Theory and Programs*; Springer Series in Optical Sciences; Springer-Verlag: Berlin Heidelberg, 2006. https://doi.org/10.1007/978-3-540-33697-6.

(288) Mackowski, D. The Extension of Mie Theory to Multiple Spheres. In *The Mie Theory: Basics and Applications*; Hergert, W., Wriedt, T., Eds.; Springer Series in Optical Sciences; Springer: Berlin, Heidelberg, 2012; pp 223–256. https://doi.org/10.1007/978-3-642-28738-1_8.

(289) T-Matrix Theory of Electromagnetic Scattering by Partciles and Its Applications: A Comprehensive Reference Database. *Journal of Quantitative Spectroscopy and Radiative Transfer* **2004**, *88* (1–3), 357–406. https://doi.org/10.1016/j.jqsrt.2004.05.002.

(290) Kahnert, F. M. Numerical Methods in Electromagnetic Scattering Theory. *Journal of Quantitative Spectroscopy and Radiative Transfer* **2003**, *79–80*, 775–824. https://doi.org/10.1016/S0022-4073(02)00321-7.

(291) Waterman, P. C. Matrix Formulation of Electromagnetic Scattering. *Proceedings of the IEEE* **1965**, *53* (8), 805–812. https://doi.org/10.1109/PROC.1965.4058.

(292) Mühlig, S.; Menzel, C.; Rockstuhl, C.; Lederer, F. Multipole Analysis of Meta-Atoms. *Metamaterials* **2011**, *5* (2–3), 64–73. https://doi.org/10.1016/j.metmat.2011.03.003.

(293) Cruzan, O. R. Translational Addition Theorems for Spherical Vector Wave Functions. *Quarterly of Applied Mathematics* **1962**, *20* (1), 33–40.

(294) Yuffa, A. J.; Scales, J. A. Object-Oriented Electrodynamic S-Matrix Code with Modern Applications. *Journal of Computational Physics* **2012**, *231* (14), 4823–4835. https://doi.org/10.1016/j.jcp.2012.03.018.

(295) Mackowski, D. W. Calculation of Total Cross Sections of Multiple-Sphere Clusters. *J. Opt. Soc. Am. A* **1994**, *11* (11), 2851. https://doi.org/10.1364/JOSAA.11.002851.
(296) Xiong, Z.; Lanham, S.; Husmann, E.; Nelson, G.; Eslamisaray, M. A.; Polito, J.; Liu, Y.; Goree, J.; Thimsen, E.; Kushner, M. J.; Kortshagen, U. R. Particle Trapping, Size-Filtering, and Focusing in the Nonthermal Plasma Synthesis of Sub-10 Nanometer Particles. *J. Phys. D: Appl. Phys.* **2022**, *55* (23), 235202. https://doi.org/10.1088/1361-6463/ac57de.
(297) Yu, P. Y.; Cardona, M. *Fundamentals of Semiconductors*; Graduate Texts in Physics; Springer Berlin Heidelberg: Berlin, Heidelberg, 2010. https://doi.org/10.1007/978-3-642-00710-1.
(298) Baranov, D. G.; Zuev, D. A.; Lepeshov, S. I.; Kotov, O. V.; Krasnok, A. E.; Evlyukhin, A. B.; Chichkov, B. N. All-Dielectric Nanophotonics: The Quest for Better Materials and Fabrication Techniques. *Optica* **2017**, *4* (7), 814. https://doi.org/10.1364/OPTICA.4.000814.
(299) Khurgin, J. B. Expanding the Photonic Palette: Exploring High Index Materials. *ACS Photonics* **2022**, *9* (3), 743–751. https://doi.org/10.1021/acsphotonics.1c01834.
(300) Kerker, M.; Wang, D.-S.; Giles, C. L. Electromagnetic Scattering by Magnetic Spheres. *J. Opt. Soc. Am.* **1983**, *73* (6), 765. https://doi.org/10.1364/JOSA.73.000765.
(301) Liu, W.; Kivshar, Y. S. Generalized Kerker Effects in Nanophotonics and Meta-Optics [Invited]. *Opt. Express* **2018**, *26* (10), 13085. https://doi.org/10.1364/OE.26.013085.
(302) Hasan, M. R.; Hellesø, O. G. Dielectric Optical Nanoantennas. *Nanotechnology* **2021**, *32* (20), 202001. https://doi.org/10.1088/1361-6528/abdceb.
(303) Kivshar, Y. All-Dielectric Meta-Optics and Non-Linear Nanophotonics. *National Science Review* **2018**, *5* (2), 144–158. https://doi.org/10.1093/nsr/nwy017.
(304) Jahani, S.; Jacob, Z. All-Dielectric Metamaterials. *Nature Nanotech* **2016**, *11* (1), 23–36. https://doi.org/10.1038/nnano.2015.304.
(305) Khurgin, J. B. How to Deal with the Loss in Plasmonics and Metamaterials. *Nature Nanotech* **2015**, *10* (1), 2–6. https://doi.org/10.1038/nnano.2014.310.
(306) Boriskina, S. V.; Cooper, T. A.; Zeng, L.; Ni, G.; Tong, J. K.; Tsurimaki, Y.; Huang, Y.; Meroueh, L.; Mahan, G.; Chen, G. Losses in Plasmonics: From Mitigating Energy Dissipation to Embracing Loss-Enabled Functionalities. *Adv. Opt. Photon.* **2017**, *9* (4), 775. https://doi.org/10.1364/AOP.9.000775.
(307) West, P. R.; Ishii, S.; Naik, G. V.; Emani, N. K.; Shalaev, V. M.; Boltasseva, A. Searching for Better Plasmonic Materials. *Laser & Photon. Rev.* **2010**, *4* (6), 795–808. https://doi.org/10.1002/lpor.200900055.
(308) Monticone, F.; Argyropoulos, C.; Alu, A. Optical Antennas: Controlling Electromagnetic Scattering, Radiation, and Emission at the Nanoscale. *IEEE Antennas Propag. Mag.* **2017**, *59* (6), 43–61. https://doi.org/10.1109/MAP.2017.2752721.
(309) Itagi, A. V.; Challener, W. A. Optics of Photonic Nanojets. *J. Opt. Soc. Am. A* **2005**, *22* (12), 2847. https://doi.org/10.1364/JOSAA.22.002847.
(310) Tzarouchis, D.; Sihvola, A. Light Scattering by a Dielectric Sphere: Perspectives on the Mie Resonances. *Applied Sciences* **2018**, *8* (2), 184. https://doi.org/10.3390/app8020184.

(311) Shamkhi, H. K.; Sayanskiy, A.; Valero, A. C.; Kupriianov, A. S.; Kapitanova, P.; Kivshar, Y. S.; Shalin, A. S.; Tuz, V. R. Invisibility and Perfect Absorption of All-Dielectric Metasurfaces Originated from the Transverse Kerker Effect. **2019**. https://doi.org/10.48550/ARXIV.1905.10538.

(312) Fu, Y. H.; Kuznetsov, A. I.; Miroshnichenko, A. E.; Yu, Y. F.; Luk'yanchuk, B. Directional Visible Light Scattering by Silicon Nanoparticles. *Nat Commun* **2013**, *4* (1), 1527. https://doi.org/10.1038/ncomms2538.

(313) Alaee, R.; Filter, R.; Lehr, D.; Lederer, F.; Rockstuhl, C. A Generalized Kerker Condition for Highly Directive Nanoantennas. *Opt. Lett.* **2015**, *40* (11), 2645. https://doi.org/10.1364/OL.40.002645.

(314) Achouri, K.; Caloz, C. *Electromagnetic Metasurfaces: Theory and Applications*; Wiley-IEEE Press: Hoboken, NJ, 2021.

(315) Liu, S.; Sinclair, M. B.; Mahony, T. S.; Jun, Y. C.; Campione, S.; Ginn, J.; Bender, D. A.; Wendt, J. R.; Ihlefeld, J. F.; Clem, P. G.; Wright, J. B.; Brener, I. Optical Magnetic Mirrors without Metals. *Optica* **2014**, *1* (4), 250. https://doi.org/10.1364/OPTICA.1.000250.

(316) Chen, H.-T.; Taylor, A. J.; Yu, N. A Review of Metasurfaces: Physics and Applications. *Rep. Prog. Phys.* **2016**, *79* (7), 076401. https://doi.org/10.1088/0034-4885/79/7/076401.

(317) Tribelsky, M. I.; Flach, S.; Miroshnichenko, A. E.; Gorbach, A. V.; Kivshar, Y. S. Light Scattering by a Finite Obstacle and Fano Resonances. *Phys. Rev. Lett.* **2008**, *100* (4), 043903. https://doi.org/10.1103/PhysRevLett.100.043903.

(318) Utyushev, A. D.; Zakomirnyi, V. I.; Rasskazov, I. L. Collective Lattice Resonances: Plasmonics and Beyond. *Reviews in Physics* **2021**, *6*, 100051. https://doi.org/10.1016/j.revip.2021.100051.

(319) Tong, J.; Suo, F.; Tobing, L. Y. M.; Yao, N.; Zhang, D.; Huang, Z.; Zhang, D. H. High Order Magnetic and Electric Resonant Modes of Split Ring Resonator Metasurface Arrays for Strong Enhancement of Mid-Infrared Photodetection. *ACS Appl. Mater. Interfaces* **2020**, *12* (7), 8835–8844. https://doi.org/10.1021/acsami.9b19187.

(320) Bourgeois, M. R.; Rossi, A. W.; Chalifour, M.; Cherqui, C.; Masiello, D. J. Lattice Kerker Effect with Plasmonic Oligomers. *J. Phys. Chem. C* **2021**, *125* (34), 18817–18826. https://doi.org/10.1021/acs.jpcc.1c05024.

(321) Gerasimov, V. S.; Ershov, A. E.; Bikbaev, R. G.; Rasskazov, I. L.; Isaev, I. L.; Semina, P. N.; Kostyukov, A. S.; Zakomirnyi, V. I.; Polyutov, S. P.; Karpov, S. V. Plasmonic Lattice Kerker Effect in Ultraviolet-Visible Spectral Range. *Phys. Rev. B* **2021**, *103* (3), 035402. https://doi.org/10.1103/PhysRevB.103.035402.

(322) Zhou, J.; Panday, A.; Xu, Y.; Chen, X.; Chen, L.; Ji, C.; Guo, L. J. Visualizing Mie Resonances in Low-Index Dielectric Nanoparticles. *Phys. Rev. Lett.* **2018**, *120* (25), 253902. https://doi.org/10.1103/PhysRevLett.120.253902.

(323) Wang, W.; Ma, X. Achieving Extreme Light Confinement in Low-Index Dielectric Resonators through Quasi-Bound States in the Continuum. *Opt. Lett.* **2021**, *46* (24), 6087. https://doi.org/10.1364/OL.445411.

(324) Kuznetsov, A. I.; Miroshnichenko, A. E.; Fu, Y. H.; Zhang, J.; Luk'yanchuk, B. Magnetic Light. *Sci Rep* **2012**, *2* (1), 492. https://doi.org/10.1038/srep00492.

(325) García-Etxarri, A.; Gómez-Medina, R.; Froufe-Pérez, L. S.; López, C.; Chantada, L.; Scheffold, F.; Aizpurua, J.; Nieto-Vesperinas, M.; Sáenz, J. J. Strong Magnetic Response of Submicron Silicon Particles in the Infrared. *Opt. Express* **2011**, *19* (6), 4815. https://doi.org/10.1364/OE.19.004815.

(326) Evlyukhin, A. B.; Novikov, S. M.; Zywietz, U.; Eriksen, R. L.; Reinhardt, C.; Bozhevolnyi, S. I.; Chichkov, B. N. Demonstration of Magnetic Dipole Resonances of Dielectric Nanospheres in the Visible Region. *Nano Lett.* **2012**, *12* (7), 3749–3755. https://doi.org/10.1021/nl301594s.

(327) De Marco, M. L.; Semlali, S.; Korgel, B. A.; Barois, P.; Drisko, G. L.; Aymonier, C. Silicon-Based Dielectric Metamaterials: Focus on the Current Synthetic Challenges. *Angew. Chem. Int. Ed.* **2018**, *57* (17), 4478–4498. https://doi.org/10.1002/anie.201709044.

(328) Yan, J.; Liu, P.; Lin, Z.; Wang, H.; Chen, H.; Wang, C.; Yang, G. Directional Fano Resonance in a Silicon Nanosphere Dimer. *ACS Nano* **2015**, *9* (3), 2968–2980. https://doi.org/10.1021/nn507148z.

(329) Li, C.-Q.; Zhang, C.-Y.; Huang, Z.-S.; Li, X.-F.; Dai, Q.-F.; Lan, S.; Tie, S.-L. Assembling of Silicon Nanoflowers with Significantly Enhanced Second Harmonic Generation Using Silicon Nanospheres Fabricated by Femtosecond Laser Ablation. *J. Phys. Chem. C* **2013**, *117* (46), 24625–24631. https://doi.org/10.1021/jp408865p.

(330) Abderrafi, K.; García Calzada, R.; Gongalsky, M. B.; Suárez, I.; Abarques, R.; Chirvony, V. S.; Timoshenko, V. Yu.; Ibáñez, R.; Martínez-Pastor, J. P. Silicon Nanocrystals Produced by Nanosecond Laser Ablation in an Organic Liquid. *J. Phys. Chem. C* **2011**, *115* (12), 5147–5151. https://doi.org/10.1021/jp109400v.

(331) Zywietz, U.; Evlyukhin, A. B.; Reinhardt, C.; Chichkov, B. N. Laser Printing of Silicon Nanoparticles with Resonant Optical Electric and Magnetic Responses. *Nat Commun* **2014**, *5* (1), 3402. https://doi.org/10.1038/ncomms4402.

(332) Zywietz, U.; Reinhardt, C.; Evlyukhin, A. B.; Birr, T.; Chichkov, B. N. Generation and Patterning of Si Nanoparticles by Femtosecond Laser Pulses. *Appl. Phys. A* **2014**, *114* (1), 45–50. https://doi.org/10.1007/s00339-013-8007-6.

(333) Fenollosa, R.; Meseguer, F.; Tymczenko, M. Silicon Colloids: From Microcavities to Photonic Sponges. *Adv. Mater.* **2008**, *20* (1), 95–98. https://doi.org/10.1002/adma.200701589.

(334) Shi, L.; Tuzer, T. U.; Fenollosa, R.; Meseguer, F. A New Dielectric Metamaterial Building Block with a Strong Magnetic Response in the Sub-1.5-Micrometer Region: Silicon Colloid Nanocavities. *Adv. Mater.* **2012**, *24* (44), 5934–5938. https://doi.org/10.1002/adma.201201987.

(335) Harris, J. T.; Hueso, J. L.; Korgel, B. A. Hydrogenated Amorphous Silicon (a-Si:H) Colloids. *Chem. Mater.* **2010**, *22* (23), 6378–6383. https://doi.org/10.1021/cm102486w.

(336) Chaâbani, W.; Proust, J.; Movsesyan, A.; Béal, J.; Baudrion, A.-L.; Adam, P.-M.; Chehaidar, A.; Plain, J. Large-Scale and Low-Cost Fabrication of Silicon Mie Resonators. *ACS Nano* **2019**, *13* (4), 4199–4208. https://doi.org/10.1021/acsnano.8b09198.

(337) Sugimoto, H.; Fujii, M. Colloidal Dispersion of Subquarter Micrometer Silicon Spheres for Low-Loss Antenna in Visible Regime. *Advanced Optical Materials* **2017**, *5* (17), 1700332. https://doi.org/10.1002/adom.201700332.

(338) Sugimoto, H.; Okazaki, T.; Fujii, M. Mie Resonator Color Inks of Monodispersed and Perfectly Spherical Crystalline Silicon Nanoparticles. *Adv. Optical Mater.* **2020**, *8* (12), 2000033. https://doi.org/10.1002/adom.202000033.

(339) Mangolini, L.; Thimsen, E.; Kortshagen, U. High-Yield Plasma Synthesis of Luminescent Silicon Nanocrystals. *Nano Lett.* **2005**, *5* (4), 655–659. https://doi.org/10.1021/nl050066y.

(340) Gresback, R.; Holman, Z.; Kortshagen, U. Nonthermal Plasma Synthesis of Size-Controlled, Monodisperse, Freestanding Germanium Nanocrystals. *Appl. Phys. Lett.* **2007**, *91* (9), 093119. https://doi.org/10.1063/1.2778356.

(341) Wang, C.; Li, D.; Lu, Z.; Song, M.; Xia, W. Synthesis of Carbon Nanoparticles in a Non-Thermal Plasma Process. *Chemical Engineering Science* **2020**, *227*, 115921. https://doi.org/10.1016/j.ces.2020.115921.

(342) Lin, P. A.; Sankaran, R. M. Plasma-Assisted Dissociation of Organometallic Vapors for Continuous, Gas-Phase Preparation of Multimetallic Nanoparticles. *Angew. Chem. Int. Ed.* **2011**, *50* (46), 10953–10956. https://doi.org/10.1002/anie.201101881.

(343) Kumar, A.; Kang, S.; Larriba-Andaluz, C.; Ouyang, H.; Hogan, C. J.; Sankaran, R. M. Ligand-Free Ni Nanocluster Formation at Atmospheric Pressure via Rapid Quenching in a Microplasma Process. *Nanotechnology* **2014**, *25* (38), 385601. https://doi.org/10.1088/0957-4484/25/38/385601.

(344) Beaudette, C. A.; Andaraarachchi, H. P.; Wu, C.-C.; Kortshagen, U. R. Inductively Coupled Nonthermal Plasma Synthesis of Aluminum Nanoparticles. *Nanotechnology* **2021**, *32* (39), 395601. https://doi.org/10.1088/1361-6528/ac0cb3.

(345) Xu, C.; Andaraarachchi, H. P.; Xiong, Z.; Eslamisaray, M. A.; Kushner, M. J.; Kortshagen, U. R. Size-Tunable Silver Nanoparticle Synthesis in Glycerol Driven by a Low-Pressure Nonthermal Plasma. *J. Phys. D: Appl. Phys.* **2022**, *55* (1), 015201. https://doi.org/10.1088/1361-6463/ac9ce9.

(346) Rowe, D. J.; Kortshagen, U. R. Boron- and Phosphorus-Doped Silicon Germanium Alloy Nanocrystals—Nonthermal Plasma Synthesis and Gas-Phase Thin Film Deposition. *APL Materials* **2014**, *2* (2), 022104. https://doi.org/10.1063/1.4865158.

(347) Coleman, D.; Lopez, T.; Yasar-Inceoglu, O.; Mangolini, L. Hollow Silicon Carbide Nanoparticles from a Non-Thermal Plasma Process. *J. Appl. Phys.* **2015**, *117* (19), 193301. https://doi.org/10.1063/1.4919918.

(348) Greenberg, B. L.; Ganguly, S.; Held, J. T.; Kramer, N. J.; Mkhoyan, K. A.; Aydil, E. S.; Kortshagen, U. R. Nonequilibrium-Plasma-Synthesized ZnO Nanocrystals with Plasmon Resonance Tunable via Al Doping and Quantum Confinement. *Nano Lett.* **2015**, *15* (12), 8162–8169. https://doi.org/10.1021/acs.nanolett.5b03600.

(349) Alvarez Barragan, A.; Ilawe, N. V.; Zhong, L.; Wong, B. M.; Mangolini, L. A Non-Thermal Plasma Route to Plasmonic TiN Nanoparticles. *J. Phys. Chem. C* **2017**, *121* (4), 2316–2322. https://doi.org/10.1021/acs.jpcc.6b08910.

(350) Beaudette, C. A.; Tu, Q.; Ali Eslamisaray, M.; Kortshagen, U. R. Plasma-Synthesized Nitrogen-Doped Titanium Dioxide Nanoparticles With Tunable Visible Light

Absorption and Photocatalytic Activity. *ASME Open Journal of Engineering* **2022**, *1*, 011010. https://doi.org/10.1115/1.4053338.

(351) Yasar-Inceoglu, O.; Lopez, T.; Farshihagro, E.; Mangolini, L. Silicon Nanocrystal Production through Non-Thermal Plasma Synthesis: A Comparative Study between Silicon Tetrachloride and Silane Precursors. *Nanotechnology* **2012**, *23* (25), 255604. https://doi.org/10.1088/0957-4484/23/25/255604.

(352) Mangolini, L.; Kortshagen, U. Plasma-Assisted Synthesis of Silicon Nanocrystal Inks. *Adv. Mater.* **2007**, *19* (18), 2513–2519. https://doi.org/10.1002/adma.200700595.

(353) Li, Z.; Kortshagen, U. R. Aerosol-Phase Synthesis and Processing of Luminescent Silicon Nanocrystals. *Chem. Mater.* **2019**, *31* (20), 8451–8458. https://doi.org/10.1021/acs.chemmater.9b02743.

(354) Firth, P.; Holman, Z. C. Aerosol Impaction-Driven Assembly System for the Production of Uniform Nanoparticle Thin Films with Independently Tunable Thickness and Porosity. *ACS Appl. Nano Mater.* **2018**, *1* (8), 4351–4357. https://doi.org/10.1021/acsanm.8b01334.

(355) Bapat, A.; Anderson, C.; Perrey, C. R.; Carter, C. B.; Campbell, S. A.; Kortshagen, U. Plasma Synthesis of Single-Crystal Silicon Nanoparticles for Novel Electronic Device Applications. *Plasma Phys. Control. Fusion* **2004**, *46* (12B), B97–B109. https://doi.org/10.1088/0741-3335/46/12B/009.

(356) Wray, P. R.; Eslamisaray, M. A.; Nelson, G. M.; Ilic, O.; Kortshagen, U. R.; Atwater, H. A. Broadband, Angle- and Polarization-Invariant Antireflective and Absorbing Films by a Scalable Synthesis of Monodisperse Silicon Nanoparticles. *ACS Appl. Mater. Interfaces* **2022**, *14* (20), 23624–23636. https://doi.org/10.1021/acsami.2c03263.

(357) Kramer, N. J.; Anthony, R. J.; Mamunuru, M.; Aydil, E. S.; Kortshagen, U. R. Plasma-Induced Crystallization of Silicon Nanoparticles. *J. Phys. D: Appl. Phys.* **2014**, *47* (7), 075202. https://doi.org/10.1088/0022-3727/47/7/075202.

(358) Xiong, Z.; Lanham, S.; Husmann, E.; Nelson, G.; Eslamisaray, M. A.; Polito, J.; Liu, Y.; Goree, J.; Thimsen, E.; Kushner, M. J.; Kortshagen, U. R. Particle Trapping, Size-Filtering, and Focusing in the Nonthermal Plasma Synthesis of Sub-10 Nanometer Particles. *J. Phys. D: Appl. Phys.* **2022**, *55* (23), 235202. https://doi.org/10.1088/1361-6463/ac57de.

(359) Ledoux, G.; Guillois, O.; Porterat, D.; Reynaud, C.; Huisken, F.; Kohn, B.; Paillard, V. Photoluminescence Properties of Silicon Nanocrystals as a Function of Their Size. *Phys. Rev. B* **2000**, *62* (23), 15942–15951. https://doi.org/10.1103/PhysRevB.62.15942.

(360) Winters, B. J.; Holm, J.; Roberts, J. T. Thermal Processing and Native Oxidation of Silicon Nanoparticles. *J Nanopart Res* **2011**, *13* (10), 5473–5484. https://doi.org/10.1007/s11051-011-0535-4.

(361) Perrey, C. R.; Carter, C. B. Insights into Nanoparticle Formation Mechanisms. *J Mater Sci* **2006**, *41* (9), 2711–2722. https://doi.org/10.1007/s10853-006-7874-z.

(362) Boisier, G.; Raciulete, M.; Samélor, D.; Pébère, N.; Gleizes, A. N.; Vahlas, C. Electrochemical Behavior of Chemical Vapor Deposited Protective Aluminum Oxide Coatings on Ti6242 Titanium Alloy. *Electrochem. Solid-State Lett.* **2008**, *11* (10), C55. https://doi.org/10.1149/1.2968109.

(363) Samélor, D.; Lazar, A.-M.; Aufray, M.; Tendero, C.; Lacroix, L.; Béguin, J.-D.; Caussat, B.; Vergnes, H.; Alexis, J.; Poquillon, D.; Pébère, N.; Gleizes, A.; Vahlas, C. Amorphous Alumina Coatings: Processing, Structure and Remarkable Barrier Properties. *Journal of Nanoscience and Nanotechnology* **2011**, *11* (9), 8387–8391. https://doi.org/10.1166/jnn.2011.5068.

(364) Avis, C.; Jang, J. High-Performance Solution Processed Oxide TFT with Aluminum Oxide Gate Dielectric Fabricated by a Sol–Gel Method. *J. Mater. Chem.* **2011**, *21* (29), 10649–10652. https://doi.org/10.1039/C1JM12227D.

(365) Amini, G.; Najafpour, G. D.; Rabiee, S. M.; Ghoreyshi, A. A. Synthesis and Characterization of Amorphous Nano-Alumina Powders with High Surface Area for Biodiesel Production. *Chemical Engineering & Technology* **2013**, *36* (10), 1708–1712. https://doi.org/10.1002/ceat.201300102.

(366) Kang, D.; Tong, S.; Yu, X.; Ge, M. Template-Free Synthesis of 3D Hierarchical Amorphous Aluminum Oxide Microspheres with Broccoli-like Structure and Their Application in Fluoride Removal. *RSC Adv.* **2015**, *5* (25), 19159–19165. https://doi.org/10.1039/C4RA13688H.

(367) Li, J.; Pan, Y.; Xiang, C.; Ge, Q.; Guo, J. Low Temperature Synthesis of Ultrafine α-Al2O3 Powder by a Simple Aqueous Sol–Gel Process. *Ceramics International* **2006**, *32* (5), 587–591. https://doi.org/10.1016/j.ceramint.2005.04.015.

(368) Karim, M. R. Synthesis of β-Alumina Particles and Surface Characterization. *TOCOLLSJ* **2011**, *4* (1), 32–36. https://doi.org/10.2174/1876530001104010032.

(369) Laishram, K.; Mann, R.; Malhan, N. A Novel Microwave Combustion Approach for Single Step Synthesis of α-Al2O3 Nanopowders. *Ceramics International* **2012**, *38* (2), 1703–1706. https://doi.org/10.1016/j.ceramint.2011.08.044.

(370) Sathyaseelan, B.; Baskaran, I.; Sivakumar, K. Phase Transition Behavior of Nanocrystalline Al₂O₃ Powders. *SNL* **2013**, *03* (04), 69–74. https://doi.org/10.4236/snl.2013.34012.

(371) Ozuna, O.; Hirata, G. A.; McKittrick, J. Pressure Influenced Combustion Synthesis of γ- and α-Al2O3 Nanocrystalline Powders. *J. Phys.: Condens. Matter* **2004**, *16* (15), 2585. https://doi.org/10.1088/0953-8984/16/15/010.

(372) Toniolo, J. C.; Lima, M. D.; Takimi, A. S.; Bergmann, C. P. Synthesis of Alumina Powders by the Glycine–Nitrate Combustion Process. *Materials Research Bulletin* **2005**, *40* (3), 561–571. https://doi.org/10.1016/j.materresbull.2004.07.019.

(373) Sherikar, B. N.; Sahoo, B.; Umarji, A. M. Effect of Fuel and Fuel to Oxidizer Ratio in Solution Combustion Synthesis of Nanoceramic Powders: MgO, CaO and ZnO. *Solid State Sciences* **2020**, *109*, 106426. https://doi.org/10.1016/j.solidstatesciences.2020.106426.

(374) Su, X.; Chen, S.; Zhou, Z. Synthesis and Characterization of Monodisperse Porous α-Al2O3 Nanoparticles. *Applied Surface Science* **2012**, *258* (15), 5712–5715. https://doi.org/10.1016/j.apsusc.2012.02.067.

(375) Sanamyan, T.; Pavlacka, R.; Gilde, G.; Dubinskii, M. Spectroscopic Properties of Er3+-Doped α-Al2O3. *Optical Materials* **2013**, *35* (5), 821–826. https://doi.org/10.1016/j.optmat.2012.10.036.

(376) Wang, J.; Ge, L.; Li, Z.; Li, L.; Guo, Q.; Li, J. Facile Size-Controlled Synthesis of Well-Dispersed Spherical Amorphous Alumina Nanoparticles via Homogeneous

Precipitation. *Ceramics International* **2016**, *42* (7), 8545–8551. https://doi.org/10.1016/j.ceramint.2016.02.081.

(377) Zhang, W. J.; Wu, X. L.; Fan, J. Y.; Huang, G. S.; Qiu, T.; Chu, P. K. Luminescent Amorphous Alumina Nanoparticles in Toluene Solution. *J. Phys.: Condens. Matter* **2006**, *18* (43), 9937. https://doi.org/10.1088/0953-8984/18/43/015.

(378) Pan, C.; Shen, P.; Chen, S.-Y. Condensation, Crystallization and Coalescence of Amorphous Al2O3 Nanoparticles. *Journal of Crystal Growth* **2007**, *299* (2), 393–398. https://doi.org/10.1016/j.jcrysgro.2006.12.006.

(379) Atrak, K.; Ramazani, A.; Taghavi Fardood, S. Green Synthesis of Amorphous and Gamma Aluminum Oxide Nanoparticles by Tragacanth Gel and Comparison of Their Photocatalytic Activity for the Degradation of Organic Dyes. *J Mater Sci: Mater Electron* **2018**, *29* (10), 8347–8353. https://doi.org/10.1007/s10854-018-8845-2.

(380) Kunath-Fandrei, G.; Bastow, T. J.; Hall, J. S.; Jaeger, C.; Smith, M. E. Quantification of Aluminum Coordinations in Amorphous Aluminas by Combined Central and Satellite Transition Magic Angle Spinning NMR Spectroscopy. *J. Phys. Chem.* **1995**, *99* (41), 15138–15141. https://doi.org/10.1021/j100041a033.

(381) Lamparter, P.; Kniep, R. Structure of Amorphous Al2O3. *Physica B: Condensed Matter* **1997**, *234–236*, 405–406. https://doi.org/10.1016/S0921-4526(96)01044-7.

(382) *Phys. Rev. B 65, 104202 (2002) - Molecular dynamics study of structural properties of amorphous $\mathrm{Al}_2\mathrm{O}_3$.* https://journals.aps.org/prb/abstract/10.1103/PhysRevB.65.104202 (accessed 2023-09-03).

(383) Snijders, P. C.; Jeurgens, L. P. H.; Sloof, W. G. Structural Ordering of Ultra-Thin, Amorphous Aluminium-Oxide Films. *Surface Science* **2005**, *589* (1), 98–105. https://doi.org/10.1016/j.susc.2005.05.051.

(384) Lee, S. K.; Lee, S. B.; Park, S. Y.; Yi, Y. S.; Ahn, C. W. Structure of Amorphous Aluminum Oxide. *Phys. Rev. Lett.* **2009**, *103* (9), 095501. https://doi.org/10.1103/PhysRevLett.103.095501.

(385) Lizárraga, R.; Holmström, E.; Parker, S. C.; Arrouvel, C. Structural Characterization of Amorphous Alumina and Its Polymorphs from First-Principles XPS and NMR Calculations. *Phys. Rev. B* **2011**, *83* (9), 094201. https://doi.org/10.1103/PhysRevB.83.094201.

(386) Stumpf, H. C.; Russell, A. S.; Newsome, J. W.; Tucker, C. M. Thermal Transformations of Aluminas and Alumina Hydrates - Reaction with 44% Technical Acid. *Ind. Eng. Chem.* **1950**, *42* (7), 1398–1403. https://doi.org/10.1021/ie50487a039.

(387) John, C. S.; Alma, N. C. M.; Hays, G. R. Characterization of Transitional Alumina by Solid-State Magic Angle Spinning Aluminium NMR. *Applied Catalysis* **1983**, *6* (3), 341–346. https://doi.org/10.1016/0166-9834(83)80106-7.

(388) Levin, I.; Brandon, D. Metastable Alumina Polymorphs: Crystal Structures and Transition Sequences. *Journal of the American Ceramic Society* **1998**, *81* (8), 1995–2012. https://doi.org/10.1111/j.1151-2916.1998.tb02581.x.

(389) Lippens, B. C.; De Boer, J. H. Study of Phase Transformations during Calcination of Aluminum Hydroxides by Selected Area Electron Diffraction. *Acta Crystallographica* **1964**, *17* (10), 1312–1321. https://doi.org/10.1107/S0365110X64003267.

(390) Morrissey, K. J.; Czanderna, K. K.; Carter, C. B.; Merrill, R. P. Growth of α-Al2O3 Within a Transition Alumina Matrix. *Journal of the American Ceramic Society* **1984**, *67* (5), c88–c90. https://doi.org/10.1111/j.1151-2916.1984.tb19521.x.

(391) Lamouri, S.; Hamidouche, M.; Bouaouadja, N.; Belhouchet, H.; Garnier, V.; Fantozzi, G.; Trelkat, J. F. Control of the γ-Alumina to α-Alumina Phase Transformation for an Optimized Alumina Densification. *Boletín de la Sociedad Española de Cerámica y Vidrio* **2017**, *56* (2), 47–54. https://doi.org/10.1016/j.bsecv.2016.10.001.

(392) Munro, M. Evaluated Material Properties for a Sintered Alpha-Alumina. *Journal of the American Ceramic Society* **1997**, *80* (8), 1919–1928. https://doi.org/10.1111/j.1151-2916.1997.tb03074.x.

(393) Krick, B. A.; Pitenis, A. A.; Harris, K. L.; Junk, C. P.; Sawyer, W. G.; Brown, S. C.; Rosenfeld, H. D.; Kasprzak, D. J.; Johnson, R. S.; Chan, C. D.; Blackman, G. S. Ultralow Wear Fluoropolymer Composites: Nanoscale Functionality from Microscale Fillers. *Tribology International* **2016**, *95*, 245–255. https://doi.org/10.1016/j.triboint.2015.10.002.

(394) Bhattacharyya, S.; Behera, P. S. Synthesis and Characterization of Nano-Sized α-Alumina Powder from Kaolin by Acid Leaching Process. *Applied Clay Science* **2017**, *146*, 286–290. https://doi.org/10.1016/j.clay.2017.06.017.

(395) Maciver, D. S.; Tobin, H. H.; Barth, R. T. Catalytic Aluminas I. Surface Chemistry of Eta and Gamma Alumina. *Journal of Catalysis* **1963**, *2* (6), 485–497. https://doi.org/10.1016/0021-9517(63)90004-6.

(396) Felbier, P.; Yang, J.; Theis, J.; Liptak, R. W.; Wagner, A.; Lorke, A.; Bacher, G.; Kortshagen, U. Highly Luminescent ZnO Quantum Dots Made in a Nonthermal Plasma. *Advanced Functional Materials* **2014**, *24* (14), 1988–1993. https://doi.org/10.1002/adfm.201303449.

(397) Thimsen, E.; Kortshagen, U. R.; Aydil, E. S. Nonthermal Plasma Synthesis of Metal Sulfide Nanocrystals from Metalorganic Vapor and Elemental Sulfur. *J. Phys. D: Appl. Phys.* **2015**, *48* (31), 314004. https://doi.org/10.1088/0022-3727/48/31/314004.

(398) Woodard, A.; Xu, L.; Barragan, A. A.; Nava, G.; Wong, B. M.; Mangolini, L. On the Non-Thermal Plasma Synthesis of Nickel Nanoparticles. *Plasma Processes and Polymers* **2018**, *15* (1), 1700104. https://doi.org/10.1002/ppap.201700104.

(399) Tavakoli, A. H.; Maram, P. S.; Widgeon, S. J.; Rufner, J.; van Benthem, K.; Ushakov, S.; Sen, S.; Navrotsky, A. Amorphous Alumina Nanoparticles: Structure, Surface Energy, and Thermodynamic Phase Stability. *J. Phys. Chem. C* **2013**, *117* (33), 17123–17130. https://doi.org/10.1021/jp405820g.

(400) Catherine, Y.; Talebian, A. Plasma Deposition of Aluminum Oxide Films. *JEM* **1988**, *17* (2), 127–134. https://doi.org/10.1007/BF02652142.

(401) Kuech, T. F.; Veuhoff, E.; Kuan, T. S.; Deline, V.; Potemski, R. The Influence of Growth Chemistry on the MOVPE Growth of GaAs and AlxGa1−xAs Layers and Heterostructures. *Journal of Crystal Growth* **1986**, *77* (1), 257–271. https://doi.org/10.1016/0022-0248(86)90310-6.

(402) Kobayashi, N.; Makimoto, T. Reduced Carbon Contamination in OMVPE Grown GaAs and AlGaAs. *Jpn. J. Appl. Phys.* **1985**, *24* (10A), L824. https://doi.org/10.1143/JJAP.24.L824.

(403) Paparazzo, E. XPS Analysis of Iron Aluminum Oxide Systems. *Applied Surface Science* **1986**, *25* (1), 1–12. https://doi.org/10.1016/0169-4332(86)90021-8.
(404) van den Brand, J.; Snijders, P. C.; Sloof, W. G.; Terryn, H.; de Wit, J. H. W. Acid−Base Characterization of Aluminum Oxide Surfaces with XPS. *J. Phys. Chem. B* **2004**, *108* (19), 6017–6024. https://doi.org/10.1021/jp037877f.
(405) McCafferty, E.; Wightman, J. P. Determination of the Concentration of Surface Hydroxyl Groups on Metal Oxide Films by a Quantitative XPS Method. *Surface and Interface Analysis* **1998**, *26* (8), 549–564. https://doi.org/10.1002/(SICI)1096-9918(199807)26:8<549::AID-SIA396>3.0.CO;2-Q.
(406) van den Brand, J.; Sloof, W. G.; Terryn, H.; de Wit, J. H. W. Correlation between Hydroxyl Fraction and O/Al Atomic Ratio as Determined from XPS Spectra of Aluminium Oxide Layers. *Surface and Interface Analysis* **2004**, *36* (1), 81–88. https://doi.org/10.1002/sia.1653.
(407) Zagrajczuk, B.; Dziadek, M.; Olejniczak, Z.; Sulikowski, B.; Cholewa-Kowalska, K.; Laczka, M. Structural Investigation of Gel-Derived Materials from the SiO2Al2O3 System. *Journal of Molecular Structure* **2018**, *1167*, 23–32. https://doi.org/10.1016/j.molstruc.2018.04.085.
(408) Boumaza, A.; Favaro, L.; Lédion, J.; Sattonnay, G.; Brubach, J. B.; Berthet, P.; Huntz, A. M.; Roy, P.; Tétot, R. Transition Alumina Phases Induced by Heat Treatment of Boehmite: An X-Ray Diffraction and Infrared Spectroscopy Study. *Journal of Solid State Chemistry* **2009**, *182* (5), 1171–1176. https://doi.org/10.1016/j.jssc.2009.02.006.
(409) Liang, D. Generalized Ellipsometry Analysis of Anisotropic Nanoporous Media: Polymer-Infiltrated Nanocolumnar and Inverse-Column Polymeric Films. 121.
(410) Schmidt, D.; Schubert, E.; Schubert, M. Generalized Ellipsometry Determination of Non-Reciprocity in Chiral Silicon Sculptured Thin Films. *physica status solidi (a)* **2008**, *205* (4), 748–751. https://doi.org/10.1002/pssa.200777906.
(411) Chang, P.-L.; Yen, F.-S.; Cheng, K.-C.; Wen, H.-L. Examinations on the Critical and Primary Crystallite Sizes during θ- to α-Phase Transformation of Ultrafine Alumina Powders. *Nano Lett.* **2001**, *1* (5), 253–261. https://doi.org/10.1021/nl015501c.
(412) Pekonen, O.; Kärkkäinen, K.; Sihvola, A.; Nikoskinen, K. Numerical Testing of Dielectric Mixing Rules By Fdtd Method. *Journal of Electromagnetic Waves and Applications* **1999**, *13* (1), 67–87. https://doi.org/10.1163/156939399X01618.
(413) Wäckelgård, E. The Experimental Dielectric Function of Porous Anodic Alumina in the Infrared Region; a Comparison with the Maxwell-Garnett Model. *Journal of Physics: Condensed Matter* **1996**, *8* (23), 4289–4299. https://doi.org/10.1088/0953-8984/8/23/019.
(414) Wormeester, H.; Kooij, E. S.; Poelsema, B. Effective Dielectric Response of Nanostructured Layers. *phys. stat. sol. (a)* **2008**, *205* (4), 756–763. https://doi.org/10.1002/pssa.200777740.
(415) Daugherty, J. E.; Graves, D. B. Particulate Temperature in Radio Frequency Glow Discharges. *Journal of Vacuum Science & Technology A* **1993**, *11* (4), 1126–1131. https://doi.org/10.1116/1.578452.
(416) *Phys. Rev. E 79, 026405 (2009) - Selective nanoparticle heating: Another form of nonequilibrium in dusty plasmas*. https://journals.aps.org/pre/abstract/10.1103/PhysRevE.79.026405 (accessed 2023-09-03).

(417) McCallum, J. C.; Simpson, T. W.; Mitchell, I. V. Time Resolved Reflectivity Measurements of the Amorphous-to-Gamma and Gamma-to-Alpha Phase Transitions in Ion-Implanted Al2O3. *Nuclear Instruments and Methods in Physics Research Section B: Beam Interactions with Materials and Atoms* **1994**, *91* (1), 60–62. https://doi.org/10.1016/0168-583X(94)96190-5.

(418) Simpson, T. W.; Wen, Q.; Yu, N.; Clarke, D. R. Kinetics of the Amorphous →γ→α Transformations in Aluminum Oxide: Effect of Crystallographic Orientation. *Journal of the American Ceramic Society* **1998**, *81* (1), 61–66. https://doi.org/10.1111/j.1151-2916.1998.tb02296.x.

(419) Eklund, P.; Sridharan, M.; Singh, G.; Bøttiger, J. Thermal Stability and Phase Transformations of γ-/Amorphous-Al2O3 Thin Films. *Plasma Processes and Polymers* **2009**, *6* (S1), S907–S911. https://doi.org/10.1002/ppap.200932301.

(420) Nakamura, R.; Shudo, T.; Hirata, A.; Ishimaru, M.; Nakajima, H. Nanovoid Formation through the Annealing of Amorphous Al2O3 and WO3 Films. *Scripta Materialia* **2011**, *64* (2), 197–200. https://doi.org/10.1016/j.scriptamat.2010.09.043.

(421) *Enhancement of nanovoid formation in annealed amorphous Al2O3 including W | Journal of Applied Physics | AIP Publishing*. https://pubs.aip.org/aip/jap/article-abstract/110/6/064324/151113/Enhancement-of-nanovoid-formation-in-annealed?redirectedFrom=fulltext (accessed 2023-09-03).

(422) Diouf, S.; Molinari, A. Densification Mechanisms in Spark Plasma Sintering: Effect of Particle Size and Pressure. *Powder Technology* **2012**, *221*, 220–227. https://doi.org/10.1016/j.powtec.2012.01.005.

(423) Kim, B.-C.; Lee, J.-H.; Kim, J.-J.; Ikegami, T. Rapid Rate Sintering of Nanocrystalline Indium Tin Oxide Ceramics: Particle Size Effect. *Materials Letters* **2002**, *52* (1), 114–119. https://doi.org/10.1016/S0167-577X(01)00377-9.

(424) Szymanski, S. F.; Seman, M. T.; Wolden, C. A. Effect of Wall Conditions on the Self-Limiting Deposition of Metal Oxides by Pulsed Plasma-Enhanced Chemical Vapor Deposition. *Journal of Vacuum Science & Technology A* **2007**, *25* (6), 1493–1499. https://doi.org/10.1116/1.2779039.

(425) Nguyen, H. M. T.; Tang, H.-Y.; Huang, W.-F.; Lin, M. C. Mechanisms for Reactions of Trimethylaluminum with Molecular Oxygen and Water. *Computational and Theoretical Chemistry* **2014**, *1035*, 39–43. https://doi.org/10.1016/j.comptc.2014.02.015.

(426) Liu, C.; Shih, K.; Gao, Y.; Li, F.; Wei, L. Dechlorinating Transformation of Propachlor through Nucleophilic Substitution by Dithionite on the Surface of Alumina. *Journal of Soils and Sediments* **2012**, *12* (5), 724–733. https://doi.org/10.1007/s11368-012-0506-0.

Appendix A

TIPS FOR THE NEXT GENERATION

"It is called research because people searched and did not find. So, we re – search."

– Ray T. Chen, 2015

The successful works in this dissertation are the fruit of years of failed endeavors, code bugs, and conceptual mistakes. This section highlights some main learning moments that may be useful to transfer to the next generation of "re – searchers."

The radiative cooling paper, discussed in Chapter 6 accompanies unpublished preliminary experimental measurements. These measurements were performed to validate that the traditional effective medium models discussed in Chapter 6 are acceptable models to describe the physical system. The measurement procedure is shown in figure A1. As discussed in Chapter 8, extracting optical parameters in this thesis is done by implicit methods. Specifically, thin film and effective medium models are run and the inputs are tuned until the best match is found with experimental reflection, transmission, and absorption data. Again, as discussed in depth in Chapter 8, it is critical to constrain as much as possible the range of the independent variables that go into your models. This requires the use of multiple measurement tools, that each come with their own experimental nonidealities and uncertainty. Furthermore, transitioning between measurement tools introduces other inherent errors.

- **The optical spot does not measure the same area between reflection, transmission, and absorption measurements. My film shows a spectrum that is not physical!**

I found that semi-transparent substrates were a great solution to this problem. For example, silicon substrates can be used in the infrared region. Prior to this solution, I had one sample for reflection and one for transmission. Though this can maximize the signal-to-noise ratio of for each measurement, it is a complete and unreliable headache! Thickness, filling fraction, spatial uniformity, and material quality often change between samples. This is particularly true of random films deposited using reactors that are not of industry standards. Using semi-transparent substrates, I could often do reflection and transmission measurements without ever unmounting the sample. When the sample did need to be unmounted, clear markers can be made.

This method will reduce the signal-to-noise ratio (SNR) for each measurement. This is a very easy problem to solve. Just average more. In the visible spectra, I would average measurements for a couple of hours. In the infrared, I would average continually for upwards of a week (~7 days).

- **How to maximize the SNR with semi-transparent samples.**

Model the measurement and the sample to find optimal conditions!

I would start with the thin-film equations and permute parameters until I reached the maximal (theoretical) signal strengths. I would then request this sample from the collaborators. This requires a deep understanding of what the measurement tool is actually measuring. The great part about modeling your measurement is that you learn much more about the measurement.

For example, ellipsometry works best near Brewster's angle. If you suspect that the Bruggeman model is likely to work, use this to vary film thickness, filling fraction, and substrate material to maximize the difference between s- and p-polarization. I simultaneously optimized SNR for all proposed measurements and found used the sample parameters that was the overall best. I was then very demanding on the film sample quality from my collaborators…. I thank Dr. Himashi deeply for putting up with this.

- **Infrared ellipsometry takes forever and my sample wasn't even good. How do I prevent this?**

Start with normal incidence FTIR. Much can be learned from this alone. Only do infrared ellipsometry as an absolute last step before any destructive techniques.

- **The particles are like fluffy soot. They easily wipe off the substrate!**

You can easily ruin a dusty plasma particle sample. First, have the collaborators deposit on substrates with wide margins. Second, use multiple layers of tape on the edges of the sample. This creates a thickness barrier on the edges of the sample to prevent brushing/scratching when measuring.

Use the ability to wipe to your advantage! I use a razor blade to scrape off all but a region of the most uniform area that is proportional to the spot size. This helps to ensure measurements of

the same area. If you are substantially off center, you will know. You measure notably less particles.

- **Use double polished wafers.**

To be honest, this may be a superstition on my part. Usually, you want to roughen the back side of a wafer to outcouple Fresnel reflections within the substrate. For random particle films, this roughness may be on the order of the thickness of the random film or one of the film layers. Additional incoherent Fresnel reflections from a double side polished substrate is easy to model. A backside layer looking like a secondary random film may not be.

- **Spend 80 – 90% of your time measuring gold standards.**

The number 1 novice mistake is turning on a measurement device and directly measuring your sample. Do not do this. Many bad measurements look like feasible measurements. Many bad measurements even look like good results.

A good measurement is 80 – 90% of your time measuring gold standards. Tune the optics, check lamp power, validate reproducible results, et cetera. Practice the procedure to remind your muscles of the motions so the entire process flows naturally. This may feel like a waste of time. It is not. The novice will try to measure directly in the hope of saving time. They will then spend the next 3 weeks trying to understand the "weirdness" in their measurement. At best they spend the entire day trying to figure out what went wrong. Just go ahead and dedicate the entire day to a single measurement up front. Make round 4+ hours or more dedicated to measuring references, processing the data, and ensuring a good match. (I automated the data processing part for this reason.)

- **Making high quality SiO2 and Si3N4 nanoparticle films**

Much work has gone into making silicon dioxide and silicon nitride particle films with minimal solar abortion and strong infrared absorption. The majority of details in this regard should be addressed by Dr. Himashi Adaraarachchi, who fabricated the particles. Magel Su also took over the experiments of this project form me. He may have additional knowledge. The primary lesson we learned is that we were extensively unsuccessful in developing high quality films by deposition silicon nanoparticles then annealing in an oxygen or nitrogen environment. Attached are examples of the annealing results. After some time, Dr. Himashi Adaraarachchi concluded the best approach was to synthesize the particle directly in the plasma chamber. A

primary reason for this is that the underlying layer system could not withstand the annealing process. This may not preclude the use of annealing altogether. But it introduces complications with any underlying fabrication post deposition of particles.

It should be noted that high quality silicon nitride nanoparticle films turned out to be a quite hard endeavor for our collaborators. The silicon nitride properties would vary often between samples under similar deposition conditions.

Figure A1. Example of silicon nanoparticles deposited on an Ag substrate and annealed at 800C for 1 hour.

Below is a miscellaneous list of common problems I encountered when developing and using electromagnetic models.

- **Parallelization and distributed computing are not panaceas.**

I was thoroughly impressed with the speed and memory improvements that can be obtained by optimizing sequential portions of code. In particular, I could achieve on the order of 100 – 1000x speed improvements before ever adding an additional processor! In truth, most code is poorly written for computational performance. For example, your Python code may rely heavily on nested for loops, even though Python is well known for being notoriously slow for such a task. In this case, vectorization or custom submodules written in C could improve your code's performance well beyond the number of cores you have available! Furthermore, this benefit comes with none of the additional complexity inherent to parallelization. In summary, do not just throw cores at the problem…

In many cases, effective parallelization is not as simple as writing sequential code, then implementing this on multiple workers. Proper parallelization is its own subject of study and should be accounted for at the beginning of algorithm design. Below is a list of questions you should answer before writing a parallel program,

- What is the expected improvement?
  I have wasted valuable time parallelizing code with little speed benefits and ballooning complexity. Look before you leap. Some programs are embarrassingly parallel, meaning the entire computational scheme is parallelizable. Finite-difference time-domain is an example of such a scheme. Though, this is not the common scenario. A quick method to determine if parallelization is worth your time is to do a back of the napkin calculation using Amdahl's Law. This states that the computational benefit of parallelizing your code is $1/(f + \frac{1-f}{n})$, were f is the fraction of the code that is strictly sequential and n is the number of available processors. This formula is assumes no computational overhead. More generally, the computation time for parallelized code is

  $$T_{parallel} = S(x) + \frac{P(x)}{n} + C(x, n),$$

  where x is the size of the problem, S is the portion of the code that is strictly sequential, P is the portion that can be parallized, and C is the communication overhead as a result of parallelization.

- How granular should I be and does this require load balancing?
  Parallelization requires overhead. Deciding on the granularity is important. Work must be distributed in appropriately sized chunks. If the chunks are too granular, the overhead of parallelization becomes the computational bottleneck. Correspondingly, load balancing is important. If the chunks are not properly distributed, the code is as slow as the slowest chunk. More sophisticated protocols can be used to poll workers and dynamically load balance. Clearly, this comes at an increased overhead cost, but is great for tasks with variable demands. In my own projects, I found load balancing was critical in distributed computing. DASK was a great software in this regard.

- How will memory management affect results?
  If is important to ask if the workers operate on shared or independent memory. This has implications on both communication overhead and synchronization. Memory allocation/deallocation can necessitate synchronization between workers depending on how the code is written. Python uses garbage collection to manage memory automatically. Though this is good for fast prototyping, it can create a headache for parallelization. An important consequence is the global interpreter lock (GIL). I

recommend reading more about the GIL. In particular you should read how the GIL limits multithreading.

- Should I use OpenMP or MPI?
  A message passing interface (MPI) enables the control of both data distribution and process synchronization, across both single and multiple nodes.

For example, parallelization requires overhead. Deciding on the granularity is important. Work must be distributed in appropriately sized chunks. If the chunks are too granular, the overhead of parallelization becomes the computational bottleneck. Correspondingly, load balancing is important. If the chunks are not properly distributed, the code is as slow as the slowest chunk. More sophisticated protocols can be used to poll workers and dynamically load balance. Clearly, this comes at an increased overhead cost, but is great for tasks with variable demands. In my own projects, I found load balancing was critical in distributed computing. DASK was a great software in this regard. Memory allocation is also a critical (and perhaps subtle) aspect of parallelization, especially for Python programs. Memory allocation/deallocation can necessitate synchronization between workers depending on how the code is written. Python uses garbage collection to manage memory automatically. Though this is good for fast prototyping, it can create a headache for parallelization. An important consequence is the global interpreter lock (GIL). I recommend reading more about the GIL. In particular you should read how the GIL limits multithreading.

- **Profile your code!**

Code is as slow as its slowest part. Focus on that. I was initially unaware of how long it took to calculate Clebsch-Gordon coefficients. Correspondingly, I spent a long time optimizing the wrong sections of code.

- **Avoid numerical integration whenever you can.**

The problem with numerical integration of continuous variables is that the dimension is in principle infinite. Sharp features and/or high frequency oscillations can quickly become a computation and memory bottleneck. Nonlinear sampling may be needed.

Whenever you are faced with a numerical integration, check if someone has mapped the solution of that integral into an equivalent series or recursive solution. If so, it is entirely possible they did

this for computational reasons. Check the research papers. It is likely worth your effort to implement. The series to solve may look scary and ugly. Recursion may feel abstract to you. That is ok.

- **Follow coding standards and protocols.**

Many (especially Ph.D. students) learn programing on the job. The resulting code is practical, but often not best practice. Standards and protocols are vital for keeping order, especially in a large open-source environment.

"A universal convention supplies all of maintainability, clarity, consistency, and a foundation for good programming habits too. What it doesn't do is insist that you follow it against your will. That's Python!"

- Tim Peters on comp.lang.python, 2001-06-16

Even if you do not plan to share your code openly, you will still greatly benefit by conforming to standards as it will prevent you from dealing with a huge list of code bugs. The Python Enhancement Protocols (https://peps.python.org/pep-0000/) are the gold-standard for writing acceptable Python code. In particular PEP 8 defines the style guide for python code. If you are combining C and Python, when you will benefit greatly by following the PEP 7 standards. PEP 257 defines the standard for code documentation. Code is read much more often than it is written. Document your code! Most compilers can generate shell docstrings automatically.